UNIVERSITAT DE BARCELONA

Hydrogel co-networks of gelatin methacryloyl and poly(ethylene glycol)diacrylate sustain 3D functional *in vitro* models of intestinal mucosa

Anna Vila Giraut

Tesi doctoral

Hydrogel co-networks of gelatin methacryloyl and poly(ethylene glycol)diacrylate sustain 3D functional *in vitro* models of intestinal mucosa

Autora:
ANNA VILA GIRAUT

Directora:
Prof. Elena Martínez Fraiz

UNIVERSITAT DE BARCELONA

Hydrogel co-networks of gelatin methacryloyl and poly(ethylene glycol)diacrylate sustain 3D functional *in vitro* models of intestinal mucosa

Memòria presentada per optar al grau de doctor per la Universitat de Barcelona

Programa de doctorat en **Nanociències**

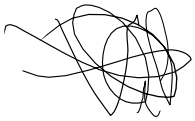

Autora: **ANNA VILA GIRAUT**

Directora:
Prof. Elena Martínez Fraiz

Tutor:
Prof. Josep Samitier Martí

Institut de Bioenginyeria de Catalunya

UNIVERSITAT DE BARCELONA

«Defensa el teu dret a pensar, perquè inclús pensar de forma errònia és millor que no pensar.»

Hipàtia de Alexandria (segle IV)

Filòsofa i matemàtica

Acknowledgements

Després d'escriure la tesi doctoral i donar gairebé per finalitzat un període molt important de la meva vida m'adono que tot això no hagués estat possible sense totes les persones que m'han estat recolzant durant aquest quatre anys de la tesi o cinc si comptem el màster. Durant aquesta etapa hi ha hagut moments de tots colors, a part d'alegries, riures i anècdotes que m'enduré i sempre les recordaré, també m'he hagut d'afrontar a reptes i passar situacions que mai hauria superat si no fos per totes les persones tant extraordinàries que m'han envoltat. És gràcies a elles que no he defallit al llarg d'aquest temps, i ara després d'aquest quatre anys tant intensos puc per fi escriure la tesi. Per altra banda i molt rellevant des del meu punt de vista és que gràcies a elles que he crescut a nivell personal. He passat de ser una "cria" quan vaig començar la tesi on hem pensava que em menjaria el món (suposo com a molts ens passa quan entrem en aquest àmbit) a esdevenir una dona amb una visió i opinió més crítica i objectiva. Degut a tots els motius anteriors, són moltes les persones a qui m'agradaria agrair el seu ajut incondicional. Tot i que serà un repte i intentaré no oblidar-me a ningú, en les següents línies voldria transmetre la meva gratitud... si no ho sé reflectir del tot si us plau, perdoneu-me.

En primer lloc, vull dirigir aquestes paraules d'agraïment a la meva directora de tesi, la Dra. Elena Martínez, per la seva dedicació i el seu esforç incondicional durant aquesta etapa. Elena, merci, per donar-me l'oportunitat de realitzar la tesi doctoral al teu costat. Moltes gràcies per tota l'ajuda, consells i guiatge al llarg d'aquests anys i per tot els coneixements i valors que m'has transmès. I sobretot moltes gràcies per la paciència que has tingut i per totes aquelles paraules reconfortants, tranquil·litzadores i encoratjadores i de sentit comú que m'has dit quan he entrat desesperada i plorant al teu despatx. Gràcies per no deixar-me defallir en els moments més difícils i per saber que sempre es pot comptar amb el teu ajut. En segon lloc, vull agrair al meu tutor, el Prof. Josep Samitier, que hagi pogut acomplir la tesi en unes instal·lacions excepcionals i sota un bon equip tècnic, així és més fàcil superar els reptes que la ciència ens posa. Moltes gràcies per l'oportunitat.

A continuació, voldria continuar els agraïments amb els quatre estudiants de doctorat, Albert, Maria, Vero i Gizem que formaven el laboratori, *Biomimetics,* quan vaig començar a entrar al món científic durant el màster. Albert, moltes gràcies, per endinsar-me en el món científic, per ensenyar-me a com fer un experiment, a com desenvolupar-me pel laboratori. Per tots els coneixements transmesos i per la teva capacitat motivadora i entusiasta que sempre has demostrat i que van ser un dels principals motius

que em van animar afrontar el repte de desenvolupar un doctorat. Per altra banda, Maria, Vero i Gizem, gràcies també per estar durant la meva primera etapa com a científica i fer-la passar més amena a base de bromes, riures i consells, sobretot en la sala dels cafès a mitja tarda durant els berenars.

Amb molt poc temps el grup *Biomimetics* va créixer exponencialment, de quatre estudiant de doctorat, va passat a ser un laboratori format per postdocs, tècnics, predocs, estudiants de màster i/o de grau. Núria, crec que mai et podré agrair tot lo que m'has aportat, la teva ajuda tant científica com personal ha estat un fort recolzament des del principi. Aquesta tesi no l'hagués pogut acabar si no hagués estat per tu, has estat sempre al meu constat i sobretot en els moments més difícils, que com ja he dit no han estat pocs. Gràcies de tot cor per tota la paciència i sobretot per suportar les meves "anades d'olla" he aprés molt de tu a nivell professional, científic, però sobretot m'ha enriquit moltíssim a nivell personal; gràcies per tota l'ajuda, consells i sobretot el temps invertit en la sala blanca. Vane gràcies per reforçar els pocs coneixements de cultiu cel·lular que tenia, per transmetre la teva passió i vocació envers a la ciència a la gent que t'envolta i sobretot per dir-me les coses de forma crítica, objectiva i sincera quan era necessari. María muchas gracias por lo que me has enseñado en el laboratorio, tus consejos sobre las Caco-2, como cortar los pilares etc y también gracias por todos los ánimos durante estos años. Gracias a Raquel que estaba sentada en el escritorio de detrás de mío y me animaba todos los días ya que siempre venida con una sonrisa. Encara que siguis l'únic postdoc noi del laboratori, en més motiu no em puc oblidar-me tu. Jordi, gràcies per les converses filosòfiques i pels teus consells envers la tesi i com afrontar-la i sobretot per tota la calma que aportes sempre mostrant-te tant tranquil i sense cap angoixa, no sé si es cosa dels físics o és el teu caràcter..., però parlar amb tu em feia reflexionar sobre la vida. Enara aunque empezamos juntas este camino y nos fuimos de congreso juntas no hemos colaborado mucho a nivel científico ya que los temas eran bastante distantes, pero sé que siempre he podido y podré contar contigo a nivel personal. Gracias por tu sonrisa y tu dulzura, no solo a nivel de comida y chocolates, la cual está enmascarada en una coraza punk, nunca lo hubiera dicho a primera vista. Malgrat només em compartit dos anyets, Aina moltes gràcies ja que has aportat molt valor al laboratori, amb el teu bon humor ens has fet riure i l'has animat, li has donat "virilla". Per cert, et vull agrair totes les correccions gramaticals i ortogràfiques en les presentacions, que han contribuït a que no fes el ridícul. També vull agrair a tots els membres de *Biomimetics* que han entrat en els últims mesos per contribuir en el creixement aquest projecte i en crear un bon caliu de treball dins del laboratori. Moltes

gràcies Jon, Vero, Livia, Angela i Eduardo. Per acabar m'agradaria donar les gràcies a als estudiants de pràctiques, els quals m'han donat l'oportunitat de poder ensenyar.

Tot seguit vull mostrar el meu sincer agraïment a *Los Ramones* per tots aquells lab meetings conjunts on les vostres contribucions i opinions relacionades amb la GelMA i la seva caracterització han estat molt valuoses. També mil gràcies a tots per fer-me sentir com una més del lab quan venia acaparar el vostre microscopi per fer fotos de les mostres, algunes de les quals han estat essencials per poder realitzar la tesi. O fins i tot quan us venia a demanar algun reactiu que sempre em rebíeu amb un somriure i amb els braços oberts, ha estat un plaer poder compartir petits moments amb vosaltres. També m'agradaria donar les gràcies a *Nanobio* per la seva ajuda essencial i desinteressada, per poder acudir a ells quan ho necessitava i sempre rebre'm amb les mans obertes. Gràcies, Anna pels consells en química i amb NMR i sobretot pel teu bon humor. Així com a la Clara, Joan, Miriam, Albert i Maider per les vostres valuoses aportacions. Finalment cal donar les gràcies aquelles persones que els he conegut en l'últim període de la tesi ja que han tingut un rol essencial per poder finalitzar-la. Moltes gràcies Loris per les discussions científiques i els comentaris i a la Claudia por su imprescindible ayuda, por su interés en mis progresos y motivación y sobre todo por las conversaciones tanto científicas como no científicas en la office de la tercera planta.

No em vull oblidar de totes aquelles persones que formen part del IBEC i que estan allà, dia a dia, per fer que la feina sigui més fàcil i amena. Gràcies a Core Facilites, Isa, Ramona, Laura, Imma, Sandra, Tania, Tere, Judit, Marina i Alicia, per resoldre tots els dubtes tècnics i de funcionament dels equips, per canviar el filtre del Mask Aligner, tot això i més ha fet que la feina fos més àgil. Voldria ressaltar en David, que et vaig conèixer com a tècnic de *Nanobio* i ara formes part de la plataforma de Core Facilites, però des de bon principi sempre t'has preocupat per nosaltres preguntant-nos en tot moment com portaven la tesi i donant-nos molts ànims per seguir endavant. Per acabar amb la comunitat del IBEC ressaltar el paper fonamental que ha tingut el departament de comunicació en la meva carrera professional, gràcies per brindar-me l'oportunitat d'impartir workshops a escoles i instituts, ha estat una experiència meravellosa. Finalment, una persona que és mereix totes les gràcies del món i més pel seu carisma, el seu bon humor, la seva alegria, el seu positivisme i altres mil coses més és l'Antonia, que té un paper invisible però indispensable, que faríem sense tu ni sense la teva alegria que transmets als passadissos del IBEC amb el *carrito* del material.

I don't want to end without thanking Dr. Amir Ghaemmaghami for the opportunity that he gave me to do an internship in his laboratory, which was essential for finishing the thesis, as well as to make me feel as another member of his team. I also need to mention the unconditional support of Edi, the postdoc who accompanied me during these four months Thank you for being in the most difficult times, for listening to me and for worrying about me when the things don't go as I expected, and, for all the scientific knowledge that you share with me. I don't want to forget my office collage Lisa, which apart of helped me a lot on improving my knowledge about immune cells and ELISAs, she was there for listening all my complaints related with sciences and life. Her cheerful and optimistic character made me go forward with positivism every day. I don't want to forget the others members of the lab Arsalan, Mitchell, Matthew and Karen. Thanks you for sharing with me the coffee breaks, which were essential to distracted me out of the lab, and for the non-scientific experiences such as the bowling day, the fencing trial or the virtual reality game.

Tanmateix a la vida no tot és feina, durant aquest quatre anys també han estat allà els amics que sempre porten felicitat. Per això vull agrair a en Joan, l'Ainara, l'Edurne, en Salvador i la Carla per fer-me esvair de la ciència. I en especial a en Marcos per totes les *xapes* i queixes que t'he donat al llarg d'aquests anys i que no han estat poques i les has escoltat amb calma i tranquil·litat.

Ara si que per acabar, el meus més sincers agraïments van dirigits a la meva família pel seu suport incondicional. Gràcies a la meva germana i la meva mare i al meu pare, tot i que som una família de poques paraules i no parlem molt, sé que encara que m'equivoqui i caigui tres, quatre cops a la mateixa pedra estareu al meu costat per ajudar-me aixecar tots els cops que faci falta. M'agradaria acabar aquestes últimes paraules donant-li les gràcies a la meva padrina del Pla per cuidar-me quan era petita i ensenyar-me tots els valors de la vida, mai no hagués pogut esdevenir la dona que sóc ara, sense tot l'amor que em va donar.

Table of contents

I. Abstract

Conventional *in vitro* cell culture models do not possess the complexity that the native tissues offer. Because of this, the functional properties of the tissues are not properly mimicked, which causes poorly predictive capabilities. Engineered tissues, which combine biofabrication and tissue engineering techniques, try to overcome this gap by providing the cells with an environment similar to the native tissue, recapitulating (I) the physicochemical and mechanical properties of the cellular matrix, (II) the multicellular complexity of the different tissue compartments, and (III) the 3D structures of the tissues. These new engineered models are key factors to improve the platforms for basic research studies, testing new drugs or modelling diseases. Among all the engineered tissues, the intestinal mucosa is not well represented. The intestinal mucosa is formed by the epithelium, which is a multicellular monolayer laying on top of the lamina propria, a connective tissue containing several cell types (mesenchymal cells, immune cells). The gold standard intestinal models are based on epithelial cell lines derived from colon cancer cells grown on the hard porous membranes of the Transwell® inserts. The lack of the intestinal stromal compartment and the growth on a hard surface give high transepithelial electrical resistance and low apparent permeability. Therefore, the development of better *in vitro* platforms, which integrates both compartments and provides epithelium-lamina propria cell interactions, is highly desirable.

In this work, we describe an easy and cost-effective method to engineer a 3D intestinal mucosa model that combines both the epithelium and the lamina propria compartments. To build the 3D scaffolds we chose hydrogels as materials to mimic the physicochemical and mechanical properties of intestinal tissue. Thus, hydrogel co-networks of gelatin methacryolyl (GelMA), a natural polymer, and poly(ethylene glycol) diacrylate (PEGDA), a synthetic polymer, are photopolymerized. On one hand, GelMA provides biodegradation and cell adhesion sequences but it lacks long-term mechanical stability. On the other hand, PEGDA, is non-biodegradable and does not present cell adhesion motifs. Nevertheless, it has good mechanical properties. By this technique, the lamina propria compartment of the intestinal mucosa can be reproduced *in vitro.* To do that, GelMA and PEGDA polymers are laden with mesenchymal cells (fibroblasts or myofibroblasts) and/or immune cells (macrophages). We demonstrated that GelMA – PEGDA hydrogel co-networks support the growth of these cells and epithelial monolayers on top of the scaffolds. Embedding fibroblasts or myofibroblasts on the hydrogel co-networks enhance the formation and the maturity of the Caco-2 epithelial monolayers, providing barrier properties similar to *in vivo*. The presence of the stromal cells, also enhances the recovery of the epithelial integrity when the epithelium is temporally

damaged. Finally, an immunocompetent model is obtained by the encapsulation of macrophages in the constructs. The presence of macrophages does not influence the formation of the epithelium. However, when the epithelial monolayer is disrupted, the presence of mesenchymal and immune cells in the stromal compartment increases cytokine secretion in a synergistic manner. Our model can successfully mimic the interactions between stromal and epithelial compartments found *in vivo* intestinal tissue, offering a potential platform to be used to study absorption and toxicity of drugs, as well as cell behaviour under physiological and pathological conditions.

II. Abbreviations

2D	Two dimensional
3D	Three dimensional
AFM	Atomic force microscopy
APS	Ammonium persulfate
ATR	Attenuated total reflectance
A.U.	Arbitrary unit
B cells	Lymphocytes B
BCA	Bicinchonic acid
BMP	Bone morphogenetic protein
BSA	Bovine serum albumin
Caco-2	Human epithelial colorectal adenocarcinoma cells
CCD-18Co	Human colon fibroblasts
DAPI	4',6-diamidino-2-phenylindole
D_{app}	Apparent diffusion coefficient
DMA	Dynamic mechanical analysis
DMEM	Dulbecco's modified eagle medium
DMSO	Dimethyl sulfoxide
DNA	Deoxyribonucleic acid
DoF	Degree of functionalization
DSB	Double strand break
ECM	Extracellular matrix
EDTA	Ethylenediaminetetraacetic acid
EGF	Epidermal growth factor
ELISA	Enzyme-linked immunosorbent assay
EthD-1-	Ethidium homodimer-1
FBS	Fetal bovine serum
FD4	FITC-dextran of 4 kDa
FD70	Rhodamine-dextran of 70 kDa
FD500	FITC-dextran of 500 kDa
FDA	Food and Drug Administration
FTIR	Fourier transform infrared
GelMA	Gelatin methacryloyl
H_2O_2	Hydrogen peroxide
HCl	Hydrochloric acid
HEPES	N-2-hydroxyethylpiperazine-N-2-ethane sulfonic acid

HT29-MTX	Goblet cells
Hyl	Hydroxylyisine
IBD	Inflammatory bowel disease
IgA	Immunoglobulin A
IR	Infrared
Irgacure D-2959	2-hydroxy-1-[4-(2-hydroxyethoxy)phenyl]-2-methyl-1-propanone
JAM	Junctional adhesion molecule
LAP	Lithium arylphosphanate
LPS	Lipopolysaccharide
Lys	Lysine
M0	Inactive macrophage
MA	Methacrylic anhydride
MMP	Metalloproteinase
MUC	Mucopolysaccharides
$NaHCO_3$	Sodium bicarbonate buffer
NIR	Near-infrared
NHS	N-hydroxysuccinimide
OCT	Optimal cutting temperature
P_{app}	Apparent permeability
PBS	Phosphate buffered saline
PDMS	Polydimethylsiloxane
PEG	Poly(ethylene glycol)
PEGDA	Poly(ethylene glycol) diacrylate
PEGDMA	Poly(ethylene glycosl) divinyl ester, poly(ethylene glycol) dimethacrylate
PEG-SH	Poly(ethylene glycol) dithiol
PET	Polyethylene terephthalate
PI	Photoinitiator
PMA	Phorbol 12-myristate 13-acetate
PMMA	Poly(methyl methacrylate)
PSA	Pressure-sensitive adhesive
RGD	Arginine-glycine-aspartic acid
ROS	Reactive oxygen species
SD	Standard deviation
SDS-PAGE	Sodium dodecyl sulfate-polyacrylamide gel electrophoresis

TBS	Tris buffer saline
T cells	Lymphocytes T
TEER	Transepithelial electrical resistance
TEMED	Tetramethylethylenediamine
TMSPMA	3-(Trimethoxysilyl)propryl methacrylate
TNBS	2,4,6-trinitrobenzene sulfonic acid
TNP	Trinitrophenyl
UV	Ultraviolet light
ZO-1	Zonula occludens-1

1. Introduction

1.1. Anatomy and physiology of the small intestine

The small intestine is an essential component of the gastrointestinal system where the digestion and absorption of nutrients take places[1,2]. It consists of a long tube, with an average of 2.5 cm in diameter and 3 m in length[3]. These dimensions make it the largest part of the gastrointestinal system, occupying most of the space of the abdominal cavity. The small intestine begins at the end of the stomach, coils through the central and inferior part of the abdominal cavity and ends into the large intestine[1,4]. It is divided into three consecutive regions. The first region is the duodenum, which connects with the stomach. The next portion is the jejunum, and the third one is the ileum, which joins the small intestine with the large intestine[1] (Figure 1.1 (a)). To properly perform its function, the small intestine has a complex organization and cellular diversity. It is composed of a wall formed by four different layers: mucosa, submucosa, *muscularis propria* and serosa or adventitia (Figure 1.1 (b and c)). The mucosa is the inner most layer of the intestinal wall and it is facing the lumen of the small intestine. Its function is to absorb nutrients and water from the intestinal lumen into the blood. Underlying this layer, there is the submucosa which is composed of highly packaged and dense connective tissue containing fibroblasts and mast cells. The main function of the submucosa is to provide structural and functional support to the mucosa through the distribution of arteries, lymphatic vessels and nerves and secretion of some enzymes[1,5]. Adjacent to the submucosa, there is the *muscularis propria*. It is composed of an inner circular smooth muscle layer and an outer longitudinal smooth muscle layer separated by the myenteric nerve plexus. The whole set is in charge of the coordination of the peristalsis movement, which aid the digested food to move through the tube[1,5]. Finally, the outer most layer of the small intestine is the adventitia or serosa, which is a single layer of smooth cells that surrounds the small intestine[5].

The intestinal mucosa is divided into three distinct layers from the lumen to the bulk of the intestinal tissue, there are the epithelium, the lamina propria and the *muscularis mucosae*[1,6] (Figure 1.1 (c)). The epithelium is a columnar epithelial layer that contains many types of cells. This cell monolayer creates a selectively permeable barrier that prevents the entrance of pathogenic agents while the nutrients and water are assimilated[6]. For its correct barrier function, it is important the regulation of the interaction between external stimuli from the lumen, such as food antigens, intestinal microbes and pathogens with the immune system[5,6,]. Beneath the epithelium and to give support to it, there is the lamina propria, a connective tissue composed of stromal cells

(mesenchymal cells which includes fibroblasts and myofibroblasts)[8] and immune system related cells (such as macrophages, monocytes, lymphocyte, dendritic cells)[7]. Moreover, the lamina propria contains a large number of blood and lymphatic vessels, which are crucial for the nutrient absorption from the lumen into the body. The third and the deepest layer of the mucosa is the *muscularis mucosae*. It consists of a thin layer of smooth muscle cells that separates the mucosa from the submucosa and aid the intestinal peristalsis motion[5] by providing a gentle movement to improve the interaction between the epithelium and the lumen content[9].

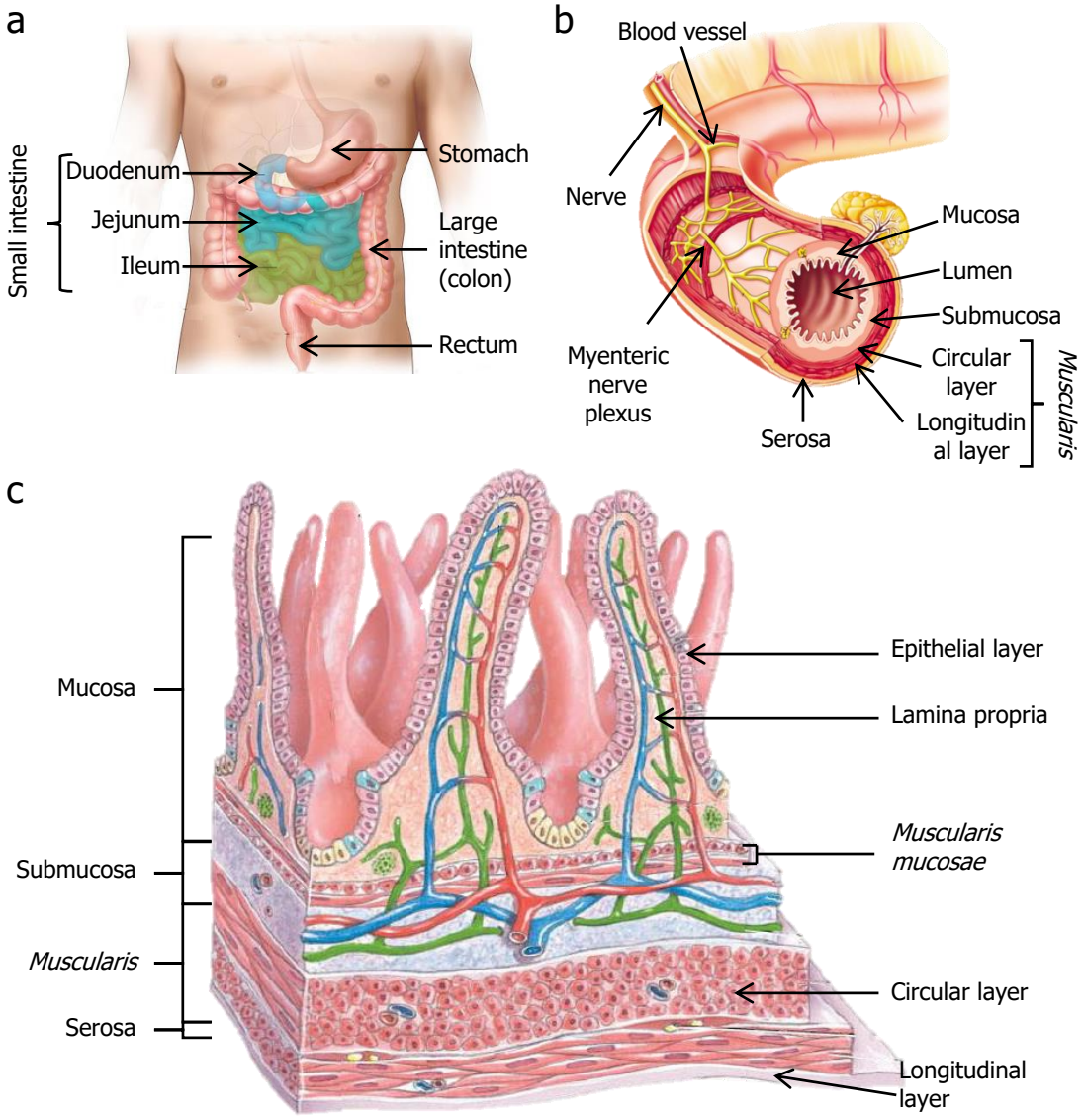

Figure 1.1. Schematic illustrations of (a) the gastrointestinal track parts (adapted from http://www.health-articles.info); (b) the small intestine anatomy (adapted from http://www.zo.utexas.edu); and (c) the four layers of the small intestinal wall and their parts (adapted from Tortora *et al.*)[1].

Apart from the complex cellular organization of the small intestine, this also has a complex structural arrangement. The small intestinal mucosa is structured with circular folds known as *plicae circularis* that enhance the digestion and nutrient absorption by increasing the surface area of the small intestine by three folds[1] (Figure 1.2 (a)). These circular folds of the mucosa and submucosa are covered with finger-like projections[1] towards the lumen, called villi (Figure 1.2 (b)). The villi are surrounded by invaginations known as crypts of Lieberkühn[10–12], forming villus-crypt units. Villus dimensions are between 0.2 – 1 mm in height[13] and between 100 – 150 µm in diameter[7,14]. Whereas the invaginations that form the crypts are between 0.3 – 0.5 mm in size[10]. Villi are found to be highly packed at a density of 20 – 40 villi·mm^{-2}, increasing the surface area for absorption and digestion of nutrients[1,7]. The villus-crypt units are covered by an epithelial cell monolayer and beneath it, there is the lamina propria supporting the structure and forming the core of the structures (Figure 1.2 (c and d)).

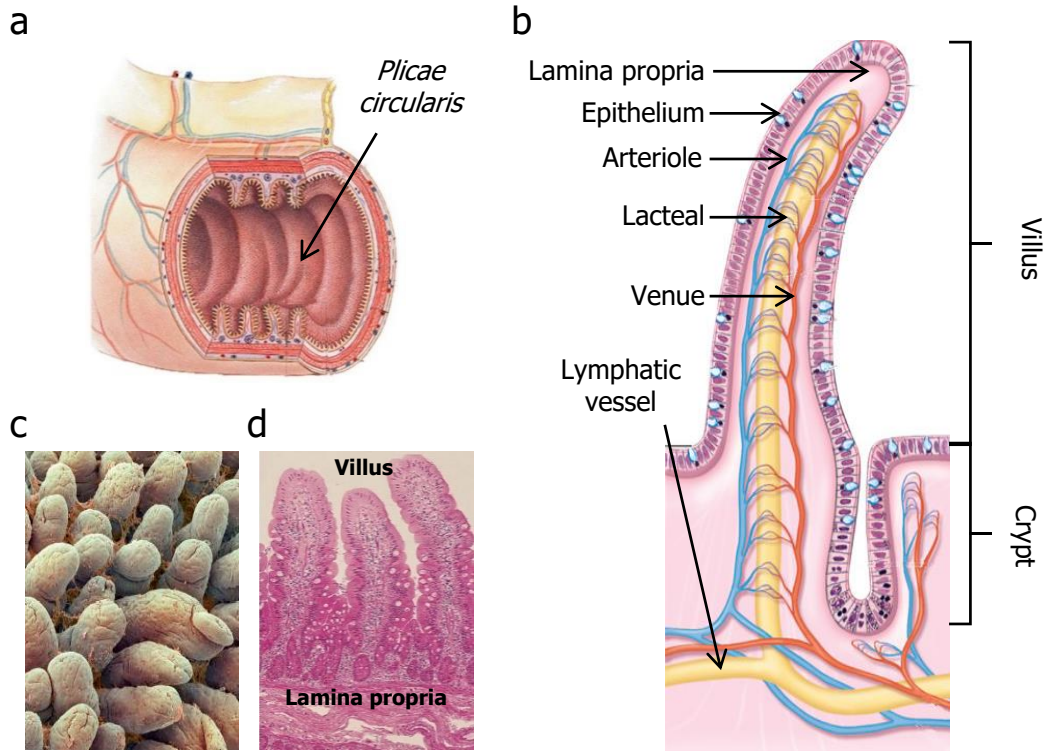

Figure 1.2. (a) Drawing of the small intestine inner wall (adapted from https://lesiukbiology.weebly.com). (b) Longitudinal cross-section representation of the villus-crypt unit (adapted from Barrett *et al.*)[12]. (c) Scanning electron micrograph of the small intestine mucosa showing villi and mucus (from Thompson *et al.*)[16]. (d) Longitudinal cross-section of the small intestine (adapted from Tortora *et al.*)[1].

The **lamina propria** is a connective tissue composed of fibrillary proteins and several cell types[14]. The main fibrillary protein is collagen, representing around 43% of

the total tissue protein[17]. In the lamina propria the most predominant subtypes of collagen are collagen type I, which provides a structure with high tensile strength to the tissue and collagen type III which gives flexibility and elasticity to the tissue[14,15,17,18]. In the lamina propria apart of the connective tissue there is a network of arterioles, venules and lymphatic vessels, known as lacteal. The network allows the absorption of nutrients from the small intestine lumen into the circulatory systems[1] (Figure 1.2 (b)). Embedded in the lamina propria there are different cell types such as stromal cells (mesenchymal cells which includes fibroblasts and myofibroblasts), smooth muscle cells[19], and immune system related cells (neutrophils, macrophages, eosinophils, lymphocytes)[20].

The **basement membrane**, which is between the epithelial monolayer and the lamina propria (Figure 1.3 (a)), is a specialised structure composed of a stable sheet of ECM components, such as collagen (predominantly collagen IV), laminin, proteoglycans, adhesives proteins and calcium binding proteins (Figure 1.3 (b)). Such ECM components are organized into a single molecular layer parallel to the surface with a thickness of 50 – 100 nm[21] and pores and cavities of 10 nm and 1 – 5 μm in diameter, respectively[22]. The main roles of this basement membrane are to support the architecture of the epithelial monolayer[16,23], and to provide cell-adhesion motifs which are essential for cell adhesion, morphology[23], migration[23,24], proliferation[23,24] and programmed death[23]. Additionally, the basement membrane reinforces the epithelium physical barrier by acting as a barrier for the penetration of cells and macromolecules[23,24].

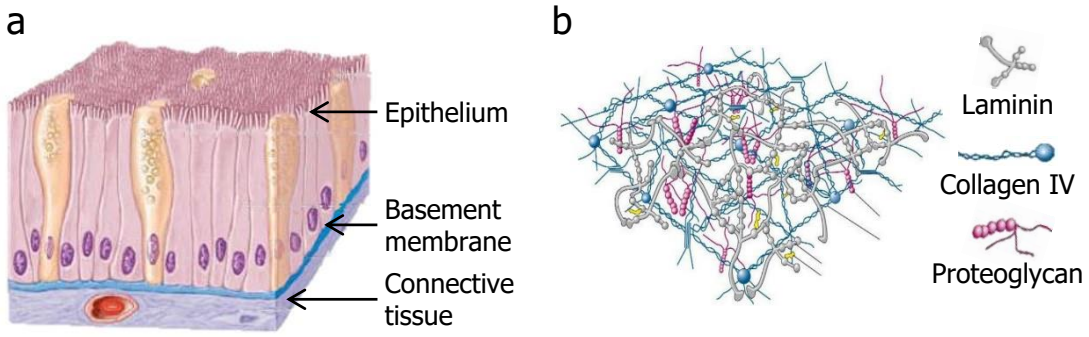

Figure 1.3. Basement membrane features. (a) Schematic drawing of the basement membrane localization in the small intestine, which is just under the epithelium providing support (adapted from Tortora *et al.*)[1]. (b) Drawing of the basement membrane organization and components (adapted from https://www.uv.es).

The **small intestinal epithelium** consists of six differentiated epithelial cell types and pluripotent intestinal epithelial stem cells[11]. Cellular distribution and organization varies along on the vertical axis of the villus-crypt units (Figure 1.4 (a)).

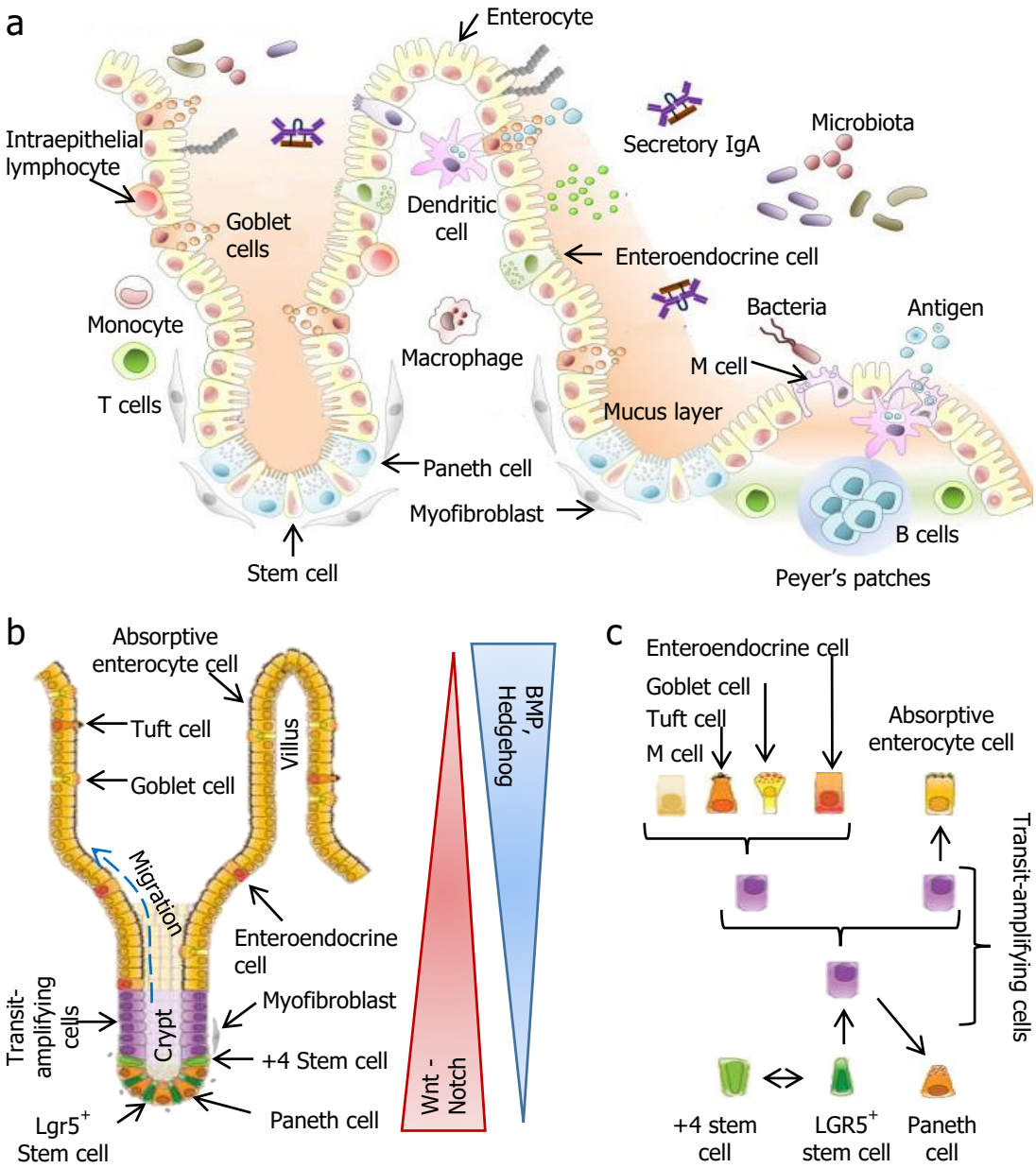

Figure 1.4. (a) General overview of the small intestinal mucosa. Enterocytes comprise the major cells type found in the crypt-villus units and secrete antimicrobial peptides. Paneth cells placed at the crypt and produce specific antimicrobial peptides. Tuft cells are localized to the follicle-associated epithelium overlying Peyer's patches and participate in antigen uptake and passage to underlying immune cells. Goblet cells produce mucus and facilitate luminal antigen transfer to dendritic cells via goblet cell-associated antigen passages. Enteroendocrine are the responsible of secreting hormones. M cells are responsible of antigen endocytosis (adapted from Allaire *et al.*)[25]. (b) Distribution of the epithelial cell types along the villi and crypt of the small intestine with the growth factor gradient. (c) Cell pathways for the differentiation. $Lgr5^+$ are settled in the base of the crypt, intercalated with Paneth cells and dividing to transit-amplifying cells. +4 Stem cells are the reservoir that differentiated to $Lgr5^5$ when there is an injury (adapted from Carulli *et al.*)[26].

The most abundant cells, around 80% of all cells in the small intestine, are absorptive enterocytes cells, which are highly polarized, columnar shaped cells in charge of digesting and absorption of nutrients and minerals from food through degradation by hydrolytic enzymes[1,7,11,27]. Another cellular type are the goblet cells which are balloon shaped cells that produce mucus through secretory granules. A third type are enteroendocrine cells, which are responsible for the secretion of a large number of hormones that regulate the digestive function[1,7,11]. Moreover, there are Tuft cells, which are scattered distributed along the whole villus-crypt units and serve to sense luminal contents[11]. Residing at the bottom of the crypts, there are the Paneth cells, which are intercalated among the intestinal stem cells and they are in charge of the intestinal stem cell niche preservation by the secretion of vital biochemical signals[11], as well as the regulation of the microbial population by the secretion of bactericidal products such as lysozymes[1,7,11]. Another cell type is Microfold cells (M cells). They are localized in the crypts next to Peyer's patches (lymphoid aggregations) and are important for passive immunity. Their main roles are the endocytosis of antigens and their transport to the intraepithelial macrophages and lymphocytes, which will then migrate through the lymphatic system reaching the lymph nodes, where the immune response is initiated[11]. Finally, the $Lgr5^+$ intestinal stem cells are located at the base of the crypts. These $Lgr5^+$ stem cells are multipotent cells, which are responsible for generating all types of mature intestinal epithelial cells. To do that, they give rise to transit amplifying cells or +4 stem cells. Transit amplifying cells migrate from the crypts to the tip of the villi while they gradually differentiate into a specific type of epithelial cell. However, Paneth cells, unlike the other epithelial cell types, they migrated downward to the crypts as they mature and reside in the crypt intercalated with the stem cells[28]. When epithelial cells become aged and reach the tip of the villus they undergo apoptosis and are ejected into intestinal lumen. Apoptosis is a process of programmed cell death, which is essential to keep the balance between the proliferative and dead cells, and thus maintain the homeostasis[29]. Epithelial monolayer is renewed very fast, within 4 – 5 days, being one of the organ in our body that self-renewed faster (Figure 1.4 (b and c))[11,25,26,30–33].

The villus-crypt unit structures are vital for the accurate intestinal homeostasis by balancing the processes of cell proliferation, differentiation and regeneration through the interconnection of different signal pathways[11,31–33]. The tissue architecture, and the equilibrium between cell regeneration and differentiation are maintained through the secretion of different signalling biomolecules such as bone morphogenetic protein (BMP), hedgehog, epidermal growth factor (EGF), Wingless/Int (Wnt) and Notch (Figure 1.4

(b))[30,32,33]. The supply of these factors are provided through intestinal stem cells that are closer associated and in direct contact with neighbouring cells such as Paneth cells and intestinal subepithelial myofibroblasts, and fibroblasts located below the basement membrane and within the lamina propria[32]. This specific cellular diversity and highly specialised cellular functionality provides the intestinal epithelium with the capabilities to perform its diverse functions.

The intestinal selective barrier function and the uptake of nutrients and minerals both are carried out due to the establishment of enterocyte cells' polarity with distinct apical and basolateral plasma membrane domains (Figure 1.5 (a))[34]. The apical membrane, which is facing the small intestinal lumen, is responsible for forming a defensive barrier against harmful organisms and for the absorption of nutrients and its area is enlarged by the presence of microvilli.

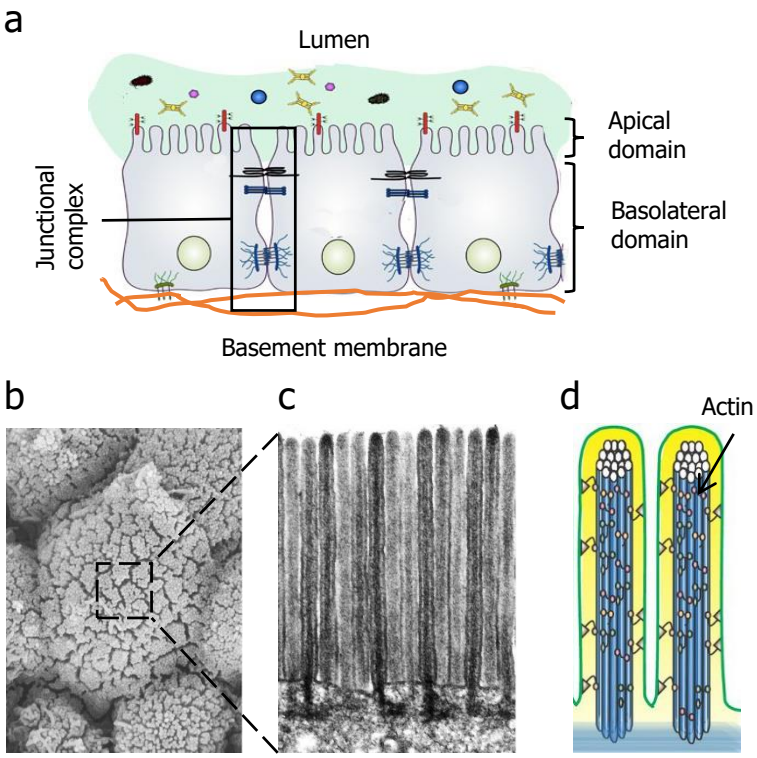

Figure 1.5. Organization of the enterocytes and the microvilli. (a) Schematic representation of the mature enterocyte morphology, showing its polarization, apical and basolateral domains, as well, the tightly adhesion to each other by junctional complex (adapted from Vancamelbeke *et al.*)[35]. (b) Top view of the villi of small intestine surface by scanning electron microscopy; (c) longitudinal cross-section of the microvilli by transmission electron microscopy. (d) Schematic illustration of microvilli showing the actin filament arrangement (adapted from Walton *et al.*)[36].

Microvilli are projections from the apical membrane of the enterocytes to the lumen of ≈1 μm. These projections are supported by a network of 20 – 30 bundles of

actin filament[1,34,36]. One single enterocyte has ≈1000 microvilli highly packed on its surface[34] ($2 \cdot 10^8$ microvilli·cm^{-2})[1] (Figure 1.5 (b – d)). The whole microvillus set is referred as brush border and improves not only the food absorption by increasing the surface area, but also the food processing by the presence of the brush-border enzymes[1].

Instead, the cell basolateral membrane is essential for establishing contact between the adjacent cells and the basement membrane[34]. A strong and close adhesion between cells is established trough junctional complexes, which are in the lateral part just below the apical membrane (Figure 1.5 (a)). The junctional complexes consist of a tight junction, adherens junction and desmosomes (Figure 1.5 (a))[34,37,38]. They provide cohesion and polarity to enterocytes, preventing the passage of nutrients, water and other molecules from the lumen into the bloodstream. Tight junctions or occluding junctions are located close to the apical domain of polarized cells forming continuous circumferential contacts.

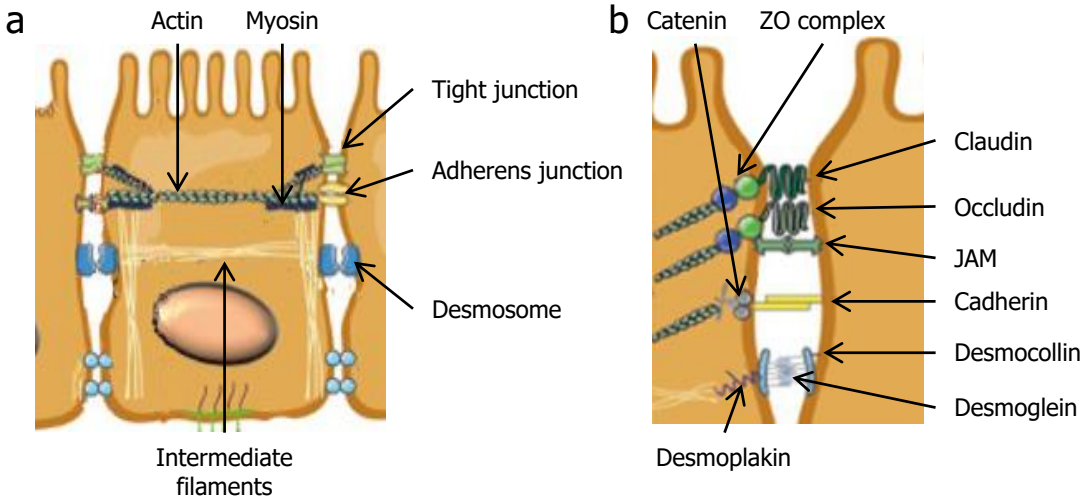

Figure 1.6. An illustration of the junctional complex and their components. (a) A general overview of the junctional complex localization (tight junction, adherens junction and desmosome) and its interaction with cytoskeleton (actin, myosin and intermediate filaments) which is the responsible of the integrity and structure of epithelial cells. (b) Zoom to show the main components of the junctional complex: tight junction (claudins, occludins, JAM and ZO which connects to actin filaments); adherens junction (cadherin binds to catenin which is connected to the actin); and desmosome (desmocollin and desmoglein and desmoplakin which connects to the intermediate filaments) (adapted from Romero *et al.*)[38].

Tight junctions are protein complexes composed of three transmembrane proteins (occludin, claudins and junctional adhesion molecules (JAM)) anchored to the cytoskeleton filaments by cytoplasmic plaque of *zonula occludens* proteins (ZO-1, ZO-2 and ZO-3) (Figure 1.5 (b)). The main function of tight junctions is sealing the apical and

the basolateral parts of the cell monolayer, therefore controlling, cellular permeability between both compartment by paracellular transport[38,39]. Adherens junctions are just below the tight junctions and consist of cadherin-catenin complexes (E-cadherin interacts with β and α catenin) which are joined to the actin finalaments[37,40]. They are required for the assembly of the tight junctions and are involved in cell-cell adhesion and intracellular signalling. Their disruption implies weak cell-cell and cell-matrix contact, ineffective epithelial cell polarization and differentiation, as well as premature apoptosis[41] (Figure 1.5 (b)). Desmosomes appear at the basal end of the cells and are comprised of a set of intracellular proteins (desmoglein, descmocllin and desmoplakin) linked to the intermediate filaments, providing mechanical strength and integrity to the tissue (Figure 1.5 (b))[37,42].

Enterocytes regulate the transport of the substances across the monolayer using two major pathways, paracellular and transcellular (Figure 1.7). The paracellular pathway is a passive transport of molecules that takes places through the channels formed between two adjacent cells (Figure 1.7 (a)). This route is characteristic of small hydrophilic molecules, which are driven by water movement due to an osmotic gradient[43]. Basically, this transport is restricted by the pore size of the epithelial tight junctions. These haves pore sizes of 5 nm and allow the diffusion of molecules ranging from 4 to 5.5 kDa while preventing the passage of larger ones[20]. In contrast, the transcellular pathway transports of molecules across the enterocyte's membrane can be mediated by passive cellular diffusion (Figure 1.7 (b)), specific membrane transporters (Figure 1.7 (c)), receptor-mediated endocytosis (transcytosis) (Figure 1.7 (d)) and by absorption into lymphatic circulation via M cells of Peyer's patches (Figure 1.7 (e)). This route is characteristic of large molecules, lipophilic compounds and nutrients. In the transcellular passive diffusion, molecules cross the apical and the basolateral membrane due to their physicochemical properties such as the size, charge and lipophobicity. Other molecules can cross the cell membrane and translocate into the cell's lumen thanks to the transcellular transport through a specific membrane transporter. In transcytosis. macromolecules are recognized by receptors, which wrap the molecules forming a vesicle and producing their endocytosis. After, crossing cells' cytosol, the vesicle arrives at the basal cell domain, where is ejected by exocytosis to the abluminal side[27,43,44]. Finally, in some cases the macromolecules go to the lymphatic circulation via M cells of Peyer's patches[44].

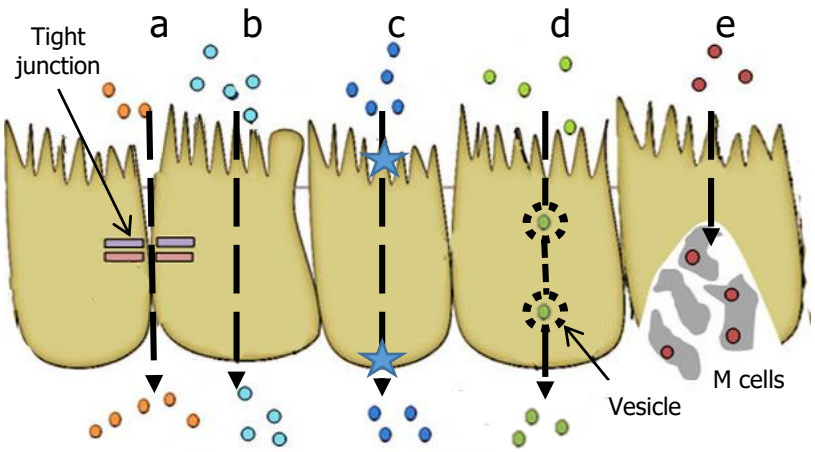

Figure 1.7. The mmechanisms to transport molecules through the epithelial membrane. Schematic drawing of the (a) paracellular and (b-e) transcellular molecule transport and absorption through the intestinal epithelium: paracellular transport via (a) tight junctions; transcellular transport via (b) passive diffusion; (c) transporter; (d) transcytosis; and (e) M cells to lymphatic circulation (adapted from Choonara *et al.*)[44].

The physical and chemical barrier that creates the epithelium and protects the organism from the entry of pathogens found in the lumen is reinforced by a layer of mucus[1,7]. Intestinal mucus is produced by goblet cells and forms a single layer that extends over the tips of the small intestine villi, covering all the epithlium[45,46]. The thickness of the mucus layer is ≈150 μm in height[47] and it is essential to prevent translocation of harmful microorganisms across the epithelial monolayer[45]. As it is viscous[48], entrapped inside the mucus matrix there are antibacterial compounds such as antibodies, lysozymes, immunoglobulin A, defensins, etc…, which are mostly produced by Paneth and enteroendocrine cells[45,46]. Moreover, the mucus layer is continually self-renewed due to the luminal movement of the nutrients and other compounds through the intestinal tube[46]. The mucus layer is composed of an extremely organized network of mucopolysaccharides (MUC), which are lubricant glycosylated proteins secreted by goblet cells[45,46], being MUC2 the most abundant[45]. Beneath the mucus layer and on top of the microvilli surface of the epithelial cells, there is the glycocalyx. This is a meshwork of carbohydrate of glycolipids and glycoproteins, including acidic MUCs, mainly transmembrane MUC3, MUC12 and MUC17, which are anchored to the cell membrane[46,49,50]. The main role of the glycocalyx is to enhance food digestion due to the large amounts of enzymes entrapped, and to prevent pathogenic infections (Figure 1.8). On top of the mucus layer there is a large amount of commensal microbiota that commonly aid with the degradation of the food and enhance its absorption by the epithelial cells[51]

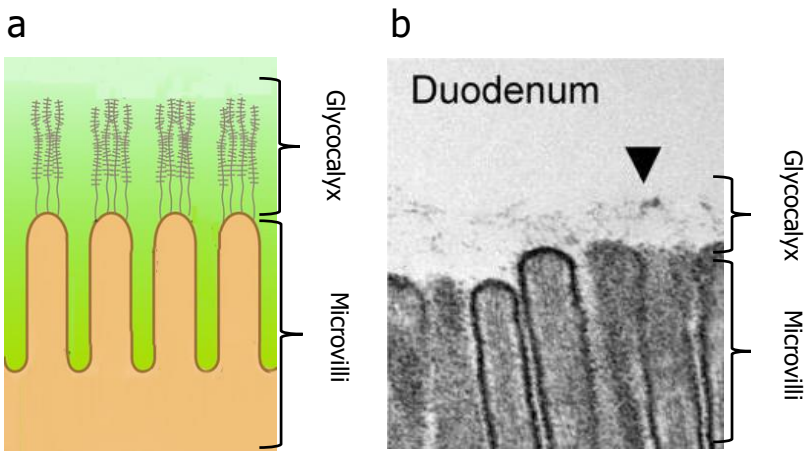

Figure 1.8. Glycocalyx on the small intestine. (a) Schematic illustration showing the microvilli on the apical membrane of the enterocytes with well-developed carbohydrate rich thick glycocalyx;. (b) Electron micrograph of duodenal microvilli with surface glycocalyx (adapted from Pelaseyed *et al.*)[44].

Apart from the barrier constituted by the mucus and the epithelial cell monolayer, pathogen colonization is prevented by the intestinal immune system related cells, which are distributed along the lamina propria. These are mainly lymphocytes (B and T cells) and non-lymphoid innate immune cells (macrophages, dendritic cells, eosinophils and mast cells)[52]. Additionally, intercalated in the epithelium and settled at the basement membrane there are T cells[52]. Around 10 – 15 T cells are interspersed every 100 epithelial cells[53]. Due to their localization they are referred as intraepithelial lymphocytes[52]. They are in direct contact with antigens, so their main function is defence against infections by preventing pathogenic entrance, extensive tissue damage, and regulating the intestinal homoeostasis[54]. On the other hand, the T cells found in the lamina propria, are known as lamina propria lymphocytes. They play a crucial role in the local immune regulation by producing high amounts of cytokines, being effector memory T cells and helping B cells to produce immunoglobulins (antibodies), especially IgA, which is the most abundant antibody in mucosal secretions and favour the maintenance of both non-invasive commensal bacteria and neutralization of invasive pathogens[20,55]. Macrophages and dendritic cells are mononuclear phagocytes[52,56]. Macrophages that reside in the lamina propria of the intestine are the most abundant cells in the intestine compared to other tissues[57]. Unlike other tissues, macrophages in the intestine are continuously renewed, for that, stem cells in the bone marrow differentiate into monocytes. Then, monocytes migrate from the bone marrow to the peripheral blood which are translocate to the intestinal mucosa while they differentiate and mature towards macrophages[57,58]. This process, known as monocyte waterfall, is a complex

process, that takes between 5 -6 days, and several changes in gene expression are needed[58]. Intestinal macrophages are essential sentinels for keeping the homeostasis in the intestine by their highly phagocytic activity.

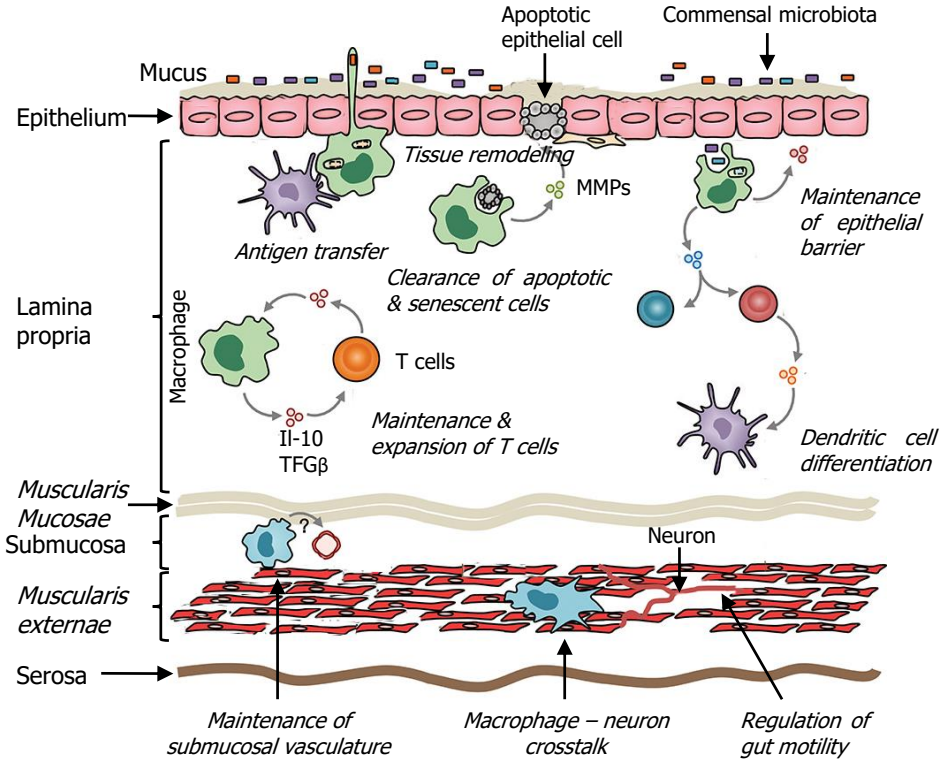

Figure 1.9. Schematic representation of the intestinal macrophage functions in the intestine to maintain its homeostasis (adapted from Bain C.C. *et al.*)[58].

Mainly their functions are (I) the degradation of apoptotic and senescent epithelial cells by the stimulation of epithelial stem cell renewal through the secretion of factors such as prostaglandin (PGE) or hepatocyte growth factor (HGF)[57,58]; (II) the aiding in the wound healing through the secretion of metalloproteinases (MMPs); (III) the phagocytosis and destruction of any pathogenic agent, such as bacteria, that break the epithelial barrier and enter to the lamina propria[57,58], macrophages can differentiate between pathogenic and commensal microorganisms by the recognition of microbial molecules secreted by the commensal microoganisms[57]; (IV) the transfer of antigens from the digested pathogen to the dendritic cells and thus present the antigen to the T cells which reside in the draining mesenteric lymph nodes; (V) the production and secretion of IL-10 and transforming growth factor beta (TGF-β) anti-inflammatory cytokines by macrophages and thus enhancing the number of T cells;[57,58]. Although macrophages are mainly found in the lamina propria, they are also present in the submucosa and *muscularis externae*, where they are involved in the integrity of the

maintenance of submucosal vasculature and in the communication between sympathetic neurons of the enteric nervous system and motility of the gut[58].

On the other hand, dendritic cells are able to migrate from the intestine to the mesenteric lymph nodes, where they initiate adaptive immune responses by activating naïve T cells upon antigen presentation [20,56]. Eosinophils are lamina propria resident cells and act as a pro–inflammatory cells by secreting cytokines, chemokines and toxic cytoplasmatic granule constituents[59]. Finally, mast cells, which are in the lamina propria and submucosa, basically, secrete components that regulate the epithelial barrier integrity, peristalsis and permeability, as well as the interaction with the local nervous system[52]. Overall, the intestinal immune system is a well coordinate set of cells that preserves the sterility and avoids the entrance of pathogenic organisms into the body. A correct immune system response involves an efficiently crosstalk between the epithelial and the immune system related cells. Epithelial cells mediate the activation of the immune innate system through secretion of antimicrobial components and can assist to program the dendritic response to antigen exposure when the innate immune system does not work[60].

1.2. Small intestine physiology and pathology

In general, five fundamental criteria are used to define a healthy gastrointestinal tract. (I) effective digestion and absorption of food (appropriate nutritional status and effective absorption of nutrients and regular bowel movement), (II) absence of illness in the gastrointestinal track (no inflammatory bowel disease, no colorectal cancer, no enzyme deficiencies), (III) common and stable intestinal microbiota (standard composition of the gut microbiome, no bacterial infection), (IV) effective immune status (effective gastrointestinal barrier function, usual mucus production, immune tolerance and no allergy, correct activity of immune cells), and (V) status of well–being (good quality of life, balanced functions of the enteric nervous system, hormones)[61]. As key players in the system, the association between commensal microbiota resident in the mucus layer with the intestinal barrier activity is essential to preserve a healthy and functional gut. Commensal microbiota is relevant in a wide variety of functions, such aiding the digestion of nutrients, regulation of the mucus synthesis produced by goblet cells, regulation of defensins secreted from Paneth cells, contribution of the tight junction protein synthesis in the epithelial cells, prevention of pathogen colonization and control

of the immune system through the secretion of immune stimulators[61,62]. Gut microbiota can be altered by drugs or pills, such as antibiotics, physiological and physical stress, aberrant peristalsis movement and modifications on the diet among other factors. If this happens, pathogenic agents can overgrow and injure the mucus layer, and the epithelial cell monolayer, resulting in the barrier damage mainly by disruption of the tight junctions. As a result of that, the intestinal paracellular permeability is increased, and pathogenic bacteria are translocated into the bloodstream causing a systemic inflammation and an inefficient absorption of the nutrients[41,61,63,64]. For example, enteropathogenic *Escherichia coli* is a bacterium that causes an inflammation of the mucosal from stomach and small intestine and provokes an increment in bowel movements causing an incorrect absorption of the fluids[65]. *E. coli* adheres directly to the surface of epithelial cells and incorporates effector proteins directly into the cell cytoplasm by syringe-like secretion systems. The effector proteins modify cellular processes, such as the synthesis of protein kinases, having a negative effect on the assembly of the tight junctions[63]. Another enteric bacterium that disrupts the tight junctions and increases the permeability is the *Vibrio cholerae.* This secretes the cytotoxic proteases hemagglutinin, which degrades the tight junctions leading to the dysregulation of intestinal ion and fluid transport[66]. Both bacteria cause diarrhoea.

Conversely, when the epithelial barrier integrity is compromised, the immune system of the intestinal mucosa contributes to the defence against pathogens and other external stimuli, such as food antigens[61]. A dysregulation of the immune system results in severe hypersensitivity reactions leading to chronic inflammatory states such as intestinal bowel disease (IBD), food allergies or celiac diseases[61].

IBD is a chronic inflammatory conditions of the gastrointestinal tract affecting 1 out of 250 individuals in the European population[67]. There are two main disorders related to IBD: Crohn's disease and ulcerative colitis. Crohn's disease affects all the gastrointestinal tract, including the small intestine, whereas ulcerative colitis only affects the colon and the rectum[67,68]. Mainly, in IBD the interaction between genetically predisposed individuals and the environment is the cause for the loss of the barrier integrity. Exposure to bacteria or other antigens produces the movement of immune cells towards the epithelia monolayer and their transmigration. This results in uncontrollable inflammatory signal cascades and abnormal immune responses against antigens, resulting in inflammation of the small intestine[35,67,69].

Food allergies are adverse multisystemic, immune–mediated reactions to ingested proteins or antigens from food. This reaction can caused the disruption of the intestinal tight junctions and enhance the intestinal permeability through the paracellular pathway, aiding the presentation of food antigens to the immune system and leading to the development of the dietary antigen-specific responses[39].

Celiac disease is an immune-mediated disorder of the small intestine that occurs in susceptible individuals when they ingested gliadin, which is a toxic component of the gluten, found in wheat or other grains. Celiac patients have aberrant tight junction structures resulting in an increment of the intestinal paracellular permeability. In a celiac person, even with a gluten-free diet, these disruptions are present. In heathy conditions, gliadin does not cross the epithelial membrane through the tight junctions. In contrast, in celiac disorders the gliadin passes through the epithelium and triggers an immune reaction[63,66].

Barrier dysfunction associated diseases, such as enteric infections, food allergies, IBD and others, have increased their prevalence over the population in the past decades[35]. These disorders are accompanied by discomfort, pain, bloating or altered motility, which can severely affect the patient's quality of life. In most of these disorders it is unclear whether the disruption of the intestinal barrier is the agent that causes the disease or it is a consequence related to the disease. A better understanding of the interaction between barrier dissociation and the pathogenic stimulus is required to improve and develop pharmacological treatments[70]. To fill this gap, predictive *in vitro* models of the small intestinal epithelium, and especially the ones that have mimic the architecture and cell distribution are required[71–73].

1.3. Conventional models of the small intestinal epithelium

Small intestine is a dynamic tissue, which high cellular complexity that has relevant roles in maintaining a human health, due to that there is an extremely necessity to obtain intestinal models. In the past decades, many research groups have been focus on better represent the *in vivo*-like physiology and anatomy of the small intestinal tissue resulting with an improvement of cell differentiation and tissue organization[72,74]. Consequently, these models will allow to obtain data more trustful and reliable, giving safer preclinical test[75]. Despite the latest advances on mimicking the small intestine physiology, the models most used and accepted by the pharmaceutical industry are

based on animal models, *ex vivo* systems or *in vitro* 2D cell cultures on a Trasnwell® setup.

1.3.1. *In vivo* animal models

Animals models have been widely employed to study the drug absorption and permeability before using them in human trials, due to they have less ethical restrictions[74]. Although, they imitate the complex physiology and interactions of the native tissues, many times they are unsuccessful to reproduce and predict human responses due to species–specific differences and the studied processes are less controllable due to the high number of other pathway that can interfered, causing unrepeatability[75]. For example, mouse's Paneth cells secrete a high amount of defensins compared to human's Paneth cells, which can make them impractical to study bacterial interaction[74]. Moreover, they are time-consuming, expensive and have ethical issues, which restrict their use[75,76]. To regulate the use of animals in scientific experiments Russell and Burch published an article for animal treatment based on the "3Rs principles"[77]. These guidelines consist on "Replace" the use of animals for alive alternatives, "Reduce" the quantity of animals for the experiments and "Refine" experiments to be less painful and stressful[73].

1.3.2. *Ex vivo* systems

Ex vivo systems are an alternative to animal models because they can minimize the difference between animal and human physiology and thus getting more trustful data. *Ex vivo* gut models are biopsy samples cultured outside the organism with similar complex cellular environments as *in* vivo, where the tissue functionality has not been lost[71]. These models can recapitulate the cellular diversity and the 3D structure of the small intestine, resulting in a better polarized and differentiated cells. This complexity is not usually found *in vitro* models. Additionally, the fact of having the tissue outside the body facilitates their manipulation and decrease the number of external parameter that can influence in the output due to the non-interaction with other tissues in the body[74]. Nevertheless, these models can only be culture for a short period of time, due to oxygen restrictions[71].

1.3.3. Standard *in vitro* 2D models

Standard *in vitro* 2D models, which are the most employed in the pharmaceutical companies or in basic research to study the small intestine are based on flat monolayers of transformed cell lines cultured onto porous plastic membranes in Transwell® inserts creating two separate apical and basolateral compartments that mimic the small intestine barrier found *in vivo* (Figure 1.9).

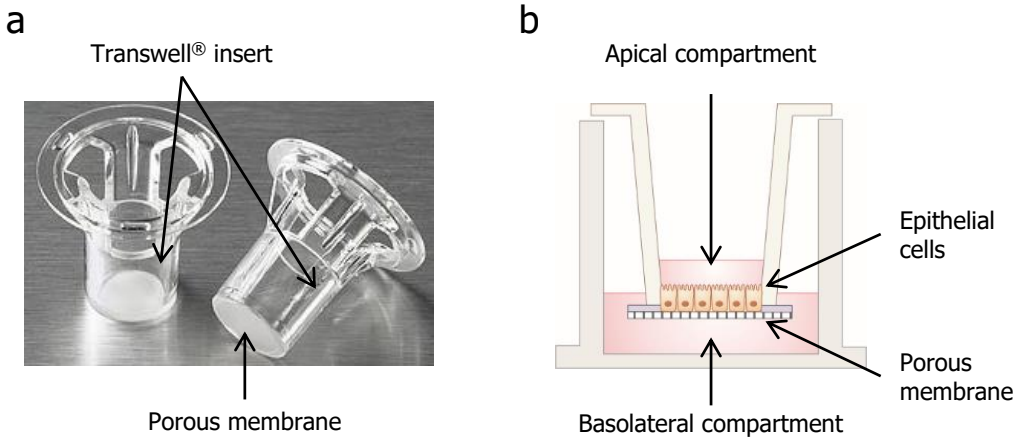

Figure 1.9. Standard 2D Transwell® inserts. (a) An image of a standard 24 well-plate Transwell® insert (from Corning). (b) Schematic drawing of *in vitro* 2D Transwell® cell culture. The epithelial cells grow on top of the porous membrane, which forms two compartments (apical and basolateral compartment).

The apical compartment, which corresponds to the upper well, mimics the intestinal lumen whereas the basolateral compartment, which corresponds to the bottom, imitates the intestinal ablumen or the inside of the intestine. To allow functional studies such as absorbance tests, the Transwell® membranes contain pores ranged between 0.1 to 12 µm. Mostly, they are composed of polycarbonate (PC), polyethylene terephthalate (PET) and polystyrene (PS), and are sometimes coated with proteins that mimic the ECM such as collagen, laminin or fibronectin to improve cell adhesion[78].

Usually, cells employed are enterocytes, being the Caco-2 cell line the gold standard in the field[79]. Caco-2 cells are an immortal human cell line derived from a human epithelial colorectal adenocarcinoma, obtained by Jorgen Fogh at the Sloan-Kettering Institute for Cancer Research in 1975[80]. Caco-2 cells spontaneously differentiate to mature enterocyte-like cells when they reach confluence in the culture. Cells begin to polarize as they grow forming a confluent, tightly-packed monolayer. During the polarization, there is a gradual reduction of cell surface, acquisition of a more columnar cell shape, and a formation of stronger and closer tight junctions. (Figure 1.10). By day

21 of culture, it is accepted that Caco-2 cells form a well-developed epithelial barrier. By this day, cells show large and uniformly distributed microvilli at their apical surfaces, forming the so called brush borders[81–83], which is also a sign of cell polarization. When Caco-2 cells are totally polarized, the expression of brush border enzymes, tight junctions and efflux and uptake transporters at both apical and basolateral compartments are comparable to those found in the native small intestine tissue. This, together with their easy handling and low culture cost, makes them ideal enterocyte-like cell candidates for *in vitro* studies[84] Consequently, pharmaceutical companies and basic research laboratories use this model for the investigation and prediction of drug absorption[85,86], toxicity[87], permeability[88] and research on intestinal transporters[89].

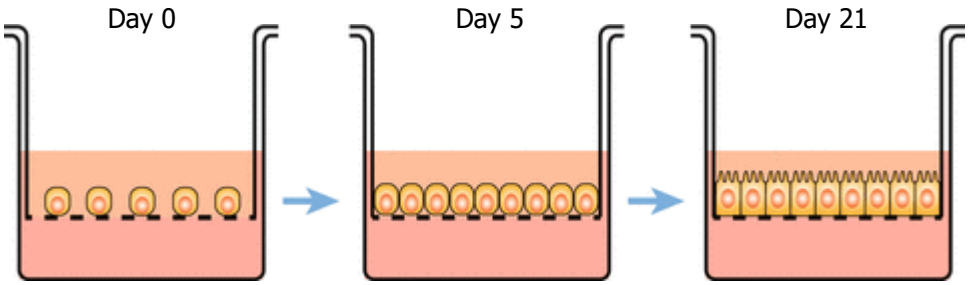

Figure 1.10. A drawing of the Caco-2 cells growing on a Transwell® insert, from low confluent (left panel) to high confluent (right panel). Caco-2 cells start to differentiate spontaneously to enterocyte-like cells when they reach the confluence. After 21 days post seeding, they present a dense microvilli on the apical side and a well-developed tight junctions in the lateral membrane, features of mature and differente small intestinal enterocytes (from Lea *et al.*) [83].

Although 2D Transwell® insert models can provide useful information on early biological responses and are suitable for high-throughput drug screening [75,90]. These models lack of the cell heterogeneity and organization, as well as tissue architecture found *in vivo*, which are important features to take into account because they modulate cell phenotype and functionality. It is well documented that Caco-2 cells grow on the hard porous Transwell® membrane, they form more densely-packed monolayers resulting in more stringent tight junctions than in *in vivo* tissue, leading to a higher transepithelial electrical resistance (TEER)[91].

Transepithelial electrical resistance (TEER) is one of the most important parameter accepted as a functional measurement of the epithelial barrier integrity and maturity. TEER can be determined by a quantitative, real-time and non-invasive measurement technique, to monitor the integrity of the tight junctions in epithelial monolayers cultured on Transwell® inserts (Figure 1.9)[92]. To measure the electrical resistance across the cell monolayer one electrode is placed in the top compartment and

the other in the bottom compartment. Then, the resistance is directly measured by an epithelial voltohmmeter (Figure 1.11 (a)) provided with chopstick electrodes (Figure 1.11 (b)) or and Endhom chamber (Figure 1.11 (c)). Electrodes are composed of silver and silver chloride (Ag/AgCl). An alternating low current (AC) signal (10 μA) with a square waveform at a frequency of 12.5 Hz is applied between the electrodes and, using the Ohm's law, the ohmic resistance is calculated. Despite electrical resistance adds up paracellular and transcellular resistances, owing to the cell membrane, the high resistance of the transcellular pathway causes that current flows mainly through the paracellular pathway. As paracellular route is regulated by tight junctions, consequently, TEER values are correlated with the strength of the tight junctions and the epithelial monolayer integrity and maturation (Figure 1.11 (d)).

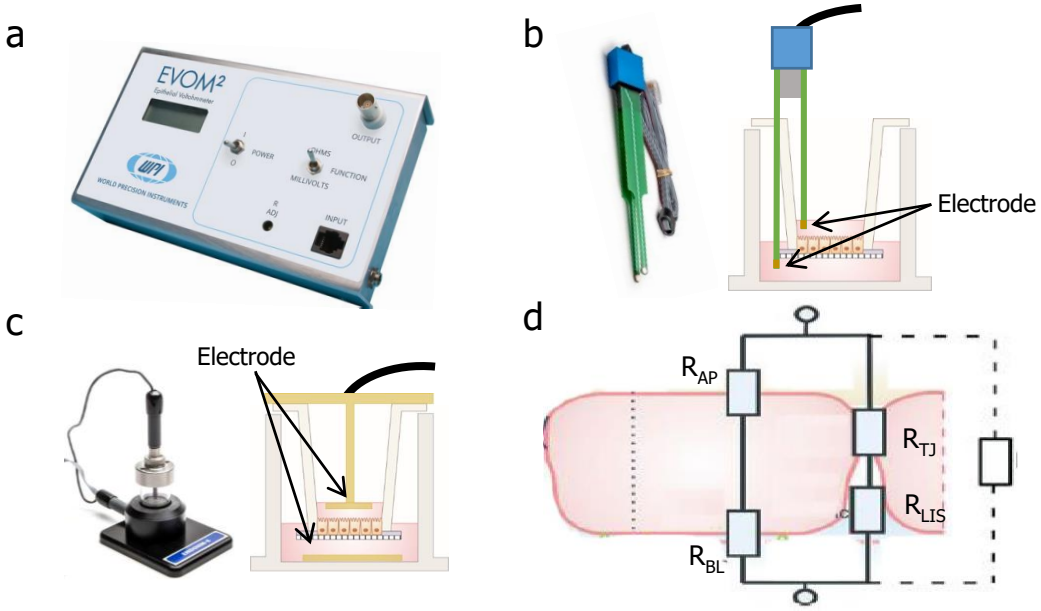

Figure 1.11. Epithelial monolayer growing on top of a porous Transwell® membrane and TEER measurements are recorded by (a) a voltohmmeter machine (from https://www.wpiinc.com). TEER can be measured by (b) chopsticks: placing a pair of electrodes one into the apical compartment and the other to the basolateral; (c) by a chamber: all the Transwell® insert is move from the well-plate and place inside the chamber. Electrodes are on top in the lid (apical side) and on the bottom of the chamber (basolateral compartment). (d) Schematic representation of the electrical resistances due to the epithelial monolayer consisting of the resistances at the apical (R_{AP}) and basal (R_{BL}) membrane (transcellular route) and the resistances of tight junctions (R_{TJ}) and resistance of lateral intercellular space (R_{LIS}) (paracellular route). Theoretically, R_{LIS} could contribute a resistance in series with the tight junction, but there is little evidence that this is physiologically significant. Overall, only R_{TJ} determines the final resistance (adapted from Srinivasan *et al.*)[99].

For a more accurate readout, the resistance created by the medium and the porous membrane without cells has to be discarded by subtracting it from the resistance giving by the cell monolayer[92,93]. TEER values measured on the standard Caco-2 model are around 1400 – 2400 $\Omega \cdot cm^{-2}$, which are much higher than the physiological TEER values reported for the native small intestine (50 – 100 $\Omega \cdot cm^{-2}$)[92] or native colon (300 – 400 $\Omega \cdot cm^{-2}$)[92].

1.4. Sophisticated *in vitro* models of small intestinal epithelium

To overcome the non-physiological data obtained by the *in vitro* 2D models, more accurate models of the small intestine are required to further understand the physiology of the small intestine tissue in healthy pathological states, and to employ them as a platforms for developing and testing pharmacological treatments and drugs[70]. These models would accelerate drug development by providing more predictive data in preclinical studies, therefore reducing the risk of failure in clinical trials[73]. In an effort to overcome these limitations 3D engineered tissues have emerged as powerful tools capable of capturing complex physiological responses *in vitro*[75].

Such engineered tissues should mimic the mechanical, physical and biological characteristics of the specific tissues. In the case of the small intestine, an ideal *in vitro* model could comprise: (I) a soft scaffold that matches the apparent elastic modulus of the intestine, (II) a multicellular epithelial population and cells from the lamina propria; creating the stromal and epithelial compartmentalization to study the crosstalk between different cell types and, if possible, mimicking the villus-crypt units, (III) a fluidic system that represents the interstitial flow, (IV) a peristatic-like movement, and (V) a mucus layer which includes the gut microbiome[73].

1.4.1. Intestinal organoids

One of the most important drawbacks to stablish *in vitro* cultures of human-derived intestinal epithelial cells is the short-term survival of primary cultures. Freshly isolated human intestinal epithelial cells die after a few hours of plating[94]. This has been associated to the lack of cell-cell and cell-matrix interactions and the absence of the proper growth factors, which lead to the induction of apoptosis and cell death[95].

A revolution in intestinal epithelial primary culture was performed by Sato *et al.*[96], who discovered a specific combination of growth factors required to support the growth of single stem cells for long culture periods. They showed that single $Lgr5^+$ stem cells from the intestinal crypts, when seeded within matrices of protein mixtures (Matrigel®), proliferate and form 3D structures called intestinal organoids or miniguts (Figure 1.12). Organoids are self-organized 3D structures that recapitulate the major features of native small intestinal tissue. Organoids exhibit a highly folded epithelium structure consisting of villus and crypt domains, and all the cell lineages found in the *in vivo* epithelium. Crypt domains form protrusions where $Lgr5^+$ stem cells, Paneth cells and proliferative transit-amplifying cells are located. In between crypts, villus-like domains populated by enterocytes, enteroendocrine and Goblet cells are found. Organoids grow forming closed structures that create a central cavity, which resembles the lumen, where the dead cells are ejected[73,97]. The renewal of the cells is similar to the *in vivo* conditions, taking about 4 – 5 days to born in the crypts, proliferate, differentiate and been death[98]. Organoids have been used to study the normal digestive physiology, developmental biology, as well as under pathological conditions of the intestine, such as inflammatory bowel diseases, cystic fibrosis, host-pathogen interactions. Additionally, they have been widely employed for testing and screening drugs and other compounds[99]. Despite the undoubtable advances in the field provided by organoids their lumen is closed, meaning that the apical surface is almost inaccessible, which makes difficult to use this model for direct experimental stimulations (drug screening and development) or imaging techniques[100]. Currently, in order to overcome this limitation and have easy access to the apical surface, organoids have been tried to culture in a monolayer[101]. Another point to consider, which limits the model, is the lack of cellular heterogeneity, organoids only contain intestinal epithelial cells, and they lack of the immune and mesenchymal cells representation, which also have a relevant contribution for the intestinal regulation and development[101]. Moreover, organoids long-term culture requires a large amount of soluble growth factors, such as R-spondin, Noggin and EGF to achieve a proper phenotype. These are expensive molecules which highly increase the cost of the experiments compared to standard cell lines. At practice, this limits their usability for basic research and large-scale analyses in a lot of laboratories[94,95].

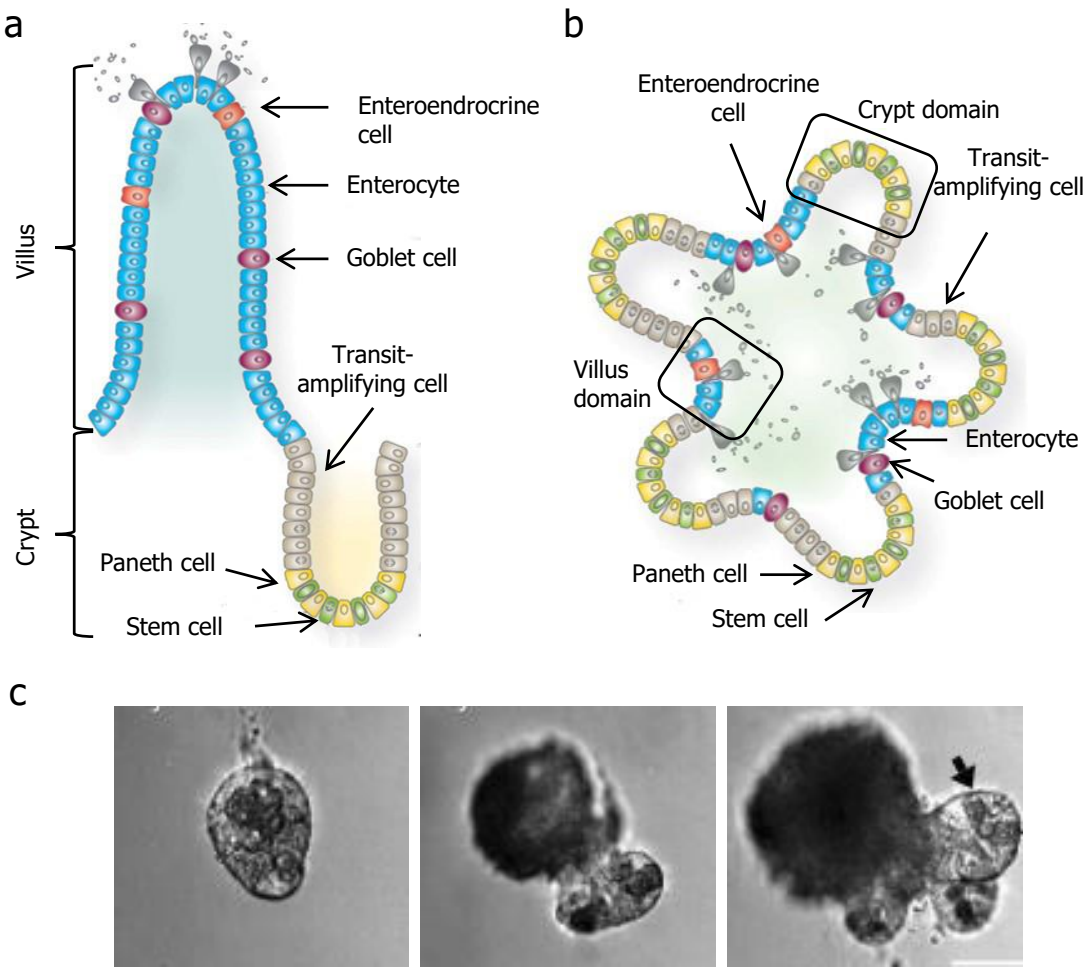

Figure 1.12. Cellular architecture of the intestinal villi–crypt structure. (a) Schematic representation of the *in vivo* small intestinal epithelium. (b) Schematic representation of an *in vitro* organoid, consisting of a central lumen lined by villus-like epithelium and associated crypt compartments (adapted from Leushacke *et al.*)[97]. (c) Bright field images showing the time course of an *in vitro* single $Lgr5^+$ stem cell growing to form the organoid. The darker zone in the center of the organoid corresponds to the lumen of the organoid where dead cells are accumulated. The arrow pointed a crypt domain (adapted from Sato *et al.*)[96].

1.4.2. Gut on chip models of the small intestine

In recent years, the development of perfused microfluidic devices mimicking organ or tissue functionalities, also called organ-on-chips, has grown significantly. Among them, gut-on-chips mimic the intestinal flow to recapitulate the shear forces sensed by cells, and the peristatic movement of the small intestine. In general, reported gut-on-a-chip devices are based on a polydimethylsiloxane (PDMS) chip fabricated using soft lithography, which contains a porous membrane of polyester or polycarbonate that creates two independent microchannels, one mimicking the lumen and the other one mimicking the stroma/endothelium. Epithelial cells are seeded on top of the porous membrane, which is usually coated by ECM proteins, while it is possible to seed other

cell types on the other microfluidic channel. In these devices, the cell culture medium is applied through the microchannel which emulates the intestinal flow of the *in vivo* intestinal tissue.

Nowadays, in the literature we can find several types of gut-on-chip platforms, however, one of the pioneers to develop a gut-on-a-chip system was Imura *et al.*[102]. The chip that they designed was similar to the previous explanation and the medium was pumped through the inlet channel using a microsyringe pump to mimic the vascular flow (Figure 1.13 (a and b)).

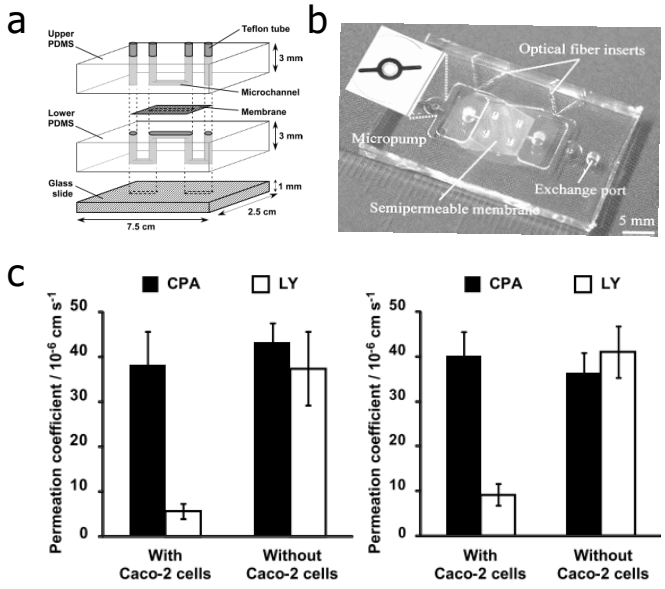

Figure 1.13. *In vitro* human gut-on-a-chip models. (a) Schematic illustration of the integrated microfluidic device. The device consists of two independent upper (AP side) and lower (BL side) PDMS chips. The semipermeable membrane on which the cells are cultivated is suspended in the cell culture chamber by sandwiching between the two PDMS chips. (b) Photograph of the gut-on-a chip device. (c) Permeability coefficients for the cyclophosphamide (CPA) molecule, which is a highly permeable compound and for the Lucifer yellow (LP) molecule, which is a non-permeable molecule, analysed on the chip device (left panel) and on the Transwell® insert (from Imura *et al.*)[102].

They used this device to evaluated intestinal absorption and compare the dynamic gut-on-a-chip devices with the static Transwell® inserts. They proved that using a microfluidic device, the results for permeation tests were more consistent with those obtained using standard Transwell® inserts, thus validating the robustness of the device (Figure 1.13 (c)). Later on, gut-on-a-chip devices were modified to better recreates the native properties and characteristics of the small intestine. For example, Kim *et al.*[103,104] introduced cyclic strain deformations to mimic the intestinal peristaltic motion. The

incorporation of peristaltic movements together with fluid flow induces villus-like formations and cell differentiation with a well-established epithelial barrier giving properties closer to the native intestinal tissue than the static Transwell® inserts. Additionally, this device allows the growth of gut microorganisms on top of a mature and differentiated epithelium without affecting their viability for long-term periods in contrast to the Transwell® inserts, where enterocytes viability decrease significantly after a few days of the co-culture with microorganisms (Figure 1.14).

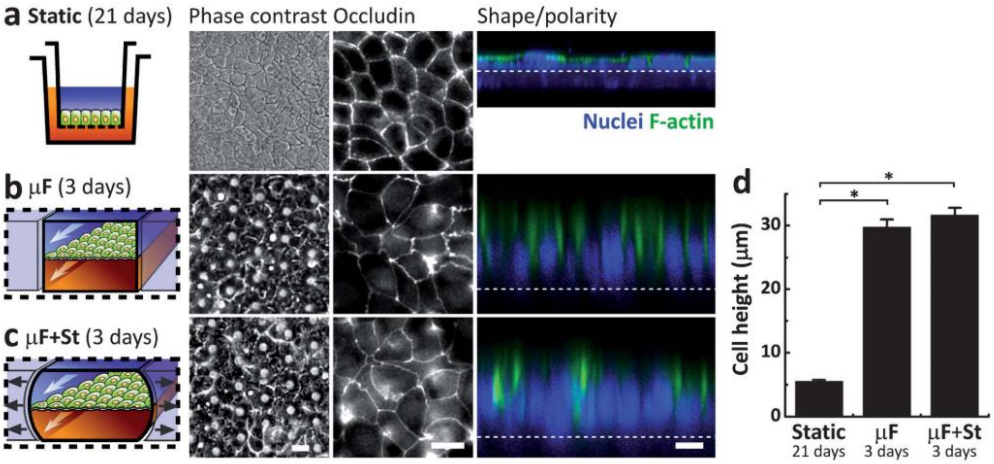

Figure 1.14. *In vitro* human gut-on-a-chip models. Morphology of the Caco-2 epithelial cells on the (a) Transwell® insert (b) in the gut-on-a-chip with flow and (c) with flow and cyclic mechanical strain. Schematic draw of the system (left panel); fluorescence images of the tight junctions (center panel); and confocal fluorescence cross section images of the epithelial cells (right panel) (nuclei in blue and F-actin in green). (d) The average height of Caco-2 cells grown in static Transwell® cultures or on the gut-on-a-chip only with microfluidics (μF) or with microfluidics and mechanical strain (μf + St) (from Kim *et al.*)[103].

Later, the same device was used to study the interaction between gut microbes, enterocytes (Caco-2 cells) and immune cells and thus examine enterocyte response under an intestinal inflammatory condition. To do that, lipopolysaccharide (LPS) and immune cells were introduced to the device through the apical and basolateral microchannels, respectively. They showed that both LPS and immune cells, when they were introduced together with the enterocytes, enterocytes increased the secretion of pro-inflammatory cytokines, which damage the epithelial barrier. With these findings they prove that their gut-on-a-chip device, due to the flow, the peristalsis-like motions and the epithelial-gut microbiome, allows to have a better control of the environment that cannot be stablished using the Transwell® inserts due to each parameter can be modulated independently of the others, suggesting that this platform can be employed for modelling and studying intestinal diseases[103,104]. Finally, Shim *et al.*[105] have upgraded

the microfluidic system through the integration of a natural scaffold made of collagen that mimics the 3D villi architecture of the human intestinal tissue. The collagen scaffold was previously developed by Sun *et al.*[106] following a complex multi-step fabrication method. Unlike the devices explained above, this chip has replaced the porous membrane with a scaffold that recapitulate the intestinal 3D architecture. On the other hand, the device only incorporates a fluid flow to provide shear stress to the cells but does not have peristaltic-like motion (Figure 1.15). They demonstrate by measuring the absorptive permeability and the activity of representative enzymes of Caco-2 enterocytes renders *in vitro* physiological results similar to the behaviour observed *in vivo.*

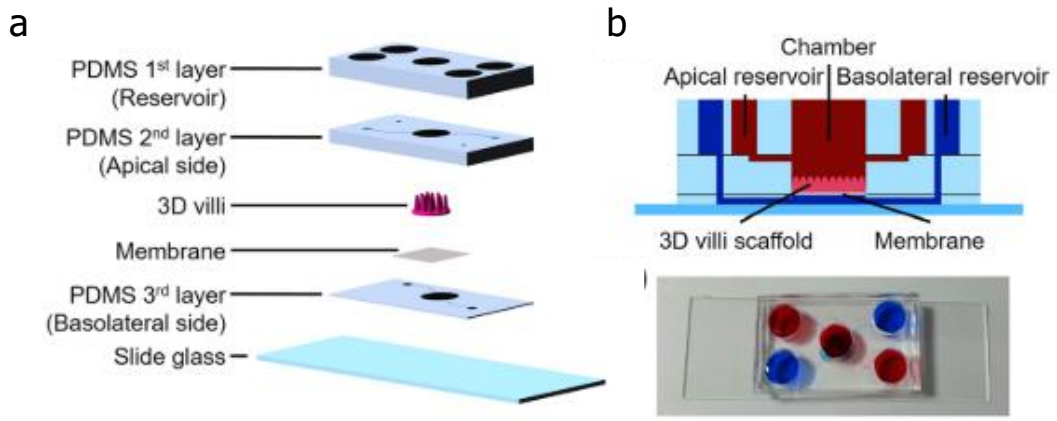

Figure 1.15. In vitro human gut-on-a-chip models. (a) Side-view of the chip. (b) A picture of the microfluidic device showing two sets of reservoirs for the apical (red) and basolateral sides (blue) (from Shim et al.)[105].

One of the major drawback of the gut-on-a-chip devices is the inability to support the lamina propria compartment just below the epithelial cells, like *in vivo* conditions where epithelial and lamina propria cells are in physical contact. Lamina propria cells, such as myofibroblast or immune cells, have been seen that play a relevant role in obtaining good physiological *in vitro* models. Another limitation of these platforms is the absorption of small and hydrophobic molecules by the PDMS, which could modify the bioavailability or absorption studies[107]. Moreover, these devices are not compatible with the standard techniques, such as TEER, and due to its dimensions are difficult to be imaged under the microscopy, without adapting the microscopy setup.

1.4.3. Engineered tissues as 3D *in vitro* models of the small intestine

Trying to overcome practical limitations of intestinal organoids and the gut-on-a-chip devices, we can find in the literature several approaches to model the small intestine *in vitro* that, inspired by tissue engineering strategies, aim to fill the gap between conventional 2D cell cultures and animal models[108,109].

To better recreate the 3D layered structure of the native intestinal mucosa tissue, engineered tissues which include both the epithelial and the lamina propria compartments have been developed[110–112]. To that end, stromal compartment is mimic by employing a thick layers of natural derived proteins, such as gelatin, collagen or Matrigel™, where cells characteristic from the lamina propria can be embedded and epithelial cells, then can be seeded on the surface. For example, Matsusaki M. *et al.*[113] mimic the lamina propria by creating a monolayer or 3D multilayer (8 layers) of normal human dermal fibroblasts (NHDF) embedded in fibronectin-gelatin nanofilms underneath of a Caco-2 epithelial monolayer (Figure 1.16(a)).

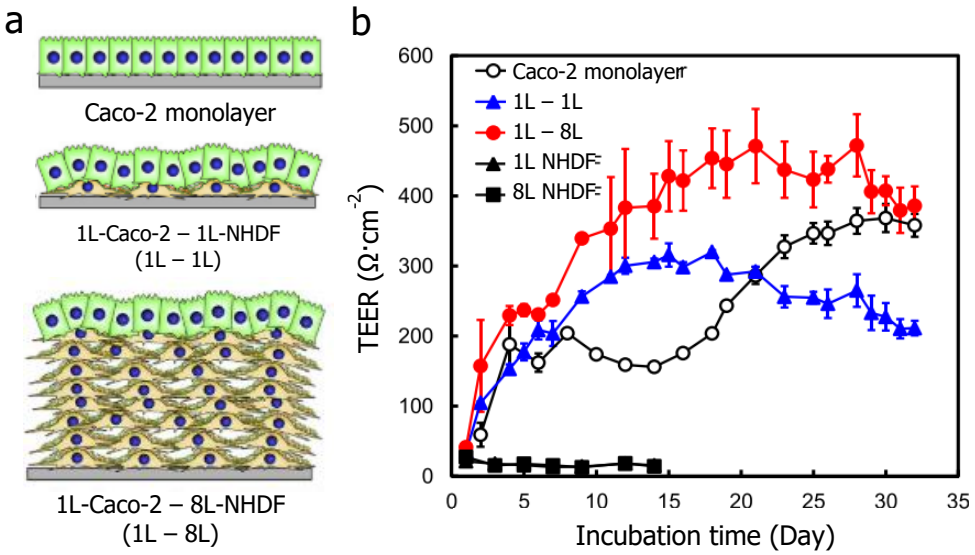

Figure 1.16. In *vitro model* of the intestinal mucosa that mimics the lamina propria by a 3D multilayer of normal human dermal fibroblasts (NHDF). (a) Schematic illustration of Caco-2 monolayer (top) and a 3D model formed by a monolayer of Caco-2 cells seeded on one layer (center) and 8 layers (bottom) of NHDF. (b) TEER values of Caco-2 cell monolayers with and without the contribution of NHDF (from Matsusaki M. *et al.*)[113].

Although, the presence of the 3D multilayer of dermal fibroblasts enhanced the Caco-2 cells growth, and thus epithelial barrier functions (TEER) were reached before compared to the Caco-2 cell monolayer without affecting the Caco-2 transporter proteins expression, the dermal fibroblasts' organization and distribution do not recreate the one

found in the native tissues (Figure 1.16 (b)). In the native tissues, cells are homogenously distributed through the lamina propria and not organized in multilayers. On the other band, Pereira *et al.*[112] developed a 3D *in vitro* model of intestinal mucosa that imitates stromal-epithelial interactions. To do that, intestinal myofibroblasts (CCD-18Co cells) were embedded in a scaffold composed of Matrigel™ onto which epithelial enterocytes (Caco-2 cells) and mucus producing cells (HT29-MTX cells) were seeded (Figure 1.17 (a and b))[112].

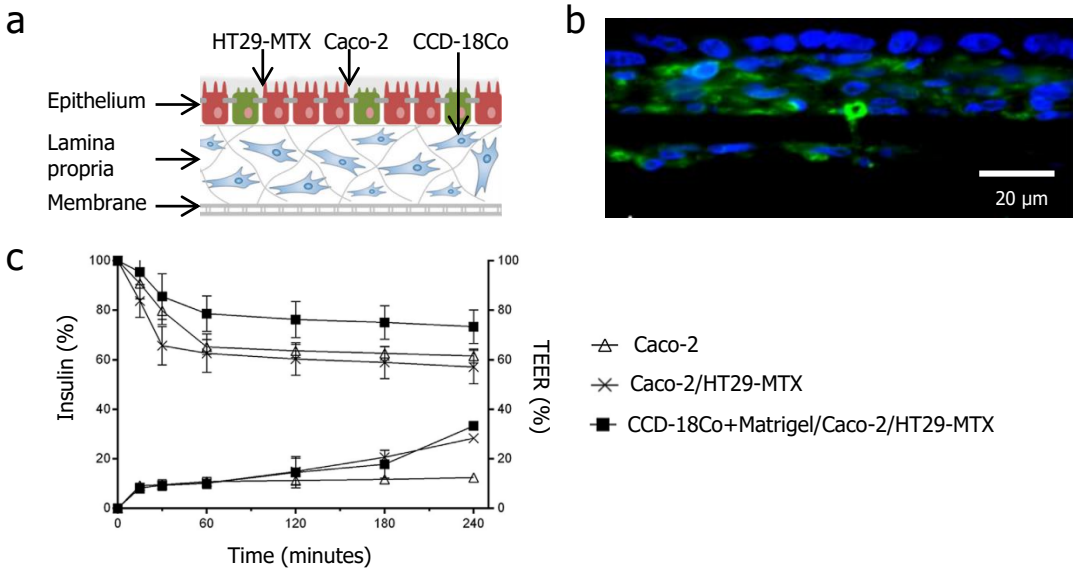

Figure 1.17. *In vitro* model of intestinal mucosa that mimics the lamina propria through encapsulation of mesenchymal cells in a 3D structure. (a) Schematic representation of the embedded CCD-18Co in the Matrigel™ while Caco-2 and HT29-MTX cells are seeded on top. (b) Immunostaining image to show cell distribution. (c) Acumulative transport of insulin and TEER values when there are goblet cells (HT29-MTX) in the model (from Pereira *et al.*)[112].

This report verified that the incorporation of 3D matrix combined with cellular heterogeneity allow to obtain more relevant physiological results due to the cell-cell and cell-matrix interaction. They showed that myofibroblasts were capable of secrete ECM matrix and thus enhance the epithelial cells growth. Due to the Caco-2 and HT29-MTX cells co-culture, the mucus layer and the interaction of myofibroblasts with epithelial cells, the model allows to obtain insulin permeability values closer to physiological data reported (Figure 1.17 (c)). Another example that incorporates the immunocompetent intestinal system was created by co-culturing immune cells (macrophages and dendritic cells) embedded in a collagen, and then epithelial enterocytes (Caco-2 cells) were seeded (Figure 1.18 (a))[114].

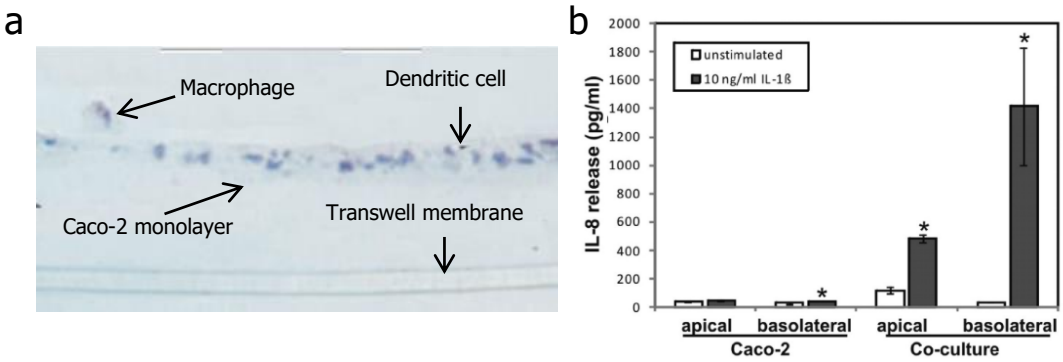

Figure 1.18. *In vitro* model of the intestinal mucosa that mimics the lamina propria through encapsulation immune cells in a 3D structure. (a) Histological image of the 3D triple co-culture with immune cells (macrophages and dendritic cells) embedded in a collagen matrix and Caco-2 cells were seeded on top on the hydrogel. (b) IL-8 protein release of Caco-2 cells in single culture or in co-culture with macrophages and dendritic cells cultivated in a Transwell® membrane (from Leonard *et al.*)[114].

This setup allows to induce an inflamed intestine through the exposure of the cells to pro-inflammatory stimuli and then Caco-2 cells response was evaluated, showing that when there were immune cells embedded in the stromal compartment, the inflammatory cytokine response was stronger than Caco-2 monoculture (Figure 1.18 (b)). This model could be a good approximation to screen drugs and molecules used to treat IBDs or to study the interaction of the nanoparticles under an inflammation state. Despite their undoubtable benefits when representing the biology of the intestinal lamina propria, these approaches have in common a compromised mechanical stability due to the degradation of the collagen natural scaffold by the cells for long-term cultures.

Apart from the engineered tissue models adapted to the Transwell® inserts, other approaches to mimic the intestinal tissue can be found in literature. For instance, Chen *et al.*[110] were pioneers in developing an *in vitro* model of small intestine that mimics the gastrointestinal tube by including a hollow lumen. (Figure 1.19). To create the scaffolds with hollow channels a multistep process is followed. First, a cylinder PMDS mold with the proper dimensions was fabricated, secondly, a screw was inserted across the cylinder mold, then the silk was deposited into the cylinder. Following that, constructs were lyophilized to polymerize the silk, and thus creating pores to the scaffold. After the process, the screw was removed to obtain a hollow channel, which mimics the lumen. Finally, stromal cells (primary human intestinal myofibroblast cells) were introduced in the core of the scaffolds by deposition them on the scaffold surface and wait for their migration into the scaffold through the pores of the construct. Then, enterocytes cells (Caco-2 cells) and mucus producing cells (HT29-MTX cells) were seeded on the surface

of the scaffold. These 3D intestinal engineered tissues enhanced the mucus secretion and its accumulation at the epithelium. Moreover, they are able to model the oxygen gradient concentrations found along the *in vivo* lumen. The oxygen gradient generated in the hollow channel was beneficial to mimic the aerobic and anaerobic conditions of the lumen and thus be able to model the luminal colonization of intestinal bacteria. Although the advantages of this model, the fabrication process of these constructs were very laborious, making not optimal for routine studies.

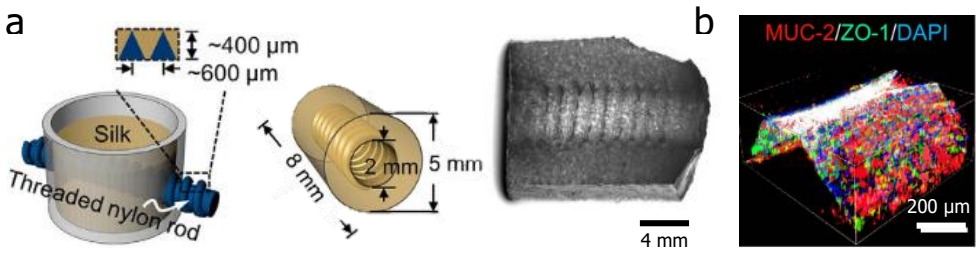

Figure 1.19. (a) Fabrication process for silk-based porous scaffolds to mimic the lumen of the small intestine. (b)A fluorescence image of a cell covered ridge (from Chen *et al.*)[115]

Despite these models represents a 3D structure that recreates the lamina propria compartment of the native intestinal tissue, they still have limitations, such as the short-term life durability of the natural scaffold due to the capability of the cells to degrade it, compromising the scaffold integrity and make them not useful for long time experiments (21 days of culture) and the complex fabrication process to get the scaffold, also make them not useful for daily experiments.

1.5. Hydrogels as scaffolds to mimic the lamina propria of the small intestine

One of the most significant limitations of the standard epithelial cell cultures based on the cell monolayers grown on Transwell® inserts is that cells are seeded on a hard substrate that does not provide the mechanical, the biochemical and the cellular environment of the stromal *in vivo* tissue. In particular, cell-matrix interactions are affected by the absence of an extracellular matrix (ECM) surrogate. The ECM is composed of a heterogeneous, dynamic and complex network of proteins and polysaccharides, which are produced, degraded and remodelled by the resident cells[116]. Generally, proteins and polysaccharides of the ECM are fibrous proteins, (collagen, elastin, fibrillin, and fibulin) adhesive glycoproteins (laminin, fibronectin, integrin,

thrombospoidin and tenascin), and glycosaminoglycans, which are heteropolysaccharides[116,117]. Moreover, it contains a high amount of water, facilitating the diffusion of nutrients, oxygen and waste products of the resident cells[118]. The composition and organization of the ECM is specific of each tissue and specie[119]. The ECM provides the physical and mechanical stability needed to maintain the tissue and organ structure. Besides that, the ECM biophysical properties (stiffness, porosity and topography) together with the biochemical cues influence to the surrounding cells in morphogenesis and homeostasis by regulating the activity of signalling molecules and the cell characteristics, such as shape, survival, proliferation, migration and differentiation through cell-matrix interactions[116,118–120]. In the case, that ECM is dysregulated and its structure is lost, this affects the cell-matrix interactions and provokes an aberrant cell functionality which can let to diseases, such as cancer[121].

The ECM is divided in the interstitial matrix, which is a mixture of polysaccharides and fibrous proteins filling the intercellular spaces, and the basement membrane, which is a thin non-cellular tissue layer beneath the epithelial cells, separating them from the connective tissue (Figure 1.20 (a)) (see section 1.1). The lamina propria lies beneath the basement membrane and is composed of an ECM containing several types of cells, such as fibroblasts, myofibroblasts, lymphocytes, macrophages, eosinophils, leukocytes, plasma cells and mast cells[122]. The lamina propria provides support to the epithelium, especially to the villi, by a spongy framework of interconnected fibroblasts and myofibroblasts[19]. In addition, it protects the epithelium from the external pathogens through the activation of its immune cells[41]. As a consequence, a scaffold mimicking the small intestinal mucosa should provide a mechanical environment similar of the *in vivo* ECM of the intestinal mucosa, allowing in parallel the attachment, the proliferation and the migration of the cells, as well as the the diffusion of secreted biomolecules, the degradation of the matrix and its remodelling.

Hydrogels are the biomaterials most widely used in the tissue bioengineering field as 3D structural supports for *in vitro* cell culture due to their resemblance to the native ECM of soft tissues[123–125] (Figure 1.20). Hydrogels are 3D networks formed from hydrophilic polymers physically or chemically crosslinked to form insoluble polymer matrices[125]. They possess a huge ability to swell when they are in contact with water-based fluids, meaning that they are capable of absorbing large amount of water into their network until reaching the equilibrium[124]. The porosity of the hydrogels ranges from 1 nm to more than 100 μm[126]. Such porosity allows the diffusion and the transport of

nutrients, oxygen and waste compounds within the network. On the other hand, the mechanical properties of the hydrogels are tuneable, being possible to match them with those of the native tissue to be modelled. Hydrogels not only have the ability to support the growth of cell monolayers on top of them, but also to sustain the culture of cells embedded inside their network[127]. These characteristics make hydrogels good candidates for *in vitro* scaffolds[128].

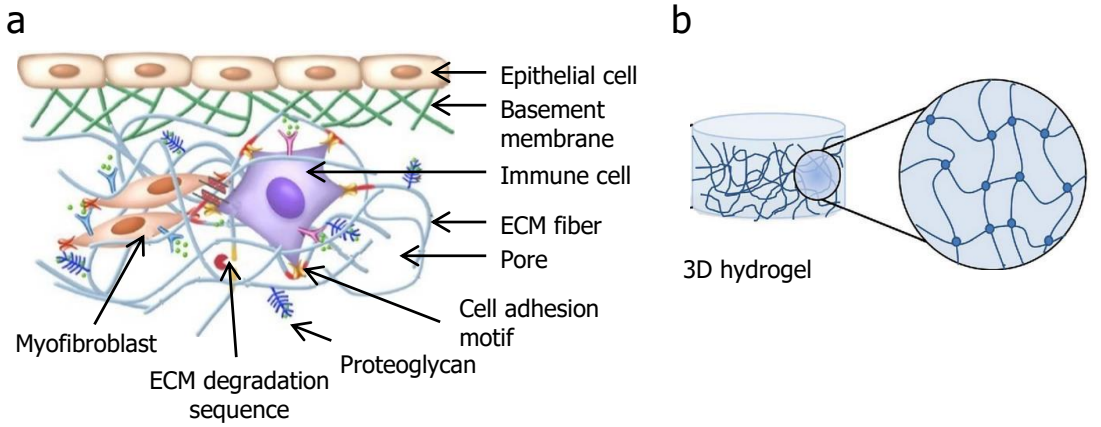

Figure 1.20. Extracellular matrix internal network. (a) Schematic illustration of the ECM features and components (adapted from Huang *et al.*)[117]. (b) Illustration of a hydrogel and its internal structure.

1.5.1. Hydrogels according to their source

Depending on the origin source of the hydrogels, they are classified as natural and synthetic hydrogels, both types have advantages and disadvantages. On one hand, natural polymers, which are extracted from tissues[129], have inherent batch-to-batch variability[128,129], however due to the high amount of tests to control de quality of the polymer after the extraction, this is not a limiting factor. Additionally, natural polymers possess biochemical cues, which are essential for cell adhesion, growth and migration[123]. Additionally, as they come from a natural source, this makes them inherently biocompatible and highly biodegradable through the cell's ability to recognise degradation motifs. This degradation is performed by matrix metalloproteinases, which are secreted by the cells, and it allows matrix remodelling, usually leading to cell proliferation and migration[130]. However, a fast degradation rate gives mechanical instability to the scaffold, and in practice this degradation limits the time needed for cell culture. In some cases, this is overcome by seeding high cell density to balance the degradation of the ECM with the production of new ECM[125,128,129]. Somoetimes, however,

the high cell densities, used to overcome the scaffold degradation, do not match the ones found in the native tissues, resulting in inaccurate *in vitro* models[8].

Collagen and Matrigel™ are the natural proteins most used as scaffolds to mimic the native ECM of tissues. Matrigel™, is a heterogeneous mixture of ECM components, mainly formed by laminin, collagen IV and enactin, with a non-defined composition. It is widely used as a ECM substitute, constituting an excellent substrate for cell growth and proliferation despite its batch-to-batch variability[131]. Unlike Matrigel™, collagen contains a single protein type, but is the most abundant protein in the ECM, so it is also widely used as a scaffold[129]. In the literature we can find small intestinal models that use either Matrigel™ or collagen as scaffolds to recreate the mucosa environment. Pereira *et al.* [112] embedded CCD-18Co intestinal myofibroblasts within a thick layer of Matrigel™ onto which Caco-2 cells and HT29-MTX cells were seeded and grew successfully. Leonard *et al.*[114] modelled the mucosa by embedding macrophages and dendritic cells in a thick collagen layer to recreate the lamina propria, and Caco-2 cells were seeded on top.

Other materials that have been used for intestinal tissue engineering are alginate[132], chitosan[133] or hyaluronic acid[134]. Alginate is a polysaccharide component derived from brown algae cell walls and some bacteria. Its structure is based on two different monomers organized into blocks (Figure 1.21 (a)).

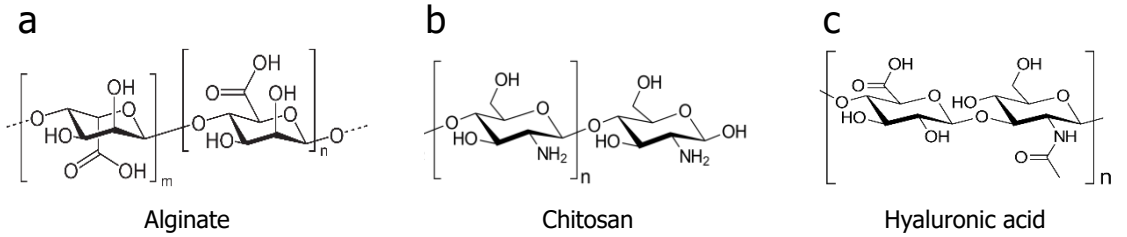

Figure 1.21. Chemical structures of some natural polymers repeat units used for fabrication of natural hydrogels applied in tissue regeneration and biomedical applications. (a) Alginate. (b) Chitosan. (c) Hyaluronic acid.

By contrast, chitosan comes from the deacetylating chitin, from the arthropods exoskeleton. It is a linear polysaccharide composed of β-(1-4)-linked D-glucosamine with randomly dispersed N-acetyl-D-glycosamine groups (Figure 1.21 (b)). Its main advantages are the low cost, easy sterilization, biocompatibility and anti-bacterial properties. However, it presents poor mechanical properties. Finally, hyaluronic acid is a component of the ECM and it is composed of D-glucuronic acid and N-acetyl-D-

glucosamine (Figure 1.21 (c)). It is rapidly degraded by hyaluronidases, which can compromise the hydrogel stability[129].

In recent years, gelatin, which is a natural polymer approved by the US Food and Drug Administration (FDA)[135 136], has emerged as a hydrogel with potential use in medical applications such as drug and cell delivery, tissue engineering or wound dressing[137]. Although it has been extensively employed in bioengineering field, to our best knowledge, it has not been used to produce engineered intestinal tissues. Gelatin is synthesised through the hydrolysis and denaturation of collagen by an acid (gelatin type A) or alkaline (gelatin type B) treatment[138]. During this process the triplex helix that forms the collagen proteins breaks down into single molecules to produce gelatin (Figure 1.22 (a))[139]. The cell adhesion sequences, arginine-glycine-aspartic acid (RGD) peptide sequences, and the matrix metalloproteinase (MMP) degradation sequences are not affected by the denaturation. Consequently, gelatin, just as collagen, exhibits a proper biocompatibility, bioactivity, biodegradability and low antigenicity[129]. In contrast, gelatin is a low cost product and the immunogenic properties of the gelatin are reduced compared with those of its precursor[140]. Despite of that, thermostability of gelatin is minimal above 37ºC, making it soluble at body temperature, and therefore compromising their mechanical integrity when used in engineered tissues[141141]. To overcome this limitation, gelatin is chemically modified by the introduction of an active group, such as acryloyl groups into -NH_2 and –OH groups of the gelatin side chain. One of the gelatin product more used in the tissue engineering field is gelatin methacryloyl (GelMA). In 2000, Van Den Bulcke *et al.* [141] synthesised GelMA polymer through the reaction of gelatin with methacrylic anhydride (MA). During this reaction, predominantly free amino groups of the lysines and hydroxilysines and some hydroxyl groups are substituted by the acryloyl groups of the MA, resulting in GelMA polymer (Figure 1.22 (b)). GelMA, unlike gelatin, is able to photocrosslink in the presence of a photoinitiator and under light exposure, resulting in a thermostable hydrogel above 37ºC[140,142,143]. It must be emphasized that the cell adhesive RGD sequences, and cell degradable MMP sequences of the gelatin are not significantly affected during the methacryloyl process[144]. Overall, these properties have pushed GelMA as an ideal candidate for clinical applications such as cell transplantation, tissue regeneration[145,146], and drug[147] or growth factor[148] delivery. However, natural derived hydrogels are not always ideal biomaterials for tissue engineering applications as they are limited by low mechanical strength and uncontrolled degradation. These limitations may be overcome by synthetic polymers.

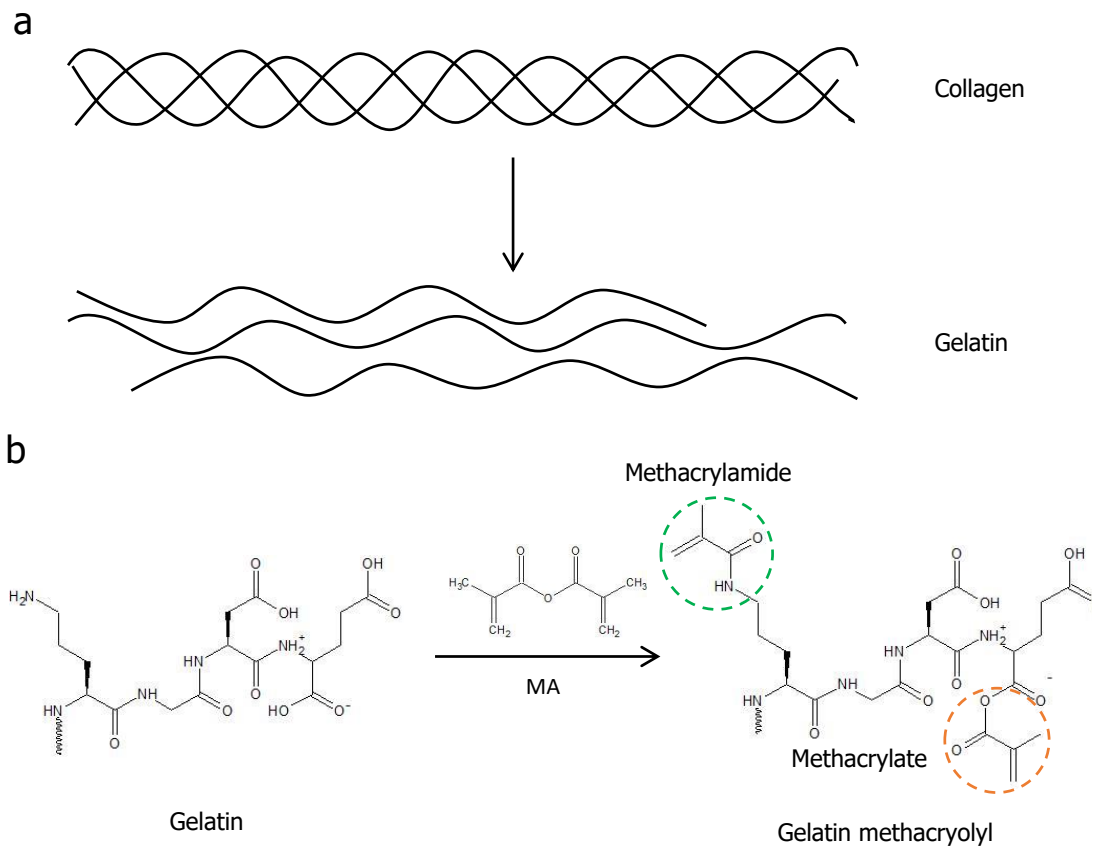

Figure 1.22. Synthesis of photocrosslinkable gelatin polymer. (a) Triplex helix that forms the collagen is denaturalized by acid or alkaline treatment to break them into single molecules, known as gelatin. (b) Covalent functionalization of the gelatin with unsaturated methacryloyl groups [H_2=CH-C(=O)–] by reaction with methacrylic anhydride (MA) to give gelatin methacryolyl (GelMA), which is a photocrosslinkable polymer. Methacryloyl groups are a mixture of methacrylamide (green circle) and methacrylate groups (orange circle), although the methacrylamide groups are the majority, around 90% of all the methacryloyl groups.

Synthetic hydrogels, which are chemically synthesised, are an alternative to their natural counterparts to mimic ECM. They can be designed with high biocompatibility and low variation in composition from batch-to-batch[149]. Additionally, synthetic hydrogels present good mechanical properties and low biodegradability, providing long-term stability to the scaffold. Some of most used synthetic polymers to form hydrogels are poly(2-hydroxyethyl methacrylate) (PHEMA), poly(vinyl alcohol) (PVA), polyvinyl pyrrolidone (PVP) and poly(ethylene glycol) (PEG) (Figure 1.23)[149]. The main drawback is that most of them fail to recapitulate essential biological features such as the bioactive sequences necessary for supporting cell adhesion, migration and proliferation[123,149]. To promote these functions, they are combined with natural derived polymers such as collagen, laminin, which contains RGD peptides, or directly with RGD sequences and MMP sequences.

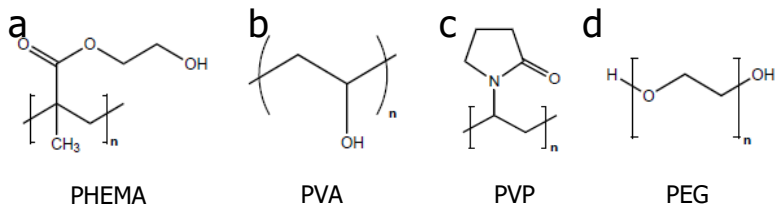

Figure 1.23. Chemical structure of some synthetic polymers used for fabrication of hydrogels applied in tissue regeneration and biomedical applications. (a) Poly(2-hydroxyethyl methacrylate) (PHEMA). (b) Poly(vinyl alcohol) (PVA). (c) Polyvinyl pyrrolidone (PVP). (d) Poly (ethylene glycol) (PEG).

PEG is the most employed synthetic biomaterial in tissue engineering. PEG has been approved by FDA in several clinical applications because its hydrophilicity, high water solubility, low cost, bioinert structure, non-immunogenicity and non-toxicity, especially when the molecular weight of PEG is above 400 Da becuase is easily excreted from the human body[136,150,151]. Moreover, its mechanical properties, can be easily tuned to achieve stiffness values matching those of native soft tissues. Despite its benefits, PEG alone cannot provide support for cell attachment and tissue formation as it does not possess cell adhesion sequences. This gap is filled by the incorporation of specific cell adhesion and cell degradation sequences to render PEG bioactive and degradable[136,152]. The improvement of PEG bioactivity is performed by modifying PEG chains through the introduction of cell adhesive peptides, such as RGD motifs or by mixing them with natural polymer[152].

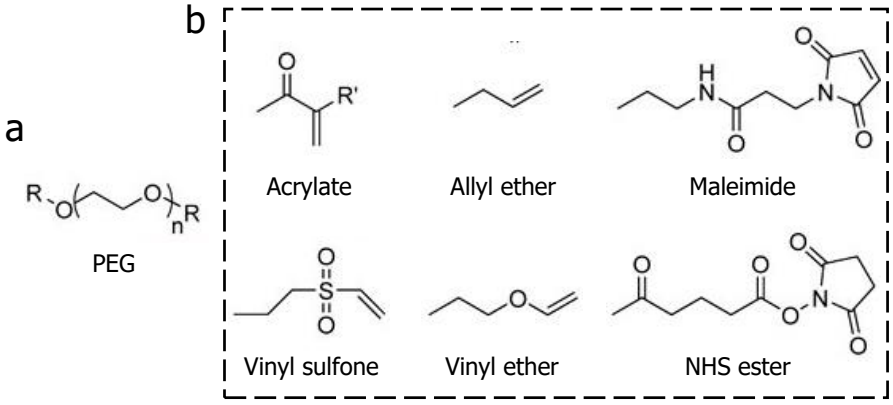

Figure 1.24. Modification of poly (ethylene glycol) polymer by covalently attaching a reactive group to the end of the chain. (a) Molecular structure of PEG, showing where the reactive chain reacts (R). (b) Possible reactive chains ends that can be incorporated to PEG polymer (R) (adapted from www.sigma.com)

PEG by itself does not polymerize, so it is chemically modified to crosslink and thus to form the hydrogels. The main modifications involve attaching to the hydroxyl

ending groups a reactive chain such as acrylate, allyl ether, maleimide, vinyl sulfone, NHS ester or vinyl ether groups (Figure 1.24). These modifications result in different PEG-based molecules such as poly(ethylene glycol) diacrylate (PEGDA), poly(ethylene glycol) divinyl ester (PEGDVE), poly(ethylene glycol) dimethacrylate (PEGDMA), and poly(ethylene glycol) dithiol (PEG-SH) (Figure 1.25).

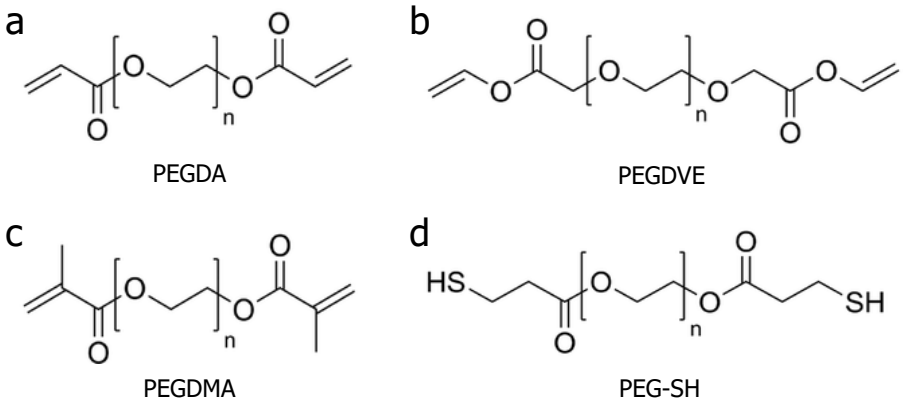

Figure 1.25. Chemical structure of PEG based polymers after adding the reactive end chain to PEG. (a) Poly(ethylene glycol) diacrylate (PEGDA); (b) Poly(ethylene glycol) divinyl ester (PEGDVE); (c) Poly(ethylene glycol) dimethacrylate (PEGDMA); and (d) Poly(ethylene glycol) dithiol (PEG-SH).

The most common method of crosslinking PEG polymers to form PEG-based hydrogels is free radical polymerization using PEG-acrylates, especially PEG-diacrylate (PEGDA) (Figure 1.25 (a)). PEGDA photocrosslinking requires the presence of a photoinitiator molecule in the pre-polymer solution which polymerize under light exposure [136].

PEGDA-based hydrogels are widely used as drug delivery[153] , as well as 3D scaffolds in the tissue engineering field, for example mimicking the cartilage[154] . Actually, PEGDA hydrogels have been used by our group to produce 3D scaffolds mimicking the small intestinal epithelium. Castaño *et al.*[155] fabricated 3D villus-like PEGDA scaffolds using a moldless photopolymerization technique. It was shown that Caco-2 cells seeded on top of the 3D constructs are capable to grow, to cover properly the scaffold, and to differentiate into mature enterocytes forming an effective epithelial barrier with TEER values that were significantly closer to *in vivo* values that conventional 2D monolayers grown on Transwell® inserts (Figure 1.26). They found that, the soft substrate and the 3D curvature provides cells with physicochemical features impacting their polarization and organization of the tight junctions. Additionally, in our group, to better visualize this cell morphology and the localization of epithelial markers in the 3D soft microstructured

PEGDA hydrogel by high–resolution and high–magnification microscopy a embedding method, which preserves the shape of the structures and does not damage the cell monolayer has been developed. In here, they corroborated that the topography and the curvature of the structures are essential in the cell phenotype[156].

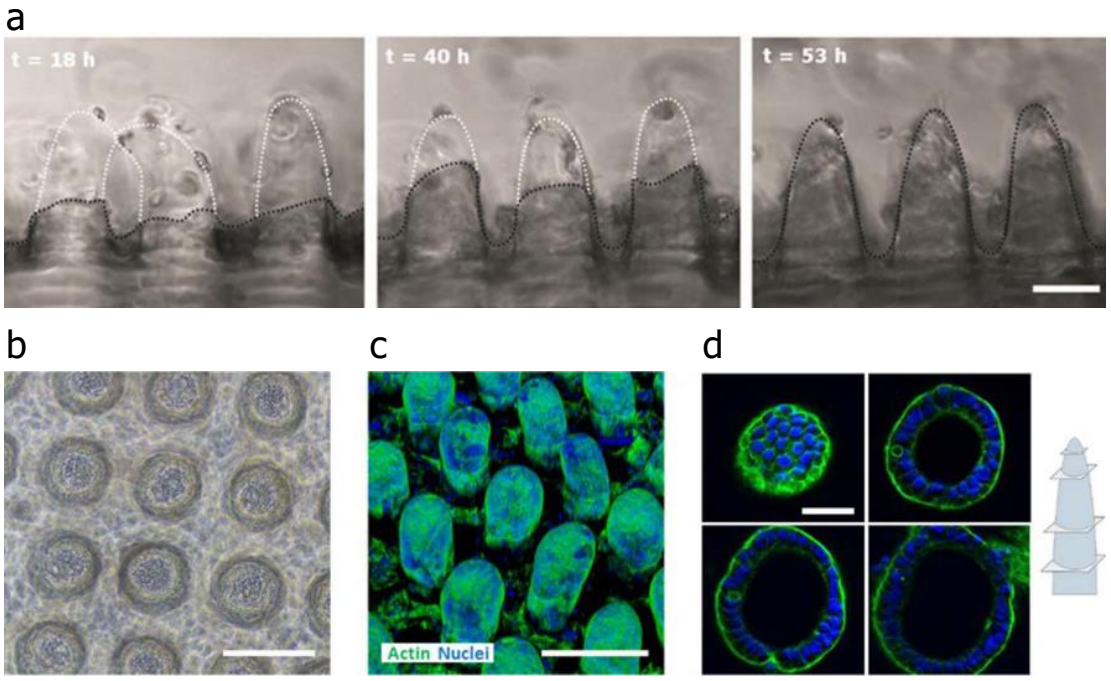

Figure 1.26. Caco-2 cell culture on PEGDA villi-like 3D scaffolds (a) Time-lapse microscopy images showing the Caco-2 cells migration upwards. (b) Top view bright field images of the villi-like PEGDA hydrogels. (c) Confocal projection of Caco-2 cells grown on the 3D scaffolds for 21 days. (d) Detailed cross-sections of a representative Caco-2 cell covered micropillar (from Castaño *et al.*)[155].

Later on, in our group these scaffolds have been used to culture the organoid-derived crypts. They showed that, villus-like PEGDA hydrogels support the growth of intestinal cells derived from organoids. Additionally, their proliferation capacity was improved by supplement the cell medium with medium derived from intestinal subepithelial myofibroblasts, suggesting that subepithelial myofibroblasts had a relevant role in the epithelial monolayer development[157]. However, major limitation of the synthetic scaffolds, such as PEGDA is the lack of long-term cell viability for embedded cells, which are needed to reproduce stromal compartment of the lamina propria, without previous modifications of the scaffold by the incorporation, for instance of cell adhesion sequences in the polymer chains.

A way of overcoming the individual drawbacks of natural and synthetic polymers while maintaining their benefits is combing both in a single hydrogel[158]. It has been

reported that the incorporation of synthetic biomaterials into GelMA hydrogels enhance GelMA physicochemical and mechanical properties. Besides this, the properties of the resulting hydrogel can be adjusted and optimized to match those of the native tissues[159] by modifying the total polymer percentage, and the ratio between natural and synthetic polymers. For example, Wang *et al.*[160] showed that the incorporation of PEGDA into GelMA hydrogels reduced the hydrogel degradation rate, providing hydrogels with good stability for up to more than 4 weeks. Moreover, the incorporation of PEGDA polymer within the hydrogel does not compromise cell viability and biocompatibility.

1.6. Crosslinking in hydrogels

1.6.1. Physically and chemically crosslinked hydrogels

Hydrogels can be physically or chemically crosslinked. Physically crosslinked hydrogels, which do not required the use of crosslinking agents or chemical modifications[161,162], are formed by molecular entanglements, hydrophobic interactions, ionic interactions, electrostatic interactions and hydrogen bonding. All these interactions are non-permanent, non-stable and weak, and they can compromise the stability of the hydrogel because sometimes they can be easily reversed and broken. However, they are sufficient to make hydrogels insoluble in aqueous solutions[163]. Although both natural and synthetic polymers may be physically crosslinked, it is mainly used to obtain hydrogels derived from natural sources. For example, Matrigel™, a natural polymer, jellifies when going from low to high temperatures. Meanwhile, poly(di(carboxyphenoxy)phosphazene) is a synthetic polymer that forms an hydrogel upon interaction with cationic ions[164].

On the other hand, chemically crosslinked hydrogels are formed through covalent bonds between the polymer chains. The resultant hydrogel network is permanently and irreversibly crosslinked, resulting in stable hydrogels over the time, with better mechanical properties and stability under physiological conditions than their physically crosslinked counterparts. However, in most cases the polymer chain needs to be modified by the incorporation of a functional group to allow the crosslinking process. Apart of the polymer modifications, sometimes an external agent is added to the polymer solution to trigger the reaction. In some cases, by-products derived of the polymerization process can be cytotoxic for cells. Predominantly, chemically crosslinked hydrogels can be created by (I) enzyme catalysed reactions, (II) click chemistry or (III)

photopolymerization. Enzymatic crosslinking reaction takes place when an enzyme is added to the polymer solution and catalyses the chemical reaction between polymer chains to form the hydrogel. There are a large number of enzymes employed for this purpose, such as transglutaminases, peroxidases, transferases, etc[161,162]. For example, transglutaminase along with calcium ions promote the formation of amide bonds between carbozamide and amine groups[165]. Hydrogels crosslinked by click chemistry are created when two reactants are linked through the interactions of two highly reactive functional groups such as thiol-vinyl, thiol-maleimide, or azide-alkyne. This reaction does not require external molecules to be initiated. However, the polymer chains need to be previously modified by the incorporation of a reactive group. Last, photocrosslinkable hydrogels are formed when a photosensitive compound is added to the polymer solution, followed by light exposure to obtain the hydrogels. Polymers are previously modified with the incorporation of a photosensitive functional group into their chains. Activation of photosensitive compound under suitable light wavelength triggers the reaction between functional groups of the polymer molecules and so chains are covalently crosslinked[161,162].

1.6.2. Polymerization mechanisms

The polymerization is the process where monomer chains react with other chains in the solution to form the 3D networks. According to the polymerization reaction mechanism, there are two types of polymerization mechanism: (I) step-growth and (II) chain- growth polymerization. The main difference between both the molecular weight dependence on the extent of monomer conversion. In the step-growth polymerization, such as click reactions, any polymer chain (monomer, oligomer, etc) that has a functional group can react independently with other active functional groups present in the solution, and there is no need to add an external agent to initiate the reaction. In this mechanism, the polymerization begins with the formation of dimers from monomers and then chains systematically increase in size until high molecular weights are achieved (Figure 1.27 (a, left panel)). Monomers are consumed early in the reaction, resulting in a slow increase of molecular weight at the beginning of the process, with high molecular weights only obtained later on, when oligomers and polymers react between them. High molecular weight polymers are achieved after long reaction times (Figure 1.27 (a, right panel))[166]. In contrast, chain-growth polymerization, such as free radical or ionic polymerization, takes place when monomers are added directly to the active sites of the

polymer chain in an arranged manner. Unlike step-growth, during chain-growth polymerization monomers react only with functional groups that have previously been activated by an initiator. This step is known as initiation step. Then, the monomers attach to the polymer chains and the reactive center is transferred to the end of the chain, referred as propagation step. This step is consecutively repeated until the reactive centers are consumed, which corresponds to termination step (Figure 1.27 (b, left panel)). This process, unlike the step-growth mechanism, gives high molecular weight polymers from the beginning of the reaction. Mainly, reaction rate depends on the initiator concentration, as well as its efficiency. Short reaction times give high molecular weight polymers (Figure 1.27 (b, right panel))[166].

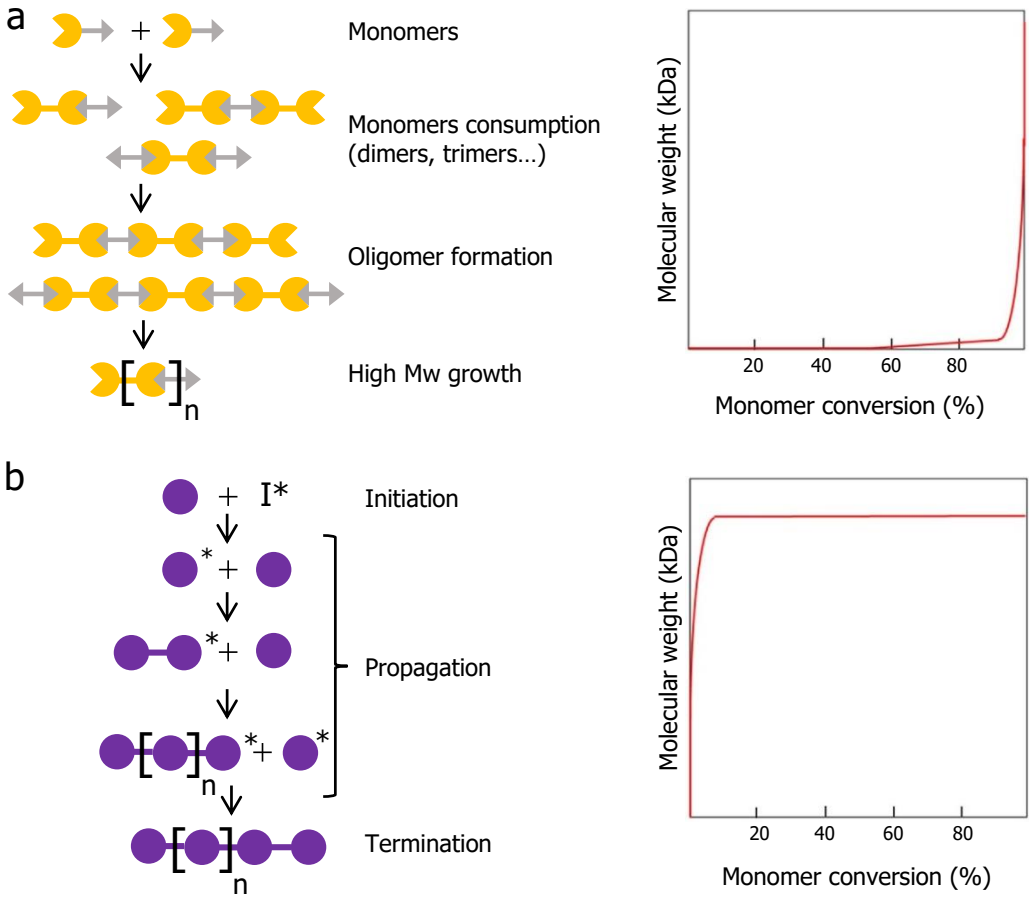

Figure 1.27. Schematic illustration (left panel) and polymerization conversion percentage (right panel) of the (a) step-growth polymerization; and (b) chain-growth polymerization. I* are radicals from the photoinitiator (adapted from Bossion *et al.*)[166].

1.6.3. Photocrosslinkable polymers to form hydrogels

Photopolymerization is the process in which the polymer solution is converted to a polymer network or a hydrogel by chain-growth mechanisms through the aid of a

photosensitive molecule, referred as photoinitiator. Free radical photopolymerization, which is a type of chain-growth, is preferred in bioengineering and biomedical applications over physical crosslinking and other covalently crosslinking reactions, such as enzymatic or click chemistry, due to its several unique advantages. These advantages include (I) a proper spatiotemporal control, (II) crosslinking under mild conditions (room temperature, aqueous solution and neutral pH), and (III) polymerization reaction takes place at high speed which decreases cell damage[167]. On the other hand, the main limitation is that the present of oxygen limits the reaction as oxygen reacts with free radicals formed and decrease the polymerization rate[136]. In the free radical polymerization to crosslink and form hydrogels, polymer solutions containing a photoinitiator are exposed under visible or UV light. The light interacts with the photoinitiator, which absorbs and triggers its decomposition into free radicals that start the polymerization process to end up with a crosslinked hydrogel network[168]. Free radical photopolymerization is divided in three steps: (I) initiation, (II) propagation, and (III) termination (Figure 1.28). In the initiation step, the photoinitiator decomposes into two reactive free radicals with unpaired electrons following a kinetic constant. Then, free radicals react with the vinyl groups (carbon-carbon double bonds) of the acrylate groups in the monomer chain to form monomers with free radicals. Then, it comes the propagation step, one electron from the free radical monomers reacts with one carbon of the vinyl groups of the polymer chains and attach to them, making the polymer chain grow. Whereas, the other electron from the free radical monomer attacks the second carbon of the double bond, creating a free radical for the whole polymer chain. This step propagates until there are not any more monomers and the termination step takes place. Termination step occurs when two unpaired electrons from the polymer chains are coupled together creating a longer polymer chain, known as combination or coupling. In other cases, although it is more rare, the polymerization can be terminated by a disproportionation reaction, in which a radical center is transferred from one polymer chain to another radical center from another polymer chain[169,170].

The presence of oxygen molecules during the free radical photopolymerization limits or inhibits the reaction. Free radicals from the photoinitiator, the monomers or the growing chains react with the oxygen in the solution, leading peroxy radicals, which have low ability to react, compromising the kinetics of the reaction and the final polymer conversion ratio[155].

1. Initiation step

1.1. Photoinitiator decomposition

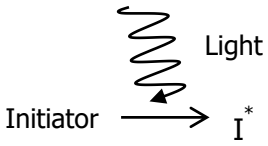

1.1. Chain activation

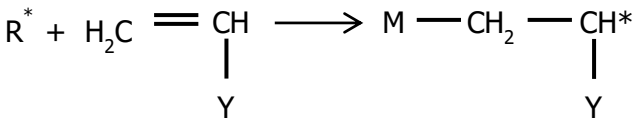

2. Propagation step

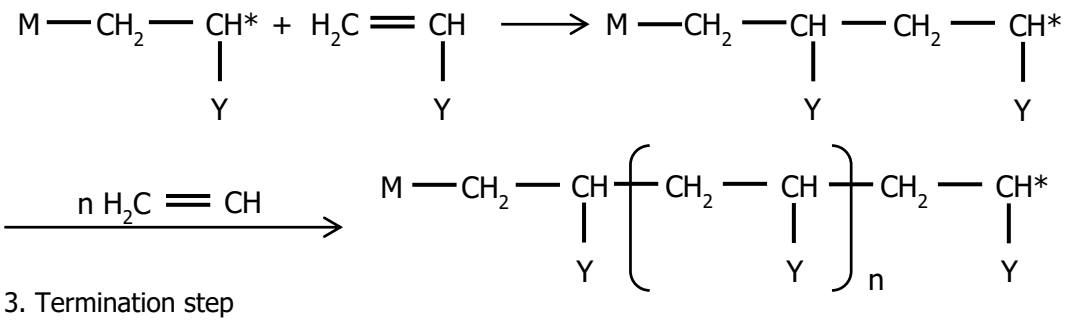

3. Termination step

a) Combination (coupling)

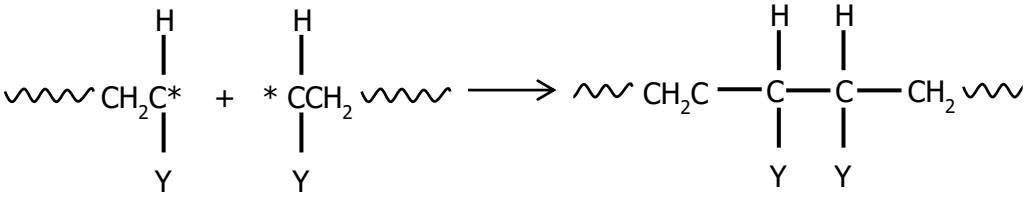

b) Disproportionation

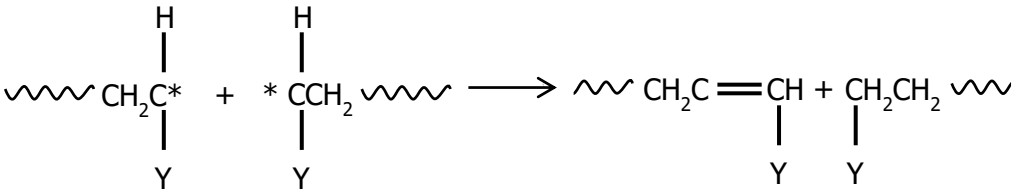

Figure 1.28. The three reaction steps during free radical photopolymerization. I* are the radicals from the photoinitiator; M is the monomer chain added (adapted from Su *et al.*)[170].

Radical photoinitiators are the most widely used to crosslink polymers to form hydrogels due to their excellent biocompatibility. Radical photoinitiators are classified into type I and type II photoinitiators. Type I photoinitiators, such as 1-[4-(2-hydroxyethoxy)-phenyl]-2-hydroxy-2-methyl-1-propanone (Irgacure D-2959) or lithium arylphosphanate (LAP,) under light irradiation, absorb photons and decay into two free

radicals leading the initiation of polymerization (Figure 1.29 (a)). In contrast, type II photoinitiators, such as eosin-Y, need co-initiators from which they can extract hydrogen atoms to generate secondary radicals and initiate the crosslinking process (Figure 1.29 (b)). This additional step makes the system quite inefficient compared with type I photoinitiators [136,171,172].

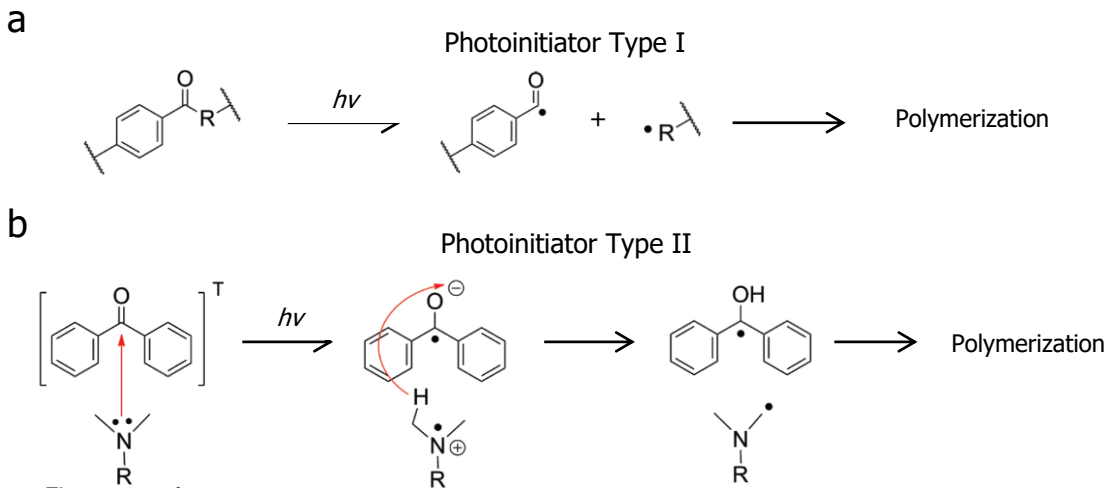

Figure 1.29. Photoinitiator activation mechanism. (a) Type I photoinitiators after light irradiation undergo cleavage and generate two radicals for initiation the polymerization. (b) Type II photoinitiators need a co-initiator to be active, after light irradiation the co-initiator transfers an electron to the photoinitiator, followed by a proton (adapted from Qin *et al.*)[172].

To this day, the most broadly employed photoinitiator in the bioengineering field is Irgacure D-2959, which absorbs mainly UV light. The main reasons are: (I) the moderate water solubility, although it is limited around 2% (w/v)[173], but sufficient for the vast majority of bio-applications, which only require 0.5% (w/v) or less, (II) the low cytotoxicity in its native form[174,175], (III) the efficient photo-dissociation into free radicals (yielding high polymerization rates)[174], and (IV) the high molar extinction coefficient under 320 nm irradiation[176]. The molar extinction coefficient for IrgacureD-2959 is 400 $M^{-1} \cdot cm^{-1}$ for exposure light wavelengths within the range 200 – 300 nm, meaning that it absorbs the light with high efficiency. However, the molar extinction coefficient decays as the wavelength gets closer to the UV-A spectrum, limiting the free radical production, as well as the polymerization efficiency. At 365 nm the molar extinction coefficient value is 4 $M^{-1} \cdot cm^{-1}$ [176].

It has been demonstrated that wavelengths below 365 nm produce phototoxicity and reduce the viability of the exposed cells[177]. To avoid that, 365 nm or higher wavelengths are used to polymerize hydrogels when they are loaded with cells. In recent

years, visible light-sensitive photoinitiators have emerged to minimize cell damaging. Nonetheless, their efficiency in triggering polymerization is limited, so they need more exposure time to crosslink hydrogels[136].

1.7. Hydrogel properties: critical parameters to consider for bioengineering applications

In tissue engineering applications, hydrogels are used as 3D scaffolds that support cell growth, proliferation and ensure proper cell functionality. To this end, the structural, biochemical and mechanical properties of hydrogels should match those found in the native tissues. Some of the relevant properties that define hydrogel networks are the swelling ratio, the elastic modulus, the diffusion coefficient, and the degradation rate. Overall, these properties are correlated one to each other and directly influenced by the degree of hydrogel crosslinking. As a general criterion, when the crosslinking degree of the hydrogels is reduced, the elastic modulus value decreases but the swelling ratio and the diffusion coefficient through the hydrogel increase. Mainly, variations on the hydrogel properties can be attributed to the mesh size modifications[178]. Mesh size (ξ) is the linear distance between two adjacent crosslinking points, so it is an estimation of the free space between the macromolecular chains. Mesh size is related to the molecular weight of the polymer chains between two neighbouring crosslinking points (M_c), either covalent bonds or physical interactions[179]. Despite there are many indirect methods to estimate ξ and M_c of a given hydrogel, the two most employed are based on the rubber elasticity theory and on the equilibrium swelling theory[125,179]. The rubber elasticity theory defines hydrogels as natural rubbers which, under a mechanical stress, they respond with an elastic deformation that recovers completely after the stimuli removal. This usually happens for deformations of less than 20%[125,179,180]. Flory[181] took benefit of this elastic behaviour of hydrogels to theoretically describe their network structure in a quantitative manner. Later on, this model was modified by Peppas[179] to be applied to the hydrogels prepared in the presence of a solvent. By applying this theory, the average molecular weight between crosslinks, M_c, is calculated with Eq. 1.1.

$$\frac{1}{M_C} = \frac{GQ^{1/3}}{RT'C_{2,r}} + \frac{2}{M_n} \qquad \textbf{Eq. 1.1}$$

Where G is the shear modulus of the hydrogel, Q is its volume swelling ratio, R is the ideal gas constant, T´ is the absolute temperature at which the shear modulus

was measured, $C_{2,r}$ is the polymer concentration in the solution before crosslinking, and M_n is the average molecular weight of the polymer[157].

In contrast, the equilibrium swelling theory is based on the swelling properties of hydrogels and it was developed by Flory and Rehner[182]. It is based on the balance between the thermodynamic force (which favours the swelling) and the stored force in the stretched polymer chains (which is against the swelling). As the hydrogel approaches the equilibrium point, the absolute value of both forces equals. At the equilibrium swelling point, the hydrogel cannot absorb any more fluid, meaning that the difference between thermodynamic force and the stored force is zero[180]. This theory calculates the M_c of a hydrogel prepared in the absence of a solvent by applying Eq. 1.2:

$$\frac{1}{M_c} = \frac{2}{M_n} - \frac{\frac{v}{V_1}\left[ln(1-v_{2,s}) + (v_{2,s}) + \chi(v_{2,s})^2\right]}{\left[{v_{2,s}}^{1}\!/_{3} - \frac{v_{2,s}}{2}\right]} \qquad \textbf{Eq. 1.2}$$

Where M_n is the number average molecular weight of the polymer chains in the absence of the crosslinking agent, υ is the specific volume of the bulk polymer (inverse of the density of the polymer), V_1 is the molar volume of water, χ is the Flory-Huggins polymer-solvent interaction parameter, and $\upsilon_{2,s}$ is the volume fraction of the polymer at swelling equilibrium. Later on, Peppas and Merrill[183] modified the Flory-Rehner theory to apply it to hydrogels prepared in the presence of a solvent, which modifies the balance between both forces. The M_c of hydrogels when they are under a solvent is calculated using Eq. 1.3:

$$\frac{1}{M_c} = \frac{2}{M_n} - \frac{\frac{v}{V_1}\left[ln(1-v_{2,s}) + (v_{2,s}) + \chi(v_{2,s})^2\right]}{(v_{2,s})\left[\left(\frac{v_{2,s}}{(v_{2,r})}\right)^{1}\!/_{3} - \frac{v_{2,s}}{2\,v_{2,r}}\right]} \qquad \textbf{Eq. 1.3}$$

Where $\upsilon_{2,r}$ is the volume fraction of the polymer at relaxed state, just after polymerization and before being submerged in the solvent.

Another critical structural parameter in hydrogel networks is the mesh size (ξ), which is directly related to M_c. ξ is obtained using the equation Eq. 1.4 and Eq.1.5 for PEGDA[125] and GelMA[184] hydrogels, respectively

$$\xi = (v_{2,s})^{-1/3}\left(2\frac{C_n^{1/2}M_c}{M_r}\right)^{1}\!/_{2}\, l \qquad \textbf{Eq. 1.4}$$

$$\xi = (v_{2,s})^{-1/3}\left(3\frac{C_n^{1/2}M_c}{M_r}\right)^{1/2} l \qquad \textbf{Eq.1.5}$$

Where M_r is the molecular weight of the repeat unit, C_n is the Flory characteristic ratio, and l is the mean length between C-C bonds and C-N bonds.

Both theories treat hydrogel networks as perfect structures, giving estimated values for ξ and M_c (Figure 1.30 (a)). Real networks have different values for ξ and M_c due to the imperfections or defects on the crosslinked network during the polymerization process, which forms physical interactions such as hydrogen and ionic bonds, loops, entanglements and dangling ends (Figure 1.30 (b))[125].

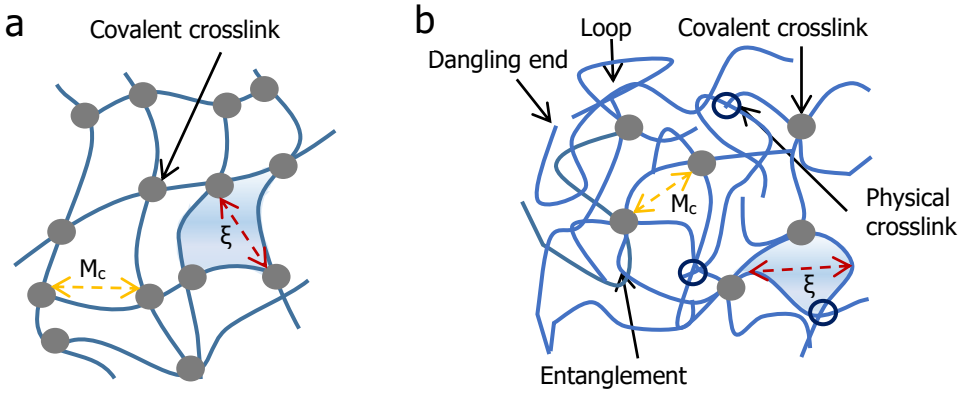

Figure 1.30. Structure of the hydrogel network. (a) In an ideal hydrogel the mesh size (ξ) and the average molecular weight between crosslinkers (M_c) are homogenous in all the hydrogel. (b) In a real hydrogel network, there are physical crosslinks, entanglements, loops and dangling ends, which create non-homogenous and dispersed values of M_c and ξ.

The mesh size of the hydrogels has direct implications on the mass transport of nutrients, oxygen, waste products and other biological molecules into, out of and within the network[185]. In hydrogels mass transport is usually driven by diffusion[186]. Diffusion consists on material movement due to a concentration gradient, from a high concentration zone to a low concentration zone. The rate and the distance that a molecule diffuses through the hydrogel network, are affected by the structural properties of the hydrogel, the interaction between the polymer chains, and the molecular weight, diameter and charge of the compound to be diffused through the hydrogel pores[186].

When developing hydrogels for biomedical applications, such as scaffolds for cell culture or for drug delivery systems, the diffusion has to be taking into account for

their proper performance. In the case of cell-laden hydrogels, the diffusion of nutrients and other components through the hydrogel network has to be efficient to ensure a continuous nutrient and waste exchange of the cells that reside inside the network[187]. This is essential for cell nutrition, proliferation, migration and functionality, including the formation of new extracellular matrix[185]. The diffusivity of the molecules within a hydrogel network is quantified by their diffusion coefficient (D), which is obtained from permeability assays (Eq. 1.6)[188]:

$$D = \frac{P_{app}\, h}{K} \qquad \textbf{Eq. 1.6}$$

Where P_{app} is the apparent permeability of the molecules through the hydrogel, h is the height of the hydrogel, and K is hydrogel/water partition coefficient.

Permeability assays can be useful to get indirect information about network properties such as mesh size when the theoretical models explained above are not valid approximations. This is the case of hydrogels consisting of two or more different polymers, such as those composed of a mixture of collagen, hyaluronic acid and poly(ethylene glycol) ether tetrasuccinimidyl glutarate[188]. In these hydrogels they get the mesh size through the correlation with the diffusivity of molecules with different size.

Finally, as mentioned above, the mesh size is also intrinsically related to the mechanical properties of the hydrogels. These are important design parameters to consider for hydrogels employed for biomedical applications. Hydrogel stiffness is a crucial factor that regulates the cell behaviour such as cell adhesion, spreading, growth, migration, functionality and cell death, of both the embedded cells[189] and the surface cells[128]. Among mechanical properties, the elastic modulus (the Young's modulus) is defined as the ability of an elastic material to resist deformation to an applied stress[190]. The Young's modulus (E) is calculated as (Eq. 1.7):

$$E = \frac{\sigma}{\varepsilon} \qquad \textbf{Eq. 1.7}$$

Where σ is the stress applied (the force divided by the area over which it is applied), and ε is the strain (the stress-induced change in length of a material divided by the its unstressed length).

For an ideally elastic soft hydrogel, the Young's modulus value is constant. However, soft hydrogels do not have a perfect and homogenous network, and, above a certain threshold, the resistance to deformation increases as the applied stress increases.

This means that the value of the Young's modulus is not constant in this regime and varies with the specific applied stress. Therefore, when performing mechanical tests, only the linear part of the stress-strain curves is analysed[191]. The most common techniques to determine the mechanical properties of hydrogels are: (I) tensile, (II) compression; and (III) indentation tests. In tensile tests, the hydrogel is placed between two clamps and then stretched for both sides to get the stress-strain curves (Figure 1.31 (a)). In compression tests, the hydrogel is hold between two clamps while a uniform load is applied, which results in the hydrogel compression (Figure 1.31 (b)). In indentation tests, a probe of a determined geometry is placed at a particular point on the hydrogel surface (Figure 1.31 (c)). Then, the probe penetrates inside the hydrogel and deforms it to a particular depth. The amount of force applied for the deformation is recorded and used to calculate the Young's modulus by applying the Hertz model[190]. Tensile and compression tests are useful to evaluate the bulk mechanical properties of hydrogels, while indentation tests are suitable to obtaining the surface mechanical properties [190,192].

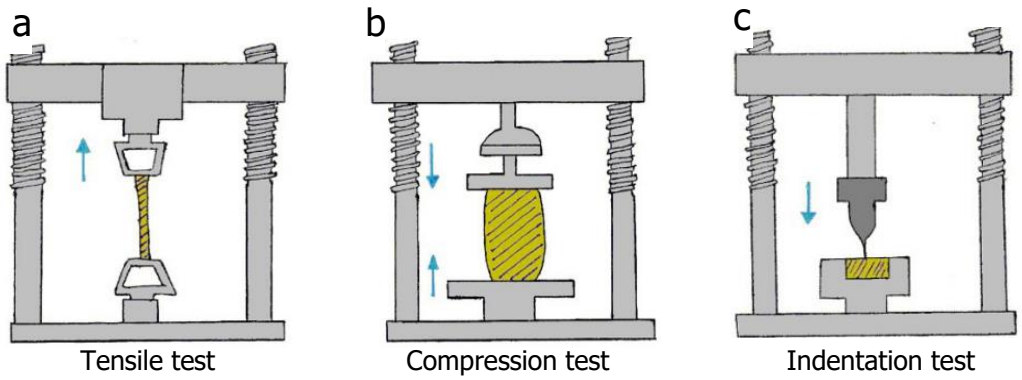

Figure 1.31. Methods used to determine the mechanical properties of the soft hydrogels. (a) Tensile test. (b) Compression test. (c) Indentation test (adapted from Vedadghavami *et al.*)[190].

Overall, the properties related to the hydrogel structure are linked together, and should be analysed at once. It is reported that, cells seeded on the surface of a material grow and proliferate better on top of stiffer surfaces[193], whereas encapsulated cells are more spread and migrate better in softer hydrogels[189]. The different requirements in the same scaffold to match the proper stiffness to achieve a high cell viability with capacity to grow, spread, migrate, proliferate and be functional for encapsulated and seeded cells, makes the developing of an accurate hydrogel challenging. In order to full fill this requirement, a part of the hydrogel type and their characteristics, the microfabrication technique employed to achieve the hydrogel is extremely important, because it can

modify the final hydrogel features. In addition, for possible futures experiments, the microfabrication technique has to be chosen weighing in the possibility of creating patterns on the hydrogel.

1.8. Microfabrication techniques for hydrogel photopolymerization

Commonly, hydrogels have been employed to mimic the mechanical properties of the ECM and thus, to better recapitulate *in vivo* tissue properties. In general, for tissue models, it has been shown that not only physicochemical and mechanical properties play a significant role for proper cell development, and cellular interactions between different cell types in the same compartment or in different compartments. Indeed, the 3D architecture of the tissue to be mimic is also a key parameter to take into account in order to achive good *in vitro* tissue models with a proper functionality.

In particular, as we mention in section 1.4 for a perfect *in vitro* small intestine model a part of the scaffold matching the range of the apparent elastic modulus of the native intestine (3 – 40 kPa)[194] and allowing stromal and epithelial compartmentalization, so the interaction between mesenchymal or immune cells with the epithelial cells; another essential parameter that would contribute in the improvement of the small intestinal model giving a more physiological data is the introduction of the villus-crypt architecture on to the scaffolds[155,156]. To achieve these features employing hydrogels as the scaffolds and photopolymerization as the crosslinking method, we need a microfabrication technique that (I) provides high cell viability and homogeneous cell distribution into the hydrogel and (II) provides a uniform cell distribution onto the hydrogels, and (III) is suitable for patterning 3D geometrical features on the hydrogels. Reviewing the literature of recent years, we have identified as the most used techniques to fabricate cell-laden hydrogels with microstructures (I) micromolding, (II) 3D bioprinting, (III) stereolithography, (IV) two-photon polymerization, and (V) photolithography[195].

1.8.1. Micromolding

Micromolding consists in replicating geometrical structures present on an original mold onto another material, which can be a hydrogel[196]. First, a hard-material

master, sometimes made of silicon-based materials, is fabricated by techniques such as photolithography, laser ablation or dry or chemical etching. Once this master is fabricated, it is durable and can be used to generate replicas for a long time[197]. Silicon masters are usually fragile and expensive to fabricate, so they are usually transferred to intermediate molds, which are flexible and easily to demold. These molds are made of polydimethylsiloxane (PDMS), through soft lithography techniques, or to other polymers such as poly(methyl methacrylate) (PMMA), ethylene tetrafluoroethylene (ETFE) polyurethane-acrylate (PUA) or Teflon® by using hot embossing approaches[198]. PDMS is usually the preferred option[197], as is a low cost material, optically transparent, non-toxic[199] and it allows the ease separation of the replica and the master avoiding its damage[196]. To then get hydrogels with defined geometry and dimensions, polymer solutions, containing (or not) cell suspension, are poured onto the PDMS molds filling the cavities, this followed by the crosslinking reaction. Finally, the structured hydrogels, which are the negative of the original molds, are carefully removed from them (Figure 1.32)[200].

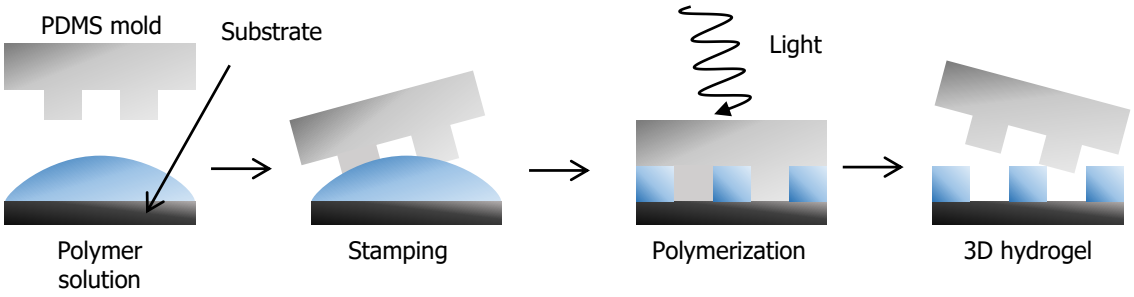

Figure 1.32. Schematic representation of the micromolding process to fabricate a hydrogel using a PDMS mold.

High cell viability of the cell-laden hydrogels has been achieved using this technique. For example, Nichol *et al.*[201] embedded cells in a square of 500 μm in width, 500 μm in elongated and 300 μm in height. Another sample that uses micromolding to generate cell-laden hydrogels is the one reported by Occhetta *et al.*[202]. They encapsulated cells in lines of 250 μm in width and 80 μm in height. We can see that many types of structures can be produced using this technique[203]. However, the soft nature of the hydrogels limits the resolution of the technique to ≈100 μm[167], making difficult to form complex geometries and high aspect ratio structures. To overcome this limitation, one can introduce extra demolding steps (I) using sacrificial molds that, for instance can be dissolved by water based solutions[204] or (II) introducing washing steps

or polymerization conditions[205], which make this method incompatible with the survival of embedded cells.

1.8.2. 3D bioprinting

3D bioprinting is a high throughput, and versatile technique that permits to obtain biomimetic and functional tissues and organs models from digital models, which embedded cells[206]. To obtain the scaffolds, the polymer solution is mixed with cells and in some cases this solution can be supplemented with other molecules such as proteins, growth factors, known as bioink. Then this bioink is dispensed in a controlled manner at desired locations, followed by the polymerization of the material[206,207]. This process is carried out in three main steps. The first one is the pre-processing step, which involves the visualization and imaging of the real construct to be model and the design of the template of the structure to be constructed using specialized software, such as AutoCAD. The second step is the bioprinting, which involves the mixture of the cells with the bionk, as well as the printing process itself, followed by polymerization. Factors related with the fabrication process, such as the bioink, and cell type, and density are chosen in this step. Finally, the third step is the post-processing step, which provides to the construct all the necessary conditions for the growth of the cell culture, such as nutrients[206]. The main techniques associated to 3D bioprinting are (I) inkjet, (II) microextrusion, and (III) laser-assisted bioprinting[206,208].

(I) Inkjet bioprintings is a non-contact technique that uses thermal, piezoelectric or electromagnetic forces to expel drops of bioink through a syringe onto a surface where the bioink crosslinks. It is a fast, low cost technique with high cell viability but the droplets are not uniform formed due to the low viscosity of the bioinks. Moreover, the needle can be obstructed[208]. The resolution is around 50 μm[206]. In the case of the bioprinting technology, the resolution is related with the minim drop size, which is secreted by the system, however, it is not the final resolution due to it depends on how the drop spreads on the surface[209]. (Figure 1.33 (a)).

(II) Microextrusion bioprinting is the most broadly used method, where a continuous layer of bioink is dispensed through a nozzle applying mechanical or pneumatic forces[208]. This technique uses high viscosity bioinks with high cell concentrations. However, cell viability is compromised due to the pressure used to

dispense the bioink, and as the nozzle can be clogged. The resolution is limited to ≈100 μm[206,207] (Figure 1.33 (b)).

(III) Laser-assisted bioprinting is a non-contact and nozzle-free technique, where clogging is avoided and thus, cell viability is enhanced. High resolution up to the level of a cell (≈10 μm) is achieved[210]. It is based on shooting laser beam pulses on an absorbing layer of a ribbon, which is pre-coated with the bioink, generating gas bubbles that propel the bioink towards the substrate. By contrast this technique is time consuming and costly[207,208] (Figure 1.33 (c)).

Despite the huge advances and extensive applications of 3D bioprinting found in literature, it still has many limitations, such as long printing times, cell death due to the mechanical forces imposed during the printing process and low biologically relevant cell densities[208].

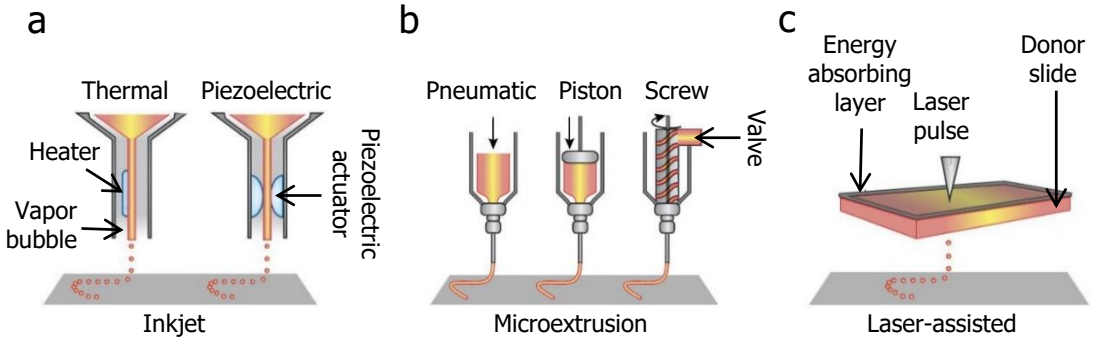

Figure 1.33. Schematic representation of the 3D bioprinter working conditions. (a) Inkjet mechanism, thermal inject method applies heat to the ink to produce air-pressure pulses that force droplets from the nozzle, unlike piezoelectric method applies ultrasounds or piezoelectric pressure to eject the droplets. (b) Microextrusion method use pneumatic, piston or screw to extrude a continuous line of bioink. (c) Laser-assisted method applies a laser beam on an absorbing substrate that lies on top of the bioink to generate droplets that fall onto a collector substrate (adapted from Murphy *et al.*)[207].

1.8.3. Stereolithography

Stereolithography builds 3D shaped construct layer-by-layer by selectively exposing a polymer solution under a specific source of light, which can be a laser beam or a digital light projector. The structure to produce is designed using a specific software, such as AutoCAD, which permits to precisely control the position of the light source. The polymer solution together with the cell suspension is deposited into a tank. Then, the polymer solution is irradiated and polymerized on a support platform. After photopolymerization of one layer, the platform is moved a defined height and then

another layer is photopolymerized on top of the previous layer. This process is repeated successively until getting the final structure[211] (Figure 1.34). The main advantage of stereolithography is the high resolution that reaches around ≈20 µm or less, due to the accurate space and time control of the applied light[212], this system allows to fabricate very complex 3D structures. The movement of the platform between each step, is the major drawback of the system because it increases a lot the time to produce one scaffold[212].

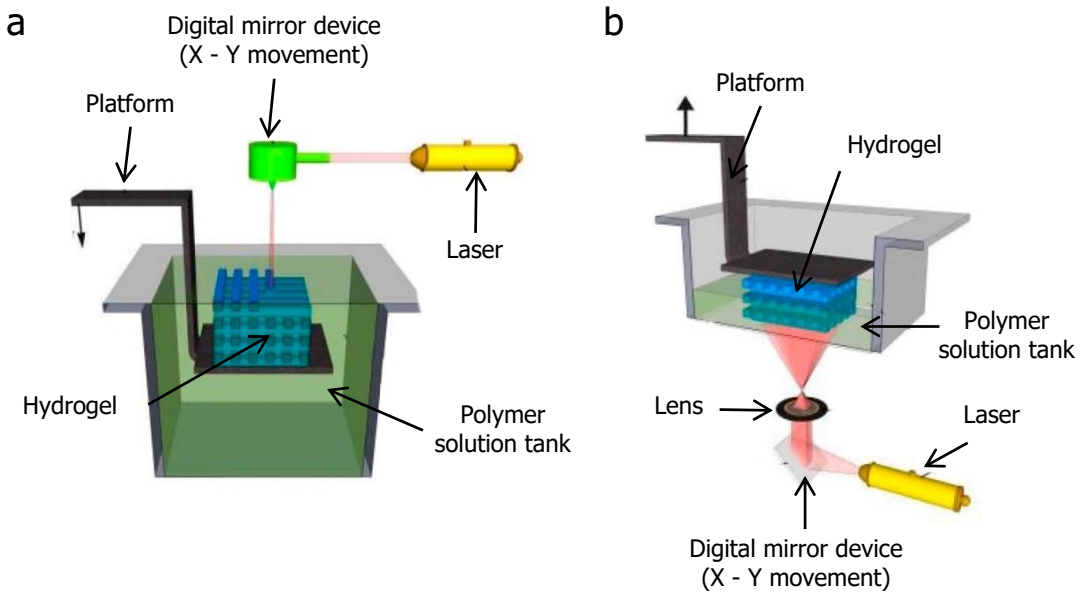

Figure 1.34. Schematic illustration of the stereolithographic technique where the polymer solution is polymerized layer by layer. (a) Bottom-up setup approach, where the beam comes from the top and platform moves down. (b) Top-down setup approach, the beam irradiates down and the platform moves up (adapted from Yao *et al.*)[167].

1.8.4. Two-photon polymerization

Two-photon polymerization is a laser-based technique for the fabrication of shaped hydrogels in a fast manner. Two-photon polymerization is based on shooting at femtoseconds near-infrared (NIR) or infrared (IR) laser beam into a well-defined focal spot of the polymer solutions. In this system polymerization only occurs when the photoinitiator is able to absorb two consequent photons, each of them providing half of the energy that is required to reach the excited state. Then, the photoinitiator disassociates into free radicals, and the polymer solution is polymerized in a defined region[167,213]. The main advantages of this technique is the use of wavelengths that do not damage the cells[214], and the fabrication of hydrogels with complex 3D architectures

with a resolution of 0.5 – 1 μm[167]. Despite its advantages, two-photon polymerization is a complex technique that faces many challenges such as high cost of the equipment, and the long time to build scaffolds. Additionally, some of the photoinitiators used, produce cytotoxic by-products causing damage to the embedded cells[167, 213].

1.8.5. Lithography-based methods

Lithography is the most used fabrication technique in microfluidics and microelectronics. It can form precise and complex 3D structures onto a substrate[215]. Lithography techniques are classified into two types (I) mask, and (II) maskless lithography. The former, usually called photolithography, needs a bidimensional mask to transfer the geometries to the substrate. In contrast, maskless lithography fabricates the structures onto the substrate through direct writing methods by using electron beams, focused ion beam or scanning probe techniques. Here, we will describe only photolithography, since it is the technique applied to fabricate our hydrogels[216]. In photolithography a pattern is transferred on a light-sensitive polymer, by placing a 2D photomask with a desired pattern on top of the polymer and applying a source of light. In the microelectronics field, a solid substrate, such as silicon wafer, is coated with thin layer of the light-sensitive polymer, known as photoresist, and a photomasks having transparent and non-transparent regions is placed in direct contact or in close proximity on top of it. The pattern is transferred using a collimated UV lamp that homogenously irradiates the photomask. Photomask can be fabricated from glass, metal or high-quality acetate sheets, the last ones are only employed to pattern structures at the micrometer scale. The light exposed regions can be crosslinked or degraded depending if the photoresist used is negative or positive, respectively. Finally, the pattern on the photoresist is developed using a solvent that eliminates the unreacted polymer, leaving the topographic structure corresponding to the photomask[215,217] (Figure 1.35 (a)). This technique allows patterning large surface areas in an easy manner. However, it requires specialized, expensive equipment for the light exposure (usually a mask aligner) and clean room facilities. By controlling the exposure dose, through the power and the exposure time, well-defined structures can be obtained, with a resolution limited by light diffraction[217].

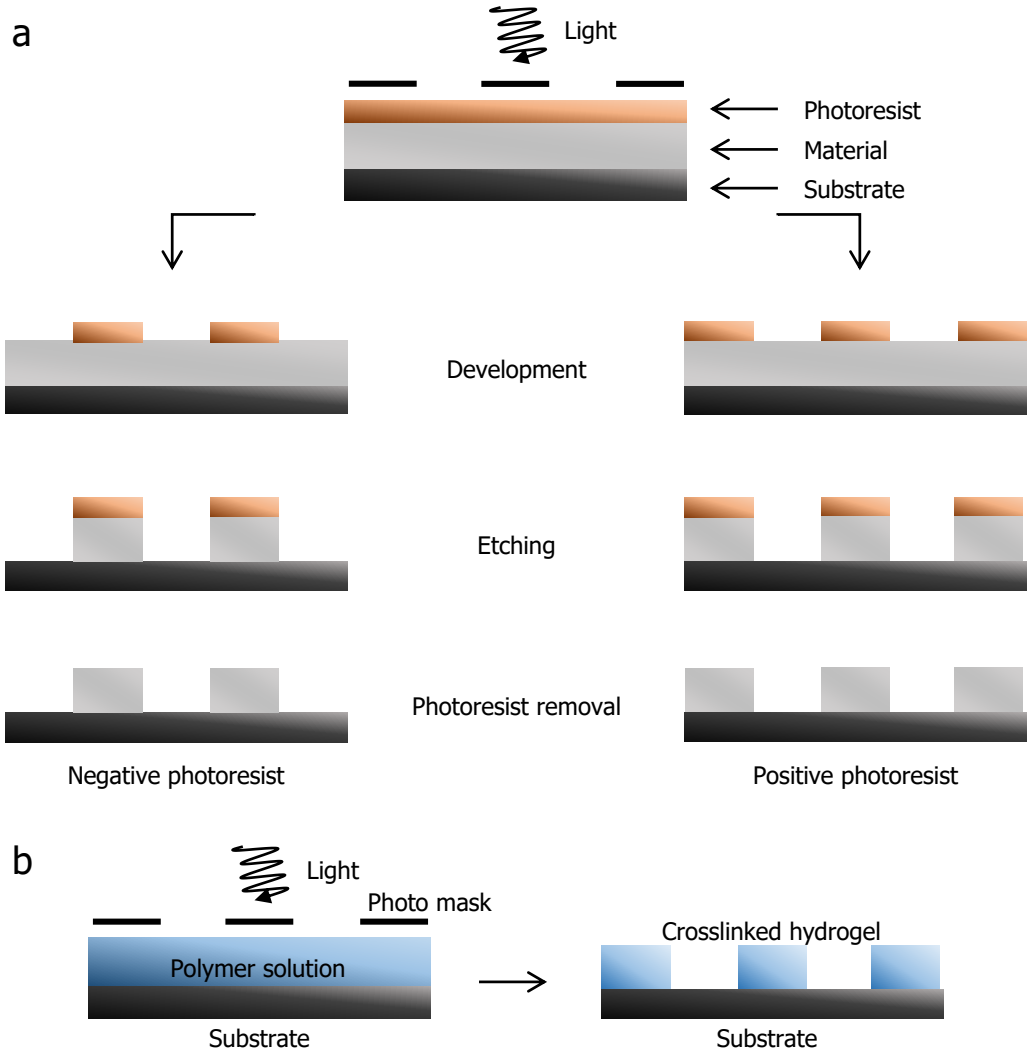

Figure 1.35. Lithography-based methods. (a) Schematic representation of the masked photolithography. The solution to pattern is disposed onto a substrate, such a glass wafer. Then, the solution is covered by a photomask, usually made of chrome, and exposed to UV light. In the case of negative photoresist, the irradiated regions crosslink the solution, which are not remove after photoresist removal. On the other hand, in positive photoresist the light exposed zones become weaker and after photoresist removal are washed away; and (b) directly polymer solution photopolymerization covered by a photomask to obtain a patterned hydrogel.

Photolithography has been adapted by others[218–220] and by our group[155] to photopolymerize hydrogels by placing the photomask on top of a container that confines the liquid polymer solution. On the light exposed regions the photoinitiator is activated and triggers the polymerization, creating a negative of the pattern of the photomask (Figure 1.35 (b)).

Nowadays, in the literature we can find some intestinal models that have been use most of the previous explained microfabrication techniques to fabricate scaffolds mimicking the villus-crypt architecture of the small intestine. For example, Wang *et al.*[205]

developed an *in vitro* model that replicates the crypt-villus features of the small intestine on top of collagen scaffolds using micromolding. Creff *et al.*[221] also achieved to patterned the crypt-villus units on top of a PEGDA hydrogel employing stereolithography. Kim *et al.*[222]fabricated villus structures through 3D bioprinting based on the layer-by-layer printing method. Finally, in our group villus-like structures on PEGDA polymer have been obtained by photolithography[155]. Although, these models imitate the 3D architecture of the small intestine and epithelial cells are cultured on top of them to mimic the epithelium. The main drawback of this models is the lack of the stromal (lamina propria) compartment. The stromal-epithelium interaction is a key parameter to have a physiological relevant *in vitro* model of the small intestine, because it directly influences on the epithelium maturation and differentiation resulting in a epithelial barrier properties closer to the physiological ones[112].

On the other hand, in literature we find models that recreate the 3D architecture of the intestine and in parallel are able to introduce the stromal and epithelial compartmentalization. Gregorio *et al.*[223] developed an *in vitro* model that mimics the intestinal topography and contains the lamina propria. However, the fabrication method employed is highly complex and time-consuming, making them impractically for daily research studies.

As the intestinal topography also plays a relevant role in the formation and maturation of the epithelium. We need to choose a technique that allows us (I) to fabricate a hydrogel that supports the compartmentalization of the lamina propria and epithelium, without affecting the viability of the embedded cells, and (II) to form villus-like patterns on the hydrogels.

2. Hypothesis and objectives

Currently, the standard *in vitro* intestinal models used in drug development or for disease modelling are restricted to bidimensional (2D) epithelial cell monolayers cultured in Transwell® inserts. These models fail in mimicking the cellular components, three-dimensional (3D) organization, and the complex functions of the intestinal mucosa. As a consequence, cells show an altered behaviour with respect to their *in vivo* counterparts, providing data that sometimes is not predictive of the human physiology. Therefore, in the last years, the development of more physiologically relevant models of intestinal mucosa to be used as *in vitro* testing platforms has become a relevant field to focus on.

The **hypothesis** of this study is if the development of an appropriate biomaterial serves as a scaffold that simulates the mechanical and physicochemical properties found in the lamina propria of the native human intestine, together with the combination of lamina propria and epithelial cells may lead to a generation of 3D *in vitro* models that better recapitulate the small intestine functions. Based on this hypothesis, the main **objective** of this study is to model a 3D intestinal mucosa *in vitro*. This model will mimic the cellular components of the lamina propria and will support the growth of functional epithelial cells. To fulfil this general objective, the **specific objectives** are itemized as:

1. To develop and characterize hydrogels that emulate the *in vivo* lamina propria features in terms of mechanical and physicochemical properties.

2. To generate a hydrogel that integrates the lamina propria cells and provide the growth of the epithelial cells.

3. To examine the interactions between epithelial cells and lamina propria cells over the functions of the epithelial barrier in healthy and pathological conditions.

3. Materials and methods

3.1. Synthesis of gelatin methacryloyl polymer

Gelatin methacryloyl (GelMA) comes from gelatin. Gelatin is a denatured and partially hydrolyzed mixture of collagen polymers from animal source. By itself it forms thermo-reversible physical interactions, but these are not stable above 37ºC. To overcome this drawback, gelatin is sometimes chemically modified by adding methacryloyl groups to the primary amine and hydroxyl groups to form GelMA polymer. When the methacryloyl group is added to primary amine this is known as methacrylamide, whereas when it is joined to the hydroxyl group is referred as methacrylate (Figure 3.1 (a)). GelMA polymer forms covalent interactions upon photopolymerization, resulting in a physically stable hydrogel adobe 37ºC using photopolymerization techniques.

Gelatin methacryloyl was prepared following a method previously described[141,142,201]. Briefly, a 10% (w/v) gelatin solution was obtained by dissolving gelatin from porcine skin type A and bloom strength 300 (Sigma-Aldrich) in phosphate buffer saline (PBS, pH 7.4) (Gibco, ThermoFischer Scientific) at 50ºC under stirring conditions for approximately 2 h. Methacrylic anhydride (MA) (Sigma-Aldrich) was added to the gelatin solution at target final concentrations and at a rate of 0.5 $mL \cdot min^{-1}$. Throughout the gelatin dissolution and the MA addition process, gelatin solution was kept always at 50ºC and under stirring to avoid phase separation. MA was left to react one hour after completing the full addition of MA. According to the final concentration of MA % (v/v) added to the gelatin, the percentage of methacryloyl groups added to the gelatin polymer are modulated. As the final concentration of MA increases, more amino and hydroxyl groups are modified. The total percentage of methacryloyl groups added to the gelatin to give GelMA is known as the degree of functionalization (DoF). The DoF affects pore size, mechanical properties, swelling behaviour and degradation of the hydrogel. Consequently, the DoF employed to form the hydrogel depends on the final purposes of the hydrogel. More information on how to calculate the DoF is explained in sections 3.2.4 and 3.2.4. During the realization of this thesis, MA concentrations tested to form GelMA polymer were 20%, 5%, 1.25% and 0.25% (v/v). To name GelMA polymer with different DoF, we refer to them according to the following criteria. We use the abbreviation for gelatin methacryloyl (GelMA) with a subindex that refers to the % (v/v) of MA added during the GelMA synthesis. In our case, we synthetized $GelMA_{20}$, $GelMA_{5}$, $GelMA_{1.25}$ and $GelMA_{0.25}$.

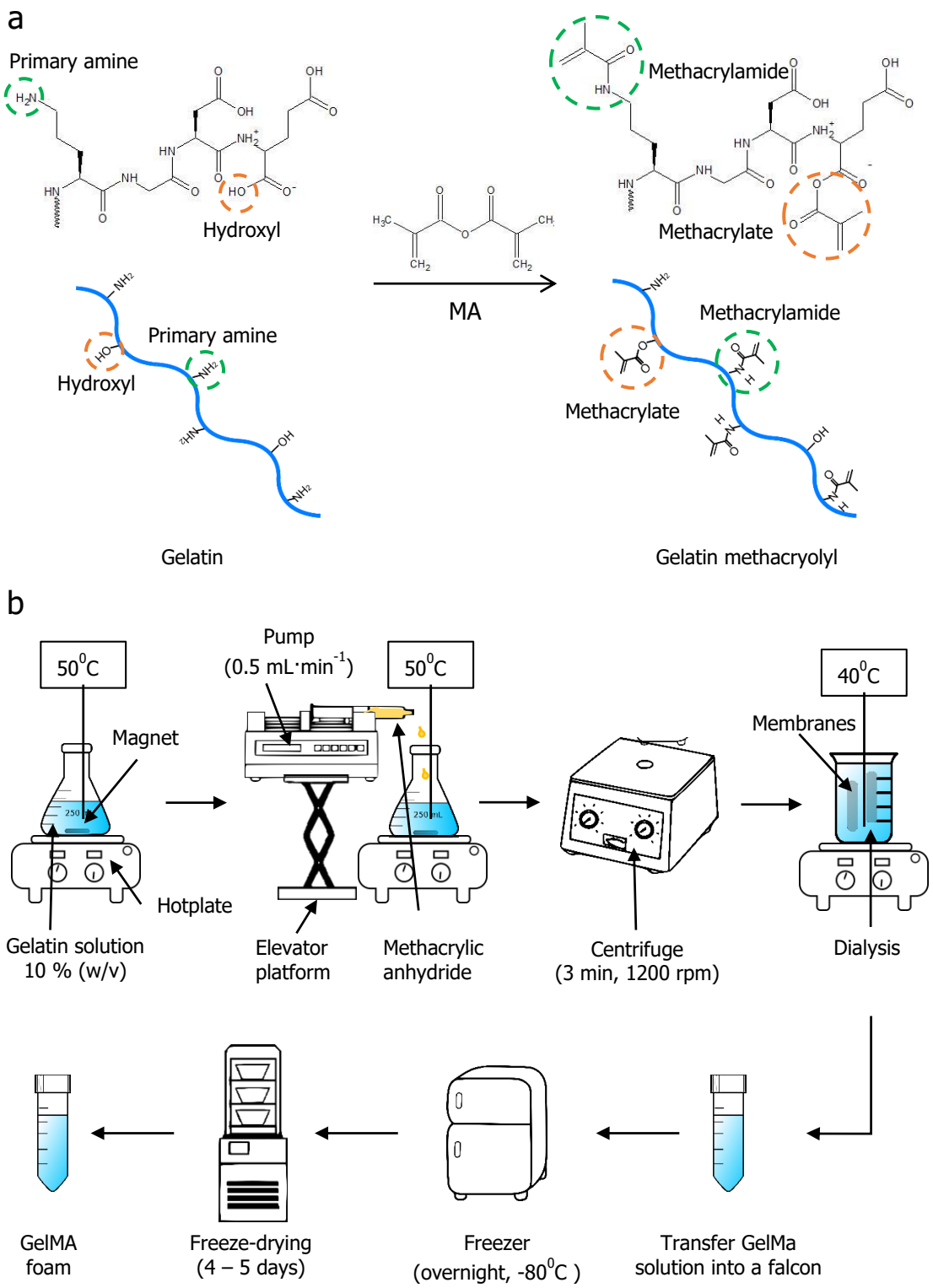

Figure 3.1. Gelatin methacryloyl (GelMA) synthesis. (a) Schematic representation showing the reaction of methacrylic anhydride (MA) with primary amine and hydroxyl groups on gelatin to form GelMA polymer. (b) Schematic illustration of the main steps of the GelMA process.

After letting the MA to react for 2 h, GelMA solution was transferred to 50 mL conical Falcons tubes (Eppendorf) and centrifuged (rotina 38R, Hettich) at 1200 rpm for

3 min at room temperature. Supernatant, which contained GelMA polymer, was decanted into a glass beaker to remove unreacted MA and other by-products, which are cytotoxic, that remained concentrated in the pellet. The reaction was stopped by adding to the supernatant two volumes of Milli-Q water at 40ºC. The resulting solution was transferred into 6 – 8 kDa of molecular weight cut-off membranes (Spectra/por, Spectrumlabs) and dialyzed against Milli-Q water at 40ºC. Milli-Q water was replaced every 4 h for 3 days. Then, the dialyzed solution was transferred into a glass beaker and the pH of the solution was adjusted to 7.4, with a pH meter (GLP21). Between 25 to 30 mL of GelMA solution was transferred in 50 mL conical Falcon tubes, covered with parafilm (Bemis) and frozen overnight at -80ºC. Finally, frozen GelMA polymer was lyophilized for 4 – 5 days (Freeze Dryer Alpha 1-4 LD Christ) until a porous white foam was obtained, which meant that GelMA was completely dehydrated. The resulting dehydrated GelMA polymer was stored at -20ºC until further use (Figure 3.1 (b)).

3.2. Gelatin methacryloyl characterization

To know if gelatin methacryloyl process had been performed accurately, GelMA polymers obtained were characterized using different techniques. Techniques used were (I) Sodium dodecyl sulfate-polyacrylamide gel electrophoresis (SDS-PAGE), (II) Fourier transform infrared (FTIR) spectroscopy, (III) Proton nuclear magnetic resonance (^{1}H-NMR) spectroscopy, and (IV) 2,4,6-trinitrobenzene sulfonic acid (TNBS) assay. On one hand, SDS-PAGE and FTIR spectroscopy were qualitative assays that allowed us to determine the presence of the methacryloyl groups into the gelatin. On the other hand, ^{1}H-NMR spectroscopy and TNBS assay were quantitative techniques that allowed us to study the degree of functionalization (DoF). The DoF is composed by the modifications in the primary amine groups and the hydroxyl groups. Here, we only quantified the DoF of the amine groups (methacrylamide groups), as the hydroxyl groups (methacrylate groups) modified are less than 10% of all the methacryloyl groups[142].

3.2.1. Molecular weight determination of GelMA samples by SDS-PAGE

The molecular weight of $GelMA_5$, $GelMA_{1.25}$ and $GelMA_{0.25}$ polymers was analysed by Sodium Dodecyl Sulfate-Polyacrylamide Gel Electrophoresis (SDS-PAGE). SDS-PAGE is a widely used technique to separate proteins by their molecular weight using an electrical field. It is based on the interaction of denaturalized proteins with an anionic

detergent (SDS) to form a highly negatively charged complex. The amount of SDS bounded to the protein is proportional to their molecular weight. Proteins charged with the SDS are loaded onto a polyacrylamide gel and a voltage is applied, producing protein migration towards the anode, which is the positive electrode. Large proteins migrate slower than small proteins, as they have more interactions with the gel pores, allowing them to be separated by their molecular weight.

To perform the SDS-PAGE, acrylamide/bis gel was fabricated. Acrylamide/bis gel is composed by two gels, the stacking and the separating gel. The stacking gel permits the proteins to concentrate in one band just above the separating gel to start migrating at the same time. Whereas the separating gel, which has a lower pore size than the stacking gel, allows the separation of proteins based on their size or molecular weight (Figure 3.2 (a)). The separating gel solution was prepared with the reagents listed in Table 3.1. All of them were added to a beaker, except the APS and TEMED, which were added just before starting the polymerization. Just after adding the APS and TEMED, which quickly triggers the radical polymerization of the gel, the resulting solution was poured in a mold consisting of two glass plates with 1.0 mm spacers between them (Figure 3.2 (b)). These plates were fixed in a casting stand which seals the open underside and laterals (Figure 3.2 (c)).

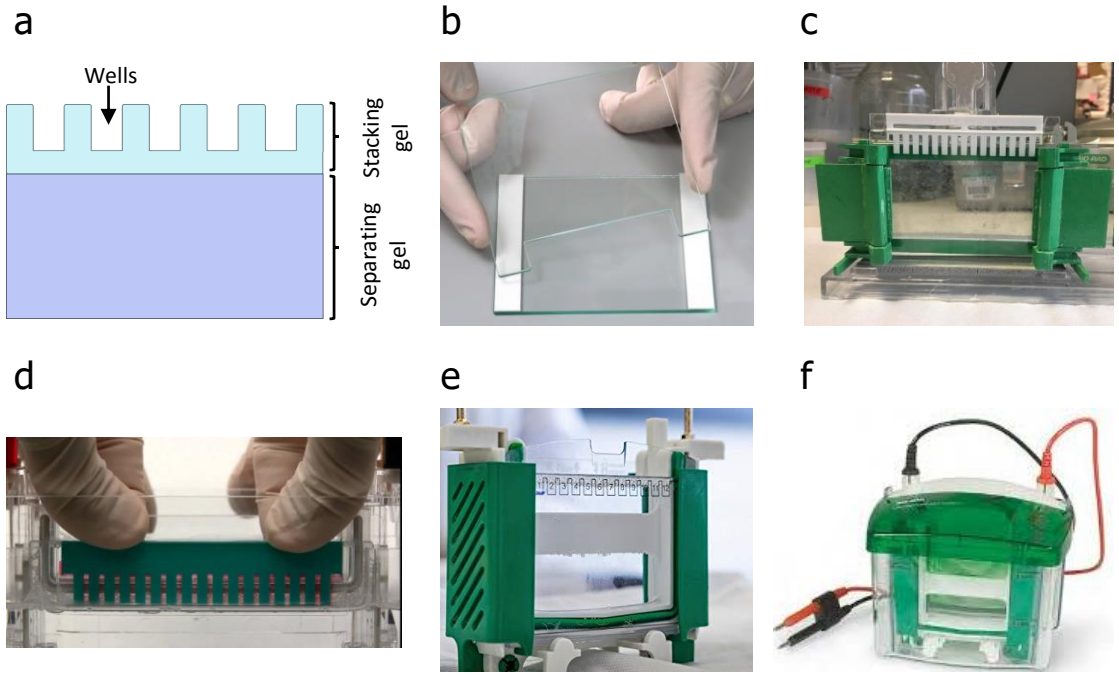

Figure 3.2. Main components of SDS-PAGE electrophoresis. (a) Schematic representation of the electrophoresis gel, showing the stacking and the separating gel; (b) glass plates; (c) casting stand with two glass plates and comb; (d) zoom of the comb; (e) clamping frame and electrophoresis assembly; and (f) electrophoresis tank.

Subsequently, the separating gel solution was covered with a thin layer of Milli-Q water to protect it from the oxygen and enhance radical polymerization. Then, Milli-Q water was removed, and the surface of the gel was dried by capillarity using filter paper. Next, the stacking gel solution (Table 3.1) was poured into the mold covering the separating gel. Immediately, a comb was inserted into it to create the wells. After polymerization, the comb was carefully removed avoiding breaking the gel (Figure 3.2 (d)). At that point, the gel could be used immediately or wrapped with damp paper and stored in the fridge at 4ºC for the next day. Samples were prepared by dissolving gelatin, $GelMA_5$, $GelMA_{1.25}$ and $GelMA0_{0.25}$ polymers at a concentration of 1 $\mu g \cdot mL^{-1}$ in PBS for 1 h at 37ºC under stirring conditions. Then, polymer solutions were mixed with the stock loading buffer 6x (Table 3.1). In a 1.5 mL Eppendorf, 100 µL sample solution, meaning that it contained 100 ng of protein, were mixed with 25 µL of the loading buffer 6x to get a final concentration of the loading buffer 1x. To calculate the amount of loading buffer need to have a final concentration of 1x, the following equation was applied (Eq. 3.1):

$$V_{initial\ LB} * C_{initial\ LB} = \left(V_{final\ sample} + V_{initial\ LB}\right) * C_{final\ LB} \qquad \textbf{Eq. 3.1}$$

Where $V_{initial\ LB}$ is the initial volume of the stock loading buffer 6x; $C_{initial\ LB}$ is the initial concentration of the stock loading buffer, in this case is 6x, $V_{final\ sample}$ is the sample volume added to the Eppendorf, in this case we added 100 µL, and $C_{final\ LB}$ is the final concentration of loading buffer needed, in this case is 1x. From here, we got that the loading buffer volume needed to have the proper dilution factor was 25 µL. An Eppendorf tube containing the samples was heated in a Eppendorf block heater for 5 min at 95ºC to break the secondary and tertiary structure of proteins (Figure 3.3). Prior to use, samples were cooled at room temperature. Acrylamide/bis gel and glass slide constructs were mounted into the electrophoresis tank (Figure 3.2 (e)).

Solutions	Components	Volume (mL)	Source
Separating gel	Milli-Q water	40.20	
	30% acrylamide/bis	33.30	Biorad
	1.5% Tris-HCl in Milli-Q, pH 6.8	25	Sigma-Aldrich
	10% SDS	1	Biorad
	APS 10x (Ammonium persulfate)	0.5	Fluka
	TEMED (Tetramethylethylenediamine)	0.05	Biorad
Stacking gel	Milli-Q water	59.52	
	0.5% Tris-HCl in Milli-Q, pH 8.8	25.52	Sigma-Aldrich

	30% acrylamide/bis	13.39	Biorad
	10 % SDS	0.98	Biorad
	APS 10x (Ammonium persulfate)	0.07	Fluka
	TEMED (Tetramethylethylenediamine)	0.74	Biorad
Loading buffer 6x	Milli-Q water	51	
	Glycerol	20	Sigma-Aldrich
	0.5 M Tris in Milli-Q¸pH 6.8	12.5	Sigma-Aldrich
	B-mercaptoethanol	10	Sigma-Aldrich
	10% SDS	4.5	Sigma-Aldrich
	Bromophenol blue	2	Sigma-Aldrich
Fixing buffer	Ethanol	50	Panreach
	Milli-Q water	40	
	Acetic acid glacial	10	Panreac
Staining buffer	Ethanol	50	Panreach
	Milli-Q water	42.25	
	Acetic acid glacial	7.5	Panreac
	Coomassie Brilliant Blue	0.25	Biorad
Detaining buffer	Milli-Q water	50	
	Methanol	45	Panreach
	Acetic acid glacial	5	Panreach
Running buffer 5x	Glycine	72.05g	Sigma-Aldrich
	Tris	15.15g	Sigma-Aldrich
	Milli-Q water	1 L	

Table 3.1. List of solutions and their reagents employed for the SDS-PAGE.

Stock Running buffer 5x (Table 3.1) was diluted at a final concentration of 1x in Milli-Q water. Then, it was poured into the electrophoresis tank, which was filled until its level reached the mark on the tank walls (Figure 3.2 (f)). Then, 24 µL of GelMA solutions, which contained 2 ng of sample, and 2.5 µL of molecular weight size marker were loaded separately onto the gel wells. The molecular weight size marker allows the calibration of the gel and to determine the molecular mass of the unknown proteins by comparing with the marker bands with the sample bands. Each band of the marker corresponds to a well-defined molecular mass protein. Electrophoresis was carried out by applying a voltage of 60 V during 30 min, this allowed the samples to be concentrated and aligned at the border between the stacking and separating gel. Afterwards, voltage was increased up to 100 V and samples started to migrate through the separating gel towards the anode. After that time, the gel was carefully removed from the glass slides

without breaking it and placed in a small container, and the stacking gel was removed from the separating gel by cutting it with a scalpel.

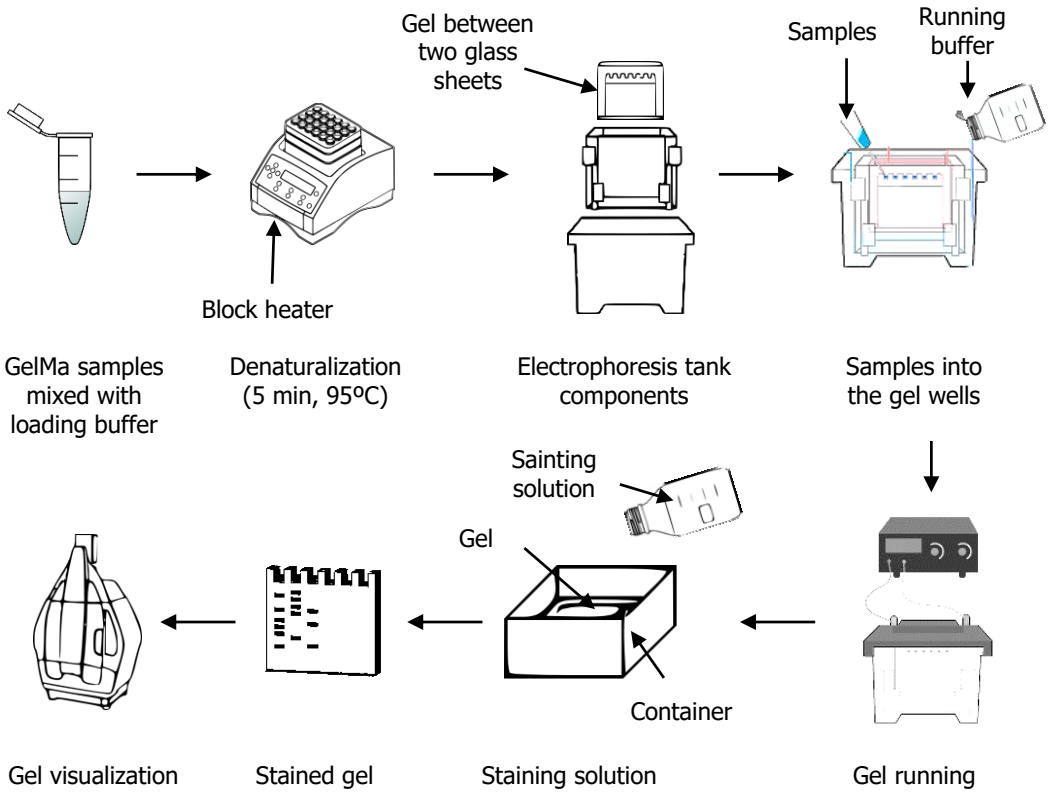

Figure 3.3. Schematic illustration of the main steps of the electrophoresis process run in order to visualize the molecular weight of the GelMA polymers.

Gels were fixed with fixing solution (Table 3.1) for 1 h at room temperature. Then, they were incubated with staining solution (Table 3.1**Table 3.1**) for 1 h 30 min at room temperature under shaking conditions, and later they were incubated overnight in the fridge at 4ºC. Coomassie Brillant Blue binds non-specifically to proteins and labels them in blue. On the next day, the stain was removed by submerging the gels in a solution (destaining solution) (Table 3.1) for 2 h in shaking conditions at room temperature. This process was repeated 3 times. White epi-images were taken with a Biomolecular Imager (ImageQuant LAS 4000, GE Healthcare). Images were analysed qualitatively using ImageJ v.149b software (http://rsb.info.nih.gov/ij, NIH). The software allowed to visualize stained bands and to determine the migration distance of the protein marker and the unknown proteins. Therefore, the molecular weight of the proteins of interest was estimated.

3.2.2. GelMA sample characterization by ATR-FTIR spectroscopy

Attenuated total reflectance-Fourier transform infrared (ATR-FTIR) spectroscopy was employed to qualitatively assess the success of the gelatin methacryloyl process by analysing the presence of specific chemical groups, such as methacrylate or methacrylamine groups into the gelatin molecule[140,224–227]. FTIR is based on the absorption of a specific frequency from infrared (IR) light when light irradiates the sample. To allow this phenomenon, the frequency of the IR light has to match the vibrational frequency of the chemical bonds in the sample[224]. For GelMA, nine characteristic IR absorption bands, known as amide A, B and I to VII, can be identified (Table 3.2)[228].

Band name	Wavelength number (cm^{-1})	Bond
Amide A	3300	N – H and O – H stretching
Amide B	3100	C – H stretching
Amide I	1600 – 1690	C = O stretching
Amide II	1480 – 1575	C – N – H stretching
Amide III	1330 – 1300	N – H stretching
Amide IV	625 – 770	O – C-N bending
Amide V	640 – 800	Out of plane N – H bending
Amide VI	540 – 610	Out of plane C = O bending
Amide VII	200	Skeletal torsion

Table 3.2. Characteristics ATR-FTIR bands of chemical bonds in GelMA.

$GelMA_{20}$ and $GelMA_{1.25}$ polymers were dissolved in PBS to a final concentration of 1% (w/v). Solutions of 1% (w/v) unmodified gelatin and 1% (v/v) MA in PBS were used as a reference. 350 µL of each solution were added into a polydimethylsiloxane (PDMS) (Sylgard 184 Silicon Elastomer, Dow Corning) mold. To fabricate this mold, PDMS polymer solution was prepared at a ratio 10:1 (w/w) between the pre-polymer and the curing agent, mixed gently and degassed under vacuum for at least 30 min. Then, it was poured between two flat poly(methyl methacrylate) (PMMA) (Goodfellow) pieces separated from each other with a spacer 2 mm thick. Next, 1 Kg weight was placed on top of the PMMA sheets and PDMS was cured at room temperature for at least 48 h. Then, circular pools were made in the PDMS by using a punch of 10 mm (AcuPunch) in diameter and were placed over a silicon wafer. GelMA polymer and reference solutions were poured in the PDMS pools and were left to dry for 1 day at room temperature. To have more concentrated samples, this step was repeated 3 times more. Polymer solutions were dried to reduce water contribution to the recorded spectra. Finally, FTIR

spectra were recorded using a spectrophotometer (Nicolet iS 10, ThermoFisher Scientific,) equipped with a diamond attenuated total reflectance (ATR) and deuterated triglycine sulphate (DTGS) detector. Spectra of all samples were collected in the range of 4000 – 800 cm^{-1} at a 4 cm^{-1} resolution and with an average of 16 scans. The raw data spectra were normalized and plotted with OriginPro 8.5 software (OriginLab, USA).

3.2.3. Determination of the degree of functionalization by ^{1}H-NMR

To quantify the degree of functionalization (DoF) of our samples, unmodified gelatin, $GelMA_{20}$, $GelMA_5$ and $GelMA_{1.25}$ polymers were dissolved at a concentration of 30 $mg \cdot mL^{-1}$ in deuterium oxide (D_2O) (Eurisotop). Samples were dissolved in a glass vial (VWR) at 65ºC for 1 hour under stirring conditions. 1 mL of each solution was transferred into a NMR tube and temperature was maintained at 37ºC to prevent sol-gel transition of the polymer solutions. ^{1}H-NMR spectra were acquired using a spectrometer (Varian INOVA 500 MHz, INOVA) and keeping the working temperature at 37ºC. Data were collected and analysed with MestReC software (Mestrelab Research). For a proper spectra interpretation, chemical sift (δ) was adjusted to the residual solvent signal, which in this case was D_2O (D_2O δ(^{1}H) =4.79 ppm) and spectra baselines were corrected using two-point baseline correction[229].

Here, the DoF estimated came from the modification of the primary amine groups from Lysine (Lys) and Hydroxylyisine (Hyl) aminoacids. DoF was calculated comparing the integral of Lys of the unmodified gelatin with the integral of Lys of the GelMA polymer. To obtain the integral of Lys, Phenylalanine (Phe) peaks (Phe δ (^{1}H) = 7.6 – 7.3 ppm) of the unmodified gelatin, $GelMA_{20}$ and $GelMA_{1.25}$ ^{1}H-NMR spectra were integrated for 5 protons and used as a reference integral. Then, Lys peaks (Lys δ (^{1}H) = 3.2 – 3.1 ppm) of unmodified gelatin and GelMA polymers were integrated. DoF of $GelMA_{20}$ and $GelMA_{1.25}$ were computed as the percentages between the Lys integral of the GelMA and the Lys integral of the unmodified gelatin (Eq. 3.2)[229]:

$$DoF\ (\%) = \left(1 - \frac{\int Lysine\ GelMA_x}{\int Lysine\ Gelatin}\right) * 100 \qquad \textbf{Eq. 3.2}$$

3.2.4. Determination of the degree of functionalization by TNBS assay

To assess the results obtained by ^{1}H-NMR, the DoF of $GelMA_5$, $GelMA_{1.25}$ and $GelMA_{0.25}$ polymers were quantified employing the Habeed Method[230]. This method is

based on the fact that free amino groups react with 2,4,6-Trinitrobenzene sulfonic acid (TNBS) to give trinitrophenyl (TNP) derivate. TNP is a compound that forms a yellow chromogenic solution that can be measured by absorbance.

Briefly, unmodified gelatin, $GelMA_5$, $GelMA_{1.25}$ and $GelMA_{0.25}$ polymers were dissolved at a concentration of 0.5 mg mL^{-1} in a sodium bicarbonate buffer solution ($NaHCO_3$, 0.1M; pH 8.4, in Milli-Q water) (Sigma-Aldrich) at 40ºC under stirring conditions. To generate a standard curve, decreasing concentration from 0.5 to 0 $mg \cdot mL^{-1}$ of gelatin were dissolved in a $NaHCO_3$ solution. Then, 100 µL of these standard gelatin solutions and 100 µL of the $GelMA_5$, $GelMA_{1.25}$ and $GelMA_{0.25}$ polymers solutions dissolved at 0.5 $mg \cdot mL^{-1}$ were pipetted in a 96 transparent well-plate (Nunc™, ThermoFisher Scientific). Next, 50 µL of 0.01% (v/v) TNBS (Sigma-Aldrich) in $NaHCO_3$ was added to each well and the mixture was incubated for 2 h at 37ºC in complete darkness. TNBS reaction was stopped by adding 50 µL of 10% (v/v) sodium dodecyl sulfate (SDS) (Sigma-Aldrich) and 25 µL of 1 M hydrochloric acid (HCl) (Panreac Applichem) to each well. SDS solubilizes gelatin and GelMA samples, and thus prevents precipitation of the samples when HCl is added. Absorbance of the resulting solutions was measured at 335 nm using a microplate reader (Infintie M200 PRO Multimode Microplate Reader, Tecan) (Figure 3.4).

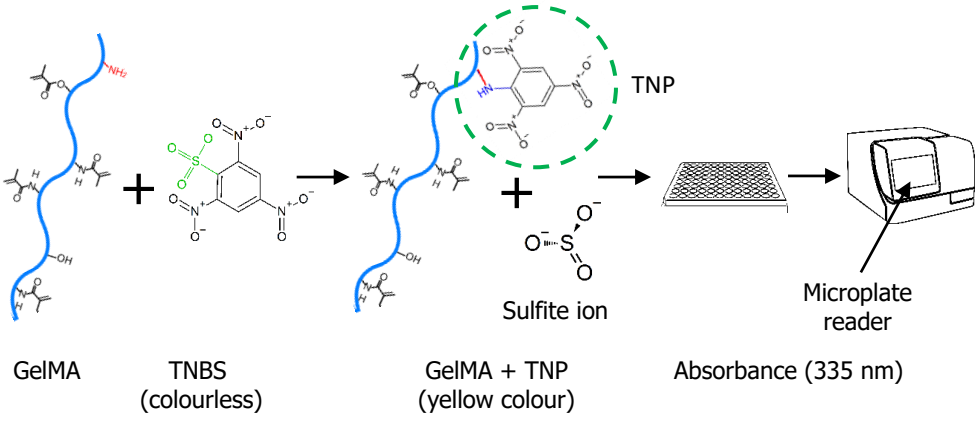

Figure 3.4. Schematic representation of the TNBS reaction with the free amino groups of GelMA to determine the degree of functionalization by a colorimetric assay.

A calibration curve that relates the absorbance of unmodified gelatin solutions with their percentage of free amino groups was established and fitted by a linear equation. Using this calibration curve, the unknown percentage of non-modified Lys in GelMA polymers (X) can be estimated from their absorbance. Finally, DoF of the GelMA

samples was calculated by subtracting the remaining free amino groups in GelMA from the total amount amino groups (Eq. 3.3)[140,229,231]:

$$DoF = (100 - X) \quad \textbf{Eq. 3.3}$$

3.3. Fabrication of GelMA, PEGDA and GelMA – PEGDA hydrogel co-networks

Photocrosslinkable hydrogels, then were made of GelMA (natural polymer), PEGDA (synthetic polymer) and GelMA – PEGDA (combination of natural and synthetic polymers). Unlike GelMA, PEGDA is a synthetic polymer composed by PEG molecules, which have been modified with one acrylate group at each end of the chain. This introduces to the PEG molecule two carbon double bonds, which are necessary to become photocrosslinkable. Hydrogels were form by free radical photopolymerization under ultraviolet light (UV) exposure. This is based on light absorption by a photoinitiator, which generates free radicals that activate the polymer carbon double bonds to generate a three-dimensional network (details are explained in section 1.6). The detailed experimental setup for the hydrogel polymerization is explained in the following sections.

3.3.1. Hydrogel polymer solution

Polymer solutions tested and concentrations of each polymer are listed in Table 3.3.

GelMA	GelMA stock % (w/v)	GelMA final % (w/v)	PEGDA stock % (w/v)	PEGDA final % (w/v)	Total macromer % (w/v)	Final polymer % (w/v)
-	0	0	10	5	5	5% PEGDA
$GelMA_5$	25	12.5	0	0	12.5	12.5% $GelMA_5$
	15	7.5	0	0	7.5	7.5% $GelMA_5$
	15	7.5	10	5	12.5	7.5% $GelMA_5$ – 5% PEGDA
	7.5	3.75	7.5	3.75	7.5	3.75% $GelMA_5$ – 3.75% PEGDA
	10	5	5	2.5	7.5	5% $GelMA_5$ – 2.5% PEGDA
	10	5	2.5	1.25	6.25	5% $GelMA_5$ – 1.25% PEGDA

$GelMA_{1.25}$	15	7.5	10	5	12.5	7.5% $GelMA_{1.25}$ – 5% PEGDA
	10	5	5	2.5	7.5	5% $GelMA_{1.25}$ – 2.5% PEGDA
	10	5	2	1.25	6.25	5% $GelMA_{1.25}$ – 1.25% PEGDA

Table 3.3. Polymer solutions employed to fabricate the hydrogels used for this thesis. $GelMA_x$ polymers of different DoF were considered. Concentrations of GelMA (in green) and PEGDA (in orange) solutions before (stock) and after mixing (final) with the photoinitiator at 0.5 %(w/v) or the other polymer are listed. Also, the total macromer concentrations (in blue) and the polymer nomenclature of the final solutions are specified.

GelMA and PEGDA polymers solutions were prepared by dissolving GelMA and PEGDA of 4000 Da in molecular weight ($PEGDA_{4000}$) (Polysciences) at the stock concentrations listed in the Table 3.3 and then diluted with the photoinitiator to the final concentration value. To do that, GelMA and PEGDA polymers were weighed in separated 10 mL glass vials and dissolved in DMEM without phenol red (Gibco, ThermoFisher Scientific) supplemented with 1% (v/v) Penicillin/Streptomycin (Sigma-Aldrich). In parallel, 1% (w/v) Irgacure D-2959 was dissolved in DMEM without phenol red supplemented with 1% (v/v) Penicillin/Streptomycin in a 5 mL glass vial. To minimize contamination, caps were sterilized by UV radiation whereas glass vials were autoclaved. Solutions were dissolved in a water bath for 2 h at 65ºC under stirring conditions and protected from light by wrapping the vial with aluminium foil. After 2 h of stirring, PEGDA and Irgacure D-2959 solutions were filtered with 0.22 µm Polyester (PET) filter (Merck-Millipore) to remove undissolved polymer (Figure 3.5). GelMA solutions were not possible to be filtered because they gelled during filtration, as the temperature drops below 37ºC.

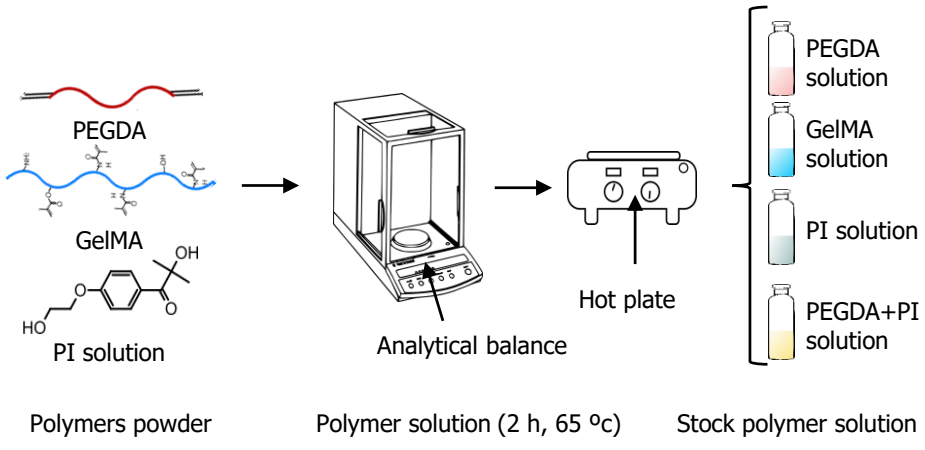

Figure 3.5. Schematic representation of the main steps for the dissolution of the GelMA, PEGDA and GelMA – PEGDA polymers.

Finally, GelMA and PEGDA solutions were mixed with photoinitiator solution in equal volumes, consequently the final concentration of the polymer and the photoinitiator were halved compared to the stock concentration. In all final polymer solutions, photoinitiator concentration remained constant at 0.5% (w/v). After mixing, polymer solutions were kept at 37ºC, under stirring conditions and protected from light for at least ≈30 min before use (Figure 3.6). For the GelMA – PEGDA hydrogels tested (Table 3.1), each polymer solution was prepared independently and then mixed to have co-network hydrogels upon photocrosslinking. To do that, GelMA and PEGDA polymer solutions were prepared as explained above with some slight modifications. Briefly, PEGDA polymer at the desired stock concentration together with Irgacure D-2959 at 1% (w/v) were weighed in the same glass vial. In parallel, GelMA polymer solution at the desired stock concentration was prepared and weighed in another glass vial. Both polymers were dissolved in DMEM without phenol red and supplemented with 1% (v/v) Penicillin/Streptomycin for 2 h at 65ºC under stirring conditions and protected from light (Figure 3.5). Following that, PEGDA polymer solution containing the photoinitiator was filtered with 0.22 µm PET filter. Finally, GelMA polymer solution and PEGDA polymer containing the photoinitiator solution were mixed at equal volumes in another glass vial. After mixing the polymer, the stock concentration of each polymer and the photoinitiator concentration was halved reduced, and thus final concentration was achieved. As with GelMA and PEGDA polymer solutions, GelMA – PEGDA polymer solutions were placed in the water bath at 37ºC, under stirring conditions and protected from light for at least ≈30 min before use (Figure 3.6).

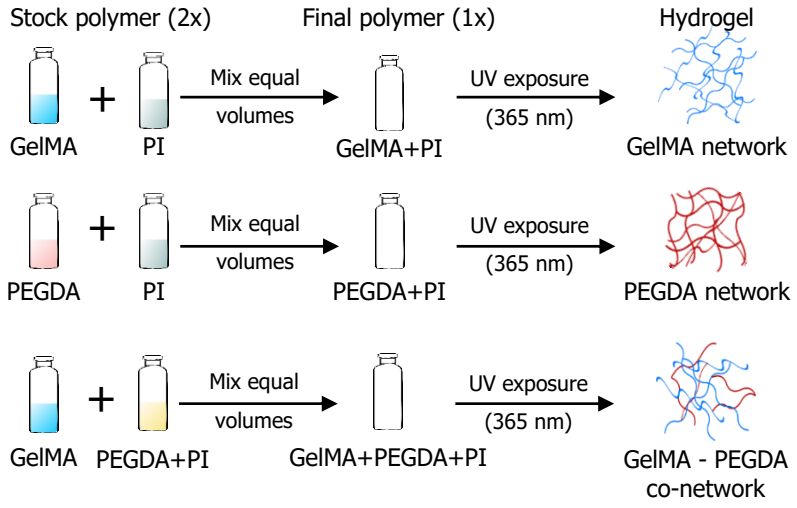

Figure 3.6. Schematic representation of the main steps for GelMA, PEGDA and GelMA – PEGDA polymer mixtures to form the hydrogels by photopolymerization.

For some of characterization hydrogel studies, GelMA, PEGDA and Irgacure D-2959 polymers were dissolved in PBS. When this happened, it is specified in the corresponding section.

3.3.2. Hydrogel polymerization setup

The experimental setup used for hydrogel polymerization was developed following a previously described methodology by our group[155,232]. Briefly, the chip to fabricate the hydrogels was made up of a PDMS sheet. To do the chip, PDMS polymer solution was prepared at a ratio 10:1 w/w between the pre-polymer and the curing agent, mixed gently and degassed under vacuum for at least 30 min. Nextt, it was poured between two flat poly(methyl methacrylated) (PMMA) (Goodfellow) pieces separated from each other with a spacer of 0.25, 0.5, 1 or 3 mm thick. Then, 1 Kg weight was placed on top of the PMMA plate and cured at room temperature for at least 48 h. After the PDMS sheet was cured, the PMMA plates were removed and the PMDS sheet was punched with a circular punch of 6.5 mm or 10 mm (AcuPunch) in diameter to create an array of circular pools. The pools served as a container for hydrogel polymer solution in order to fabricate the hydrogel with specific dimensions. Then, two inlet channels were cut with the help of a scalpel (Paramount) on opposite sides of the circular pool, to facilitate the insertion of the polymer solution. PDMS pools were mounted on top of polystyrene (PS) supports (ThermoFisher Scientific). Next, PDMS pools were covered with a silanized circular 12 mm diameter glass coverslip (VWR) or with a circular 12 mm Tracketc® polyethylene terephthalate (PET) membranes with 5 µm pore size (Sabeu GmbH & Co). To avoid leakage of polymer solution and minimize oxygen diffusion through the PET membranes pores, a non-silanized circular 18 mm diameter glass coverslip (VWR) was placed on top of the PET membrane. Glass coverslips and PET membranes, which acted as a substrate, were silanized to improve adhesion of the hydrogel to them. This step was essential to maintain the hydrogel in an aqueous solution for a long time without detaching from the substrate. Silanization is a process that coats the surface of some materials (glass, silicon, ceramics) with a silane molecule due to the interaction of the hydroxyl groups on the material with the alkoxy groups on the silane[233]. Briefly, glass coverslips or PET membranes were placed into a glass Petri dish and treated using an oxygen plasma apparatus (UV/ozone ProCleanar, Bioforce Nanoscience) for 15 min. Immediately after the UV plasma treatment, silane solution was poured into the substrates container. Silane solution was done by mixing 2% (v/v)

3-(Trimethoxysilyl)propryl methacrylate (TMSPMA) (Sigma-Aldrich) and 3% (v/v) diluted glacial acetic acid in ethanol at 96% (v/v). Diluted glacial acetic acid solution was prepared at a ratio 1:10 (v/v) between glacial acetic acid stock and Milli-Q water. Then, the silane solution was incubated for 2 h on a shaker at room temperature. Finally, silane solution was rinsed and substrates were washed gently with ethanol at 96% (v/v), dried for 1 h in the oven at 65ºC and stored under vacuum conditions to have an oxygen-free and low humidity atmosphere, which prevents the deterioration of the functionalization before being used. During UV oxygen plasma treatment, silicon oxides on the substrate surface react to the hydroxyl groups produced by radicals from the oxygen plasma treatment to activate the substrate surface. Then, silane molecules in the solution react with hydroxlyl groups of the substrate surface and form a stable siloxane bonds resulting in a silane monolayer on the substrate (Figure 3.7). In this case, TMSPMA were chose because it has a methacrylate group that reacts with acrylate groups of PEGDA or methacryloyl groups of GelMA[233]. Through this reaction, hydrogel adheres better to the substrate surface, and as a result hydrogels immersed in an aqueous solution do not detached so easily from the substrate.

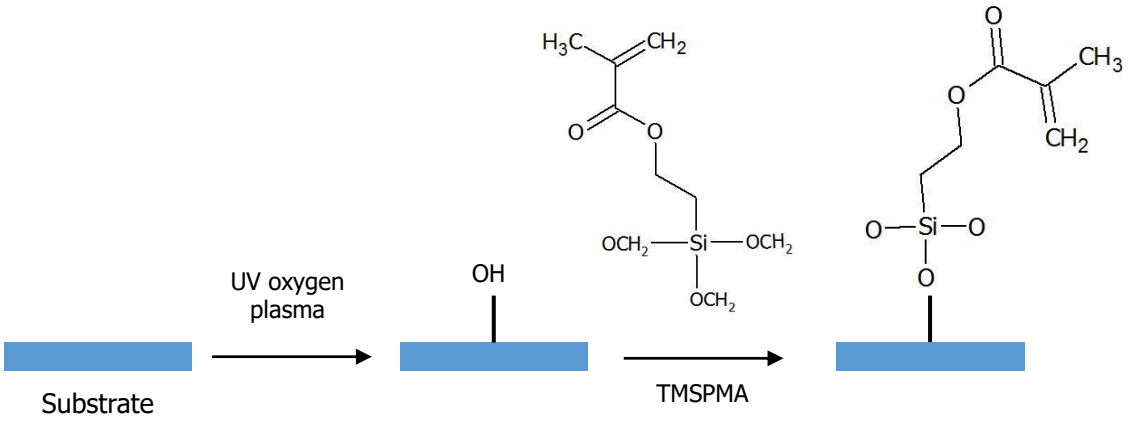

Figure 3.7. Schematic illustration of the silanization process. The solid substrates, such as glass or PET membranes were exposed to UV oxygen plasma to introduce hydroxyl-activated groups on their surfaces. Then, the silane TMSPMA was added and reacted with the hydroxyl-activated surface through siloxane covalent bond.

Disc-shaped hydrogels were fabricated by pouring the polymer solution into the PDMS pool array and exposed them to UV light (Figure 3.8 (a – c)). It was important to always keep the solution at 37ºC, and the material used for hydrogel fabrication, such as pipette tips, supports and PDMS chips, were warmed at 65ºC. This step is necessary to prevent gelation of GelMA-containing solutions.

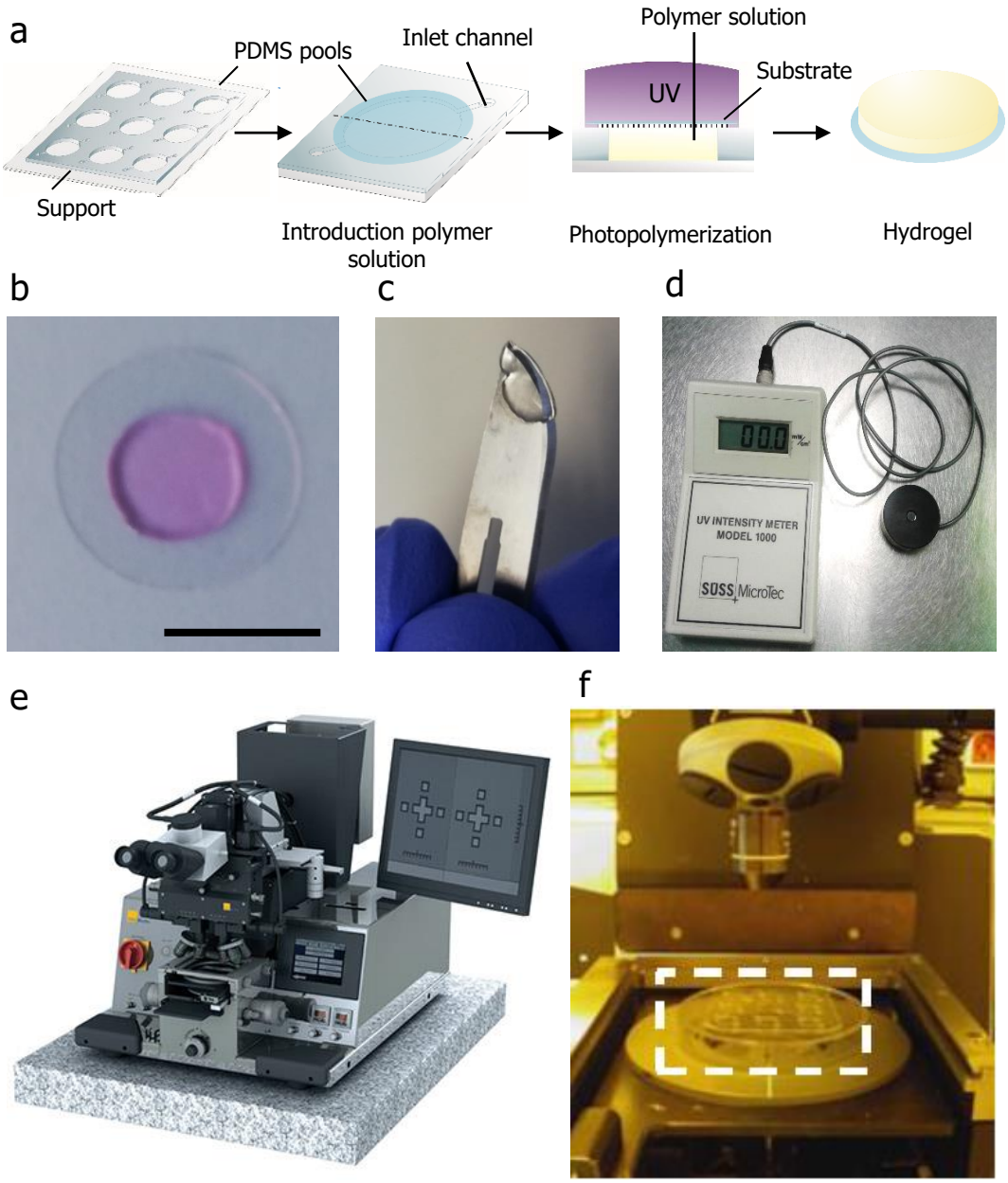

Figure 3.8. Hydrogel fabrication setup. (a) Schematic drawing of photocrosslinking process employed. Polymer solution was poured into PDMS pools, which were covered with a glass coverslip or a porous membrane, both acting as substrates. Then the substrates were UV exposed. (b) Photographs of 7.5% (w/v) $GelMA_{1.25}$ – 5% (w/v) PEGDA hydrogel crosslinked using an energy dose of 1.88 J/cm^2 on top of a glass coverslip, scale bar 10 mm; and (c) the same hydrogel after detaching it from the glass coverslip. (d) Photograph of the UV intensity meter, Model 1000, Suss MicroTech. (e) Photograph of the Mask Aligner MJB4, Suss MicroTech (from https://www.suss.com/). (f) Photograph of the PMDS chip placed on the Mask Aligner (from Castaño *et al.*[232]).

UV light exposure took place in a MJB4 Mask Aligner (MJB4, Suss MicroTech) located at the IBEC MicroFabSpace (Figure 3.8 (d and f)). This mask aligner was equipped with a mercury short arc lamp (OSR HBO 350 W/S) and an I-line filter. This I-

line filter was placed to prevent sample irradiation for wavelengths lower and higher than 365±10 nm (Figure 3.9) to minimize the UV damage on encapsulated cells. Before each exposure, the incidental power density on the surface of the samples was measured using a UV-intensity meter (Model 1000, Suss MicroTech) placed at the same position of the sample (Figure 3.8 (d)). Hydrogels were manufactured using a constant energy dose (ε) (J·cm^{-2}). As the incidental power density fluctuated daily, to maintain constant the energy dose in all the experiments, UV exposure time for a specific energy dose was corrected based on the incidental power density (P) (mW·cm^{-2}) measured just before the exposure (Eq. 3.4).

$$t = \frac{\varepsilon}{P} \qquad \textbf{Eq. 3.4}$$

For each experiment, these parameters are listed in the corresponding material and method section.

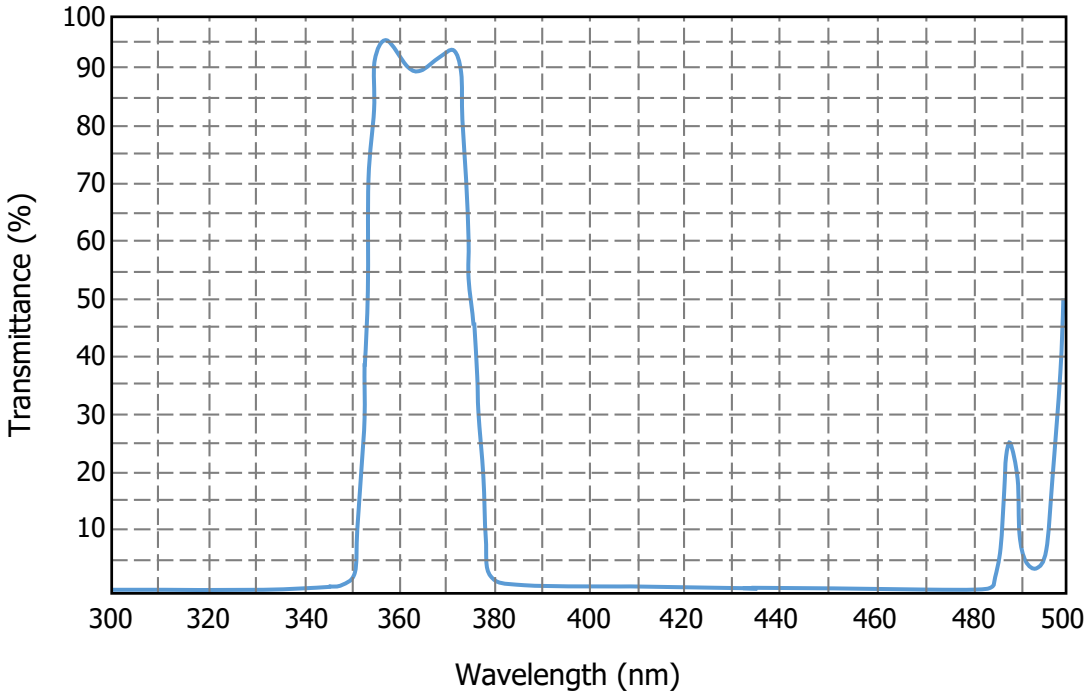

Figure 3.9. Intensity distribution at the spectral region of the mercury short arc lamp set when the I-line filter is implemented in the mask aligner.

After UV exposure, the unreacted polymer and photoinitiator were washed out with warm PBS at 37ºC. Then, samples were placed into a 24 well-plate and kept submerged in PBS at 4ºC to reach the equilibrium swelling before further characterization.

3.4. Characterization of GelMA hydrogel networks and GelMA – PEGDA hydrogel co-networks

After fabrication of the GelMA, PEGDA and GelMA – PEGDA hydrogels co-networks, the mechanical and physicochemical properties of the hydrogels were characterized in order to find one that (I) supports the growth of epithelial cells, (II) allows for the incorporation of a stromal compartment and (III) is suitable for long-term cell culture.

3.4.1. Analysis of co-network homogeneity

The presence of GelMA and the microscopic homogeneity of GelMA – PEGDA co-networks were determined by the fluorescent labelling of the GelMA chains using NHS-Rhodamine (Sigma-Aldrich). NHS groups are esters able to react with primary amine groups of GelMA molecule to form stable amine bonds, resulting in a labelled fluorescently GelMA molecule. On the contrary, PEGDA chains lack of primary amine groups, so NHS groups do not react with them and they remain non-fluorescence.

To study co-network homogeneity, hydrogels of 10 mm in diameter and 1 mm in thickness were obtained from dissolving 7.5% (w/v) $GelMA_5$, 5% (w/v) PEGDA and 7.5% (w/v) $GelMA_5$ – 5% (w/v) PEGDA. All the polymer solutions contained 0.5% (w/v) Irgacure D-2595 and were exposed to a UV dose of 3.00 $J \cdot cm^{-2}$. Hydrogels were swollen for at least 3 days at 4ºC in PBS in a 24 well-plate. Firstly, NHS-Rhodamine, which is water insoluble, was diluted in DMSO at a 20 mM stock concentration and was vortexed to enhance dilution. The 20 mM of NHS-Rhodamine was then diluted in PBS at different concentrations (2 mM, 0.2 mM and 0.02 mM). Hydrogels were placed in a 24 well-plate, and 0.5 mL of the different NHS-Rhodamine solutions were added. The 24 well-plate was covered with aluminium foil and incubated overnight at 4ºC in shaking conditions. During the incubation NHS groups of the Rhodamine were allowed to react with primary amine groups of $GelMA_5$ chains. On the next day, NHS-Rhodamine solutions were rinsed and 1 mL of PBS was added and incubated for 2 h at 4ºC under shaking. This step was repeated 3 additional times. Finally, hydrogels were left overnight at 4ºC with PBS under shaking conditions. Then, the fluorescence of the hydrogels was visualized. For this purpose, a drop of Fluoromount-G® mounting solution (SoutherBiotech) was placed on a rectangular glass coverslip of 24 mm x 60 mm (VRW) and hydrogels were deposited on top of the drop. The fluorescence of the hydrogels was imaged using a confocal

microscopy (LSM 800, Zeiss) located at the IBEC MicroFabSpace installations. Z-stack images (2 µm between each image) were obtained from the first 50 µm of the hydrogels and were acquired using a 40x objective. Capture parameters were kept constant during the acquisition time for all the hydrogels. Fluorescence intensity of each hydrogel was analysed by ImageJ software. The intensity was measured from the maximum Z projections to allow for comparisons.

3.4.2. Mass swelling analysis

Swelling is a relevant factor in hydrogels because it is connected with their degree of crosslinking and their porosity. The largest the crosslinking degree of the hydrogel, the smallest is the pore size and lowest is the capacity of retaining water inside the network. As a result of that, the diffusion of the nutrients and oxygen inside of the hydrogel can be compromised. Another factor to consider is the equilibrium swelling time, after which the hydrogels cannot arrest more water. At that point, the weight and dimensions of the hydrogel are constant and the physicochemical and mechanical properties remain unchanged over time. The equilibrium swelling time and the mass swelling ratio were determined for all the hydrogels listed in Table 3.4. The polymer solutions and hydrogels were fabricated following the methodology described in section 3.3. To perform this study, polymer solutions were dissolved in PBS.

Swelling analysis were performed following the method previously used in our laboratory[157]. GelMA, PEGDA and GelMA – PEGDA hydrogels of 10 mm in diameter and 1 mm in height were obtained by photopolymerization with a UV dose of 3.00 $J \cdot cm^{-2}$ onto glass coverslips. Right after polymerization, hydrogels were weighed (m_c). Then, they were kept submerged in PBS at 37ºC to induce swelling for one week with 1 mL of PBS in a 24 well-plate. During this time, hydrogels were weighted at different time points, from 15 min till 7 days. Before weighing, hydrogels were carefully manipulated and wiped with a KimWipe tissue (Kimtech Science) to remove any excess of liquid. After each measurement, PBS was rinsed and exchanged for new filtered PBS to prevent fungi or microbial contamination. At a certain time, hydrogels arrive to equilibrium swelling and keep a constant weight over time (m_s). After swelling, PBS was removed, and samples were dried overnight at room temperature. The lid of the 24 well-plate was removed to facilitate water evaporation. Next day, hydrogels were placed in the oven at 50ºC

(Memert) for 4 h 30 min to remove all the residual water and were weighed once more at dry state (m_d).

GelMA DoF	GelMA final % (w/v)	PEGDA final % (w/v)	Total macromer % (w/v)	Hydrogel tested % (w/v)
$GelMA_5$	12.5	0	12.5	12.5% $GelMA_5$
	7.5	0	7.5	7.5% $GelMA_5$
$GelMA_{1.25}$	12.5	0	12.5	12.5% $GelMA_{1.25}$
	7.5	0	7.5	7.5% $GelMA_{1.25}$
$GelMA_{0.25}$	12.5	0	12.5	12.5% $GelMA_{0.25}$
	7.5	0	7.5	7.5% $GelMA_{0.25}$
-	0	12.5	12.5	12.5% PEGDA
	0	7.5	7.5	7.5% PEGDA
$GelMA_5$	7.5	5	12.5	7.5% $GelMA_5$ – 5% PEGDA
	3.75	3.75	7.5	3.75% $GelMA_5$ – 3.75% PEGDA

Table 3.4. List of the hydrogels tested for mass swelling analysis.

Later, for cellular experiments, hydrogels were fabricated on top of circular 12 mm Tracketc® PET membranes. As the fabrication conditions were slightly different compared to the glass coverslips because PET membranes tend to absorb UV light behaving as filters[155], mass swelling ratio was determined again for the new parameters. Moreover, the mass swelling analysis protocol explained above was modified to facilitate hydrogel manipulation and swelling measurements. In the following paragraphs, these modifications are explained.

In particular, hydrogels grown on PET membranes, were photopolymerized with an UV dose of 1.88 $J \cdot cm^{-2}$. As previously, right after polymerization, hydrogels were weighed (m_c) and were also weighted once they arrived to the equilibrium swelling (m_s). Finally, samples were detached from glass coverslip, placed to a 1.5 mL Eppendorf (Eppendorf), covered with parafilm and frozen overnight at -80ºC. Frozen samples were lyophilized with a freeze-dryer machine (Freeze Dryer Alpha 1-4 LD Christ) for at least 1 day and weighed once more to obtain the dry weight (m_d).

After obtaining the experimental values for equilibrium and dry weights (m_S and m_d), the mass swelling ratio was calculated following Eq. 3.5[201]:

$$Mass\ swelling\ ratio = \frac{m_s - m_d}{m_d} \qquad \textbf{Eq. 3.5}$$

For statistics, three hydrogels for each condition were analysed. Data were plotted with OriginPro 8.5 software (OriginLab, USA) as the mean ± standard deviation.

3.4.3. Characterization of the network properties of GelMA and PEGDA hydrogels

Molecular diffusion is an important network property of the hydrogels affecting mass transport, which correlates with the mesh size (ξ) and the molecular weight between two consecutive crosslinking points (M_c). To estimate the mesh size of GelMA and PEGDA samples, we used the Peppas and Merrill[183] theory, which was adapted from Flory-Rehner theory[182], and takes into account hydrogels formed in water or in solvent solutions. Further details of this theory are found in section 1.7. Disc-shaped hydrogels tested were $GelMA_5$, $GelMA_{1.25}$, $GelMA_{0.25}$ and PEGDA hydrogels containing two different total macromer concentrations (7.5% (w/v) and 12.5% (w/v)) and polymerized at a UV dose of 3.00 J·cm^{-2} on top of glass coverslips. Additionally, some $GelMA_5$ hydrogels polymerized at a UV dose of 1.88 J·cm^{-2} on PET membranes were also characterized. The measured masses of the hydrogels right after fabrication (m_c), in equilibrium swelling (m_s), and in their dry state (m_d) were used to calculate their polymer volume fraction in the relaxed ($v_{2,r}$) and swollen ($v_{2,s}$) states. The relaxed state is the state of the hydrogel immediately after polymerization, while the swollen state is the state of hydrogel once it is placed into the water[234]. Relaxed and swollen state polymer volume fraction values are obtained using Eq. 3.6 and Eq. 3.7, respectively.

$$v_{2,r} = \left[1 + \frac{(q_F - 1) * \rho_p}{\rho_{sol}}\right]^{-1} \quad \textbf{Eq. 3.6}$$

$$v_{2,s} = \left[1 + \frac{(q_w - 1) * \rho_p}{\rho_{water}}\right]^{-1} \quad \textbf{Eq. 3.7}$$

Where ρ_p, ρ_{sol} and ρ_{water} are the gelatin, the solvent and the water densities, respectively, q_F is the weight fraction of hydrogel after curing ($q_F = \frac{m_c}{m_d}$), and q_w is the weight fraction of hydrogel after equilibrium swelling ($q_w = \frac{m_s}{m_d}$).

To estimate the average molecular weight between two crosslinks the following equation was resolved:

$$\frac{1}{M_c} = \frac{2}{M_n} - \frac{\frac{v}{V_1} * \left[ln(1 - v_{2,s}) + (v_{2,s}) + \chi * (v_{2,s})^2\right]}{(v_{2,s}) * \left[\left(\frac{v_{2,s}}{(v_{2,r})}\right)^{1/3} - \frac{v_{2,s}}{2\, v_{2,r}}\right]} \quad \textbf{Eq. 3.8}$$

Where M_n is the average molecular weight of the polymer, υ is the specific volume of bulk polymer (inverse of the density of the polymer), V_1 is the molar volume of water, χ is the Flory-Huggins polymer-solvent interaction parameter, $v_{2,r}$ and $v_{2,r}$ are described previously. Once M_c was obtained, the mesh size was computed as described by Canal and Peppas model (Eq. 3.9)[235].

$$\xi = \left(\overline{r_0^2}\right)^{1/2} * \left(v_{2,s}\right)^{-1/3} \quad \textbf{Eq. 3.9}$$

Where $\overline{r_0^2}$ is the root mean square average end to end distance of the GelMA or PEGDA polymer chains in the unperturbed state and is calculated by Eq. 3.10:

$$\left(\overline{r_0^2}\right)^{1/2} = l * n^{1/2} * C_n^{1/2} \quad \textbf{Eq. 3.10}$$

Where C_n is the Flory characteristic ratio for GelMA or PEG and l is the mean length between bonds and it depends on the polymer molecules. For GelMA molecules, l is the mean length between one C – C bond and two C – N bonds, whereas for PEG, l is the mean length between C – C and C – O bonds. Finally, n is the number of bond vectors per a chain and it depends on the polymer used. As a result, GelMA (Eq. 3.11) and PEGDA (Eq. 3.12) have different equations[184].

$$n = 3 * \frac{M_c}{M_r} \quad \textbf{Eq. 3.11}$$

$$n = 2 * \frac{M_c}{M_r} \quad \textbf{Eq. 3.12}$$

Table 3.5 summarizes the parameters used to calculate the molecular weight between crosslinks and the mesh size of GelMA and PEGDA hydrogel networks. For statistics, three hydrogels for each condition were analysed. Data were plotted with OriginPro 8.5 software (OriginLab, USA) as the mean ± standard deviation.

Parameters	GelMA	Reference	PEGDA	Reference
M_n (kDa)	87.50	[184]	4.00	Datasheet
$\boldsymbol{l}$ (nm)	0.139	[184]	0.146	[157,184]
M_r (g·mol^{-1})	94.70	[184]	44.00	[157,184]

ν $(cm^2 \cdot g^{-1})$	0.741	[184]	0.893	[157,184]
C_n	8.26	[184]	4.00	[157,184]
X (nm)	0.497	[184]	0.426	[157,184]
ρ_p $(g \cdot cm^{-3})$	1.35	[236]	1.12	[157]
ρ_{sol} $(g \cdot cm^{-3})$	1.00	*	1.00	*
ρ_{water} $(g \cdot cm^{-3})$	1.00	[157]	1.00	[157]

Table 3.5. Parameters used for the calculation of M_c and ξ of GelMA and PEGDA hydrogel networks. * Solvent density is assumed to be the same of the water density.

This model is only suited to determine quantitatively the mesh size and average molecular weight between crosslinking of homopolymeric hydrogels, it is not well suited for the GelMA – PEGDA hydrogel co-networks[237].

3.4.4. Study of the diffusion properties and mesh size for GelMA hydrogels and GelMA – PEGDA hydrogel co-networks

The Flory-Rehner model[182] modified by Peppas and Merril[183,235] is not well suited to determine the mesh size of GelMA – PEGDA hydrogels co-networks[237]. Therefore, we performed some empirical approximations to know about the mesh size of our co-networks by checking the diffusion profiles of dextran fluorescent molecules of different molecular weights when passing through the GelMA – PEGDA hydrogel co-networks.

Dextran molecules of 4 kDa (FITC-Dextran, FD4), 70 kDa (Rhodamine-Dextran, FD70) and 500 kDa (FITC-Dextran, FD500) (all from Sigma-Aldrich) with hydrodynamic diameters of 1.4, 6.0 and 14.7 nm, respectively, were selected to study their diffusion coefficients through the networks. $GelMA_5$ hydrogels of 12.5% and 7.5% (w/v) polymer concentrations and $GelMA_5$ – PEGDA hydrogels of 7.5% (w/v) – 5% (w/v) and 3.75% (w/v) – 3.75% (w/v) polymer concentrations, all containing 0.5% (w/v) of Irgacure D-2595, were fabricated on top of porous PET membranes using a UV dose of 1.88 $J \cdot cm^{-2}$. Hydrogels were 6.5 mm in diameter and 1 mm in height. After fabrication, they were kept on a 24 well-plate with PBS for 3 days, until swelling was completed. After swelling, hydrogels were mounted on 24-well polycarbonate Transwell® filter inserts (Corning Costar) using double-sided pressure-sensitive adhesive (PSA) rings (Adhesives Research). Briefly, polycarbonate membranes of the commercial Transwell® inserts were removed completely by a scalpel. Swollen hydrogels were removed from the PBS solutions and dried carefully to remove excess of water on the membrane with a KimWipe

tissue. Then, the protective layer of an adhesive ring of 15 mm outer diameter and 6 mm inner diameter was removed, and the ring was stack onto the commercial Transwell® insert. The second protective layer of the PSA ring was removed and the PET membrane with the hydrogel was placed on top of the adhesive ring, with the hydrogel facing towards inside the insert. Finally, a second adhesive ring was placed to ensure an accurate adhesion between membrane and adhesive ring, and thus minimize leakage through the borders (Figure 3.10).

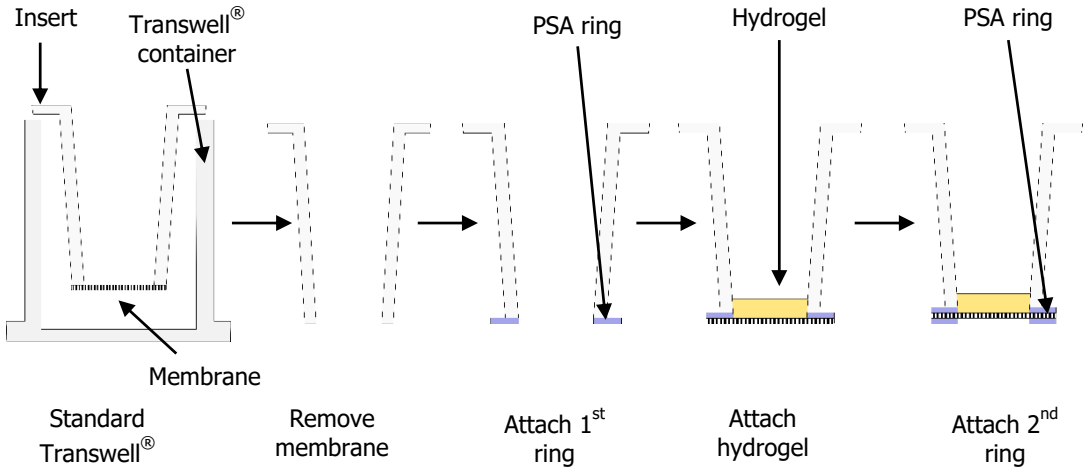

Figure 3.10. Schematic illustration of the process to mount hydrogels on standard Transwell® inserts.

Once the hydrogels were placed on the commercial Transwell® inserts, the apical and basolateral compartments were filled with 200 µL of and 600 µL of PBS, respectively, and incubated overnight in the oven at 37ºC. The next day, dextrans FD4, FD70, and FD500 were diluted at 0.25 $mg \cdot mL^{-1}$ in PBS and filtered with a 0.22 µm PET filter. Each one was prepared in a different glass vial in order to use them separately and thus preventing the blockage of the diffusion of the smallest dextrans through the pores by the largest dextrans due to the interactions with the hydrogel networks. The PBS solution from the inserts was rinsed and 200 µL of dextran solution was loaded in the apical chamber while into the basolateral chamber 600 µL of PBS were added. At several time points, ranging from 0 to 240 min, 50 µL were sampled from the basolateral compartment and replaced with 50 µL of PBS. Then, the collected samples were transferred to 96 black well-plates and FITC or Rhodamine fluorescence was measured at excitation/emission wavelengths of 490/525 nm and 540/625 nm, respectively, using a microplate reader (Infinite M200 PRO Multimode, Tecan). During all the experiment, Transwell® inserts were incubated at 37ºC (Figure 3.11).

To quantitatively link dextran concentrations with fluorescence values, standard curves for each dextran were produced. Standard curves were obtained by plotting fluorescence readouts on Y-axis versus the known dextran concentrations on X-axis and performing linear fittings. Finally, fluorescence values of each dextran over time obtained from the basolateral compartments were converted to known dextran concentrations.

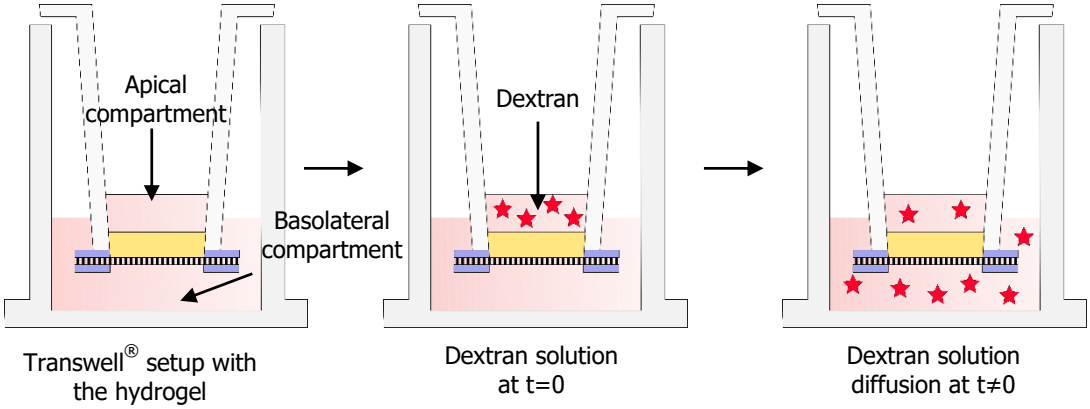

Figure 3.11. Schematic representation of the diffusion assay. After mounting the hydrogel in the insert, dextran solution was added to the apical part (t=0). Driven by a gradient concentration, dextrans diffuse to the basolateral compartment, if the pore size of the hydrogels are larger than the dextran diameter.

The mass transfer of the dextran molecules in the basolateral compartment at each time point was calculated by Eq. 3.13:

$$Mass\ tranfer = C_n * V_r \qquad \textbf{Eq. 3.13}$$

Where C_n is the experimental dextran concentration in the solution at time n and V_r is the total volume of the solution in the basolateral chamber. To calculate the total mass transfer accounting for the mass removed at each time point, a correction factor was applied (Eq. 3.14).

$$Total\ mass\ tranfer = V_s * \left(\sum_{n=1}^{n} C_{n-1}\right) + C_n * V_r \qquad \textbf{Eq. 3.14}$$

Where V_s is the collected volume, C_n is the concentration of dextrans in the solution at given time point, and V_r is the total volume of the basolateral chamber. Finally, the apparent permeability (P_{app}) of the dextran through the network was computed by Eq. 3.15:

$$P_{app} = \frac{dQ/dt}{C_0 * A} \quad \textbf{Eq. 3.15}$$

Where C_0 is the initial concentration in the apical chamber, A is the area of the hydrogel surface, and dQ/dt is the dextran transport rate, which is defined as the slope obtained from linear regression of dextran transport amount[238]. Then, the apparent diffusion coefficients (D_{app}) for each dextran were calculated following the model described by Kontturi L. (Eq. 3.16)[188]:

$$D_{app} = \frac{P_{app} \cdot h}{K} \quad \textbf{Eq. 3.16}$$

Where h is the height of the hydrogel, K is the hydrogel-water partition coefficient (assumed to be 1), and P_{app} is the apparent permeability. For statistics at least two hydrogels for each condition were analysed. Data were plotted with OriginPro 8.5 software (OriginLab, USA) as the mean ± standard deviation.

3.4.5. Mechanical properties of GelMA and GelMA – PEGDA hydrogels

The mechanical properties of hydrogels are important physical cues to take into account when creating hydrogels for cell culture. Cell phenotype, cytoskeleton organization, proliferation and migration can be modulated by changing the mechanical properties of hydrogels[239]. The mechanical properties of GelMA and GelMA – PEGDA hydrogels were analysed and compared among samples with different degree of GelMA functionalization, total macromer composition and content of each of the polymers.

For the first set of hydrogels the mechanical properties were analysed by dynamic mechanical analysis (DMA). DMA is a method to characterize mechanical properties of bulk hydrogels. $GelMA_5$ and PEGDA hydrogels at concentrations of 12.5% (w/v) and 7.5% (w/v), and $GelMA_5$ – PEGDA hydrogel co-networks at concentrations of 7.5% (w/v) – 5% (w/v) and 3.75% (w/v) – 3.75% (w/v) were fabricated on top of glass coverslips covered with porous PET membranes, to mimic the exposure conditions for the hydrogels used for cell culture. Hydrogels discs of 10 mm in diameter and about 3 mm in height were photopolymerized with an energy dose of 3.76 $J \cdot cm^{-2}$. We applied the double of the dose employed for cell encapsulation (see section 3.8) to ensure photopolymerization across entire thickness of the hydrogel. After swelling in PBS, hydrogels were detached from the glass coverslip and dried with a tissue. Due to the

different swelling rates, the diameters of hydrogels were no longer comparable, so they were punched to obtain consistent 10 mm diameter samples. Sample heights were accurately determined using a high precision calliper (Mitutoyo Corporation). A Zwick-Roell Zwichi Z0.5TN testing machine (Zwick Roell Group) was used to obtain stress (σ) – strain (ϵ) curves from compression assays at room temperature (Figure 3.12 (a – c)). Samples were placed between the compression clamps for the measurements. To reduce hydrogel dehydration during the measurement, a couple of Milli-Q water drops were placed on top of the hydrogel before starting the measurements.

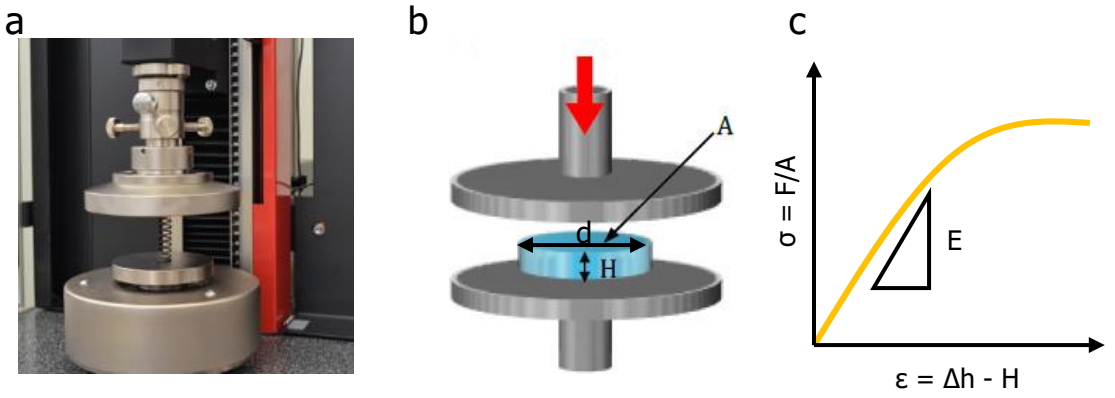

Figure 3.12. Mechanical testing analysis by Dynamic mechanical analysis (DMA). (a) Photograph of the Zwick-Roell Zwicki machine. (b) Schematic representation of the compression test, where F is the force applied, A is the hydrogel area, H is the initial height of the hydrogel and d is the diameter. (c) Representation of stress (σ)-strain (ε) curve to compute the Young's modulus.

Stress-strain curves were recorded by applying a limiting strain rate of 5% min^{-1} and a maximum strain of 50%. An initial load of 5 mN was applied to facilitate the precise contact between the hydrogel and the compression plates. The settings used were in agreement with the ones found in the literature[240]. Raw data obtained were analysed with TestXpert II, v3.41 analysis software, introducing the hydrogel area (A) and Poisson ratio (ν). Hydrogel area was 0.785 cm^2 and Poisson ratio was assumed to be 0.5, as was found in the literature[241,242]. Knowing these values, the software calculated the values for stress and strain using Eq. 3.17 and Eq. 3.18, respectively:

$$\sigma = \frac{F}{A} \qquad \textbf{Eq. 3.17}$$

$$\epsilon = \frac{\Delta h}{h} \qquad \textbf{Eq. 3.18}$$

Where F is the normal force applied perpendicular to the hydrogel area, Δh is the variation of hydrogel height, and h is the initial hydrogel height. The apparent elastic

modulus (E) was determined from the slope of the linear region of the stress-strain curves, corresponding to a strain of 10 – 20%. For statistics, three hydrogels of each condition were inspected. Data were plotted with OriginPro 8.5 software (OriginLab, USA) as the mean ± standard deviation.

The mechanical properties for a second set of hydrogels were determined by atomic force microscopy (AFM). While DMA provides bulk properties, the mechanical properties obtained by AFM are mainly from the surface of the hydrogel. For cells cultured on top of the substrates, stiffness measured by AFM maybe more representative than the DMA as cells sense mainly a few micrometers under them. For AFM measurements, $GelMA_5$ – PEGDA and $GelMA_{1.25}$ – PEGDA disc-shaped hydrogels at concentrations of 7.5% (w/v) – 5% (w/v), 5% (w/v) – 2.5% (w/v), 5% (w/v) – 1.25% (w/v) were fabricated on top of silanized glass coverslips covered with porous PET membranes. Hydrogel discs of 6.5 mm in diameter and 0.5 mm in height were photopolymerized with an energy dose of 1.88 $J \cdot cm^{-2}$. AFM studies were performed on swollen hydrogels.

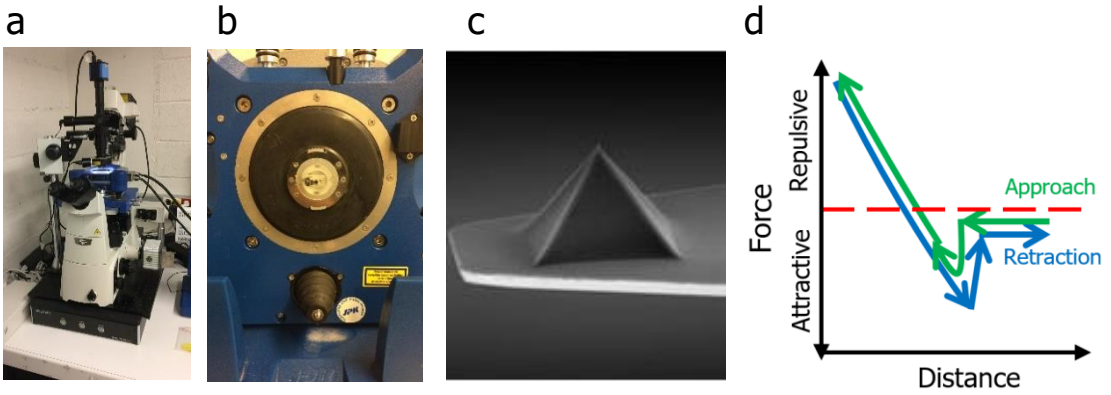

Figure 3.13. Mechanical testing analysis by Atomic Force Microscopy (AFM). (a) The Nikon Ti inverted microscope in which the AFM is mounted. (b) NanoWizard® 4 Bioscience AFM. (c) A pyramidal tip. (d) Schematic representation of an approach and retraction curve.

NanoWizard® 4 Bioscience AFM (JPK Instruments) mounted onto a Nikon Ti inverted microscope was used to perform the measurements (Figure 3.13 (a and b)). Indentations were performed on the surface of the samples using silicon nitride pyramidal tips (NanoWorld) with nominal spring constants of 0.08 $N \cdot m^{-1}$ (PNP-TR-50) and cantilever approach/retraction speeds of 0.5 $\mu m \cdot s^{-1}$ and 1 $\mu m \cdot s^{-1}$ (Figure 3.13 (c)). All the measurements were conducted at room temperature. After calibration of the sensitivity, force (F)-displacement (z) curves were measured on the surface. The curves consist on two parts: one part is the approach curve where the cantilever starts to

approach to the sample until touching it, and the other part is the retraction curve where the cantilever moves away from the hydrogel surface (Figure 3.13 (d)). The apparent elastic modulus was obtained from the approach curve by applying Hook's law and the Hertz model[190]. All the data were analysed with the JPK data analysis software and were presented as the mean ± standard deviation.

3.4.6. Degradation studies of GelMA and GelMA – PEGDA hydrogels

Our hydrogels contain GelMA, which is a natural-derived polymer coming from collagen, a protein of the extracellular matrix. Consequently, GelMA can be degraded by matrix metalloproteinases, which are enzymes capable of degrading extracellular matrix proteins. Hydrogel degradation is an essential physical process to study to have good stability for long-term cell culture scaffolds while allowing the cells to remodel their microenvironment.

Degradation was examined for a first set of disc-shaped hydrogels, $GelMA_5$ at concentrations of 12.5% (w/v) and 7.5% (w/v), and $GelMA_5$ – PEGDA at concentrations of 7.5% (w/v) – 5% (w/v) and 3.75% (w/v) – 3.75% (w/v), which were mixed with 0.5% (w/v) of Irgacure D-2959 and dissolved in PBS. Hydrogels of 10 mm diameter and 1 mm thickness were fabricated on top of 12 mm glass coverslips after exposure to an UV dose of 3.00 $J \cdot cm^{-2}$ to ensure complete hydrogel crosslinking. For a second set of disc-shaped hydrogels, $GelMA_5$ – PEGDA and $GelMA_{1.25}$ – PEGDA at concentrations of 7.5% (w/v) – 5% (w/v), 5% (w/v) – 2.5% (w/v) and 5% (w/v) – 1.25% (w/v) were mixed with 0.5% (w/v) of Irgacure D-2959 and dissolved with DMEM without phenol red supplemented with 1% Penicillin/Streptomycin. Hydrogels of 10 mm diameter and 1 mm thickness were fabricated on top of 12 mm glass coverslips topped with PET membranes and irradiated by applying an UV dose of 1.88 $J \cdot cm^{-1}$. After fabrication, for both sets of hydrogels, samples were meticulously removed from their glass coverslips using a scalpel and were placed inside of a 1.5 mL Eppendorf tube containing 1 mL PBS for 3 days to achieve the equilibrium swelling. After swelling, hydrogels were placed in an oven at 37ºC for 1 day to temper them. Then, PBS was rinsed and 1 mL of collagenase type II (Sigma-Aldrich) at 2.5 $U \cdot mL^{-1}$ dissolved in filtered PBS at 37ºC was added to each Eppendorf ensuring that hydrogels were entirely submerged into the solution. Hydrogels were incubated at 37ºC for an efficient collagenase activity. At several time points, ranged from 0 h to 96 h or until all the hydrogel was degraded, collagenase solution was

removed from the hydrogel by centrifuging the samples for 5 min at 8000 rpm. Then, the solutions were decanted and the remaining hydrogels were washed twice by adding 1 mL of Milli-Q water, centrifuged again for 5 min at 8000 rpm, and supernatant was decanted. After the second centrifugation, hydrogels were frozen at -20ºC and stored until further use. At the end of the experiment, hydrogels were frozen overnight at - 20ºC and then freeze-dried (Freeze Dryer Alpha 1-4 LD Christ) and weighed. The mass remaining percentage for each hydrogel at each time point was determined by applying Eq. 3.19:

$$Mass\ remaining\ (\%) = \frac{M_{(t)}}{M_{(t=0)}} \cdot 100 \qquad \textbf{Eq. 3.19}$$

Where $M_{(t=0)}$ is the mass at time 0, and $M_{(t)}$ is the mass after incubation with collagenase for the different time points. Finally, mass remaining *versus* time graphs were plotted to compare the degradation behaviour of the samples. For statistics three hydrogels for each condition were analysed. Data were plotted with OriginPro 8.5 software (OriginLab, USA) as the mean ± standard deviation.

3.4.7. Gel fraction studies of the GelMA-PEGDA hydrogels co-networks

Gel fraction is the percentage of solid crosslinked polymer after UV exposure and it depends on the crosslinking degree. To investigate the gel fraction, disc-shape hydrogels (10 mm diameter and 1 mm height) of $GelMA_5$ – PEGDA and $GelMA_{1.25}$ – PEGDA at 7.5% (w/v) – 5% (w/v), 5% (w/v) – 2.5% (w/v) and 5% (w/v) – 1.25% (w/v) with 0.5% (w/v) Irgacure D-2959 were fabricated on top of 12 mm non-silanized glass coverslips covered with PET membranes by applying a range of UV exposure dose from 0 to 10 $J \cdot cm^{-2}$. After hydrogel fabrication, swelling was not performed to keep the non-crosslinked polymer inside the hydrogels. Hydrogels were detached from the glass coverslips, placed inside 1.5 mL Eppendorfs, frozen at -80ºC overnight and freeze-dried (Freeze Dryer Alpha 1-4 LD Christ) overnight. Then, the dried hydrogels were weighed $(M_{fabrication})$. This weight accounted the contribution of crosslinked and non-crosslinked polymer. Then, 1.2 mL of filtered Milli-Q water was added in each Eppendorf ensuring that the hydrogels were entirely submerged and incubated at 37ºC. Milli-Q water was used instead of PBS to avoid salt crystal deposition on the hydrogels. Milli-Q water was replaced with fresh Milli-Q water by centrifuging hydrogels at 8000 rpm for 5 min and decanting the supernatant. Removing supernatant with the pipette induced hydrogel

damage since they were transparent and difficult to visualize. This step was done for 3 consecutive days. On the third day, after decanting the supernatant, hydrogels were frozen at -80ºC overnight, freeze-dried (Freeze Dryer Alpha 1-4 LD Christ) overnight and weighed again $(M_{swollen})$. To this weight value it only contributed the crosslinked polymer, as during the swelling period non-crosslinked material was leached. After getting all weight values for the different UV energy doses applied, the gel fraction percentages were calculated by Eq. 3.20:

$$Gel\ fraction\ (\%) = \frac{M_{swollen}}{M_{fabrication}} \cdot 100 \qquad \textbf{Eq. 3.20}$$

Finally, gel fraction percentages as a function of the UV energy dose were plotted with OriginPro 8.5 software (OriginLab, USA) as the mean ± standard deviation. Statistics were done by analysing three hydrogels from each condition.

3.5. Cell culture

3.5.1. NIH/3T3 fibroblasts cell culture

NIH/3T3 fibroblast cell line (ATCC® CRL-1658™) was purchased from American Type Culture Collection (ATCC, USA). NIH/3T3 cell line was established by George Todaro and Howard Green in 1962. The cells are originally derived from Swiss mouse embryonic fibroblast cells. In our case, NIH/3T3 cells were used as a cell model to mimic fibroblast population in the stromal compartment of the intestinal tissue. NIH/3T3 fibroblasts were chosen because they are easy to grow and are commonly used to test toxicity and biocompatibility of the polymers[243]. Moreover, NIH/3T3 fibroblasts have been extensively used in co-cultures with murine cells, as well as with human cells as feeder layers[244].

To start the cell culture, a cryotube™ vial (ThermoFisher Scientific) containing $1 \cdot 10^6$ NIH/3T3 fibroblasts in 1 mL was removed from the liquid nitrogen tank. Fibroblasts were thawed by adding 200 µL of cell culture medium at room temperature into the cryotube™ vial. The new medium was pipetted up and down few times to favour the defrosting of the frozen medium. Then, 200 µL of cell suspension was transferred into a 15 mL Falcon tube (ThermoFisher Scientific) containing 9 mL of culture medium. This step was repeated several times, until all the frozen medium was dissolved and medium of the cryotube™ vial was fully transferred into the Falcon tube. Freezing medium is

composed of 10% (v/v) of dimethyl sulfoxide (DMSO) (Sigma-Aldrich) diluted in cell culture medium for NIH/3T3 cells. DMSO is added to avoid ice crystals formation during freezing and minimize cell damage. Otherwise, as the DMSO is toxic for the cells, to improve cell viability is relevant to minimize the time that cells are in contact with it during the thawing by quickly diluting the freezing medium with contains the fibroblasts into fresh NIH/3T3 cell culture medium. Cell culture medium for NIH/3T3 fibroblasts was composed of high glucose Dulbecco's modified eagle medium (DMEM) phenol red (Gibco, ThermoFisher Scientific), supplemented with 10% (v/v) of fetal bovine serum (FBS) (Gibco, ThermoFisher Scientific) and 1% (v/v) of Penicillin/Streptomycin (Sigma-Aldrich). From now on, we will refer to this medium as "fibroblast complete DMEM medium". Then, the Falcon tube which contained the cells was centrifuged at 1200 rpm for 5 min. Supernatant was discarded and cell pellet collected in the Falcon tube was scratched and resuspended in 10 mL of fibroblast complete DMEM medium warmed at 37ºC. Finally, cells were seeded in 75 cm^2 cell culture treated flasks (Nunc™, ThermoFisher Scientific) and were grown in an incubator (New Brunswick) at 37ºC and 5% CO_2. Fibroblast complete DMEM medium was exchanged every other day until cells reached the confluence. When fibroblasts reached 90% of confluence, they were passaged to a new flask. At that point, fibroblast complete DMEM medium was rinsed, and cells were washed once with 5 mL of PBS warmed at 37ºC. Cells were detached from the flask by adding 3 mL of 0.25% (v/v) Trypsin – EDTA warmed at 37ºC (Gibco, ThermoFisher Scientific) and incubating them at 37ºC between 3 and 5 min. After, NIH/3T3 cells, which were resuspended in Trypsin – EDTA solution, were pipetted up and down to favour disruption of cell aggregates and were transferred into a 50 mL conical Falcon tube (ThermoFisher Scientific) containing 7 mL of warmed fibroblast complete DMEM medium. Cells were counted using a Neubauer chamber (Sigma-Aldrich) and a specific volume that contained our desired number of cells was placed in a 15 mL Falcon tube. Fibroblast solutions were centrifuged at 1200 rpm for 5 min, supernatant was decanted and cells were resuspended in a specific volume of fibroblast complete DMEM medium to achieve the desired cell density for the cell passage, which was between $2 \cdot 10^5$ to $3 \cdot 10^5$ cells in a 75 cm^2 flask, or to use them for a specific experiment. Details about the fibroblast cell density for individual experiments are described in each corresponding section.

3.5.2. Human colon myofibroblast (CCD-18Co) cells

CCD-18Co cell line (ATCC® CRL-1459™) was kindly provided by Prof. Amir Ghaemmaghami (Life Sciences Building, University of Nottingham, United Kingdom). The CCD-18Co cells are normal human intestinal fibroblasts/myofibroblasts derived from a biopsy colon tissue of a black female infant of 2.5 months old. In our case, CCD-18Co cells were used as cell model to mimic the myofibroblasts population of the lamina propria compartment of the intestinal tissue.

To start the cell culture, a cryotube™ vial of CCD-18Co cells, containing approximately $2.5 \cdot 10^5$ cells, was taken out from the liquid nitrogen tank, and thawed following the same methodology as explained above for NIH/3T3 cells. After thawing, CCD-18Co cells were expanded in a 25 cm^2 flasks in high glucose DMEM phenol red, supplemented with 10% (v/v) of FBS, 1% (v/v) of Penicillin/Streptomycin, and 1% (v/v) of non-essential amino acids. When cells got the maximum confluence, they were treated with 1 mL of 0.25% (v/v) Trypsin – EDTA warmed at 37ºC, incubating them at 37ºC for 5 min. To inhibit the effect of the Trypsin – EDTA solution, cell suspension was diluted in complete DMEM medium. Then, a Neubauer chamber was used to count the cell density and a certain volume of the cell suspension, with the desired cell number was placed in a 10 mL Falcon. For the passage of the CCD-18Co cells, which was done once per week, cells were seeded at a density of $3 \cdot 10^5$ cells in a 75 cm^2 cell culture flask or $1 \cdot 10^5$ cells in a 25 cm^2 cell culture flask. The cell density employed in each of the individual experiments is described in each section. After seeding, cells in the flask or within the hydrogels were maintained inside an incubator at 37ºC and 5% CO_2 and cell culture medium was exchanged every 3 – 4 days.

3.5.3. Human epithelial colorectal adenocarcinoma (Caco-2) cell culture

Caco-2 cell line (ATCC® HTB-37™) was courteously supplied by the Physiology Department from the Faculty of Pharmacy (University of Barcelona). Caco-2 cell line was used as a model of the intestinal epithelial monolayer because it is the most popular *in vitro* model for drug permeability studies in the pharmaceutical industry[79,83,245]. Caco-2 cell line is derived from human epithelial colorectal adenocarcinoma cells and was established by Jorgen Fogh. Caco-2 cells are able to differentiate and polarize to resemble the enterocytes of the small intestine under specific cell culture conditions. Due

to this differentiation, Caco-2 cells express a well-differentiated brush border, tight junctions, microvilli and nutrient transporters[79].

To begin the cell culture, a cryotube™ vial which contained $1 \cdot 10^6$ Caco-2 cells in 1 mL was removed from the liquid nitrogen tank. Cells were thawed as before, and expanded in a 75 cm^2 cell culture flask in high glucose DMEM phenol red, supplemented with 10% (v/v) of FBS, 1% (v/v) of Penicillin/Streptomycin, and 1% (v/v) of non-essential amino acids. This is the same culture medium used for the CCD-18Co cells. To refer to both media from now on, we will name them as CCD-18Co/Caco-2 complete DMEM medium. Caco-2 cells were maintained in an incubator at 37ºC with 5% CO_2 and medium was exchanged every 3 days. Caco-2 cells were passaged when the confluence reached between 80% – 90%. Cells were detached adding 3 mL of 0.25% (v/v) Trypsin – EDTA into the cell culture flask and incubating them at 37ºC for 5 – 7 min. Then, cell suspension was diluted in CCD-18Co/Caco-2 complete DMEM medium and the cell density was adjusted by counting the cells in the Neubauer chamber. The cell suspension with the desired amount of cells for the passage, which was around $2 \cdot 10^5$ cells, was seeded in a 75 cm^2 cell culture flask. For each experiment, the cell density is detailed in the corresponding section. After seeding, cells were maintained at 37ºC in an incubator with 5% (v/v) CO_2. Cell medium was exchanged every 2- 3 days and cell passage was done once a week.

3.5.4. THP-1 cell culture

THP-1 (ATCC® TIB-202™) cell line was warmly provided by Dr. Loris Rizzello (Molecular Bionics group, IBEC, Spain). THP-1 cells are monocyte-like line derived from peripheral blood of a 1-year old male patient suffering from acute monocytic leukemia. These cells have been used to study monocyte/macrophage immune responses due to their facility to differentiate into macrophage-like cells under a stimulus[246]. We used THP- 1 cell line as cell model to provide the basic immunocompetent characteristics of the lamina propria compartment from the intestinal tissue.

To start the cell culture, a cryotube™ vial, which contained $5 \cdot 10^6$ of THP-1 cells in 1 mL was removed from the liquid nitrogen tank. THP-1 cells were thawed by adding 200 µL of cell culture medium at room temperature into the cryotube™ vial and pipetted up and down few times, to favour the defrosting of the frozen medium. Then, 200 µL of cell suspension was transferred into a 15 mL Falcon tube containing 9 mL culture

medium. This step was repeated several times, until all the frozen medium was dissolved and medium of the cryotube™ vial was completely transferred into the Falcon tube. Then, the Falcon tube which contained the cells was centrifuged at 400 g for 5 min under the minimum deceleration rate. For THP-1 cells, this is an important parameter to take into account to have a proper pellet deposition and avoid the damage of the cells. Then, the supernatant was discarded using a serological pipette and the cell pellet was resuspended in 20 mL of warm culture medium to achieve a cell density of $\approx 2 \cdot 10^5$ cells·mL^{-1}. THP-1 cell culture medium was composed of RPMI 1640 phenol red (Gibco, ThermoFisher Scientific), supplemented with 10% (v/v) of FBS, 1% (v/v) of Penicillin/Streptomycin, 1% (v/v) of sodium pyruvate (Gibco, ThermoFisher Scientific), 1% (v/v) of HEPES (4-(2-hydroxyethyl)-1-piperazineethanesulfonic acid) (Gibco, ThermoFisher Scientific) and 0.1% (v/v) of β-mercaptoethanol (Gibco, ThermoFisher Scientific). β-mercaptoethanol was added just before using the medium, as it is an instable and highly degradable compound. From now on, we will refer to THP-1 medium as THP-1 complete RPMI medium. THP-1 monocyte cells, which are non-adherent cells, were seeded in a 75 cm^2 cell culture flask and grew at 37ºC and 5% CO_2 in the incubator. 10 mL or 15 mL of THP-1 complete RPMI medium was added every three or four days in order to maintain cell density lower than $8 \cdot 10^5$ cells · mL^{-1}. THP-1 monocyte cells were passaged when cell density was $\approx 8 \cdot 10^5$ cells·mL^{-1}. Cell density did not exceed $1 \cdot 10^6$ cells·mL^{-1}, because for higher cell densities cells stop dividing, formed clumps and did not behaviour properly. For the passaging, cell suspension was directly pipetted up and down in the flask to break cell aggregates. Then, a sample was taken and cells were counted in the Neubauer chamber. A specific volume of cell suspension with the desired number of cells was transferred into a 15 mL Falcon tube, and centrifuged according to the conditions explained above. Finally, the supernatant was removed and the pellet was resuspended with the proper volume of THP-1 complete RPMI medium. To passage the cells, they were seeded at a cell density between $1 \cdot 10^5 - 2 \cdot 10^5$ cells·mL^{-1}. For the experiments, THP-1 monocyte cells were differentiated to macrophage-like cells, we will refer them as M0. To do that, $8 \cdot 10^6$ cells were resuspended in 7 mL of differentiation cell culture medium and were seeded on a Petri dish (ThermoFisher Scientific). This differentiation medium was composed of RPMI 1640 phenol red, supplemented with 10% (v/v) of FBS, 1% (v/v) of Penicillin/Streptomycin, 1% (v/v) of sodium pyruvate, 1% (v/v) of HEPES and 50 ng·mL^{-1} of phorbol 12-myristate 13-acetate (PMA) (Sigma-Aldrich). PMA was freshly added into the medium at the moment of the differentiation step. Then, cells were left on the differentiation medium for 3 days. Unlike the

undifferentiated THP-1, which were non-adherent cells, M0 became highly adherent cells. On the third day, M0 cells were detached from the Petri dish. To do that, differentiated medium was rinsed and cells were washed with 3 mL of PBS warm at 37ºC. Then, 3 mL of Accutase® solution were added to the cell monolayer, which was incubated for 10 min at 37ºC and 5% CO_2. The unattached cells were transferred to a 15 mL Falcon tube containing 7 mL of THP-1 complete medium. To increase cell detachment M0 cells were carefully scratched with a cell scraper (VWR) by adding 2 mL of THP-1 complete medium. Finally, cell suspension was transferred to a new 15 mL Falcon (Figure 3.14). At that point, cells were counted and divided to the desired cell density for the experiments. Further details related with cell density for each experiment are provided in the corresponding sections.

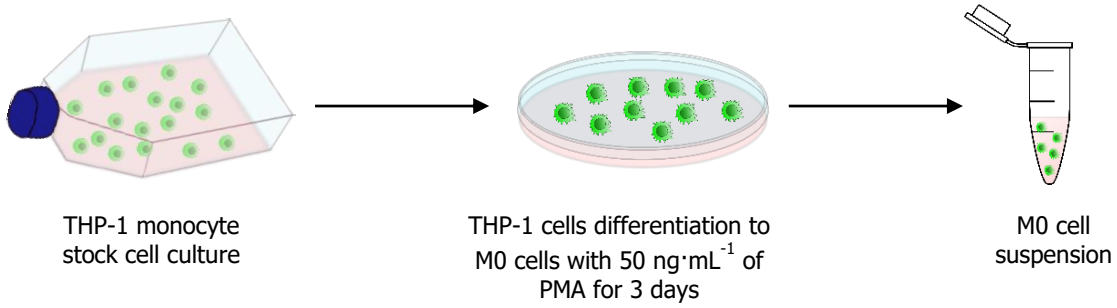

Figure 3.14. THP-1 monocyte-like cells differentiation process to macrophage-like cells (M0).

3.6. Determination of photoinitiator (Irgacure D-2959) cytotoxicity concentration

In this thesis, the method chosen to fabricate the hydrogels was free radical photopolymerization under UV light. To do that, GelMA and/or PEGDA polymer solutions were mixed with a photoinitiator to trigger the crosslinking reaction upon light irradiation (the detailed process is explained in section 3.3). As photoinitiators can be cytotoxic at relatively low concentrations, such concentration was first optimized to minimize the damage of the cells encapsulated within the hydrogels.

The photoinitiator chosen was 2-Hydroxy-4'-(2-hydroxyethoxy)-2-methylpropiophenone (Irgacure D-2959) (Sigma-Aldrich), as it was found to be the most cytocompatible UV photoinitiator for many cell types[175,247]. Irgacure D-2959 maximum concentration before inducing cell death was determined through AlamarBlue® cell viability assay (ThermoFisher Scientific). The assay solution contains a blue-coloured and

non-fluorescent molecule (resazurin), which is reduced by metabolically active cells to form a red-coloured and highly fluorescent molecule (resorufin). Colour changes are measured by fluorescence or absorbance.

NIH/3T3 fibroblasts at 10^4 cells·well^{-1} were seeded in a 96 transparent well-plate and were incubated overnight at 37ºC and 5% CO_2 in fibroblast complete DMEM medium. On the next day, a set of Irgacure D-2959 solutions containing concentrations of the photoinitiator ranging from 0 to 1% (w/v) were studied. Irgacure D-2959 was diluted in fibroblast complete DMEM medium at 65ºC for 1 h in a glass vial under stirring conditions and protected from light by wrapping it with aluminium foil. Solutions were sterilized by filtering them using a 0.22 µm PET filter inside the biological safety cabinet (Teslar). Then, cell medium of the 96 well-plate was removed, 100 µL of Irgacure D-2959 at different concentrations were added in the corresponding wells, and cells were left for 2 h in the incubator at 37ºC and 5% CO_2. After this time, the photoinitiator was rinsed, cells were washed with PBS warmed at 37ºC, and 100 µL of warmed fibroblast complete DMEM medium was added to each well. Cells were incubated overnight at 37ºC and 5% CO_2 to reduce the stress suffered while being in contact with the photoinitiator. Prior AlamarBlue® cell viability assay, a standard curve was done by seeding $24{\cdot}10^3$ – $12{\cdot}10^3$ – $6{\cdot}10^3$ – $3{\cdot}10^3$ – $1.5{\cdot}10^3$ – $0.75{\cdot}10^3$ – 0 cells in a 96 well-plate and waiting for 2 h for cell adhesion. Then, 100 µL solution of 10% (v/v) AlamarBlue® solution diluted in fibroblast complete DMEM medium was added to the cells used for the calibration curve, and to the cells exposed to the photoinitiator. 96 well-plates were placed inside the incubator for 5 h. After that time, 50 µL of the AlamarBlue® solution was transferred from each well to a new 96 well-plate. Finally, data readout was achieved by measuring the absorbance at 570 nm. Then, for the calibration curve a linear fit was made to correlate the absorbance values with the known cell number. Total cell numbers were converted into percentages normalizing by the samples without photoinitiator. Data were plotted with OriginPro 8.5 software (OriginLab, USA) as the mean ± standard deviation. For the statistics three replicates were done for each condition (n=3).

3.7. Biocompatibility studies of the hydrogels for cell culture

From the results obtained of the physicochemical and mechanical characterization of GelMA hydrogels and GelMA – PEGDA hydrogel co-networks, the

networks formed by 7.5% (w/v) $GelMA_5$ and 7.5% (w/v) $GelMA_5$ – 5% (w/v) PEGDA were selected to perform the initial cellular assays. First of all, these hydrogel compositions were tested to know if they were suitable for (I) the loading of lamina propria cells (NIH/3T3 fibroblasts) within their network, and (II) the growth of epithelial cells (Caco-2 cells) on their surface. These experiments were performed with hydrogels fabricated on glass coverslips to facilitate their manipulation.

3.7.1. NIH/3T3 cells encapsulated in GelMA and GelMA – PEGDA hydrogel co-network

From solutions of 7.5% (w/v) $GelMA_5$ and 7.5% (w/v) $GelMA_5$ – 5% (w/v) PEGDA with 0.5% (w/v) Irgacure D-2595, cell-laden hydrogels were fabricated applying an UV dose of 1.50 J·cm^2. Disc-shaped hydrogels were 10 mm in diameter and 0.250 mm in height. Height was reduced to ensure nutrients and oxygen diffusion inside the hydrogel. The number of cells per hydrogels was computed with the volume of the disc (V_{disc}) and applying Eq. 3.22:

$$V_{disc} = \pi * r^2 * h \qquad \textbf{Eq. 3.21}$$

$$Number\ of\ cells\ in\ one\ hydrogel = \frac{Encapsulation\ cell\ density}{V_{disc}} \qquad \textbf{Eq. 3.22}$$

Where r is the radius of the hydrogel disc, h is its height, and the encapsulation cell density refers to the density in solution (5·10^6 cells·mL^{-1}). NIH/3T3 fibroblasts were treated as described in section 3.5.1. The volume containing the number of cells needed to fabricate 1 or more hydrogels was transferred in a 1.5 mL Eppendorf tube and centrifuged at 1200 rpm for 5 min. Then, supernatant was removed, and pellet was resuspended with the necessary volume of the polymer solution (≈20 µL (Eq. 3.21) per hydrogel). Finally, the cell-laden polymer solution was introduced in the PDMS pools (10 mm in diameter and 0.250 mm in height) and hydrogels were fabricated on silanized glass coverslips (12 mm in diameter) by exposing them to an UV energy dose of 1.50 J·cm^{-2} (Figure 3.15). Unreacted polymer chains and photoinitiator were washed out with warm fibroblast complete DMEM medium, which was additionally supplemented with 10% of Penicillin/Streptomycin and 1/250 of Normocin™ (Invitrogen) to avoid contamination. Then, cell-laden hydrogels were transferred into a sterile 24 well-plate. Normocin™ at 1/500 was added to the fibroblast complete DMEM medium to avoid a

possible contamination owing to the non-sterile working conditions. Cell-laden hydrogels were maintained at 37ºC and 5% CO_2 in the incubator, exchanging medium every 2 days. Live/Dead™ viability/cytotoxicity assay and immunofluorescence (see sections 3.10.2 and 3.10.3 for further details) were carried out at different days, from day 1 to day 21 of culture.

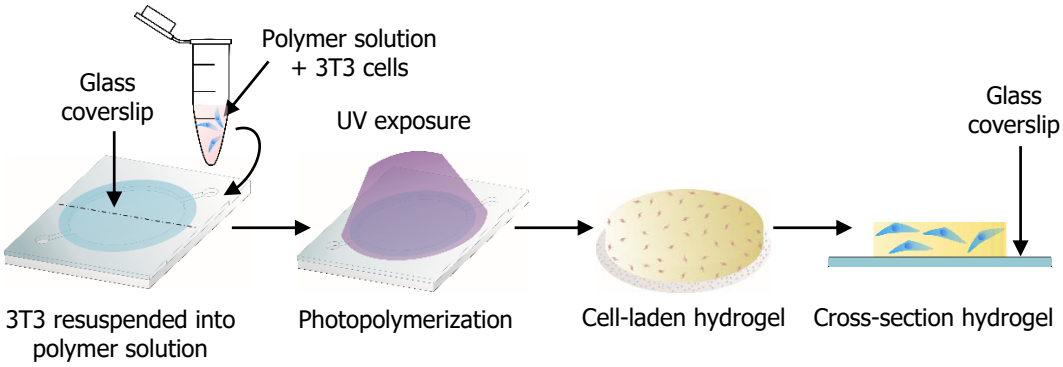

Figure 3.15. Schematic drawing of the process to fabricate NIH/3T3 cell-laden hydrogels on top of glass coverslips.

3.7.2. Caco-2 cell growth on GelMA hydrogel networks and GelMA – PEGDA hydrogel co-networks

Polymer solutions at concentrations of 7.5% (w/v) $GelMA_5$ and 7.5% (w/v) $GelMA_5$ – 5% (w/v) PEGDA with 0.5% (w/v) Irgacure D-2595 were prepared in PBS. Disc-shaped hydrogels (10 mm diameter and 1 mm height) were fabricated on top of silanized 12 mm glass coverslips using UV exposure doses of 1.50 $J \cdot cm^{-2}$. Unreacted polymer chains and photoinitiator were washed out with PBS warm at 37ºC. Hydrogels were changed to a new sterile 24 well-plate under the biological safety cabinet, PBS supplemented with 10% of Penicillin/Streptomycin was added and kept for 3 days. After swelling, PBS was removed, and Caco-2 cells were seeded at a density of $7.5 \cdot 10^5$ $cells \cdot cm^{-2}$. Cells were seeded by adding a drop of cells on top of the hydrogel confine them on the hydrogel surface sample. To do that, $5.9 \cdot 10^5$ Caco-2 cells were resuspended in 50 µL of CCD-18Co/Caco-2 complete DMEM medium, placed as a drop on top of the hydrogels ($A_{10\ mm}$ = 0.79 cm^2) and left to adhere on the hydrogel for 3 – 4 h. Afterwards, 500 µL of CCD-18Co/Caco-2 complete DMEM medium was carefully added in the well to avoid cell removal (Figure 3.16).

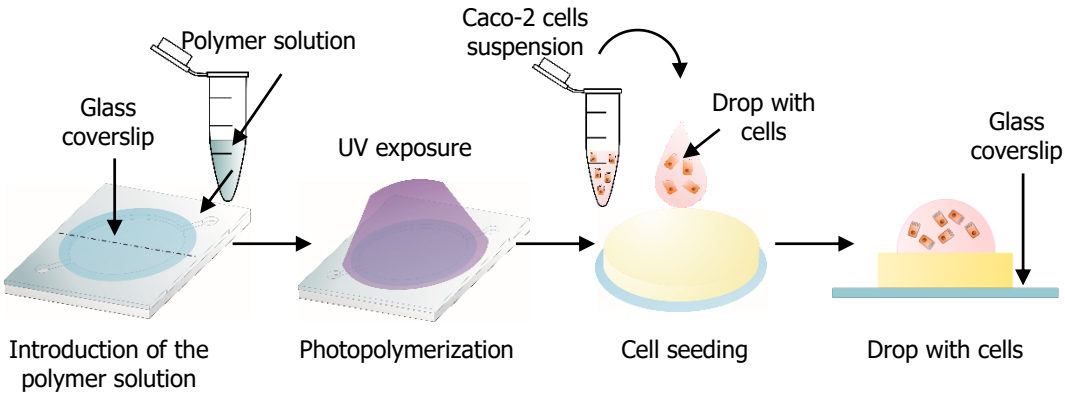

Figure 3.16. Schematic drawing of the epithelial cells seeding on a hydrogel fabricated on top of a glass coverslip. PDMS pool was covered with a glass coverslip that acted as a substrate, followed of a UV exposure. Finally, Caco-2 cells were seed by placing a drop of cells on the center of the hydrogel surface.

Cell growth and formation of epithelial monolayers was followed for up to 21 days taking pictures with the stereoscope microscopy. Finally, images were analysed by ImageJ software and cell surface coverage percentage was calculated by Eq. 3.23:

$$Surface\ coverage\ (\%) = \frac{Cell\ covered\ area}{Hydrogel\ area} \cdot 100 \qquad \textbf{Eq. 3.23}$$

3.8. Fabrication of the lamina propria of the 3D intestinal mucosa model

The intestinal epithelium consists of a monolayer of tightly interconnected epithelial cells laying on top of the basement membrane. Just below the basement membrane there is the lamina propria, also named stromal tissue, which together with the epithelium forms the intestinal mucosa. The lamina propria has a large variety of cells, including fibroblasts, myofibroblasts, endothelial or immune cells residing within its ECM[248]. The epithelial monolayer together with the lamina propria form a semipermeable barrier that allows the absorption of nutrients and other necessary compounds while protects the human body of undesirable luminal contents[41]. For that reason, it is relevant to study the barrier function of the epithelium on the presence of a compartment representing the lamina propria, as the extracellular matrix and the cellular crosstalk are important factors in the epithelial cell behaviour.

The lamina propria compartment of the intestinal mucosa was mimicked by embedding lamina propria cells during the hydrogel polymerization process. Cells need

the proper transport of nutrient and oxygen when they are inside the hydrogels, as well as the removal of the cell waste. This transport is limited by diffusion and is essential for cell survival and function[249]. In here, we investigated two different setups to provide cells with good mass transport. On one hand, we used a perfusion bioreactor, which was developed in our lab by Valls M. *et al.*[250,251]. On the other hand, we used an adapted version of commercial Transwell® inserts. Both setups are explained in detail in the following sections.

To mimic the lamina propria, NIH/3T3, CCD-18Co, THP-1 differentiated to macrophages (M0) or a co-culture of CCD-18Co and M0 were treated as explained above in section 3.5. Depending on the goal of the experiment, one cell type or another were employed. Trypsinized cells were resuspended in polymer solutions, which were maintained at 37ºC before polymerization to prevent gelling. Hydrogels without embedded cells were also included in the experiment as controls. The hydrogel dimensions (6.5 mm diameter and 0.5 mm high), the substrate (silanized PET membranes of 5 µm pore size), the UV energy dose (1.88 $J \cdot cm^{-2}$), and the polymer dissolution medium (DMEM without phenol red supplemented with 1% (v/v) Penicillin/Streptomycin) were kept constant for all the experiments. Other parameters such as (I) the encapsulated cell density, (II) the degree of functionalization, and (III) the concentration of GelMA and PEGDA polymers were modified to optimize the output. Their corresponding values are reported in each experimental section.

Hydrogel polymerization was carried out as it is explained in section 3.3.2. Once we got the cell-laden hydrogel on top of a PET membrane, non-crosslinked polymer was washed out with warm cell culture medium supplemented with 10% (v/v) Penicillin/Streptomycin and 1/250 of Normocin™. Finally, cell-laden hydrogels were inserted either within the perfusion bioreactors (Figure 3.17 (a)) or in the Transwell® inserts (Figure 3.18 (a)). Live/Dead™ viability/cytotoxicity assays and immunofluorescence assays were used to analyse cell viability and distribution inside the hydrogels. For these experiments, NIH/3T3 fibroblasts were employed.

3.8.1. Perfusion bioreactor setup

To investigate if cell growth and viability on our hydrogels is limited by the mass transfer restrictions imposed by polymer composition, a proof of concept experiment was performed. In this experiment, the mass transfer supply through the whole thickness of

the hydrogel was forced by using a perfusion setup. To that end, NIH/3T3-laden hydrogels (cell density 5·10 cells·mL^{-1}), made of 7.5% (w/v) GelMA$_5$ – 5% (w/v) PEGDA and 0.5% (w/v) Irgacure D-2959, were inserted in the perfusion chambers of the bioreactor. Such perfusion bioreactor (Figure 3.17 (b)) was composed of a medium reservoir (Sartorius Stedim) connected through gas-permeable platinum cured silicone tubing (1.6 mm inner diameter x 3.2 mm outer diameter) (ThermoFisher Scientific) to a PharMed® BPT 3-Stop pump tubing (0.89 mm inner diameter) (ThermoFisher Scientific). Another piece of silicone tubing connected the pump tubing to a four port luer manifold (ThermoFisher Scientific, Spain), where the culture medium was equally distributed in four branches throughout flow restrictors (L25915-250D2 microfluidic channels, Leventon, WerfenLife Company). A high fidelity de-bubbling system (Leventon, WerfenLife Company) was installed before perfusion chambers to avoid entrapment of bubbles inside them. The perfusion chambers were assembled with another four port luer manifold, which was attached to a gas exchanger, composed of 3 m of gas-permeable platinum-cured silicone tubing coiled around a falcon tubing. Finally, the gas exchanger was connected to the medium reservoir to close the circuit. All connections between the components were performed using male and female polyvinylidene fluoride (PVDF) luer lock connectors (1.6 mm inner diameter tubing) (Value Plastics). The perfusion chamber used was a Swinnex filter holder of 13 mm (Merck Millipore). Samples were placed inside the chamber and held in place using two gaskets. All the components were sterilized by either autoclave (high pressure saturated steam at 121ºC) or 70% ethanol with subsequent autoclaved distilled water rinse to remove any remaining ethanol. The whole system was placed inside an incubator with temperature and CO_2 control (37ºC and 5% CO_2)[250]. A continuous perfusion of fibroblast complete DMEM medium at 0.4 mL·min^{-1} was applied by connecting the pump tubing to a multichannel peristaltic pump (REGLO Digital, 2 channels) (Ismatec). Fibroblast complete DMEM medium was exchanged every other day. L-ascorbic acid at 50 µg·mL^{-1} (Sigma-Aldrich) was freshly added to cell culture medium to stimulate the production of extracellular matrix[252].

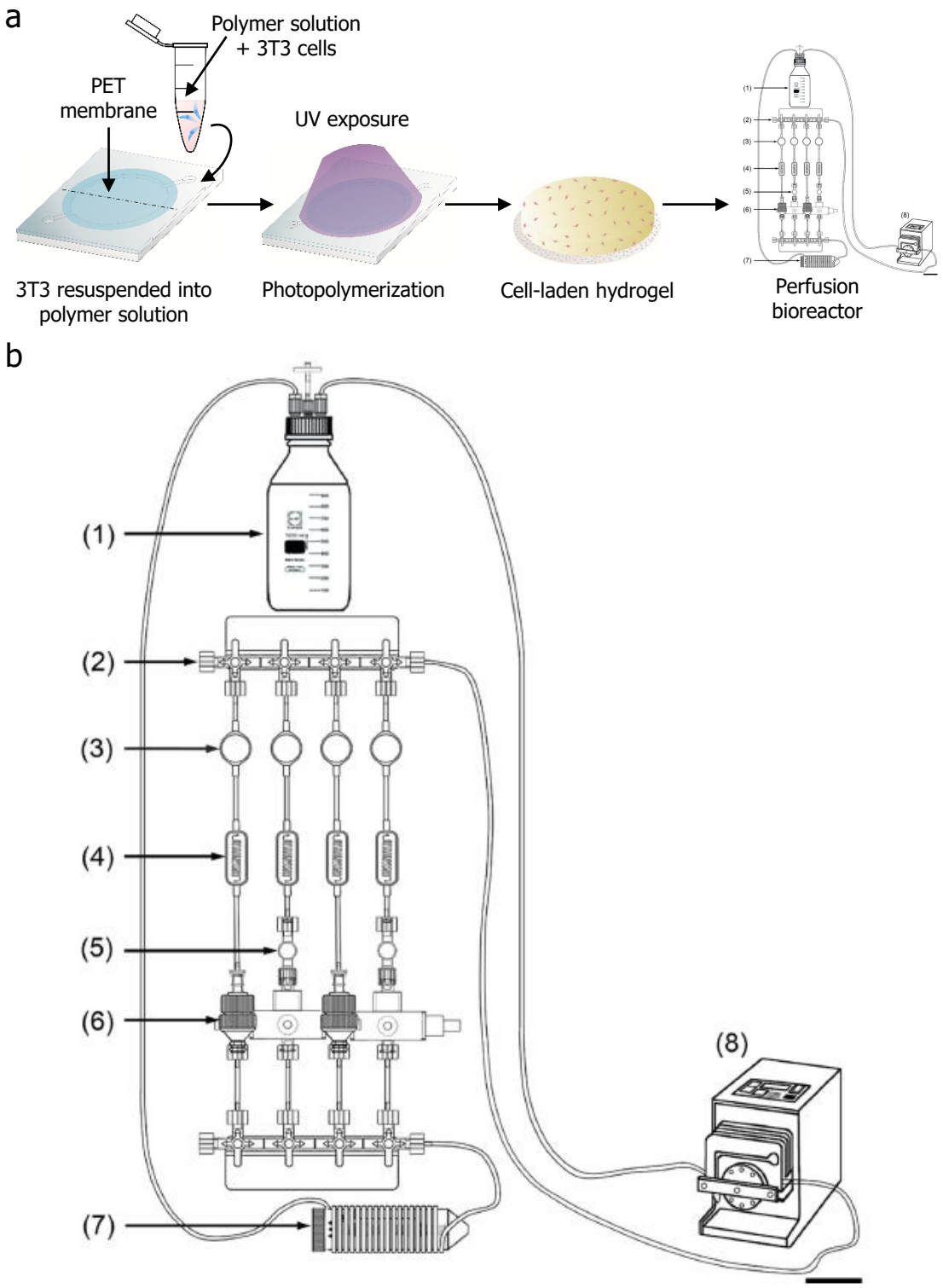

Figure 3.17. Cell-laden hydrogel cultured in a perfusion bioreactor. (a) Schematic drawing of the 3T3 cell-laden hydrogel fabricated on top of a PET membrane, then it was placed in a bioreactor. (b) The bioreactor was composed of a (1) medium reservoir, a (2) luer manifold, (3) de-bubbling systems, (4) flow restrictors, (5) in-line luer injection ports, (6) perfusion chambers, a (7) gas exchanger and a (8) persitatiltic pump. It supported up to four chambers to culture multiple tissue constructs under the same physicochemical conditions. Scale bar 4 cm (from Valls M. *et al.*[250]).

The experiment was carried out until day 21 after cell encapsulation and a total of 4 cell-laden hydrogels were placed inside the bioreactor. At the following time points, 3 days, 7 days, 14 days and 21 days, the state of the encapsulated cells was examined. To do that, one hydrogel sample was taken out from one bioreactor chamber at each time point. Samples were divided into two equal parts. Half of the hydrogel was used to study cell viability by Live/Dead™ viability/cytotoxicity assay (see section 3.10.2) while the other half of the sample was fixed and used for immunofluorescence analysis (see section 3.10.3). Each time a hydrogel was removed from the bioreactor one branch was closed, consequently, the flow rate of the peristaltic pump was adjusted to achieve a constant flow over time.

3.8.2. Cell culture on hydrogels mounted on Transwell® insert

Commercial Transwell® inserts are commonly used for *in vitro* intestinal studies, such as drug permeability[79,88] or drug absorption[79,245] due to their cost effectiveness and easy handling (Figure 3.18 (b and c)).

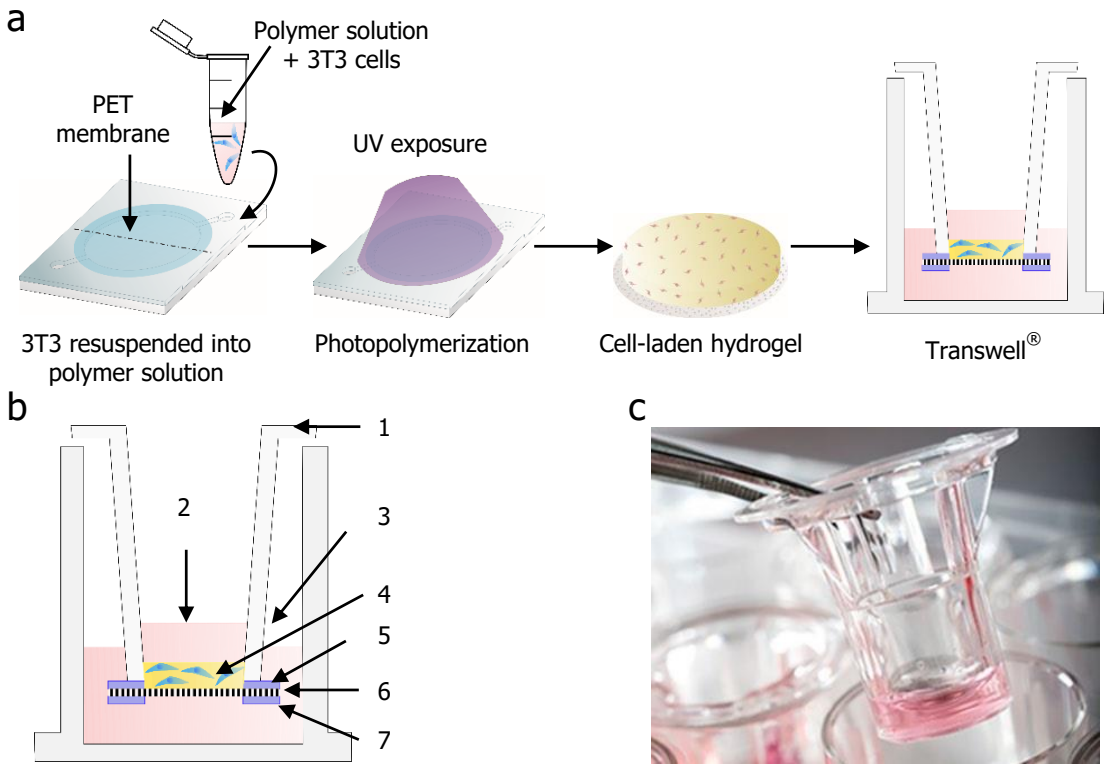

Figure 3.18. Transwell® cell culture setup. (a) Cell-laden hydrogel placed on commercial Transwell® inserts. The hydrogel adhesion to the Transwell® insert was the same as explained in Figure 3.10. (b) Main parts of the Transwell® setup, (1) insert, (2) apical compartment, (3) basolateral compartment, (4) hydrogel, (5) 1st PSA ring, (6) PET membrane, and (7) 2nd PSA ring. (c) Photograph of a 24 Transwell® well-plate.

To investigate cell viability in this setup, NIH/3T3-laden hydrogels (cell density $5 \cdot 10$ cells$\cdot mL^{-1}$) made of 7.5% (w/v) $GelMA_5$ – 5% (w/v) PEGDA and 0.5% (w/v) Irgacure D-2959 were mounted on a 24-well Transwell® filter insert using double-sided PSA rings, following the same methodology as explained in section 3.4.4. After mounting, fibroblast complete DMEM medium was quickly added in the apical (200 µL) and basolateral (600 µL) compartments. Hydrogels were incubated at 37ºC and 5% CO_2, exchanging the medium every other day. The medium was supplemented with freshly L-ascorbic acid at 50 µg$\cdot mL^{-1}$. The experiments were carried out until day 21 of culture. At different time points, samples were demounted from the Transwell® inserts and divided into two equal parts. One part was used to study cell viability by Live/Dead™ viability/cytotoxicity assay (see section 3.10.2) while the other half of the sample was fixed and used for immunofluorescence analysis (see section 3.10.3).

3.9. Fabrication of the 3D model of the intestinal mucosa

Cell-laden GelMA – PEGDA hydrogels containing either NIH/3T3 cells or CCD-18Co cells were produced as described above to fabricate the lamina propria compartment of intestinal mucosa models. After fabrication, the constructs were mounted into Transwell® inserts. Then, the following day, Caco-2 cells were seeded on top of the cell-laden hydrogels to represent the epithelial component of the small intestinal tissue. To do that, the medium in the Transwell® inserts was rinsed out, and 200 µL of Caco-2 cells resuspended at a cellular density of $7.5 \cdot 10^5$ cells$\cdot cm^{-2}$ in CCD-18Co/Caco-2 complete DMEM medium were added into the apical compartment. The basolateral side was filled with 600 µL of CCD-18Co/Caco-2 complete DMEM medium (Figure 3.19). Control experiments were performed by seeding Caco-2 cells on equivalent cell-free hydrogels or leaving samples of cell-laden hydrogels without seeding Caco-2 cells. Additionally, Caco-2 cells were seeded on top of 24-well polycarbonate membranes of Transwell® inserts (0.4 µm pore size) at a density of $7.5 \cdot 10^5$ cells$\cdot cm^{-2}$. Cells were cultured for 21 days, exchanging the medium every other day. For all the samples, the medium composition used was CCD-18Co/Caco-2 complete DMEM medium. In some experiments, L-ascorbic acid was freshly added every time that the medium was exchanged.

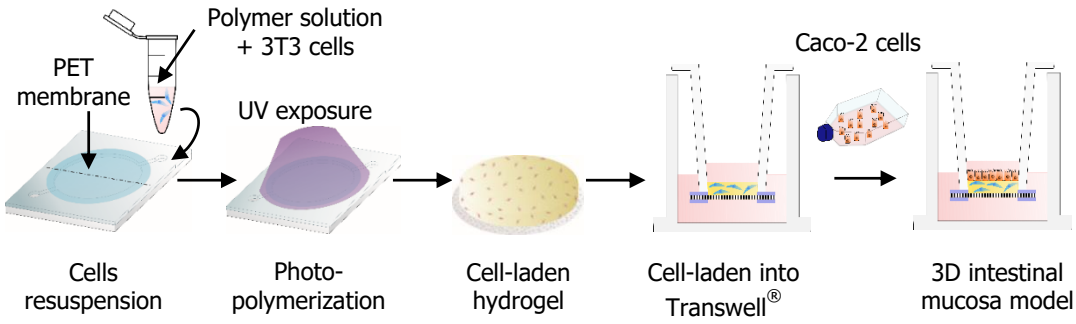

Figure 3.19. Scheme of the fabrication steps of the 3D model of the intestinal mucosa. First of all, cell-laden hydrogel was placed on a Transwell® insert and then epithelial cells were seeded on top in order to get the 3D intestinal mucosa model.

3.10. Cell characterization of the 3D models of the intestinal mucosa

3.10.1. Genotoxicity effects of UV exposure on cell-laden hydrogels

It is well reported that DNA is damaged when cells are exposed directly to UV light[253]. Despite UV does not produce DNA double strand breaks (DSB) directly, it produces cyclobutane pyrimide dimers or pyrimidine-pyrimidine 6-4 photoproducts (Figure 3.20 (a)). These end up forming DNA breaks because of the unsuccessful attempted replication of DNA at sites containing the UV induced damage. Then, DNA is cleaved generating DSBs, at which there is a histone H_2AX phosphorylation on serine 139[254] (Figure 3.20 (b)). Histone H_2AX modifications are easily detected by immunofluorescence. To evaluate the possible DNA damage produced in the cell-laden hydrogels due to UV light irradiation, fibroblast-laden hydrogels at a concentration of 5% (w/v) $GelMA_{1.25}$ – 1.25% (w/v) PEGDA and fibroblasts cell density of $7.5 \cdot 10^6$ cell·mL^{-1} were fabricated by applying an energy dose of 1.88 J·cm^{-2}. As it was mentioned in previous sections, the UV light used for the fabrication of the samples was limited to a wavelength of 365 nm, as a filter was used to cut the lower and upper wavelengths. Just after fabrication hydrogels were placed on a 24 well-plate, and one hydrogel was treated with 500 µL of hydrogen peroxide (H_2O_2) (Sigma-Aldrich) at 1 mM dissolved in fibroblast complete DMEM medium for 30 min, whereas the other sample remained untreated and was incubated only with fibroblast complete DMEM medium. H_2O_2 molecules are reactive oxygen species (ROS) that can easily diffuse inside the cells and react with DNA to induce DSBs, causing high levels of histone H_2AX phosphorylation.

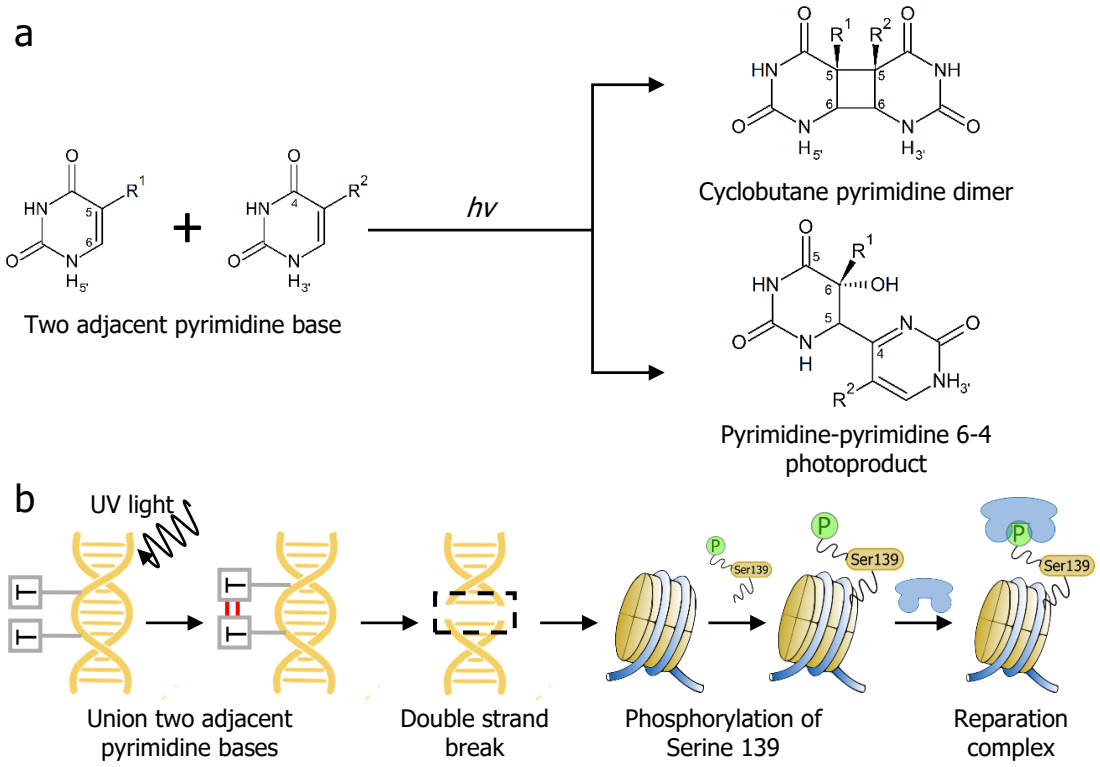

Figure 3.20. Effects of UV exposure on the DNA. (a) UV-photons are absorbed by DNA resulting the union of two adjacent pyrimidine bases to form cyclobutane pyrimidine dimers and pyrimidine-pyrimidine 6-4 photoproducts. (b) Schematic representation of DNA damage by the UV light. After the union of two adjacent pyrimidine bases, the DNA double strand breaks, causing the phosphorylation of serine 139 in the histone complex, followed by the recruitment of the DNA reparation complex.

Additionally, to have positive and negative controls of the assay, NIH/3T3 cells were seeded at a density of $5 \cdot 10^4$ cell·mL^{-1} on sterilized 12 mm glass coverslips and incubated overnight at 37ºC and 5% CO_2. Positive controls were treated with 1 mM of H_2O_2 solution for 30 min, while negative controls were kept untreated, cultured only with fibroblast complete DMEM medium. Finally, one sample of each condition was fixed to later analyse DNA damage by immunofluorescence using mouse anti-phospho-histone H_2AX (Ser 139) (Millipore) (Table 3.6), as primary antibody. DAPI (4',6-diamidino-2-phenylindole) at a concentration of 5 µg·mL^{-1} (ThermoFisher Scientific) was used to correlate the phosphorylated cells in the histone H_2AX with their nuclei. Immunofluorescence was performed as described in section 3.10.3. Fluorescence for the four different sample conditions was imaged using a confocal microscopy (LSM 800, Zeiss), located at the IBEC MicroFabSpace installations. Z-stacks images (1 µm distance between each image) from cell-laden hydrogels and snapshots from the positive and negative controls were acquired using a 63x oil objective. Capture parameters were maintained constant for all images, so the signal from cell-laden hydrogels could be

compared with the controls. Images were analysed with ImageJ software. Cell-laden z-stacks images were treated to obtain z-stack maximum intensity projections. Then, the presence or absence of the anti-phospho-histone H_2AX (Ser 139) was analysed qualitatively by comparison.

3.10.2. Live/Dead™ cell viability/cytotoxicity assay

The viability of the embedded cells within the hydrogels was determined by the Live/Dead™ viability/cytotoxicity assay kit (Invitrogen). The kit is an easy two-colour assay that determines cell viability based on cells plasma membrane integrity and esterase activity. It has two components, calcein AM and ethidium homodimer-1. On one hand, live cells convert the non-fluorescent calcein AM molecule to an intensely fluorescent calcein molecule by intracellular esterase enzyme. Calcein molecule is kept inside the cell, producing a green fluorescence molecule at 852 nm/515 nm excitation/emission wavelengths. On the other hand, ethidium homodimer-1 (EthD-1) penetrates into cells that have a broken membrane and binds to DNA. The interaction between ethidium homodimer-1 and DNA changes the conformation of the ethidium homodimer-1, which then becomes a red-fluorescence molecule at 530 nm/635 nm excitation/emission wavelengths[255] (Figure 3.21).

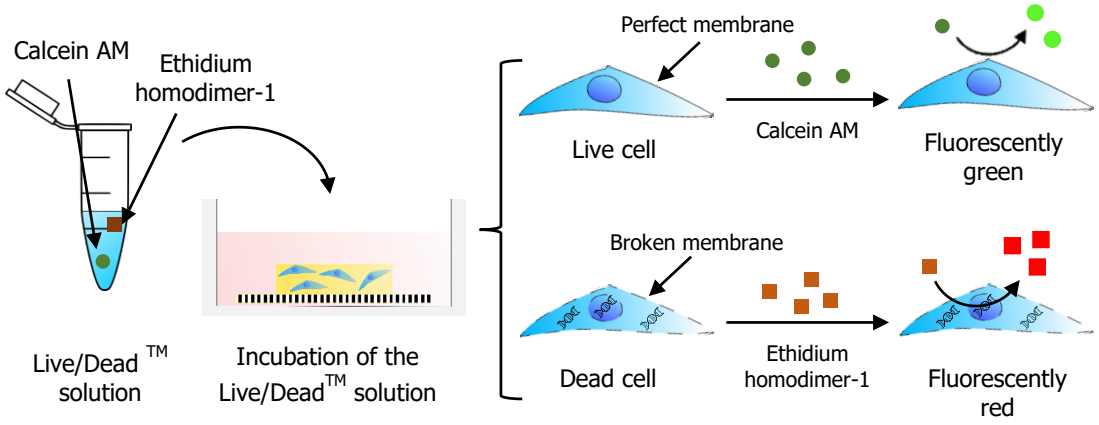

Figure 3.21. Live/Dead™ viability/cytotoxicity assay. The test contains calcein AM and ethidium homodimer-1, both molecules are non-fluorescent. Calcein AM is modified by intracellular esterases of the live cells to give green fluorescence molecules. By contrast, ethidium homodimer-1 interacts directly with the DNA of the dead cells giving red fluorescence molecules.

To analyse the cell viability, cell-laden hydrogels were removed either from the 24 well-plates (hydrogels on a glass coverslip), from the inside perfusion chambers of the bioreactor or from the Transwell® inserts and were transferred to new sterile 24 well-

plates inside the biosafety cell culture cabinet. Hydrogels were washed out to remove residual esterases from the medium that remained inside the hydrogel pores by adding 1 mL of PBS warmed at 37ºC under shaking conditions for 3 min. This step was repeated three times to ensure the total removal of the esterases. During washing steps, Live/Dead™ working solution was prepared. EthD-1 at 2 mM was diluted to a final concentration of 4 µM EthD-1, whereas calcein AM at 4 mM was diluted to 2 µM calcein AM. EthD-1 and calcein AM were diluted in the same PBS solution. Finally, Hoechst Reagent 33342 (5 $\mu g \cdot mL^{-1}$) (Invitrogen) was added to the EthD-1-calcein working solution. Live/Dead™ working solution was vortexed to ensure the proper mixing of the reagents. After washing, Live/Dead™ working solution was added directly to the hydrogels. Hydrogels were incubated for 20 min in the incubator at 37ºC and 5% CO_2. Following that, they were washed twice with PBS at 37ºC for 3 min under shaking conditions. A PDMS of the same diameter and height as the hydrogels was placed on a large glass coverslip (600 x 24 mm) (Menzel Gläser, ThermoFisher Scinetific) and filled with a PBS drop. Finally, with the aid of forceps the hydrogels were inverted and mounted onto glass coverslips. Fluorescence images were taken using an inverted confocal microscope (SPE, Leica) located at IRB Advanced Digital Microscopy Unit or confocal scanning microscope (LSM800, Zeiss) present at the IBEC MicroFabSpace installations. Images were acquired using 10x or 20x dry objectives to visualize all the cells across the hydrogel thickness. Cell viability analysis were done by acquiring a set of z-stack images (10 µm step between each z-stack) of the whole hydrogels. Images were treated using ImageJ software. Mainly, image contrast and brightness were adjusted manually in order to visualize better the embedded cells. Then, cell viability quantification was performed manually stack by stack and the percentage of viable cells at each time point was calculate computing the Eq. 3.24:

$$Cell\ viablity\ (\%) = \frac{Total\ number\ of\ live\ cells}{Total\ number\ of\ cells} * 100 \qquad \textbf{Eq. 3.24}$$

Data were plotted as the mean ± standard deviation. Routinely, one hydrogel of each condition was employed to perfom the Live/Dead™ viability/cytotoxicity assay

3.10.3. Immunofluorescence assay

Morphology and distribution of embedded cells (NIH/3T3 fibroblasts, CCD-18Co or THP-1), as well as cellular morphology and polarization markers for epithelial cells (Caco-2 cells) were studied by immunofluorescence. Samples were removed from either

the 24 well-plates, the perfused bioreactor or the Transwell® inserts and placed in a new 24 well-plate. Then, samples were washed with PBS warmed at 37ºC for 3 min under shaking conditions. Next, samples were fixed with 10% neutral buffered formalin solution (Sigma-Aldrich) for 1 h at 4ºC under shaking conditions. Hydrogels were washed three times with PBS for 5 min at room temperature. Cell membrane permeabilization was done with 0.5% (v/v) Triton-X (Sigma-Aldrich) in PBS at 4ºC for 1 h, followed by three washings steps with PBS at room temperature for 5 min under shaking conditions. A blocking step was necessary to prevent non-specific binding of the antibodies. A blocking solution, containing 1% (w/v) bovine serum albumin (Sigma-Aldrich), 3% (v/v) donkey serum (Millipore) and 0.3% (v/v) Triton-X in PBS, was added to the samples and incubated for 2 h at 4ºC, under shaking conditions. Afterwards, the primary antibody solution, consisting of 0.1% (w/v) bovine serum albumin, 0.3% (v/v) donkey serum, 0.2% (v/v) Triton-X and primary antibodies in PBS, was incubated overnight at 4ºC under shaking. After this time, constructs were washed three times with PBS for 5 min. The combination of primary antibodies changed as a function of the cell type and the desired outcome of the study. The primary antibodies used are listed in Table 3.6. ZO-1 and β-catenin cell markers were used to study the epithelial cell polarization. ZO-1, also known as zona occludens-1, is a protein from the tight junction complex, whose expression increases upon cell polarization. On the other hand, β-catenin is a protein that forms part of the adherens junction complex. Adherens junctions are localized just below the tight junctions and aid to the proper adhesion between cells. Ki-67 is a nuclear protein marker of proliferative cells and was used to check the proliferation capacity of the embedded cells. This marker is present during all the cell cycle process but not in the quiescent cells. Human collagen IV was used to check the production of collagen by NIH/3T3 cells and CCD-18Co in the cell-laden hydrogels. Collagen IV is the main component of the basement membrane.

Target molecule	**Host**	**Concentration (μg·mL^{-1})**	**Source**
ZO-1	Goat	2	Abcam
β-catenin	Rabbit	1	Abcam
Human collagen IV	Goat	1.6	Biorad
Ki 67	Rabbit	0.31	Abcam
Phospho-histone H_2AX (Ser 139)	Mouse	5	Millipore

Table 3.6. List of primary antibodies used for immunofluorescence analysis. They were used to characterize the embedded cells and epithelial cells.

After incubation with the primary antibody solution and the washing steps, hydrogels were incubated with the secondary antibody solution, which was composed by 0.1% (w/v) bovine serum albumin, 0.3% (v/v) donkey serum and secondary antibodies (Table 3.7) or/and Rhodamine-Phalloidin in PBS. Rhodamine-Phalloidin was used to stain filamentous actin (F-actin) and thus, check the cell cytoskeleton morphology. For the epithelial cells, it was also used to check their surface coverage. Finally, samples were incubated with DAPI at a concentration of 5 $\mu g \cdot mL^{-1}$ between 30 min - 60 min at 4ºC and washed three times with PBS. All the steps were carried out under shaking conditions. Then, the hydrogels were mounted to be observed with a fluorescence or a confocal microscope. To avoid cell smashing and hydrogel damage, a PDMS spacer of the same dimensions of the hydrogels was placed on a large glass coverslip (60 mm x 24 mm). The hole of PDMS spacer was filled with a drop of Fluoromount-G® mounting solution, following that, the hydrogels were inverted facing downwards onto the glass coverslip, and inserted inside the PDMS hole. Finally, a glass coverslip was placed on top of the membrane to ensure the sealing. One hand, for the surface coverage studies, images were taken using a fluorescence inverted microscope (Axio vert.A1, Zeiss), access kindly provided by the Biosensors for bioengineering group from IBEC. Images were treated with ImageJ software. On the other hand, a closer view of the samples was imaged using a confocal laser-scanning microscope (LSM 800, Zeiss) located at IBEC MicroFabSpace facilities, and the acquired Z-stacks were processed using ImageJ software.

Target molecule	Chromogen	Host	Concentration ($\mu g \cdot mL^{-1}$)	Source
Phalloidin	Rhodamine	-	0.07	Cytoskeleton
Goat	Alexa 488	Donkey	4	Invitrogen
Mouse	Alexa 548	Donkey	4	Invitrogen
Rabbit	Alexa 647	Donkey	4	Invitrogen

Table 3.7. List of secondary antibodies used for immunofluorescence analysis. They were used to characterize the embedded cells and epithelial cells.

3.10.4. Immunofluorescence of hydrogel histological sections

For a better visualization of the embedded cells across the entire height of the hydrogels, after fixation some hydrogels were embedded using optimal cutting temperature (OCT) compound, and cross-sectioned using a microtome-cryostat. Briefly, after fixation, samples were incubated overnight with 30% sucrose (Sigma-Aldrich) at

4ºC, and then embedded in OCT (Tissue-Tek® O.C.T. Compound, Sakura® Finetek). Tissue sections (≈7 µm in thickness) were cut, placed on glass slides, air dried, and stored at -20 ºC for further analysis. For the immunostaining, the glass slides with the samples were taken out from the freezer and were warmed at room temperature for 5 min. Then, they were placed vertically, rehydrated by carefully throwing PBS with a Pasteur pipette, dried with a tissue avoiding to touch the hydrogels, and placed on a handmade humidity chamber to avoid evaporation of the solutions during the immunofluorescence steps. To permeabilize the cell membranes, 100 µL drops of permeabilization solution were placed on top of the hydrogel slides, covered with parafilm, and incubated for 1 h at 4ºC in static conditions. Then, samples were washed with PBS and dried. Next, 100 µL drops of blocking solution were placed on top of the samples, covered with parafilm and incubated for 2 h at 4ºC under static conditions. After rinsing, 50 µL drops of primary antibody solution were deposited on top of the hydrogels, covered with parafilm and incubated overnight at 4ºC. The following day, samples were washed with PBS and then, 50 µL drops of secondary antibody solution were placed on top of the samples, covered with parafilm and incubated 2 h at 4ºC. Slides were then rinsed gently with PBS and 100 µL drops of DAPI at a concentration of 5 $\mu g \cdot mL^{-1}$ were incubated for 1 h at 4ºC and washed with PBS. Finally, hydrogel slides were mounted by adding Fluoromount G® mounting solution, and were covered with glass coverslips. Samples were observed using a confocal laser-scanning microscope (LSM 800, Zeiss) located at IBEC MicroFabSpace facilities. Acquired Z-stacks were processed using ImageJ software.

3.10.5. Hematoxylin-eosin staining hydrogel histological section

Alternatively, some samples of the NIH/3T3-laden hydrogels co-cultured with the Caco-2 cells were embedded in paraffin and stained for hematoxylin-eosin. These samples were embedded in an automatic tissue processor machine (Tissue Tek VIP, Sakura) following routine procedures, resulting in paraffin-embedded sections of about 3 µm thick. After being cut and air dried, these samples were further dried overnight at 60ºC and then stored at room temperature. Hematoxylin and eosin staining were carried out by the Histopathology Facility services from IRB at PCB. Images were taken using an fluorescence inverted microscope (Axio vert.A1, Zeiss). The brightness and contrast levels of the acquired images were processed using ImageJ software.

3.10.6. Transepithelial electrical resistance measurement

The transepithelial electrical resistance (TEER) is a quantitative parameter that can be used to evaluate the integrity and the tightness of cellular barrier in non-invasive, low-cost and real-time *in vitro* assays[92,256]. TEER measurements are usually performed in Transwell® inserts, where cells grow on a porous membrane forming a tight monolayer, that when becoming confluent and mature, creates an electrical resistance between the two compartments. To measure the resistance, a pair of electrodes is placed into the Transwell® inserts, one electrode in the apical side and another in the basolateral compartment. A 12.5 Hz square-wave in low alternating current (AC) is applied through the electrodes, and the voltage across the cell barrier is measured through an EVOM^2 epithelial voltohmmeter (WPI world precision instruments). Equipped with an Endohm-6G culture camber (World precision Instruments) (Figure 3.22). Values were monitored every two days throughout the culture period (21 days) and by applying the Ohm's law, the resistance of the monolayer is extracted[92].

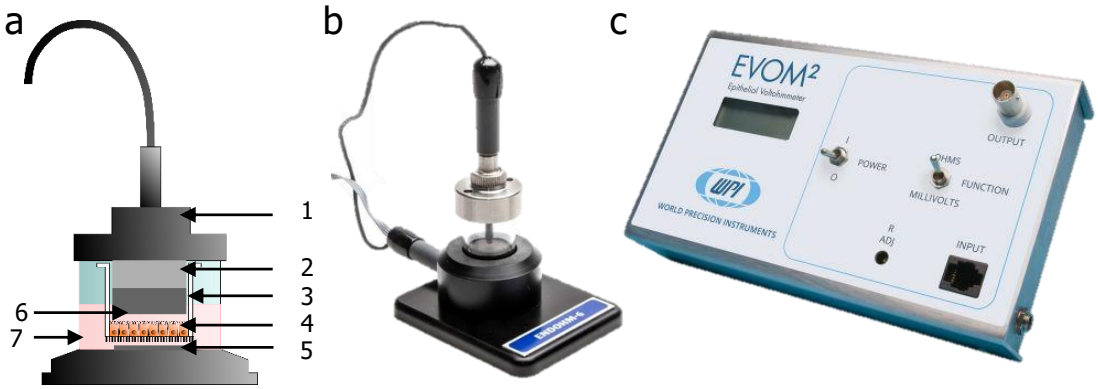

Figure 3.22. Setup of TEER measurements by a voltohmmeter. (a) Scheme of Endohm-6 chamber with a Transwell® insert placed inside. The chamber is composed by (1) cap, (2) electrode, (3) Transwell® insert, (4) cell monolayer, (5) electrode, (6) apical compartment, and (7) basolateral compartment. (b) Photograph of the Endohm-6 chamber with a circular disc Ag/AgCl electrodes. (c) EVOM^2 epithelial voltohmmeter.

Before starting the measurements, samples were removed from the incubator and left for 20 min at room temperature to stabilize and avoid misreading of the TEER values. Endohm-6G culture chamber was filled with 1 mL of cell culture medium. Then, a Transwell® insert was picked up, inserted into the Endohm-6G culture cup and the total resistance value (R_{total}) was recorded. Total resistance values were corrected by subtracting the blank resistance (R_{blank}) to the total resistance value measured each day. Blank resistance was given by the porous PET membrane or the hydrogel placed on

the membrane just before seeding the Caco-2 epithelial cells. The resistance value that was obtained after subtracting the blank was the resistance coming only from cell monolayer (R_{cell}). It is obtained by applying Eq. 3.25:

$$R_{cell} = R_{total} - R_{blank} \quad \textbf{Eq. 3.25}$$

Finally, cell resistance was normalized by multiplying it with the total insert surface area (A_{insert}) (Eq. 3.26). The A_{insert} of our samples was 0.33 cm^2. Data were plotted with OriginPro 8.5 software, as the mean ± standard deviation.

$$TEER = R_{cell} * A_{insert} \quad \textbf{Eq. 3.26}$$

During the first days of the culture, TEER values remained low, as the epithelial monolayer is not yet well-formed and the tight junctions between the cells had not been established. As the cells divided and the monolayer became more compact, the tight junctions are narrower and the resistance between both compartments increases. Finally, when the epithelial monolayer reached its maximum confluence at that moment the cells are well-polarized and the tight junctions between cells are very narrowed, TEER values reached their maximum and are constant over time.

3.10.7. Apparent permeability assay

Passive absorption or apparent permeability of a drug or nutrient through the intestinal epithelium is measured using the Caco-2 cell line after its differentation[257–259]. The apparent permeability, P_{app}, is defined as the initial flux of compound through the membrane, normalized by membrane surface area and donor concentration (Eq. 3.27):

$$P_{app} = \frac{dQ/dt}{C_0 * A} \quad \textbf{Eq. 3.27}$$

Where C_0 is the initial concentration in the apical chamber, A is the area of the hydrogel and dQ/dt is the molecule transport rate, which is defined as the slope obtained from linear regression of the transport amount[238]. P_{app} values are computed by adapting a straight line to the initial portion of the recorded amounts of molecules that make it to the receiver compartment. Sometimes, there is a lagging period, so the first time points of the curve should be discarded[257].

After 21 days of cell culture, the apparent permeability coefficient was measured using dextrans fluorescently labelled. FD4 (FITC-dextran of 4 kDa) and FD70 (Rhodamine-dextran of 70 kDa) were employed as model compounds mimicking the paracellular transport through the tight junctions of the epithelial layer. Additionally, insulin apparent permeability was studied as model drug. Firstly, FD4 and FD70 were weighted inside the same glass vial and were dissolved in DMEM without phenol red at a concentration of 0.5 $mg \cdot mL^{-1}$. In parallel, insulin was weighted in another glass vial at a concentration of 0.5 $mg \cdot mL^{-1}$ and dissolved in DMEM without phenol red. Then, both solutions were gently shacked to ensure the dissolution of the dextrans and the insulin. Before adding the solutions into the cell culture, they were sterilized by filtering them with 0.22 µm PET filter inside the biosafety cabinet, were placed into a 15 mL Falcon tube protected from light and were maintained at 37ºC. Afterwards, the samples were removed from the incubator and left for 20 min at room temperature. Next, TEER was measured and cells were washed twice with DMEM without phenol red warmed at 37ºC prior starting the permeability assay. Following that, 200 µL of dextran solution or insulin solution were added to the apical side of the Transwell® insert and 600 µL of DMEM without phenol red were added to the basolateral compartment. For each sample, 50 µL solution from the basolateral compartment were recovered at given time points, from 0 to 180 min, and placed into a 96 black well-plate. Simultaneously, to keep constant the volume in the basolateral side, 50 µL of DMEM without phenol red were added every time that a sample was removed from the basolateral part. During the experiment, cells were incubated at 37ºC on a horizontal shaker at 50 rpm. Finally, FD4 and FD70 fluorescence were measured using a microplate reader (Infinite M200 PRO Multimode microplate reader, Tecan) at 495/520 and 540/625 excitation/emission wavelengths, respectively, or by an insulin ELISA kit. To relate fluorescence values of the collected samples with molecule concentrations, standard curves for FD4, FD70 and insulin were generated from 0.5 $mg \cdot mL^{-1}$ (FD4 and FD70) or 0.25 $mg \cdot mL^{-1}$ (insulin) to 0 $mg \cdot mL^{-1}$. P_{app} values were computed by a linear fitting of the initial portion of the recorded amounts in the receiver compartment. Data were plotted with OriginPro 8.5 software as the mean ± standard deviation.

3.10.8. Disruption and recovery of the tight junctions of the epithelial barrier

The impact of the stromal cells on barrier recovery after tight junction disruption was studied by disrupting the barrier with ethylenediaminetetra acetic acid (EDTA). EDTA

is a molecule that acts as a calcium ion chelator. Calcium ions, which are present in cell culture medium, are necessary to maintain the structure and conformation of proteins involved in the tight junctions[260]. EDTA in the medium restrains calcium ions, resulting in their rupture. As a consequence, the epithelial monolayer is disrupted, and this can be observed as a drastic drop in TEER values compared to the initial value[261]. This rupture is reversible, once EDTA is removed from the medium, the tight junctions are formed again and the epithelial barrier integrity is recovered[262].

This study was performed on fibroblasts cell-laden hydrogels (fibroblasts density $5 \cdot 10^6$ cells·mL^{-1}) and non-cell laden hydrogels both of them composed of 7.5% (w/v) $GelMA_5$ – 5 % (w/v) PEGDA. After 21 days of cell culture, epithelial barrier was disrupted with EDTA (Sigma-Aldrich). First of all, cell culture medium from the Transwell® inserts was removed and a solution of 5 mM EDTA in CCD-18Co/Caco-2 complete DMEM medium and pH adjusted at 7.5 was added to the apical (200 µL) and the basolateral (600 µL) Transwell® compartments. After 5 min of EDTA incubation, samples were gently washed with PBS and apical and basolateral sides were filled with CCD-18Co/Caco-2 complete DMEM medium. The epithelial barrier disruption and recovery was monitored through recording the TEER values before EDTA and after EDTA removal from 0 h to 24 h. During the experiment, hydrogels were kept in the incubator at 37ºC and 5% CO_2. The changes in TEER values for the recovery phase were obtained by calculating the TEER slopes from 1 h to 6 h after removing EDTA. Data were plotted with OriginPro 8.5 software as the mean ± standard deviation.

3.11. Inflammatory stimulation of the 3D model of the intestinal mucosa

Inflammatory bowel diseases (IBDs), which include Crohn's disease and ulcerative colitis, are chronic intestinal inflammation and tissue destruction due to an inappropriate inflammatory response to intestinal microbes mediated by the innate and adaptive immune [69,263]. One molecule that triggers IBDs is the lipopolysaccharide (LPS), which is present in the outer membrane of Gram-negative bacteria[264]. To mimic an inflammatory status of the small intestine, macrophages were included in the lamina propria compartment of our hydrogels in order to provide immunocompetence activity. Macrophages were chosen because they represent the largest immune cell population in

the intestinal lamina propria. THP-1 monocyte cell line was chosen, to carry out these experiments because they can be easily differentiated to macrophages-like cells (M0).

3.11.1. Characterization of the cells on the hydrogel-based intestinal mucosa constructs

M0 (cell density $6.5 \cdot 10^6$ cell·mL^{-1}), CCD-18Co (cell density $6.5 \cdot 10^6$ cell·mL^{-1}), and co-culture of CCD-18Co and M0 (total cell density $13 \cdot 10^6$ cell·mL^{-1}) cell-laden hydrogels composed of 5% (w/v) $GelMA_{1.25}$ – 1.25% (w/v) PEGDA were fabricated using an UV energy dose of 1.88 J·cm^{-2} (Figure 3.23 (a)). Some of them were kept without epithelial cells, and others were seeded with Caco-2 cells at a density of $7.5 \cdot 10^5$ cells·cm^{-2} (Figure 3.23 (b)). Samples were kept in the incubator at 37ºC, and 5% CO_2, exchanging the medium every two days. The barrier integrity developed by the epithelial cells was monitored every two days throughout the culture period (21 days) by measuring TEER (see section 3.10.6). Cell viability on cell-laden hydrogels without epithelium was evaluated through Live/Dead™ viability/cytotoxicity assay at 3 and 14 days after encapsulation (see section 3.10.2). Images of the whole thickness of the cell-laden hydrogels were taken at a z-stack of 10 µm with the confocal scanning microscope (LSM, 800, Zeiss) located at the IBEC MicroFabSpace installations. Image processing was performed using ImageJ software. Images were analysed qualitatively by projecting their maximum intensity and the distribution was visualized by 3D reconstructions of the constructs. Moreover, cell morphology, proliferation and ECM secretion were evaluated at days 3 and 7 after encapsulation. For that, cells were fixed, cross-sectioned, and examined by immunofluorescence following the same protocol as described in section 3.10.4. Images were taken with a confocal scanning microscope (LSM, 800, Zeiss) and processed using ImageJ software. For the cell-laden hydrogels with epithelial barriers, the surface coverage of the epithelial cells was analysed by immunofluorescence at days 7 and 21 after seeding. Epithelial cells were labelled with β-catenin and DAPI (see section 3.10.3). Fluorescence images of the entire hydrogel surfaces were done using confocal laser scanning microscopy (TCS SP5, Leica) equipped with a 10x dry or 63x oil objectives, located at IRB Advanced Digital Microscopy Unit.

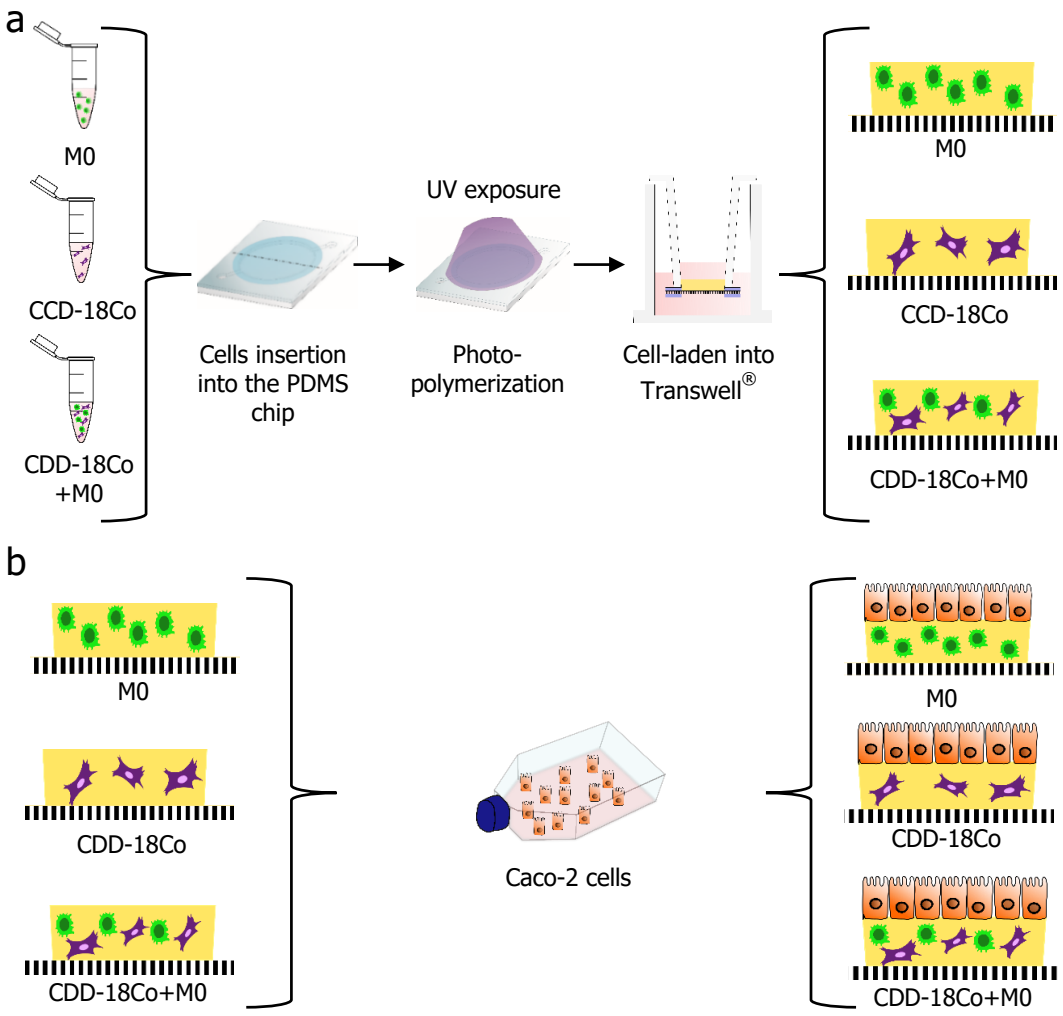

Figure 3.23. Schematic representation of the 3D intestinal mucosa containing immune and stromal cells. (a) Hydrogels with M0, CCD-18Co, and M0+CCD-18Co cells embedded were fabricated and mounted into Transwell® inserts. (b) Caco-2 cells were seeded on top of the M0, CCD-18Co, and M0+CCD-18Co cell-laden hydrogels to mimic the epithelial barrier.

3.11.2. LPS treatment

To perform an inflammatory stimulation in our 3D models of the intestinal mucosa, cell-laden hydrogels with and without epithelial barriers were treated with LPS from *Escherichia coli O26:B6* (Sigma-Aldrich) after 14 days and 21 days of culture, respectively. The TEER values of the samples that had the epithelial compartment were recorded. At day 14 or 21, the cell culture medium was removed and replaced by THP- 1 complete DMEM medium without β-mercaptoethanol, where FBS was reduced from 10% (v/v) to 2% (v/v). Cells were incubated in this medium for 18 h before LPS stimulation. After this time, some hydrogels were treated with LPS by adding to the apical side 200 µL of 5 $mg \cdot mL^{-1}$ LPS solution dissolved in THP-1 complete DMEM medium without β-mercaptoethanol and with 2% (v/v) FBS. In the basolateral chamber, 600 µL of THP-1

complete DMEM medium without β-mercaptoethanol and with 2% (v/v) FBS was added. On the other hand, some hydrogels remained untreated by replacing the medium on the apical and basolateral compartments for fresh THP-1 complete DMEM medium without β-mercaptoethanol and with 2% (v/v) FBS. Untreated and LPS-treated hydrogels were incubated at 37ºC in a 5% CO_2 for 6 h. Then, for the samples with epithelial monolayer, TEER was measured again. Moreover, for non-epithelial samples and epithelial samples medium from apical and basolateral sides was exchanged to THP-1 complete DMEM medium without β-mercaptoethanol and 10% (v/v) FBS. Supernatant was collected during (I) cell culture period from day 0 to day 21, (II) before the LPS-treatment, and (III) after LPS-treatment, to study cytokine release by Enzyme-Linked Immunosorbent Assay (ELISA) assays (see section 3.11.3).

3.11.3. Cytokine release profiles

Cytokines are small secreted proteins released by cells which have important roles on (I) the interaction and communication between cells, (II) the proliferation of antigen specific effector cells, and (III) the mediation of the local and systemic inflammation[265,266]. Different cytokines can have similar functions, and they can act on the same cells that secreted them, on the nearby cells or on distant. Cytokines can be classified into pro-inflammatory or anti-inflammatory. Pro-inflammatory cytokines are related with the up regulation of inflammatory reactions, and some of them are IL-1β, IL-6 or TNF-α. Anti-inflammatory cytokines are immunoregulatory molecules that control the pro-inflammatory cytokine responses, and some examples are IL-4, IL-10, IL-11 and IL-13[266]. Cytokines produced by the intestinal immune system are relevant to maintain the homeostasis of the intestinal tissue. Moreover, a dysregulation on the secretion profile of these the cytokines can produce inflammation of the intestine and may result in inflammatory bowel diseases such as Crohn's disease or ulcerative colitis.

Cytokines were analysed using an ELISA test, which is based on an antigen-antibody reaction resulting in a strong coloured solution when the cytokine is present in the medium. ELISA assay is widely used because is a simple and cost-effective technique with a high specificity and sensitivity. To perform our analysis, sandwich ELISA, which uses two antibodies to detect the antigen, was chosen. First, a capture antibody is immobilized on a well-plate, then, the plate is blocked to avoid non-specific absorption of other proteins. Following that, the sample is added, the antigen reacts with the

immobilized capture antibody, and is sandwiched with another antibody called detection antibody. After, the anchored detection antibody is recognized by an enzyme-labelled antibody, such as horseradish peroxidase (HRP) which gives a colour to the solution when a chemical substrate is added[267].

Human IL-8, human IL-10, human IL-6 and human TGF-β cytokine release profiles were assayed with ELISA kit (DuoSet® ELISA, R&D Systems). IL-8 is a chemoattractant and pro-inflammatory cytokine produced by immune cells, as well as epithelial cells. IL-10 is an anti-inflammatory cytokine mainly secreted by M1 macrophages and directs macrophage polarization to an immunosuppressive phenotype. IL-6 is a pro-inflammatory cytokine produced by M2 macrophages. Finally, TGF-β (Transforming growth factor beta) is secreted by fibroblasts or myofibroblasts and it acts as an anti-inflammatory cytokine. To analyse cytokine profiles, medium was collected at days 7, 14, 21 of culture and after LPS-treatment. Untreated samples were added as controls. Media from both apical and basolateral compartments were gathered in a 0.5 mL Eppendorf and frozen at -20ºC. ELISA assay protocol provided by the manufacturer was slightly modified to adapt it from a96 well-plate to a 384 well-plate. Each kit has its specific antibodies and standard molecule working concentrations (Table 3.8).

Cytokine	Source & Lot	Reagent	Stock concentration	Working concentration
IL-8	R&D systems P210528	Capture	480 µg·mL^{-}	4.00 µg mL^{-1}
		Detection	1.20 µg·mL^{-}	20.0 ng mL^{-1}
		Standard	100 ng·mL^{-}	31.2-2000 pg·mL^{-1}
		Streptavidin-HRP	N/A	40 fold dilution
IL-10	R&D systems P204890	Capture	240 µg·mL^{-}	2.00 µg mL^{-1}
		Detection	3.00 µg·mL^{-}	50.0 ng mL^{-1}
		Standard	150 ng·mL^{-}	31.2-2000 pg·mL^{-1}
		Streptavidin-HRP	N/A	40 fold dilution
IL-6	R&D systems P20859	Capture	240 µg·mL^{-}	2.00 µg mL^{-1}
		Detection	3.00 µg·mL^{-}	50.0 ng mL^{-1}
		Standard	180 ng·mL^{-}	9.38-600 pg·mL^{-1}
		Streptavidin-HRP	N/A	40 fold dilution
TGF-β	R&D systems P192323	Capture	240 µg·mL^{-}	2.00 µg mL^{-1}
		Detection	3 µg·mL^{-}	50.0 ng mL^{-1}
		Standard	190 ng·mL^{-}	31.2-2000 pg·mL^{-1}
		Streptavidin-HRP	N/A	40 fold dilution

Table 3.8. List of cytokines used and their reagents, as well as the stock and working concentrations employed to do the ELISA tests.

Reagents of ELISA kit were resuspended and stored in aliquots following the instructions provided with the kit. Briefly, a transparent 384 well-plate was coated by adding 50 µL of capture antibody solution diluted in filtered PBS to the working concentration, and incubating this solution overnight at room temperature. The plate was covered with an adhesive film and wrapped with an aluminium foil to prevent evaporation. Next day, solution was aspirated and washed three times by adding 100 µL of 0.05% (v/v) Tween® 20 (Sigma-Aldrich) in PBS (Wash Buffer) to each well, removing it by inverting the plate, and blotting it against clean paper tissues. Blocking of the plate surfaces was performed by adding 100 µL of reagent diluent buffer , which is composed of 0.1% (w/v) BSA and 0.05% (v/v) Tween® in Tris buffer saline (TBS) (ThermoFisher Scientific) with the pH adjusted at 7.4. This buffer was incubated for 2 h and 30 min, at room temperature. Afterwards, the well-plate was washed three times as it was described above. Meanwhile, samples and standard reagents were thawed in ice to minimize protein degradation by proteases from the medium. Then, they were diluted in the reagent diluent buffer to fit within detection limit of the kit. 25 µL of samples or standard reagents diluted solution were added to the corresponding well and were incubated for 2 h at room temperature. The well-plate was washed three times and afterwards, 25 µL of the detection antibody solution diluted in the reagent diluent buffer to the working concentration were added in the corresponding well for 2 h at room temperature. Then, a washing step was repeated three times. Next, 25 µL of Streptavidin-HRP in reagent diluent buffer diluted to the corresponding working concentration were added to each well for 20 min at room temperature. After incubation, the plate was washed again and 25 µL of substrate solution were added and incubated for 20 min at room temperature. The substrate solution (R&D Systems), which is a kit composed of the substrate A and B, was prepared by mixing substrate solution A reagent and substrate solution B reagent in equally volumes. Finally, to stop the reaction, 15 µL of 2N Sulfuric acid (H_2SO_4) (Stop solution) (Fluka) were mixed with the substrate solution in the well. In this step, the colour of the solution turned to yellow if there were cytokines attached to the capture antibodies. During all the steps of the ELISA assay, the well-plate was sealed with a plate sealer (R&D Systems) to prevent solution evaporation and covered with aluminium foil to protect Streptavidin-HRP from the light exposure. To finalize the assay, the absorbance of each well was immediately measured at 450 nm with a plate reader (Benchmark Plus Microplate Reader, Bio-Rad). Optical imperfections coming from the plate were corrected by subtracting absorbance values at 540 nm from absorbance values at 450 nm.

For the standard solutions, technical replicas were performed in triplicates. For sample solutions, technical replicas were not performed. However, there were at least two biological replicas of each condition. The absorbance of the blank solutions was subtracted for each replica. Curves relating absorbance with concentrations were created by plotting the absorbance values versus the concentration of the standards reagents in logarithmic scale, and fitting the curve by a four parameters logistic (4-PL) equation. If samples were diluted, cytokine concentration values obtained were corrected by the dilution factor. All the data were processed using GraphPad Prism 6 software. Graph were plotted with OriginPro 8.5 software (OriginLab) as the mean ± standard deviation.

3.12. Fabrication of 3D villus-like GelMA – PEGDA hydrogel co-networks

GelMA – PEGDA hydrogel co-networks including 3D villus-like microstrutures were fabricated by free radical photopolymerization under UV light exposure of polymer solutions using a photomask. First GelMA – PEGDA polymer solutions were prepared as explained in section 3.3.1 and were polymerized using a setup similar to the one used to fabricate disc-shaped hydrogels (section 3.3.2). However, in this setup the support had a black background to prevent light scattering and a 2D photomask was included to selectively confine light irradiation in specific regions, which will form the villus structures. The GelMA – PEGDA solution was introduced into a chip 1 mm or 0.5 mm high through the input channels. Previously, the PDMS container was covered with a PET membrane, which acted as a substrate, and an 18 mm glass coverslip to prevent polymer solution leakage through the membrane pores. An acetate photomask with the desired pattern was placed on top of the chip covering entirely the polymer solution container (Figure 3.24 (a)). The photomask designs were based on either an array of transparent circular spots 100 µm in diameter and 100 µm of space between them, which gave a density of 25 windows·mm^{-2}, or an array of spots 150 µm in diameter and 300 µm of space between them (density of 12.5 windows·mm^{-2}). These parameters were chosen based on the *in vivo* anatomical dimensions of the human villi of the intestine, which range between 0.2 – 1 mm in height[13] and between 100 – 150 µm in diameter[7,14] and 20 – 40 villi·mm^{-2} villi surface density[1] (Figure 3.24 (b and c)). The photomasks were designed using AutoCAD software (Autodesk) and printed on acetate films (CAD/Art

Services). After UV light exposure, microstructured hydrogels were washed with PBS at 37ºC in order to eliminate the non-crosslinked polymer solution.

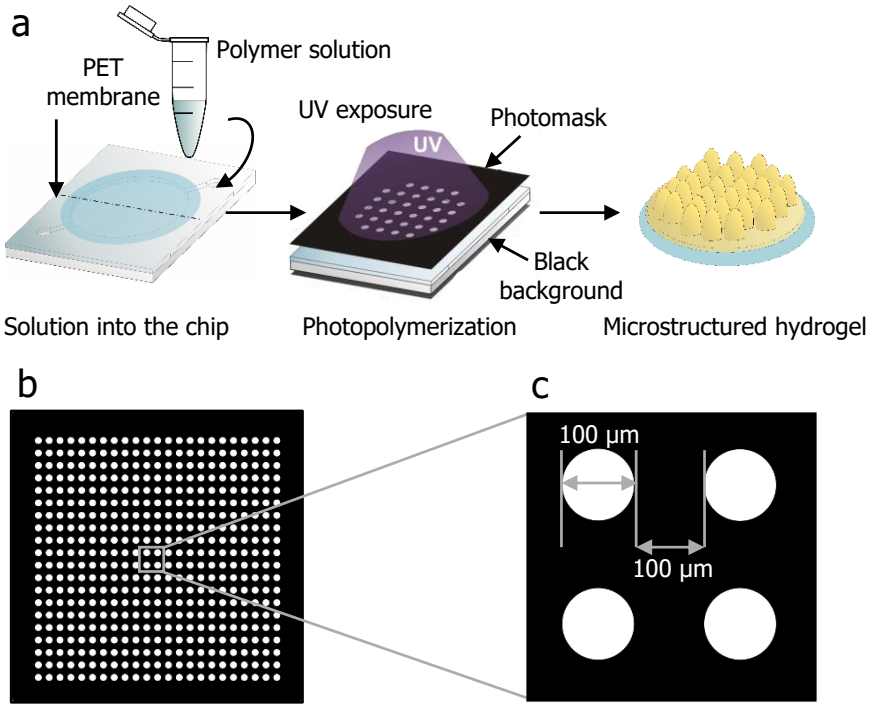

Figure 3.24. Scheme of the microfabrication process of 3D villus-like hydrogels. (a) Simplified scheme of the fabrication procedure on GelMA – PEGDA hydrogels. In the first step, polymer solution was introduced to the chip, which contained a black bottom. Then, the polymer solution was exposed to the UV light, through the photomask. Finally, hydrogel was washed to remove the non-crosslinked material. (b) Drawing of the photomask design used to microstructure hydrogels. (c) Zoom of the photomask to visualize better the pattern and the dimensions of the UV-transparent windows.

3.12.1. Morphological assessment of the 3D villus-like microstructured hydrogel co-networks

The height of 3D villus-like microstructures patterned on the hydrogel co-networks was analysed as a function of UV energy dose used in the fabrication process. To do that, microstructures were fabricated using 7.5% (w/v) $GelMA_5$ – 5% (w/v) PEGDA polymer solution, which was photopolymerized applying a range of UV energy doses from 4.9 to 7.7 $J \cdot cm^{-2}$. After swelling in PBS, hydrogels were placed in a 6 well-plate, covered with a few drops of PBS. Then, hydrogels were carefully cross-sectioned under a bright field microscopy. PET membranes, which served as supports to fabricate the hydrogel, were held with the tweezers and an array of villi-like structures was cut using a scalpel. Then, the array was tilted horizontally and imaged using a bright field microscopy (Nikon Eclipse Ts2) (Figure 3.25 (a)).

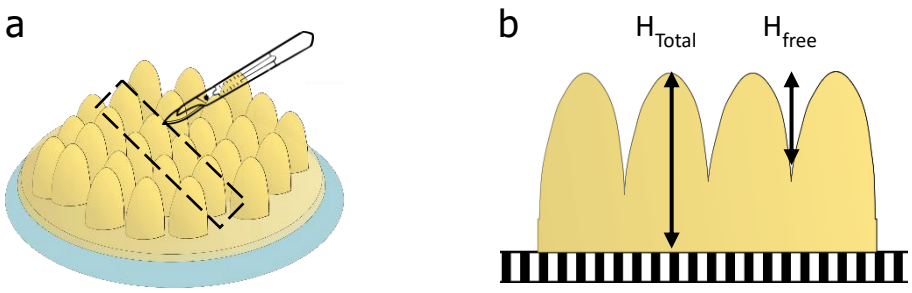

Figure 3.25. 3D villus-like hydrogels sample cutting. (a) Simplified scheme of the sectioning process. (b) Drawing of the cross-sectioned hydrogels showing the H_{total} (the total height of villus-like microstructures) and H_{free} (the free height of villus-like microstructures).

Images were analysed using ImageJ software. The total height of the villus-like structures (H_{total}) was determined by measuring the height from the tip of the microstructures until the bottom. In some cases, there was hydrogel crosslinked between the microstructures, so their free height was shorter than their total height. This free height of the villus-like structures (H_{free}) was obtained by measuring the distance between their tips till the first layer of crosslinked polymer (Figure 3.25 (b)).

3.12.2. Fabrication of a lamina propria compartment on the 3D villus-like hydrogels

To achieve 3D villus-like hydrogel co-networks including the lamina propria compartments, NIH/3T3 cells were encapsulated into microstructured hydrogel co-networks. After dissolving the polymer solution (see section 3.3.1), the cell pellet was obtained following the methodology explained in section 3.5.1. The polymer solution containing the cells was photopolymerized following the method described in section 3.9. Briefly, the NIH/3T3 cells (cell density of $5 \cdot 10^6$ cells·mL^{-2}) were resuspended in a 7.5% (w/v) $GelMA_5$ – 5% (w/v) PEGDA solution and 3D villus-like hydrogels of 0.5 mm height and 6.5 mm diameter were crosslinked on top of a PET membrane by applying an energy dose of 7.70 J·cm^{-2}. The 3D villus-like structures with embedded fibroblasts were then mounted on Transwell® inserts using double-sided PSA rings, following the same methodology as explained in section 3.4.4. After mounting each hydrogel, fibroblast complete DMEM medium was quickly added in the apical (200 µL) and the basolateral (600 µL) compartments of the Transwell® inserts (Figure 3.26). Hydrogels were incubated at 37ºC and 5% CO2, exchanging the fibroblast complete DMEM medium every other day. The experiment was carried out until day 21 after cell encapsulation, a

total of 5 cell-laden hydrogels were fabricated. At the following time points, 3 days, 7 days, 10 days, 14 days and 21 days, the state of the embedded cells was analysed. To do that, one hydrogel sample was demounted from the Transwell® insert and the cell viability inside the 3D villi-like structures was analysed by Live/Dead™ viability/cytotoxicity assay kit (see section 3.10.2).

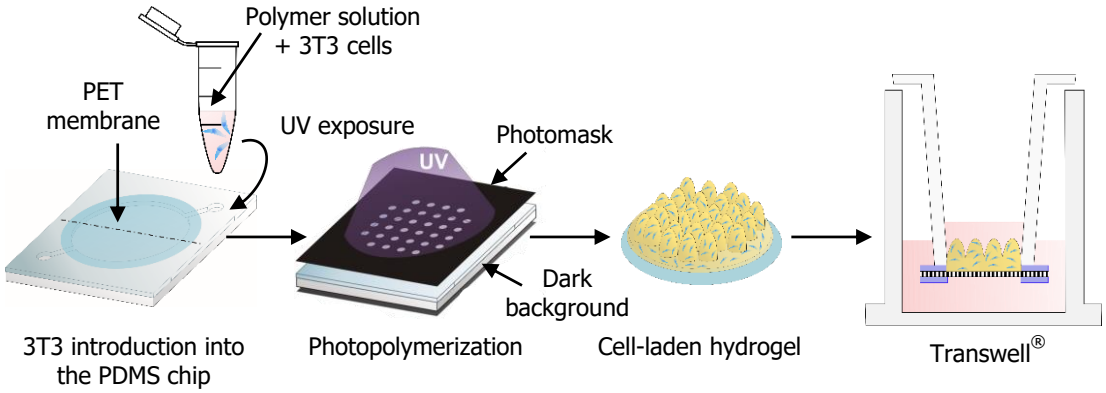

Figure 3.26. Schematic drawing of the NIH/3T3 cell-laden 3D villi-like hydrogel fabricated on top of a PET membrane. A black bottom was provided to the chip, to avoid light scattering. Then, PDMS pools were covered with a PET membrane that acted as substrate. NIH/3T3 resuspended in the polymer solution were introduced to the pools, pools were covered by the photomask and exposed to UV light. Finally, the hydrogels were mounted.

3.13. Data analysis and statistics

Data are presented as the mean ± standard deviation (SD). The graphs were plotted using OriginPro 8.5 software (OriginLab). In the case of normal distributions, differences between groups were compared through a one-way analysis of variance (ANOVA) applying a Turkey's test. Replicates of each experiment are indicated in the figure legends of the results. Differences were considered as statistically significant if $p<0.05$.

4. Results

4.1. Fabrication and characterization of gelatin methacryloyl

Firstly, we verified that the gelatin methacryloyl (GelMA) polymer obtained after the reaction between gelatin and methacrylic anhydride (MA) was properly synthetized. GelMA was prepared following a reported process where MA reacted with gelatin molecules to get GelMA, the degree of functionalization (DoF) of batches of newly synthesized GelMA were characterized. DoF is an essential parameter to check to guarantee the reproducibility of the GelMA synthesis procedure, needed to fabricate hydrogels with controllable mechanical and physicochemical properties. The DoF of GelMA chains was studied by different techniques and is reported in the following sections.

4.1.1. Qualitative analysis of the degree of functionalization of GelMA

To qualitatively analyse the modifications in the gelatin polymer, attenuated total reflectance-Fourier transform infrared (ATR-FTIR) and proton nuclear magnetic resonance (^{1}H-NMR) measurements were carried out.

ATR-FTIR is a well know technique used to study the chemical bonds and the secondary structure of polypeptides. It determines the chemical bonds by measuring the intensity of the light absorbed when the vibration frequencies of the bounds are the same as the infrared frequencies irradiated[228]. The ATR-FTIR spectra of $GelMA_{20}$, $GelMA_{1.25}$, unmodified gelatin, and MA polymer solutions dissolved at 1% (w/v) were examined (Figure 4.1 (a)). The broad signal between 3300 to 3250 cm^{-1} corresponded to the N – H stretching vibration from the peptide bonds and O – H stretching vibration from hydroxyl groups of amide A. Around 3050 cm^{-1} it appeared the C – H stretching for the amide B. In the 1600 cm^{-1} region, the first peak that appeared was the C = O stretching for amide I, the second peak corresponded to C – N – H deformation for the amide II, and the third one for amide III was the N – H stretching[224,268]. ATR-FTIR spectra of GelMA and unmodified gelatin did not show any distinguishable difference between them. Gelatin is a heterogeneous, large and complex molecule, which contains several types of chemical bonds. The complex spectrum of the unmodified gelatin could mask the new signals coming from the introduction of MA in the gelatin to produce GelMA. Overall, FTIR spectra was not a suitable method to confirm methacrylation reaction.

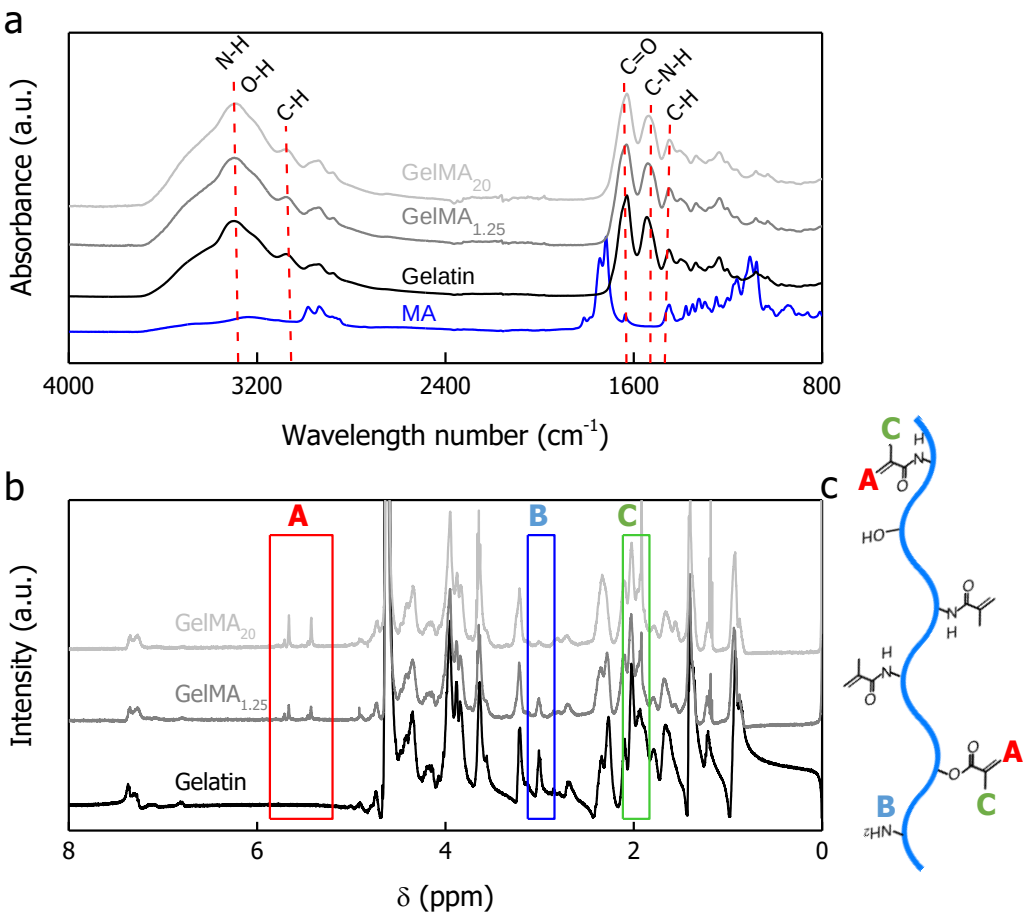

Figure 4.1. Characterization of the methacryation process. (a) Attenuated total reflectance-Fourier-transform infrared spectroscopy (ATR-FITR) spectra of methacrylic anhydride (MA) (blue line), unmodified gelatin (back line), GelMA$_{1.25}$ (dark grey line) and GelMA$_{20}$ (light grey line) where the absorption bands of the main bonds are marked with a dashed red line. (b) Proton nuclear magnetic resonance (^{1}H-HMR) spectra of unmodified gelatin (black line), and gelatin methacrylate for GelMA$_{1.25}$ (dark grey line) and for GelMA$_{20}$ (light grey line). In the spectra appears specific bands at 5.3 ppm and 5.6 ppm (red square, A) which correspond to the acrylic protons incorporated to the lysines or hydroxylysines residues. There is a disappearance of the band at 3 ppm (blue square, B) which correlates with the decrease of free amino groups from the modified lysines or hydroxylysines. The new band at 1.9 ppm (green square, C) refers to the methyl protons from the methacryloyl groups (c) Schematic representation of GelMA molecule that correlates the bands of the ^{1}H-NMR spectra and chemical groups.

^{1}H-NMR spectroscopy was performed also to qualitatively assess the methacrylation of the synthesized GelMA. ^{1}H-NMR spectra of unmodified gelatin and the two gelatin methacrylate with different DoF (GelMA$_{20}$ and GelMA$_{1.25}$) are represented in Figure 4.1 (b). As it can be seen, both GelMA spectra are rather different from gelatin spectrum. Three different signals appear in GelMA spectra due to the reaction between MA with amine groups (-NH$_2$) of lysines (Lys) or hydroxylysines (Hyl) resulting into the incorporation of methacryloyl groups in the gelatin chain to form the GelMA

molecule[142,229,269]. In the recent years it has been seen that when there is an excess of MA, this one reacts with the hydroxyl groups (-OH) of aminoacid residues and resulting in the incorporation of methacryloyl groups to the gelatin molecule. The methacryloyl groups attached to the $–NH_2$ are known as methacrylamide groups, while the methacryloyl groups attached to the –OH are known as methacrylate groups[142,229,269]. Gelatin methacryloyl is the general name given to gelatin after the methacrylation process and encompasses the two previous modifications. As it is shown in Figure 4.1 (b), the incorporation of the methacryloyl group caused the apparition of three new bands. Two of them at 5.3 ppm and 5.6 ppm, corresponding to the acrylic protons incorporated into the lysine or hydroxylysine residues ($C\mathbf{H_2}=C(CH_3)CNH$-). Next to the 5.6 ppm signal region, sometimes it appeared a small peak corresponding to the double bonds from the acrylic protons incorporated into hydroxyl groups. However, in the spectrum, the peak is difficult to see because the percentage of modified hydroxyl groups is very small[142,231]. The third band, which is at 1.9 ppm, is assigned to methyl protons of the new methacryloyl groups ($CH_2=C(C\mathbf{H_3})CO$-) incorporated into the lysine, hydroxylysine residues or hydroxyl groups. In contrast, the peak at 3 ppm, which correspond to the methylene protons of the free lysine or hydroxylysine residues (NH_2-$C\mathbf{H_2}CH_2CH_2CH_2$-), decreased markedly in GelMA spectra, especially the one with a higher degree of functionalization ($GelMA_{20}$)[189,229,231]. Overall, methacrylic anhydride reaction with the free amino groups from the lysines, hydroxylysines residues or hydroxyl groups in gelatin polymer to get GelMA polymer was achieved, and thus the success of the gelatin methacrylation process was confirmed.

4.1.2. Quantitative analysis of the degree of GelMA functionalization

In addition, the methacrylation process was quantitatively analysed to get the DoF of GelMA polymers. DoF was determined by two different methods. The first one was through ^{1}H-NMR spectrum, comparing the decrease in the peaks of lysines of the GelMA spectra to the one of the unmodified gelatin spectrum. The second method was TNBS assay, which is a colorimetric assay (more information about calculations in section 3.2.3 and 3.2.4, respectively). Both methods are widely used in the literature[140,189]. However, they provide an estimation of the DoF because they only take into account the methacrylamide groups resulting from the modification of amino groups from lysine or hydroxylisine residues, whereas functionalization of hydroxyl groups is not considered.

In the last few years, modifications on the ^{1}H-NMR setup and new colorimetric assays have been introduced to quantify the methacrylate groups in GelMA polymer, providing a more accurate quantitative analysis of the degree of GelMA functionalization. Regarding ^{1}H-NMR spectroscopy, an internal reference such as TMPS is added to simultaneously quantify methacrylamide and methacrylate groups. Concerning TNBS assay, it is complemented by performing in parallel another colorimetric assay, known as Fe(III)-hydroxaminic assay, which quantifies the methacrylate groups. Therefore, the sum of the two assays gives the total DoF for GelMA[229,231]. However, when methacrylic anhydride is not in excess, it mainly reacts with free amino groups of lysine and hydroxylysine[231]. We hypothesised that, as we added a low percentage of methacrylic anhydride, this was not able to react with the hydroxyl groups, so the percentage of methacrylamide groups incorporated to the gelatin is a good approximation to the DoF.

Figure 4.2 shows the DoF calculated by ^{1}H-NMR for $GelMA_{20}$ and $GelMA_{1.25}$ (Figure 4.2 (a)), and by TNBS assay for $GelMA_{5}$ and $GelMA_{1.25}$ (Figure 4.2 (b)).By varying the % (v/v) of methacrylic anhydride added to gelatin, GelMA polymers with different DoF were achieved. Decreasing the percentage of MA (v/v) decreased the DoF, meaning that less free amine groups were modified, resulting in GelMA polymers containing fewer crosslinking points. DoF affects the mechanical properties of the final hydrogel, and might impact cellular behavior[270,271]. Therefore, hydrogels containing GelMA polymer with high DoF are claimed to provide better mechanical stability and environment for cell culture than hydrogels with low DoF[272]. On the other hand, despite MA was added 4x excess in $GelMA_{20}$ polymer compared to $GelMA_{5}$, both polymers had similar DoFs ($GelMA_{20}$ (^{1}H-NMR) = 80.7 ± 1.3% and $GelMA_{5}$ (TNBS) = 75.4 ± 2.1%). We presume that this is the case because MA was unable to react with the remaining unreacted lysine or hydroxilysine aminoacids due to the 3D structural conformation of gelatin masking the ε-amine groups. Moreover, non-significant differences were obtained between both analytical techniques to determine the DoF ($GelMA_{1.25}$ (1H-NMR) = 54.7 ± 2.5%; and $GelMA_{1.25}$ (TNBS) = 51.4% ± 3.7) (Figure 4.2). We assume that both methods were robust and truthful. For simplicity and practicality, to quantify the DoF in this thesis, we mostly used the TNBS assay.

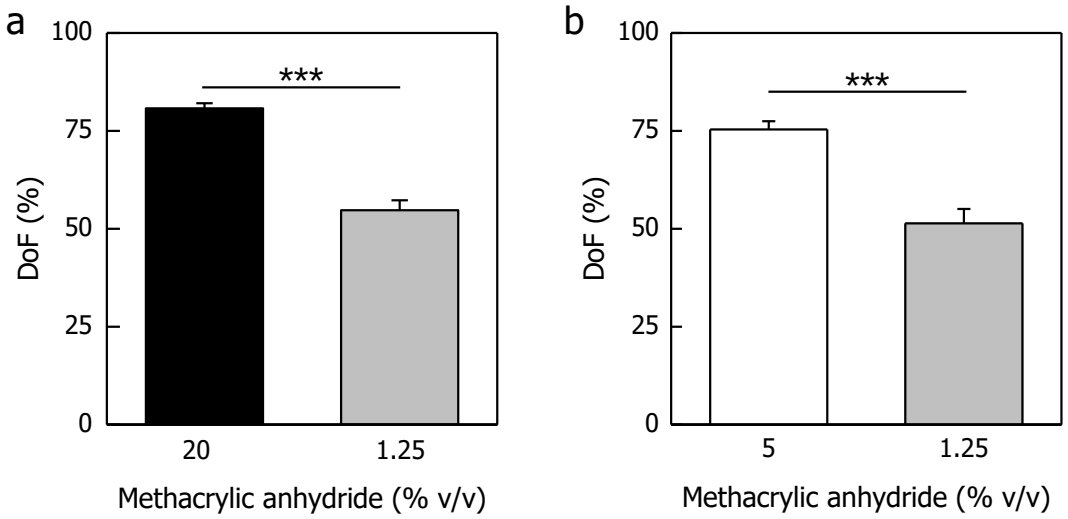

Figure 4.2. Quantification of the degree of functionalization of different GelMA polymer batches by (a) ^{1}H-NMR technique, for $GelMA_{20}$ (black) and $GelMA_{1.25}$ (grey) (n=3, N=1). (b) TNBS assay, for $GelMA_{5}$ (white) and $GelMA_{1.25}$ (grey) (n=1 with 3 technical repetitions, N=2). Values are shown as the mean ± SD. ***p<0.001.

4.2. Determination of GelMA molecular weight

The molecular weight is the sum of the atomic weights of all the atoms that forms a molecule and it is measured in Daltons (Da) or $g \cdot mol^{-1}$. Here, the molecular weight distribution of GelMA polymers was compared with unmodified gelatin to known if it was affected by the addition of methacryloyl groups. For that, sodium dodecyl sulfate-polyacrylamide gel electrophoresis (SDS-PAGE) with 10% (v/v) bis/acrylamide gels was performed for unmodified gelatin and GelMA polymers ($GelMA_{5}$, $GelMA_{1.25}$ and $GelMA_{0.25}$). Figure 4.3 shows a photo of the electrophoresis results. In the first column there is a molecular weight size marker, which is a set of standard bands of known molecular weights that are used to determine approximately the size of the unknown molecule. In the other columns there are our gelatin and GelMA samples. We found out that unmodified gelatin displayed three protein bands at ≈250, ≈130 and ≈110 kDa. The first band (≈250 kDa) corresponded to the β-chain. The second (≈130 kDa) and the third (≈110 kDa) bands were the α_1-chain and the α_2-chain, respectively. The molecular weight of β-chain is twice the α-chains because it is composed of two α-chains covalently crosslinked[273]. These three bands from the unmodified gelatin were the same as reported in the literature for collagen and gelatin polymers[273,274]. This means that the process of hydrolysis of collagen to obtain gelatin did not affect the molecular weight of β-, α_1-, α_2-chains. Analysing GelMA polymer bands, $GelMA_{0.25}$ presented the same three bands

(matching for β-, α_1-, α_2- chains) as in gelatin. These results showed that the molecular weight of the gelatin chains remained unaffected by low methacrylation process. In $GelMA_5$ and $GelMA_{1.25}$, bands corresponding to β-, α_1-, α_2- chains were not that clearly visible. However, this did not necessarily mean that gelatin was degraded by high amounts of MA. We presume that Comassiee Brilliant Blue dye interacted with the basic side chains of aminoacids, which included lysine aminoacids among others [275]. As lysines were modified during the methacrylation process, the dye was unable to attach to lysines or hydroxylisine residues, resulting in unstained bands.

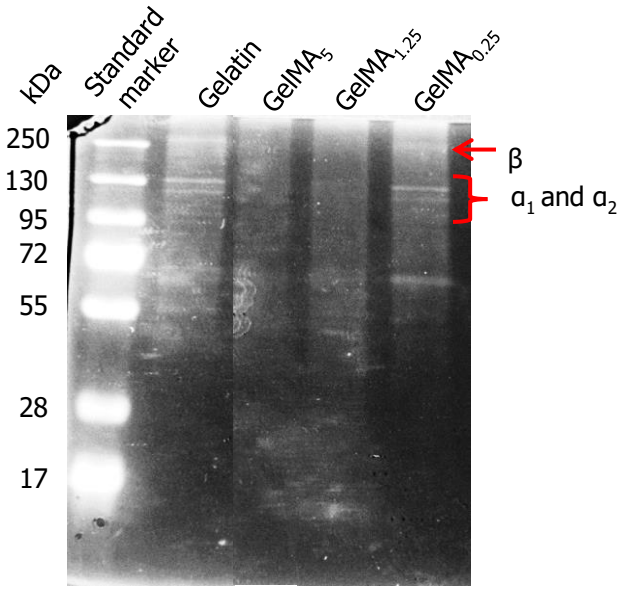

Figure 4.3. SDS-PAGE analysis of unmodified gelatin and GelMA at different degree of functionalization ($GelMA_5$, $GelMA_{1.25}$ and $GelMA_{0.25}$). Molecular weight of the standard marker is indicated on the left-hand side, whereas β-, α_1- and α_2- chains are on the right-hand side of the image.

4.3. Fabrication of GelMA and PEGDA hydrogel networks

The DoF of the GelMA polymer affects hydrogel pore size and mechanical properties[201]. Therefore, properties such as swelling dynamics, total mass swelling, mesh size and average molecular weight between crosslinking points were studied for hydrogel networks obtained from GelMA with different DoFs. In addition, these properties were also studied for PEGDA hydrogels.

To fabricate the hydrogels, we used an adapted version of a published protocol developed previously in our laboratory[155]. GelMA and PEGDA polymer solutions were dissolved in PBS and their polymerization was tested (more information about the concentrations and conditions are explained in each section below). Unlike PEGDA

polymer, GelMA polymer physically crosslinks at temperatures below 37ºC, making GelMA solutions more difficult to handle than PEGDA solutions. During the hydrogel fabrication, PDMS chips, supports and pipette tips were kept warmed to avoid physical crosslinking of GelMA as this would entrap GelMA molecules and affect the photocrosslinking process. The previously designed setup to form PEGDA hydrogels was suitable to polymerize GelMA polymers under UV light, however the material needed to be previously warmed to avoid jellification and perform a proper polymerization process.

4.3.1. Analysis of physicochemical properties of GelMA and PEGDA hydrogel networks

After the successful hydrogel formation, we studied the following network parameters: (I) swelling dynamics up to the equilibrium behaviour, (II) total mass swelling, (III) mesh size, and (IV) average molecular weight between crosslinked points. To do that, solutions of $GelMA_5$, $GelMA_{1.25}$ and PEGDA at concentrations of 12.5% and 7.5% (w/v) of total polymer content were dissolved in PBS and disc-shaped hydrogels were fabricated using a UV dose of 3 $J \cdot cm^{-2}$. $GelMA_{0.25}$ was not further characterized because it is reported to have weak mechanical properties[201]. On the other hand, the total polymer concentration was set at a maximum of 12.5% (w/v) because it is reported that concentrations higher than 15% (w/v) have low degradation rates and induce low viability of encapsulated cells, making them unsuitable candidates for medical applications[276]. The minimum polymer concentration used was 7.5% (w/v) because lower concentrations produce hydrogels with high degradation rates and short-term stability[201]. To determine the swelling dynamics and the time needed to achieve the equilibrium, swelling of the hydrogels was monitored daily by a gravimetric method to determine the amount of stored water. As it is observed in Figure 4.4 (a), the amount of stored water in $GelMA_{1.25}$ and PEGDA hydrogels increased over time, reaching up to 30.8 mg and 18.2 mg for $GelMA_{1.25}$ hydrogels, and up to 67.5 mg and 55.5 mg for PEGDA hydrogels, for low and high polymer concentrations, respectively. In contrast, $GelMA_5$ hydrogels had poor capacity to absorb water inside their network, only retaining between 2.6 mg and 0.5 mg of water for the low and high total macromer contents, respectively. Comparing the hydrogels according to their total polymer concentrations, those containing higher polymer concentrations diminished their capacity to store water (Figure 4.4 (a)). This is consequence of a more compact network. Water absorption in $GelMA_{1.25}$ and PEGDA hydrogels was more pronounced during the first hours of swelling.

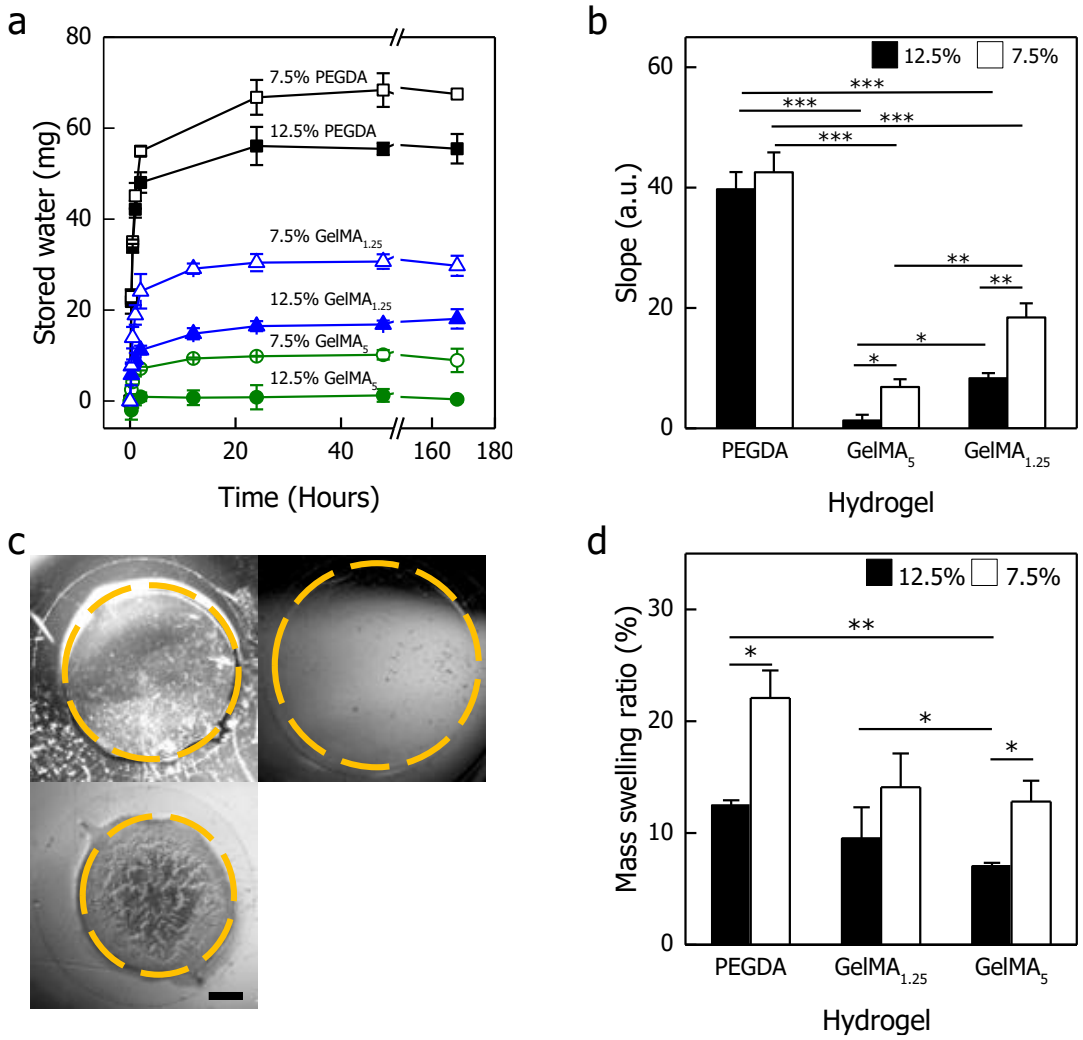

Figure 4.4. Characterization of swelling properties from hydrogels composed of PEGDA and GelMA polymers. (a) Variation of absorbed water by PEGDA (black, square), $GelMA_5$ (green, circle) and $GelMA_{1.25}$ (blue, triangle) hydrogels as a function of time. High (12.5% (w/v) (fill) and low 7.5% (w/v) (hollow)) concentrations of PEGDA and GelMA are represented. (b) Slope of the water amount absorbed by PEGDA, $GelMA_5$ and $GelMA_{1.25}$ hydrogels at a 12.5% (w/v) (black) and 7.5% (w/v) (white) during the first hour of swelling. (c) Images of 7.5% (w/v) PEGDA disc-shaped hydrogel fabricated applying an UV energy dose of 3 $J \cdot cm^{-2}$ after fabrication (top-left), at the equilibrium swollen state (top-right) and at the dry state (bottom-left). Scale bar: 1 mm. (d) Mass swelling ratio of hydrogels made of PEGDA, $GelMA_5$ and $GelMA_{1.25}$ at 12.5% (w/v) (black) and 7.5% (w/v) (white). Values are shown as the mean ± SD (at least n=2). * $p<0.05$, **$p<0.01$ and ***$p<0.001$

Figure 4.4 (b) shows the slope of the curve obtained from the amount of water absorbed during the first hour of swelling. No significant differences were observed in PEGDA hydrogels between the low and high macromer content. However, in GelMA samples there were significant differences among samples with different macromer content. After some time, the hydrogels could not absorb more water inside their networks. At that point, known as the equilibrium swelling point, hydrogel weights were

stable and constant (Figure 4.4 (a)). Although swelling was carried out for 7 days to ensure hydrogels were completely swollen, $GelMA_{1.25}$ hydrogels reached swelling equilibrium after 12 hours. Whereas, PEGDA hydrogels arrived at the swelling equilibrium after 24 hours. Weight values measured after hydrogel fabrication (m_c), at the equilibrium swollen state (m_s) and at the dry state (m_d) (Figure 4.4 (c)) were used to calculate, among other parameters, the mass swelling ratio (for further information about calculations see sections 3.4.2). For all polymers, higher polymer contents led to significant decrease in hydrogel swelling ratio (Figure 4.4 (d)). This is consistent with denser network structures having high crosslinking densities, smaller pores, and less capacity to hold water inside them. On the other hand, for the same GelMA amount, decreasing the DoF increased the mass swelling ratio, as it decreases the crosslinking points, providing hydrogels with larger pores and more capacity to store water. Our results are in agreement with previously published literature[201,231,269]. In contrast, maintaining the total concentration of GelMA or PEGDA polymer constant, the swelling ratio of GelMA hydrogels was significantly lower than that of PEGDA hydrogels. This is consequence of GelMA chains having more crosslinking points spread all over their chains than PEGDA chains, which only had two crosslinking points at their ends. Furthermore, GelMA molecule is more hydrophobic than PEGDA, causing a reduction of their interaction with water molecules and consequently, the mass swelling ratio decreases. These results show that hydrogel swelling can be tuned easily in our hydrogels by modifying the DoF of GelMA polymers and/or the total GelMA or PEGDA polymer concentrations.

In addition to the mass swelling ratio analysis, mesh size (ξ) and average molecular weight between crosslinking points (M_c) were determined (Figure 4.5). Pore size is related to molecule diffusivity through the hydrogel network, and is a key parameter to guarantee the supply of nutrients and oxygen to embedded cells. In our case, the mesh size and the average molecular weight between crosslinking points of $GelMA_5$, $GelMA_{1.25}$ and PEGDA at final polymer concentrations of 12.5% and 7.5% (w/v) were determined using Peppas and Merrill equilibrium swelling theory in the presence of water,[182] which is an adaptation of the original theory developed by Flory-Rehner[183] (see section 3.4.3). Comparing the M_c values of $GelMA_5$ and $GelMA_{1.25,}$ represented in Figure 4.5 (a), we observe that decreasing the DoF, and therefore decreasing crosslinking points, the M_c increased. However, when the DoF was maintained constant, M_c increased when the total polymer content was decreased. The same tendency was seen in PEGDA hydrogels. In both types of polymers, the M_c values decreased significantly when

compared with the average molecular weight of their single chains, which are $87.5 \cdot 10^3$ Da ($g \cdot mol^{-1}$) for GelMA and $4 \cdot 10^3$ Da ($g \cdot mol^{-1}$) for PEGDA. One would expect that the M_c value obtained for PEGDA hydrogels would be similar to the molecular weight of single chains because the reaction points are at the end of the PEGDA molecules. However, network defects, such as unreacted ends, intramolecular lops, and physical entanglement are present in the hydrogel network[277], resulting in decreased M_c values (62 – 68% lower than the molecular weight of single chains). On the other hand, M_c of GelMA hydrogels was greatly reduced compared to the M_c of single GelMA chains (up to 85 – 96%). This was consistent because unlike PEGDA, GelMA molecule has more crosslinking points distributed throughout its structure.

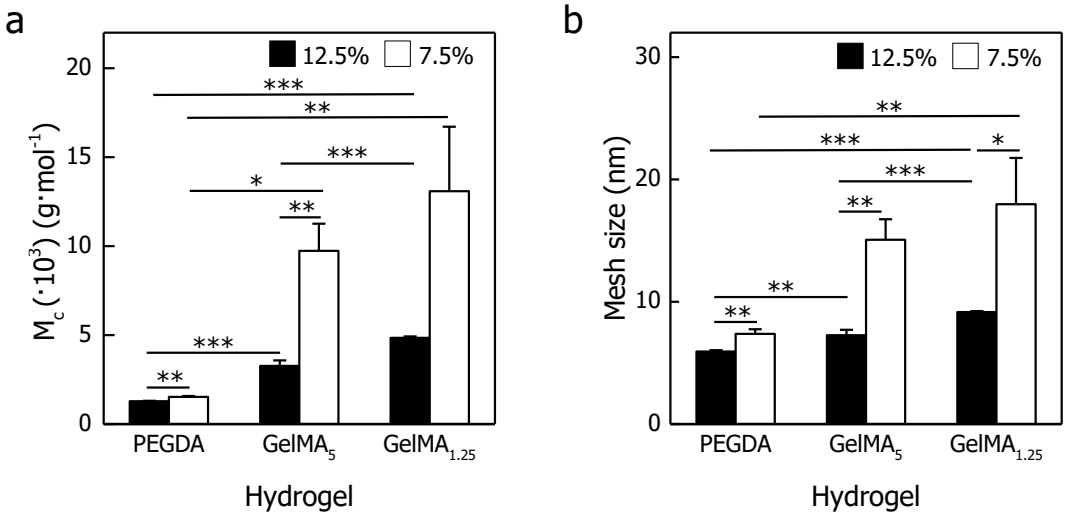

Figure 4.5. Characterization of hydrogel network properties through Peppas and Merrill theory. (a) Average molecular weight between crosslinks (M_c). (b) Mesh size (ξ) for PEGDA, $GelMA_5$ and $GelMA_{1.25}$ hydrogels fabricated applying an UV energy dose of 3 $J \cdot cm^{-2}$ at final polymer concentrations of 12.5% (w/v) (black) and 7.5% (w/v) (white). Values are shown as the mean ± SD (with almost n=2). * $p<0.05$, ** $p<0.01$, and *** $p<0.001$.

As it is expected, hydrogel mesh size correlates with M_c. Mesh size for $GelMA_5$, $GelMA_{1.25}$ and PEGDA hydrogels at 12.5% (w/v) were estimated to be 5.9±0.1 nm, 7.3±0.4 nm and 9.2±0.1 nm, respectively, while for hydrogels at 7.5% (w/v) were 7.4±0.4 nm, 15.1±1.7 nm and 18±3.8 nm, respectively (Figure 4.5 (b)). PEGDA mesh size values were comparable with the ones previously reported in our laboratory, which for 10% and 5% (w/v) were 11.8 nm and 8.2 nm, respectively[157]. The mesh size of GelMA hydrogels was higher than that of PEGDA hydrogels, as predicted by M_c values. Comparing the polymer content of the same material, the mesh size of hydrogels containing 12.5% (w/v) polymer was significantly lower than hydrogels containing 7.5%

(w/v). Finally, we observe that mesh size of GelMA hydrogels increased as the DoF decreased, this being especially relevant for hydrogels composed of 12.5% (w/v). Sarveswaran *et al.* [184] calculated that the mesh size of 5 – 20% (w/v) GelMA hydrogels was around 21.2 nm, which is in agreement with our results. This demonstrates that varying the degree of functionalization and/or the total polymer concentration, the hydrogel mesh size can be easily tuned. Frequently, mesh size of GelMA and PEGDA hydrogels have been estimated through SEM images. However, SEM images can lead to misleading information, due to chain collapse during dehydration and freeze-drying process[276], which causes an overestimation of the pore size values. Overall, these results demonstrate that the differences found in the hydrogel networks depend on their polymer concentration, and the DoF of GelMA polymer. These parameters can be easily tuned to match the network properties needed for the final setup. As different applications, such as tissue engineering, or drug and/or protein delivery[125], have their own requirements, it is relevant to finely adjust these parameters.

It is reported that cells encapsulated in GelMA hydrogels with a DoF between 50% to 70% were able to spread and form cell-cell contacts, although these were less pronounced in hydrogels with 70% functionalization[269]. Moreover, the viability of cells embedded in these hydrogels was high[189,269]. Our purpose is to have hydrogels that support cell encapsulation, cell spreading and cell proliferation. In parallel, these hydrogels should allow remodelling of the cellular matrix without compromising its mechanical properties and displaying long-term stability. To fulfil all the above-mentioned requirements, $GelMA_5$ polymer was chosen for further characterization studies.

4.4. Fabrication and characterization of GelMA – PEGDA hydrogel co-networks

Once the GelMA and PEGDA hydrogel networks were characterized, and $GelMA_5$ polymer was selected to perform further experiments, the next step was to fabricated and characterized GelMA – PEGDA hydrogel co-networks. To that end, $GelMA_5$ – PEGDA, $GelMA_5$ and PEGDA polymer powders were dissolved in DMEM without phenol red supplemented with 1% (v/v) Penicillin/Streptomycin or in PBS, and their polymerization was tested employing the same setup mentioned above. GelMA – PEGDA and GelMA polymer solutions were polymerized under a UV exposure doses ranging from 1 $J \cdot cm^{-2}$

to 3.76 J·cm^{-2}. However, when applying UV energy doses lower than 3 J·cm^{-2}, PEGDA polymer solutions did not crosslink at the macromer concentrations tested. Overall, for all the GelMA – PEGDA solutions tested, UV energy doses of less than 1 J·cm^{-2} led to poorly crosslinked networks or non-crosslinking at all. After successful hydrogel formation, the physicochemical and the mechanical properties of the co-networks, such as homogeneity, mass swelling ratio, mesh size, degradation rate and molecular diffusion were studied and are reported in the following sections.

4.4.1. Analysis of co-network homogeneity

GelMA polymer has been shown to precipitate in GelMA – PEGDA co-networks when using high concentrations of PEG polymers of high molecular weight[278]. To study the co-network homogeneity of GelMA – PEGDA hydrogels, GelMA chains were fluorescently labelled with NHS-Rhodamine after hydrogel fabrication. To do that, 7.5% (w/v) GelMA$_5$ – 5% (w/v) PEGDA disc-shaped hydrogels 10 mm in diameter and 1 mm in height were fabricated onto silanized glass coverslips by applying a UV energy dose of 3.00 J·cm^{-2} to the polymer solution dissolved in PBS. Additionally, 7.5% (w/v) GelMA$_5$ and 5% (w/v) PEGDA disc-shaped hydrogels were fabricated and labelled with NHS-Rhodamine as positive and negative controls, respectively. NHS-Rhodamine concentrations from 0.02 to 20 mM were tested to find the best staining parameters (Figure 4.6 (a)). We could visually observe by eye that even after extensive washings, the hydrogels dyed with the two highest NHS-Rhodamine concentrations were stained in red. Meanwhile, hydrogels stained with the lowest NHS-Rhodamine concentration remained visually transparent (Figure 4.6 (b)). The distribution of labelled GelMA$_5$ chains within the hydrogel networks was visualized through confocal microscopy. It was found that Rhodamine was homogenously distributed throughout all the volume in GelMA hydrogel networks and GelMA – PEGDA hydrogel co-networks. On the other hand, PEGDA hydrogels were not labelled with NHS-Rhodamine as expected for polymers that do not contain any primary amine groups. Concerning GelMA – PEGDA hydrogels, precipitation of GelMA polymer did not occur when it was mixed and polymerized with PEGDA. This suggests that at the microscopic level no phase-segregation occurred, and the polymerization process results in homogenous co-networks at least at that scale (Figure 4.6 (c)). The fluorescence intensity of the images was quantitatively evaluated by ImageJ software. The fluorescence intensity of PEGDA hydrogels was the lowest with a value of 12.3 while for GelMA$_5$ hydrogels it was the highest with a value of 106.6.

PEGDA hydrogels exhibited a basal fluorescence intensity due to the entrapment of Rhodamine dye inside the hydrogel network and the non-specific interactions between PEGDA chains and Rhodamine molecule. On the other hand, in $GelMA_5$ – PEGDA hydrogels fluorescence intensity was about 20% lower in comparison to $GelMA_5$ hydrogels, presumably due to the PEGDA content in the structure.

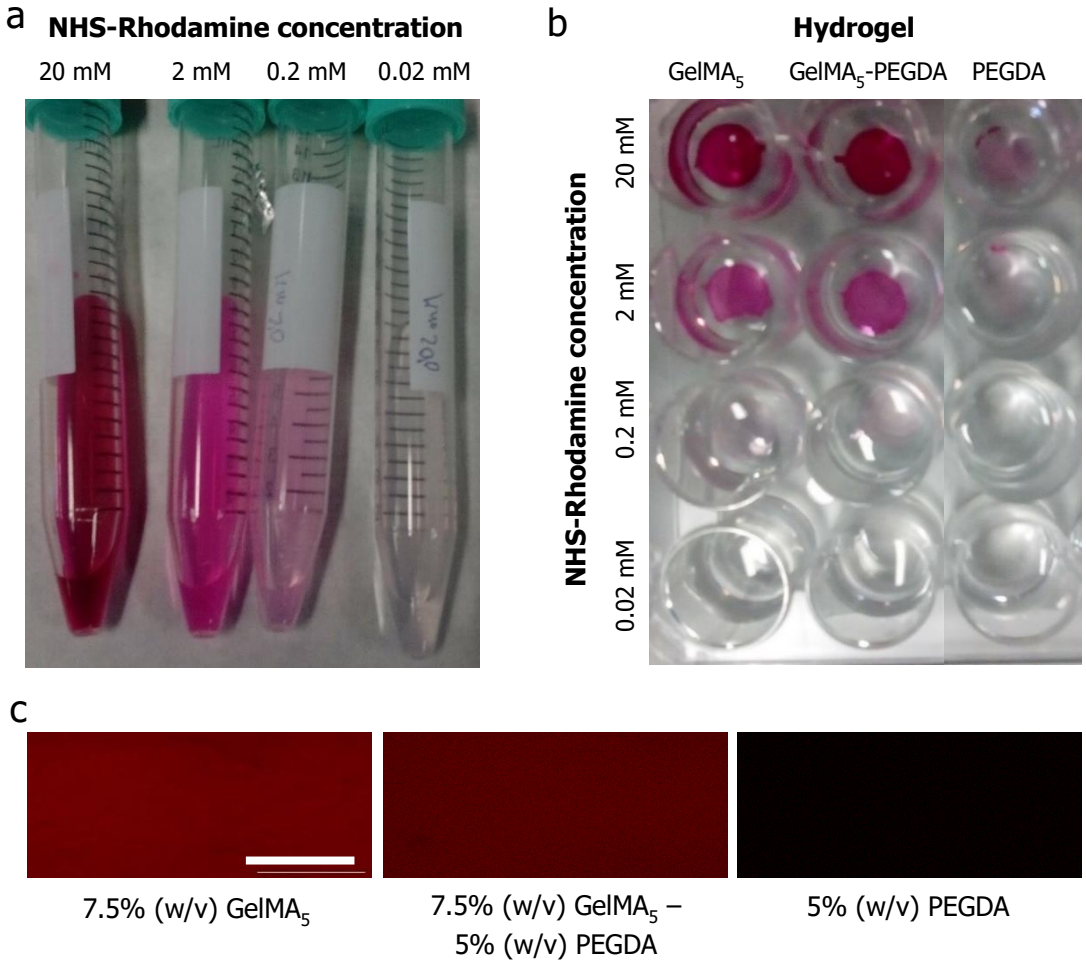

Figure 4.6. NHS-Rhodamine staining for co-network homogeneity analysis. (a) Photo of NHS-Rhodamine solutions at concentrations from 20 to 0.02 mM. (b) Photos of $GelMA_5$, $GelMA_5$ – PEGDA and PEGDA hydrogels stained with NHS-Rhodamine. After exhaustive washings Rhodamine dye at higher concentrations was still entrapped in the network, giving a red colour visible by eye. (c) Confocal images of polymer networks and co-networks containing 7.5% (w/v) $GelMA_5$ (left), 7.5% (w/v) $GelMA_5$ – 5% (w/v) PEGDA (middle) and 5% (w/v) PEGDA (right), showed homogeneous staining for GelMA chains. Scale bars = 50 µm.

4.4.2. Characterization of the swelling properties of GelMA hydrogel networks and GelMA – PEGDA hydrogel co-networks

Here, in order to make the fabrication process cell friendly for encapsulation, we changed the PBS used to dissolve the polymer by cell culture medium (DMEM without

phenol red, supplemented with 1% Penicillin/Streptomycin). The solution chosen did not contain phenol red or other supplements, such as FBS to minimize the UV absorption or diffraction due to these components. Two more changes made to polymerize the hydrogel were (I) the reduction of UV energy dose from 3 J·cm^{-2} to 1.88 J·cm^{-2}, and (II) the placement of a PET membrane on top of the glass coverslip to simulate the light absorption obtained when hydrogels are fabricated directly on the membranes. To study the swelling properties, disc-shaped hydrogels of 10 mm in diameter and 1 mm in height were produced from GelMA$_5$ polymer solutions with final concentrations of 12.5% and 7.5% (w/v); and GelMA$_5$ – PEGDA polymer solutions with concentrations of 7.5% (w/v) – 5% (w/v) and 3.75% (w/v) – 3.75% (w/v), having a total macromer concentrations of 12.5% and 7.5% (w/v) respectively. As mentioned above, PEGDA hydrogels did not crosslinked under these conditions.

Figure 4.7 shows that hydrogels of higher macromer percentages (12.5% (w/v)) significantly decreased their swelling ratios regarding polymer composition. Higher macromer contents provide more crosslinking groups, which leads to denser networks.

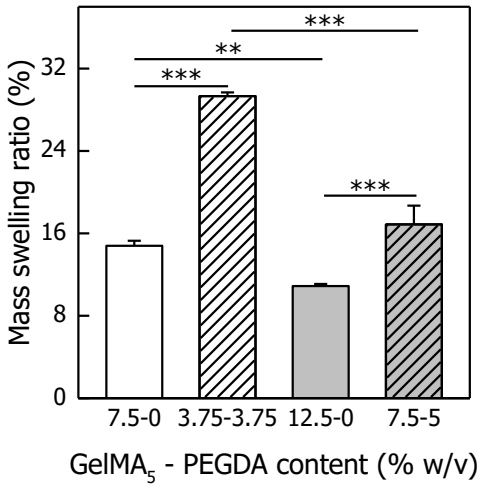

Figure 4.7. Mass swelling ratio for GelMA$_5$ networks and GelMA$_5$ – PEGDA co-networks: 7.5 – 0 (7.5% w/v GelMA$_5$), 3.75 – 3.75 (3.75% w/v GelMA$_5$ – 3.75% w/v PEGDA), 12.5 – 0 (12.5% w/v GelMA$_5$), 7.5 – 5 (7.5% w/v GelMA$_5$ – 5% w/v PEGDA), fabricated applying an energy dose of 1.88 J·cm^{-2}**.** Values are shown as the mean ± SD (n=3). **p<0.01 and ***p<0.001.

On the other hand, the influence of PEGDA incorporation into GelMA$_5$ was studied. Keeping the final concentration of the total polymer constant, the swelling ratio of GelMA$_5$ hydrogels was significantly lower than that of GelMA$_5$ – PEGDA hydrogels. When PEGDA was added to 7.5% (w/v) GelMA$_5$ samples, the swelling ratio increased by 100%, however, when PEGDA was added to the 12.5% (w/v) GelMA$_5$ samples, it

increased only 54% (Figure 4.7). GelMA molecules have more crosslinking points spread all over the chain compared to PEGDA molecules, which only have two at the end of the chain. As a consequence, increasing the GelMA content resulted in a more packed network. Furthermore, GelMA chains are more hydrophobic than PEGDA molecules, thus their interaction with water molecules is lower. All of these results are in agreement with previous findings[277].

4.4.3. Analysis of diffusion properties in GelMA hydrogel networks and GelMA – PEGDA hydrogel co-networks

Diffusion is a passive or net movement of matter from higher concentration regions to lower concentration regions, known as concentration gradient[238]. To supply the lack of intravascular systems and enhance cell viability, cell function and differentiation of encapsulated cells, mass transport of nutrients and oxygen has to reach effectively into hydrogel core[276,279]. Although diffusion in hydrogels is a relevant parameter to be analysed in scaffolds for tissue regeneration[24], sometimes it is not properly considered. Diffusion is directly correlated with the mesh size of the network, as this should to be at least equal or larger than the diameter of the diffusive species[280]. Both the pore size of the hydrogel networks and co-networks and the diffusion coefficient of relevant biomolecules have been calculated mainly through theoretical models such as Peppas and Merrill (mesh size)[183] or Peppas and Reinharts (diffusion values)[280]. However, these theoretical models are not well-suited to determine quantitatively the mesh size or diffusion properties of hydrogels composed by two or more polymers[237], such as our GelMA – PEGDA hydrogels. To fill the lack of theoretical models, we experimentally studied diffusion in our samples. For that, we analysed the diffusion profiles of dextran fluorescent molecules of different molecular weights as they passed through $GelMA_5$ (12.5% (w/v) and 7.5% (w/v)) and $GelMA_5$ – PEGDA (7.5% (w/v) – 5% (w/v) and 3.75% (w/v) – 3.75% (w/v)) hydrogels. Disc-shaped hydrogels were fabricated on top of porous PET membranes (5 µm pore size) using an UV dose of 1.88 $J \cdot cm^{-2}$ and were mounted on 24 well Transwell® inserts. To examine the diffusion profiles, we used three dextrans fluorescently labelled of different sizes: (I) FD4 (4 kDa), (II) FD70 (70 kDa), and (III) FD500 (500 kDa). We chose these dextrans because their hydrodynamic diameters (2.8 nm, 11.6 nm and 32 nm for FD4, FD70 and FD500, respectively) covered the range of diameters for most of the biomolecules (more details in section 3.4.4). Then, the permeability, which was measured as the mass diffused from

the apical to the basolateral chambers of the Transwell® devices was analysed for the three dextrans. Our results showed that the smallest dextran (FD4) could easily pass from the apical to the basolateral chamber through the hydrogel network and co-networks. There was a gradual increase in the total mass as a function of time, until reaching 0.5 µg at 90 min after the dextran loading into the apical part. The diffusion of the medium (FD70) and the large dextran (FD500) was more restricted. After 90 min the diffused mass of FD70 and FD500 was 5x lower than FD4 dextran, meaning that diffusion was hindered by the hydrogel (Figure 4.8 (a)). From these results we could presumably deduce that the average mesh size of the hydrogel is much smaller than the FD70 hydrodynamic diameter.

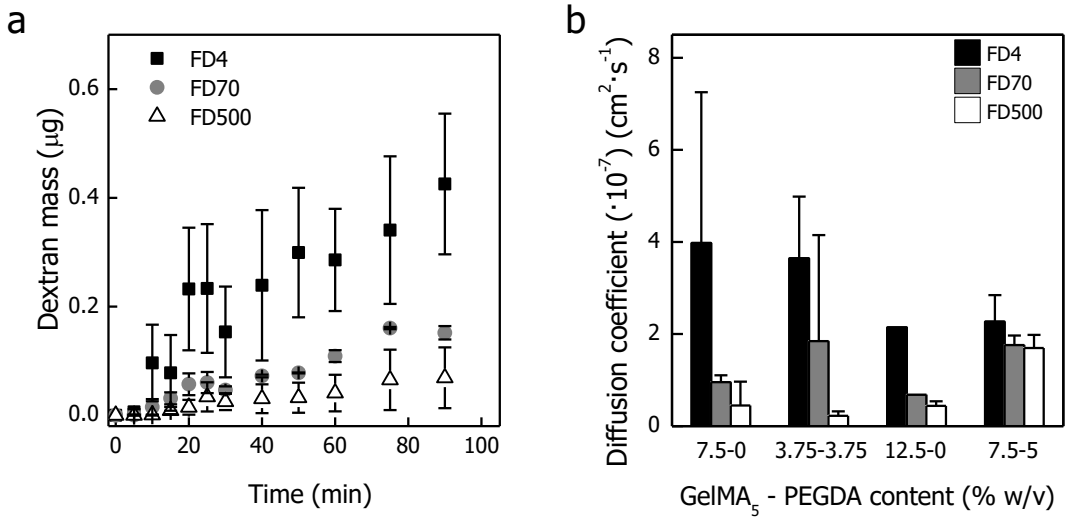

Figure 4.8. Diffusion studies of three different dextran molecules: FD4 (4 kDa), hydrodynamic diameter of 2.8 nm (black colour); FD70 (70 kDa), hydrodynamic diameter of 11.6 nm (grey colour), and FD500 (500 kDa), with a hydrodynamic diameter of 32 nm (white colour). (a) Permeability of different dextran molecules through $GelMA_5$ 7.5% (w/v) hydrogels. (b) Diffusion coefficient values of the three different dextrans for $GelMA_5$ networks and $GelMA_5$ – PEGDA co-networks: 7.5– 0 (7.5% w/v $GelMA_5$), 3.75 – 3.75 (3.75% w/v $GelMA_5$ – 3.75% w/v PEGDA), 12.5 – 0 (12.5% w/v $GelMA_5$), 7.5 – 5 (7.5% w/v $GelMA_5$ – 5% w/v PEGDA), fabricated applying an energy dose of 1.88 $J \cdot cm^{-2}$**.** Plotted values represent the mean ± SD (with almost n = 2).

Finally, diffusion coefficients for FD4, FD70 and FD500 were evaluated for all the different hydrogel compositions (Figure 4.8 (b)). The molecular weight of the dextrans influenced the diffusivity, smaller dextrans showed higher diffusion than bigger dextrans. When hydrogels were loaded with FD4, the diffusion coefficient decreased with increasing polymer concentration. Nevertheless, the diffusion coefficients of FD70 and FD500 dextrans were not significantly altered with increasing macromer content. The reason might be that even for the hydrogels with the lowest polymer concentrations, the

networks were dense enough to hinder the passage of large molecules. Actually, we had determined that mesh size for $GelMA_5$ hydrogels decreased from ≈15 nm to ≈7 nm when the macromer content was increased from 7.5% to 12.5% (w/v) $GelMA_5$ (see section 3.4.2). These mesh size values should not affect the permeability of the FD4 and FD70 molecules, which have hydrodynamic diameters of 2.8 nm and 11.6 nm, respectively. Meanwhile, for the FD500 molecule, whose hydrodynamic diameter is 32 nm, the permeability should be null. As it can be appreciated in (Figure 4.8 (b)), the diffusion coefficients of FD70 through the hydrogels were ≈0.5x 10^{-7} – 2x 10^{-7} $cm^2 \cdot s^{-1}$, which were quite similar to the FD500 values. The reasons for the low permeability of the FD70 might be the inhomogeneity of the mesh size through the hydrogel and the interactions of FD70 with the polymer chains. These results agreed with the ones published in literature. Kaemmerer *et al.* [281] reported that the diffusion coefficient of FD70 through similar GelMA hydrogels[281] to be ≈2.3x 10^{-7} $cm^2 \cdot s^{-1}$. Despite other method was used to calculate the diffusion, the correlation of the results validates the effectiveness of our setup to study this process. Keeping the macromer content constant and comparing PEGDA – containing hydrogels to $GelMA_5$ hydrogels, for the 3.75% (w/v) $GelMA_5$ – 3.75% (w/v) PEGDA no significant differences in diffusivity properties for the three dextrans were noticed. The reason might be that the addition of PEGDA did not significantly modify the mesh size of the hydrogel co-networks. However, for the 7.5% (w/v) $GelMA_5$ – 5% (w/v) PEGDA hydrogels, FD70 and FD500 diffusion coefficients were reduced. These results support that there is a correlation between GelMA and PEGDA proportions, which affect hydrogel mesh sizes, and the diffusion profile of the molecules tested. Similar results were reported by Wang *et al.*[160].

4.4.4. Mechanical properties of GelMA hydrogel network and GelMA – PEGDA hydrogel co-networks

The mechanical properties of $GelMA_5$ and $GelMA_5$ – PEGDA hydrogels were evaluated by a compression uniaxial mechanical test after swelling. Disc-shaped hydrogels (10 mm in diameter and 3 mm in thick) of 12.5% (w/v) and 7.5% (w/v) $GelMA_5$ and 3.75% (w/v) – 3.75% (w/v) and 7.5% (w/v) – 5% (w/v) $GelMA_5$ – PEGDA, were dissolved in DMEM without phenol red, supplemented with 1% Penicillin/Streptomycin, and were polymerized using a UV dose of 3.76 $J \cdot cm^{-2}$. The effects on the hydrogel mechanical properties as a function of the total polymer concentration and the addition of PEGDA polymer to the $GelMA_5$ hydrogels were studied.

For the conditions employed to perform the assay, the stress-strain curves recorded did not show any sample failure, even at the maximum strain level applied of 50% (Figure 4.9 (a)). All tested hydrogels presented a linear behaviour demonstrating that they behaved as elastomers. Young's moduli, or better said, apparent elastic moduli (E) were determined from the slope of the linear part of the stress-strain curves, which ranged from 10% to 20% of the total strain for all the hydrogels tested.

Elastic moduli was found to significantly increase when increasing the total polymer content of the hydrogels, for both $GelMA_5$ and $GelMA_5$ – PEGDA samples (Figure 4.9 (b)). This increment was attributable to the formation of denser and more compact hydrogel networks, resulting in harder, less deformable hydrogels. For example, for 7.5% (w/v) $GelMA_5$ hydrogels, E value was 13.2±0.2 kPa, and raised up to 49.70±3.98 kPa for 12.5% (w/v) $GelMA_5$ hydrogels, with almost a 4-fold increase. Similar modulus values were reported in the literature. Nichol *et al.*[201] reported values of 35 kPa and 20 kPa for 15% (w/v) and 10% (w/v) GelMA hydrogels, respectively. In another work, Mamaghani *et al.*[282] measured apparent elastic moduli of 8.2±2.1 kPa for 5% (w/v) GelMA hydrogels, and 65.5±4.7 kPa for 15% (w/v) GelMA hydrogels.

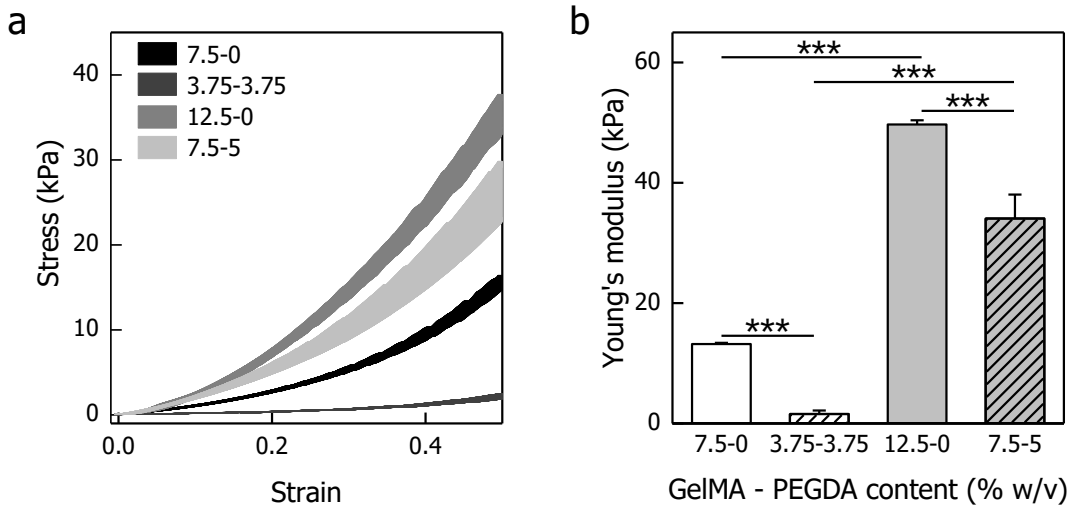

Figure 4.9. Analysis of the mechanical properties by compression test for $GelMA_5$ and $GelMA_5$ – PEGDA hydrogels fabricated by applying an energy dose of 3.76 $J \cdot cm^{-2}$. (a) Stress-strain curves of 7.5% – 0% (w/v) $GelMA_5$ (dark), 3.75% (w/v) $GelMA_5$ – 3.75% (w/v) PEGDA (dark grey), 12.5% – 0% (w/v) $GelMA_5$ (grey) and 7.5% (w/v) $GelMA_5$ – 5% (w/v) PEGDA (light grey). (b) Young's moduli of the mentioned $GelMA_5$ and $GelMA_5$ – PEGDA hydrogels measured after swelling. Values are shown as the mean ± SD (n=3). ***p<0.001.

Regarding hydrogel composition, keeping the total macromer content constant, the addition of PEGDA led to a significantly decrease in the elastic modulus. Particularly,

apparent elastic modulus was found to decrease drastically (≈85% decrease) for hydrogels with low macromer content (7.5% (w/v)) when PEGDA was added. Unlike, for hydrogels with higher macromer content (12.5% (w/v)), Young's modulus did not drop that much (≈15% decrease). This fact might be attributed to the ratio between $GelMA_5$ – PEGDA macromers. For the hydrogels with higher total polymer concentration, this ratio was 1:0.7, while for lower total polymer concentrations, this ratio was 1:1. Adding PEGDA to GelMA hydrogels resulted in a less packed network with increased water storage capacity, and consequently, elastic modulus values decreased. Therefore, by co-polymerizing $GelMA_5$ polymer with PEGDA polymer, the mechanical properties of the resulting hydrogels could be tailored to fulfil our requirements. The apparent elastic moduli for our hydrogels ranged from 2 to 50 kPa were comparable to those reported for soft tissues *in vivo* values, ranging from 1 to 100 kPa[283].

4.4.5. Degradation rate of GelMA hydrogel networks and GelMA – PEGDA hydrogel co-networks

GelMA polymer is obtained after functionalization of gelatin polymer, which is a natural polymer derived from denatured collagen[231,284]. GelMA, like its precursor, exhibits enzymatic-sensitive degradation sites[231,284]. These sequences are recognized by enzymes regulators of the matrix remodelling, known as matrix metalloproteinases (MMPs). These enzymes are responsible for degrading extracellular matrix proteins, such as collagen, laminin, fibronectin, among others. Mainly, collagen is degraded to gelatin molecules and then into peptides. The main responsible for gelatin degradation are MMP-2 and MMP-9, which are secreted by cells[285]. In previous works, Pedron *et al.*[284] found that cells were able to express high levels of MMP-2 and MMP-9 when they were encapsulated in $GelMA_5$ hydrogel network and $GelMA_5$ – PEGDA hydrogel co-networks. For tissue engineering, biodegradability of hydrogels is a relevant feature to consider. A good control of degradability properties would ideally lead to a gradual replacement of the artificial scaffold, which acts as a temporary ECM, by cell-secreted ECM[286]. *In vitro*, degradability properties are important to create hydrogels suitable for long-term cell. Previously, Benton *et al.*[271] and Hutson *et al.*[240] studied the enzymatic degradation of $GelMA_5$ and $GelMA_5$ – PEGDA hydrogels using 2.5 $U \cdot mL^{-1}$ collagenase type II. Hence, we compared the biodegradability of $GelMA_5$ and $GelMA_5$ – PEGDA hydrogels following their experimental approach. Briefly, the hydrogel samples were incubated with collagenase at 2.5 $U \cdot mL^{-1}$ at 37ºC and the changes in hydrogel weight were monitored over the time.

After that, the remaining polymer masses were calculated by applying Eq. 3.19 (see section 3.4.6). Figure 4.10 shows the percentage of mass remaining over time when the different samples were incubated with collagenase. $GelMA_5$ hydrogels containing 12.5% and 7.5% (w/v) of macromer content were completely degraded after incubation with collagenase for 24 h and 4 h, respectively. When $GelMA_5$ polymer was mixed with PEGDA to form $GelMA_5$ – PEGDA hydrogel co-networks, hydrogel degradation rates were delayed. The cause of this was that PEGDA chains did not contain enzyme-biodegradable sequences. Our results prove that samples containing 7.5% (w/v) – 5% (w/v) of $GelMA_5$ – PEGDA were only degraded by 30% after 96 h of collagenase incubation, and thus the mechanical integrity of the samples was preserved after this assay. Meanwhile, the $GelMA_5$ hydrogels containing the same amount of macromers (7.5% (w/v)) were totally degraded after 24 h of collagenase incubation. Our data were comparable with the values published in a previous study where GelMA hydrogels containing 5% (w/v) and 10% (w/v) of macromers were fully degraded after 12 h and 24 h, respectively, whereas GelMA – PEGDA hydrogels containing 10% (w/v) – 5% (w/v) of macromers still had 60% of the initial mass after 48 h of collagenase incubation[240].

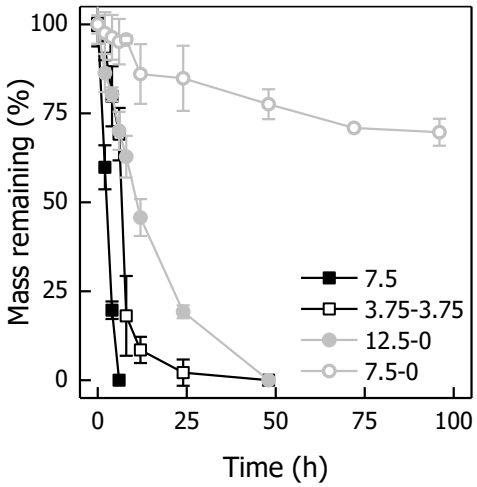

Figure 4.10. Degradation rate studies for $GelMA_5$ and $GelMA_5$ – PEGDA hydrogels. Percentage of mass remaining after incubation of the different hydrogels with collagenase II. The tested hydrogels were 7.5% – 0% (w/v) $GelMA_5$ (black, filled square), 3.75% (w/v) $GelMA_5$ – 3.75% (w/v) PEGDA (black, hollow square), 12.5% – 0% (w/v) $GelMA_5$ (grey, filled circle) and 7.5% (w/v) $GelMA_5$ – 5% (w/v) PEGDA (grey, hollow circle) and were fabricated using a UV energy dose of 3.00 $J \cdot cm^{-2}$. Data are represented as the mean ± SD (n=3).

PEGDA molecule is a synthetic and non-biodegradable polymer as it does not present enzymatic degradation sites. On one hand, in $GelMA_5$ – PEGDA hydrogel co-networks, collagenase cannot cleave PEGDA. Additionally, PEGDA polymers hide the

degradation motifs that are present in GelMA chains, hampering sample degradation. Any attempt to provide cells with artificial ECM environments should synchronize the degradation rate needed for matrix remodelling with the rate of production of new ECM by the laden cells[286]. We found that modulating the ratio between $GelMA_5$ and PEGDA macromers, we can tailor hydrogel degradation profiles, providing samples with long-term mechanical integrity due to PEGDA component. Whereas, cellular attachment, spreading, proliferation and secretion of ECM by cells is possible due to GelMA component.

After analysing both the physicochemical and the mechanical properties of our $GelMA_5$ and $GelMA_5$ – PEGDA hydrogels, we selected 7.5% (w/v) $GelMA_5$ – 5% (w/v)) PEGDA hydrogel co-networks to continue with their characterization and cellular studies due to their low degradability, appropriate mechanical properties and mechanical stability.

4.4.6. Gel fraction of $GelMA_5$ – PEGDA hydrogel co-networks

As pointed out during the hydrogel characterization studies, the co-network properties, such as mass transfer or mechanical properties, can be modified by changing the total macromer content and the percentages of each component. Additionally, in our system another key parameter that influences the network properties is the hydrogel crosslinking density, which could in turn be tuned by the UV exposure dose. Therefore, we did proceed to characterized the gel fraction (crosslinking degree) of 7.5% (w/v) $GelMA_5$ – 5% (w/v) PEGDA hydrogels as a function of the UV energy dose. To do that, disc-shaped hydrogels (10 mm in diameter and 1 mm in height) were polymerized applying increasing UV energy doses. Then, hydrogels were dried and weighted right after fabrication ($M_{fabrication}$) and after having reached equilibrium swelling ($M_{swollen}$). Gel fraction percentages were computed by Eq. 3.20 (details in section 3.4.7) and plotted against the energy exposure doses (Figure 4.11).

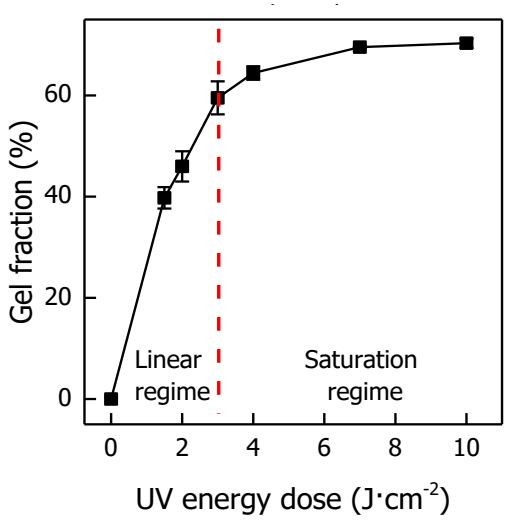

Figure 4.11. Gel fraction (crosslinking degree) for $GelMA_5$ – PEGDA hydrogels of 7.5% (w/v) $GelMA_5$ – 5% (w/v) PEGDA composition, and polymerized under a range of UV energy doses. Gel fraction has two regimes (red striped line divides both regimes), the linear (left) and the saturation regime (right). Data are represented as the mean ± SD (n=3).

As it can be seen from Figure 4.11, gel fraction curve shows two regimes, a linear region and a saturation region. In the linear region, gel fraction increases linearly from 0 to 59.5±2.6% as the UV energy dose applied went from 0 to 3 $J{\cdot}cm^{-2}$. From these results we can infer that the previous hydrogel samples containing 7.5% (w/v) $GelMA_5$ – 5% (w/v) PEGDA of polymer, which were fabricated using a UV energy dose of 1.88 $J{\cdot}cm^{-2}$, possessed a crosslinking degree of ≈42%, which fits in the linear region. Having hydrogels with low crosslinking degrees might be beneficial for cell encapsulation, as the pore size is larger, favouring mass transport. On the other hand, for UV energy doses equal or greater than 3 $J{\cdot}cm^{-2}$, the percentage of polymer crosslinking was maintained, with gel fraction percentages ranging between 64.4±1.3% and 70.3±0.9% (maximum value obtained). Despite of increasing the applied dose energy, the polymer crosslinking efficiency never reached its maximum of 100%, but results point out that there is ≈30% of unreacted polymer. We hypothesized that this might be due to PEGDA chains forming closed loops and, thus, hindering further crosslinking, or to GelMA chains forming physical crosslinks that were not stable and were leached when performing the gel fraction experiments.

Overall, our $GelMA_5$ hydrogel networks and $GelMA_5$ – PEGDA hydrogel co-networks were highly tunable matrices in which water content, pore size, mechanical properties, degradability and crosslinking density may be tailored to suit the requirements of tissue-specific microenvironments.

After hydrogel characterization, cellular experiments were carried out employing the $GelMA_5$ – PEGDA (7.5% (w/v) – 5% (w/v)) hydrogel co-networks with a crosslinking degree of ≈42%. As pointed above, this hydrogel was selected on the bases of a good compromise between degradability, mechanical integrity, and nutrients/oxygen transfer into the core hydrogel. Additionally, to compare the effects on cell behaviour when PEGDA polymer was introduced in the scaffold, we used as control $GelMA_5$ (7.5% (w/v)) hydrogels.

4.5. Cytocompatibility studies

4.5.1. Determination of photoinitiator cytotoxicity

Before analyzing the cytocompatibility of the selected hydrogels, we studied whether the photoinitiator and/or the UV light applied to polymerize the hydrogels allowed cell survival. When photoinitiators are exposed to specific light wavelengths they absorb photons and produce reactive species, such as free radicals, which are essential to initiate polymer crosslinking. At the same time, these reactive species can react with the proteins or DNA from the cells included in the polymer solution, resulting in cell damage or even cell death[247]. Currently, one of the most used photoinitiator is Irgacure D-2959. However, this photoinitiator is toxic for the cells above certain concentrations[175]. Irgacure D-2959 cytotoxicity is therefore a critical parameter that must be evaluated to ensure proper cell viability. To do this, NIH/3T3 cells were chosen as a cell line model because they are ease to culture, and they are extensively used in literature for material toxicity studies[243]. NIH/3T3 cells were incubated with Irgacure D-2959 concentrations ranging from 0 to 1% (w/v), in absence of UV light. As a positive control, cells incubated with fibroblast complete DMEM medium were employed. After photoinitiator treatment, cell viability was determined by AlamarBlue® assay. Cell viability of control samples was 100±16.7%. Fibroblasts incubated with 0.1% (w/v) Irgacure D-2959 did not present differences in cell survival in comparison with the positive control (Figure 4.12 (a)). However, increasing photoinitiator concentration higher cytotoxicity was observed. Specially, there was a dramatic decrease in cell viability when photoinitiator concentrations were above 0.5% (w/v). As no statistically significant differences were noticed between 0.3% and 0.5% (w/v), the photoinitiator concentration to polymerize our hydrogels was fixed at 0.5% (w/v). It is reported that photoinitiator concentrations

lower than 0.5% (w/v) cause hydrogels to have low crosslinking degrees, requiring more UV energy dose to achieve the desired properties[232].

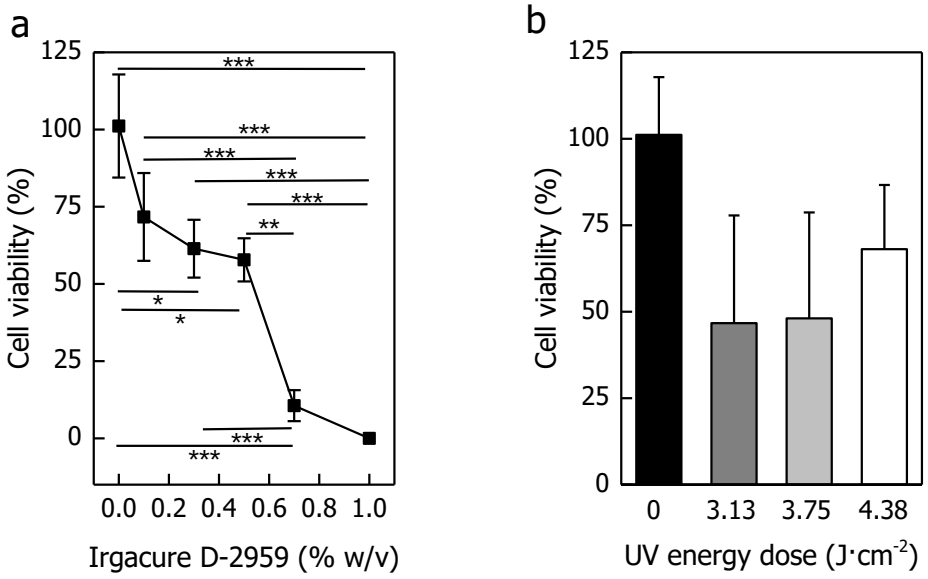

Figure 4.12. NIH/3T3 cell viability for different photoinitiator concentrations and UV energy doses. (a) Effects of Irgacure D-2959 concentration on NIH/3T3 cell viability (n=3). (b) Effects of UV energy dose when the wavelength range is from 260 to 500 nm on the NIH/3T3 viability in the absence of Irgacure D-2959. Values are shown as the mean ± SD (n=3). *p<0.05, **p<0.01 and ***p<0.001.

In addition, the effects of UV energy dose in cell viability in absence of Irgacure D-2959 were examined. To do that, NIH/3T3 cells were exposed to 3.13, 3.75, and 4.38 $J \cdot cm^{-2}$ using a UV mercury short arc lamp (OSR HBO 350 W/S), which had a spectral range from 260 to 500 nm. Cells not exposed to UV light were used as a positive control. As shown in Figure 4.12 (b), high energy doses decreased cell viability down to half of the control cells. However, we need to keep in mind that this was not the real fabrication conditions. Here, cells were exposed directly to UV light, without the polymer solutions or photoinitiator, which in a real scenario will absorb light and attenuate the UV effects. Moreover, a wide UV spectrum band was used, and it is known that wavelengths below 350 nm produce cell damage and an increase cell death[177]. Again, in the real experiments, light was filtered at 365 nm.

4.5.2. Qualitative cell viability studies of encapsulated NIH/3T3 cells in GelMA hydrogel networks and GelMA – PEGDA hydrogel co-networks

To investigate if $GelMA_5$ and $GelMA_5$ – PEGDA macromer concentrations and photoinitiator concentrations were biocompatible, non-cytotoxic, and therefore allow the survival of embedded cells, qualitative cell viability tests were carried out. To do that, NIH/3T3 fibroblast cells, at initial density of $5 \cdot 10^6$ cells·mL^{-1}, were mixed with 7.5% (w/v) $GelMA_5$ and 7.5% (w/v) $GelMA_5$ – 5% (w/v) PEGDA polymer solutions with the photoinitiator at 0.5% (w/v). Cells loaded into the polymer solutions were exposed to a UV dose of 1.50 J·cm^{-2} to form disc-shaped hydrogels (10 mm in diameter and 0.250 mm in thick) onto glass coverslips in order to simplify hydrogel manipulation. UV energy dose was reduced compared to discs photopolymerized on top of PET membranes (1.88 J·cm^{-2}), as glass does not absorb so much energy (more details in section 3.7.1). To account for the nutrient and oxygen diffusion restriction from the bottom of the hydrogel due to the glass coverslip, hydrogels height was reduced to 0.250 mm. The viability of the embedded cells was qualitatively evaluated through Live/Dead™ viability/cytotoxicity assay and samples were imaged under a confocal microscope. Figure 4.13 shows the confocal images of the fluorescent signals through the different days of cell culture for 7.5% (w/v) $GelMA_5$ samples (Figure 4.13 (a and b)) and 7.5% (w/v) $GelMA_5$ – 5% (w/v) PEGDA hydrogels (Figure 4.13 (c and d)). The upper panels show top views with the maximum intensity projections including the whole thickness of the samples. The lower panels show the 3D reconstructions of the hydrogels and provide information of cell position along their thickness. Maximum intensity projections showed that the majority of fibroblasts were alive (green staining), although some dead cells (red staining) could be visualized, mainly for days 1 and 7 (Figure 4.13 (a and c)). The first days of cell culture after encapsulation, it has been shown that short-term cell viability might decrease due to the stress induced by the photocrosslinking process (UV irradiation, presence of radical species), and to the swelling caused by the incubation with cell culture medium. This tendency was shown to be reduced for later time points of the cell culture (days 14 and 21). Through these results, we would like to emphasize that the hydrogel fabrication method allowed to get a homogenous cell distribution through the entire thickness of the hydrogel after its fabrication (days 1 and 7).

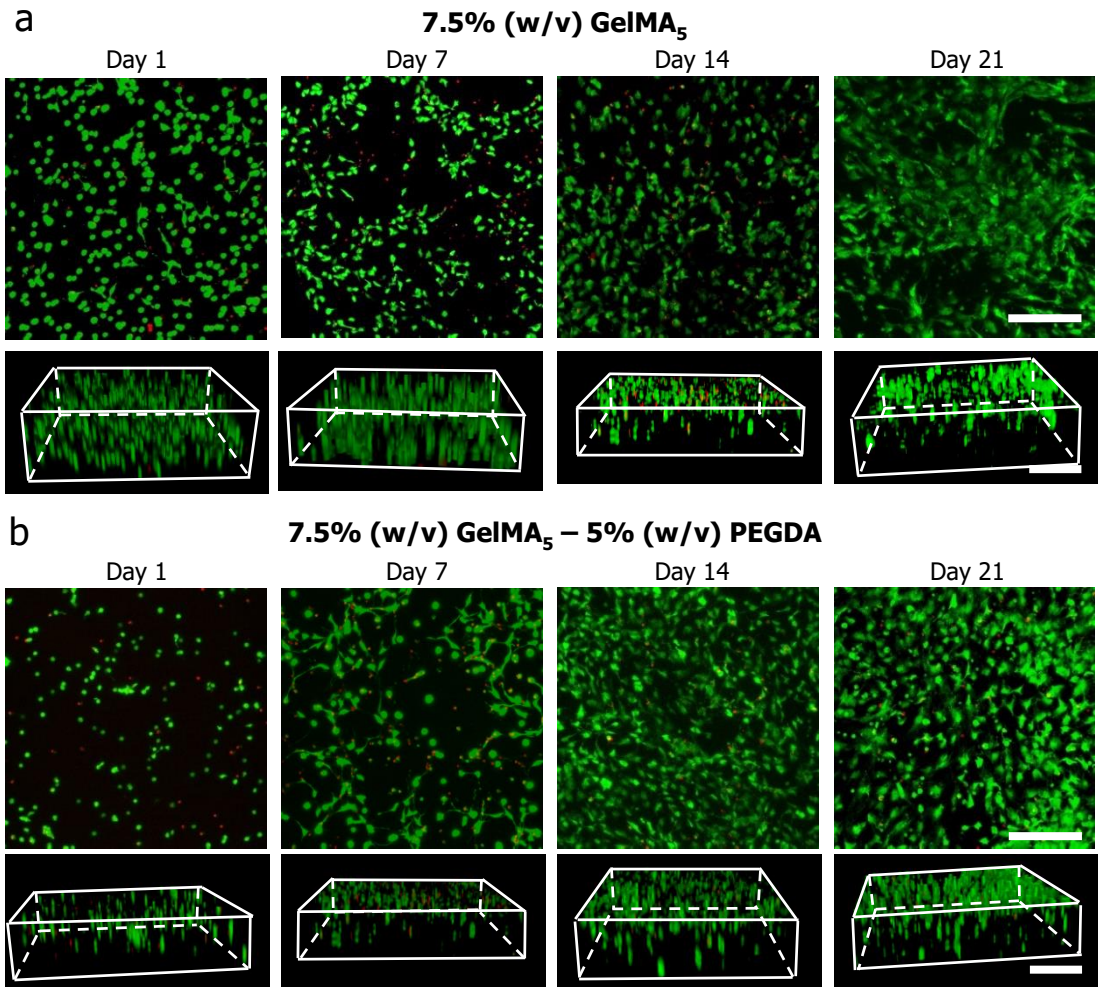

Figure 4.13. Evaluation of the cytotoxicity of $GelMA_5$ and $GelMA_5$ – PEGDA polymer solutions and the fabrication process of NIH/3T3 laden hydrogels at days 1, 7, 14 and 21. Maximum intensity projections and 3D reconstructions of (a) 7.5% (w/v) $GelMA_5$ and (b) 7.5% (w/v) $GelMA_5$ – 5% (w/v) PEGDA hydrogels showing cell viability (live cells stain in green, dead cells in red) and the spatial distribution of the NIH/3T3 embedded in the hydrogels. Scale bars: 200 μm.

However, as cell culture time was going on, the amount of fibroblasts inside the hydrogel decreased and the density at or near the hydrogel surfaces increased (Figure 4.13 (b and d)). We attributed cell diminished population inside the hydrogel to mass transport constrains limiting nutrient and oxygen permeability through diffusion and hypothesized that this could be improved by a better cell culture configuration addressing these limitations. These results agree with previous findings where 3D environments have been reported to decrease cell metabolic activity and induce growth arrest compared to 2D equivalents, leading the cells to be in a steady state when they are cultured for long time periods[112,193]. On the other hand, and according to the results found in the enzymatic degradation experiments, we visually observed that the

mechanical integrity of 7.5% (w/v) $GelMA_5$ hydrogel networks was diminished after 14 days of culture, resulting in a loss of hydrogel shape and less defined contours; whereas 7.5% (w/v) $GelMA_5$ – 5% (w/v) PEGDA hydrogel co-networks maintained their mechanical stability during the three weeks of cell culture.

Overall, this qualitative experiment demonstrated that 7.5% (w/v) $GelMA_5$ – 5% (w/v) PEGDA polymer solutions and the encapsulation process designed resulted in hydrogels that allow cell survival and sustain mechanical integrity for at least 21 days of cell culture.

4.5.3. Growth studies of epithelial colorectal adenocarcinoma cells on GelMA hydrogel networks and GelMA – PEGDA hydrogel co-networks

In parallel, the ability of the 7.5% (w/v) $GelMA_5$ and 7.5% (w/v) $GelMA_5$ – 5% (w/v) PEGDA hydrogel samples to support adhesion, growth and formation of an epithelial monolayer on their surface by the epithelial colorectal adenocarcinoma (Caco-2) cells was also qualitatively investigated. Caco-2 cell line was used in our experiments as a model of the epithelial compartment of the intestinal mucosa because it is the gold-standard to study intestinal barrier properties[79,83,245,287]. Hydrogel discs (10 mm diameter and 1 mm thickness; without cells encapsulated) were fabricated following the method explained in section 3.7.2. Caco-2 cells were seeded on top of them at a density of $7.5 \cdot 10^5$ cells·cm^{-2}. Caco-2 cells growth was monitored by taking pictures of the whole hydrogel surface for up to 2 weeks. Figure 4.14 shows that Caco-2 cells were able to attach on both hydrogel surfaces (see pictures of Figure 4.14 (a and b), at day 2 of cell culture). Therefore, we assumed that the material was also biocompatible for Caco-2 cells and that the cell adhesion motifs provided by GelMA molecules (RGD sequences) were functional, and were not altered or degraded during neither the methacrylation process nor the hydrogel photopolymerization. However, in both hydrogels Caco-2 cells were not able to form a complete monolayer covering all the substrates. Despite of that, cell surface coverage on $GelMA_5$ – PEGDA hydrogels was slightly better than on $GelMA_5$ hydrogels (Figure 4.14 (c)). This might be related to its higher stiffness, which has been reported to affect cell behaviour such as cell adhesion, cycle activity, differentiation, proliferation and migration[288,289]. For instance, Kim J and Asthagiri A[288] reported that on soft substrates, the proliferation rate of Madin-Darby canine kidney (MDCK) epithelial

cells was low. However, when hydrogel stiffness increased, cells became more proliferative.

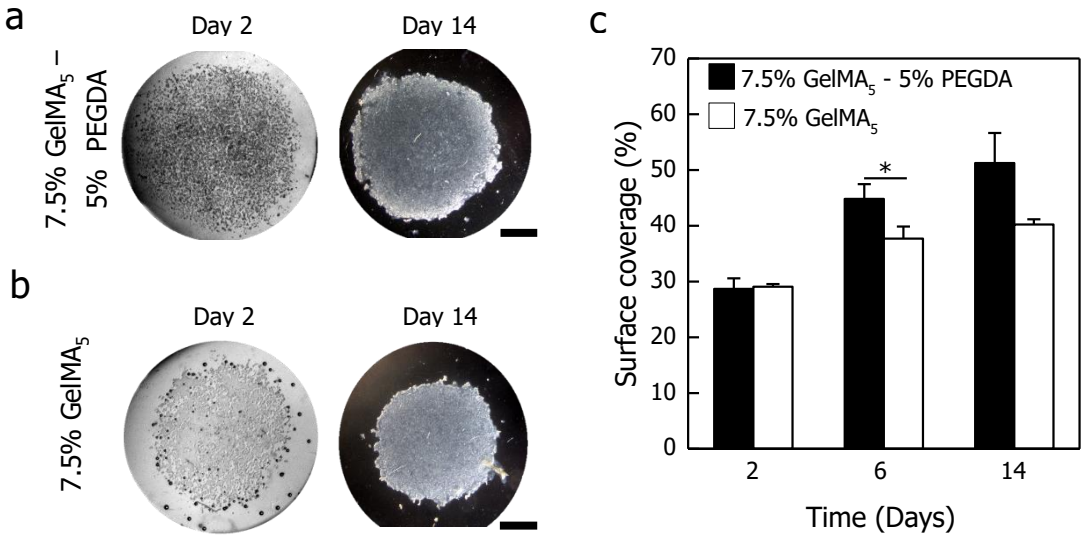

Figure 4.14. Evaluation of the surface coverage of the epithelial cell monolayer formed on top of GelMA – PEGDA and GelMA hydrogels fabricated on glass coverslips. Stereoscope images of Caco-2 cells growing on (a) 7.5% (w/v) $GelMA_5$ – 5% (w/v) PEGDA and (b) 7.5% (w/v) $GelMA_5$ hydrogels after 2 and 14 days of culture. Scale bar: 2 mm. (c) Percentage of the surface coverage as a function of cell culture time. Values are shown as the mean ± SD (n=3). *$p<0.05$.

To sum up these experiments we can conclude that the addition of PEGDA into the GelMA network hydrogel did not modify the ability for cells to recognize cell adhesion sequences provided by GelMA molecules. This has been observed because GelMA – PEGDA hydrogels (I) did not compromise the viability of fibroblasts after their encapsulation, and (II) sustained Caco-2 cell adhesion for long time periods. Therefore, we selected GelMA – PEGDA hydrogel co-networks as good candidate matrices to create modes of intestinal mucosa, and we focused the next set of cellular experiments on these hydrogels.

4.6. Genotoxicity effects of UV exposure on cell-laden GelMA – PEGDA hydrogel co-networks

DNA damage of the encapsulated cells right after UV exposure was other significant factor to be studied before going further with cell experiments. Exposure of cells to UV light does not always directly result in cell death. Nonetheless, indirectly, UV light induces DNA break generating double-strand breaks (DSBs), which trigger the

phosphorylation of histone H_2AX on Ser-139 (γ-H_2AX). This is a specific and sensitive marker of the presence of DSBs in nuclear chromatin[254,290]. Phosphorylation of histone H_2AX is essential for the recruitment of DNA repair proteins at the sites containing damaged chromatin, as well as to inhibit cell cycle progression. Consequently, phosphorilated-H_2AX can act as an anchor holding the broken DNA ends in close proximity facilitating the repairing of the broken DNA[253,254]. Without this mechanism, DNA ends can drifting apart, forming inappropriate re-joining of chromatin fragments and thus, resulting in genetic translocations and other abnormalities that can lead to aberrant cell behaviour or even cell death.[253]

In our case, the phosphorylation of histone H_2AX was used to detect the potential genotoxic effects that UV can produce to the exposed cells. Histone H_2AX phosphorylation occurs during early stages after UV exposure, whereas DSBs decrease progressively over the time because the DNA are repareid[291,292]. To check this phosphorylation, GelMA – PEGDA disc-shaped hydrogels laden with NIH/3T3 fibroblasts were fabricated by applying an energy dose of 1.88 $J \cdot cm^{-2}$. After UV exposure, cells were left for 30 min to activate the DNA repairing mechanism. Then, samples were fixed and the presence of DSBs was analysed by checking at the phosphorylation of histone H_2AX on Ser-139 (γ-H_2AX) within cell nuclei (DAPI) through immunofluorescence. Images were taken by a confocal microscope. As positive controls, fibroblast-laden hydrogels and fibroblasts seeded on glass coverslips were incubated with peroxidase (H_2O_2) to induce DNA damage. Additionally, non-treated fibroblasts seeded on glass coverslips were used as negative control. Figure 4.15 (a and c) shows the maximum intensity projections obtained after analysing a thickness of 20 μm from the hydrogel surfaces. Figure 4.15 (b and d) shows cells on top of the glass coverslips. Figure 4.15 (a) shows that encapsulated fibroblasts stained negative for γ-H_2AX. There was no colocalization of DAPI and γ-H_2AX, indicating the absence of DSBs. Similar results were found for negative controls (Figure 4.15 (b)). However, for positive controls, γ-H_2AX was positively labelled and colocalized with DAPI, meaning that phosphorylation occurred and resulted in DNA damage (Figure 4.15 (c and d)).

We should have in mind that short wavelengths corresponding to UVC (from 100 nm to 200 nm) and UVB (from 280 nm to 315 nm) spectra have more energy, and consequently, they are more susceptible to produce DSBs on the DNA. In this case, cell-laden hydrogels were fabricated using a wavelength of 365 nm corresponding to the less energetic UVA (from 315 nm to 400 nm) spectrum. In view of these results we can

hypothesize that, for this short-time period studied, the wavelength used to fabricate our cell-laden hydrogels produces few DSBs, and most of them could be repaired after UV light exposure.

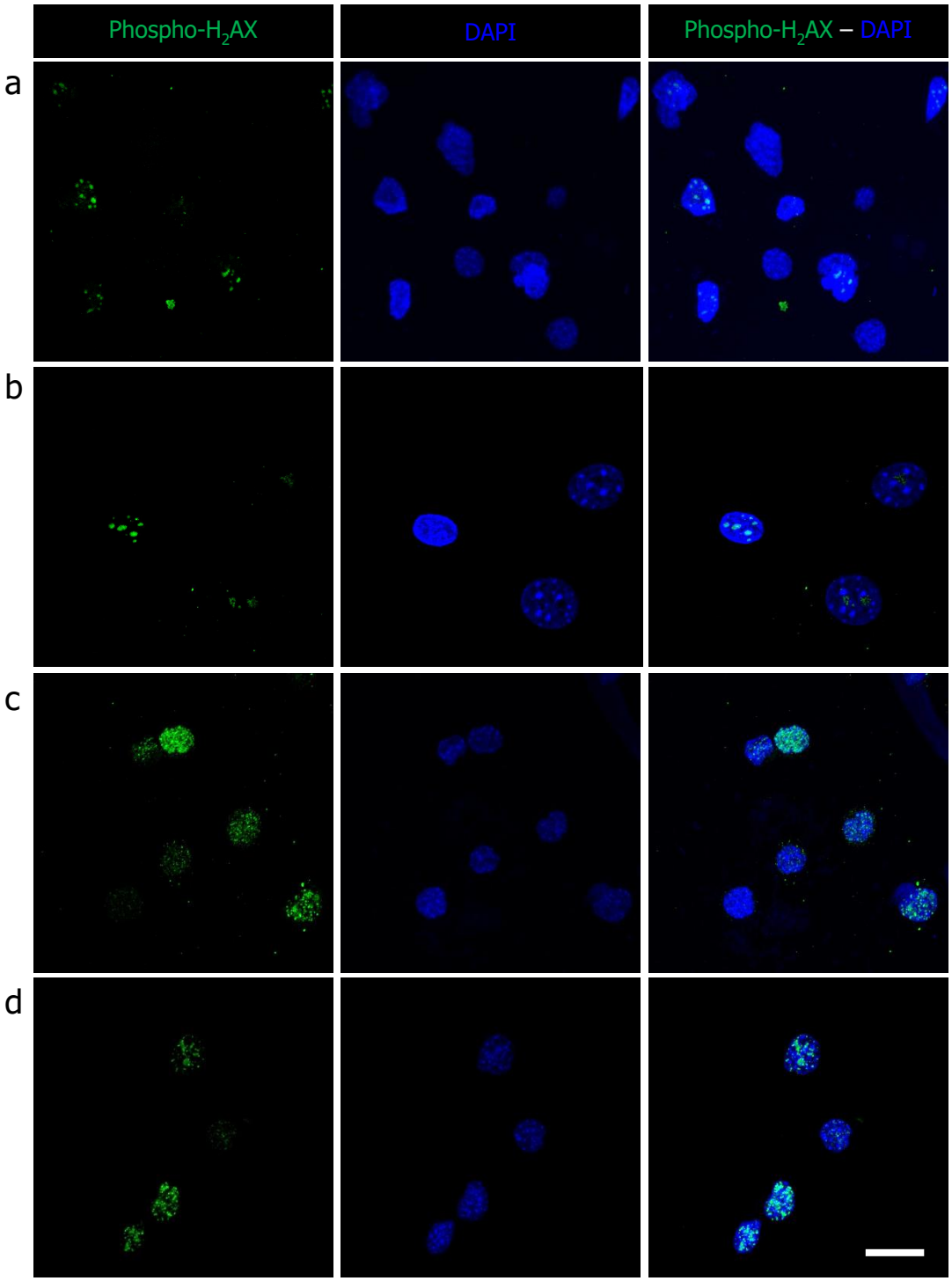

Figure 4.15. Evaluation of UV damage by immunostaining for Pospho-H_2AX and DAPI, and their colocalization. (a) Fibroblast-laden hydrogels, (b) untreated fibroblasts on top of a glass coverslip (negative control), (c) fibroblast-laden hydrogels treated with H_20_2 (positive control) and (d) fibroblasts on top of a glass coverslip treated with H_20_2 (positive control). Scale bar: 20 μm.

4.7. GelMA – PEGDA hydrogel co-networks support stromal cell encapsulation and epithelial cell attachment

The above results show that our $GelMA_5$ hydrogel networks and $GelMA_5$ – PEGDA hydrogel co-networks were highly tuneable matrices in which water content, pore size, mechanical properties, and degradability could be tailored to match the requirements of tissue-specific microenvironments. In addition, the first cellular experiments carried out to investigate the cytocompatibility of polymers, hydrogels and fabrication conditions demonstrated that both hydrogels were suitable as scaffolds for cell culture. The hydrogels that will be further used in cellular experiments were selected based on the material degradation results, apparent elastic modulus values and preliminary viability cell experiments. Long culture times (usually 3 weeks for the correct differentiation of the Caco-2 cells)[293] and elastic moduli in the range of the *ex vivo* small intestine tissue (3 – 30 kPa)[294] were considered as initial requirements for the formation of a functional intestinal epithelial barrier and the development of a relevant in *in vitro* model of intestinal mucosa. According to our results, the hydrogel co-networks formed by 7.5% $GelMA_5$ – 5% PEGDA polymers were selected for the cellular experiments.

Once decided the polymer composition, we focused on mimicking better the *in vivo* intestinal tissue conditions in our cell culture setup. Thus, apical and basolateral compartments were simulated using commercial well-plates of Transwell® inserts, which are highly used in *in vitro* epithelial monolayer studies. In these cell culture devices, cells grown as monolayers on top of hard polymer porous membranes that separate both apical and basolateral compartments. Such setup favours cell differentiation, polarization and formation of functional epithelial tissue barriers. Moreover, it is easy to study the permeability of molecules across cell monolayers, and to monitor TEER periodically without compromising cell monolayer integrity[295].

4.7.1. Fibroblast-laden GelMA – PEGDA hydrogel co-networks to mimic the stromal compartment of the intestinal mucosa

To properly fit the hydrogels into the commercial Transwell® inserts, their diameter was reduced to 6.5 mm. The hydrogel thickness selected was 0.5 mm, considering that cell viability was limited by oxygen diffusion and computing the maximum hydrogel thickness for NIH/3T3 cell survival (3 mm considering $2 \cdot 10^7$ cells·mL^{-1})[296]. NIH/3T3 fibroblasts, at initial cell loading of $5 \cdot 10^6$ cells·mL^{-1}, were mixed

with the 7.5% (w/v) $GelMA_5$ – 5% (w/v) PEGDA polymer solution together with the photoinitiator and exposed to a UV dose of 1.88 $J \cdot cm^{-2}$. Disc-shaped hydrogels were fabricated on porous membranes and mounted on Transwell® inserts (see section 3.8.2). Viability of the encapsulated cells was evaluated through Live/Dead™ viability/cytotoxicity assays and confocal microscopy over the cell culture time. One day after encapsulation, cells were evenly distributed throughout the hydrogel and, although there were some non-viable cells (stained in red), most of them were alive (stained in green) (Figure 4.16 (a and b)).

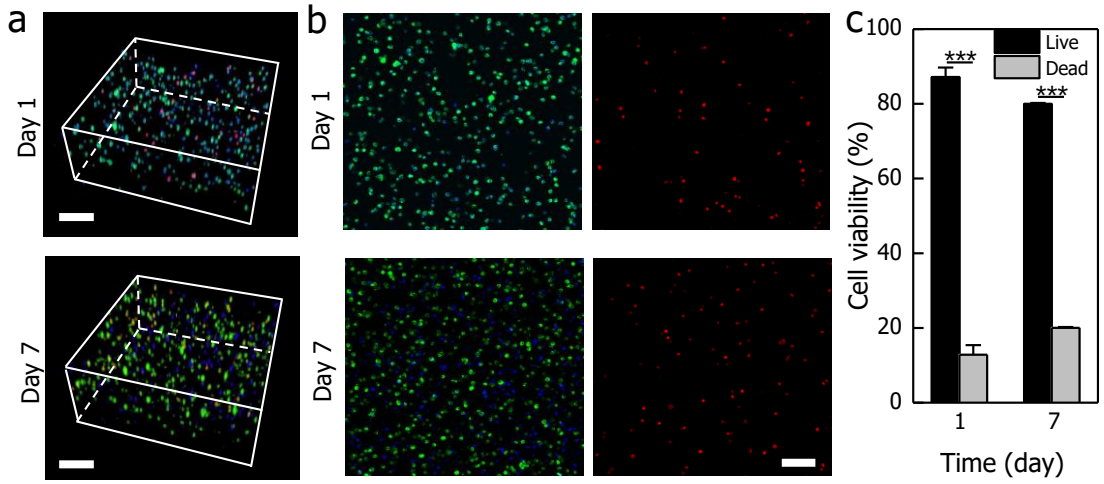

Figure 4.16. Analysis of fibroblast viability into $GelMA_5$ – PEGDA hydrogels co-networks mounted into Transwell® inserts (a) Confocal 3D reconstructions of the hydrogel co-networks showing the spatial distribution of the NIH/3T3 embedded cells at days 1 and 7 (live cells stain in green, dead cells in red). Hoechst Reagent was used to stain the nuclei. Scale bars: 200 μm. (b) Maximum intensity projections of samples shown in panel (a). Scale bar: 100 μm. (c) Quantification of cell viability at days 1 and 7 after encapsulation based on Live/Dead™ viability/cytotoxicity staining. Values are the mean ± SD (n=3). ***p<0.001.

Overall, cell viability, computed as the ratio between alive and dead cells, was more than 85% right after encapsulation (Figure 4.16 (c)). At 7 days of culture, the cells were homogeneously dispersed along the thickness of the hydrogels (Figure 4.16 (a), lower panels) and cell viability was maintained, as non-statistically significant values were measured (Figure 4.16 (c)). On the contrary, after 14 and 21 days of culture, cells were preferentially found at or near the hydrogel surfaces.

To better analyse the behaviour of cells when embedded in the hydrogels, cell morphology and functionality were studied by immunofluorescence. For that purpose, at day 7 some samples were fixed and stained for different cell markers. Figure 4.17 shows the confocal images of DAPI (cell nuclei marker), F-actin (cytoskeleton cellular marker),

Ki-67 (cell proliferation marker) and collagen IV (secreted ECM protein, related to cell functionality). Upper panels show maximum intensity projections of the whole hydrogel thickness. Whereas, the lower panels show 3D reconstructions of the hydrogel, providing information of cell distribution, morphology and functionality as a function of the hydrogel thickness.

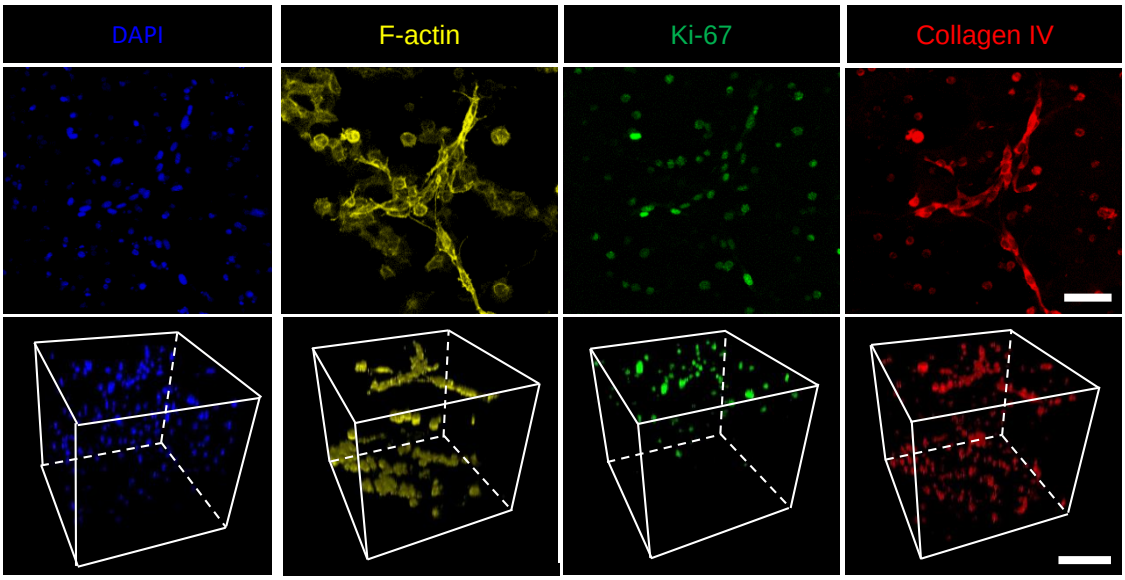

Figure 4.17. Analysis of fibroblast morphology into $GelMA_5$ – PEGDA hydrogels co-networks mounted into Transwell® inserts to mimic the stromal compartment of the intestinal mucosa. Immunostaining for DAPI, F-actin, Ki-67 and Collagen IV after 7 days in culture shown as maximum intensity projections (top panels) and confocal 3D reconstructions (bottom panels). Scale bars: 50 µm (top) and 100 µm (bottom panels).

At day 7, DAPI labelling shows that cells were homogeneously distributed throughout the hydrogel, regardless of whether they were close to the hydrogel surface or in the core. F-actin marker allowed us to study the cell morphology. As it can be seen in the 3D reconstruction, the cells inside the hydrogel showed spherical shapes and, as they were closer to hydrogel surface, cells became more elongated and spread, this indicated by their spindle-like morphology. This was attributed to cell growth restrictions in the core of the hydrogels. Actually, as it can be appreciated in the Ki-67 immunostaining, the proliferative capacity of the fibroblasts that were closer to the hydrogel surface was higher than that of cells growing inside the hydrogel, which proliferated less or were in growth arrest[297]. Finally, collagen IV, which is a relevant protein presents both in the stromal compartment of the intestinal mucosa and in the basement membrane as essential component, was tested to analyse the functionality of the fibroblasts. Fibroblasts have the capacity to produce collagen IV and thus, contribute to the ECM remodelling. Collagen IV immunostainings showed that embedded fibroblasts

cultured for 7 days were functional, as they had the ability to actively synthetize collagen IV regardless of their position within the hydrogel volume. Despite the low proliferation capacity and the spherical shape of the fibroblasts within the hydrogel, they remained viable and functional, meaning that GelMA – PEGDA hydrogels can be used to encapsulate fibroblasts without altering their functions.

In general, these results showed that GelMA – PEGDA hydrogels allowed embedding of cells without affecting their functionality. However, in terms of cell viability, these data did not represent an improvement with respect to the samples cultured on the glass coverslips. Therefore, at this point we decided to study if cell viability of the embedded fibroblasts was improved by enhancing mass transport through the hydrogel using a perfusion bioreactor.

4.7.2. Perfusion bioreactor enhances mass transport through the hydrogel

We hypothesize that the low proliferation, the growth arrest and the circular morphology obtained for cells embedded on our GelMA – PEGDA hydrogels could be associated to hypoxic conditions and mass-transport issues inherent to the 3D cell culture microenvironment[279,283]. To test whether this cellular behaviour is directly linked to the mesh properties of our 7.5% (w/v) $GelMA_5$ – 5% (w/v) PEGDA hydrogel co-network, which restricts oxygen and nutrient diffusion, we conducted a pilot experiment by perfusing the cell medium through the hydrogel during the culture. The perfusion should improve limitations originated from diffusion-related mass transport constrains. To do that, fibroblast-laden hydrogels were fabricated from 7.5% (w/v) $GelMA_5$ – 5% (w/v) PEGDA polymer solutions following the same protocol as stated above for hydrogels mounted in Transwell® inserts. After photopolymerization, hydrogels were transferred into a bioreactor chamber and cultured under perfusion during 21 days. The perfused bioreactor consisted of four independent chambers mounted in parallel. This parallel system allowed us to culture under the same physicochemical conditions four hydrogels, overcoming the variability coming from the cell culture conditions[59] (Figure 4.18).

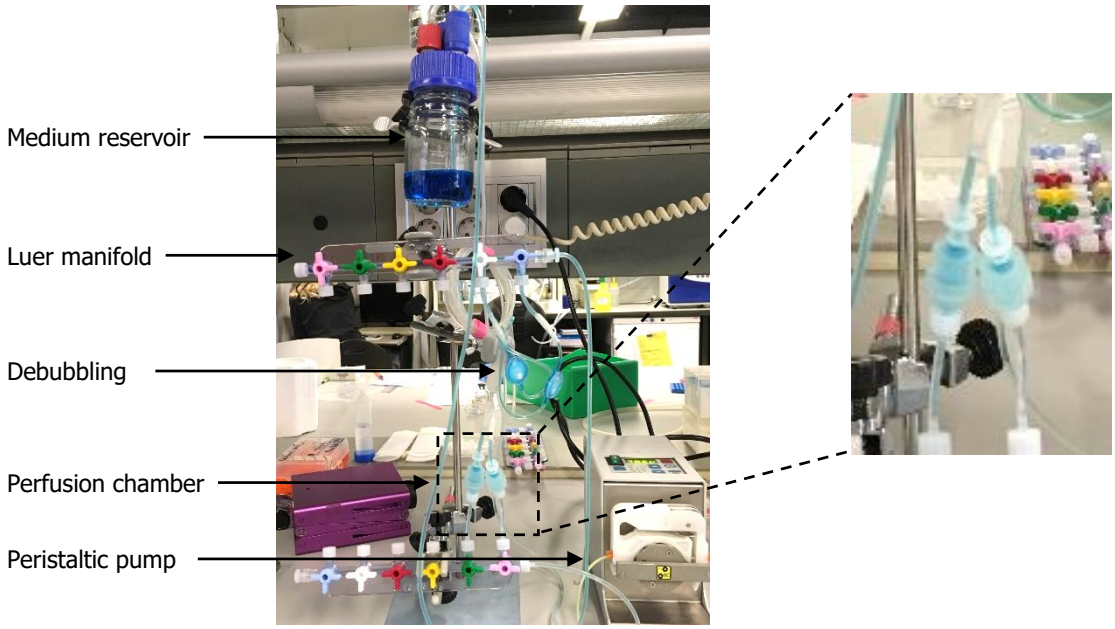

Figure 4.18. Photo of the perfusion bioreactor setup and a zoom of the perfusion chambers, where the cell-laden hydrogels are placed inside.

Regarding the medium flow passing through the hydrogel, it might exert a very high shear stress to the encapsulated cells due to the small size of the hydrogel pores. It has been reported that high shear stress can modify cell behaviour or can even induce cell death via apoptosis[298]. In order to minimize that damage coming for the shear stress, we applied a flux rate of 0.1 mL·min^{-1} to each branch of the bioreactor. To better analyse that the perfusion bioreactor could benefit the mass transport and thus enhance the cell distribution inside the hydrogel along the cell culture period, a set of hydrogels mounted on Transwell® inserts were analysed in parallel. Live/Dead™ viability/cytotoxicity assays were performed at different time points and were evaluated by analysing the confocal images, where Z-stacks were performed along the whole thickness of the samples (≈0.5 mm). As shown in Figure 4.19, for both bioreactor and Transwells® inserts, cell viability was excellent in all the scaffolds tested for up to 21 days, as dead cells (stained in red) could not be distinguished. At day 3 of culture, cell viability and distribution in samples cultured under perfusion (Figure 4.19, left upper row) and in Transwell® (Figure 4.19, left lower row) were similar, meaning that continuous perfusion did not produced obvious detrimental effects on cells due to the shear stress. Remarkably, after 14 and 21 days of cell culture, fibroblast cultured within the bioreactor were homogenously distributed throughout the entire hydrogel (Figure 4.19, middle and right upper row), contrary to what happened for the fibroblasts cultured on Transwell® inserts (Figure 4.19, middle and right lower row).

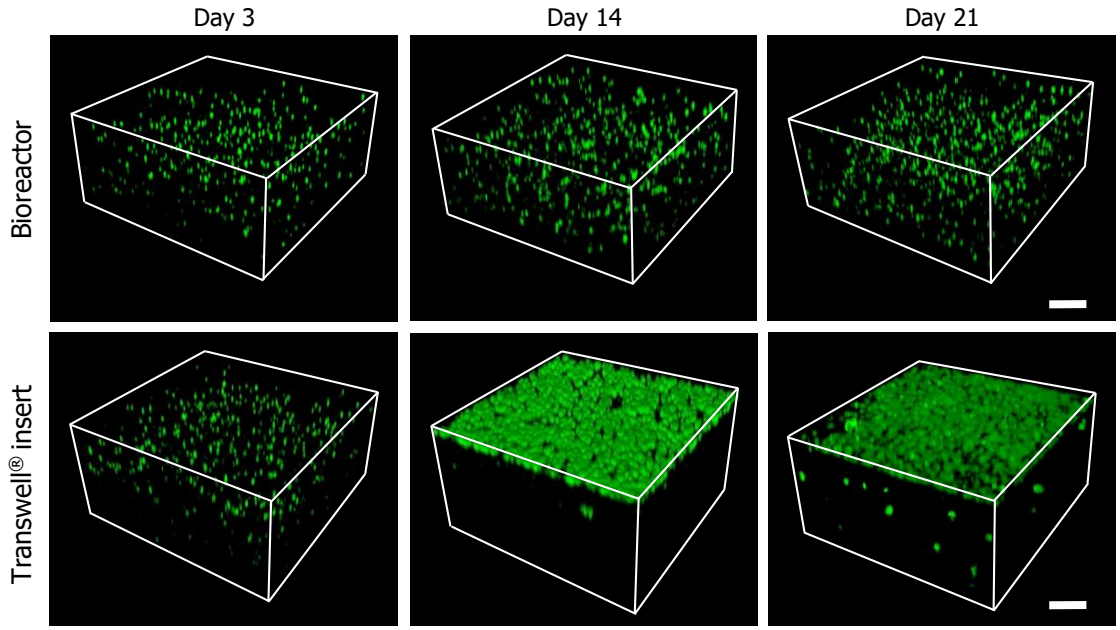

Figure 4.19. Comparison between hydrogels cultured in the bioreactor (upper panels) and in the Transwell® inserts (bottom panels). Confocal 3D reconstruction of the whole hydrogel thickness showing the spatial distribution of the NIH/3T3 embedded cells at days 3 (left), 14 (middle) and 21 (right) after Live/Dead™ viability/cytotoxicity assay. Live cells are labelled in green and dead cells are labelled in red. Scale bars: 200 μm.

We attribute these results to the fact that cell medium perfusion was efficiently providing nutrients and oxygen to the cells embedded into the hydrogel core. This data evidence that embedded cells remained highly viable for long-term cell culture, meaning that the hydrogel was biocompatible and did not present any relevant cellular toxicity. Therefore, the most influential factor determining a homogenous cell distribution along all the hydrogel thickness was the mass transport.

While results from Figure 4.19 show that cell viability was good, we did not observed any significant increase in the cell population cultured under perfusion. Therefore, these experiments were completed by analysing cell distribution, spreading, proliferation and ECM protein synthesis and secretion by immunostaining cell nuclei (DAPI), actin cytoskeleton (F-actin), proliferation (Ki-67 marker) and collagen IV synthesis, of the embedded fibroblasts cultured for 21 days in bioreactors and Transwell® insert (Figure 4.20). At day 21, DAPI labelling shows that in the bioreactor fibroblasts still were inside the hydrogel, while on the surface were not growing. However, fibroblasts placed in the Transwell® insert behaved inversely, there were no cells inside the hydrogel, while the surface was almost entirely covered. F-actin staining showed

that, within the bioreactor, the cells within and on the surface of the hydrogel had a spherical shape. Thus, despite mass transfer was improved, it was not enough to change the cell morphology and spreading compared to the Transwell® conformation.

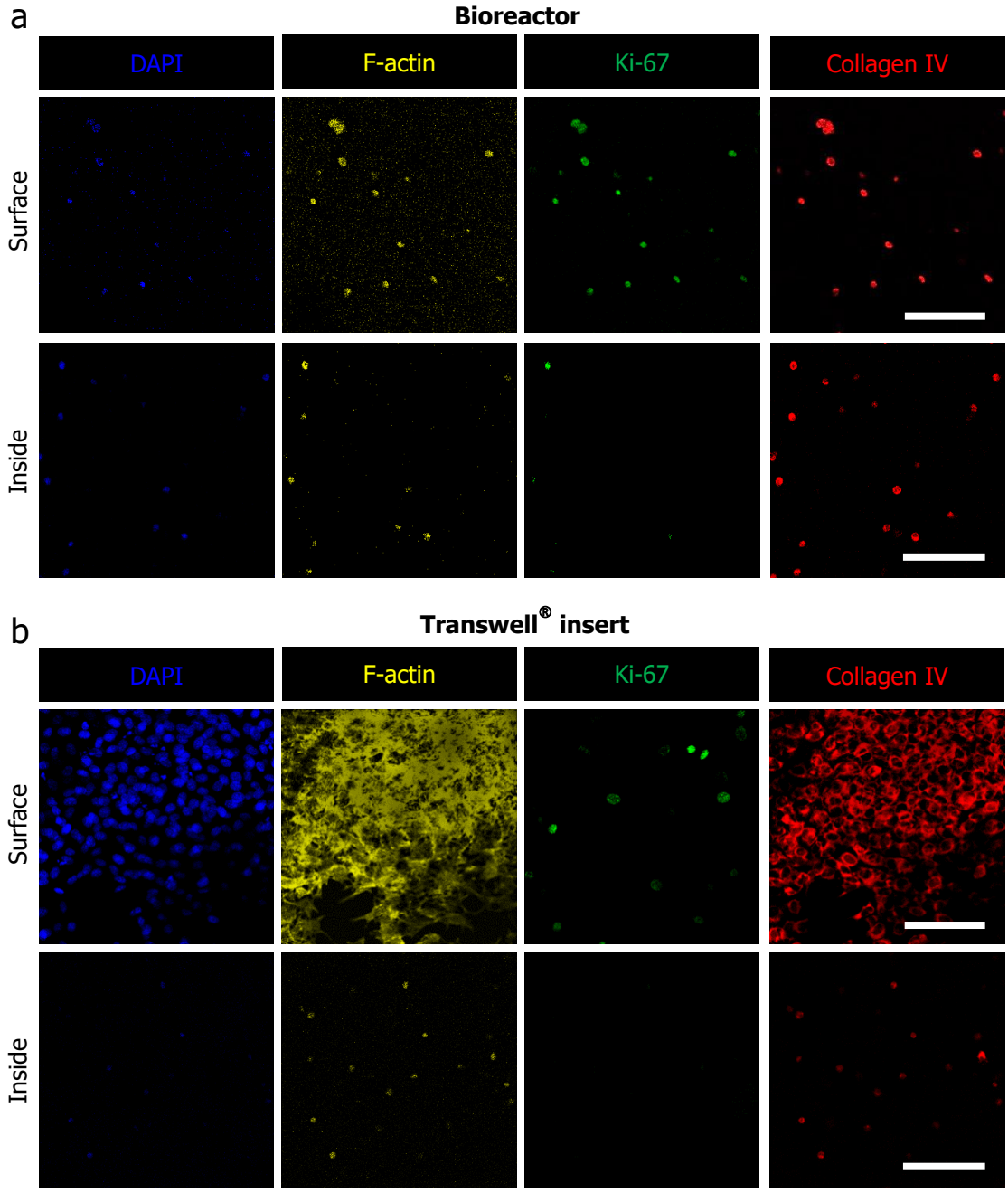

Figure 4.20. Immunostaining analysis of fibroblasts embedded in GelMA$_5$ – PEGDA hydrogel co-networks. Hydrogels were mounted in (a) perfusion bioreactor and (b) Transwell® inserts, and stained for DAPI, F-actin, Ki-67 and Collagen IV after 21 days in culture. Images are stacks from the surface (a and b top panels) and from the inside (a and b bottom panels) of the hydrogels. Scale bars: 100 μm.

This suggested that hydrogel stiffness was the main parameter restricting cell spreading. It has been published in the literature that morphology and cell spreading depend on matrix stiffness, as harder is the network where cells are embedded, the less capacity have to elongate[189,269,272,281]. It seemed that matrix is also directly linked to cell proliferation, as it can be appreciated in Ki-67 immunostainings that fibroblasts next to the hydrogel surface were more proliferative than cells within the hydrogel core[297], this happening in both setups. Finally, fibroblasts in the bioreactor independently of their position within the hydrogel, had the ability to actively synthetize collagen IV. However, comparing the collagen IV immunostaining images with those of the Transwells® inserts, we did not see any potential improvement in the cell functionality.

These results validate that fibroblasts were functional within GelMA – PEGDA hydrogels. Although they appeared to be in growth arrest, they were alive and could act as a feeder layer. Actually, it is well reported that growth-arrested feeder cells co-cultured with epithelial cells enhance cell proliferation and differentiation through the release of growth factors to the culture media[244,299,300]. For these reasons we decided to continue our cellular experiments using the 7.5% (w/v) $GelMA_5$ – 5% (w/v) PEGDA hydrogel co-networks.

4.7.3. Caco-2 cells on GelMA – PEGDA hydrogel co-networks mimic the epithelial compartment of the intestinal mucosa

We have seen in a previous section that our GelMA – PEGDA hydrogel co-networks were non-toxic for epithelial cells and supported their adhesion. However, on the hydrogels fabricated onto glass coverslips, Caco-2 cells never covered entirely all the surface forming a packed monolayer. We hypothesized that this might be related to improper mass transfer, as this was restricted at the basolateral part of the cells. Traditionally, this drawback has been solved on conventional cultures of Caco-2 monolayers by using Transwell® inserts. The insert separates the apical compartment, corresponding to the intestinal lumen, from the basal one, which represents the stroma and the blood vessels[73], mimicking more accurately the epithelial barrier conditions of the *in vivo* intestine[301]. Following this rationale, hydrogels were included in Transwell® inserts to culture the epithelial cells. Disc-shaped hydrogels 6.5 mm in diameter and 0.5 mm in height were photocrosslinked using 7.5% (w/v) $GelMA_5$ – 5% (w/v) PEGDA polymer solutions and applying a UV exposure dose of 1.88 $J \cdot cm^{-2}$. The samples were

fabricated onto porous polymeric membranes and mounted in Transwell® inserts. Then, Caco-2 cells, at cell density of $7.5 \cdot 10^5$ cells·cm^{-2}, were seeded on the surface of the samples and were grown for 21 days. At day 21, Caco-2 cell samples were fixed, and the epithelial monolayers were characterized by immunostaining cell nuclei (DAPI) and cell cytoskeleton (F-actin). Then, the surface of the immunostained samples was visualized under a fluorescent microscope. Representative immunofluorescence images of the whole hydrogel surface were taken to analyse the epithelial monolayer coverage (Figure 4.21). DAPI and F-actin stainings in Figure 4.21 (a) revealed the consistent formation of densely packed monolayers of Caco-2 cells that were homogeneously distributed throughout the hydrogel surface To better visualize cell distribution, representative images were taken at large magnification (Figure 4.21 (b)). These images demonstrate that epithelial monolayers were perfectly formed without any hole and cells were growing in a flat monolayer without forming 3D clumps.

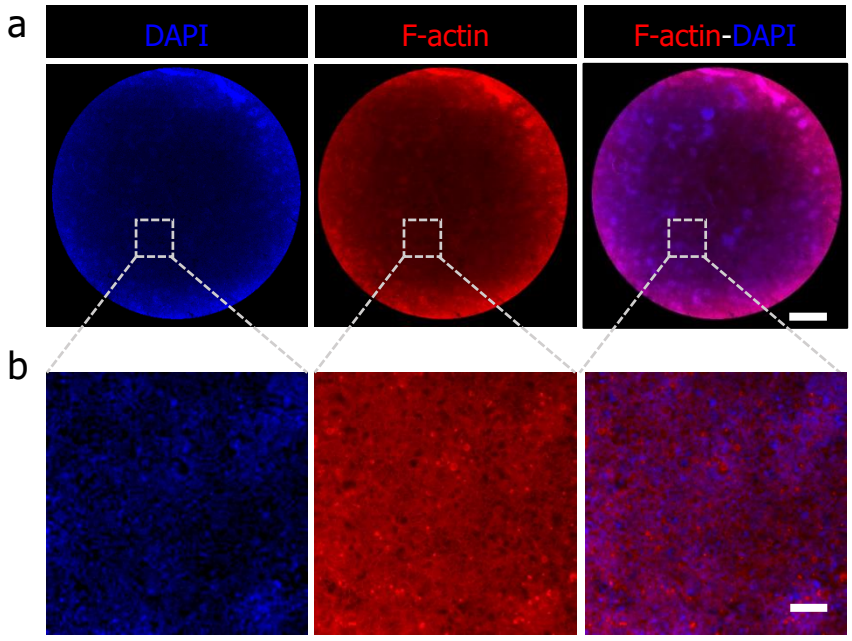

Figure 4.21. Epithelial cell monolayer formed on top of 7.5% (w/v) $GelMA_5$ – 5% (w/v) PEGDA hydrogel co-networks at day 21. (a) Immunostaining for DAPI (left), F-actin (center) markers and merge of both markers (right) showing the whole hydrogel surface. Scale bar: 1mm. (b) Higher magnification images of the epithelial cell monolayers. Scale bar: 100µm.

After being cultured for 21 days, Caco-2 cells should exhibit features of mature enterocytes. To check this, cells were immunostained for two epithelial markers involved in cell-cell adhesion and visualized under a confocal microscope. The markers were ZO-1, which is a protein involved in the tight junctions located in the apical part of the cells, and β-catenin, which is a protein that forms part of the adherens junctions located just

under the tight junctions. Caco-2 cells are correctly mature and polarized when ZO-1 appears in the apical part of the cells, while the β-catenin is mainly localized in the basolateral part. Confocal images revealed the typical cobblestone-like shape of epithelial layers (Figure 4.22 (a)), while the cross-sections (Figure 4.22 (b)) showed columnar, highly polarized cells exhibiting apical F-actin and ZO-1 expression, with β-catenin expression confined to the basolateral side of the monolayers.

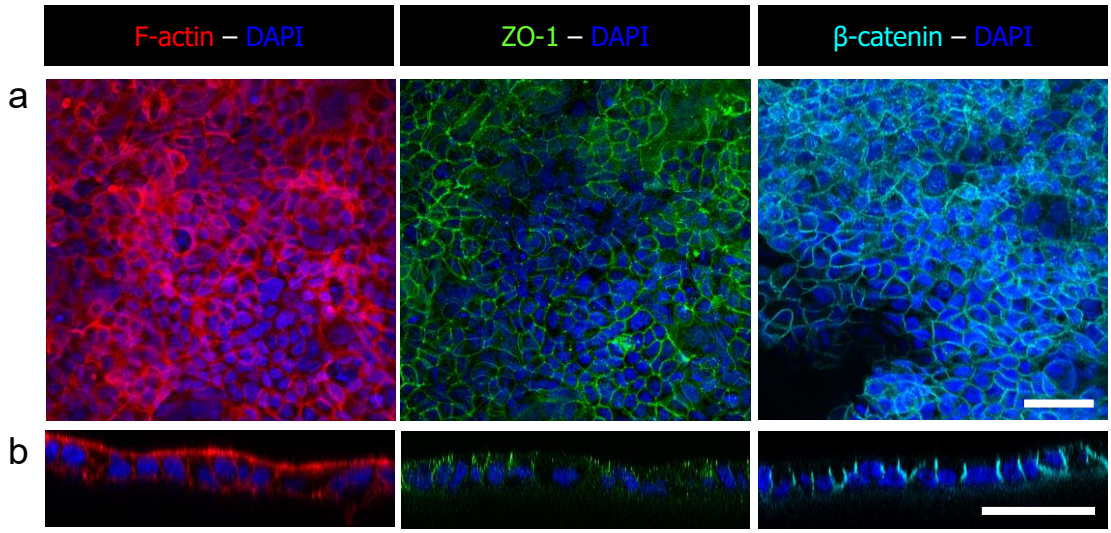

Figure 4.22. Epithelial cell monolayer formed on top of 7.5% (w/v) $GelMA_5$ – 5% (w/v) PEGDA hydrogel co-networks at day 21. (a) Maximum intensity projections of immunostainings for F-actin, ZO-1 and β-catenin, on the epithelial cell monolayers formed on top of the hydrogel con-networks and (b) orthogonal sections of the images from panel (a). DAPI was used to stain the cell nuclei. Scale bars: 50 μm.

No differences between the epithelial monolayer grew on top of the hydrogel surface and on top of a hard porous Transwell® membrane (Figure 4.23), for the immunostaing of F-actin and ZO-1 makers. In both case, cells showed a columnar shape and they were well-polarized. These results demonstrate that Caco-2 cells grow, forming a well-compact and well-polarized monolayer on our 7.5% (w/v) $GelMA_5$ – 5% (w/v) PEGDA hydrogel co-networks.

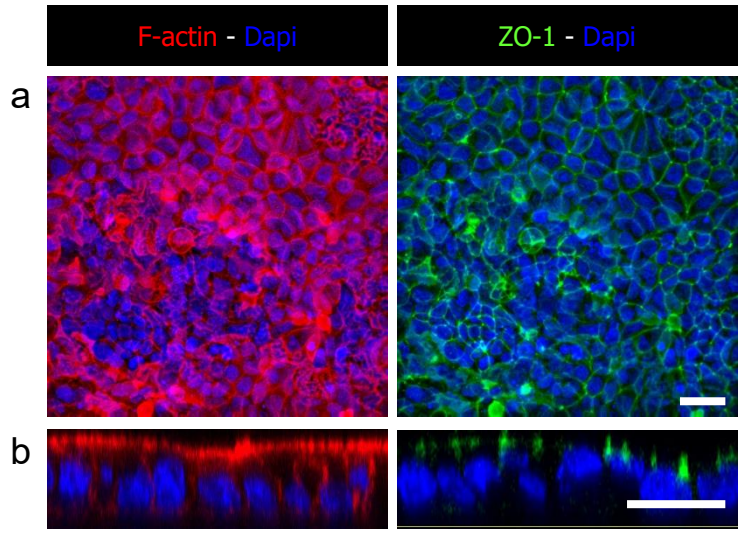

Figure 4.23. Epithelial cell monolayer formed on a top of a hard porous membrane of Transwell insert (a) Maximum intensity projections of immunostainings for F-actin, and ZO-1 on the epithelial cell monolayer, and (b) orthogonal sections, of the images from panel a. DAPI was used to stain the nuclei. Scale bars: 25 μm. Images kindly provided by Dra. Maria Garcia.

4.8. GelMA – PEGDA hydrogel co-networks used to mimic simultaneously epithelial and stromal compartments of the intestinal mucosa

After separately characterized the suitability of our GelMA – PEGDA hydrogel co-networks to sustain viability and functionality of encapsulated fibroblasts and the growth and maturity of monolayers of Caco-2 epithelial cells, both cell types were co-cultured in a physiological manner to model *in vitro* the intestinal mucosa including both the stromal and the epithelial compartment on the 7.5% $GelMA_5$ – 5% PEGDA hydrogels. NIH/3T3 fibroblast-laden 7.5% (w/v) $GelMA_5$ – 5% (w/v) PEGDA hydrogels were combined with the culture of Caco-2 monolayers on top of them. To this objective, NIH/3T3 cells at a density of $5 \cdot 10^6$ cells·mL^{-1} were encapsulated in hydrogels and mounted in Transwell® inserts. The day after, Caco-2 cells at a density of $7.5 \cdot 10^5$ cells·cm^{-2} were seeded on top of the cell-laden hydrogels. Then, the constructs were cultured for 21 days (details in section 3.9). After this period, samples were characterized by histological processing to be able to obtain information of both the epithelial layer and the stromal section. Remarkably, histological studies analogous to the ones routinely performed with *ex vivo* tissues could be performed because the hydrogels presented good mechanical integrity to be successfully processed. Hydrogels were cut transversely in sections of 3 μm in thickness. Hematoxylin-eosin staining of the construct cross-

sections was performed to have a general view of the cells within the hydrogel. Staining presented in Figure 4.24 (a) revealed the formation of a continuous epithelial cell monolayer on top of the constructs and a homogenous distribution of fibroblasts throughout the hydrogel co-networks. Fibroblasts looked rounded and, although they were evenly distributed, the cell density was low.

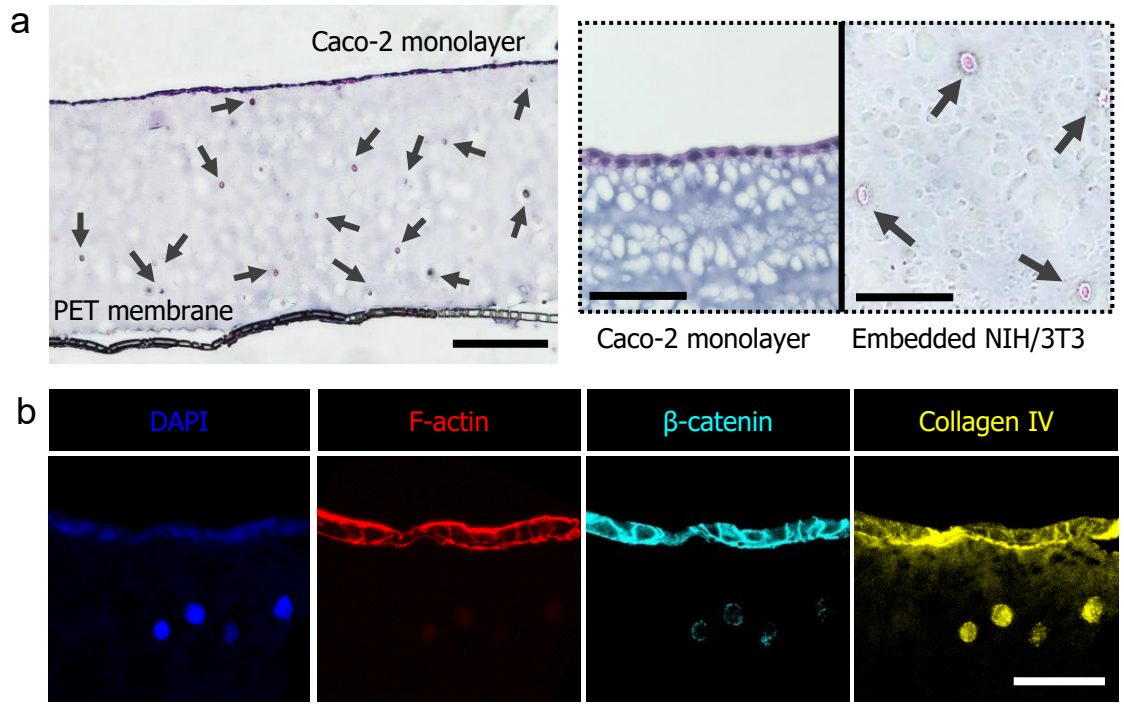

Figure 4.24. NIH/3T3 fibroblasts and Caco-2 epithelial cell co-cultured in the hydrogel co-networks. (a) Cross-section of hematoxylin-eosin stained samples showing the formation of an intact epithelial monolayer at the top and a uniform distribution of the NIH/3T3 fibroblasts (arrows) throughout the hydrogel (left panel). The right panel show detailed views of both cell types. Scale bars: 150 μm (left) and 50 μm (right). (b) Immunostainings for F-actin, β-catenin, and Collagen IV of a co-cultured sample in hydrogel co-networks. DAPI was used to stain the cell nuclei. Scale bar: 50 μm.

To have a more detailed information of the epithelial cells' polarity and maturity and of the fibroblasts morphology and functionality, we conducted immunostaining assays on the histological cuts. Staining targeted actin cytoskeleton, β-catenin as epithelial cell marker, and collagen IV as a functional marker for the fibroblasts. Images in Figure 4.24 (b) demonstrate the presence of apical F-actin and basolateral β-catenin on the Caco-2 cell monolayer, which confirmed their correct polarization. Whereas, fibroblasts were mostly rounded shape but expressed collagen IV, which appeared within the cells, and it seemed that they also secreted it, as collagen IV signal appeared to be accumulated at the epithelial basement membrane. This suggests the capacity of fibroblasts in being functional by secreting ECM proteins within our model.

Based on these results, our 7.5% (w/v) $GelMA_5$ – 5% (w/v) PEGDA hydrogel co-networks were suitable scaffolds to be used for long-term cell culture, as well as to simultaneously model both compartments, the stromal and the epithelial. Additionally, it seemed that when fibroblasts cells were co-cultured with the epithelial cells, they were able to secret more collagen IV, especially under the epithelial monolayer while Caco-2 cells had better polarization characteristics than when they were cultured alone on the hydrogels.

4.8.1. Evaluation of the effects of the stromal component on the barrier properties of the epithelium in the *in vitro* model of intestinal mucosa

Once generated a 3D tissue-like construct that mimicked some basic features of the intestinal mucosa, we employed it to assess *in vitro* the effect of fibroblasts on the intestinal epithelial monolayer growth and barrier function. As functional hallmarks for epithelial barrier integrity and permeability, we measured the transepithelial electrical resistance (TEER) and the apparent permeability (P_{app}) to paracellular model compounds of the epithelial monolayers grown under different experimental conditions depicted in Figure 4.25 (a)**.** Disc-shaped hydrogel samples made of 7.5% (w/v) $GeLMA_5$ – 5% (w/v) PEGDA polymer solutions laden with fibroblasts were fabricated onto porous membranes, mounted on Transwell® inserts and seeded with Caco-2 cells following the methods previously described. As controls, we used (I) hydrogel discs with only embedded fibroblasts, (II) discs without fibroblasts but with Caco-2 cells on top, and (III) plastic porous membranes with Caco-2 growing directly on top of them (Figure 4.25 (a)). For all the conditions, cells were cultured up to 21 days. During this period, several characterizations were conducted to evaluate the *de novo* growth of the epithelial monolayer with and without the presence of the fibroblasts, and the impact of these cells on the TEER and P_{app} of the mucosa-like constructs. After 8 days of culture, the morphology of Caco-2 cell monolayers grown onto fibroblast-laden hydrogels or without fibroblasts were analysed by immunostaining of cell nuclei (DAPI) and actin cytoskeleton (F-actin). Images showed that on hydrogels without the fibroblasts embedded within, the epithelial cells formed a discontinuous layer with dome-shaped structures. In contrast, Caco-2 cells formed a continuous and flat epithelial monolayer that fully covered the hydrogel surface when they were seeded on fibroblast-laden hydrogels (Figure 4.25 (b)).

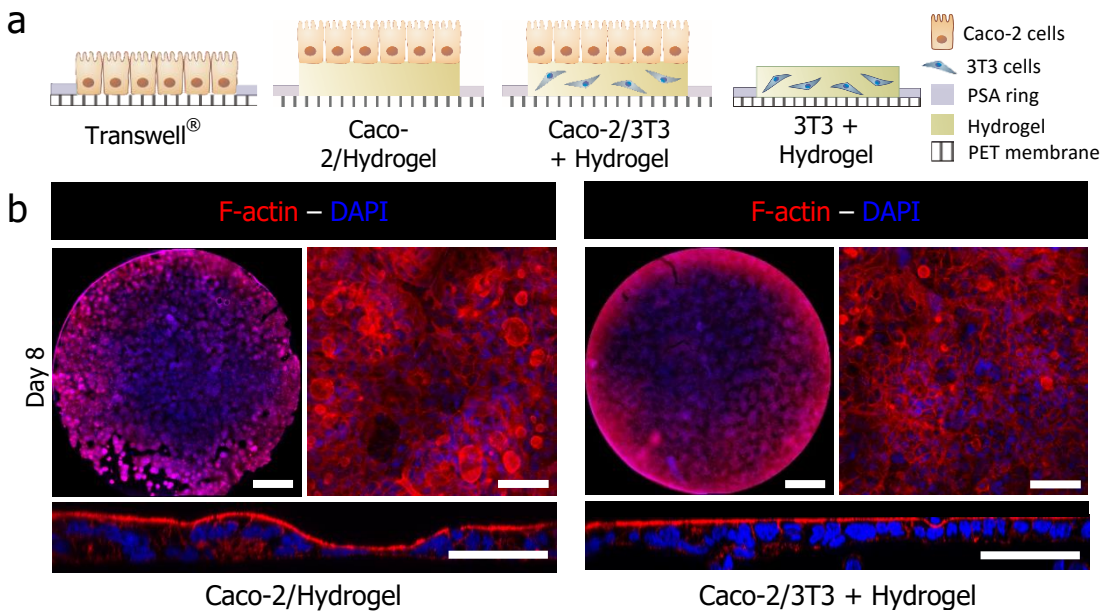

Figure 4.25. (a) Schematic illustration of the analyzed cell culture configurations. (b) Immunostainings for F-actin and nuclei of the entire Transwell® membrane surface (0.33 cm^2) showing the epithelial monolayer grown on top of hydrogel co-networks without (left) and with (right) embedded NIH/3T3 cells after 8 days in culture. Right and bottom panels show detailed cross-section views of the formation of the epithelial monolayer on top of the hydrogels. Scale bars: 1 mm, 50 µm and 50 µm, respectively.

TEER, which is directly related to the tightness of the epithelial barrier, was monitored for the different sample conditions along the 21 days of the experiments. TEER values increased for all samples including epithelial cells with increasing culture time (Figure 4.26 (a)), indicating the formation of an epithelial monolayer with effective barrier properties. In contrast, fibroblast-laden hydrogels without epithelial cells on top did not show TEER values significantly different from the background, therefore demonstrating that the increase in TEER was due to the formation of epithelial barriers and not linked to any significant electrical resistance provided by the hydrogel and/or the NIH/3T3 cells. By day 21 of culture, TEER values of Caco-2 epithelial monolayers grown on hydrogels were significantly lower (up to 4-fold) than for cells grown on hard Transwell® inserts (Figure 4.26 (a)). As TEER vales of cells grown in Transwell® inserts are recognized as being non-physiologically representative of the *in vivo* permeability (meaning that the barrier formed is too tight compared to *in vivo* tissue), however, our hydrogels provide an improved representation of the barrier properties.

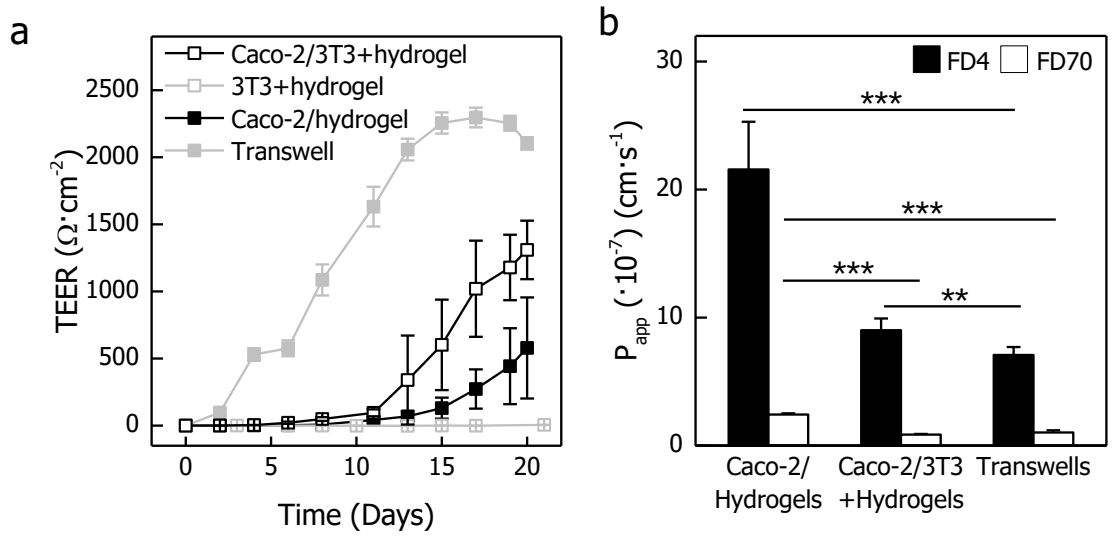

Figure 4.26. Study of the epithelial barrier properties. (a) Transepithelial electrical resistance (TEER) as a function of cell culture time for epithelial monolayers grown on Transwell® inserts (grey), on top of hydrogel co-networks with (white), without (black) embedded NIH/3T3 fibroblasts, and embedded NIH/3T3 fibroblast without epithelial monolayers (hollow grey). (b) Apparent permeability (P_{app}) of FITC-dextran 4 kDa (FD4) (black) and Rhodamine-dextran 70 kDa (FD70) (grey) through epithelial monolayers grown on Transwell® inserts, and on top of hydrogel co-networks with and without embedded NIH/3T3 fibroblasts. Values are the mean ± SD (n=3). **p < 0.005 and ***p<0.001.

Monitoring TEER also provides information about the growth dynamics of the epithelial monolayers. It should be noted that TEER values of Caco-2 cell monolayers grown on hard porous membranes increased already after 2 – 3 days in culture, while cells grown on 7.5% (w/v) $GelMA_5$ – 5% (w/v) PEGDA hydrogel co-networks did not show an increase until 11 – 12 days of culture. This indicates a delay in epithelial layer formation when cells were grown on hydrogel substrates. It has been shown that the physical properties of cellular microenvironments play a crucial role in regulating cell division[302], collective cell migration[303], and, more importantly, in the maturing of tight junctions[304]. We therefore attribute the delay in epithelial monolayer formation and lower TEER values in the hydrogel-containing samples to the soft mechanical properties of the 7.5% (w/v) $GelMA_5$ – 5% (w/v) PEGDA hydrogels, apparent elastic modulus of about 35 kPa, compared to the Transwell® inserts, which is between 2 and 3 GPa[305]. This is also in agreement with previous findings for soft natural[106,112] or synthetic hydrogels[155], which yield physiologically realistic TEER values, while hard porous membranes typically result in unrealistically high ones[306]. Comparing the samples with and without fibroblasts, the slope of the TEER curve, which provides information about changes in TEER over time, differed significantly between them. The presence of fibroblasts clearly accelerated the

formation of the epithelial monolayer and the development of tight junctions, leading to TEER values increased by 2.5-fold by day 21 ((Figure 4.26 (a)).

The role of the fibroblasts in the paracellular transport through the tight junctions of the epithelial monolayers was also investigated. To that aim, at day 21 of cell culture, the apparent permeability for all the samples having Caco-2 cells was evaluated by using fluorescently labelled dextran molecules of different and well-defined molecular weights as tracers: FITC-dextran 4 kDa (FD4) and Rhodamine-dextran 70 kDa (FD70). Consistent with the lower TEER values, the epithelial barriers formed onto both hydrogels with and without fibroblasts were significantly more permeable to FD4 dextrans than those formed on Transwell® inserts (Figure 4.26 (b)). These data are also in agreement with TEER indications about the tightness of the monolayer among the hydrogel samples. Those containing embedded fibroblasts showed less epithelial permeability than those without fibroblasts (Figure 4.26 (b)). Paracellular permeability is size dependent and inversely proportional to the molecular weight of the molecule tested. In the case of FD70 dextran, which exhibits a hydrodynamic radius of 11.6 nm, it was employed as control to test that epithelial barriers formed restricted the paracellular transport of larger molecules.

Overall, the previous data seem to suggest that the presence of embedded fibroblasts within the hydrogel co-networks had beneficial effects on the formation of continuous and uniform epithelial monolayers, enhancing the maturity of the tight junctions, and that the tissue-like mucosa construct developed could be of use in *in vitro* assays for drug absorption and permeability. To prove this point, permeability studies were carried out using a relevant biomedical drug. Insulin, which has a hydrodynamic radius of 2 nm[307], was selected for this purpose. Its apparent permeability across Caco-2 epithelial monolayers grown onto fibroblast-laden 7.5% (w/v) $GelMA_5$ – 5% (w/v) PEGDA hydrogels was studied. Figure 4.27 shows the total percentage of insulin that was able to permeate the epithelial monolayer from the apical to the basolateral compartment as a function of time. We can observe that the insulin permeation through the epithelial monolayer was linear and was not restricted by the tight junctions of the epithelial monolayer. Moreover, when epithelial cells were grown on these 7.5% (w/v) $GelMA_5$ – 5% (w/v) PEGDA hydrogel samples, insulin P_{app} coefficient obtained was 6±1 x 10^{-8} $cm \cdot s^{-1}$. The obtained value was an order of magnitude higher than reported values for conventional Caco-2 monolayers on Transwell® membranes[308,309]. This correlates well with the lower TEER values observed for hydrogel constructs.

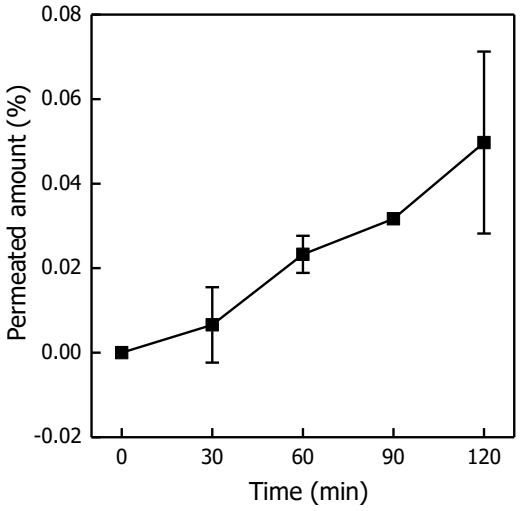

Figure 4.27. Permeability studies of insulin through fibroblast-laden 7.5% (w/v) $GelMA_5$ – 5% (w/v) PEGDA hydrogels when an epithelial monolayer is well-formed after 21 days of cell culture. Values are the mean ± SD (n=2).

Altogether, our results demonstrate that Caco-2 cells grown on fibroblast-laden GelMA – PEGDA hydrogel co-networks yield an improved physiological barrier compared to conventional Caco-2 cells growth on plastic porous membranes, as TEER and permeability values are more similar to those found in *in vivo* intestinal studies[310].

4.8.2. Effects of stromal components on the recovery of the barrier function of the intestinal epithelium

As a next step, the 3D model of the intestinal mucosa was used to mimic *in vitro* the disruption and recovery process of the epithelial barrier integrity. This is a common occurrence under intestinal and systemic diseases, such as inflammatory bowel diseases, autoimmune disease and other metabolic diseases[67]. To conduct these experiments, epithelial monolayers were grown for 21 days on 7.5% (w/v) $GelMA_5$ – 5% (w/v) PEGDA hydrogels with and without fibroblasts embedded in the hydrogel, as previously described in section 3.9. Once functional epithelial barriers were formed (being these monitored through TEER measurements), tight junctions were disrupted to increase the barrier permeability. For this purpose, cells were treated with a solution of EDTA, which is a calcium-chelating agent, for 5 min. After this time, EDTA was removed and the epithelial integrity was monitored by measuring TEER values just after removing the EDTA solution and at several times points for a recovery period of 24 hours.

As show in Figure 4.28 (a), the treatment with EDTA reduced the TEER values in both samples to basal levels, confirming the disruption of the epithelial barrier. After removing EDTA, TEER values were progressively recovered corresponding with the restoration of the tight junctions and the reestablishment of the epithelial barrier function. Interestingly, TEER recovered faster in epithelial monolayers grown on fibroblast-laden hydrogels than in those formed on hydrogels without fibroblasts (Figure 4.28 (b)). These results indicate that the presence of stromal fibroblasts in our model, apart from enhancing the growth and the maturity of Caco-2 monolayers giving barrier properties closer to those of the native intestinal tissue, also had an impact in the recovery rate of the epithelial barrier when there is a temporary disruption of the tight junctions.

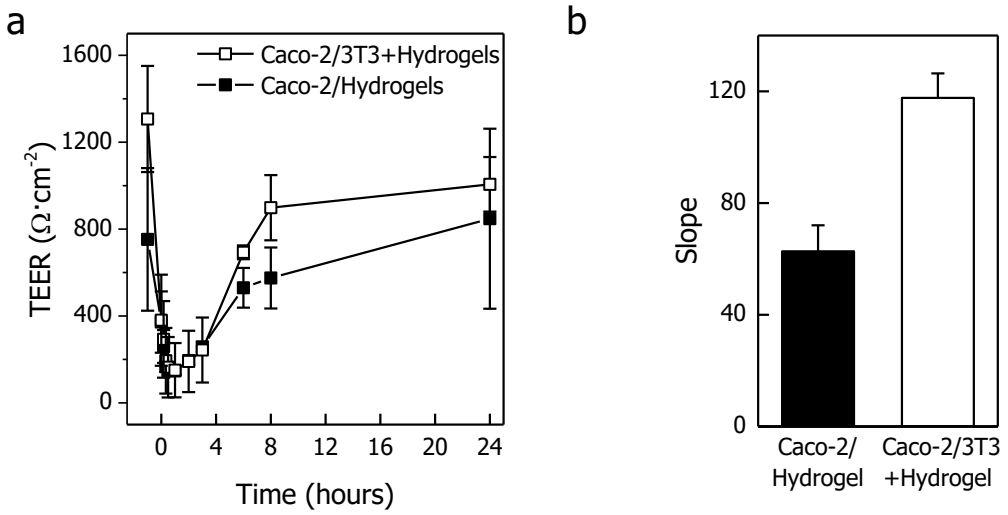

Figure 4.28. Effect of the stromal compartment on the epithelial barrier restoration after its disruption. (a) TEER evolution after EDTA treatment of the epithelial monolayer grown on hydrogel co-networks in the presence or absence of fibroblasts embedded in the matrix. (b) Change of TEER over time from panel (a). Values are the mean ± SD (n=3). **p < 0.005 and ***p<0.001.

Analysing all the results obtained with the hydrogel co-network composed of 7.5% (w/v) $GelMA_5$ – 5% (w/v) PEGDA macromer content, the setup developed might act as a first approach of an *in vitro* 3D model of the small intestinal mucosa. On one hand, epithelial cells grew on top of these hydrogels forming a functional epithelial barrier. On the other hand, the hydrogels supported the encapsulation of fibroblasts without affecting cell viability and functionality, and thus, emulating properly the stromal compartment. Overall, this platform allows us to simultaneously have the epithelial and

stromal compartment, obtaining an *in vitro* model that better mimics the native properties of the small intestine.

4.9. Optimization of hydrogel co-network composition for an improved 3D model of the intestinal mucosa

Despite being an improvement of the standard model for *in vitro* intestinal studies, the intestinal mucosa model developed so far still had some shortcomings. Specifically, although 7.5% (w/v) $GelMA_5$ – 5% (w/v) PEGDA hydrogel composition presented an excellent stability and sustained the culture of viable fibroblasts for up to 21 days of culture, the growth and spreading of the encapsulated cells was restrained. Fibroblasts adopted a round-shape and a restricted migratory phenotype, resulting in an impaired interaction between them and the epithelial cells. It has been reported that in cells with round morphology, their migration and proliferation are limited[311,312]. We attributed the cell growth arrest within our hydrogels to the densely packed co-networks, resulting in tiny mesh sizes (a few nanometers) and relatively high stiffness values[312–314]. This was supported from the diffusion coefficients studies, as FD4 (2.8 nm diameter) dextran molecules diffused freely through the hydrogels while FD70 (11.8 nm diameter) or FD500 (32 nm diameter) dextran molecules did not. Therefore, fibroblasts were alive and secreted collagen IV, but their support to the epithelium was basically through paracrine mechanisms. Other fibroblasts functions, such as ECM remodelling, were not observed even if the hydrogel contained cell-degradable material (gelatin). It has been reported that in networks with high crosslinking density, cell growth and invasion decrease dramatically, and the secretion of MMPs by fibroblasts is impaired[315].

To better recapitulate the *in vivo* functionality of fibroblasts within the stromal compartment of the intestinal mucosa, our efforts were then focused in improving the mass transport properties and matrix remodelling capabilities of our hydrogel co-networks. To accomplish this, we aimed to develop hydrogels with larger pores without compromising their mechanical stability and the functionality of the epithelial monolayers. As we have previously seen, polymer mesh size can be tuned by modifying the total macromer content and/or decreasing the crosslinking points of GelMA chains by decreasing their DoF. Thus, we explored these options. To do that, the total macromer content was reduced from 12.5% (w/v) to 7.5% (w/v) and 6.25% (w/v) and the DoF of

GelMA polymer was changed from 75.7±2.1% ($GelMA_5$) to 51.4%±3.7 ($GelMA_{1.25}$). Table 4.1 contains the new hydrogel formulations assayed.

GelMA	GelMA content % (w/v)	PEGDA content % (w/v)	Total macromer % (w/v)	Polymer solution composition
$GelMA_5$	7.5	5	12.5	7.5% (w/v) $GelMA_5$ – 5% (w/v) PEGDA
	5	2.5	7.5	5% (w/v) $GelMA_5$ – 2.5%(w/v) PEGDA
	5	1.25	6.25	5% (w/v) $GelMA_5$ – 1.25% (w/v) PEGDA
$GelMA_{1.25}$	7.5	5	12.5	7.5% (w/v) $GelMA_{1.25}$ – 5% (w/v) PEGDA
	5	2.5	7.5	5% (w/v) $GelMA_{1.25}$ – 2.5% (w/v) PEGDA
	5	1.25	6.25	5% (w/v) $GelMA_{1.25}$ – 1.25% (w/v) PEGDA

Table 4.1. New hydrogel formulations tested to improve the 3D model of the intestinal mucosa.

4.9.1. Characterization of hydrogel co-networks obtained from optimized GelMA – PEGDA formulations

First, the hydrogels obtained from the new polymer formulations (Table 4.1) were physicochemically and mechanically characterized. Swelling behaviour, mechanical properties (apparent elastic modulus), degradation properties and gel fraction (crosslinking degree) were evaluated to choose the most suitable candidate to have an optimized cell co-culture platform. In these studies, polymer formulations (Table 4.1) were dissolved in DMEM without phenol red, supplemented with 1% Penicillin/Streptomycin and photopolymerized using a UV dose of 1.88 $J \cdot cm^{-2}$ to form GelMA – PEGDA hydrogel discs. For swelling behaviour analysis, degradation studies and gel fraction, dimensions of the hydrogel discs were 10 mm in diameter and 1 mm in thickness and were polymerized on non-silanized glass coverslips. Whereas, for the mechanical tests, hydrogel disc dimensions were 6.5 mm in diameter and 0.5 mm in thickness and were fabricated on silanized glass coverslips.

4.9.2. Swelling analyses

For swelling analyses, hydrogels formed from GelMA – PEGDA polymers described in Table 4.1 were incubated in PBS at 37ºC and the increment of weight as a function of time was measured. Figure 4.29 presents the amount of water retained by the $GelMA_5$ – PEGDA (Figure 4.29 (a)) and the $GelMA_{1.25}$ – PEGDA (Figure 4.29 (b))

hydrogel co-networks. All samples followed the same pattern shown for GelMA and PEGDA hydrogels networks studied in section 4.3.1. Briefly, hydrogels had high capacity to absorb water during the first hour after their fabrication. Then, this capacity diminished, and finally the amount of retained water was kept constant at the equilibrium swelling. For both types of hydrogels, containing $GelMA_5$ or $GelMA_{1.25}$, the swelling equilibrium was reached after 24 h of incubation in PBS regarding their DoF. There were non-statistically significant differences between samples in the amount of water absorbed at the equilibrium, neither comparing the total macromer content nor the DoF of the GelMA.

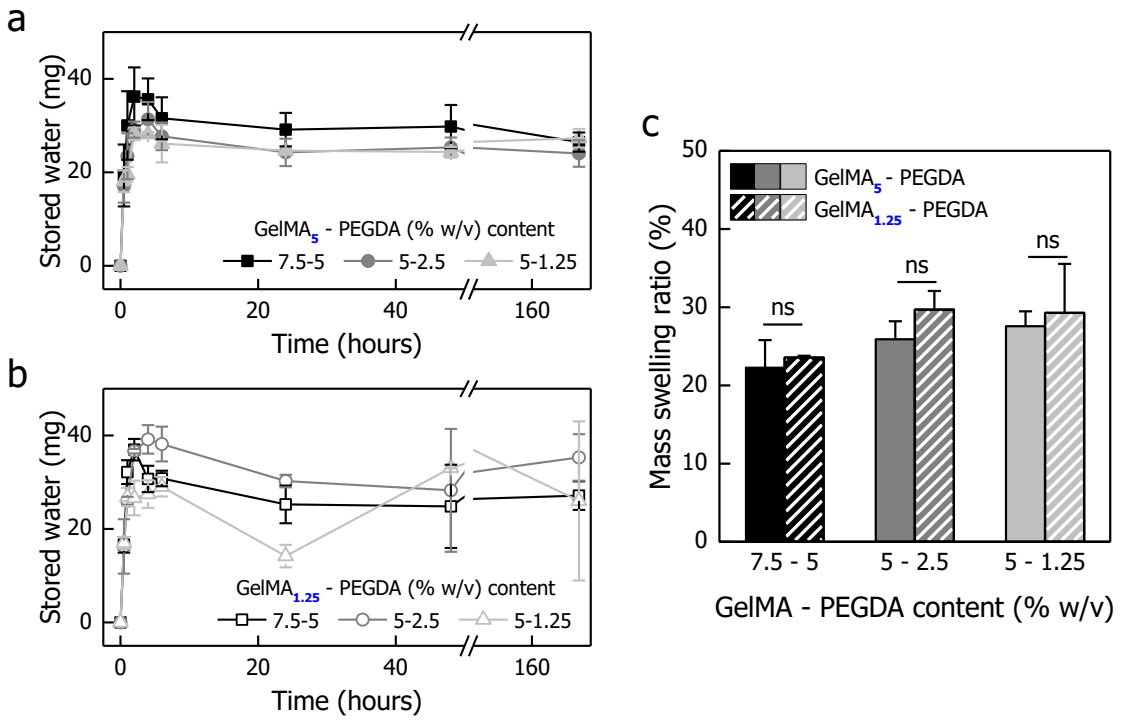

Figure 4.29. Analysis of the swelling properties of hydrogels composed of GelMA – PEGDA polymers at different macromer concentrations: 7.5% (w/v) – 5% (w/v) (dark), 5% (w/v) – 2.5% (w/v) (grey) and 5% (w/v) – 1.25% (w/v) (light grey). Amount of stored water in the (a) $GelMA_5$ – PEGDA or (b) $GelMA_{1.25}$ – PEGDA co-networks as a function of time. (c) Mass swelling ratio for the different $GelMA_5$ – PEGDA (solid) and $GelMA_{1.25}$ – PEGDA (stripes) hydrogels. ns means no significant differences. Results are represented as the mean ± SD (almost n=3).

In parallel, mass swelling ratio was evaluated as a function of the total macromer content depending on GelMA DoF. The different DoF did not results in statistically significant differences between the samples. Also, no significant differences were found for samples with different macromer content but there was a tendency of increasing swelling ratio while the total macromer content was decreased (Figure 4.29

(c)). These results suggest that the parameter that affects most the water uptake is the macromer content.

4.9.3. Mechanical properties

After reaching the equilibrium swelling, hydrogels were tested by AFM to determine their mechanical properties. We decided to use AFM instead of DMA as hydrogel's surface stiffness has been reported to affect cell-hydrogel interaction and consequently cell behaviour[316]. Figure 4.30 (a) shows the approach Force – Distance curve obtained for 7.5% (w/v) $GelMA_5$ – 5% (w/v) PEGDA and 5% (w/v) $GelMA_5$ – 1.25% (w/v) PEGDA hydrogels. The curve from 7.5% (w/v) $GelMA_5$ – 5% (w/v) PEGDA hydrogel corresponds to a relatively hard surface, while the curve from 5% (w/v) $GelMA_5$ – 1.25% (w/v) PEGDA hydrogel corresponds to a softer sample.

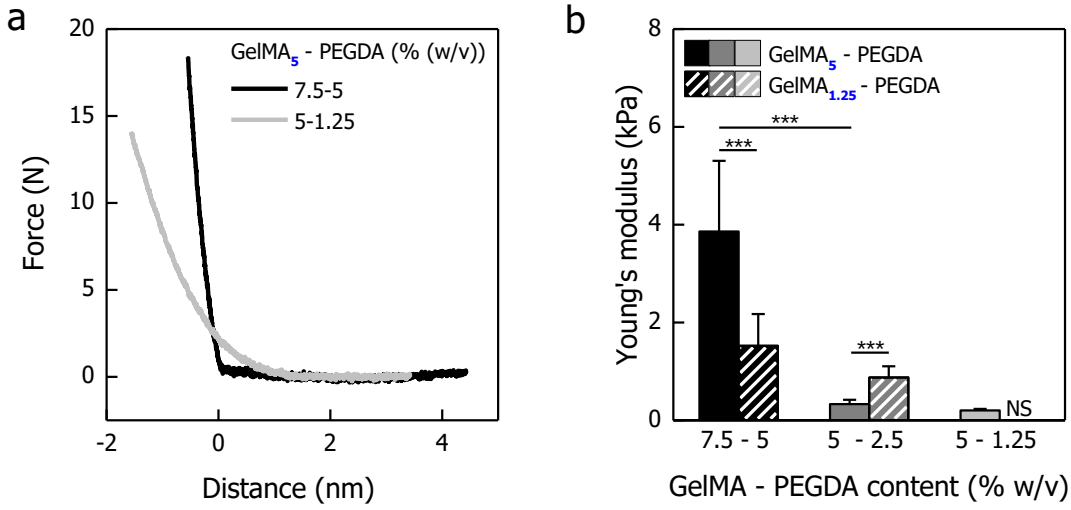

Figure 4.30. Analysis of the mechanical properties by AFM for new hydrogel formulations composed of GelMA – PEGDA and photopolymerized using an energy dose of 1.88 $J \cdot cm^{-1}$. (a) Force-Distance curve of 7.5% (w/v) $GelMA_5$ – 5% (w/v) PEGDA (black line) and 5% (w/v) $GelMA_5$ – 1.25% (w/v) PEGDA (grey line). (b) Elastic modulus values for hydrogels: 7.5% (w/v) $GelMA_5$ – 5% (w/v) PEGDA (solid-black bar), 5% (w/v) $GelMA_5$ – 2.5% (w/v) PEGDA (solid-grey bar), 5% (w/v) $GelMA_5$ – 1.25% (w/v) PEGDA (solid-light grey bar), 7.5% (w/v) $GelMA_{5.25}$ – 5% (w/v) PEGDA (stripped-black bar), 5% (w/v) $GelMA_{1.25}$ – 2.5% (w/v) PEGDA (stripped-grey bar). NS means that the sample was unable to be measured. Results are represented as the mean ± SD (n=3). ***p<0.001.

The slope from the AFM curves allowed us to obtain the values of the Young's modulus for hydrogel samples (Figure 4.30 (b)). Elastic moduli significantly decreased as the total amount of macromer decreased. For samples containing $GelMA_5$ (high DoF) the surface elastic moduli decreased from 3.9 kPa to 0.2 kPa, when the total polymer

content decreased from 12.5% (w/v) to 6.25% (w/v). On the other hand, when maintaining the polymer concentration, decreasing the DoF of GelMA results in a decrease in the Young's moduli. GelMA molecules with the lowest DoF have fewer crosslinking points, providing hydrogels with softer surfaces. In particular, for the 5% (w/v) $GelMA_{1.25}$ – 1.25% (w/v) PEGDA sample, hydrogel surface was so soft that the Young modulus could not be measured. These results agree with other studies published in the literature. For example, Schuurman *et al.*[317] reported that the elastic modulus of GelMA hydrogels increase with increasing GelMA concentration, while Chen *et al.*[318] demonstrated that the elastic modulus of GelMA hydrogels was higher containing GelMA polymers with a high DoF. These results show that by adjusting the total macromer content and the DoF of GelMA polymer, hydrogels with different stiffness were obtained, even if their swelling ratio had not been significantly modified. We expected that these hydrogels, which had softer mechanical properties than the previous ones tested, would allow embedded cells to be less restrained within the hydrogel network, and thus improve cell spreading and growth.

4.9.4. Degradation studies

Degradation of the hydrogels containing $GelMA_{1.25}$, with total macromer contents of 12.5% (w/v), 7.5% (w/v) and 6.25% (w/v) was tested. However, for practical purposes, we only added in the study the hydrogel composed of $GelMA_5$ with a final macromer content of 12.5% (w/v) for comparison, assuming that the other formulations with $GelMA_5$ will present degradation profiles that will behave in a monotonous trend. For this, hydrogels were incubated with collagenase and after specific time points, this was removed, and the weight of the samples was measured by a gravimetric method. The mass remaining percentages along time for the four hydrogels tested are presented in Figure 4.31 (a). Based on these results, after 2 h with collagenase, hydrogels containing $GelMA_{1.25}$ and total macromer concentrations of 7.5% (w/v) and 6.25% (w/v) were totally degraded, while the one containing 12.5% (w/v) needed 4 hours to complete its degradation. These results revealed that in our samples degradation rate can be tuned by adjusting the total macromer content of the polymer formulations. On the other hand, for the 12.5% (w/v) hydrogel containing GelMA with higher DoF, 31.1±29.2% of the initial mass was still remaining after 4 hours of collagenase, being totally degraded after 8 hours of incubation (Figure 4.31 (b)). The degradation was more accelerated in the GelMA hydrogels that had low DoF ($GelMA_{1.25}$)

than in ones with high DoF ($GelMA_5$) because their networks had fewer crosslinking points. As the network formed was less densely packed, consequently, the degradation sequences were more accessible to collagenase molecules to be degraded. Additionally, as non-statistically significant differences were found when comparing hydrogels with increased PEGDA amounts, this suggests that at the PEGDA concentration range tested, the presence of PEGDA chains did not hinder the GelMA degradation sequences. Altogether, the results prove that degradation rate of our GelMA – PEGDA hydrogel co-networks can be tuned by the DoF of GelMA polymer and the total macromer concentration.

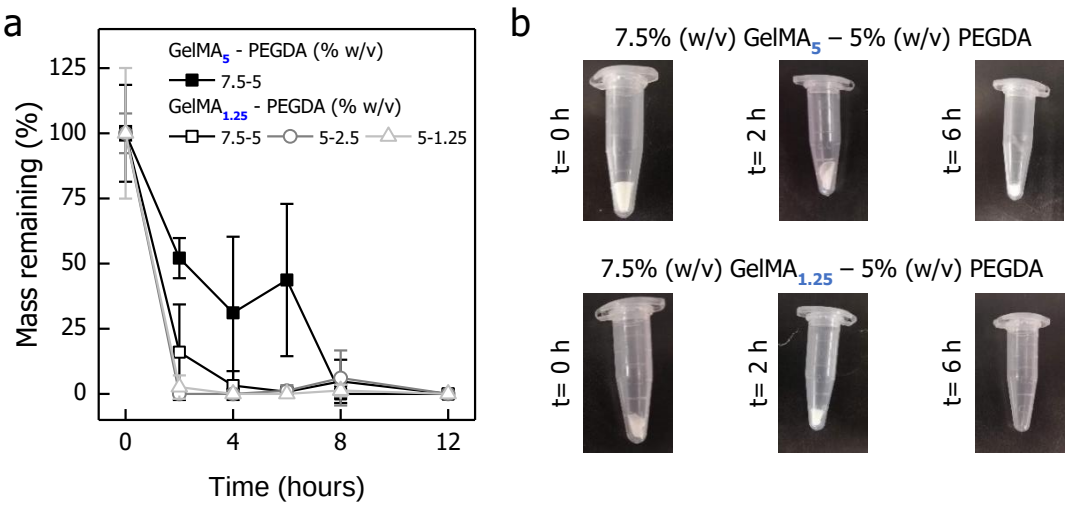

Figure 4.31. Degradation for hydrogel formulations composed of GelMA – PEGDA polymers at different macromer concentrations. (a) Graph shows the mass remaining of the hydrogels after incubation with collagenase at different time points. The concentrations tested were 7.5% (w/v) $GelMA_5$ – 5% (w/v) PEGDA (black-solid square), 7.5% (w/v) $GelMA_{1.25}$ – 5% (w/v) PEGDA (black-hollow square), 5% (w/v) $GelMA_{1.25}$ – 2.5% (w/v) PEGDA (grey-hollow circle) and 5% (w/v) $GelMA_{1.25}$ – 1.25% (w/v) PEGDA (light grey-hollow triangle). Values are represented as the mean ± SD (n=3). (b) Pictures of the hydrogels at 0 h, 2 h, and 6 h after being treated with collagenase solution.

4.9.5. Gel fraction measurements

Gel fraction or crosslinking degree, which is a measurement of the polymerization reaction efficiency, was determined for the hydrogels made of polymer formulations described in Table 4.1 as a function of the UV energy exposure dose. As it can be appreciated in Figure 4.32, the gel fraction displayed similar trends for samples containing $GelMA_5$ or $GelMA_{1.25}$. Moreover, the polymerization curves were comparable to the ones obtained previously described for 7.5% $GelMA_5$ – 5% PEGDA (section 4.4.6). The crosslinking degree increased as the energy dose applied increased until energy

doses of ≈4 J·cm^{-2}. After that, despite the energy dose was increased, the crosslinking degree did not change, suggesting that at that point the maximum possible conversion had already been achieved. When applying an energy dose of 2 J·cm^{-2}, close to the one used to fabricate our hydrogels, the degree of crosslinking was not significantly changed between hydrogels. All samples, regarding their macromer content or DoF of the GelMA polymer, showed a similar crosslinking degree, with gel fraction values around ≈42%.

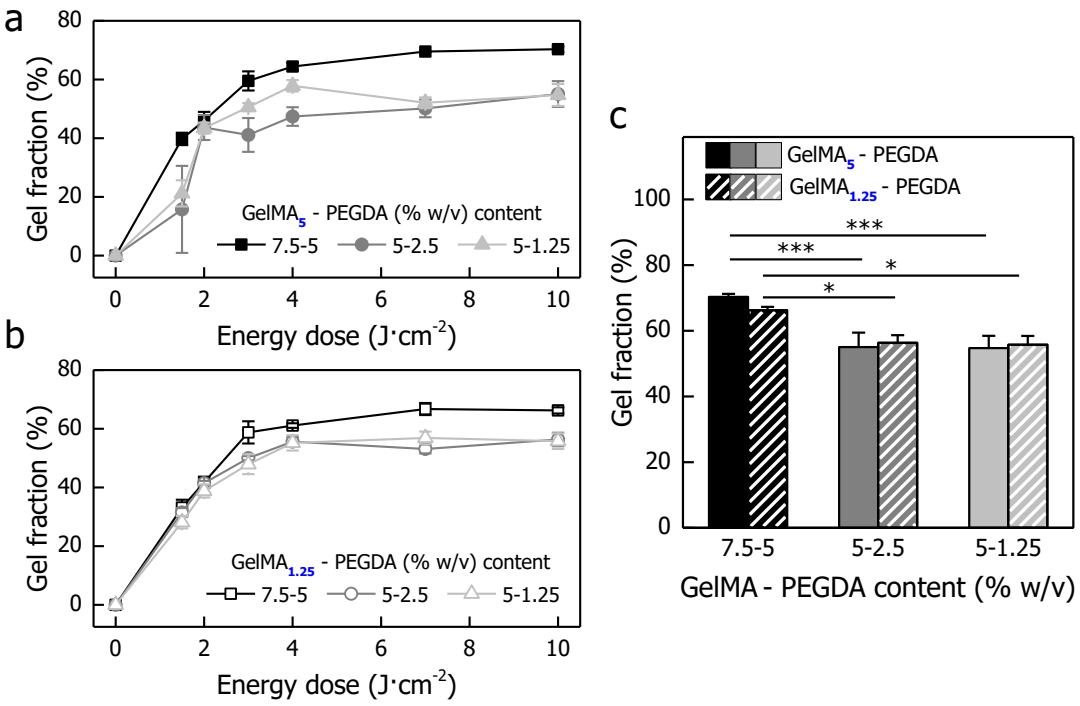

Figure 4.32. Gel fraction or crosslinking degree for new hydrogel formulations composed of GelMA – PEGDA polymers at different macromer concentrations: 7.5% (w/v) – 5% (w/v) (dark), 5% (w/v) – 2.5% (w/v) (grey) and 5% (w/v) – 1.25% (w/v) (light grey). The degree of crosslinking was examined as a function of UV energy dose for (a) GelMA$_5$ – PEGDA (solid squares) and (b) GelMA$_{1.25}$ – PEGDA (hollow circles) co-networks. (c) Maximum gel fraction value after polymerizing GelMA$_5$ – PEGDA (solid) and GelMA$_{1.25}$ – PEGDA (stripes) hydrogels under an UV energy dose of 10 J·cm^{-2}. Values are showed as the mean ± SD (n=3). **p<0.005 and ***p<0.001.

In contrast, for energy doses higher than 4 J·cm^{-2}, the gel fraction values obtained did not significantly change with the DoF of GelMA, but they showed a statistically significant dependence on the total macromer content of the polymer (Figure 4.32 (c)). Van Nteuwenhove *et al.*[319] reported that for GelMA hydrogels with a degree of functionalization of 72% the gel fraction obtained was 94%, while for GelMA hydrogels with a degree of functionalization of 95% the gel fraction was 98%. We hypothesize that the gel fraction values did not present any significant differences when the DoF of GelMA was changed because the DoF between GelMA$_5$ (75.4±2.1%) and GelMA$_{1.25}$

(51.4±3.7%) did not differ enough to obtain differences in the gel fraction. In other words, the number of crosslinking points in hydrogels containing $GelMA_{1.25}$ were already enough to efficiently crosslink all the GelMA molecules between them and, thus, gel fraction was not modified. However, the density of crosslinking points is increased in the samples with higher DoF, which results in modifications of the mechanical and physicochemical properties of the hydrogels.

Overall, the analysis of all the characterization studies performed for the hydrogel formulations listed in Table 4.1 suggests that decreasing the total macromer content and/or the DoF of GelMA could be beneficial to improve the results of the cell experiments without compromising the stability of the platform. We have found that decreasing the DoF of GelMA polymer, the mechanical and degradation properties were highly affected, while when decreasing the total macromer content in GelMA – PEGDA formulations these properties did not change so drastically. For this reason, first we decided to focus our efforts in studying the effects that decreasing the total macromer content of the GelMA – PEGDA formulations had on the cell behaviour, both on the stromal and on the epithelial cells.

4.10. Influence of the total macromer composition of GelMA – PEGDA hydrogel co-networks to mimic the intestinal mucosa

In this study, we explored the effects of diminishing the total macromer content on the suitability of GelMA – PEGDA hydrogels to produce *in vitro* tissue models of the intestinal mucosa. According to the results obtained in the previous sections, decreasing the total macromer content increases hydrogel swelling and decreases significantly the mechanical properties of the networks obtained. Hydrogels containing GelMA polymers of high DoF ($GelMA_5$) and two total macromer compositions (7.5% and 6.25% (w/v)) were included in this study.

4.10.1. Effects of total macromer content on the fibroblasts embedded within GelMA – PEGDA hydrogel co-networks

To evaluate cell behaviour on the hydrogels formed from these polymer solutions, hydrogels with and without encapsulated fibroblasts were fabricated. Polymer

solutions (5% (w/v) $GelMA_5$ – 2.5% (w/v) PEGDA and 5% (w/v) $GelMA_5$ – 1.25% (w/v) PEGDA) were mixed with the photoinitiator at a concentration of 0.5% (w/v). For the fibroblast-laden hydrogels, NIH/3T3 fibroblasts were added to the mixture at a density of $5 \cdot 10^6$ cells·mL^{-1}. Then, disc-shaped hydrogels were obtained on porous membranes by UV exposure at a dose of 1.88 J·cm^{-2}, and were mounted on Transwell® inserts (see section 3.8.2). Results on cell behaviour were compared to 7.5% (w/v) $GelMA_5$ – 5% (w/v) PEGDA hydrogels (with 12.5% (w/v) of the total macromer content) reported in previous sections of this manuscript.

The distribution, the morphology and the ability to synthesize collagen IV of the NIH/3T3 cells embedded in the hydrogels were examined through immunostaining after 8 days in culture, as it has been reported that for embedded single cells there is a lag period of 7 days from encapsulation to their spreading[313,320,321]. Figure 4.33 shows representative fluorescent confocal microscopy pictures for the surface and the inside of the hydrogels at day 8 after encapsulation. DAPI (nuclear marker) signal shows that for both 5% (w/v) $GelMA_5$ – 2.5% (w/v) PEGDA and 5% (w/v) $GelMA_5$ – 1.25% (w/v) PEGDA hydrogels, NIH/3T3 were found in larger amounts on the surface that at inside the samples. F-actin signal revealed that cells on the surface had a spread morphology and well-developed actin cytoskeleton. Paying close attention to the F-actin signal inside of the hydrogels, we could observe a loss of the cell round shape and filopodia formation at their edges. Regarding cell proliferative capacity (Ki-67 marker), in general inside the hydrogels cells had low proliferation compared to the surface. Collagen IV staining showed that for both hydrogels NIH/3T3 cells were functionally active by producing and secreting collagen IV. Although this trend was more noticeable on the surface than inside the hydrogel, this ability was not limited by the cell localization. Comparing the immunostainings of these two hydrogels that contain total macromer contents of 7.5% (w/v) and 6.25% (w/v) (Figure 4.33) with the previous hydrogel that has a total macromer content of 12.5% (w/v) (Figure 4.17) at day 8 and 7, respectively, we could observe that the main difference is the morphology of the encapsulated cells.

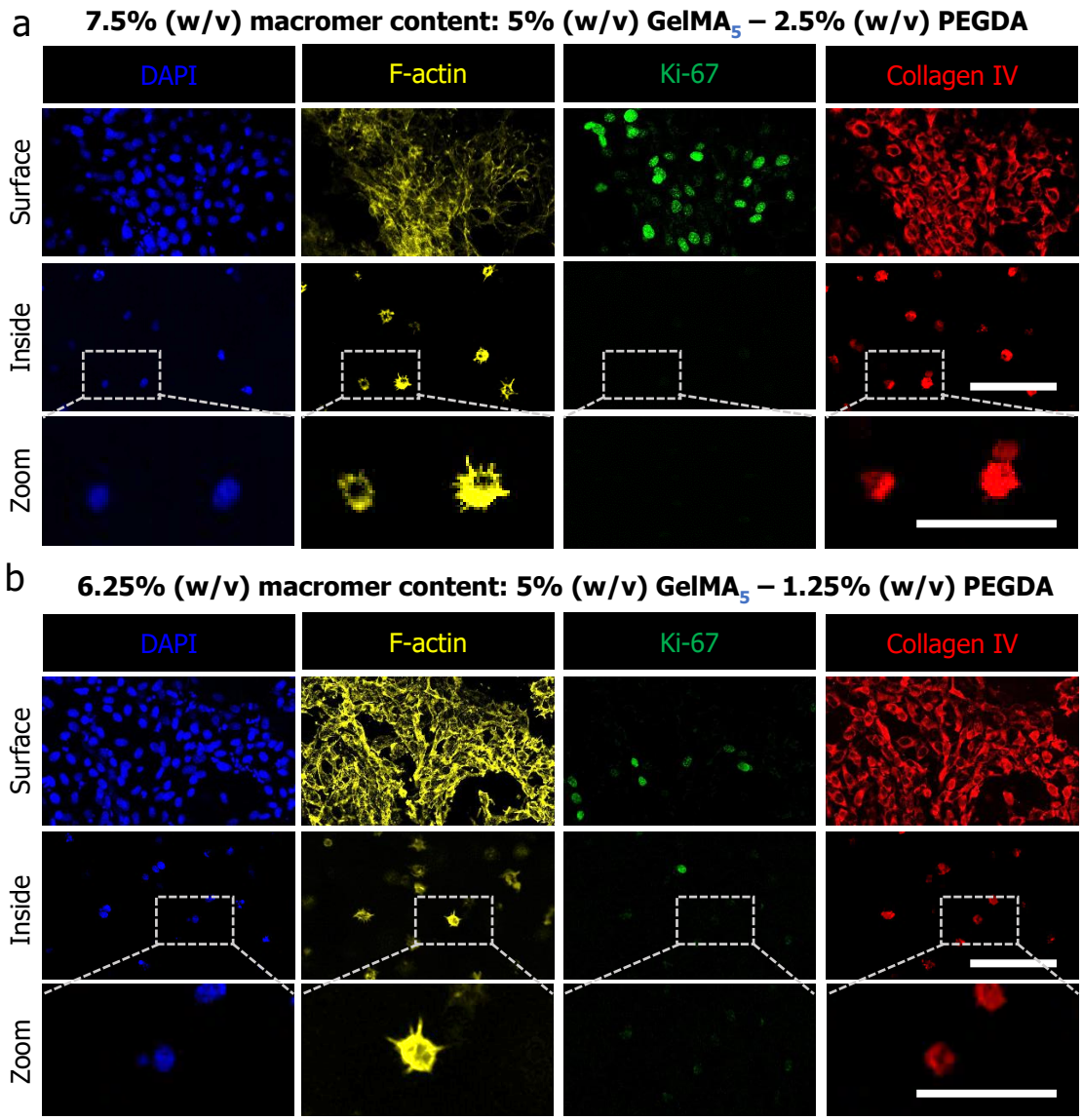

Figure 4.33. Immunostaining for DAPI, F-actin, Ki-67 and Collagen IV at day 8 after NIH/3T3 cells encapsulation in (a) 5% (w/v) $GelMA_5$ – 2.5% (w/v) PEGDA and (b) 5% (w/v) $GelMA_5$ – 1.25% (w/v) PEGDA, showing stacks of the hydrogel surface (top panels), of inside the hydrogel (middle panels), and a zoom (bottom panels). Scale bars: 100 μm (top and middle panels) and 50 μm (bottom panels).

To evaluate how cell morphology evolved over cell culture time on these hydrogels, samples were analysed at day 15 of culture, following the same immunostaining as in day 8. Figure 4.34 shows that cells grew well on the surface of both hydrogel co-networks. Furthermore, after 15 days of culture, again both hydrogels retained cells in their inside (DAPI staining). Remarkably, analysing the actin cytoskeleton, we observed that the encapsulated cells presented a much less rounded shape and an increase in the formation of filopodia compared to day 8 of culture. On the

other hand, the synthesis of collagen IV was not altered, indicating that the fibroblasts retained their functionality after being encapsulated for 15 days

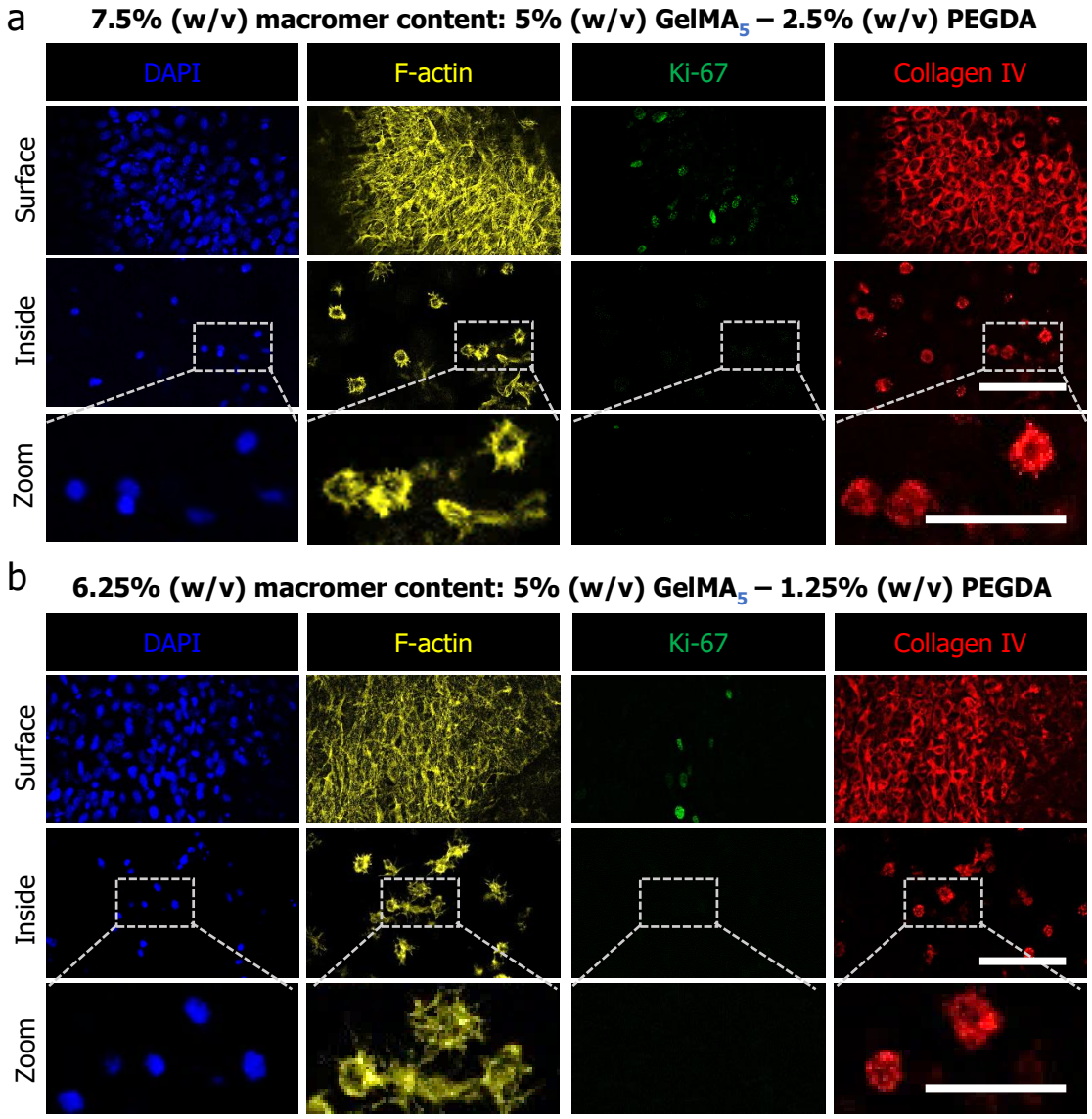

Figure 4.34. Immunostaining for DAPI, F-actin, Ki-67 and Collagen IV at day 15 after NIH/3T3 cells encapsulation in (a) 5% (w/v) $GelMA_5$ – 2.5% (w/v) PEGDA and (b) 5% (w/v) $GelMA_5$ – 1.25% (w/v) PEGDA, showing stacks of the hydrogel surface (top panels), of inside the hydrogel (middle panels), and a zoom (bottom panels). Scale bars: 100 μm (top and middle panels) and 50 μm (bottom panels).

At 15 days of culture, it was visible that cells encapsulated in the samples containing the lowest total macromer content (6.25% (w/v)) exhibited more spread morphologies. Nevertheless, to get quantitative data about cell morphological features with respect to the macromer content of the hydrogels, the F-actin signal was used to compute the circularity of the embedded fibroblasts (Figure 4.35). We found statistically significant differences in cell circularity for both days 8 and 15 of cell culture. At both

time points hydrogels with less macromer content (6.5% (w/v)) permitted further spreading of the cells embedded within them.

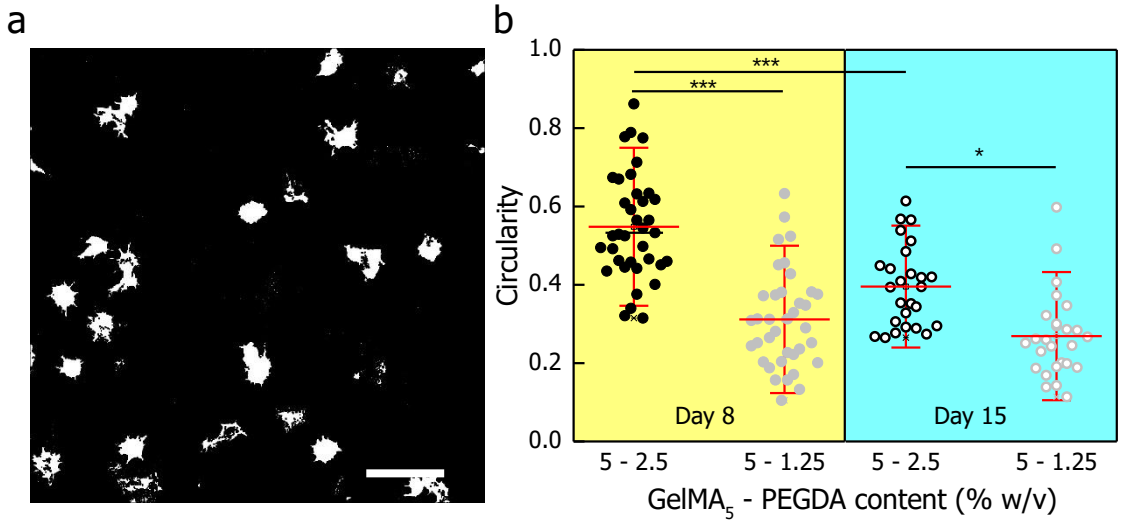

Figure 4.35. Cell morphology studies by analyzing the circularity of embedded cells. (a) A binary image of 5% (w/v) $GelMA_5$ – 1.25% (w/v) PEGDA at day 15. Scale bar: 50 µm. (b) Plot of the circularity of fibroblasts embedded in 5% (w/v) $GelMA_5$ – 2.5% (w/v) PEGDA and 5% (w/v) $GelMA_5$ – 1.25% (w/v) PEGDA hydrogels after 8 days in culture (light yellow) and 15 days in culture (light blue). Values are showed as the mean ± SD (Day 8 n=37; Day 15 n=26). *p<0.05, ***p<0.001.

These data suggested that decreasing the total amount of polymer content, the embedded cells were less restrained by the hydrogel matrix and were able to start spreading.

4.10.2. Effects of total macromer content of the growth of epithelial cells on top of GelMA – PEGDA hydrogel co-networks

Subsequently, the growth of the Caco-2 epithelial monolayers was studied on the 5% (w/v) $GelMA_5$ – 2.5% (w/v) PEGDA and 5% (w/v) $GelMA_5$ – 1.25% (w/v) PEGDA hydrogels that did not contain embedded fibroblast. To do that, both 7.5% (w/v) and 6.25% (w/v) hydrogel co-networks without fibroblasts were fabricated on porous membranes applying a UV energy dose of 1.88 $J \cdot cm^{-2}$, and were mounted on Transwell® inserts (see section 3.8.2). Then, Caco-2 cells were seeded, at a density of $7.5 \cdot 10^6$ $cells \cdot cm^{-2}$, on top of the hydrogel surfaces. The growth of the epithelial monolayers was tracked periodically by measuring TEER values for a period of 21 (Figure 4.36). The evolution of the TEER values with the cell culture time was similar for both types of

hydrogels. As we noticed with the 12.5% (w/v) hydrogels (reported in section 4.8.1), there was a lag period of about 8 to 10 days for the epithelial monolayer formation and maturation, followed by an period of exponential growth. Finally, around day 18 of cell culture, the epithelial monolayer was completely packed and, thus, the TEER values reached a plateau. As it is shown in Figure 4.36, there were no significant differences in the TEER values between both hydrogel formulations tested, suggesting that the quality of both epithelial monolayers formed was similar. At this point, we should recall that there were no differences in the hydrogel stiffness values obtained by AFM measurements (Figure 4.30 (b)).

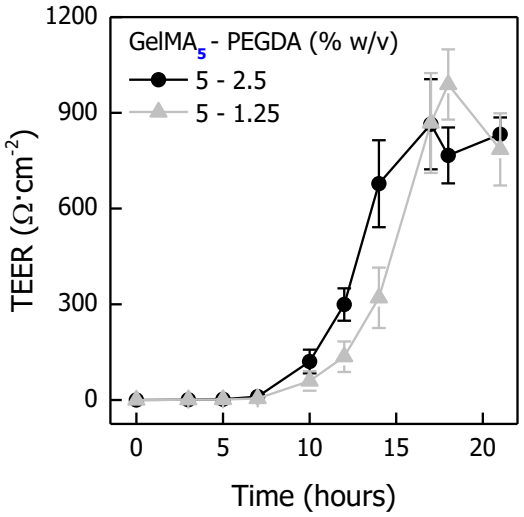

Figure 4.36. Transepithelial electrical resistance (TEER) as function of cell culture time for epithelial cells cultured on top of hydrogels composed of 5% (w/v) $GelMA_5$ – 2.5% (w/v) PEGDA (black-solid circles) and 5% (w/v) $GelMA_5$ – 1.25% PEGDA (light grey-solid triangles). Values are presented as the mean ± SD (n=4).

In general, these results show that decreasing the total macromer content of the hydrogel formulations, and so the stiffness of the hydrogels, did not affect the formation of a well-developed epithelial barrier. It is noteworthy that the decrease of the total polymer content favoured the mass transport of molecules within the hydrogel, causing fibroblasts to be more spread. According to these results, we decided to continue our studies employing the hydrogel with less polymer content (6.25% (w/v)). The next step was to study whether the DoF of GelMA might also positively influence on the shape and the functionality of the embedded fibroblasts due to the modification of mass transport within the hydrogel co-networks without affecting the properties of the epithelial barriers.

4.11. Influence of the degree of functionalization of GelMA polymer in the epithelial monolayer formation onto GelMA – PEGDA hydrogel co-networks

To check for the impact of the DoF of the GelMA polymer on the performance of the intestinal mucosa constructs, we decided to set the total macromer content as 6.25%(w/v) and investigate if by using $GelMA_{1.25}$ instead of $GelMA_5$ the resulting hydrogel co-network was still able to sustain the growth of functional epithelial monolayers. For this purpose, disc-shaped hydrogels (without fibroblasts) were fabricated from 5% (w/v) $GelMA_{1.25}$ – 1.25% (w/v) PEGDA polymer solutions as stated above and were mounted on Transwell® inserts. Caco-2 cells were seeded on their surface at a density of $7.5 \cdot 10^5$ cells·cm^{-2} and were cultured for 21 days. Their performance was benchmarked with samples fabricated from 5% (w/v) $GelMA_5$ – 1.25% (w/v) PEGDA and with Caco-2 cells cultured on the porous membranes of Transwell® inserts. Caco-2 cells growth and formation of epithelial barrier were studied by monitoring TEER over the cell cultured period. Finally, at day 21 of cell culture, we evaluated the apparent permeability of the monolayers. As controls, TEER and P_{app} was also evaluated for samples without cells on top to discard significant impacts of the hydrogels in the electrical resistance or permeability properties.

TEER values obtained for the monolayers growing on the hydrogels (Figure 4.37 (a)), shows that they presented diminished TEER values with respect to the samples grown on Transwells® and that TEER was basically zero on hydrogels without cells (data not represented in the graph). In addition, on the samples containing $GelMA_{1.25}$, TEER at day 21 was half of the value obtained for samples with the same polymer content but fabricated with $GelMA_5$. This contrasts with the non-significant differences produced in the TEER values obtained for hydrogels containing $GelMA_5$ when the macromer content was changed (Figure 4.36). Therefore, it appears that on our hydrogels the epithelial barrier formation is mostly influenced by the DoF of GelMA polymer and not by the total macromer content within the range of parameters assayed.

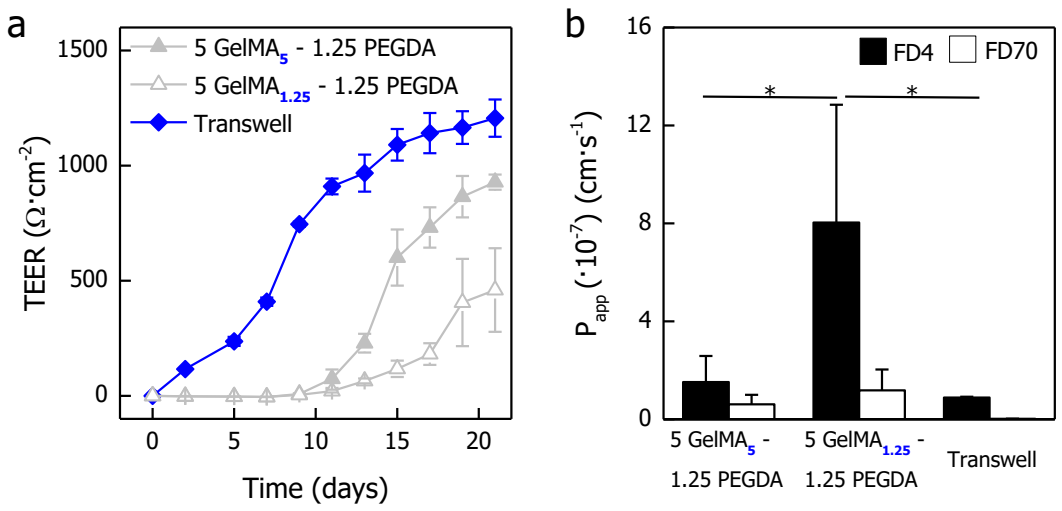

Figure 4.37. Epithelial barrier properties of GelMA – PEGDA hydrogels co-networks of high and low DoF. (a) TEER evolution as function of cell culture time on hydrogels with a total macromer content of 6.25% (w/v) and on Transwells® inserts. (b) P_{app} of FITC-dextran 4 kDa (FD4) (black) and Rhodamine-dextran 70 kDa (FD70) (white) at day 21 of culture on hydrogels with a total macromer content of 6.25% (w/v) and on Transwells® inserts. Values are the mean ± SD (n=3). *p<0.05.

To further characterize the epithelial barriers formed, we investigated their apparent permeability to small size dextran (FD4) as a tracer for paracellular transport through tight junctions while the medium size dextran (FD70) was used as a positive control to confirm that tight junctions were tightly formed and corroborate that big size molecules were not able to pass through the epithelial monolayers (Figure 4.37 (b)). First, we checked that the apparent permeability for these compounds when no cells were present was larger (≈$3 \cdot 10^{-5}$ cm·s^{-1}), so the gels themselves were not creating a permeability barrier. Hydrogels without cells did not place any physical restriction on the mobility and diffusion of molecules at least up to 12 nm of hydrodynamic radius. When the cell barriers were present, for the FD4 dextran molecules, the permeability was enhanced by ≈10-fold for the hydrogels containing GelMA polymer of low DoF (5% (w/v) $GelMA_{1.25}$ – 1.25% (w/v) PEGDA) compared to the hydrogels with the same amount of macromers but GelMA polymer of high DoF (5% (w/v) $GelMA_5$ – 1.25% (w/v) PEGDA), as well as for monolayers grown onto porous membranes (Figure 4.37 (b)). These findings agreed with the low TEER values measured for monolayers grown on the 5% (w/v) $GelMA_{1.25}$ – 1.25% (w/v) PEGDA hydrogels. Regarding FD70, non-significant differences were found on the epithelial monolayers formed on the samples containing $GelMA_{1.25}$ or $GelMA_5$. This indicates that despite the differences on the FD4 permeability,

the epithelial monolayer on top of both hydrogels was well-formed, because it did not allow the permeability of larger molecules such as FD70.

In general, these results indicated that regardless of the total macromer content of the hydrogel, the DoF of GelMA polymer was a relevant factor that affected the formation of the epithelial monolayers. We hypothesized that the alterations in the epithelial barrier caused by the changes on the DoF of GelMA polymer were due to the changes in the mechanical properties of the hydrogels. The fact that hydrogel stiffness affects cell behaviour is in agreement with other studies found in the literature[193,288]. We then considered the epithelial monolayers obtained on these soft hydrogels (low DoF, low macromer content) as more physiologically relevant barriers than the ones growing on standard hard porous membranes, which exhibit TEER values that do not correlate well with *in vivo* TEER measurements[306].

4.12. GelMA – PEGDA hydrogel co-networks of low macromer content and low degree of functionalization of GelMA to develop 3D models of the intestinal mucosa

4.12.1. Studies of cell density variation within the stromal compartment

Tissue engineered constructs of the intestinal mucosa were then generated taking into consideration the results of the previous sections and using GelMA of low DoF and polymer solutions of low macromer content. As we just measured, Caco-2 epithelial monolayers were able to grow on top of them and formed functional tissue barriers. Regarding the stromal component, it has been reported that when working with scaffolds with low mechanical stability and integrity, increasing the cell density might be beneficial due to the higher production and secretion of ECM components, such as collagen, by the embedded cells[322,323]. Varying cell density, cell to cell distance is decreased and, consequently, the paracrine signalling profile between cells is altered, modulating cell behavior[324].

Following these findings, we decided to increase the density of the encapsulated cells, 1.5 and 2-folds. To do that, NIH/3T3 fibroblasts, at densities of $7.5 \cdot 10^6$ cells·mL^{-1}

and $10 \cdot 10^6$ cells·mL^{-1}, were mixed with GelMA – PEGDA polymer solutions composed of 6.25% (w/v) macromer content and $GelMA_{1.25}$ polymer (5% (w/v) $GelMA_{1.25}$ – 1.25% (w/v) PEGDA). Disc-shaped hydrogels were fabricated as previously explained and mounted on Transwell® inserts. Caco-2 cells were then seeded onto the hydrogel surfaces one day after encapsulation and the constructs were cultured for 21 days. For comparison, hydrogels containing the same macromer content (6.25% (w/v)) but $GelMA_5$ (high DoF) in their formulation (5% (w/v) $GelMA_5$ – 1.25% (w/v) PEGDA) were also added to the experiment. On all these samples, the formation of epithelial monolayers was studied through periodic monitoring of the TEER values for 21 days. TEER values were normalized the values obtained at day 21 for the hydrogels containing $GelMA_{1.25}$ and an initial density of encapsulated cells of $7.5 \cdot 10$ cells·mL^{-1}. These results were plotted in Figure 4.38.

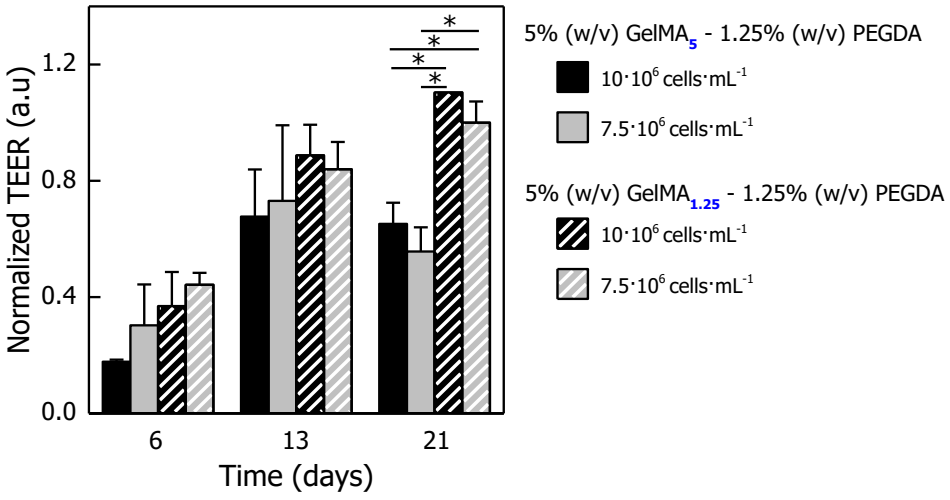

Figure 4.38. TEER measurements to evaluate the epithelial monolayer formation when Caco-2 cells were seeded on top of 5% (w/v) $GelMA_5$ – 1.25% (w/v) PEGDA (solid) or on 5% (w/v) $GelMA_{1.25}$ – 1.25% (w/v) PEGDA (striped), and the density of the encapsulated cells were $10 \cdot 10^6$ cells·mL^{-1} (black) or $7.5 \cdot 10^6$ cells·mL^{-1} (light grey). Values are presented as the mean ± SD. (almost n=2 or 3). *$p<0.05$

TEER was increasing through the culture period and its maximum values at day 21 did not present any significant differences between the two fibroblast densities employed on the same polymer formulation. Nevertheless, at day 21 TEER values were higher on the samples fabricated with the GelMA polymer with the lowest DoF ($GelMA_{1.25}$) than on the samples containing GelMA with high DoF ($GelMA_5$). Noticeable, this was the opposite when Caco-2 cells grown in the absence of fibroblasts (Figure 4.37 (a)). This

result points out the potential key role of the stromal compartment in the growth of the epithelial monolayers.

To gain more insights, firstly fibroblasts distribution and morphology were examined periodically taking representative bright field pictures from the bulk of the hydrogels (Figure 4.39). Figure 4.39 shows that for the low polymer content (6.25% (w/v)) the embedded cells were found within the hydrogel during the 21 of cell culture independently of the DoF of the GelMA polymer,.

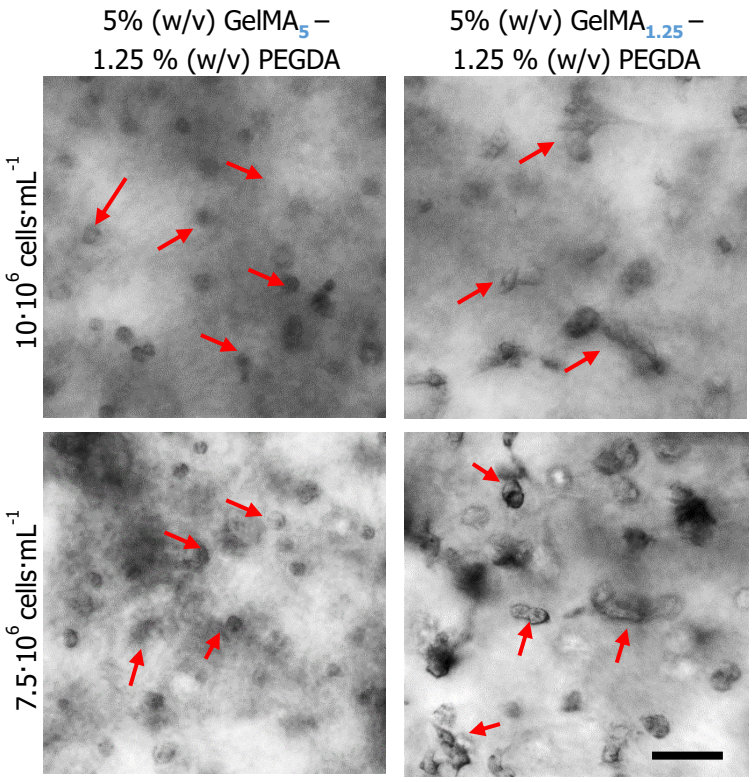

Figure 4.39. Bright field images of fibroblasts embedded in 5% (w/v) $GelMA_5$ – 1.25% (w/v) PEGDA (left) and 5% (w/v) $GelMA_{1.25}$ – 1.25% (w/v) PEGDA (right) co-networks at a density of $10 \cdot 10^6$ cells·mL^{-1} (upper panels) and $7.5 \cdot 10^6$ cells·mL^{-1} (bottom panels) at day 21 after cell encapsulation. Red arrows show the fibroblasts inside the hydrogel co-networks. Scale bar: 50 µm.

When comparing these results with those obtained for hydrogels with high macromer content (12.5% (w/v)), we can conclude that cell distribution is affected by the total macromer content. Decreasing the percentage of polymer creates a less densely packed network and improves the diffusion of molecules. Because of that, cells were uniformly distributed along the whole thickness of the hydrogels.

Regarding hydrogels containing GelMA polymer with low DoF ($GelMA_{1.25}$), we saw that fibroblasts acquired a more stretched morphology than in samples with GelMA

polymer of high DoF ($GelMA_5$). This change in cell morphology might be due to the significant changes in the mechanical properties. In soft hydrogels ($GelMA_{1.25}$) fibroblasts were elongated and spread over all hydrogel whereas in the harder hydrogels ($GelMA_5$) fibroblasts have a more rounded shape. These results are in agreement with the ones reported by Li *et al.*[189] who found that cells showed round morphologies within hydrogels with high degree of functionalization and high stiffness . Finally, with respect to the two cell densities studied ($10 \cdot 10^6$ cell·mL^{-1} and $7.5 \cdot 10^6$ cell·mL^{-1}) no differences in cell distribution or morphology were visually appreciated on the bright field images (Figure 4.39). Altogether, these results indicated that the microenvironment conditions such as matrix stiffness were more relevant than the encapsulation cell density to influence the cellular response.

To better characterize the tissue engineered constructs formed on the 5% (w/v) $GelMA_{1.25}$ – 1.25% (w/v) PEGDA hydrogels, samples were histologically processed and cross-sections were immunostained and imaged by confocal microscopy (Figure 4.40). Images of cell nuclei (DAPI), and actin cytoskeleton (F-actin) showed the presence of two distinctive compartments the epithelial monolayer and the stromal region. Cells forming the epithelial monolayer appear to be columnar in shape and polarized (F-actin was accumulated at their apical side) and their nuclei, particularly at day 21 (Figure 4.40 (b)), wew highly elongated and oriented with the large axes of a fitting ellipse perpendicular to the surface (Figure 4.40 (a)). On the other hand, the distribution, the morphology and the ability to secrete ECM proteins by the fibroblasts encapsulated was also qualitatively evaluated. Both at days 14 and 21 of the culture, DAPI signal confirmed the presence of fibroblasts within the bulk of the hydrogels. F-actin signal clearly showed that, in contrast with the results obtained for previous formulations of the hydrogel co-networks (Figure 4.24), the embedded fibroblasts were well spread. In addition, some cells in the hydrogel core were arranged perpendicularly to the epithelial monolayer and presented a migrating phenotype. Actually, at both days 14 and 21, we identified fibroblasts clusters right below the epithelial monolayer, thus confirming that the network allowed cell migration and the intimate interaction between the two cell types.

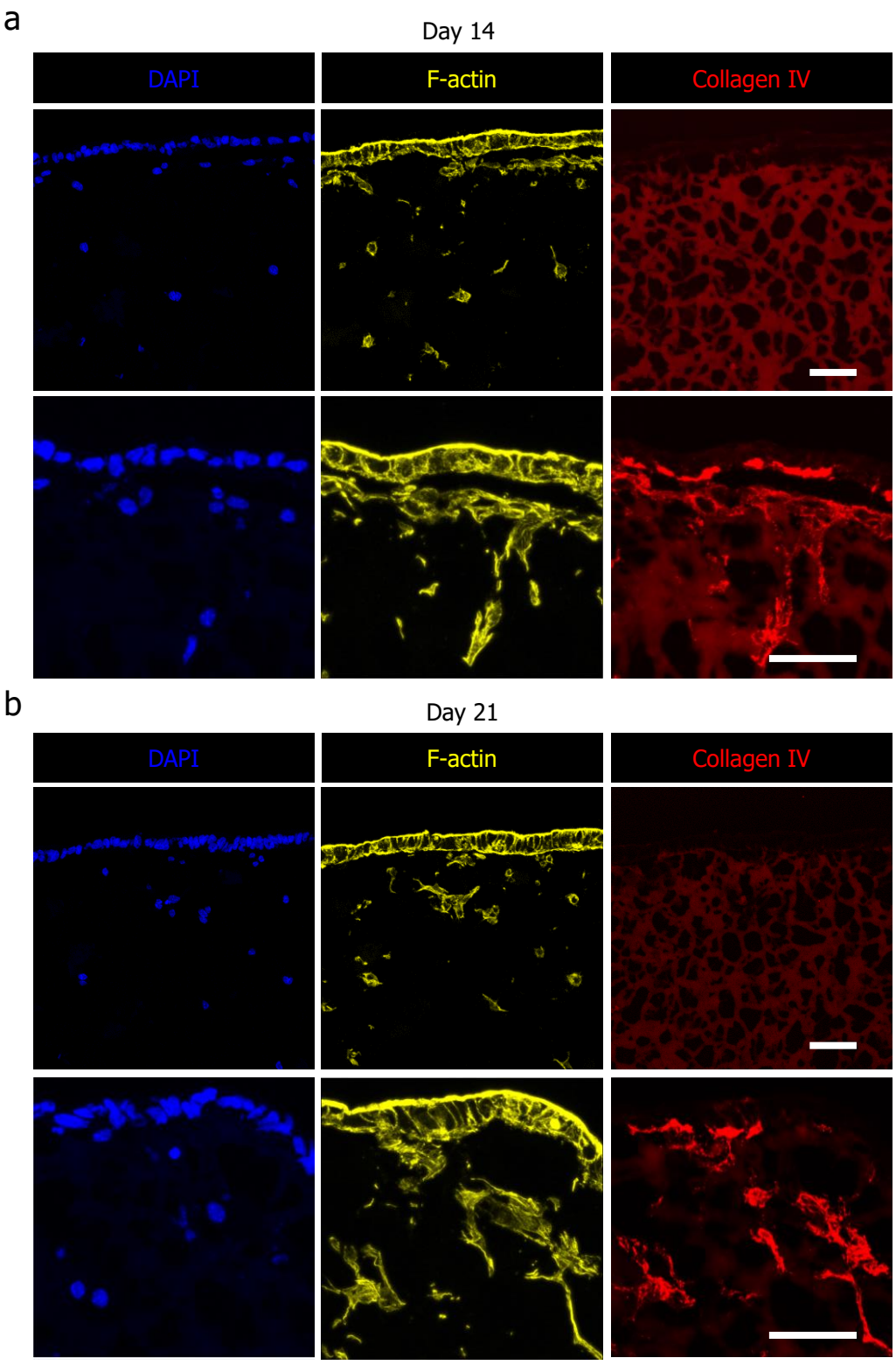

Figure 4.40. Interaction between Caco-2 and NIH/3T3 cells in 5% (w/v) $GelMA_{1.25}$ – PEGDA hydrogels. Samples were immunostained for DAPI, F-actin and Collagen IV at day (a) 14 and (b) day 21, after seeding the Caco-2 cells. General view of the cell distribution (a and b top panels) and a detailed view of the cell morphology (a and b bottom panels). Scale bar: 50 μm.

Finally, expression of collagen IV was observed within the fibroblast cytoplasm and accumulated under the epithelial basement membrane, suggesting that the fibroblasts were able to synthetize and secrete ECM proteins. This results are in contrast with those obtained for the hydrogel composition with high macromer content (12.5% (w(v)) and high DoF ($GelMA_5$) previously described. Overall, based on our results, we can propose our GelMA – PEGDA hydrogel co-networks composed of 5% (w/v) $GelMA_{1.25}$ – 1.25% (w/v) PEGDA polymers as good candidates to produce *in vitro* models of the intestinal mucosa due to the capability to better recapitulate *in vivo* interactions between epithelial and stromal cells.

4.13. Generation of a biomimetic *in vitro* model of the intestinal mucosa

In all the previous experiments, we used a murine embryonic fibroblast cell line to mimic the stromal compartment of the tissue engineered intestinal mucosa. The reasons for this choice were twofold. First, NIH/3T3 cells are a well-standardized cell model easy to handle and with a high proliferative capacity. Second, NIH/3T3 cells have been used as the gold standard feeder layers to support the culture of other cells, including stem cells[244]. However, to produce a biomimetic model of the human intestinal mucosa, it would be interesting to use a more appropriate cell source for the stromal compartment. As Caco-2 cells are epithelial cells from human colon, we then chose CCD-18Co cell line. CCD-18Co are cells from human neonatal colon, which have already been used to mimic the myofibroblast cells found in the stromal component of *in vitro* intestinal models[112,301,325]. It has been reported that one of the major functions of the *in vivo* myofibroblasts is to support the growth and differentiation of the epithelial layer[326–328]. It is known that CCD-18Co cell line plays a relevant role in the regulation of the intestinal response, influencing epithelial cell proliferation, differentiation or cytokine release[329]. For the above mentioned reasons, we selected CCD-18Co cells to mimic the functions of the *in vivo* myofibroblasts in the intestinal mucosa tissue.

We then studied the influence of CCD-18Co cells on the growth of the epithelial monolayers and on the epithelial barrier integrity. CCD-18Co cells at a density of $7.5 \cdot 10^6$ cells·mL^{-1} were mixed with 5% (w/v) $GelMA_{1.25}$ – 1.25% (w/v) PEGDA polymer solution and disc-shaped hydrogel co-networks were fabricated following the previous reported protocol (section 3.8.2 and 3.9). Hydrogel samples were then mounted in Transwell®

inserts and Caco-2 cells at a density of $7.5 \cdot 10^6$ cells·cm^{-2} were seeded on top. As controls, (I) hydrogel samples with CCD-18Co cells but without Caco-2 cells, (II) hydrogels without CCD-18Co but with Caco-2 cells, and (III) Caco-2 cells grown on hard porous membranes of Transwell® inserts were added to the experiments.

TEER measurements were performed throughout the cell culture period to monitor the epithelial barrier formation. As depicted in Figure 4.41, TEER increased as a function of time in all samples that had epithelial cells. TEER values for samples only having CCD-18Co were undistinguishable from the background, so even at relatively high loading densities the cell-laden hydrogels did not create electrical resistance. The epithelial monolayer formed on the hard porous membrane of the Transwell® inserts presented high TEER values, which is in agreement with the literature[259]. On the contrary, Caco-2 cells seeded on the hydrogels exhibited much lower TEER values. Upon including CCD-18Co cells within the hydrogels, TEER values of the epithelial barrier considerably increased, analogously to what happened when including the NIH/3T3 cells. Moreover, TEER parameter started to increase at earlier time culture points than for samples void of fibroblasts. Therefore, the presence of the myofibroblasts appeared as enhancing both the growth rate of the epithelial monolayers and the tightness of the barriers formed.

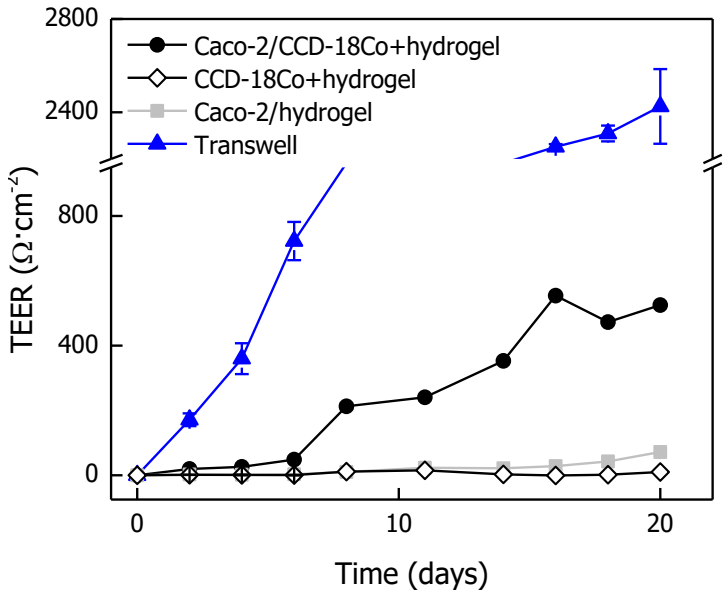

Figure 4.41. TEER values of Caco-2 cells seeded on hydrogels with and without CCD-18Co cells (myofibroblasts) or in Transwell® inserts. Additionally, hydrogels containing only CCD-18Co cells were included in the study. Values are shown as the mean ± SD (n=3 until day 7; n=2 until day 14, n=1 until day 20, except for Transwell® inserts n=3).

In literature, it has been considered the positive role of stromal cells, and myofibroblasts in particular, on the restoration of the intestinal epithelial barriers. Effects derived from cell-cell contact interactions, paracrine signalling and remodelling of ECM have been proposed to contribute to barrier restoration events[326,328]. Conventional *in vitro* models used to these cell-cell effects are based on a monoculture of Caco-2 monolayers on top of Transwell® inserts and stromal cells on the bottom of the well-plate. Therefore, the cells of both compartments are not in close contact as are in the native tissue. Consequently, cell-cell physical interactions, paracrine signalling, as well as matrix remodelling, within those simplistic setups are not well represented[330]. In here, we used our 3D model of the intestinal mucosa to explore the cell interaction between stroma and epithelial compartment. To do that, the tissue engineered constructs containing the CCD-18Co and Caco-2 cells, were histologically cut and immunostained for the nuclei (DAPI), cytoskeleton (F-actin) and cell functionality (Collagen IV) and imaged by confocal microscopy. Figure 4.42 shows that the model developed allow us to mimic the two compartments of the intestinal tissue, the epithelial monolayer and the stromal region. Analysing the epithelial monolayer it was observed that at day 7 (Figure 4.42 (a)), cell nuclei did not acquire the columnar shape and F-actin appeared in the apical and basolateral parts, so cells were not well polarized. However, at day 20 of culture, cells forming the epithelial monolayer were completely polarized, with their nuclei elongated perpendicularly to the basement membrane, columnar shape, and F-actin mainly found in the apical region (Figure 4.42 (b)). In relation to the stromal compartment, the DAPI signal shows that during the three weeks of cell culture the distribution of CCD-18Co cells throughout the GelMA – PEGDA hydrogel co-networks remained homogenous. In addition, comparing the first and the third week of cell culture, the density of the encapsulated cells did not decrease, indicating that hydrogel co-networks supported the growth of embedded cells.

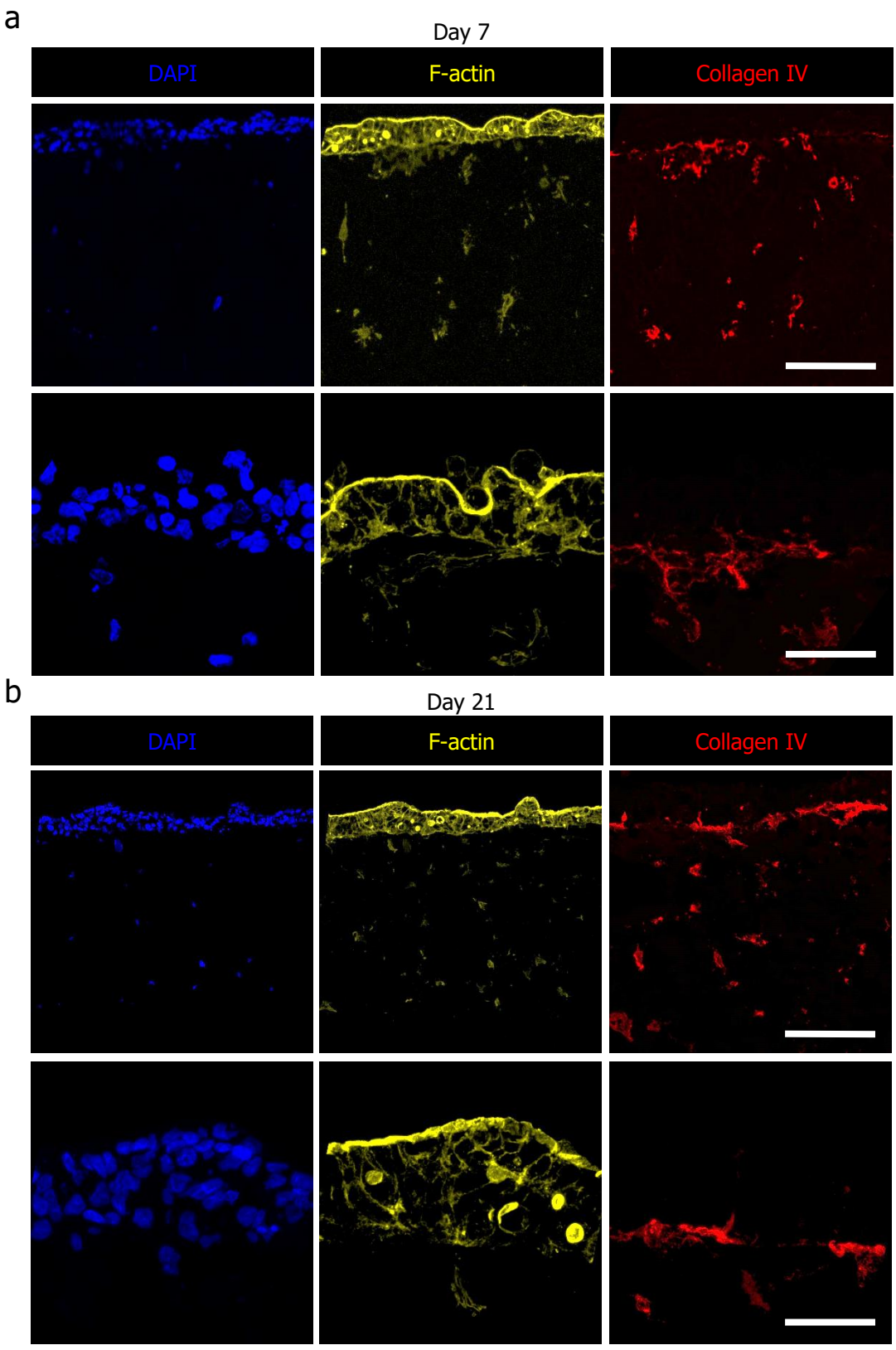

Figure 4.42. Immunostaining for DAPI, F-actin and Collagen IV of 5% (w/v) $GelMA_{1.25}$ – 1.25% (w/v) PEGDA hydrogel co-networks with embedded CCD-18Co myofibroblasts and epithelial monolayers after (a) 7 days and (b) 21 days in culture. Images show an overview of the cell distribution inside the hydrogel (top panel) and cell organization under the epithelial layer (bottom panel). Scale bars: 200 μm (top panel) and 50 μm (bottom panel).

Analysing the cytoskeleton morphology through the F-actin staining, almost all embedded cells were stretched, elongated, and in some cases, were perpendicular to the surface, suggesting a migrating phenotype toward the epithelial monolayer. In particular, at day 21 we could identify aggregations of CCD-18Co right below the epithelial monolayer, where epithelial cells and myofibroblasts appeared to be in intimate physical contact. The CCD-18Co were also able to synthesize and secrete collagen IV at both days of cell culture. Collagen IV could be seen within the cell cytoplasm and also accumulated at the epithelial basement membrane (Figure 4.42 (bottom panels)). Overall, CCD-18Co cell-laden hydrogels made of 5% (w/v) $GelMA_{1.25}$ – 1.25% (w/v) PEGDA polymer solutions support the growth of epithelial cells with improved TEER values with respect to the standard monolayers, and properly mimic the cell-cell and cell-matrix interactions existing in the *in vivo* tissue.

4.14. Introduction of immunocompetent features to the stromal compartment of the intestinal mucosa

It has been reported that the intestinal epithelial behaviour is regulated through interactions of epithelial cell with cells in the stroma (lamina propria), such as intestinal subepithelial myofibroblasts[73,76] and immune cells[7]. In the previous sections, we have shown the development of an 3D model of the small intestinal mucosa that recapitulates *in vitro* epithelial – myofibroblast interactions similar to the *in vivo* tissue. As a next step, we propose to provide this model with some immunocompetence properties by the introduction of immune cells within the stromal compartment. If functional, this model can be key in the study of pathological situations such as inflammatory bowel diseases[331] or allergic food reactions[332].

Macrophages play a relevant role in regulating multiple tissue repair processes because of their relation to all stages of tissue healing through their phenotypic plasticity[333]. Intestinal macrophages are one of the largest populations of macrophages in the body. They are primarily concentrated just underneath the epithelial monolayer, and they act the first line of body's defence when the barrier integrity is compromised[110]. Macrophages are key in maintaining the intestinal homeostasis, by phagocytosis and degradation of microorganisms and dead tissue cells as well as production of mediators that drive epithelial cell renewal[52]. Due to these factors, we decided to introduce macrophages into our intestinal mucosa model to mimic some immunocompetence

properties. As macrophage cell model, we chose the THP-1 cell line. This line comes from human leukemia monocytes[246] and it is widely used to study monocyte/macrophage immune responses[246,334] because it can be easily differentiated from monocytes to macrophages by adding a small amount of phorbol 12-myristate 13-acetate (PMA) to the THP-1 cell culture medium[334]. Additionally, other advantages are the low level of variability in their phenotype[334] and the fast average doubling time[246].

4.14.1. Cell viability and morphological studies of the immunocompetent stromal compartment

First, we evaluated the viability of THP-1 cells after the encapsulation process and culture within GelMA – PEGDA hydrogel co-networks. As *in vivo* immune cells co-exist in the stromal compartment with other cell types, also the viability of THP-1 cells encapsulated with CCD-18Co was evaluated in this experiment. To do this, THP-1 monocytes were differentiated to macrophages (M0) thought PMA stimulation. After their differentiation, M0 cells were detached from the Petri dish and were mixed with 5% (w/v) $GelMA_{1.25}$ – 1.25% (w/v) PEGDA polymer solutions adding or not CCD-18Co myofibroblasts. Samples were photopolymerized as previously explained (sections 3.3 and 3.8.2), mounted on Transwell® inserts and cultured for 14 days. As controls, hydrogels loaded with CCD-18Co were also included in the experiments. Samples containing one single cell type were loaded with $6.5 \cdot 10^6$ cells·mL^{-1}, while samples containing both immune cells and myofibroblasts were loaded with $13 \cdot 10^6$ cells·mL^{-1} in total, in an equal ratio of immune cells and myofibroblasts.

Cell viability was evaluated through Live/Dead™ viability/cytotoxicity assay and confocal microscopy images were taken at different time points. At day 3 after encapsulation, cell viability was extremely high as almost no dead cells were labelled (stained in red) in the three cell-laden hydrogels (Figure 4.43 (a)). In addition, all cells were homogenously distributed throughout the entire thickness of the samples (Figure 4.43 (b)). These results indicate that short-term immune cell viability was not compromised by the UV exposure process, the presence of free radical species and/or the co-culture with the CCD-18Co cells.

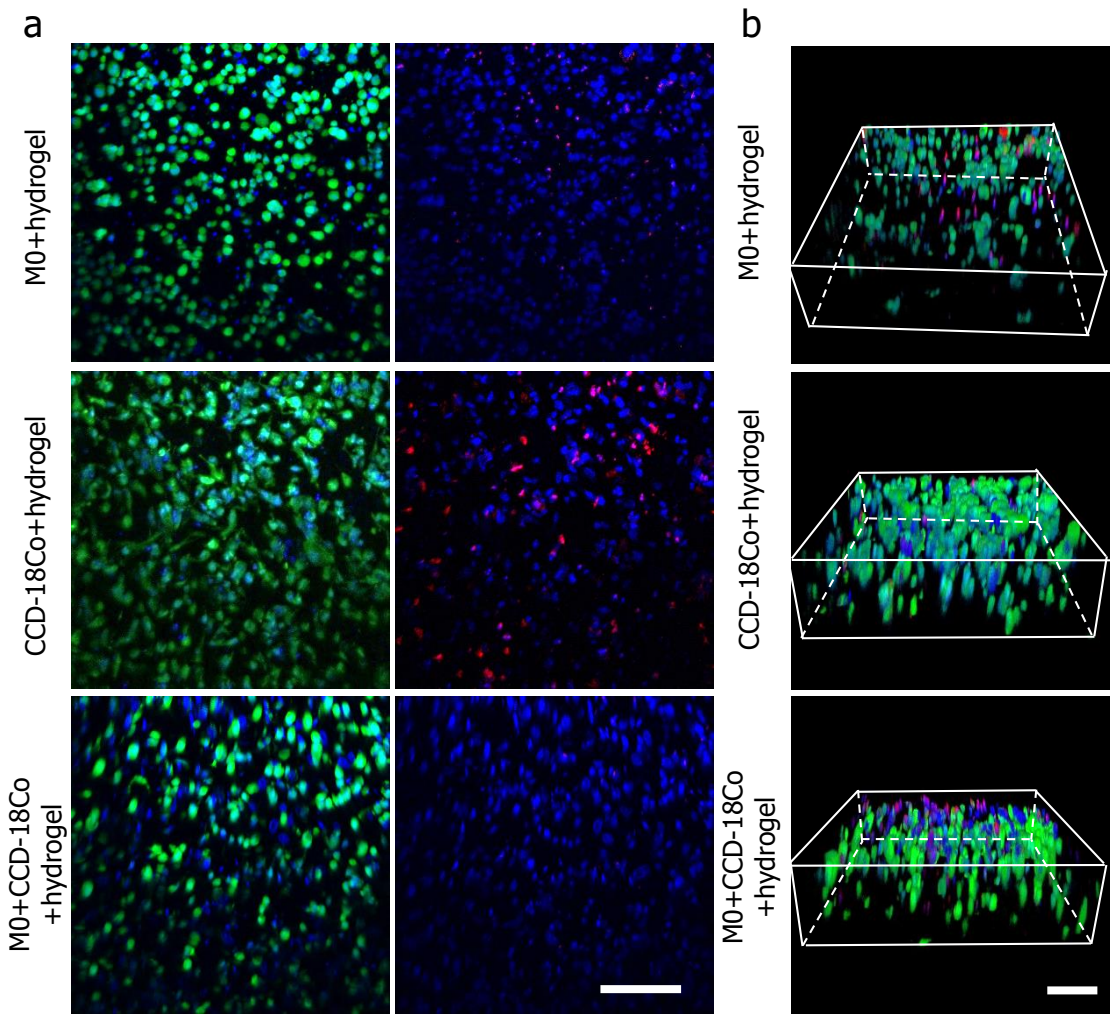

Figure 4.43. Viability studies for the monocultures of M0 (top panel), CCD-18Co (middle panel) and the co-culture M0+CCD-18Co (bottom panel) embedded in 5% (w/v) $GelMA_{1.25}$ – 1.25% (w/v) PEGDA hydrogel co-networks at day 3 after encapsulation. (a) Maximum intensity projections of samples after Live/Dead™ viability/cytotoxicity assay (live cells stained in green, dead cells in red). Hoechst Reagent was used to stain the nuclei. Scale bars:100 μm. (b) Confocal 3D reconstructions of the hydrogel co-networks showing the spatial distribution of cells shown in panel (a). Scale bar: 50 μm.

Thereafter, we checked if cell viability was sustained for longer culture time periods, so Live/Dead™ viability/cytotoxicity assays were performed at day 14 after the encapsulation process. We found that, for all the samples cells were mostly alive (stained in green) (Figure 4.44 (a)).Despite the different cell types on the co-cultures cannot be distinguished from Live/Dead™ viability/cytotoxicity assay, we could actually differentiate them according to their morphology. M0 cells were rounded whereas CCD-18Co cells were elongated and spread. Moreover, we observed that M0 cells were seen as single cells homogenously distributed through the hydrogels at day 3, whereas over time they formed clusters.

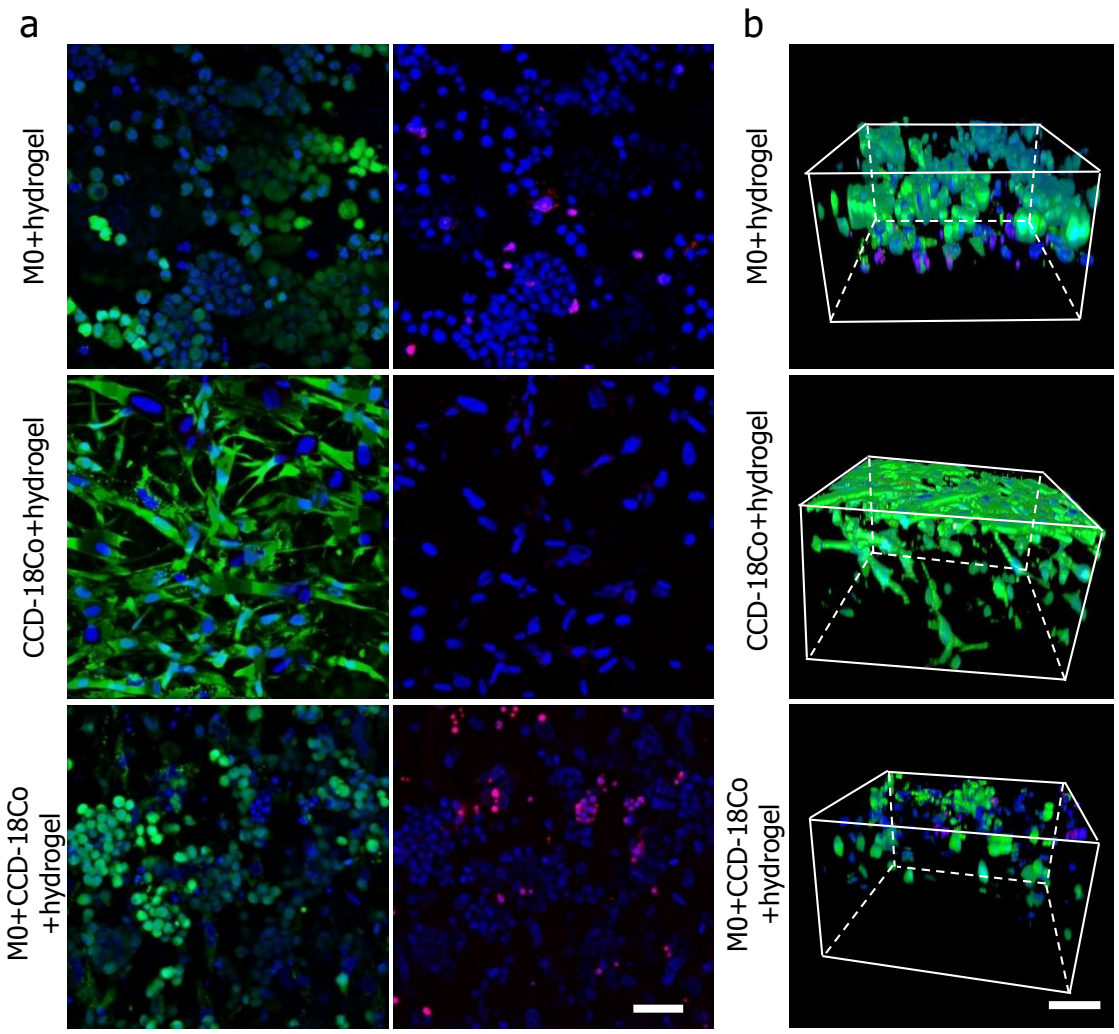

Figure 4.44. Viability studies for the monocultures of M0 (top panel), CCD-18Co (middle panel) and the co-culture M0+CCD-18Co (bottom panel) embedded in 5% (w/v) $GelMA_{1.25}$ – 1.25% (w/v) PEGDA hydrogel co-network at day 14 after encapsulation. (a) Maximum intensity projections of samples after Live/Dead™ viability/cytotoxicity assay (live cells stained in green, dead cells in red). Hoechst Reagent was used to stain the nuclei. Scale bars:100 μm. (b) Confocal 3D reconstruction of the hydrogel co-networks showing the spatial distribution of cells shown in panel (a). Scale bar: 50 μm.

At day 14 CCD-18Co cells were found mainly at the hydrogel surface, although this tendency was less pronounced in the presence of the M0 (Figure 4.44 (b)). Regarding M0 cells, we observed that they proliferate along the cell culture time, forming clusters of increasing size. However, when M0 cells were co-cultured with the CCD-18Co myofibroblasts, M0 clusters were smaller. Maybe this could be due to the high cellular density in the co-culture system compared with the monocultured constructs, this inhibiting cell proliferation. Nevertheless, at this point is worth considering that M0 cells are supposed to not be proliferative after being differentiated from THP-1 monocytes[335]. This fact disagrees with our experimental findings, which show proliferation of these cell

type for both the monocultures and the co-cultures. We then hypothesize that M0 cells when growing for a long time without any additional stimuli that keep them differentiated (no PMA treatment), can revert their phenotype back to THP-1 monocytes. This will rely on the fact that M0 are highly plastic cells and will agree with the experimental observations, as THP-1 are they highly proliferative. Additionally, in favour of our hypothesis, Spano *et al.*[336] showed that after 72 h of PMA withdrawal, the differentiated THP-1 treated with low PMA doses were dedifferentiated, as they detached from the cell culture surface and their proliferative capacity was restored.

To gain better insight on the cell proliferation within the hydrogels, we then performed immunostainings on histological cuts of the samples containing M0 and CCD-18Co monocultures after 3 and 7 days of culture. The presence of cells and their morphology was checked by DAPI (nuclei) and F-actin (actin cytoskeleton) staining while proliferation was checked through the staining of Ki-67 nuclear marker. Maximum intensity projection images for M0 cells (Figure 4.45) and CCD-18Co myofibroblasts (Figure 4.46) were analysed.

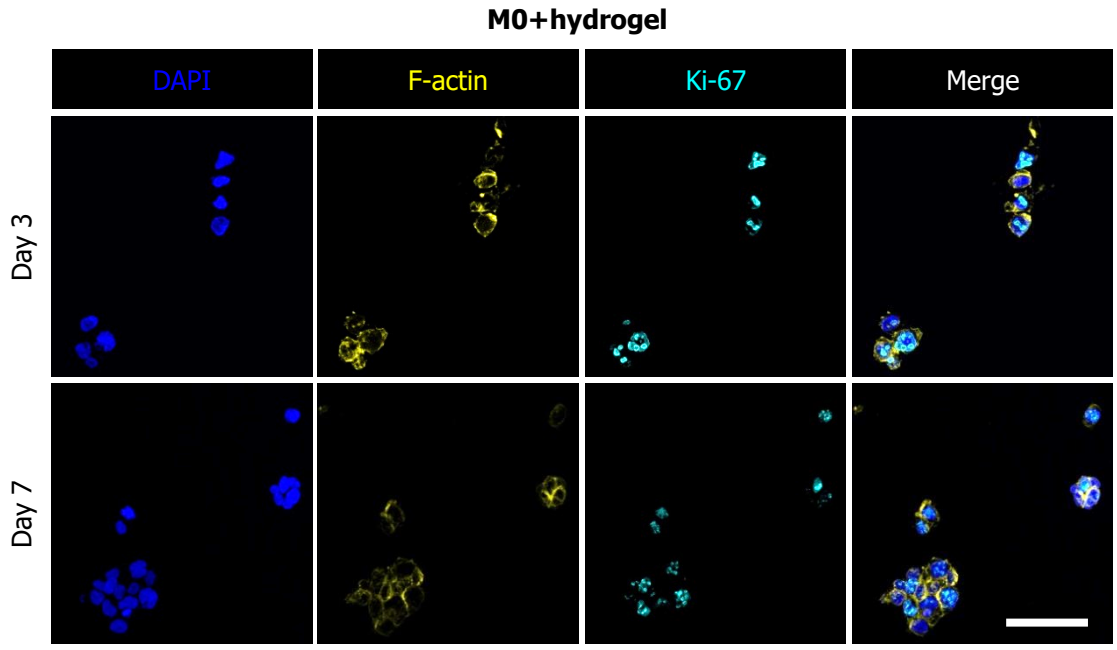

Figure 4.45. Immunostaining for DAPI, F-actin and Ki-67 markers of M0-laden hydrogels after 3 (top panel) and 7 days (bottom panel) in culture. Images show maximum intensity projections. Scale bar: 50 μm.

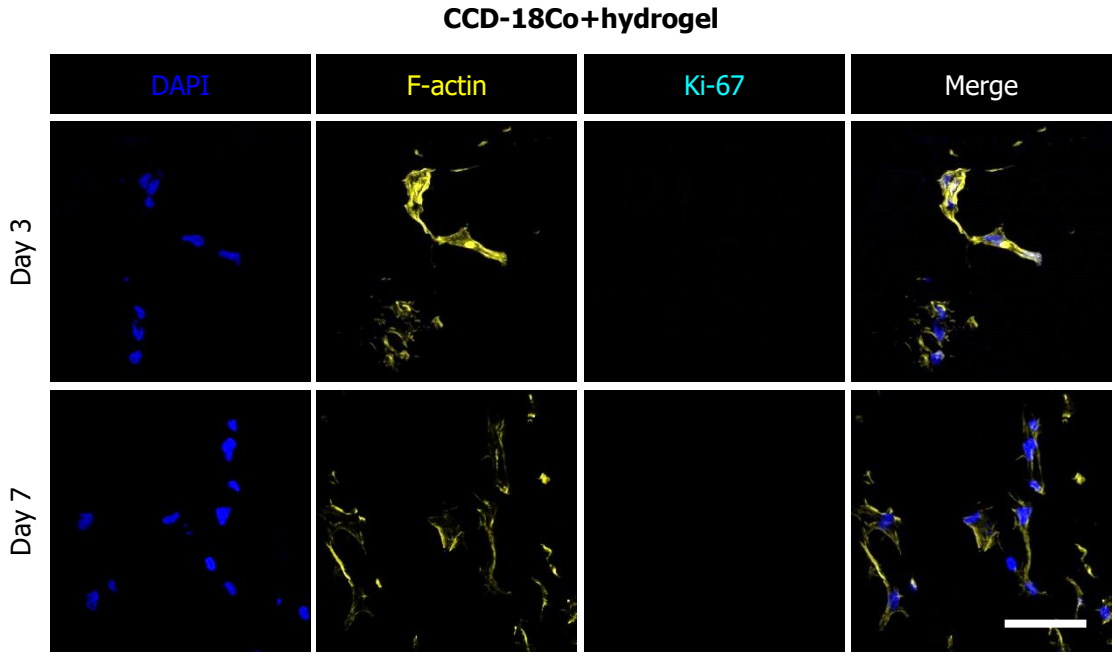

Figure 4.46. Immunostaining for DAPI, F-actin and Ki-67 markers of CCD-18Co-laden hydrogels after 3 (top panel) and 7 days (bottom panel) in culture. Images show maximum intensity projections. Scale bar: 50 μm.

DAPI images showed that at day 3, M0 cells were scattered as single cells through the samples, but at day 7 they formed clusters. Whereas, myofibroblasts were well-distributed inside the hydrogels at both days. In addition, F-actin images revealed that M0 cells remained rounded, while myofibroblasts acquired an elongated shape. Finally, Ki-67 stainings showed that M0 cells tested positive for both time points. Whereas, myofibroblasts were negative for Ki-67 marker for both time points. Ki-67 stanings confirmed the observations of the Live/Dead™ viability/cytotoxicity assay, where we suggested that M0 cells became highly proliferative after being encapsulated and PMA was withdrawn from the medium.

On the other hand, to check the ability to synthesize collagen IV of the CCD-18Co cells, we performed immunostainings on histological cuts of the samples after 3 and 7 days of culture. Maximum intensity projection images of the collagen IV showed that M0 cells were not able to synthesize collagen IV (Figure 4.47), while CCD-18Co myofibroblasts were, appearing in the cell cytoplasm both at day 3 and 7 of the cell culture (Figure 4.48).

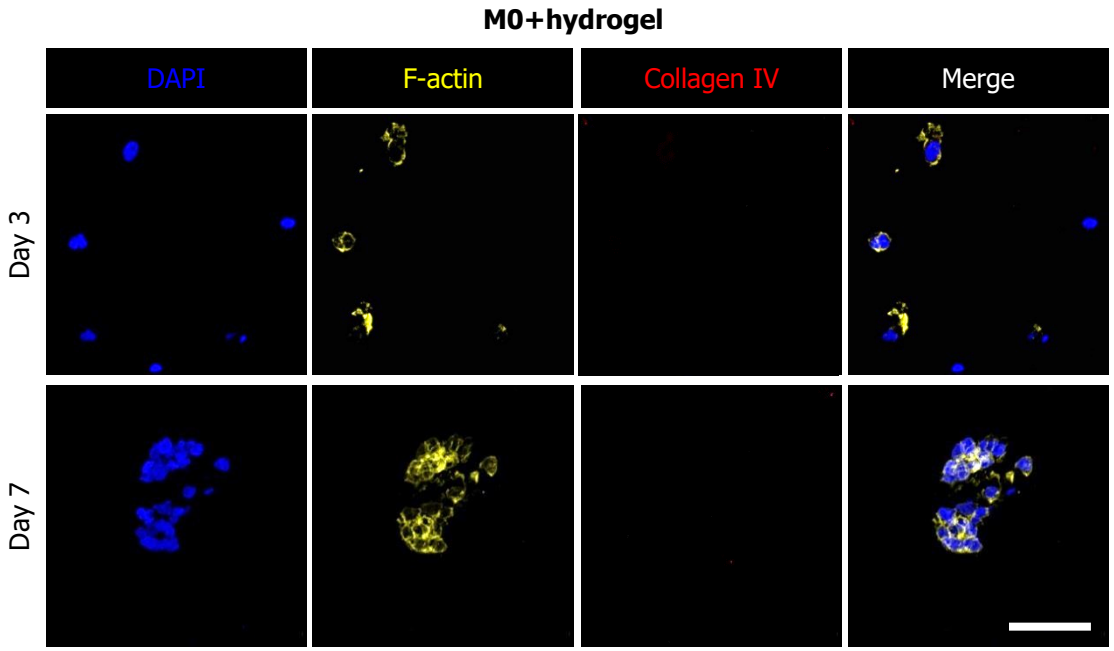

Figure 4.47. Immunostaining for DAPI, F-actin and Collagen IV markers of M0-laden hydrogels after 3 (top panel) and 7 days (bottom panel) in culture. Images show maximum intensity projections. Scale bar: 50 μm.

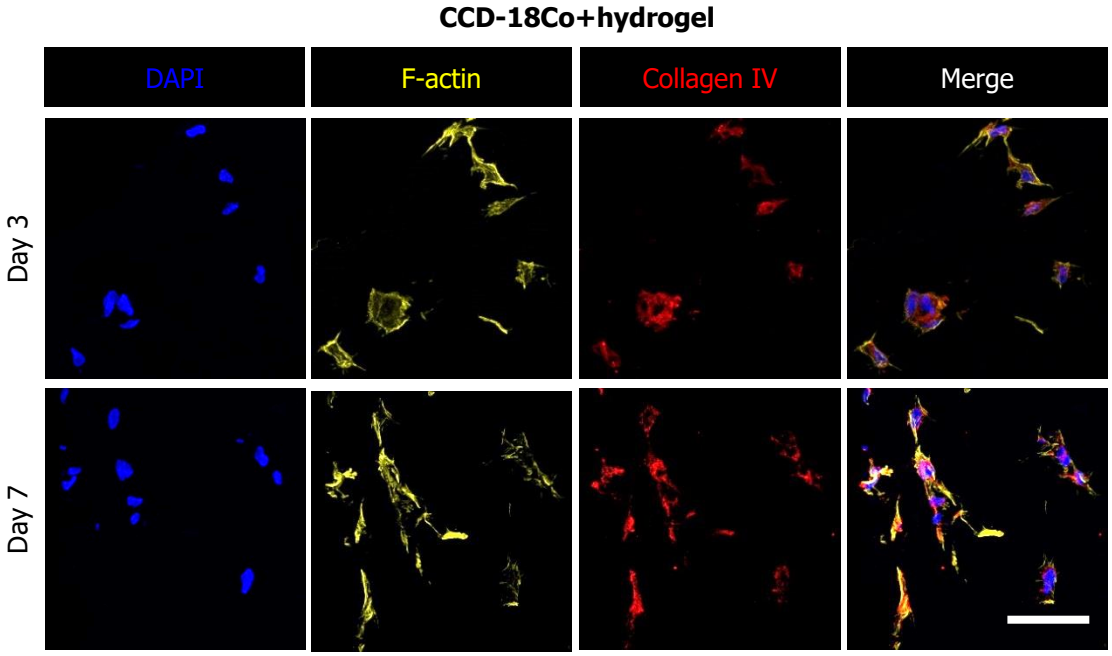

Figure 4.48. Immunostaining for DAPI, F-actin and Collagen IV markers of CCD-18Co-laden hydrogels after 3 (top panel) and 7 days (bottom panel) in culture. Images show maximum intensity projections. Scale bar: 50 μm.

After analysing the samples containing cell monocultures, hydrogels containing both immune cells and myofibroblasts were also immunostained using the same markers and were fluorescently imaged at day 14 of culture (Figure 4.49). At this time point,

DAPI and F-actin stains showed CCD-18Co mostly at the surface of the hydrogels, while M0 cells (here identified by the rounded and clustered morphology) remained in the hydrogel core. Remarkably, some of the M0 cells stained positive for Ki-67 marker, meaning that they could maintain a certain proliferative capacity for long-term culture periods. Additionally, some of the M0 clusters were surrounded by spread CCD-18Co cells with a well-developed F-actin cytoskeleton, therefore suggesting a certain degree of interaction between the M0 cells and CCD-18Co myofibroblasts.

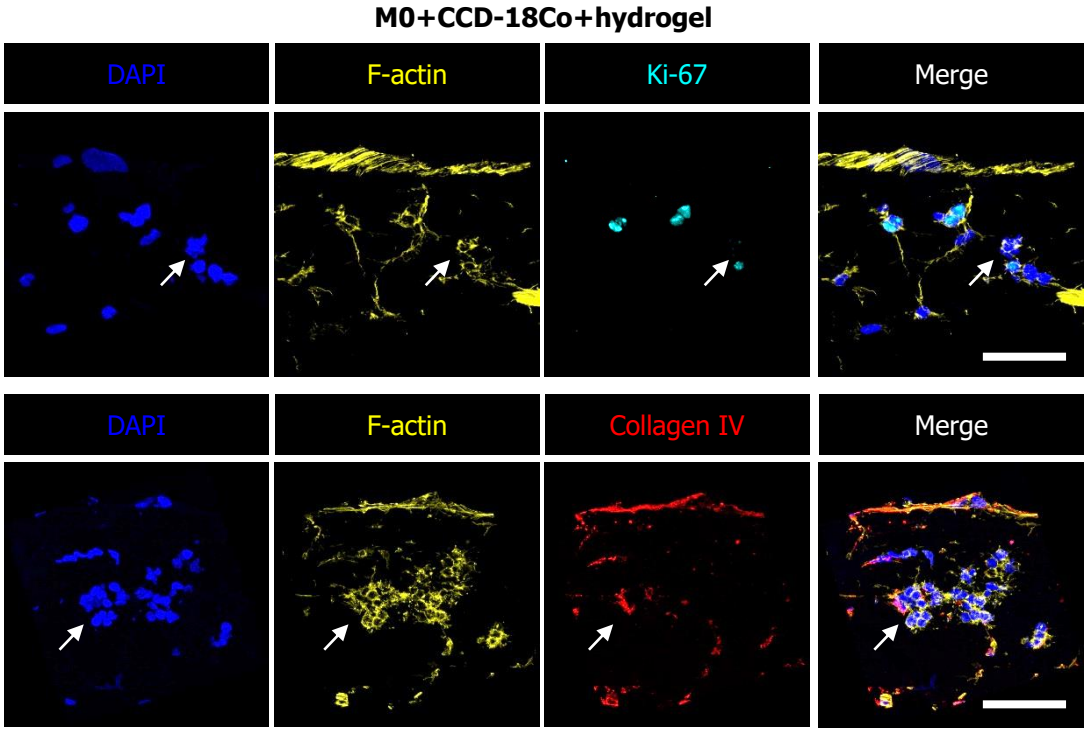

Figure 4.49. Immunostaining for DAPI, F-actin, Ki-67(top panel) and Collagen IV (bottom panel) of 5% (w(v) $GelMA_{1.25}$ – 1.25% (w/v) PEGDA hydrogel cross-sections containing M0+CCD-18Co co-cultures at day 14. Images show maximum intensity projections. The withe arrows show some of the M0 cells. Scale bar: 50 µm.

4.14.2. Evaluation of the immunocompetent response of the stromal compartment under a pathogenic stimulus

After evaluating cell viability, distribution, and morphology of the immune cells in the GelMA – PEGDA hydrogel co-networks, we then studied the immunocompetent response of the stromal compartment. Immune cells play a crucial role in regulating intestinal inflammation when the homeostasis of the intestinal tissue has been dysregulated. This might happen by an alteration of the commensal microbiota in the gut or a pathogenic infection through the exposure of some components from pathogenic microorganisms, such as lipopolysaccharides (LPS)[20,332]. LPS are molecules found in the

outer membrane of Gram-negative bacteria and strongly activate the immune system, specially the innate system, where the macrophages have an important role[25]. LPS stimulus causes the secretion of several cytokines such as TNFα, IL-1, IL-6, IL-8, IL-10, IL-15 and TGF-β[337].

To study cell cytokine expression and release, the supernatant of the hydrogel cultures was collected at day 7 and at day 13 of culture, and after stimulating the samples with LPS at day 14. Cytokines tested were IL-8, IL-6, IL-10 and TGF-β. Their concentration was determined through ELISA assays of the supernatant. Samples non-stimulated with LPS were added as controls. For the four cytokines studied, IL-10 and TGF-β were not secreted during cell encapsulation and after LPS stimulation or were below the detection limit of the ELISA kit used, for that reason their results are not shown in this manuscript.

First, we checked the basal expression of the selected cytokines by the cell lines in 2D cultures, measuring the cell culture media obtained from M0 and CCD-18Co stocks without LPS stimulation. Figure 4.50 shows the basal levels of the cytokine release for IL-6 and IL-8. We found that M0 cells secreted IL-8 at low concentrations and almost an undetectable amount of IL-6. On the contrary, detectable levels of IL-6 were secreted by CCD-18Co cells, which did not secrete IL-8.

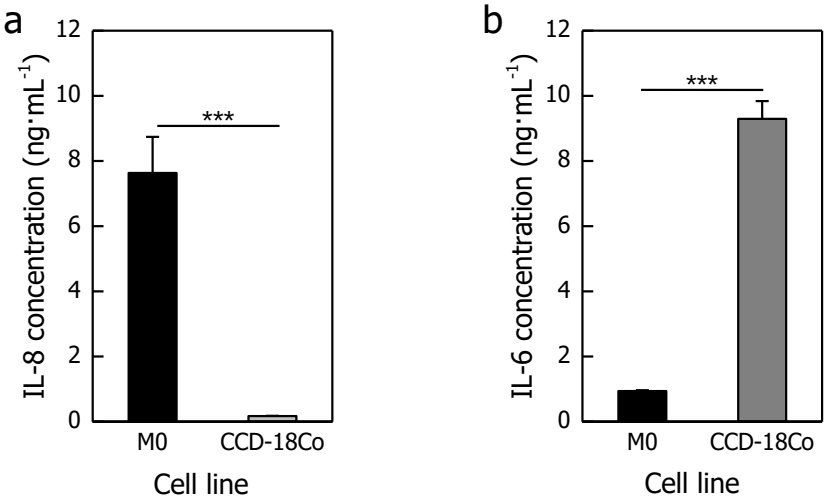

Figure 4.50. Basel levels of the cytokines (a) IL-8 and (b) IL-6 expressed by M0 (black) and CCD-18Co (dark grey) cell lines from the stocks without LPS stimulation. Values were represented as the mean ± SD (almost n=3). ***p<0.001.

When embedded in the hydrogels, this tendency was maintained. IL-6 was detected on CCD-18Co-laden hydrogels, meaning that the cytokine was both secreted

by the cells and able to diffuse through the hydrogel porous network. IL-6 secretion was maintained over the cell culture period tested. On the other hand, IL-8 was detected on the M0-ladden hydrogels, so again it was secreted by the cells and effectively diffused through the hydrogel. Contrary to the IL-6 profile, IL-8 levels decreased with the culture time, despite in the previous section we saw that M0 cell population increased. For the hydrogels containing both cell types, higher amounts of both cytokines were detected (Figure 4.51). Overall, we could establish that IL-6 and IL-8 cytokines were expressed and secreted in certain basal concentrations by CCD-18Co myofibroblasts and M0 cells, respectively. When embedded in our hydrogels, the cells did not lose the capacity of secreting such molecules, which could actually diffuse through the co-network porous structure reaching the cell culture media. In addition, when combining both cell types with the hydrogels, it seemed that a synergistic effect appeared and the cytokine concentrations detected were higher than the simple addition of the monoculture secretions. These results agree with the ones found in the literature. Watanabe *et al.*[338] found that synovial fibroblasts co-cultured with monocytes for 12 days secreted levels of IL-6 and IL-8 significantly higher than those of the respective monocultures. Additionally, these results are in agreement with the ones Ma *et al.*[339] were they saw that the release of IL-6 by cardiac fibroblasts and macrophages was low or absent, respectively. However, when they were co-cultured together the secretion of IL-6 was enhanced.

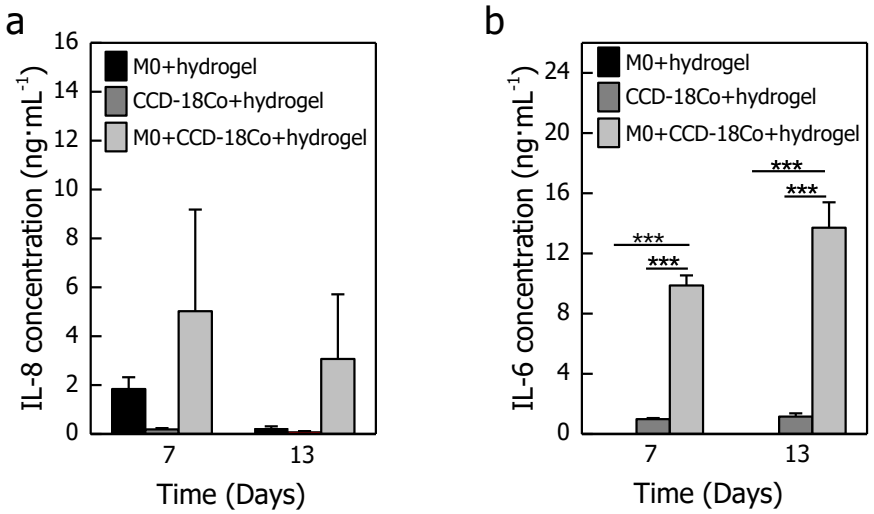

Figure 4.51. Profile of (a) IL-8 and (b) IL-6 cytokines secreted by monocultures of hydrogels laden with M0 and CCD-18Co cells (black and dark grey, respectively) and co-cultures of M0+CCD-18Co cells (light grey). Measurements were performed at days 7 and 13 after encapsulation. Values were represented as the mean ± SD (almost n=3). ***p<0.001.

Then, in another experiment, at day 14 of the cell culture we proceed to stimulate the cells embedded in the hydrogels with adding LPS and measuring the concentration of IL-8 and IL-6. The untreated LPS samples were used as controls. The results are plotted in Figure 4.52. For IL-8, statistically significant enhanced secretion was found when comparing treated and untreated samples, except for the hydrogels containing only CCD-18Co myofibroblasts. Also, for the LPS-treated samples, the concentration of IL-8 found in the co-cultures was significantly higher than the one in monocultures (Figure 4.52 (a)). Regarding IL-6, LPS-stimulation was effectively triggering secretion in hydrogels containing both M0 cells and CCD-18Co (Figure 4.52 (b)).

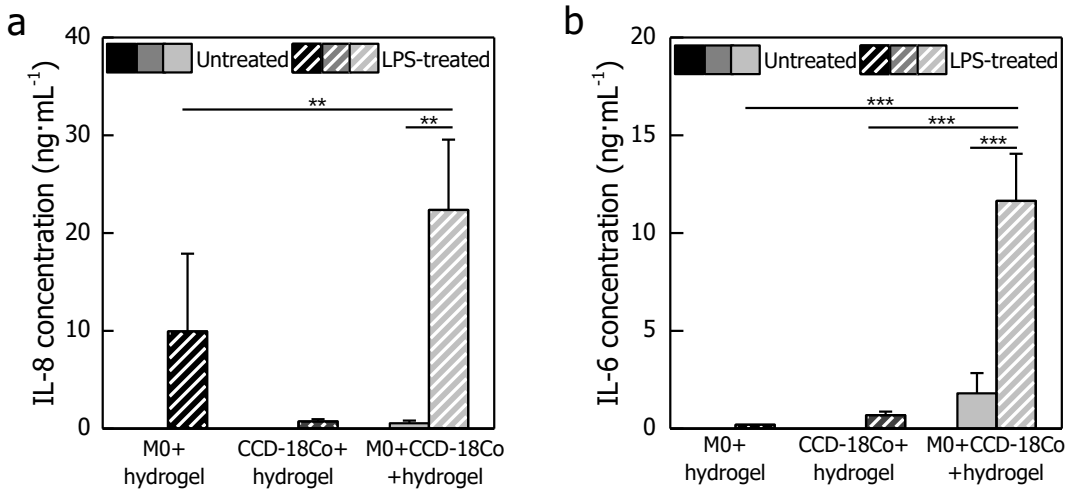

Figure 4.52. . Cytokine levels of (a) IL-8 and (b) IL-6 expressed after LPS treated (solid colors) and untreated (stripped colors) for samples with embedded M0 (black), CCD-18Co (dark grey), and M0+CCD-18Co (light grey) cells. Values were shown as the mean ± SD (almost n=3). **p<0.005; ***<0.001.

Taken into account the above results, we saw that the incorporation of the immune system into the stromal compartment modulated the fibroblast responses without compromising them. All together, we suggest that this platform that incorporates the immunocompetent compartment could be used as a potential construct to better imitate functions of the lamina propria of the native intestinal mucosa.

4.15. Introduction of the immunocompetent stromal compartment into the biomimetic *in vitro* model of the intestinal mucosa tissue

As a next step, we studied the characteristics of the epithelial monolayers when grown on top of the $GelMA_{1.25}$ – PEGDA hydrogels containing myofibroblasts and macrophages to evaluate the performance of our *in vitro* model of intestinal mucosa. Our hypotheses is that the introduction of the immune system to the *in vitro* model should not compromise the epithelial monolayer formation, as similar strategies have been previously reported using macrophage-Caco-2 co-cultures[340]. On the other hand, as it is demonstrated in previous sections of this manuscript, myofibroblasts contribute to form a better epithelial barrier. Based on the existing knowledge, we speculate that, upon epithelial damage, the main role of the myofibroblasts would be remodelling the ECM to decrease the time for wound healing[223]. Meanwhile, the role of the macrophages would be an increment of pro-inflammatory cytokines, such as IL-6 or IL-8, because they act as chemotactic molecules for the recruitment of other immune cells[340]. In order to study our hypotheses by using our model of the intestinal mucosa, the stromal compartment was produced by mixing M0 cells and CCD-18Co myofibroblasts with 5% (w/v) $GelMA_{1.25}$ – 1.25% (w/v) PEGDA polymer solutions, which were photocrosslinked following the previously established methodology to create cell-laden hydrogels. Hydrogels containing single populations of M0 cells, single populations of myofibroblasts and both cell types were included in the study. Then, hydrogels were mounted in Transwell® inserts, seeded with Caco-2 cells and cultured for up to 21 days. The growth of the epithelial monolayers was checked by performing DAPI (nuclei marker) and β-catenin (protein from the adherend junctions) immunostainings of the samples after 7 and 21 days of cell culture and imaging the whole Transwell® area of the samples. At day 7, immunofluorescence images (Figure 4.53) show that on hydrogels containing myofibroblasts and myofibroblasts with macrophages epithelial monolayers that fully covered the entire hydrogel surface were formed. In contrasts, epithelial cells seeded on hydrogels containing only M0 adhered very poorly to the sample surface and formed a discontinuous monolayer with dome-shape epithelial structures. This resulted in the absolute loss of the epithelial layer on the surfaces after 3 weeks of cell culture.

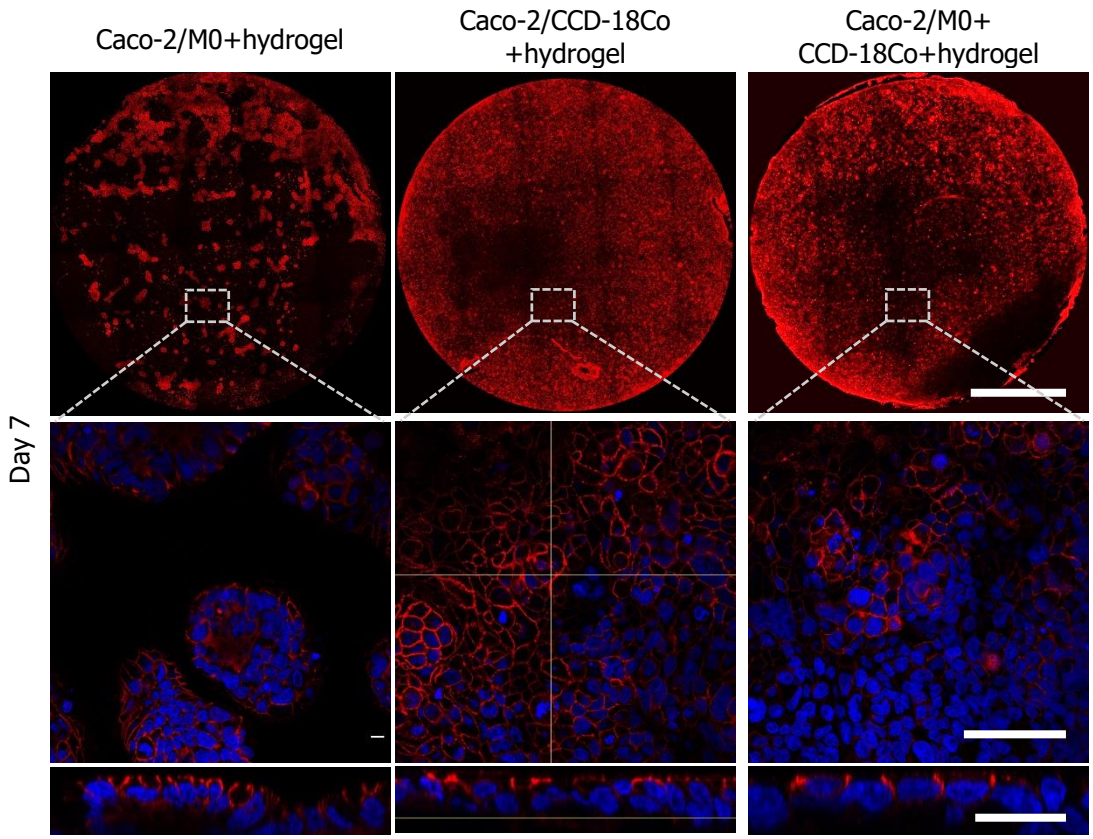

Figure 4.53. Caco-2 cells grown on top of 5% $GelMA_{1,25}$ – 1.25% (w/v) PEGDA hydrogel co-networks containing M0 (left panels) cells, CCD-18Co myofibroblasts (middle panels) and the co-culture of M0 cells with CCD-18Co myofibroblasts (right panels) after 7 days of cell culture. Top panels show tile-scan images of the entire hydrogel surface (0.33 cm^2) (Scale bar: 2 mm), middle panels are magnification images (Scale bar: 75 µm) and bottom panels are cross-section views of the corresponding samples (Scale bar: 50 µm).

However, at day 21 hydrogels containing either myofibroblasts, or the co-cultures were fully covered with monolayers formed by cells with the typical cobblestone epithelial morphology (Figure 4.54). Analysing the cross section images from day 21, on the hydrogels containing myofibroblasts and M0 cells, Caco-2 cells were more polarized than on hydrogels containing myofibroblasts. Cell nuclei were more elongated and all most all of them were perpendicular to the surface compared to the samples with a single population of myofibroblasts embedded in the hydrogels.

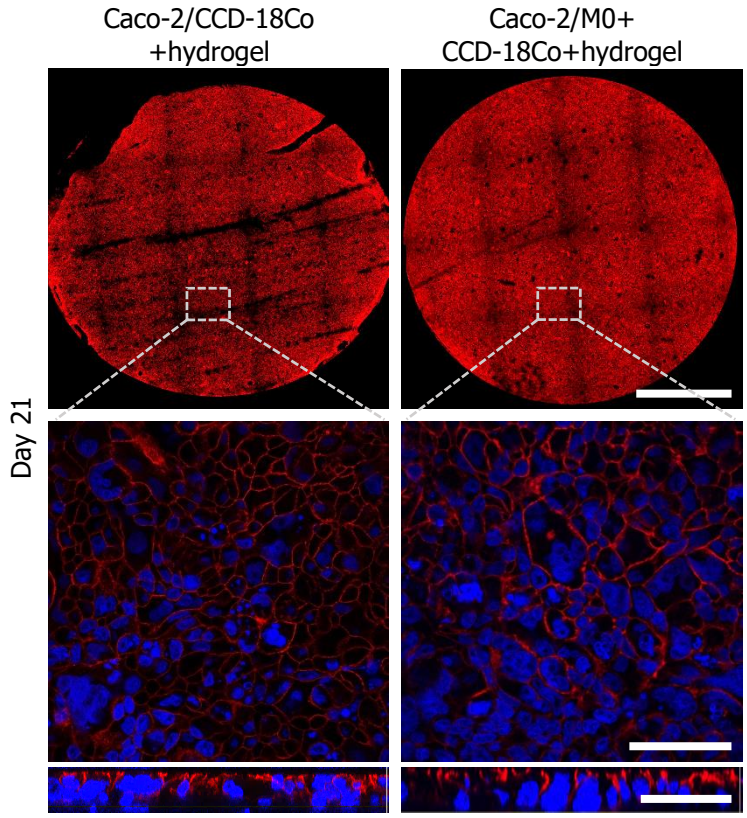

Figure 4.54. Caco-2 cells grown on top of 5% $GelMA_{1,25}$ – 1.25% (w/v) PEGDA hydrogel co-networks containing CCD-18Co myofibroblasts (left panels) and the co-culture of M0 cells with CCD-18Co myofibroblasts (right panels) after 21 days of cell culture. Top panels show tile-scan images of the entire hydrogel surface (0.33 cm^2) (Scale bar: 2 mm), middle panels are magnification images (Scale bar: 75 µm) and bottom panels are cross-section views of the corresponding samples (Scale bar: 50 µm).

To quantitatively determine potential differences among the quality of the epithelial barrier formed, TEER was monitored for the samples in which Caco-2 cells were able to grow. As can be observed in Figure 4.55**,** TEER values increased in such samples up to a saturation value, which corresponded to the formation of a mature packed and dense epithelial monolayer. TEER values of the epithelial barrier formed on top of the hydrogels either containing the monoculture (myofibroblasts) or the co-culture (M0+myofibroblasts) did not show significant differences. This suggests that the presence of the M0 cells did not interfere in the epithelial barrier formation and the homeostatic properties of the intestine were maintained. Mainly, the epithelial barrier development was influenced by the presence of myofibroblasts. These results are in agreement with the previous immunostaining, in which the epithelial monolayer cultured on hydrogels containing M0 cells were barely formed. Whereas, Caco-2 cells on hydrogels with myofibroblasts, either monoculture or co-culture, grew correctly.

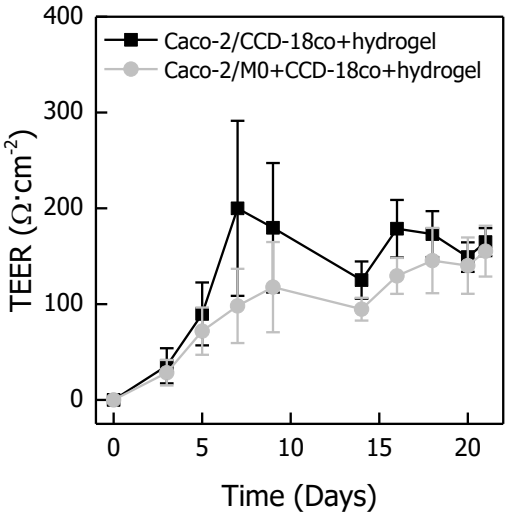

Figure 4.55. TEER values as a function of cell culture time for epithelial monolayers grown on top of 5% (w/v) $GelMA_{1.25}$ – 1.25% (w/v) PEGDA hydrogel co-networks with embedded CCD-18Co cells (black square) and with M0+CCD-18Co co-cultures (light grey circles). Values are the mean ± SD (n=3).

Then, after 21 days of culture, we mimicked a disruption of the epithelial barrier by treating the samples with LPS. In the presence of our immunocompetent mucosa model we expect that, as previously shown, inflammatory cytokines will be released and contribute to the restoration of the barrier as *in vivo*. Results showed that in the presence of LPS, the epithelial monolayers were damaged and TEER values were reduced around 25% compared with untreated samples (Figure 4.56 (a)).

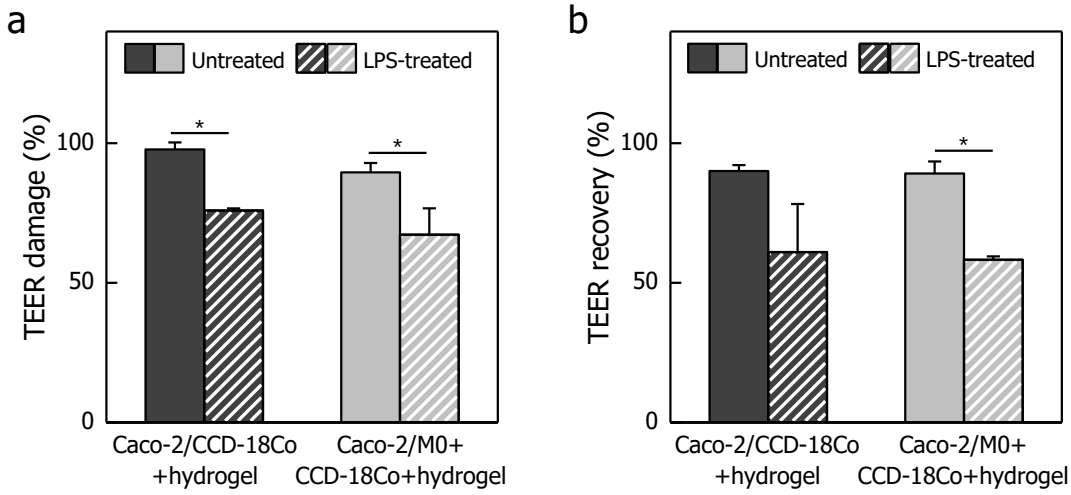

Figure 4.56. *In vitro* model of intestinal inflammation. (a) Change in the TEER of the epithelial monolayers grown on 5% (w/v) $GelMA_{1.25}$ – 1.25% (w/v) PEGDA hydrogels in the presence of CCD-18Co cells (black) or M0+CCD-18Co co-cultures (dark grey) after LPS treatment (stripped) and without LPS treatment (solid). (b) Epithelial layer recovery after 24 h of LPS removal. Values are shown as the mean ± SD (TEER damage n=3; TEER recovery n=2). *$p < 0.05$

This percentage of damage did not change with or without the presence of M0 cells in the model. This result is in agreement with the literature, where it has been found that treating the epithelial barrier with LPS was not enough to produce a relevant disruption on it[115].

Thereafter, we monitored the epithelial barrier restoration by checking the recovery of the TEER values after 24 h once the LPS was removed from the system. We saw that TEER values were not totally recovered (only around ≈70%) and we did not find significant differences with the samples containing or not the M0 cells (Figure 4.56 (b)). As TEER recovery did not show any significant changes due to the presence of the M0 cells, we decided to check for the concentrations of IL-8 and IL-6 cytokines released to the medium in our experimental conditions (Figure 4.57). For IL-8, which we saw that is secreted mostly by M0 cells and we did see a clear increase with LPS treatment in the hydrogels that contained these cells. A similar trend was reported by Kämpfer *et al.*[340], they found that IL-8 in co-cultures of THP-1 and Caco-2 cells was release in small amounts when they were untreated. However, when the co-culture was treated to mimic inflammation, the amount of IL-8 released was highly increased. Regarding IL-6, we did not observe any statistically significant differences between the treated and untreated samples, regarding the samples contained or not M0. However, and consistent with our previous findings, the concentration of IL-6 when both cell types were in the hydrogel was much higher than in the absence of M0.

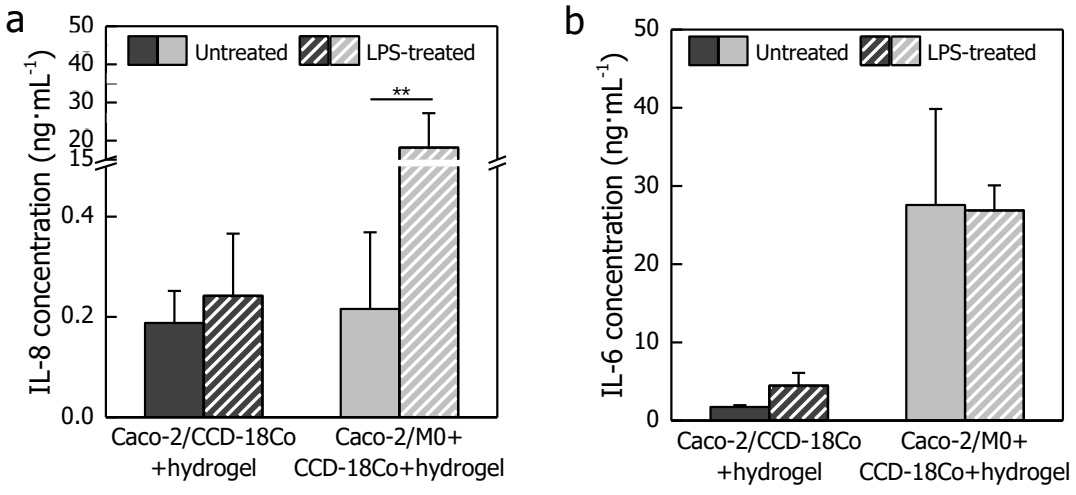

Figure 4.57. Modelling intestinal inflammation. Cytokine levels of (a) IL-8 and (b) IL-6 expressed after LPS treatment (stripped colours) and untreated (solid colours) by monocultures of embedded CCD-18Co myofibroblasts (dark grey) and co-cultures of embedded M0 cells and CCD-18Co myofibroblasts (light grey). Values were shown as the mean ± SD (almost n=3). **p<0.005.

Although LPS treatment did not significantly disrupt the epithelial barrier, as TEER values decreased only around ≈25%, the addition of LPS to our *in vitro* intestinal mucosa model elicited a cell response by efficiently increasing the secretion of IL-8 on the hydrogels containing M0 cells. This indicates that the immune system cells (M0) did not lose their function after being encapsulated for a long-period of time and were able to react under an external stimulus such as LPS triggering an inflammatory response. We hypothesize that TEER did not fully recovery after 24 h because the exposure of the cells to LPS might have induced cell death. LPS, unlike EDTA molecule, can trigger the production of other cytokines such as TNF-α (tumour necrosis factor alpha) by the immune cells. TNF-α is known to be linked to the activation of apoptotic mechanism[342]. We suggest that TNF-α can provoke the death of the epithelial cells, and therefore TEER will take longer to recover.

4.16. GelMA – PEGDA microstructured hydrogel co-networks as biomimetic *in vitro* models of the intestinal mucosa

A realistic physiological *in vitro* model of the intestinal mucosa should replicate properly the mechanical properties of the ECM, the stromal-epithelial interactions and the 3D architecture of the native intestine. The intestinal epithelium has a complex morphology based on crypt-villus units. Villi are finger-like projections, between 0.2 – 1 mm in height and 100 – 200 μm in diameter and have a density of 20 – 40 villi·mm^{-2}. Whereas, crypts are epithelium invaginations that surround the villus[1,4]. Until now, we have obtained an *in vitro* model that is able to recapitulate the stromal-epithelial interactions of the intestinal tissue. Finally, to have a more functional *in vitro* 3D model of intestinal mucosa, we checked if the GelMA – PEGDA hydrogels could be microstructured to achieve the villus-like structures. Hydrogels can be microstructured by several methods such as micromolding[200], 3D bioprinting[195], stereolithography[211], two-photon polymerization[213] and lithography-based methods[215]. Out of all these techniques, to obtain the villus-like structures on our GelMA – PEGDA samples we selected a lithography-based technique, in particular photolithography. This method has been recently developed and optimized in our group to fabricate 3D villus-like PEGDA scaffolds[155].

4.16.1. Fabrication and morphological characterization of 3D villus-like microstructured hydrogel co-networks

To fabricate hydrogels containing microstructures similar in morphology and dimensions to the villi of the intestinal tissue, the photocrosslinking process described in the previous sections of this thesis (section 3.3.2) was modified by employing a 2D photomask, which will produce patterns of light exposed regions (see section 3.12). Our photomask contained arrays of UV transparent, circular windows of 100 μm in diameter spaced 100 μm, which mimicked the native villus dimensions and their density in the small intestine[1]. This photomask was used to polymerize 7.5% (w/v) $GelMA_5$ – 5% (w/v) PEGDA polymer solutions within PDMS pools of 1 mm or 0.5 mm in height, following the schematics depicted in Figure 3.24 (a). The presence of the 2D photomasks made necessary to introduce some technical modifications in the polymerization layout, such as the presence of a dark layer at the bottom of the pools (see details in section 3.12). Such modifications required to optimize the range of exposure energy doses to obtain hydrogel co-networks with enough mechanical integrity (gel fraction values above 50-60%). Figure 4.58 shows the gel fraction values as a function of the exposure energy doses obtained for 7.5% (w/v) $GelMA_5$ – 5% (w/v) PEGDA polymer solutions with this setup (disc-shaped hydrogels were employed for these experiments). The gel fraction increases linearly as a function of the energy dose applied, until reaching saturation at 4 $J \cdot cm^{-2}$.

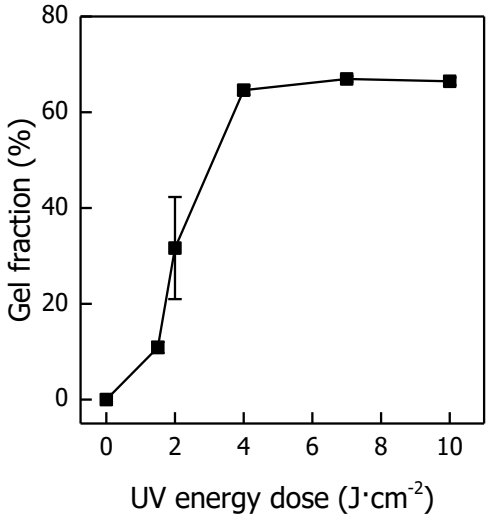

Figure 4.58. Gel fraction or crosslinking degree of 7.5% (w/v) $GelMA_5$ – 5% (w/v) PEGDA hydrogel co-networks polymerized under a range of UV energy doses when a dark bottom is placed under the PDMS chip to minimize light reflection.

When employing the 2D photomask and energy doses from 4.9 to 7.7 J·cm^{-2}, a wide variety of micropillars were obtained (Figure 4.59). We obtained pillars without crosslinked material between them, so they form single microstructures (Figure 4.59 (a)) and we also obtained, pillars that were completely joined by the polymerization of the hydrogel of the non-exposed UV regions (Figure 4.59 (b and c)). However, despite maintaining constant the energy dose applied and the macromer content of the polymer solution, the reproducibility of this process was very low and replicates were difficult to obtain.

Figure 4.59. Images of the cross-sections of the microstructured hydrogels showing a single row of the villus-like structures. It can be easily appreciated material crosslinking between pillars, which increases when the energy dose applied increases (a) 4.9, (d) 5.9, and (e) 7.5 J·cm^{-2}. The borders of the pillars are marked in yellow. Scale bar: 500 µm.

The lack of the reproducibility could be because of (I) the presence of the photomask induced light scattering that produced overexposure in some regions[155], sometimes even embedding completely the pillars; (II) the diffusion of free radicals of the irradiated regions into the non-irradiated regions produced hydrogel polymerization of the non-irradiated regions[279]; and (III) the microfabrication process was very much depending on environmental parameters, showing day-to-day hard to reproduce results. In particular, we identified the fabrication and sterilization process of the PDMS pools as key elements triggering huge variability in the photopolymerization process. The acrylate-photopolymerization reaction that we are using is inhibited by the presence of oxygen, which is stored within the PDMS material. In previous works, acrylic acid was used to minimize this effect when photocrosslinking PEGDA[155], but it was avoided here to make the crosslinking process cell-friendly. Nevertheless, and despite the process yield efficiency was not very good, micropillars resembling villus-like structures could be obtained using 7.5% (w/v) $GelMA_5$ – 5% (w/v) PEGDA polymer solutions and energy doses of 7.70 J·cm^{-2}.

Once these fabrication parameters were set, we proceeded to investigate if the technological set up was able to support the embedding of NIH/3T3 fibroblasts. To do that, fibroblasts at a density of 10^6 cells·mL^{-1} were mixed with 7.5% (w/v) $GelMA_5$ – 5% (w/v) PEGDA polymer solutions and polymerized using a photomask and an energy dose of 7.70 J·cm^{-2}. Through this process, fibroblast-laden hydrogels with micropillars resembling intestinal villi were produced. Once fabricated, the samples were mounted on Transwell® inserts and cultured for 21 days. At several time points along the cell cultured period, the viability of the embedded cells was analysed by Live/Dead™ viability/cytotoxicity assay, combined with DAPI staining. Results are show as representative maximum intensity projections of the fluorescence signal in Figure 4.60. At day 3, few cells could be observed in the pictures, but the majority remained viable and were located inside the core of the villus-like microstructures, thus indicating that cells were able to withstand the microfabrication procedure. By day 7 of culture, NIH/3T3 cells remained mostly viable but started to be localized preferentially on the surface of the 3D microstructures. Also, more cells were visible, therefore suggesting cell proliferation.

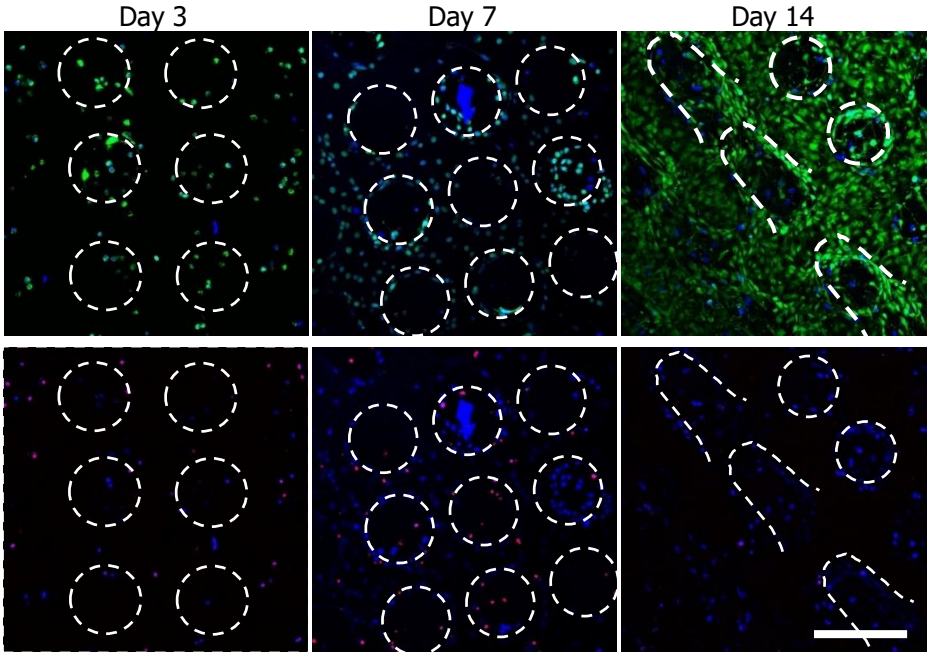

Figure 4.60. Analysis of fibroblasts viability into 3D villus-like microstructured 7.5% (w/v) $GelMA_5$ – 5% (w/v) PEGDA hydrogel co-networks mounted in Transwell® inserts at day 3 (left panel), day 7 (middle panel) and day 14 (right panel) of culture using Live/Dead™ viability/cytotoxicity assay. Alive cells are stained in green (top panels) whereas dead cells are labelled in red (bottom panels). DAPI was used to stain the nuclei. Microstructures are outlines in white colour to better visualized due to its transparency under the confocal microscopy. Scale bars: 200 µm.

At day 14, cells were viable and had proliferated, covering the 3D microstructures. Most of them were located at the surface, as fluorescence signal was very poor within the core of the microstructures. We attribute this to the fact that the cells that were in the core of the 7.5% (w/v) $GelMA_5$ – 5% (w/v) PEGDA hydrogels were in growth arrest due to the low mass transfer and therefore they did not proliferate. Whereas fibroblasts that were closer to the surface found the environmental conditions more favourable and were able to proliferate, covering the 3D microstructured hydrogels. These results are in agreement with fibroblast-laden 7.5% (w/v) $GelMA_5$ – 5% (w/v) PEGDA disc-shaped hydrogel co-netwoks, explained early in this manuscript (section 3.8). On the other hand, as it is shown in Figure 4.61, from day 21, some pillars were collapsed, bended and fell on the PET membrane. We suggest that this might be due to (I) the increase in cell density over the cell culture, exceeding the weight that the 3D microstructures could support or (II) the mounting process of the hydrogels in the Transwell® inserts. Nonetheless, in general, the shape of the microstructures fabricated on the hydrogels was maintained throughout the cell culture time.

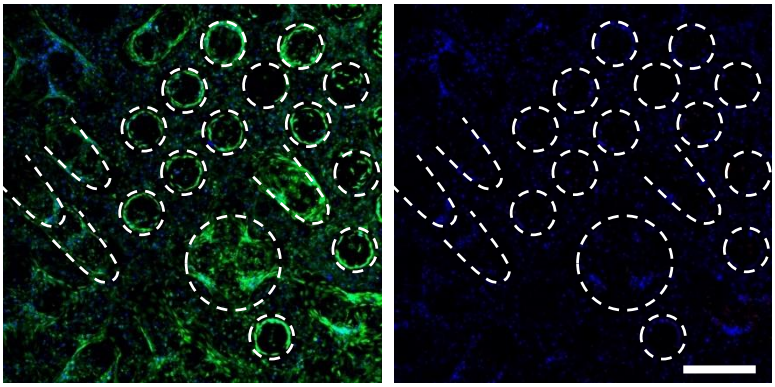

Figure 4.61. Analysis of fibroblast viability into 3D villus-like microstructured 7.5% (w/v) $GelMA_5$ – 5% (w/v) PEGDA hydrogel co-networks mounted in Transwell® inserts at day 21 of cell culture using Live/Dead™ viability/cytotoxicity assay. Alive cells are stained in green (right panel) whereas dead cells are labelled in red (right panel). DAPI was used to stain the nuclei. Scale bars: 200 µm.

This pilot experiment demonstrated that 7.5% (w/v) $GelMA_5$ – 5% (w/v) PEGDA polymer solutions can be combined with our original photolithography-based fabrication setup to successfully produce 3D hydrogel microstructures with morphology and dimensions similar to the villi of the *in vitro* intestine. By employing this process, fibroblasts could be loaded within the 3D villus-like hydrogels and were able to grow without compromising the shape of the microstructures. However, similar to the results obtained for the disc-shaped hydrogels detailed in section 4.7.1, the polymer formulation

employed (GelMA of high DoF and high macromer content) likely restricted the growth of the cells within the core of the 3D micropillars. Whereas, cells on the surface grew and proliferate. To mitigate these drawbacks, changes in the polymer formulation were suggested and implemented in this thesis. However, when applying the photolithography-based fabrication approach to the new polymer formulations (5% (w/v) $GelMA_{1.25}$ – 5% (w/v) PEGDA polymer solutions) to mimic the native morphology of the small intestine, the crosslinking degree could not be properly controlled. When we used a photomask containing arrays of UV transparent, circular windows of 100 µm in diameter and spaced 100 µm and a PDMS pool of 1 mm height, after applying energy doses from 4 to 4.5 $J \cdot cm^{-2}$ hydrogel polymer solution was unable to crosslink. Nevertheless, when the photomask was replaced by one containing arrays of UV transparent, circular windows of 300 µm in diameter and spaced 150 µm and the energy dose applied was 4 $J \cdot cm^{-2}$ villus-like microstructured hydrogels were obtained either of 1 mm or 0.5 mm in height (Figure 4.62). However, due to the low reaction efficiency and the high dimensions of the villus-like microstructures and the small space between them, there was undesired crosslinked hydrogel between the micropillars. To prevent the hydrogel formation between the micropillars, we decreased the energy dose up to 3 $J \cdot cm^{-2}$ and we saw that the crosslinking degree could not be properly controlled. Employing the same conditions (energy dose and polymer solution formulation), some days microstructured hydrogels were obtained while other days did not polymerize.

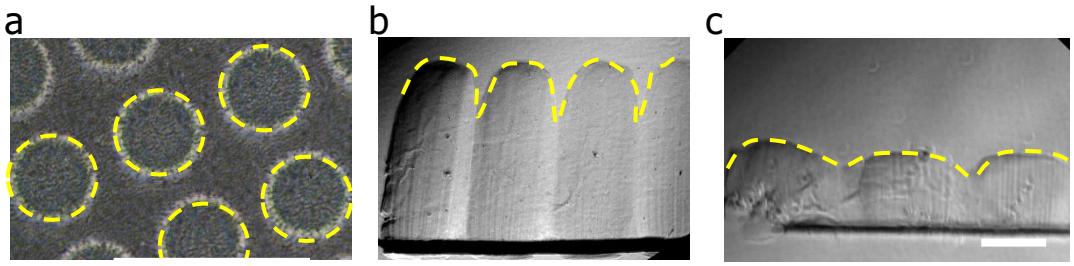

Figure 4.62. Images of the 3D villi-like microstructured 5% (w/v) $GelMA_{1.25}$ – 1.25% (w/v) PEGDA hydrogel co-networks polymerized applying an energy dose of 4 $J \cdot cm^{-2}$ (a) top view and cross-section of the hydrogel photopolymerized using a PDMS pool of (b) 1 mm height and (c) 0.5 mm height. Borders of the hydrogels are marked in yellow. Scale bar: 250 µm

Despite the lack of reproducibility in the patterning of the microstructures on GelMA – PEGDA hydrogel co-networks, these results demonstrate that if we manage to get the villus-like hydrogels, they could support the growth of fibroblasts for long-term period without significantly affecting the stability of the hydrogel. Due to these favourable results, currently in the laboratory are working and optimizing a 3D

bioprinting method to achieve a better control of the GelMA – PEGDA hydrogel crosslinking. The pilot experiments show that (I) 3D villus-like microstructures patterned on the GelMA – PEGDA hydrogel co-network can be fabricated and (II) the microstructured construct support the embedding of the NIH/3T3 cells and the growth of Caco-2 cells on top.

5. Discussion

The small intestine forms part of the gastrointestinal system. The main functions of the small intestine are the digestion and absorption of nutrients and minerals from food, as well as the protection against pathogenic infections or other external agents. To properly develop these roles, the mucosa, which is the outer layer of the small intestinal wall, has a crucial role[1]. In the mucosa there are the epithelial and stromal compartments, and the crosstalk between the different cell components (such as epithelial cells, myofibroblasts and immune cells) plays an important role in the regulation of fundamental biological processes related to the maintenance of healthy intestinal tissue. It has been demonstrated that the secretion of factors by the cells of the intestinal epithelium and the cells of the stromal tissue is bidirectional and modulates cell growth, differentiation, proliferation and functionality[8,343–345]. Myofibroblasts, in the stromal compartment, are located underneath of the epithelial monolayer and give mechanical support to the epithelium thought the production, secretion and deposition of collagen[346]. Additionally, myofibroblasts are responsible of regulating the behaviour of the epithelial cells by enhancing their differentiation through the release of growth factors and/or cytokines[112,347,348]. On the other hand, the behaviour of the immune cells, which reside in the stromal tissue, is modulated mainly by the epithelial cells. The immune-epithelial crosstalk is essential to trigger a proper immune response when the epithelial monolayer has been damaged due to an external stimulus, such an infection[7,343]. Due to the complex 3D architecture and cell organization of the small intestine, it is essential to develop *in vitro* models that mimic accurately the physiological and morphological conditions of the native small intestinal tissue.

Nowadays, most of the *in vitro* models of the intestinal mucosa that are being used to study the absorption, permeability or toxicity of molecules are limited to monoculture of the Caco-2 cells on a hard porous Transwell® membranes[88,349]. Although Transwell® inserts allow to replicate the luminal (apical) and abluminal (basolateral) compartments as in the native intestine, they are restricted only to the culture of epithelial monolayers, whereas the stromal compartment is not represented. Moreover, the stiffness of the porous membrane (2 GPa)[350] is much higher than that of the epithelial basement membrane (3 – 40 kPa)[194]. As a consequence, these models do not represent correctly neither cell–cell interactions and cell distribution, nor the mechanical properties of the tissue. Therefore, the results obtained by these models are not always comparable with those expected *in vivo.* Under these non-physiological conditions, Caco-2 cells grow forming tight junctions far too stiff, with very small pores restricting the transport through the paracellular pathway. This has a direct impact on the permeability studies,

resulting in underestimated results for drug absorption, as well as TEER values (1400 – 2400 $\Omega \cdot cm^{-2}$) much are higher than those found for the native small intestine (50 – 100 $\Omega \cdot cm^{-2}$)[92] or native colon (300 – 400 $\Omega \cdot cm^{-2}$)[92]. For that reasons, there is a great commitment to find alternative models of the small intestine that better recapitulate the barrier function *in vitro*. In recent years, advances in the field have yield small intestine models that mimic the cell-ECM interactions[110–113,205]. However, these models still have some drawbacks, such as (I) high complex fabrication methods, which are time-consuming, expensive, and unsuitable for cell encapsulation, (II) use of biomaterials coming from natural origin, which affects their long-term mechanical stability and reduces their life span, and (III) incompatibility with conventional measurements, such as TEER or permeability assays.

One major step when developing tissue engineered models of the intestinal mucosa is the choice of the scaffold for cell culture. It is desirable that its mechanical properties, porous structure, water content, cell remodelling capabilities and mass transport are as similar as possible to the ECM of the stromal component or lamina propria to faithfully replicate cell-matrix interactions found *in vivo.* In addition, the material must be non-toxic for the cells and has to provide enough adhesive and degradation sequences to the cells. Moreover, Caco-2 epithelial cell cultures need 21 days to mature, so the degradability of the scaffold should match with the ability of the cells to remodel the matrix with new ECM, and thus not compromise the mechanical integrity of the constructs.

To be able to fit these requirements, GelMA – PEGDA hydrogel co-networks were chosen as scaffolds to mimic the stromal-epithelial interactions of the intestine. To check the effects of the PEGDA polymer on the physicochemical and mechanical properties of the co-networks, we have compared them with hydrogel networks only containing GelMA polymer. GelMA is a natural polymer derived from gelatin (denaturalized collagen), however, gelatin cannot be UV photocrosslinked. As we had selected photopolymerization as the technique to fabricate our hydrogels, to overcome this inconvenience, gelatin was modified to obtain GelMA. We have been able to demonstrate that the modification of gelatin did not affect its molecular weight, and that has not been degraded during the process. Like gelatin, GelMA has cell adhesion motifs and is highly biodegradable[142,201]. To minimize biodegradability, PEGDA (one of the most used polymers for biomedical purposes), a synthetic, UV photocrosslinkable, bioinert and non-biodegradable polymer, which can withstand long-term cell cultures but lacks of

bioadhesion sequences[240], was introduced to have GelMA – PEGDA polymer solutions. Although it has been shown that GelMA precipitates when it is mixed with high concentrations of PEG polymer of high molecular weigth[278], our GelMA – PEGDA hydrogel co-networks were homogenously distributed and no polymer aggregates were detected during the photopolymerization.

The addition of PEGDA to the GelMA hydrogel networks results in the modification of the hydrogel swelling properties. PEGDA significantly increased the swelling of hydrogels due to its high hydrophilicity. As the ECM has high water content, around of ≈75%[351], hydrogels with high capacity to store water are a good option to mimic the physiological environment of the tissue. A crucial parameter for the growth and functionality of the cells residing inside the hydrogel is the diffusivity of molecules within the material. Nutrients, macromolecules, growth factors and oxygen need to pass freely through the hydrogel, and thus arrive to the embedded cells. Here, our GelMA – PEGDA hydrogels allowed the diffusion of metabolites and other biomolecules with hydrodynamic diameter of 2.8 nm (MW of 4 kDa), while for molecules of hydrodynamic diameter of 11.2 nm (MW of 70 kDa), the diffusion was restricted or even prevented. For GelMA and GelMA – PEGDA hydrogels, FD4 diffusion coefficient is ≈2 $\mu m^2 \cdot s^{-1}$, consequently the diffusion of the nutrients of the cell culture medium, which have molecular weights ranging between 0.6 – 0.1 Da[184] is permitted. On the other hand, media is supplemented with fetal bovine serum, which is a mixture of macromolecules, proteins in particular, such as serum albumin (MW of ≈66 kDa)[352]. As it has seen for the FD70 dextran molecule, which have a similar molecular weight than the macromolecules, diffusion of them within the hydrogels was low due to the small pore size, as a consequence of that embedded cells were alive but in growth arrest.

Moreover, an appropriate scaffold for stromal-epithelial cell growth requires mechanical properties that permit the growth of epithelial cells forming a mature and well-differentiated monolayer, as well as the growth, the differentiation and the functionality of stromal cells within the core of the hydrogel, which acts as an artificial ECM. In our case, the GelMA – PEGDA hydrogel co-networks studied had apparent elastic modulus values within the physiological range of the small intestine (3 – 40 kPa)[194], meaning that they might be good candidates to be used as scaffolds to mimic this tissue. Biodegradability is a relevant factor to take into account for *in vitro* models of the intestinal mucosa because when used with enterocyte cell lines such as Caco-2 cells, they need to maintain stability for at least 21 days. Although in literature one can find

scaffolds that allow to study the interactions between stromal and epithelial components, they are based on natural hydrogels such as GelMA or Matrigel™. The main problem when using natural hydrogels for long-term cell culture is that the fast hydrogel degradation that does not match with the secretion of ECM by the cells[9,16]. To overcome this inconvenience, Matsusaki M. *et al.*[113] replaced the hydrogel for a 3T3 multilayer and then Caco-2 cells were seeded on top. However, the physiological conditions of the native intestine were not well-represented because in the small intestinal mucosa, stormal cells are homogenously distributed inside the ECM and not arranged layer by layer. In our experiments, hydrogels composed of only GelMA polymers were quickly degraded when incubated with collagenase, so we did not consider them suitable for long-term cell cultures. On the contrary, GelMA – PEGDA hydrogel co-networks were considered as good potential candidates to be used as scaffolds because their degradation rate could be modified to match that required for long-term cell cultures. Another relevant factor to consider is the gel fraction or crosslinking degree of our hydrogel. This parameter is an indicator of how densely packed is the internal network of the hydrogel and it is important for the survival of the embedded cells. Here, we demonstrated that using photocrosslinkable polymers, such as GelMA and PEGDA polymers, to form the hydrogels, the gel fraction could be easily tuned in order to achieve the desire physicochemical and mechanical properties of our scaffolds. In our case, we chose a GelMA – PEGDA crosslinking degree of ≈40% because we wanted a stable hydrogel for growing the epithelial monolayer, providing physiological values of TEER and apparent permeability. Additionally, at the same time, the scaffold must have low crosslinking degree to form less packed networks, and thus to allow the growth of the embedded cells without losing their functionality, such as the production of collagen.

Here, we demonstrate that changes on the content of GelMA and PEGDA polymers, together with changes on the final macromer content allow to tune the swelling, mesh size, diffusion, degradability, apparent elastic modulus and gel fraction of the scaffolds to make them similar to the extracellular matrices of the small intestinal mucosa. Here, we take advantage of the good mechanical and physicochemical properties of GelMA – PEGDA hydrogel co-networks to replicate the stromal and epithelial compartments of the intestinal mucosa. First of all, we corroborated that neither the materials used (GelMA and PEGDA polymers, and photoinitiator) nor the technique chosen (UV photopolymerization) to fabricate the hydrogels were toxic for cells. For the photoinitiator, toxicity studies were performed on 2D monolayers of NIH/3T3 cells instead of embedding them into the 3D dimensional hydrogel matrices. This was done

to create a more dramatic environment for the cells, as they were in direct contact with the photoinitiator for a long time compared to the encapsulation process. Also in this process, the effects of free radicals on the cells were minimized through the reaction with the polymer chains to form the hydrogel. The 2D results demonstrated that concentrations higher than 0.5% (w/v) produced high rate of cell death. Willams C.G. *et al.* [175] showed that low photoinitiator concentrations increased considerably cell survival. However, for us decreasing the photoinitiator concentration was not beneficial because it required increasing the UV energy dose to get hydrogels with good properties. Regarding cell damage due to the UV light exposure during the fabrication process of the hydrogels, this was studied in encapsulated NIH/3T3 cells. It is well-documented that UV light induces the phosphorylation of the DNA, and consequently produces DNA alterations such as DNA double strand breaks[290]. We have seen that our system, which uses an I-line filter (365 nm±10 nm), did not cause drastic DNA damage or this was so minimal that it could be repaired by DNA repair mechanisms.

It is reported in the literature that the stiffness of the hydrogels does not have a significant effect on cell viability of the encapsulated cells, however it can modulate their phenotype and functionality[189]. Cells in low rigidity hydrogels are more elongated and spread compared with those in hydrogels with higher stiffness, which show rounded-shape[189]. Despite that the apparent elastic modulus of the hydrogels were similar to those of the native intestinal tissue, the cells embedded had round-shapes and preferred to grow on the surface of the hydrogels than in their core. To maintain good cell viability for prolonged culture time, the system needs a good efficiency on the exchange of nutrients, macromolecules, oxygen and growth factors from the medium to the bulk of the hydrogel and vice versa. Mass transfer mainly depends on the scaffold size, porosity and diffusion rate[353]. In static culture conditions, mass transfer is limited to distances of 100 – 200 μm[353–355]. Diffusion limitations of the molecules usually are highly improved by introducing a perfusion system into cell cultures. When we placed the hydrogels in the perfusion bioreactor, the low diffusivity of the molecules was mitigated, and this favoured a homogeneous cell distribution along the entire hydrogel thickness. This corroborates that GelMA – PEGDA hydrogels were suitable for cell culture. Remarkably, even if cells appeared to be in growth arrest, they were functional in the sense that they could synthesize collagen. Therefore, we considered that our GelMA – PEGDA hydrogels were suitable to emulate the cellular component of the stromal compartment of the intestinal mucosa.

On the other hand, viability, growth, migration, differentiation, and death of the cells seeded onto the scaffold surfaces are affected by the scaffold stiffness. It is reported that stiffer surfaces favour cell proliferation and differentiation[193]. Our GelMA – PEGDA hydrogel co-networks with an apparent elastic modulus of ≈40 kPa showed that Caco-2 cells could grew forming an epithelial monolayer on their surfaces and expressing the epithelial markers, so they allowed to mimic the epithelium of the intestinal mucosa. When both stromal and epithelial compartments were in direct contact, we observed a synergetic effect between both cell types. Additionally, cells within the stromal compartment remained homogenously distributed through the hydrogels, while the epithelial monolayers were more compact with less cell aggregates. To trustworthy *in vitro* studies, models of undamaged, epithelial monolayers of mature cells are fundamental to mimic the native intestinal mucosa. One of the most widely used methods to examine the epithelial barrier properties is the study of the tight junctions. Tight junctions formation is essential to achieve an accurate epithelial cell polarity and maturity[356]. TEER and permeability measurements are quantitative methods to measure the integrity, maturity and tightness of epithelial barrier. We found that when Caco-2 cells were grown on hydrogel co-networks, and especially those containing NIH/3T3 cells, TEER and permeability measurements were closer to the *in vivo* values of the intestine compared to Caco-2 monolayers grown on the hard porous membranes of the Transwell® inserts. One of the goals of *in vitro* models is to simplify the *in vivo* interactions in a setup that is physiologically relevant, and thus study pathological conditions under correct physiological parameters. Using our 3D small intestinal mucosa model to mimic the barrier disruption, we found that the tight junctions restoration and therefore the epithelial monolayer functionality returned faster to physiological values in the hydrogels containing NIH/3T3 cells. In our intestinal mucosa model, physical interactions between NIH/3T3 cells in the stromal compartment with the Caco-2 cells in the epithelial compartment did not take place, as the NIH/3T3 cells appeared not to be able to migrate through the hydrogel due to matrix restrictions. This suggested that the main interaction between them was through paracrine signalling. It is reported that growth, proliferation, differentiation and maturity of the epithelial cells are accelerated when they are co-cultured with NIH/3T3 cells in Transwell® inserts because of the paracrine factors, such as hepatocyte growth factor (HGF)[357] or keratinocyte growth factor (KGF)[330], which are secreted by fibroblasts.

We demonstrated that the inclusion of stromal-epithelial interactions aided to obtain an *in vitro* model that better recapitulates the physiological parameters of the *in*

vivo small intestinal tissue. Although the embedded cells in hydrogels had a rounded-shape and the collagen secretion was not improved, we took advantage of the high cell viability after hydrogel fabrication and we modified the GelMA – PEGDA hydrogel co-networks to enhance NIH/3T3 cell spreading and proliferation. Most papers in the literature perform cellular experiments using hydrogels with GelMA polymers of high DoF and/or high total macromer contents to have dense structures to reduce degradation and improve scaffold stability. However, this prevents cell spreading, proliferation and migration[160,358]. This drawback can be mitigated if cells are embedded within less dense hydrogel networks[269]. Here, we have demonstrated that cells lost their round-shapes and started to acquire a spread morphology by decreasing the total polymer of the hydrogels. Moreover, cell growth arrest was avoided when the DoF of GelMA polymer was diminished. In that situation, the hydrogel matrix was less crosslinked and cells were less constrained, allowing them to spread and migrate until they were positioned underneath of the epithelial monolayer. This cell distribution resembled that of the native intestinal mucosa, where the fibroblasts are located underneath the epithelial monolayer[91]. The production, the secretion, and the deposition of collagen by the fibroblasts just below the epithelial cells indicates that they were functional and were providing mechanical support to the epithelium. The degradation of the hydrogel matrix was compensated by their high capacity of producing collagen to remodel the matrix, and thus the stability of the hydrogel was not affected. In addition, we could show that these modifications in the hydrogel formulation did not cause any alterations on the formation of the epithelial monolayers. The epithelium grew on top of the hydrogels containing fibroblasts and formed an effective tissue barrier, with TEER values close to those found in the intestinal mucosa *in vivo*. Despite in our intestinal mucosa model we used NIH/3T3 fibroblasts, which are from murine origin, and we co-cultured them with Caco-2 epithelial cells (human origin), we observed synergetic effects between both cell types. Actually, there are many works in literature that use NIH/3T3 fibroblast in co-cultures together with epithelial cell lines from human origin on which also find crosstalk between them [359,360].

Anyway, to minimize specie differences and as an improvement of our model, NIH/3T3 fibroblasts were replaced by CCD-18Co myofibroblast cell line, which comes from human colon cells. It has been seen that CCD-18Co cells enhance the proliferation and differentiation of Caco-2 epithelial cells[330]. Aside from that, CCD-18Co myofibroblasts have a great ability to degrade and synthesize ECM components, such as collagen, playing a key role in the remodelling of the matrix[112]. In this model, we showed that

CCD-18Co produced a large amount of collagen that was deposited under the epithelial monolayer. The experiments also showed that, in addition to the physical cell interactions between the stromal and the epithelial compartments, paracrine signals were also present. The combination of collagen deposition with paracrine signals are crucial factors to enhance epithelial cell proliferation, as well as differentiation and maturity. After 21 days, Caco-2 cells seeded on CCD-18Co-laden hydrogels formed epithelial monolayers with barrier properties closer to the native tissue compared to Caco-2 cell monolayers formed on hydrogels that did not contain cells embedded or monolayers grown on the hard porous Transwell® membranes.

In the native small intestinal mucosa tissue, the immune system has a crucial role to protect it against external infections and, thus, maintain tissue homeostasis. Intestinal mucosa models that contain immune cells into their stromal compartment still are a challenge. Some of the reported studies only investigate the interaction between immune cells and epithelial cells without taking into account the contribution of the fibroblasts or myofibroblasts[114,340]. Actually, *in vitro* intestinal mucosa models formed by an epithelial compartment and a stromal compartment containing a co-culture of immune cells and myofibroblasts had not been reported previously to the best of our knowledge. When examining the effects of the encapsulation process on M0 cells (THP-1 cells differentiated to macrophages), we found that they remained viable during the 21 days of culture, and they had a high proliferative capacity that caused them to grow forming clusters inside the hydrogel. In addition, when M0 cells were co-cultured with CCD-18Co cells in the GelMA – PEGDA hydrogel co-networks to mimic the stromal compartment, their introduction did not alter the behaviour of myofibroblasts. The functionality of the macrophages was evaluated by LPS treatment. We found that M0 cells responded to an external stimulus by the production of cytokines and specially, this response was increased in the co-culture, suggesting that there was a synergetic effect that allowed to overcome the epithelial damage faster than in the monoculture system. When epithelial cells were grown on top of hydrogels containing the co-culture (M0+CCD-18Co) or the monoculture (CCD-18Co cells), the epithelial monolayer was successfully formed after 21days. However, epithelial monolayer was not formed on top of M0-laden hydrogels. This demonstrated that macrophages did not contribute in the formation of the epithelial monolayer and only myofibroblasts had a positive effect in the epithelial cells growth and differentiation. This reaffirms the importance of myofibroblasts-epithelial crosstalk in the modulation of the epithelial cell behaviour,

resulting in a well-oriented epithelium with a columnar morphology and physiological barrier properties.

Epithelial monolayer has a relevant role in acting as a physical barrier that avoids the entrance of pathogens, antigens or other harmful molecules which might be present in the lumen of the mucosa tissue. Tight junctions are in charge of forming a well-developed epithelial barrier. Downregulation of the tight junctions by external stimuli provokes an increase of the paracellular permeability causing the permeation of external molecules, which activates the immune system resulting in an inflammation of the intestine[361]. Here, we induced an inflammatory intestinal mucosa model by LPS exposure. We found that LPS treatment significantly disrupted the epithelial barrier in hydrogels containing the CCD-18Co monoculture and the M0+CCD-18Co co-culture. However, we did not observed differences in the recovery of the epithelium between hydrogels containing the monoculture or the co-culture. We point out that no differences have been noticed because LPS apart from indirectly affecting tight junctions, can produce epithelial cell death. We suggested that, if epithelial cells die during the LPS treatment, unlike tight junctions, the recovery of the epithelium properties due to the cell death took more time to be repaired, for that reason we thought that 24 hours after the LPS treatment were not enough to see the effects on the TEER recovery.

Overall, our results suggest that the introduction of PEGDA polymer into GelMA polymers to produce GelMA – PEGDA hydrogel co-networks is beneficial to have long-term scaffolds without losing mechanical stability. On the other hand, both the photopolymerization process and the GelMA – PEGDA constructs show to be highly biocompatible for both the embedded and the seeded cells. Embedded fibroblasts and myofibroblasts can grow and are able to produce collagen IV and thus remodel the hydrogel matrix for ECM components, whereas macrophages are able to respond to external stimuli, such as LPS molecules and activate an immune response. In reference to epithelial cells on top of the GelMA – PEGDA hydrogel co-networks, these cells are able to form an epithelial barrier with properties closer to the physiological one. Taking into account all of that, we have demonstrated that our 3D *in vitro* model of the intestinal mucosa allows to mimic the cellular spatial distribution of the *in vivo* small intestine tissue (stromal and epithelial compartment). This *in vitro* model would be helpful to understand better the cell-matrix and cell-cell interactions that take place in the *in vivo* intestine under physiological conditions, as well as to study the pathological conditions when they are emulated by external stimuli.

6. Conclusions

1. GelMA – PEGDA hydrogel co-networks have been developed successfully in this thesis to model the native human intestine. The physicochemical and mechanical properties of the material, such as hydrogel co-network homogeneity, degradation rate, diffusion coefficient, swelling ratio and Young's modulus, have been identified and studied. Evaluating the influence of the above parameters and selecting the ones that have provided the most promising results, GelMA – PEGDA hydrogel co-networks with similar physicochemical and mechanical properties to those of the human intestine have been obtained. GelMA – PEGDA hydrogels fabricated are mechanically stable and adequate for long-term cell culture, generating a suitable lamina propria-like hydrogel environment.

2. The methodology employed to fabricate the hydrogels and the polymer solution are highly compatible with optimal process reproducibility, cell survival, and cell functionality. Optimization of crosslinking parameters and polymer solutions for the proper physiology of the cells modelling the lamina propria have been performed. The low Young's modulus values of the surfaces of the GelMA – PEGDA hydrogels do not hinder or affect the epithelial cell growth. Epithelial monolayers with accurate barrier properties are formed on top of the hydrogels.

3. The combination of both lamina propria and epithelium compartments in the GelMA – PEGDA hydrogel co-networks to better recreate the *in vivo* intestinal mucosa features has been fulfilled. The presence of a lamina propria microenvironment has allowed to have (I) crosstalk between lamina propria cells, epithelial cells and the surrounding matrix and (II) suitable arrangement of the cell distribution, providing to our *in vitro* model with more physiologically relevant features, such as enhanced epithelial cell proliferation and barrier permeability.

4. The *in vitro* intestinal mucosa model developed has applicability in modelling pathological intestinal dysfunctions. This has been examined by mimicking (I) a wound repair process by disruption of the tight junctions and (II) an intestine inflammation by LPS exposure. In both cases, the results vary depending on the cells that constitute the lamina propria compartment. These results verify that cell-cell contacts and cell-matrix interactions are necessary to have more functional *in vitro* models of the intestinal tissue.

5. The results demonstrate that our model provides a simplistic but still meaningful approach to obtain more physiologically relevant *in vitro* epithelial models at the cellular and functional levels. It can therefore be used to improve predictions of intestinal permeability in drug studies or to implement better epithelial disease models where an accurate reproduction of the interaction between different cell compartments is of crucial importance.

7. References

1. Tortora, G. J. & Derrickson, B. *Principles of Anatomy & Physiology 14th Edition*. *Wiley* (2014).
2. Practice, C. *Gastrointestinal tract 4: anatomy and role of the jejunum and ileum*. 115: 43–46 (2019).
3. Helander, H. F. & Fändriks, L. *Surface area of the digestive tract – revisited*. Scandinavian Journal of Gastroenterology 49: 681–689 (2014).
4. Hall, J. E.; Guyton, A. C. *Guyton and Hall Textbook of Medical Physiology. Journal of Chemical Information and Modeling* vol. 53 (2015).
5. Volk, N. & Lacy, B. *Anatomy and Physiology of the Small Bowel*. Gastrointestinal Endoscopy Clinics of North America 27: 1–13 (2017).
6. Buckley, A. & Turner, J. R. *Cell biology of tight junction barrier regulation and mucosal disease*. Cold Spring Harbor Perspectives in Biology 10: 1–16 (2018).
7. Peterson, L. W. & Artis, D. *Intestinal epithelial cells: Regulators of barrier function and immune homeostasis*. Nature Reviews Immunology 14: 141–153 (2014).
8. Powell, D. W., Pinchuk, I. V, Saada, J. I., Chen, X. & Mifflin, R. C. *Mesenchymal cells of the intestinal lamina propria.* Annual review of physiology 73: 213–237 (2011).
9. Uchida, K. & Kamikawa, Y. *Muscularis mucosae - The forgotten sibling*. Journal of Smooth Muscle Research 43: 157–177 (2007).
10. Campbell, J., Berry, J. & Liang, Y. *Shackelford's Surgery of the Alimentary Tract Anatomy and Physiology of the Small Intestine*. Shackelford's Surgery of the Alimentary Tract 817–841 (2019).
11. Clevers, H. *The intestinal crypt, a prototype stem cell compartment.* Cell 154: 274–284 (2013).
12. Barret, K. E., Barman, S. M., Boitno, S. & Brooks, H. L. *Ganong's Review of Medical Physiology*. Developmental Medicine & Child Neurology 4: (2016).
13. J., L.-A., S., G. & R., B. *Multiple micronutrient supplementation improves small bowel histological architecture and absorptive area in zambian adults*. Annals of Nutrition and Metabolism 63: 1354 (2014).
14. Kelly, P., Menzies, I., Crane, R., Zulu, I., Nickols, C., Feakins, R., Mwansa, J., Mudenda, V., Katubulushi, M., Greenwald, S. & Farthing, M. *Responses of small intestinal architecture and function over time to environmental factors in a tropical population*. American Journal of Tropical Medicine and Hygiene 70: 412–419 (2004).
15. Thompson, C. M., Proctor, D. M., Suh, M., Haws, L. C., Kirman, C. R. & Harris, M. A. *Assessment of the mode of action underlying development of rodent small intestinal tumors following oral exposure to hexavalent chromium and relevance to humans*. *Critical Reviews in Toxicology* vol. 43 (2013).
16. Li, a C. Y. & Thompson, R. P. H. *Basement membrane components.* Journal of clinical pathology 56: 885–887 (2003).
17. Bühler, R. B., Sennes, L. U., Tsuji, D. H., Mauad, T., Ferraz Da Silva, L. & Saldiva, P. N. *Collagen type I, collagen type III, and versican in vocal fold lamina propria*. Archives of Otolaryngology - Head and Neck Surgery 137: 604–608 (2011).
18. Muñoz-Pinto, D., Whittaker, P. & Hahn, M. S. *Lamina propria cellularity and collagen composition: an integrated assessment of structure in humans.* The Annals of otology, rhinology, and laryngology 118: 299–306 (2009).
19. Roulis, M. & Flavell, R. A. *Fibroblasts and myofibroblasts of the intestinal lamina propria in physiology and disease*. Differentiation 92: 116–131 (2016).
20. Sun, M., He, C., Cong, Y. & Liu, Z. *Regulatory immune cells in regulation of intestinal inflammatory response to microbiota.* Mucosal immunology 8: 969–978 (2015).
21. Yurchenco, P. D. *Basement membranes: cell scaffoldings and signaling platforms.* Cold Spring Harbor perspectives in biology 3: 1–27 (2011).
22. Takeuchi, T. & Gonda, T. *Distribution of the pores of epithelial basement membrane in the rat small intestine.* The Journal of veterinary medical science 66: 695–700 (2004).
23. Timpl, R. *Macromolecular organization of basement membranes.* Current opinion in cell biology 8:

618–624 (1996).

24. Weber, M. *Basement membrane proteins.* Kidney international 41: 620–628 (1992).

25. Allaire, J. M., Crowley, S. M., Law, H. T., Chang, S.-Y., Ko, H.-J. & Vallance, B. A. *The Intestinal Epithelium: Central Coordinator of Mucosal Immunity.* Trends in immunology 39: 677–696 (2018).

26. Carulli, A. J., Samuelson, L. C. & Schnell, S. *Unraveling intestinal stem cell behavior with models of crypt dynamics.* Integrative biology : quantitative biosciences from nano to macro 6: 243–257 (2014).

27. Snoeck, V., Goddeeris, B. & Cox, E. *The role of enterocytes in the intestinal barrier function and antigen uptake*. Microbes and Infection 7: 997–1004 (2005).

28. Lueschow, S. R. & McElroy, S. J. *The Paneth Cell: The Curator and Defender of the Immature Small Intestine*. Frontiers in Immunology 11: (2020).

29. Ramachandran, A., Madesh, M. & Balasubramanian, K. A. *Apoptosis in the intestinal epithelium: Its relevance in normal and pathophysiological conditions*. Journal of Gastroenterology and Hepatology 15: 109–120 (2000).

30. van der Flier, L. G. & Clevers, H. *Stem Cells, Self-Renewal, and Differentiation in the Intestinal Epithelium*. Annual Review of Physiology 71: 241–260 (2009).

31. Barker, N. *Adult intestinal stem cells: Critical drivers of epithelial homeostasis and regeneration*. Nature Reviews Molecular Cell Biology 15: 19–33 (2014).

32. Spit, M., Koo, B. K. & Maurice, M. M. *Tales from the crypt: Intestinal niche signals in tissue renewal, plasticity and cancer*. Open Biology 8: (2018).

33. Crosnier, C., Stamataki, D. & Lewis, J. *Organizing cell renewal in the intestine: Stem cells, signals and combinatorial control*. Nature Reviews Genetics 7: 349–359 (2006).

34. Schneeberger, K., Roth, S., Nieuwenhuis, E. E. S. & Middendorp, S. *Intestinal epithelial cell polarity defects in disease: lessons from microvillus inclusion disease.* Disease models & mechanisms 11: (2018).

35. Vancamelbeke, M. & Vermeire, S. *The intestinal barrier: a fundamental role in health and disease.* Expert review of gastroenterology & hepatology 11: 821–834 (2017).

36. Walton, K. D., Freddo, A. M., Wang, S. & Gumucio, D. L. *Generation of intestinal surface: an absorbing tale.* Development (Cambridge, England) 143: 2261–2272 (2016).

37. Henderson, P., Van Limbergen, J. E., Schwarze, J. & Wilson, D. C. *Function of the intestinal epithelium and its dysregulation in inflammatory bowel disease*. Inflammatory Bowel Diseases 17: 382–395 (2011).

38. Salvo Romero, E., Alonso Cotoner, C., Pardo Camacho, C., Casado Bedmar, M. & Vicario, M. *The intestinal barrier function and its involvement in digestive disease*. Revista Española de Enfermedades Digestivas 108: 686–695 (2015).

39. Assimakopoulos, S. F. *Enterocytes' tight junctions: From molecules to diseases*. World Journal of Gastrointestinal Pathophysiology 2: 123 (2011).

40. Perez-Moreno, M. & Fuchs, E. *Catenins: Keeping Cells from Getting Their Signals Crossed*. Developmental Cell 11: 601–612 (2006).

41. Turner, J. R. *Intestinal mucosal barrier function in health and disease.* Nature reviews. Immunology 9: 799–809 (2009).

42. Garrod, D. & Chidgey, M. *Desmosome structure, composition and function*. Biochimica et Biophysica Acta - Biomembranes 1778: 572–587 (2008).

43. Ménard, S., Cerf-Bensussan, N. & Heyman, M. *Multiple facets of intestinal permeability and epithelial handling of dietary antigens*. Mucosal Immunology 3: 247–259 (2010).

44. Choonara, B. F., Choonara, Y. E., Kumar, P., Bijukumar, D., du Toit, L. C. & Pillay, V. *A review of advanced oral drug delivery technologies facilitating the protection and absorption of protein and peptide molecules*. Biotechnology Advances 32: 1269–1282 (2014).

45. Schroeder, B. O. *Fight them or feed them: How the intestinal mucus layer manages the gut microbiota*. Gastroenterology Report 7: 3–12 (2019).

46. Linden, S. K., Sutton, P., Karlsson, N. G., Korolik, V. & McGuckin, M. A. *Mucins in the mucosal barrier to infection.* Mucosal immunology 1: 183–197 (2008).

47. Atuma, C., Strugala, V., Allen, A. & Holm, L. *The adherent gastrointestinal mucus gel layer: thickness and physical state in vivo.* American journal of physiology. Gastrointestinal and liver physiology 280: G922-9 (2001).

48. Strocchi, A. & Levitt, M. D. *A reappraisal of the magnitude and implications of the intestinal unstirred layer.* Gastroenterology 101: 843–847 (1991).

49. Pelaseyed, T., *et al. The mucus and mucins of the goblet cells and enterocytes provide the first defense line of the gastrointestinal tract and interact with the immune system.* Immunological reviews 260: 8–20 (2014).

50. Schneider, H., Pelaseyed, T., Svensson, F. & Johansson, M. E. V. *Study of mucin turnover in the small intestine by in vivo labeling.* Scientific reports 8: 5760 (2018).

51. Rescigno, M. *The intestinal epithelial barrier in the control of homeostasis and immunity*. Trends in Immunology 32: 256–264 (2011).

52. Mowat, A. M. & Agace, W. W. *Regional specialization within the intestinal immune system*. Nature Reviews Immunology 14: 667–685 (2014).

53. Ferguson, A. *Intraepithelial lymphocytes of the small intestine.* Gut 18: 921–937 (1977).

54. Ma, H., Tao, W. & Zhu, S. *T lymphocytes in the intestinal mucosa: defense and tolerance*. Cellular and Molecular Immunology 16: 216–224 (2019).

55. Gutzeit, C., Magri, G. & Cerutti, A. *Intestinal IgA production and its role in host-microbe interaction.* Immunological reviews 260: 76–85 (2014).

56. Cerovic, V., Bain, C. C., Mowat, A. M. & Milling, S. W. F. *Intestinal macrophages and dendritic cells: What's the difference?* Trends in Immunology 35: 270–277 (2014).

57. Wang, S., Ye, Q., Zeng, X. & Qiao, S. *Functions of Macrophages in the Maintenance of Intestinal Homeostasis*. Journal of Immunology Research 2019: 1–8 (2019).

58. Bain, C. C. & Schridde, A. *Origin, Differentiation, and Function of Intestinal Macrophages*. Frontiers in Immunology 9: (2018).

59. Jung, Y. & Rothenberg, M. E. *Roles and regulation of gastrointestinal eosinophils in immunity and disease.* Journal of immunology (Baltimore, Md. : 1950) 193: 999–1005 (2014).

60. Schleimer, R. P., Kato, A., Kern, R., Kuperman, D. & Avila, P. C. *Epithelium: at the interface of innate and adaptive immune responses.* The Journal of allergy and clinical immunology 120: 1279–1284 (2007).

61. Bischoff, S. C. *'Gut health': a new objective in medicine?* BMC medicine 9: 24 (2011).

62. Mai, V. & Draganov, P. V. *Recent advances and remaining gaps in our knowledge of associations between gut microbiota and human health.* World journal of gastroenterology 15: 81–85 (2009).

63. König, J., Wells, J., Cani, P. D., García-Ródenas, C. L., MacDonald, T., Mercenier, A., Whyte, J., Troost, F. & Brummer, R.-J. *Human Intestinal Barrier Function in Health and Disease.* Clinical and translational gastroenterology 7: e196 (2016).

64. Rios-Arce, N. D., Collins, F. L., Schepper, J. D., Steury, M. D., Raehtz, S., Mallin, H., Schoenherr, D. T., Parameswaran, N. & McCabe, L. R. *Epithelial Barrier Function in Gut-Bone Signaling.* Advances in experimental medicine and biology 1033: 151–183 (2017).

65. Sattar, SBA; Singh, S. *Bacterial Gastroenteritis*. *Treasure Island* https://www.ncbi.nlm.nih.gov/books/NBK513295/ (2019).

66. Groschwitz, K. R. & Hogan, S. P. *Intestinal barrier function: molecular regulation and disease pathogenesis.* The Journal of allergy and clinical immunology 124: 3–20; quiz 21–22 (2009).

67. Chelakkot, C., Ghim, J. & Ryu, S. H. *Mechanisms regulating intestinal barrier integrity and its*

pathological implications. Experimental & molecular medicine 50: 103 (2018).

68. Baumgart, D. C. & Sandborn, W. J. *Inflammatory bowel disease: clinical aspects and established and evolving therapies.* Lancet (London, England) 369: 1641–1657 (2007).

69. Gu, P. & Feagins, L. A. *Dining With Inflammatory Bowel Disease : A Review of the Literature on Diet in the Pathogenesis and Management of IBD*. Inflammatory Bowel Diseases XX: 1–11 (2019).

70. González-González, M., Díaz-Zepeda, C., Eyzaguirre-Velásquez, J., González-Arancibia, C., Bravo, J. A. & Julio-Pieper, M. *Investigating Gut Permeability in Animal Models of Disease*. Frontiers in Physiology 9: 1962 (2019).

71. Pearce, S. C., Coia, H. G., Karl, J. P., Pantoja-Feliciano, I. G., Zachos, N. C. & Racicot, K. *Intestinal in vitro and ex vivo models to study host-microbiome interactions and acute stressors*. Frontiers in Physiology 9: (2018).

72. Dosh, R. H., Jordan-Mahy, N., Sammon, C. & Le Maitre, C. L. *Tissue Engineering Laboratory Models of the Small Intestine*. Tissue Engineering - Part B: Reviews 24: 98–111 (2018).

73. Costa, J. & Ahluwalia, A. *Advances and Current Challenges in Intestinal in vitro Model Engineering: A Digest.* Frontiers in bioengineering and biotechnology 7: 144 (2019).

74. Williams, C. F., Walton, G. E., Jiang, L., Plummer, S., Garaiova, I. & Gibson, G. R. *Comparative Analysis of Intestinal Tract Models*. Annual Review of Food Science and Technology 6: 329–350 (2015).

75. Torras, N., García-Díaz, M., Fernández-Majada, V. & Martínez, E. *Mimicking Epithelial Tissues in Three-Dimensional Cell Culture Models.* Frontiers in bioengineering and biotechnology 6: 197 (2018).

76. Pusch, J., Votteler, M., Göhler, S., Engl, J., Hampel, M., Walles, H. & Schenke-Layland, K. *The physiological performance of a three-dimensional model that mimics the microenvironment of the small intestine.* Biomaterials 32: 7469–7478 (2011).

77. Tannenbaum, J. & Bennett, B. T. *Russell and Burch's 3Rs then and now: the need for clarity in definition and purpose.* Journal of the American Association for Laboratory Animal Science : JAALAS 54: 120–132 (2015).

78. Benam, K. H., *et al. Engineered In Vitro Disease Models*. Annual Review of Pathology: Mechanisms of Disease 10: 195–262 (2015).

79. Meunier, V., Bourrié, M., Berger, Y. & Fabre, G. *The human intestinal epithelial cell line Caco-2; pharmacological and pharmacokinetic applications*. Cell Biology and Toxicology 11: 187–194 (1995).

80. Fogh, J; Trempe, G. *Human Tumor Cells In Vitro*. in *Plenum* 115–141 (1975).

81. Smetanová, L., Stětinová, V., Svoboda, Z. & Kvetina, J. *Caco-2 cells, biopharmaceutics classification system (BCS) and biowaiver.* Acta medica (Hradec Kralove) 54: 3–8 (2011).

82. Vachon, P. H. & Beaulieu, J. F. *Transient mosaic patterns of morphological and functional differentiation in the Caco-2 cell line.* Gastroenterology 103: 414–423 (1992).

83. Lea, T. *Caco-2 Cell Line*. *The Impact of Food Bioactives on Health: in vitro and ex vivo models* (Springer International Publishing, 2015).

84. Awortwe, C., Fasinu, P. S. & Rosenkranz, B. *Application of Caco-2 cell line in herb-drug interaction studies: Current approaches and challenges*. Journal of Pharmacy and Pharmaceutical Sciences 17: 1–19 (2014).

85. Hidalgo, I. J., Raub, T. J. & Borchardt, R. T. *Characterization of the human colon carcinoma cell line (Caco-2) as a model system for intestinal epithelial permeability.* Gastroenterology 96: 736–749 (1989).

86. Hilgers, A. R., Conradi, R. A. & Burton, P. S. *Caco-2 cell monolayers as a model for drug transport across the intestinal mucosa.* Pharmaceutical research 7: 902–910 (1990).

87. Kang, T., Guan, R., Chen, X., Song, Y., Jiang, H. & Zhao, J. *In vitro toxicity of different-sized ZnO nanoparticles in Caco-2 cells.* Nanoscale research letters 8: 496 (2013).

88. Hubatsch, I., Ragnarsson, E. G. E. & Artursson, P. *Determination of drug permeability and prediction of drug absorption in Caco-2 monolayers*. Nature Protocols 2: 2111–2119 (2007).

89. Brück, S., Strohmeier, J., Busch, D., Drozdzik, M. & Oswald, S. *Caco-2 cells – expression, regulation and function of drug transporters compared with human jejunal tissue*. Biopharmaceutics and Drug Disposition 38: 115–126 (2017).

90. Artursson, P., Palm, K. & Luthman, K. *Caco-2 monolayers in experimental and theoretical predictions of drug transport*. Advanced Drug Delivery Reviews 64: 280–289 (2012).

91. Li, N., Wang, D., Sui, Z., Qi, X., Ji, L., Wang, X. & Yang, L. *Development of an improved three-dimensional in vitro intestinal mucosa model for drug absorption evaluation*. Tissue engineering. Part C, Methods 19: 708–719 (2013).

92. Srinivasan, B., Kolli, A. R., Esch, M. B., Abaci, H. E., Shuler, M. L. & Hickman, J. J. *TEER measurement techniques for in vitro barrier model systems.* Journal of laboratory automation 20: 107–126 (2015).

93. Chen, S., Einspanier, R. & Schoen, J. *Transepithelial electrical resistance (TEER): a functional parameter to monitor the quality of oviduct epithelial cells cultured on filter supports.* Histochemistry and cell biology 144: 509–515 (2015).

94. Ren, H. J., Zhang, C. L., Liu, R. D., Li, N., Li, X. G., Xue, H. K., Guo, Y., Wang, Z. Q., Cui, J. & Ming, L. *Primary cultures of mouse small intestinal epithelial cells using the dissociating enzyme type I collagenase and hyaluronidase*. Brazilian Journal of Medical and Biological Research 50: 1–11 (2017).

95. Aldhous, M. C., Shmakov, A. N., Bode, J. & Ghosh, S. *Characterization of conditions for the primary culture of human small intestinal epithelial cells*. Clinical and Experimental Immunology 125: 32–40 (2001).

96. Sato, T., Vries, R. G., Snippert, H. J., van de Wetering, M., Barker, N., Stange, D. E., van Es, J. H., Abo, A., Kujala, P., Peters, P. J. & Clevers, H. *Single Lgr5 stem cells build crypt-villus structures in vitro without a mesenchymal niche.* Nature 459: 262–265 (2009).

97. Leushacke, M. & Barker, N. *Ex vivo culture of the intestinal epithelium: strategies and applications*. Gut 63: 1345–1354 (2014).

98. Meneses, A., Schneeberger, K., Kruitwagen, H., Penning, L., van Steenbeek, F., Burgener, I. & Spee, B. *Intestinal Organoids—Current and Future Applications*. Veterinary Sciences 3: 31 (2016).

99. Zachos, N. C., Kovbasnjuk, O., Foulke-Abel, J., In, J., Blutt, S. E., de Jonge, H. R., Estes, M. K. & Donowitz, M. *Human Enteroids/Colonoids and Intestinal Organoids Functionally Recapitulate Normal Intestinal Physiology and Pathophysiology*. Journal of Biological Chemistry 291: 3759–3766 (2016).

100. Bartfeld, S. & Clevers, H. *Stem cell-derived organoids and their application for medical research and patient treatment*. Journal of Molecular Medicine 95: 729–738 (2017).

101. Wallach, T. E. & Bayrer, J. R. *Intestinal Organoids*. Journal of Pediatric Gastroenterology and Nutrition 64: 180–185 (2017).

102. Imura, Y., Asano, Y., Sato, K. & Yoshimura, E. *A microfluidic system to evaluate intestinal absorption.* Analytical sciences : the international journal of the Japan Society for Analytical Chemistry 25: 1403–1407 (2009).

103. Kim, H. J., Huh, D., Hamilton, G. & Ingber, D. E. *Human gut-on-a-chip inhabited by microbial flora that experiences intestinal peristalsis-like motions and flow.* Lab on a chip 12: 2165–2174 (2012).

104. Kim, H. J., Li, H., Collins, J. J. & Ingber, D. E. *Contributions of microbiome and mechanical deformation to intestinal bacterial overgrowth and inflammation in a human gut-on-a-chip.* Proceedings of the National Academy of Sciences of the United States of America 113: E7-15 (2016).

105. Shim, K. Y., Lee, D., Han, J., Nguyen, N. T., Park, S. & Sung, J. H. *Microfluidic gut-on-a-chip with three-dimensional villi structure*. Biomedical Microdevices 19: (2017).

106. Sung, J. H., Yu, J., Luo, D., Shuler, M. L. & March, J. C. *Microscale 3-D hydrogel scaffold for biomimetic gastrointestinal (GI) tract model.* Lab on a chip 11: 389–392 (2011).

107. Bein, A., Shin, W., Jalili-Firoozinezhad, S., Park, M. H., Sontheimer-Phelps, A., Tovaglieri, A., Chalkiadaki, A., Kim, H. J. & Ingber, D. E. *Microfluidic Organ-on-a-Chip Models of Human Intestine*. Cellular and Molecular Gastroenterology and Hepatology 5: 659–668 (2018).

108. Pampaloni, F., Reynaud, E. G. & Stelzer, E. H. K. *The third dimension bridges the gap between cell culture and live tissue.* Nature reviews. Molecular cell biology 8: 839–845 (2007).

109. Mattei, G., Giusti, S. & Ahluwalia, A. *Design criteria for generating physiologically relevant in vitro models in bioreactors*. Processes 2: 548–569 (2014).

110. Chen, Y., Lin, Y., Davis, K. M., Wang, Q., Rnjak-Kovacina, J., Li, C., Isberg, R. R., Kumamoto, C. A., Mecsas, J. & Kaplan, D. L. *Robust bioengineered 3D functional human intestinal epithelium*. Scientific Reports 5: 1–11 (2015).

111. De Gregorio, V., Imparato, G., Urciuolo, F. & Netti, P. A. *3D stromal tissue equivalent affects intestinal epithelium morphogenesis in vitro*. Biotechnology and Bioengineering 115: 1062–1075 (2018).

112. Pereira, C., Araújo, F., Barrias, C. C., Granja, P. L. & Sarmento, B. *Dissecting stromal-epithelial interactions in a 3D in vitro cellularized intestinal model for permeability studies*. Biomaterials 56: 36–45 (2015).

113. Matsusaki, M., Hikimoto, D., Nishiguchi, A., Kadowaki, K., Ohura, K., Imai, T. & Akashi, M. *3D-fibroblast tissues constructed by a cell-coat technology enhance tight-junction formation of human colon epithelial cells.* Biochemical and biophysical research communications 457: 363–369 (2015).

114. Leonard, F., Collnot, E.-M. & Lehr, C.-M. *A three-dimensional coculture of enterocytes, monocytes and dendritic cells to model inflamed intestinal mucosa in vitro.* Molecular pharmaceutics 7: 2103–2119 (2010).

115. Chen, Y., Lin, Y., Davis, K. M., Wang, Q., Rnjak-Kovacina, J., Li, C., Isberg, R. R., Kumamoto, C. A., Mecsas, J. & Kaplan, D. L. *Robust bioengineered 3D functional human intestinal epithelium*. Scientific Reports 5: 13708 (2015).

116. Yi, S., Ding, F., Gong, L. & Gu, X. *Extracellular Matrix Scaffolds for Tissue Engineering and Regenerative Medicine.* Current stem cell research & therapy 12: 233–246 (2017).

117. Huang, G., Li, F., Zhao, X., Ma, Y., Li, Y., Lin, M., Jin, G., Lu, T. J., Genin, G. M. & Xu, F. *Functional and Biomimetic Materials for Engineering of the Three-Dimensional Cell Microenvironment*. Chemical Reviews 117: 12764–12850 (2017).

118. Gattazzo, F., Urciuolo, A. & Bonaldo, P. *Extracellular matrix: a dynamic microenvironment for stem cell niche.* Biochimica et biophysica acta 1840: 2506–2519 (2014).

119. Kusindarta, D. L. & Wihadmadyatami, H. *The Role of Extracellular Matrix in Tissue Regeneration*. in *Tissue Regeneration* vol. 20 S23-29 (InTech, 2018).

120. Kim, Y., Ko, H., Kwon, I. K., Kwon, I. K. & Shin, K. *Extracellular Matrix Revisited: Roles in Tissue Engineering.* International neurourology journal 20: S23-29 (2016).

121. Sainio, A. & Järveläinen, H. *Extracellular matrix macromolecules: potential tools and targets in cancer gene therapy*. Molecular and Cellular Therapies 2: 14 (2014).

122. Andersson, K.-E. & McCloskey, K. D. *Lamina propria: the functional center of the bladder?* Neurourology and urodynamics 33: 9–16 (2014).

123. González-Díaz, E. C. & Varghese, S. *Hydrogels as Extracellular Matrix Analogs.* Gels (Basel, Switzerland) 2: 469–484 (2016).

124. Geckil, H., Xu, F., Zhang, X., Moon, S. & Demirci, U. *Engineering hydrogels as extracellular matrix mimics.* Nanomedicine (London, England) 5: 469–484 (2010).

125. Slaughter, B. V., Khurshid, S. S., Fisher, O. Z., Khademhosseini, A. & Peppas, N. A. *Hydrogels in regenerative medicine.* Advanced materials (Deerfield Beach, Fla.) 21: 3307–3329 (2009).

126. Ganji, F., Vasheghani-Farahani, S. & Vasheghani-Farahani, E. *Theoretical description of hydrogel swelling: A review*. Iranian Polymer Journal (English Edition) 19: 375–398 (2010).

127. Caliari, S. R. & Burdick, J. A. *A practical guide to hydrogels for cell culture.* Nature methods 13: 405–414 (2016).

128. Tibbitt, M. W. & Anseth, K. S. *Hydrogels as extracellular matrix mimics for 3D cell culture.* Biotechnology and bioengineering 103: 655–663 (2009).

129. Catoira, M. C., Fusaro, L., Di Francesco, D., Ramella, M. & Boccafoschi, F. *Overview of natural hydrogels for regenerative medicine applications*. Journal of Materials Science: Materials in Medicine 30: (2019).

130. Bott, K., Upton, Z., Schrobback, K., Ehrbar, M., Hubbell, J. A., Lutolf, M. P. & Rizzi, S. C. *The effect of matrix characteristics on fibroblast proliferation in 3D gels*. Biomaterials 31: 8454–8464 (2010).

131. Hughes, C. S., Postovit, L. M. & Lajoie, G. A. *Matrigel: a complex protein mixture required for optimal growth of cell culture.* Proteomics 10: 1886–1890 (2010).

132. Capeling, M. M., *et al. Nonadhesive Alginate Hydrogels Support Growth of Pluripotent Stem Cell-Derived Intestinal Organoids*. Stem Cell Reports 12: 381–394 (2019).

133. Zakhem, E. & Bitar, K. *Development of Chitosan Scaffolds with Enhanced Mechanical Properties for Intestinal Tissue Engineering Applications*. Journal of Functional Biomaterials 6: 999–1011 (2015).

134. Esposito, A., Mezzogiorno, A., Sannino, A., De Rosa, A., Menditti, D., Esposito, V. & Ambrosio, L. *Hyaluronic acid based materials for intestine tissue engineering: A morphological and biochemical study of cell-material interaction*. Journal of Materials Science: Materials in Medicine 17: 1365–1372 (2006).

135. Drugbank. *Gelatin*. https://www.drugbank.ca/drugs/DB11242.

136. Choi, J. R., Yong, K. W., Choi, J. Y. & Cowie, A. C. *Recent advances in photo-crosslinkable hydrogels for biomedical applications.* BioTechniques 66: 40–53 (2019).

137. Jaipan, P., Nguyen, A. & Narayan, R. J. *Gelatin-based hydrogels for biomedical applications*. MRS Communications 7: 416–426 (2017).

138. Lee, B. H., Lum, N., Seow, L. Y., Lim, P. Q. & Tan, L. P. *Synthesis and characterization of types A and B gelatin methacryloyl for bioink applications*. Materials 9: 1–13 (2016).

139. Gyles, D. A., Castro, L. D., Silva, J. O. C. & Ribeiro-Costa, R. M. *A review of the designs and prominent biomedical advances of natural and synthetic hydrogel formulations*. European Polymer Journal 88: 373–392 (2017).

140. Sun, M., Sun, X., Wang, Z., Guo, S., Yu, G. & Yang, H. *Synthesis and Properties of Gelatin Methacryloyl (GelMA) Hydrogels and Their Recent Applications in Load-Bearing Tissue.* Polymers 10: (2018).

141. Van Den Bulcke, A. I., Bogdanov, B., De Rooze, N., Schacht, E. H., Cornelissen, M. & Berghmans, H. *Structural and rheological properties of methacrylamide modified gelatin hydrogels*. Biomacromolecules vol. 1 31–38 (2000).

142. Loessner, D., Meinert, C., Kaemmerer, E., Martine, L. C., Yue, K., Levett, P. A., Klein, T. J., Melchels, F. P. W., Khademhosseini, A. & Hutmacher, D. W. *Functionalization, preparation and use of cell-laden gelatin methacryloyl-based hydrogels as modular tissue culture platforms*. Nature protocols 11: 727–746 (2016).

143. Dong, Z., Yuan, Q., Huang, K., Xu, W., Liu, G. & Gu, Z. *Gelatin methacryloyl (GelMA)-based biomaterials for bone regeneration*. RSC Advances 9: 17737–17744 (2019).

144. Shin, S. R., *et al. Reduced Graphene Oxide-GelMA Hybrid Hydrogels as Scaffolds for Cardiac Tissue Engineering.* Small (Weinheim an der Bergstrasse, Germany) 12: 3677–3689 (2016).

145. Radhakrishnan, J., Krishnan, U. M. & Sethuraman, S. *Hydrogel based injectable scaffolds for cardiac tissue regeneration*. Biotechnology Advances 32: 449–461 (2014).

146. Toh, W. S. & Loh, X. J. *Advances in hydrogel delivery systems for tissue regeneration*. Materials Science and Engineering: C 45: 690–697 (2014).

147. Luo, Z., Sun, W., Fang, J., Lee, K., Li, S., Gu, Z., Dokmeci, M. R. & Khademhosseini, A. *Biodegradable Gelatin Methacryloyl Microneedles for Transdermal Drug Delivery.* Advanced healthcare materials 8: e1801054 (2019).

148. Jeon, O., Wolfson, D. W. & Alsberg, E. *In-situ formation of growth-factor-loaded coacervate microparticle-embedded hydrogels for directing encapsulated stem cell fate.* Advanced materials (Deerfield Beach, Fla.) 27: 2216–2223 (2015).

149. Lutolf, M. P. & Hubbell, J. A. *Synthetic biomaterials as instructive extracellular microenvironments for morphogenesis in tissue engineering*. Nature Biotechnology 23: 47–55 (2005).

150. D'souza, A. A. & Shegokar, R. *Polyethylene glycol (PEG): a versatile polymer for pharmaceutical applications.* Expert opinion on drug delivery 13: 1257–1275 (2016).

151. Gyles, D. A., Castro, L. D., Silva, J. O. C. & Ribeiro-Costa, R. M. *A review of the designs and prominent biomedical advances of natural and synthetic hydrogel formulations*. European Polymer Journal 88: 373–392 (2017).

152. Zhu, J. *Bioactive modification of poly(ethylene glycol) hydrogels for tissue engineering.* Biomaterials 31: 4639–4656 (2010).

153. Hanna, K., Yasar-Inceoglu, O. & Yasar, O. *Drug Delivered Poly(ethylene glycol) Diacrylate (PEGDA) Hydrogels and Their Mechanical Characterization Tests for Tissue Engineering Applications*. MRS Advances 3: 1697–1702 (2018).

154. Nguyen, Q. T., Hwang, Y., Chen, A. C., Varghese, S. & Sah, R. L. *Cartilage-like mechanical properties of poly (ethylene glycol)-diacrylate hydrogels*. Biomaterials 33: 6682–6690 (2012).

155. Castaño, A. G., García-Díaz, M., Torras, N., Altay, G., Comelles, J. & Martínez, E. *Dynamic photopolymerization produces complex microstructures on hydrogels in a moldless approach to generate a 3D intestinal tissue model.* Biofabrication 11: 025007 (2019).

156. Altay, G., Tosi, S., García-Díaz, M. & Martínez, E. *Imaging the Cell Morphological Response to 3D Topography and Curvature in Engineered Intestinal Tissues*. Frontiers in Bioengineering and Biotechnology 8: (2020).

157. Altay, G. *Towards the development of biomimetic in vitro models of intestinal epithelium derived from intestinal organoids*. TDX (Tesis Doctorals en Xarxa) (2019).

158. Pérez, R. A., Won, J.-E., Knowles, J. C. & Kim, H.-W. *Naturally and synthetic smart composite biomaterials for tissue regeneration.* Advanced drug delivery reviews 65: 471–496 (2013).

159. Xiao, S., Zhao, T., Wang, J., Wang, C., Du, J., Ying, L., Lin, J., Zhang, C., Hu, W., Wang, L. & Xu, K. *Gelatin Methacrylate (GelMA)-Based Hydrogels for Cell Transplantation: an Effective Strategy for Tissue Engineering*. Stem Cell Reviews and Reports 15: 664–679 (2019).

160. Wang, Y., Ma, M., Wang, J., Zhang, W., Lu, W., Gao, Y., Zhang, B. & Guo, Y. *Development of a Photo-Crosslinking, Biodegradable GelMA/PEGDA Hydrogel for Guided Bone Regeneration Materials.* Materials (Basel, Switzerland) 11: 6–8 (2018).

161. Hu, W., Wang, Z., Xiao, Y., Zhang, S. & Wang, J. *Advances in crosslinking strategies of biomedical hydrogels*. Biomaterials Science 7: 843–855 (2019).

162. Parhi, R. *Cross-Linked Hydrogel for Pharmaceutical Applications: A Review.* Advanced pharmaceutical bulletin 7: 515–530 (2017).

163. Maitra, J. & Shukla, V. K. *Cross-linking in Hydrogels - A Review*. American Journal of Polymer Science 4: 25–31 (2014).

164. Allcock, H. R. & Kwon, S. *An ionically crosslinkable polyphosphazene: poly[bis(carboxylatophenoxy)phosphazene] and its hydrogels and membranes*. Macromolecules 22: 75–79 (1989).

165. McHale, M. K., Setton, L. A. & Chilkoti, A. *Synthesis and in vitro evaluation of enzymatically cross-linked elastin-like polypeptide gels for cartilaginous tissue repair.* Tissue engineering 11: 1768–1779.

166. Bossion, A., Heifferon, K. V., Meabe, L., Zivic, N., Taton, D., Hedrick, J. L., Long, T. E. & Sardon, H. *Opportunities for organocatalysis in polymer synthesis via step-growth methods*. Progress in Polymer Science 90: 164–210 (2019).

167. Yao, H., Wang, J. & Mi, S. *Photo processing for biomedical hydrogels design and functionality: A review*. Polymers 10: 1–27 (2017).

168. Kawamoto, M., Ito, Y. & Matsuda, T. *Photochemical processed materials*. *Photochemistry for Biomedical Applications: From Device Fabrication to Diagnosis and Therapy* (2018).

169. Bowman, C. N. & Kloxin, C. J. *Toward an enhanced understanding and implementation of*

photopolymerization reactions. AIChE Journal 54: 2775–2795 (2008).

170. Su, W.-F. *Principles of Polymer Design and Synthesis*. *Extracts* (2013).

171. Shih, H. & Lin, C.-C. *Visible-Light-Mediated Thiol-Ene Hydrogelation Using Eosin-Y as the Only Photoinitiator*. Macromolecular Rapid Communications 34: 269–273 (2013).

172. Qin, X. H., Ovsianikov, A., Stampfl, J. & Liska, R. *Additive manufacturing of photosensitive Hydrogels for tissue engineering applications*. BioNanoMaterials 15: 49–70 (2014).

173. Fouassier, J.-P., Burr, D. & Wieder, F. *Water-soluble photoinitiators: Primary processes in hydroxy alkyl phenyl ketones*. Journal of Polymer Science Part A: Polymer Chemistry 29: 1319–1327 (1991).

174. Rouillard, A. D., Berglund, C. M., Lee, J. Y., Polacheck, W. J., Tsui, Y., Bonassar, L. J. & Kirby, B. J. *Methods for photocrosslinking alginate hydrogel scaffolds with high cell viability.* Tissue engineering. Part C, Methods 17: 173–179 (2011).

175. Williams, C. G., Malik, A. N., Kim, T. K., Manson, P. N. & Elisseeff, J. H. *Variable cytocompatibility of six cell lines with photoinitiators used for polymerizing hydrogels and cell encapsulation.* Biomaterials 26: 1211–1218 (2005).

176. Fairbanks, B. D., Schwartz, M. P., Bowman, C. N. & Anseth, K. S. *Photoinitiated polymerization of PEG-diacrylate with lithium phenyl-2,4,6-trimethylbenzoylphosphinate: polymerization rate and cytocompatibility*. Biomaterials 30: 6702–6707 (2009).

177. Kappes, U. P., Luo, D., Potter, M., Schulmeister, K. & Rünger, T. M. *Short- and long-wave UV light (UVB and UVA) induce similar mutations in human skin cells.* The Journal of investigative dermatology 126: 667–675 (2006).

178. Nicodemus, G. D. & Bryant, S. J. *Cell encapsulation in biodegradable hydrogels for tissue engineering applications.* Tissue engineering. Part B, Reviews 14: 149–165 (2008).

179. Chai, Q., Jiao, Y. & Yu, X. *Hydrogels for Biomedical Applications: Their Characteristics and the Mechanisms behind Them.* Gels (Basel, Switzerland) 3: 6 (2017).

180. Peppas, N. A., Hilt, J. Z., Khademhosseini, A. & Langer, R. *Hydrogels in Biology and Medicine: From Molecular Principles to Bionanotechnology*. Advanced Materials 18: 1345–1360 (2006).

181. Flory, P. J., Rabjohn, N. & Shaffer, M. C. *Dependence of elastic properties of vulcanized rubber on the degree of cross linking*. Journal of Polymer Science 4: 225–245 (1949).

182. Flory, P. J. & Rehner, J. *Statistical mechanics of cross-linked polymer networks I. Rubberlike elasticity*. The Journal of Chemical Physics 11: 512–520 (1943).

183. Peppas, N. A. & Merrill, E. W. *Crosslinked poly(vinyl alcohol) hydrogels as swollen elastic networks*. Journal of Applied Polymer Science 21: 1763–1770 (1977).

184. Sarveswaran, K., Kurz, V., Dong, Z., Tanaka, T., Penny, S. & Timp, G. *Synthetic Capillaries to Control Microscopic Blood Flow.* Scientific reports 6: 21885 (2016).

185. Loh, Q. L. & Choong, C. *Three-dimensional scaffolds for tissue engineering applications: Role of porosity and pore size*. Tissue Engineering - Part B: Reviews 19: 485–502 (2013).

186. Drury, J. L. & Mooney, D. J. *Hydrogels for tissue engineering: Scaffold design variables and applications*. Biomaterials 24: 4337–4351 (2003).

187. Offeddu, G. S., Axpe, E., Harley, B. A. C. & Oyen, M. L. *Relationship between permeability and diffusivity in polyethylene glycol hydrogels*. AIP Advances 8: (2018).

188. Kontturi, L.-S., Collin, E. C., Murtomäki, L., Pandit, A. S., Yliperttula, M. & Urtti, A. *Encapsulated cells for long-term secretion of soluble VEGF receptor 1: Material optimization and simulation of ocular drug response.* European journal of pharmaceutics and biopharmaceutics : official journal of Arbeitsgemeinschaft fur Pharmazeutische Verfahrenstechnik e.V 95: 387–397 (2015).

189. Li, X., Chen, S., Li, J., Wang, X., Zhang, J., Kawazoe, N. & Chen, G. *3D Culture of Chondrocytes in Gelatin Hydrogels with Different Stiffness.* Polymers 8: (2016).

190. Vedadghavami, A., Minooei, F., Mohammadi, M. H., Khetani, S., Rezaei Kolahchi, A., Mashayekhan, S. & Sanati-Nezhad, A. *Manufacturing of hydrogel biomaterials with controlled mechanical properties*

for tissue engineering applications. Acta Biomaterialia 62: 42–63 (2017).

191. McKee, C. T., Last, J. A., Russell, P. & Murphy, C. J. *Indentation versus tensile measurements of young's modulus for soft biological tissues*. Tissue Engineering - Part B: Reviews 17: 155–164 (2011).

192. Wilson, S. L., Ahearne, M., El Haj, A. J. & Yang, Y. *Mechanical characterization of hydrogels and its implications for cellular activities*. RSC Soft Matter 171–190 (2014).

193. Wells, R. G. *The role of matrix stiffness in regulating cell behavior.* Hepatology (Baltimore, Md.) 47: 1394–1400 (2008).

194. Johnson, L. A., Rodansky, E. S., Sauder, K. L., Horowitz, J. C., Mih, J. D., Tschumperlin, D. J. & Higgins, P. D. *Matrix stiffness corresponding to strictured bowel induces a fibrogenic response in human colonic fibroblasts*. Inflammatory Bowel Diseases 19: 891–903 (2013).

195. Yanagawa, F., Sugiura, S. & Kanamori, T. *Hydrogel microfabrication technology toward three dimensional tissue engineering*. Regenerative Therapy 3: 45–57 (2016).

196. Sen, A. K., Raj, A., Banerjee, U. & Iqbal, S. R. *Soft Lithography, Molding, and Micromachining Techniques for Polymer Micro Devices*. in *Methods in Molecular Biology* vol. 1906 13–54 (2019).

197. McDonald, J. C., Duffy, D. C., Anderson, J. R., Chiu, D. T., Wu, H., Schueller, O. J. A. & Whitesides, G. M. *Fabrication of microfluidic systems in poly(dimethylsiloxane)*. Electrophoresis 21: 27–40 (2000).

198. Zhou, W. *Nanoimprint Lithography: An Enabling Process for Nanofabrication*. (Springer Berlin Heidelberg, 2013).

199. Qin, D., Xia, Y. & Whitesides, G. M. *Soft lithography for micro- and nanoscale patterning*. Nature Protocols 5: 491–502 (2010).

200. Khademhosseini, A., Eng, G., Yeh, J., Fukuda, J., Blumling, J., Langer, R. & Burdick, J. A. *Micromolding of photocrosslinkable hyaluronic acid for cell encapsulation and entrapment.* Journal of biomedical materials research. Part A 79: 522–532 (2006).

201. Nichol, J. W., Koshy, S. T., Bae, H., Hwang, C. M., Yamanlar, S. & Khademhosseini, A. *Cell-laden microengineered gelatin methacrylate hydrogels*. Biomaterials 31: 5536–5544 (2010).

202. Occhetta, P., Sadr, N., Piraino, F., Redaelli, A., Moretti, M. & Rasponi, M. *Fabrication of 3D cell-laden hydrogel microstructures through photo-mold patterning*. Biofabrication 5: (2013).

203. Yeh, J., Ling, Y., Karp, J. M., Gantz, J., Chandawarkar, A., Eng, G., Blumling, J., Langer, R. & Khademhosseini, A. *Micromolding of shape-controlled, harvestable cell-laden hydrogels*. Biomaterials 27: 5391–5398 (2006).

204. Sen, A. K., Raj, A., Banerjee, U. & Iqbal, S. R. *Soft Lithography, Molding, and Micromachining Techniques for Polymer Micro Devices*. Lab on a Chip 7: 13–54 (2019).

205. Wang, Y., Gunasekara, D. B., Reed, M. I., DiSalvo, M., Bultman, S. J., Sims, C. E., Magness, S. T. & Allbritton, N. L. *A microengineered collagen scaffold for generating a polarized crypt-villus architecture of human small intestinal epithelium*. Biomaterials 128: 44–55 (2017).

206. Vijayavenkataraman, S., Yan, W. C., Lu, W. F., Wang, C. H. & Fuh, J. Y. H. *3D bioprinting of tissues and organs for regenerative medicine*. Advanced Drug Delivery Reviews 132: 296–332 (2018).

207. Murphy, S. V. & Atala, A. *3D bioprinting of tissues and organs*. Nature Biotechnology 32: 773–785 (2014).

208. Bishop, E. S., Mostafa, S., Pakvasa, M., Luu, H. H., Lee, M. J., Wolf, J. M., Ameer, G. A., He, T. C. & Reid, R. R. *3-D bioprinting technologies in tissue engineering and regenerative medicine: Current and future trends*. Genes and Diseases 4: 185–195 (2017).

209. Tran, V. & Wen, X. *Rapid prototyping technologies for tissue regeneration*. in *Rapid Prototyping of Biomaterials* 97–155 (Elsevier, 2014).

210. Guillotin, B., Souquet, A., Catros, S., Duocastella, M., Pippenger, B., Bellance, S., Bareille, R., Rémy, M., Bordenave, L., Amédée, J. & Guillemot, F. *Laser assisted bioprinting of engineered tissue with high cell density and microscale organization*. Biomaterials 31: 7250–7256 (2010).

211. Melchels, F. P. W., Feijen, J. & Grijpma, D. W. *A review on stereolithography and its applications in biomedical engineering*. Biomaterials 31: 6121–6130 (2010).

212. Manapat, J. Z., Chen, Q., Ye, P. & Advincula, R. C. *3D Printing of Polymer Nanocomposites via Stereolithography*. Macromolecular Materials and Engineering 302: 1–13 (2017).

213. Ciuciu, A. I. & Cywiński, P. J. *Two-photon polymerization of hydrogels-versatile solutions to fabricate well-defined 3D structures*. RSC Advances 4: 45504–45516 (2014).

214. Wloka, T., Czich, S., Kleinsteuber, M., Moek, E., Weber, C., Gottschaldt, M., Liefeith, K. & Schubert, U. S. *Microfabrication of 3D-hydrogels via two-photon polymerization of poly(2-ethyl-2-oxazoline) diacrylates*. European Polymer Journal 122: 109295 (2020).

215. Tran, K. T. M. & Nguyen, T. D. *Lithography-based methods to manufacture biomaterials at small scales*. Journal of Science: Advanced Materials and Devices 2: 1–14 (2017).

216. Pimpin, A. & Srituravanich, W. *Reviews on micro- and nanolithography techniques and their applications*. Engineering Journal 16: 37–55 (2012).

217. del Barrio, J. & Sánchez-Somolinos, C. *Light to Shape the Future: From Photolithography to 4D Printing*. Advanced Optical Materials 7: (2019).

218. Tsang, V. L., Chen, A. A., Cho, L. M., Jadin, K. D., Sah, R. L., DeLong, S., West, J. L. & Bhatia, S. N. *Fabrication of 3D hepatic tissues by additive photopatterning of cellular hydrogels*. The FASEB Journal 21: 790–801 (2007).

219. Gumuscu, B., Bomer, J. G., van den Berg, A. & Eijkel, J. C. T. *Photopatterning of Hydrogel Microarrays in Closed Microchips*. Biomacromolecules 16: 3802–3810 (2015).

220. Liu, J., Zheng, H., Poh, P. S. P., Machens, H.-G. & Schilling, A. F. *Hydrogels for Engineering of Perfusable Vascular Networks.* International journal of molecular sciences 16: 15997–16016 (2015).

221. Creff, J., Courson, R., Mangeat, T., Foncy, J., Souleille, S., Thibault, C., Besson, A. & Malaquin, L. *Fabrication of 3D scaffolds reproducing intestinal epithelium topography by high-resolution 3D stereolithography*. Biomaterials 221: 119404 (2019).

222. Kim, W. & Kim, G. H. *An innovative cell-printed microscale collagen model for mimicking intestinal villus epithelium*. Chemical Engineering Journal 334: 2308–2318 (2018).

223. De Gregorio, V., Imparato, G., Urciuolo, F. & Netti, P. A. *Micro-patterned endogenous stroma equivalent induces polarized crypt-villus architecture of human small intestinal epithelium.* Acta biomaterialia 81: 43–59 (2018).

224. Rahali, K., Ben Messaoud, G., Kahn, C. J. F., Sanchez-Gonzalez, L., Kaci, M., Cleymand, F., Fleutot, S., Linder, M., Desobry, S. & Arab-Tehrany, E. *Synthesis and Characterization of Nanofunctionalized Gelatin Methacrylate Hydrogels.* International journal of molecular sciences 18: 2938–2950 (2017).

225. Martineau, L., Peng, H. & Pang, S. *Development of a novel biomaterial: Part II. Evaluation of a photo cross-linking method*. Defence R&D Canada - Toronto Technical Report (2005).

226. Fares, M. M., Shirzaei Sani, E., Portillo Lara, R., Oliveira, R. B., Khademhosseini, A. & Annabi, N. *Interpenetrating network gelatin methacryloyl (GelMA) and pectin-g-PCL hydrogels with tunable properties for tissue engineering*. Biomaterials Science 6: 2938–2950 (2018).

227. Aldana, A. A., Malatto, L., Rehman, M. A. U., Boccaccini, A. R. & Abraham, G. A. *Fabrication of Gelatin Methacrylate (GelMA) Scaffolds with Nano- and Micro-Topographical and Morphological Features.* Nanomaterials (Basel, Switzerland) 9: (2019).

228. Kong, J. & Yu, S. *Fourier Transform Infrared Spectroscopic Analysis of Protein Secondary Structures*. Acta Biochimica et Biophysica Sinica 39: 549–559 (2007).

229. Claaßen, C., Claaßen, M. H., Truffault, V., Sewald, L., Tovar, G. E. M., Borchers, K. & Southan, A. *Quantification of Substitution of Gelatin Methacryloyl: Best Practice and Current Pitfalls.* Biomacromolecules 19: 42–52 (2018).

230. Habeeb, A. F. *Determination of free amino groups in proteins by trinitrobenzenesulfonic acid.* Analytical biochemistry 14: 328–336 (1966).

231. Zhu, M., Wang, Y., Ferracci, G., Zheng, J., Cho, N.-J. & Lee, B. H. *Gelatin methacryloyl and its*

hydrogels with an exceptional degree of controllability and batch-to-batch consistency. Scientific reports 9: 6863 (2019).

232. Garcia Castaño, A. *Engineering poly (ethylene glycol) diacrylate-based microstructures to develop an in vitro model of small intestinal epithelium*. TDX (Tesis Doctorals en Xarxa) (2017).

233. Yuk, H., Zhang, T., Lin, S., Parada, G. A. & Zhao, X. *Tough bonding of hydrogels to diverse non-porous surfaces.* Nature materials 15: 190–196 (2016).

234. Carr, D. A. & Peppas, N. A. *Molecular structure of physiologically-responsive hydrogels controls diffusive behavior.* Macromolecular bioscience 9: 497–505 (2009).

235. Canal, T. & Peppas, N. A. *Correlation between mesh size and equilibrium degree of swelling of polymeric networks.* Journal of biomedical materials research 23: 1183–1193 (1989).

236. Zhao, W. B. *Gelatin. Polymer Data Handbook*. in *The Polymer Data Handbook* (Oxford University Press, 1999).

237. Okeowo, O. & Dorgan, J. R. *Multicomponent swelling of polymer networks*. Macromolecules 39: 8193–8202 (2006).

238. Brodin, B., Steffansen, B. & Nielsen, C. U. *Passive diffusion of drug substances: the concepts of flux and permeability*. Molecular Biopharmaceutics 135–151 (2010).

239. Ahearne, M. *Introduction to cell-hydrogel mechanosensing.* Interface focus 4: 20130038 (2014).

240. Hutson, C. B., Nichol, J. W., Aubin, H., Bae, H., Yamanlar, S., Al-Haque, S., Koshy, S. T. & Khademhosseini, A. *Synthesis and characterization of tunable poly(ethylene glycol): gelatin methacrylate composite hydrogels.* Tissue engineering. Part A 17: 1713–1723 (2011).

241. Anseth, K. S., Bowman, C. N. & Brannon-Peppas, L. *Mechanical properties of hydrogels and their experimental determination*. Biomaterials 17: 1647–1657 (1996).

242. Ahearne, M., Yang, Y., El Haj, A. J., Then, K. Y. & Liu, K.-K. *Characterizing the viscoelastic properties of thin hydrogel-based constructs for tissue engineering applications.* Journal of the Royal Society, Interface 2: 455–463 (2005).

243. Rejmontová, P., Capáková, Z., Mikušová, N., Maráková, N., Kašpárková, V., Lehocký, M. & Humpolíček, P. *Adhesion, Proliferation and Migration of NIH/3T3 Cells on Modified Polyaniline Surfaces.* International journal of molecular sciences 17: 1–8 (2016).

244. Hynds, R. E., Bonfanti, P. & Janes, S. M. *Regenerating human epithelia with cultured stem cells: feeder cells, organoids and beyond*. EMBO Molecular Medicine 10: 139–150 (2018).

245. Bailey, C. A., Bryla, P. & Malick, A. W. *The use of the intestinal epithelial cell culture model, Caco-2, in pharmaceutical development*. Advanced Drug Delivery Reviews 22: 85–103 (1996).

246. Chanput, W., Mes, J. J. & Wichers, H. J. *THP-1 cell line: An in vitro cell model for immune modulation approach*. International Immunopharmacology 23: 37–45 (2014).

247. Sabnis, A., Rahimi, M., Chapman, C. & Nguyen, K. T. *Cytocompatibility studies of an in situ photopolymerized thermoresponsive hydrogel nanoparticle system using human aortic smooth muscle cells.* Journal of biomedical materials research. Part A 91: 52–59 (2009).

248. Hunyady, B., Mezey, E. & Palkovits, M. *Gastrointestinal immunology: cell types in the lamina propria--a morphological review.* Acta physiologica Hungarica 87: 305–328 (2000).

249. Bland, E., Dréau, D. & Burg, K. J. L. *Overcoming hypoxia to improve tissue-engineering approaches to regenerative medicine.* Journal of tissue engineering and regenerative medicine 7: 505–514 (2013).

250. Valls Margarit, M. *Development of an advanced 3D culture system for human cardiac tissue engineering*. TDX (Tesis Doctorals en Xarxa) (2017).

251. Valls-Margarit, M., *et al. Engineered Macroscale Cardiac Constructs Elicit Human Myocardial Tissue-like Functionality.* Stem cell reports 13: 207–220 (2019).

252. Caballero, D. & Samitier, J. *Topological Control of Extracellular Matrix Growth: A Native-Like Model for Cell Morphodynamics Studies.* ACS applied materials & interfaces 9: 4159–4170 (2017).

253. Podhorecka, M., Skladanowski, A. & Bozko, P. *H2AX Phosphorylation: Its Role in DNA Damage Response and Cancer Therapy.* Journal of nucleic acids 2010: (2010).

254. Halicka, H. D., Huang, X., Traganos, F., King, M. A., Dai, W. & Darzynkiewicz, Z. *Histone H2AX phosphorylation after cell irradiation with UV-B: relationship to cell cycle phase and induction of apoptosis.* Cell cycle (Georgetown, Tex.) 4: 339–345 (2005).

255. Invitrogen Molecular Probes. *LIVE/DEAD Viability/Cytotoxicity Kit for mammalian cells*. Product Information, Catalog number: MP 03224 1–7 (2005).

256. Arık, Y. B., van der Helm, M. W., Odijk, M., Segerink, L. I., Passier, R., van den Berg, A. & van der Meer, A. D. *Barriers-on-chips: Measurement of barrier function of tissues in organs-on-chips.* Biomicrofluidics 12: 042218 (2018).

257. Palumbo, P., Picchini, U., Beck, B., Van Gelder, J., Delbar, N. & DeGaetano, A. *A general approach to the apparent permeability index*. Journal of Pharmacokinetics and Pharmacodynamics 35: 235–248 (2008).

258. Stockdale, T. P., Challinor, V. L., Lehmann, R. P., De Voss, J. J. & Blanchfield, J. T. *Caco-2 Monolayer Permeability and Stability of Chamaelirium luteum (False Unicorn) Open-Chain Steroidal Saponins*. ACS Omega 4: 7658–7666 (2019).

259. Artursson, P. & Karlsson, J. *Correlation between oral drug absorption in humans and apparent drug permeability coefficients in human intestinal epithelial (Caco-2) cells.* Biochemical and biophysical research communications 175: 880–885 (1991).

260. Wang, X., Wang, N., Yuan, L., Li, N., Wang, J. & Yang, X. *Exploring tight junction alteration using double fluorescent probe combination of lanthanide complex with gold nanoclusters.* Scientific reports 6: 32218 (2016).

261. Han, X., Zhang, E., Shi, Y., Song, B., Du, H. & Cao, Z. *Biomaterial-tight junction interaction and potential impacts*. Journal of Materials Chemistry B 7: 6310–6320 (2019).

262. Noach, A. B. J., Kurosaki, Y., Blom-Roosemalen, M. C. M., de Boer, A. G. & Breimer, D. D. *Cell-polarity dependent effect of chelation on the paracellular permeability of confluent caco-2 cell monolayers*. International Journal of Pharmaceutics 90: 229–237 (1993).

263. Park, J. H., Peyrin-Biroulet, L., Eisenhut, M. & Shin, J. Il. *IBD immunopathogenesis: A comprehensive review of inflammatory molecules.* Autoimmunity reviews 16: 416–426 (2017).

264. Guo, S., Al-Sadi, R., Said, H. M. & Ma, T. Y. *Lipopolysaccharide causes an increase in intestinal tight junction permeability in vitro and in vivo by inducing enterocyte membrane expression and localization of TLR-4 and CD14.* The American journal of pathology 182: 375–387 (2013).

265. Sanchez-Munoz, F., Dominguez-Lopez, A. & Yamamoto-Furusho, J.-K. *Role of cytokines in inflammatory bowel disease.* World journal of gastroenterology 14: 4280–4288 (2008).

266. Zhang, J.-M. & An, J. *Cytokines, inflammation, and pain.* International anesthesiology clinics 45: 27–37 (2007).

267. Sakamoto, S., Putalun, W., Vimolmangkang, S., Phoolcharoen, W., Shoyama, Y., Tanaka, H. & Morimoto, S. *Enzyme-linked immunosorbent assay for the quantitative/qualitative analysis of plant secondary metabolites.* Journal of natural medicines 72: 32–42 (2018).

268. Modaresifar, K., Hadjizadeh, A. & Niknejad, H. *Design and fabrication of GelMA/chitosan nanoparticles composite hydrogel for angiogenic growth factor delivery*. Artificial Cells, Nanomedicine and Biotechnology 46: 1799–1808 (2018).

269. Pepelanova, I., Kruppa, K., Scheper, T. & Lavrentieva, A. *Gelatin-Methacryloyl (GelMA) Hydrogels with Defined Degree of Functionalization as a Versatile Toolkit for 3D Cell Culture and Extrusion Bioprinting.* Bioengineering (Basel, Switzerland) 5: (2018).

270. Engler, A. J., Sen, S., Sweeney, H. L. & Discher, D. E. *Matrix elasticity directs stem cell lineage specification.* Cell 126: 677–689 (2006).

271. Benton, J. A., DeForest, C. A., Vivekanandan, V. & Anseth, K. S. *Photocrosslinking of gelatin macromers to synthesize porous hydrogels that promote valvular interstitial cell function.* Tissue engineering. Part A 15: 3221–3230 (2009).

272. Fu, Y., Xu, K., Zheng, X., Giacomin, A. J., Mix, A. W. & Kao, W. J. *3D cell entrapment in crosslinked thiolated gelatin-poly(ethylene glycol) diacrylate hydrogels.* Biomaterials 33: 48–58 (2012).

273. Piluso, S., Weigel, T., Lendlein, A. & Neffe, A. T. *Synthesis and characterization of gelatin fragments obtained by controlled degradation*. Macromolecular Symposia 309–310: 199–204 (2011).

274. Chi, C. F., Cao, Z. H., Wang, B., Hu, F. Y., Li, Z. R. & Zhang, B. *Antioxidant and functional properties of collagen hydrolysates from Spanish mackerel skin as influenced by average molecular weight*. Molecules 19: 11211–11230 (2014).

275. Tal, M., Silberstein, A. & Nusser, E. *Why does Coomassie Brilliant Blue R interact differently with different proteins? A partial answer*. Journal of Biological Chemistry 260: 9976–9980 (1985).

276. Miri, A. K., Hosseinabadi, H. G., Cecen, B., Hassan, S. & Zhang, Y. S. *Permeability mapping of gelatin methacryloyl hydrogels.* Acta biomaterialia 77: 38–47 (2018).

277. Daniele, M. A., Adams, A. A., Naciri, J., North, S. H. & Ligler, F. S. *Interpenetrating networks based on gelatin methacrylamide and PEG formed using concurrent thiol click chemistries for hydrogel tissue engineering scaffolds*. Biomaterials 35: 1845–1856 (2014).

278. Hönig, W. & Kula, M.-R. *Selectivity of protein precipitation with polyethylene glycol fractions of various molecular weights*. Analytical Biochemistry 72: 502–512 (1976).

279. Figueiredo, L., Pace, R., D'Arros, C., Réthoré, G., Guicheux, J., Le Visage, C. & Weiss, P. *Assessing glucose and oxygen diffusion in hydrogels for the rational design of 3D stem cell scaffolds in regenerative medicine*. Journal of Tissue Engineering and Regenerative Medicine 12: 1238–1246 (2018).

280. Nafea, E. H., Marson, A., Poole-Warren, L. A. & Martens, P. J. *Immunoisolating semi-permeable membranes for cell encapsulation: focus on hydrogels.* Journal of controlled release : official journal of the Controlled Release Society 154: 110–122 (2011).

281. Kaemmerer, E., Melchels, F. P. W., Holzapfel, B. M., Meckel, T., Hutmacher, D. W. & Loessner, D. *Gelatine methacrylamide-based hydrogels: An alternative three-dimensional cancer cell culture system*. Acta Biomaterialia 10: 2551–2562 (2014).

282. Mamaghani, K. R., Naghib, S. M., Zahedi, A., Rahmanian, M. & Mozafari, M. *GelMa/PEGDA containing graphene oxide as an IPN hydrogel with superior mechanical performance*. Materials Today: Proceedings 5: 15790–15799 (2018).

283. Swift, J., *et al. Nuclear lamin-A scales with tissue stiffness and enhances matrix-directed differentiation.* Science (New York, N.Y.) 341: 1240104 (2013).

284. Pedron, S. & Harley, B. A. C. *Impact of the biophysical features of a 3D gelatin microenvironment on glioblastoma malignancy.* Journal of biomedical materials research. Part A 101: 3404–3415 (2013).

285. Jabłońska-Trypuć, A., Matejczyk, M. & Rosochacki, S. *Matrix metalloproteinases (MMPs), the main extracellular matrix (ECM) enzymes in collagen degradation, as a target for anticancer drugs.* Journal of enzyme inhibition and medicinal chemistry 31: 177–183 (2016).

286. Wang, K., Wu, L.-Y., Dou, C.-Z., Guan, X., Wu, H.-G. & Liu, H.-R. *Research Advance in Intestinal Mucosal Barrier and Pathogenesis of Crohn's Disease.* Gastroenterology research and practice 2016: 9686238 (2016).

287. Sun, H., Chow, E. C. Y., Liu, S., Du, Y. & Pang, K. S. *The Caco-2 cell monolayer: usefulness and limitations.* Expert opinion on drug metabolism & toxicology 4: 395–411 (2008).

288. Kim, J. H. & Asthagiri, A. R. *Matrix stiffening sensitizes epithelial cells to EGF and enables the loss of contact inhibition of proliferation*. Journal of Cell Science 124: 1280–1287 (2011).

289. Skardal, A., Mack, D., Atala, A. & Soker, S. *Substrate elasticity controls cell proliferation, surface marker expression and motile phenotype in amniotic fluid-derived stem cells.* Journal of the mechanical behavior of biomedical materials 17: 307–316 (2013).

290. Hanasoge, S. & Ljungman, M. *H2AX phosphorylation after UV irradiation is triggered by DNA repair intermediates and is mediated by the ATR kinase.* Carcinogenesis 28: 2298–2304 (2007).

291. Schiele, N. R., Chrisey, D. B. & Corr, D. T. *Gelatin-based laser direct-write technique for the precise*

spatial patterning of cells. Tissue Engineering - Part C: Methods 17: 289–298 (2011).

292. Stewart, G. S., Wang, B., Bignell, C. R., Taylor, A. M. R. & Elledge, S. J. *MDC1 is a mediator of the mammalian DNA damage checkpoint.* Nature 421: 961–966 (2003).

293. Cai, Y., Xu, C., Chen, P., Hu, J., Hu, R., Huang, M. & Bi, H. *Development, validation, and application of a novel 7-day Caco-2 cell culture system.* Journal of pharmacological and toxicological methods 70: 175–181 (2014).

294. Liao, D., Yang, J., Zhao, J., Zeng, Y., Vinter-Jensen, L. & Gregersen, H. *The effect of epidermal growth factor on the incremental Young's moduli in the rat small intestine.* Medical engineering & physics 25: 413–418 (2003).

295. Ghaffarian, R. & Muro, S. *Models and methods to evaluate transport of drug delivery systems across cellular barriers.* Journal of visualized experiments : JoVE e50638 (2013).

296. Yanagawa, F., Kaji, H., Jang, Y.-H., Bae, H., Yanan, D., Fukuda, J., Qi, H. & Khademhosseini, A. *Directed assembly of cell-laden microgels for building porous three-dimensional tissue constructs.* Journal of biomedical materials research. Part A 97: 93–102 (2011).

297. Lei, Y., Gojgini, S., Lam, J. & Segura, T. *The spreading, migration and proliferation of mouse mesenchymal stem cells cultured inside hyaluronic acid hydrogels.* Biomaterials 32: 39–47 (2011).

298. Freed, L. E. & Vunjak-Novakovic, G. *Cultivation of cell-polymer tissue constructs in simulated microgravity.* Biotechnology and bioengineering 46: 306–313 (1995).

299. Llames, S., García-Pérez, E., Meana, Á., Larcher, F. & del Río, M. *Feeder Layer Cell Actions and Applications*. Tissue Engineering Part B: Reviews 21: 345–353 (2015).

300. Hynds, R. E., Gowers, K. H. C., Nigro, E., Butler, C. R., Bonfanti, P., Giangreco, A., Prêle, C. M. & Janes, S. M. *Cross-talk between human airway epithelial cells and 3T3-J2 feeder cells involves partial activation of human MET by murine HGF*. PLoS ONE 13: 1–18 (2018).

301. Pereira, I., Lechanteur, A. & Sarmento, B. *3D Model Replicating the Intestinal Function to Evaluate Drug Permeability*. in vol. 1817 107–113 (2018).

302. Uroz, M., Wistorf, S., Serra-Picamal, X., Conte, V., Sales-Pardo, M., Roca-Cusachs, P., Guimerà, R. & Trepat, X. *Regulation of cell cycle progression by cell-cell and cell-matrix forces.* Nature cell biology 20: 646–654 (2018).

303. Sunyer, R., Conte, V., Escribano, J., Elosegui-Artola, A., Labernadie, A., Valon, L., Navajas, D., García-Aznar, J. M., Muñoz, J. J., Roca-Cusachs, P. & Trepat, X. *Collective cell durotaxis emerges from long-range intercellular force transmission.* Science (New York, N.Y.) 353: 1157–1161 (2016).

304. Rowart, P., Erpicum, P., Krzesinski, J.-M., Sebbagh, M. & Jouret, F. *Mesenchymal Stromal Cells Accelerate Epithelial Tight Junction Assembly via the AMP-Activated Protein Kinase Pathway, Independently of Liver Kinase B1.* Stem cells international 2017: 9717353 (2017).

305. Pasman, T., Grijpma, D., Stamatialis, D. & Poot, A. *Flat and microstructured polymeric membranes in organs-on-chips.* Journal of the Royal Society, Interface 15: (2018).

306. Le Ferrec, E., Chesne, C., Artusson, P., Brayden, D., Fabre, G., Gires, P., Guillou, F., Rousset, M., Rubas, W. & Scarino, M. L. *In vitro models of the intestinal barrier. The report and recommendations of ECVAM Workshop 46. European Centre for the Validation of Alternative methods.* Alternatives to laboratory animals : ATLA 29: 649–668 (2014).

307. Smith, M. I., Foderà, V., Sharp, J. S., Roberts, C. J. & Donald, A. M. *Factors affecting the formation of insulin amyloid spherulites.* Colloids and surfaces. B, Biointerfaces 89: 216–222 (2012).

308. Wood, K. M., Stone, G. M. & Peppas, N. A. *The effect of complexation hydrogels on insulin transport in intestinal epithelial cell models.* Acta biomaterialia 6: 48–56 (2010).

309. Liu, J., Werner, U., Funke, M., Besenius, M., Saaby, L., Fanø, M., Mu, H. & Müllertz, A. *SEDDS for intestinal absorption of insulin: Application of Caco-2 and Caco-2/HT29 co-culture monolayers and intra-jejunal instillation in rats.* International journal of pharmaceutics 560: 377–384 (2019).

310. Gupta, V., Doshi, N. & Mitragotri, S. *Permeation of insulin, calcitonin and exenatide across Caco-2 monolayers: measurement using a rapid, 3-day system.* PloS one 8: e57136 (2013).

311. Chicurel, M. E., Chen, C. S. & Ingber, D. E. *Cellular control lies in the balance of forces.* Current opinion in cell biology 10: 232–239 (1998).

312. Kutty, J. K., Cho, E., Soo Lee, J., Vyavahare, N. R. & Webb, K. *The effect of hyaluronic acid incorporation on fibroblast spreading and proliferation within PEG-diacrylate based semi-interpenetrating networks*. Biomaterials 28: 4928–4938 (2007).

313. Lee, H.-J., Sen, A., Bae, S., Lee, J. S. & Webb, K. *Poly(ethylene glycol) diacrylate/hyaluronic acid semi-interpenetrating network compositions for 3-D cell spreading and migration.* Acta biomaterialia 14: 43–52 (2015).

314. Vila, A., Torras, N., Castaño, A. G., García-Díaz, M., Comelles, J., Pérez-Berezo, T., Corregidor, C., Castaño, Ó., Engel, E., Fernández-Majada, V. & Martínez, E. *Hydrogel co-networks of gelatine methacrylate and poly(ethylene glycol) diacrylate sustain 3D functional in vitro models of intestinal mucosa.* Biofabrication 12: 025008 (2020).

315. Lutolf, M. P., Lauer-Fields, J. L., Schmoekel, H. G., Metters, A. T., Weber, F. E., Fields, G. B. & Hubbell, J. A. *Synthetic matrix metalloproteinase-sensitive hydrogels for the conduction of tissue regeneration: engineering cell-invasion characteristics.* Proceedings of the National Academy of Sciences of the United States of America 100: 5413–5418 (2003).

316. Kloxin, A. M., Kloxin, C. J., Bowman, C. N. & Anseth, K. S. *Mechanical properties of cellularly responsive hydrogels and their experimental determination*. Advanced Materials 22: 3484–3494 (2010).

317. Schuurman, W., Levett, P. A., Pot, M. W., van Weeren, P. R., Dhert, W. J. A., Hutmacher, D. W., Melchels, F. P. W., Klein, T. J. & Malda, J. *Gelatin-methacrylamide hydrogels as potential biomaterials for fabrication of tissue-engineered cartilage constructs.* Macromolecular bioscience 13: 551–561 (2013).

318. Chen, Y.-C., Lin, R.-Z., Qi, H., Yang, Y., Bae, H., Melero-Martin, J. M. & Khademhosseini, A. *Functional Human Vascular Network Generated in Photocrosslinkable Gelatin Methacrylate Hydrogels.* Advanced functional materials 22: 2027–2039 (2012).

319. Van Nieuwenhove, I., Salamon, A., Peters, K., Graulus, G.-J., Martins, J. C., Frankel, D., Kersemans, K., De Vos, F., Van Vlierberghe, S. & Dubruel, P. *Gelatin- and starch-based hydrogels. Part A: Hydrogel development, characterization and coating*. Carbohydrate Polymers 152: 129–139 (2016).

320. Anderson, S. B., Lin, C.-C., Kuntzler, D. V. & Anseth, K. S. *The performance of human mesenchymal stem cells encapsulated in cell-degradable polymer-peptide hydrogels.* Biomaterials 32: 3564–3574 (2011).

321. Loessner, D., Stok, K. S., Lutolf, M. P., Hutmacher, D. W., Clements, J. A. & Rizzi, S. C. *Bioengineered 3D platform to explore cell-ECM interactions and drug resistance of epithelial ovarian cancer cells.* Biomaterials 31: 8494–8506 (2010).

322. Wang, L., Sheshareddy, K., Weiss, M. L. & Detamore, M. S. *Effect of initial seeding density on human umbilical cord mesenchymal stromal cells for fibrocartilage tissue engineering.* Tissue engineering. Part A 15: 1009–1017 (2009).

323. Zhou, H., Weir, M. D. & Xu, H. H. K. *Effect of cell seeding density on proliferation and osteodifferentiation of umbilical cord stem cells on calcium phosphate cement-fiber scaffold.* Tissue engineering. Part A 17: 2603–2613 (2011).

324. Kim, K., Dean, D., Mikos, A. G. & Fisher, J. P. *Effect of initial cell seeding density on early osteogenic signal expression of rat bone marrow stromal cells cultured on cross-linked poly(propylene fumarate) disks.* Biomacromolecules 10: 1810–1817 (2009).

325. de Bruyn, J. R., van den Brink, G. R., Steenkamer, J., Buskens, C. J., Bemelman, W. A., Meisner, S., Muncan, V., Te Velde, A. A., D'Haens, G. R. & Wildenberg, M. E. *Fibrostenotic Phenotype of Myofibroblasts in Crohn's Disease is Dependent on Tissue Stiffness and Reversed by LOX Inhibition.* Journal of Crohn's & colitis 12: 849–859 (2018).

326. Lahar, N., Lei, N. Y., Wang, J., Jabaji, Z., Tung, S. C., Joshi, V., Lewis, M., Stelzner, M., Martín, M. G. & Dunn, J. C. Y. *Intestinal subepithelial myofibroblasts support in vitro and in vivo growth of human small intestinal epithelium*. PLoS ONE 6: 1–9 (2011).

327. Lei, N. Y., *et al. Intestinal subepithelial myofibroblasts support the growth of intestinal epithelial*

stem cells. PloS one 9: e84651 (2014).

328. Powell, D. W., Mifflin, R. C., Valentich, J. D., Crowe, S. E., Saada, J. I. & West, A. B. *Myofibroblasts. II. Intestinal subepithelial myofibroblasts*. American Journal of Physiology-Cell Physiology 277: C183–C201 (1999).

329. Giménez-Bastida, J. A., Surma, M. & Zieliński, H. *In vitro evaluation of the cytotoxicity and modulation of mechanisms associated with inflammation induced by perfluorooctanesulfonate and perfluorooctanoic acid in human colon myofibroblasts CCD-18Co*. Toxicology in Vitro 29: 1683–1691 (2015).

330. Visco, V., Bava, F. A., D'Alessandro, F., Cavallini, M., Ziparo, V. & Torrisi, M. R. *Human colon fibroblasts induce differentiation and proliferation of intestinal epithelial cells through the direct paracrine action of keratinocyte growth factor.* Journal of cellular physiology 220: 204–213 (2009).

331. Antoni, L. *Intestinal barrier in inflammatory bowel disease*. World Journal of Gastroenterology 20: 1165 (2014).

332. Tokuhara, D., Kurashima, Y., Kamioka, M., Nakayama, T., Ernst, P. & Kiyono, H. *A comprehensive understanding of the gut mucosal immune system in allergic inflammation*. Allergology International 68: 17–25 (2019).

333. Barthes, J., Dollinger, C., Muller, C. B., Liivas, U., Dupret-Bories, A., Knopf-Marques, H. & Vrana, N. E. *Immune assisted tissue engineering via incorporation of macrophages in cell-laden hydrogels under cytokine stimulation*. Frontiers in Bioengineering and Biotechnology 6: 1–17 (2018).

334. Qin, Z. *The use of THP-1 cells as a model for mimicking the function and regulation of monocytes and macrophages in the vasculature*. Atherosclerosis 221: 2–11 (2012).

335. Richter, E., Ventz, K., Harms, M., Mostertz, J. & Hochgräfe, F. *Induction of Macrophage Function in Human THP-1 Cells Is Associated with Rewiring of MAPK Signaling and Activation of MAP3K7 (TAK1) Protein Kinase*. Frontiers in Cell and Developmental Biology 4: (2016).

336. Spano, A., Barni, S. & Sciola, L. *PMA withdrawal in PMA-treated monocytic THP-1 cells and subsequent retinoic acid stimulation, modulate induction of apoptosis and appearance of dendritic cells*. Cell Proliferation 46: 328–347 (2013).

337. Rossol, M., Heina, H., Undine, M., Quandt, D., Klein, C., Sweet, M. J. & Hauschildt, S. *LPS-induced Cytokine Production in Human Monocytes and Macrophages*. Critical Reviews™ in Immunology 31: 2162–6472 (2011).

338. Watanabe, S., Ogura, N., Akutsu, M., Kawashima, M., Hattori, T., Yano, T., Ito, K. & Kondoh, T. *Pro-inflammatory Cytokine Production in Co-culture of Human Monocytes and Synovial Fibroblasts from the Human Temporomandibular Joint*. International Journal of Oral-Medical Sciences 15: 107–113 (2017).

339. Ma, F., Li, Y., Jia, L., Han, Y., Cheng, J., Li, H., Qi, Y. & Du, J. *Macrophage-Stimulated Cardiac Fibroblast Production of IL-6 Is Essential for TGF β/Smad Activation and Cardiac Fibrosis Induced by Angiotensin II*. PLoS ONE 7: e35144 (2012).

340. Kämpfer, A. A. M., Urbán, P., Gioria, S., Kanase, N., Stone, V. & Kinsner-Ovaskainen, A. *Development of an in vitro co-culture model to mimic the human intestine in healthy and diseased state*. Toxicology in Vitro 45: 31–43 (2017).

341. Wang, F., Graham, W. V., Wang, Y., Witkowski, E. D., Schwarz, B. T. & Turner, J. R. *Interferon-γ and Tumor Necrosis Factor-α Synergize to Induce Intestinal Epithelial Barrier Dysfunction by Up-Regulating Myosin Light Chain Kinase Expression*. The American Journal of Pathology 166: 409–419 (2005).

342. Miura, M., Friedlander, R. M. & Yuan, J. *Tumor necrosis factor-induced apoptosis is mediated by a CrmA-sensitive cell death pathway.* Proceedings of the National Academy of Sciences 92: 8318–8322 (1995).

343. Wittkopf, N., Neurath, M. F. & Becker, C. *Immune-epithelial crosstalk at the intestinal surface*. Journal of Gastroenterology 49: 375–387 (2014).

344. Kurashima, Y. & Kiyono, H. *Mucosal Ecological Network of Epithelium and Immune Cells for Gut Homeostasis and Tissue Healing*. Annual Review of Immunology 35: 119–147 (2017).

345. Nowarski, R., Jackson, R. & Flavell, R. A. *The Stromal Intervention: Regulation of Immunity and Inflammation at the Epithelial-Mesenchymal Barrier*. Cell 168: 362–375 (2017).

346. Kurashima, Y., Tokuhara, D., Kamioka, M., Inagaki, Y. & Kiyono, H. *Intrinsic control of surface immune and epithelial homeostasis by tissue-resident gut stromal cells*. Frontiers in Immunology 10: 1–9 (2019).

347. Bosman, F. T., de Bruïne, A., Flohil, C., van der Wurff, A., ten Kate, J. & Dinjens, W. W. *Epithelial-stromal interactions in colon cancer.* The International journal of developmental biology 37: 203–211 (1993).

348. Shaker, A. & Rubin, D. C. *Intestinal stem cells and epithelial-mesenchymal interactions in the crypt and stem cell niche.* Translational research : the journal of laboratory and clinical medicine 156: 180–187 (2010).

349. Yu, J., Carrier, R. L., March, J. C. & Griffith, L. G. *Three dimensional human small intestine models for ADME-Tox studies*. Drug Discovery Today 19: 1587–1594 (2014).

350. MITSOMWANG, P., NAGASAWA, S., CHAIJIT, S., FUJIKURA, M. & MUTOH, Y. *Effect of Underlay Stiffness on Cutting Profile of Polycarbonate Sheet during Wedge Indentation Process*. Journal of Advanced Mechanical Design, Systems, and Manufacturing 6: 1168–1179 (2012).

351. Atala, A., Lanza, R., Mikos, T. & Nerem, R. *Principles of Regenerative Medicine*. (Academic Press, 2008).

352. Hong, X., Meng, Y. & Kalkanis, S. N. *Serum proteins are extracted along with monolayer cells in plasticware and interfere with protein analysis*. Journal of Biological Methods 3: 51 (2016).

353. Salehi-Nik, N., Amoabediny, G., Pouran, B., Tabesh, H., Shokrgozar, M. A., Haghighipour, N., Khatibi, N., Anisi, F., Mottaghy, K. & Zandieh-Doulabi, B. *Engineering Parameters in Bioreactor's Design: A Critical Aspect in Tissue Engineering*. BioMed Research International 2013: 1–15 (2013).

354. Schmid, J., Schwarz, S., Meier-Staude, R., Sudhop, S., Clausen-Schaumann, H., Schieker, M. & Huber, R. *A Perfusion Bioreactor System for Cell Seeding and Oxygen-Controlled Cultivation of Three-Dimensional Cell Cultures*. Tissue Engineering Part C: Methods 24: 585–595 (2018).

355. MUSCHLER, G. F., NAKAMOTO, C. & GRIFFITH, L. G. *ENGINEERING PRINCIPLES OF CLINICAL CELL-BASED TISSUE ENGINEERING*. The Journal of Bone and Joint Surgery-American Volume 86: 1541–1558 (2004).

356. YU, Q. & YANG, Q. *Diversity of tight junctions (TJs) between gastrointestinal epithelial cells and their function in maintaining the mucosal barrier*. Cell Biology International 33: 78–82 (2009).

357. Göke, M., Kanai, M. & Podolsky, D. K. *Intestinal fibroblasts regulate intestinal epithelial cell proliferation via hepatocyte growth factor.* The American journal of physiology 274: G809-18 (1998).

358. Billiet, T., Gevaert, E., De Schryver, T., Cornelissen, M. & Dubruel, P. *The 3D printing of gelatin methacrylamide cell-laden tissue-engineered constructs with high cell viability*. Biomaterials 35: 49–62 (2014).

359. Viney, M., Bullock, A., Day, M. & MacNeil, S. *Co-culture of intestinal epithelial and stromal cells in 3D collagen-based environments*. Regenerative Medicine 4: 397–406 (2009).

360. Uenoyama, Y., Seno, H., Fukuda, A., Sekikawa, A., Nanakin, A., Sawabu, T., Kawada, M., Kanda, N., Suzuki, K., Yada, N., Fukui, H. & Chiba, T. *Hypoxia induced by benign intestinal epithelial cells is associated with cyclooxygenase-2 expression in stromal cells through AP-1-dependent pathway*. Oncogene 25: 3277–3285 (2006).

361. Lee, S. H. *Intestinal Permeability Regulation by Tight Junction: Implication on Inflammatory Bowel Diseases*. Intestinal Research 13: 11 (2015).

8. Resum en català

Els models convencionals de cultiu cel·lular *in vitro* no representen correctament ni la complexitat ni la organització cel·lular dels teixits natius. Aquesta manca de les propietats fisiològiques, fa que la majoria de models utilitzats per fer estudis *in vitro* donin uns resultats significativament poc fisiològics i no comparables amb els trobats en condicions *in vivo.*

Teixits obtinguts mitjançant la combinació de tècniques de bioenginyeria i de biofabricació volen reduir les distàncies entre els models *in vitro* i els teixits natius. Per fer-ho, es vol proporcionar a les cèl·lules un entorn similar al del teixit natiu a través de la imitació (I) de les estructures 3D dels teixits; (II) de la complexitat multicel·lular present en els diferents compartiments que formen el teixit; i (III) de les propietats fisicoquímiques i mecàniques de la matriu cel·lular. Aquests nous models de teixits que s'estan desenvolupant i estudiant són un factor clau per millorar les plataformes actuals utilitzades tant en les investigacions bàsiques (interacció entre cèl·lules o entre les cèl·lules i la matriu), com en el desenvolupament de nous fàrmacs, o en la modelització de malalties. Actualment entre tots els models de teixits dissenyats, els models relacionats amb la mucosa intestinal estan poc desenvolupats, generant un buit important en aquest sector.

La mucosa intestinal està formada per l'epiteli i la làmina propria. L'epiteli és una capa multicel·lular, formada per cèl·lules epitelials que recobreix la part superior de la làmina propia. La làmina propria, o compartiment estromal, esta format per teixit connectiu on resideixen diversos tipus cel·lulars, com les cèl·lules mesenquimals i les cèl·lules immunològiques. El model intestinal més utilitzat, tant en la industria com en la recerca, està basat en un cultiu 2D de línies cel·lulars epitelials derivades de cèl·lules cancerígenes de còlon sobre una membrana porosa i dura dels inserts de Transwell®. La falta del compartiment estromal, la poca heterogeneïtat cel·lular i el creixement de les cèl·lules en una superfície dura, la qual la seva duresa és més elevada que la corresponent al teixit *in vivo* fa que en aquests models, les cèl·lules epitelials formin una monocapa més densa i compacta comparada amb la del intestí natiu. Com a resultat de la incorrecta representació, els resultats obtinguts són enganyosos en comparació amb els obtinguts *in vivo.* Per tal de poder superar aquest buit, és fonamental el desenvolupament d'una plataforma *in vitro,* que reprodueixi correctament les propietats mecàniques del intestí i que a més a més integri els dos compartiments, tant l'estromal com l'epitelial. D'aquesta forma les interaccions entre cèl·lula-cèl·lula i cèl·lula-matriu seran més semblants a les reals, proporcionat resultats més acurats.

En aquest treball es descriu un mètode simple i rendible per obtenir un model 3D de la mucosa intestinal, que combina tant el compartiment epitelial com l'estromal o lamina propria. Per construir les mostres, escollim els hidrogels com a material per imitar les propietats fisicoquímiques i mecàniques del intestí. A més a més, també ens permet obtenir els dos compartiments. Els hidrogels són polímers que un cop polimeritzats formen xarxes tridimensionals amb un alt contingut d'aigua, i porositat, facilitant la difusió de nutrients i oxigen tant a l'interior com a l'exterior del hidrogel. Per obtenir els hidrogels, es barreja gelatina metacrilada (GelMA), un polímer natural, amb poly(ethylene glycol) diacrylate (PEGDA), un polímer sintètic, i es polimeritza sota la llum UV (λ= 365 nm). Per una banda, la GelMA proporciona seqüències de biodegradació i adhesió cel·lular, però té molta inestabilitat mecànica, resultant inapropiada per cultius cel·lulars a llarg termini. D'altra banda, el PEGDA, no té seqüències biodegradables ni d'adhesió cel·lular, però proporciona bona estabilitat mecànica fent que els hidrogels siguin aptes per cultius cel·lulars de períodes llargs. Abans d'utilitzar els hidrogels com a plataforma pel cultiu cel·lular, les seves propietats fisicoquímiques i mecàniques es van analitzar i estudiar, per tal de trobar un hidrogel que permetés el cultiu fins a 21 dies sense comprometre la seva estructura i a més a més que les propietats mecàniques fossin semblants a les del intestí prim.

Un cop verificades aquestes propietats, els hidrogels van ser utilitzats com a potencials plataformes per modelitzar els dos compartiments de la mucosa intestinal, la lamina pròpia i l'epiteli. Per fer-ho els polímers de GelMA i PEGDA es van dissoldre, barrejar amb cèl·lules mesenquimals (fibroblasts o miofibroblasts) i/o cèl·lules del sistema immunològic (macròfags) i es van abocar en uns motllos de PDMS. Finalment van ser exposats sota la llum UV. A continuació, es van muntar en els inserts de Transwell® i es van sembrar sobre aquests hidrogels les cèl·lules epitelials. En aquesta tesi, hem demostrat, que les co-xarxes de GelMA – PEGDA són aptes per mantenir una bona viabilitat de les cèl·lules encapsulades, tant de les cèl·lules mesenquimals (fibroblasts i miofibroblasts) com de les immunològiques (macròfags). A més a més, també suporten el creixement de la monocapa epitelial en la seva superfície. Per altra banda, demostrem mitjançant l'estudi de la resistència elèctrica transepitelial i la permeabilitat de diverses molècules que la incorporació de cèl·lules mesenquimals a la co-xarxa d'hidrogel de GelMA – PEGDA milloren la formació i la maduresa de la monocapa epitelial donant unes propietats de barrera similars a les del intestí humà,. A més a més, la presencia de fibroblasts dins de la co-xarxa del hidrogel, millora la recuperació de la barrera epitelial quan aquesta ha estat danyada espontàniament durant un període curt.

Finalment, en el nostre model 3D de la mucosa intestinal s'ha incorporat el sistema immunocompetent a través de l'encapsulació de macròfags en les co-xarxes d'hidrogels de GelMA – PEGDA. Hem validat que la presència de macròfags no influeix en la formació de l'epiteli, i que són només el fibroblasts o miofibroblasts que tenen un paper beneficial en la seva formació i maduració. Per altra banda, hem estudiat com influeix la presència només d'un tipus cel·lular (macròfags o miofibroblasts) o els dos tipus cel·lulars (macròfags+miofibroblasts) encapsulats en l'hidrogel a la monocapa epitelial quan hi ha un dany a per la presencia de lipopolisacàrdis (LPS), que és una molècula present a la membrana exterior dels bacteris gramnegatius. Hem observat, que quan en la barrera epitelial la seva integritat es veu compromesa, la resposta per fer front a la lesió, la qual es va valorar a través de l'estudi dels nivells de citoquines seretades després de la estimulació amb LPS, la secretació és més elevada quan en el compartiment estromal hi ha el co-cultiu (macròfags i miofibroblasts). Això ens suggereix que hi ha un efecte sinèrgic entre els dos tipus cel·lulars per reparar el dany en la barrera epitelial.

Els resultats obtinguts al llarg d'aquesta tesi són compatibles amb la hipòtesi inicial en la qual l'obtenció d'un material amb propietats fisicoquímiques i mecàniques similars a la de la làmina pròpria del intestí humà, juntament amb el co-cultiu de cèl·lules de la lamina propia i les epitelials ha permès desenvolupar un model 3D de la mucosa intestinal *in vitro* amb propietats fisiològiques més semblants a la del intestí prim humà, proporcionant uns resultats més acurats. Arribats en aquests punt, el model s'hauria de seguir desenvolupant per ser utilitzat com a plataforma per testar la permeabilitat i toxicitat de molècules o per estudiar models de malalties en que les interaccions epiteli – stroma són essencials.

9. Appendix:

Journal articles

IOP Publishing Biofabrication 12 (2020) 025008 https://doi.org/10.1088/1758-5090/ab5f50

Biofabrication

PAPER

RECEIVED
29 August 2019

REVISED
26 November 2019

ACCEPTED FOR PUBLICATION
5 December 2019

PUBLISHED
7 February 2020

Hydrogel co-networks of gelatine methacrylate and poly(ethylene glycol) diacrylate sustain 3D functional *in vitro* models of intestinal mucosa

Anna Vila[1,5], Núria Torras[1,5], Albert G Castaño[1], María García-Díaz[1], Jordi Comelles[1], Teresa Pérez-Berezo[1], Carmen Corregidor[1], Óscar Castaño[1,2,3], Elisabeth Engel[1,2,4], Vanesa Fernández-Majada[1,6] and Elena Martínez[1,2,3,6]

[1] Institute for Bioengineering of Catalonia (IBEC), The Barcelona Institute of Science and Technology (BIST), Barcelona, Spain
[2] Centro de Investigación Biomédica en Red (CIBER), Madrid, Spain
[3] Electronics and Biomedical Engineering, University of Barcelona (UB), Barcelona, Spain
[4] Materials Science and Metallurgical Engineering, Polytechnical University of Catalonia (UPC), Barcelona, Spain
[5] Equal contribution.
[6] Authors to whom any correspondence should be addressed.

E-mail: vfernandez@ibecbarcelona.eu **and** emartinez@ibecbarcelona.eu

Keywords: gelatine methacrylate, poly(ethylene glycol) diacrylate, GelMA-PEGDA co-networks, intestinal mucosa, epithelial-stromal interactions, intestinal barrier function, intestinal permeability

Supplementary material for this article is available online

Abstract

Mounting evidence supports the importance of the intestinal epithelial barrier and its permeability both in physiological and pathological conditions. Conventional *in vitro* models to evaluate intestinal permeability rely on the formation of tightly packed epithelial monolayers grown on hard substrates. These two-dimensional models lack the cellular and mechanical components of the non-epithelial compartment of the intestinal barrier, the stroma, which are key contributors to the barrier permeability *in vivo*. Thus, advanced *in vitro* models approaching the *in vivo* tissue composition are fundamental to improve precision in drug absorption predictions, to provide a better understanding of the intestinal biology, and to faithfully represent related diseases. Here, we generate photo-crosslinked gelatine methacrylate (GelMA)—poly(ethylene glycol) diacrylate (PEGDA) hydrogel co-networks that provide the required mechanical and biochemical features to mimic both the epithelial and stromal compartments of the intestinal mucosa, i.e. they are soft, cell adhesive and cell-loading friendly, and suitable for long-term culturing. We show that fibroblasts can be embedded in the GelMA-PEGDA hydrogels while epithelial cells can grow on top to form a mature epithelial monolayer that exhibits barrier properties which closely mimic those of the intestinal barrier *in vivo*, as shown by the physiologically relevant transepithelial electrical resistance (TEER) and permeability values. The presence of fibroblasts in the artificial stroma compartment accelerates the formation of the epithelial monolayer and boosts the recovery of the epithelial integrity upon temporary barrier disruption, demonstrating that our system is capable of successfully reproducing the interaction between different cellular compartments. As such, our hydrogel co-networks offer a technologically simple yet sophisticated approach to produce functional three-dimensional (3D) *in vitro* models of epithelial barriers with epithelial and stromal cells arranged in a spatially relevant manner and near-physiological functionality.

1. Introduction

The intestinal epithelium consists of a layer of tightly packed interconnected epithelial cells sitting on a collagen-based basal lamina that separates it from the stromal tissue (named lamina propria) below. The intestinal lamina propria contains many cell types including fibroblasts, myofibroblasts, endothelial and

IOP Publishing Biofabrication 12 (2020) 025008 A Vila et al

immune cells embedded in a matrix [1]. The intestinal epithelium in combination with the lamina propria form the intestinal mucosa, which acts as a pseudo-permeable barrier and ensures adequate containment of undesirable luminal contents while preserving the ability to absorb nutrients and beneficial substances [2]. It has been suggested that these barrier and permeability functions of the intestinal mucosa could play a crucial role in both physiological and pathological conditions [3]. For instance, intestinal drug permeability is a key parameter to take into account in the early stages of drug discovery [4, 5]. At the same time, intestinal barrier dysfunction leading to an increased intestinal permeability has been associated to numerous health conditions such as inflammatory bowel diseases, irritable bowel syndrome, celiac disease, obesity, and metabolic diseases [6]. Whether the inflammation associated with these diseases is a cause or a consequence of the increased intestinal permeability is still not fully understood [7]. Traditionally, intestinal permeability studies have been performed *in vivo* or using animal mucosal tissue explants. Although valuable, these experiments provide few mechanistic insights due to the complexity of the *in vivo* environment [8]. Conversely, *in vitro* models, which mostly use transformed epithelial cell lines grown as monolayers, provide a limited and simplistic representation of only the epithelial component of the intestinal mucosa. However, it has been demonstrated that epithelium-stroma interactions are important to maintain the intestinal mucosa integrity [9]. Thus, the development of more physiologically relevant 3D intestinal mucosa-like *in vitro* models that represent the epithelial and the stromal compartments of the tissue in a spatially relevant manner would be instrumental to reduce the gap between *in vitro* epithelial cell-based models and *in vivo* experiments.

Engineered tissues represent a new paradigm in the field of cell-based *in vitro* assays. They combine biofabrication and tissue-engineering components to provide *in vitro* models with tissue-like characteristics such as 3D architecture, multicellularity, cell-matrix interactions and near-*in vivo* functionality [10–13]. As such, engineered tissues hold the potential to deliver huge improvements over current reductionist cell culture monolayers, opening new research avenues by providing better tools for basic research, disease modeling, and drug testing. However, examples of engineered tissues recreating the intestinal mucosa and, more specifically, including stromal and epithelial components, are scarce. In a pioneering work, collagen hydrogels were used to embed primary mouse fibroblasts and produce a 3D model of the intestinal mucosa that included lamina propria and epithelial cells [14]. This models yielded improved predictions on drug permeability with respect to standard *in vitro* cultures based on tightly packed Caco-2 cell monolayers on Transwell®, which typically show abnormally high TEER values and low permeability values [14]. However, this model used fibroblasts with a low passage number to represent the stromal component, which compromises its adoption in routine long-term applications. A different study employed fibronectin-gelatine nanofilms to produce 3D-multilayer structures consisting of normal dermal fibroblasts underneath a monolayer of epithelial Caco-2 cells [15]. The authors showed that the presence of multiple layers of dermal fibroblasts accelerates Caco-2 epithelial monolayer formation and enhances epithelial barrier function. In contrast, a more recent study showed how CCD-18Co intestinal fibroblasts embedded in Matrigel® were able to sustain the growth of epithelial cells, sitting on top of them, through the production of ECM proteins. The CCD-18Co fibroblasts interfered with barrier robustness by getting intercalated between the epithelial cells [16]. The discrepancies reported with respect to the effects of stromal fibroblasts on the epithelial barrier performance is likely due to differences in experimental set-ups, particularly regarding the origin and density of the fibroblasts, the thickness of the construct, and the 3D organization of the epithelial and stromal compartments. As the literature in the field is sparse, further analysis of the impact of fibroblasts on the maintenance of the epithelial barrier maintenance is needed to elucidate the underlying mechanisms.

Thus far, most approaches to engineer 3D *in vitro* models of the intestinal mucosa that represent both the epithelial and stromal compartments, have employed hydrogels of natural origin as extracellular matrices (ECM). Typically, hydrogels are the preferred choice because they possess a high water content, mechanical properties that are similar to those in the native ECM of soft tissues, and confer diffusion-driven solute transport properties [17, 18]. A major drawback of natural hydrogels is that they are highly biodegradable. On the one hand, this biodegradability allows for cell matrix remodeling, which can have positive effects on cell proliferation and migration [19, 20]. On the other hand, it limits the available time for cell culturing and compromises the mechanical stability of the engineered tissues. Often, this problem is overcome by increasing the density of cells on the scaffold. However, this typically results in a density of cells that exceeds physiologically realistic levels in the native lamina propria and thus further removes these models from being able to faithfully represent *in vivo* conditions [21].

In this work, we report a simple strategy to engineer a 3D model of the small intestinal mucosa that includes both the epithelium and the stroma components. With this aim, we employ hydrogels based on the co-polymerization of gelatine methacrylate (GelMA) and poly(ethylene glycol) diacrylate (PEGDA) polymers to produce cell-laden constructs. GelMA provides cell-adhesive and biodegradable moieties, but its mechanical robustness is insufficient to sustain long-term cultures [17]. Conversely, PEGDA is

IOP Publishing Biofabrication 12 (2020) 025008 A Vila et al

a synthetic, non-degradable polymer that forms mechanically stable networks. We demonstrate that GelMA-PEGDA hydrogel co-networks generated by photopolymerization possess tuneable physicochemical and mechanical properties depending on their polymer composition and total macromer content. For a particular co-network composition, we proved that fibroblasts-laden hydrogels support the formation of a mature epithelial monolayer, providing an engineered *in vitro* model of the epithelial and stromal compartments. We then demonstrate that while our approach is sufficiently simple to be used with conventional cell culture systems, it also possesses the necessary complexity to recapitulate the relevant epithelial-stromal interactions, yielding realistic TEER values and an improved representation of the permeability of drug model compounds. The model can therefore be used to improve the predictive accuracy of state-of-the-art *in vitro* systems.

2. Materials and methods

2.1. GelMA synthesis and characterization

Gelatine methacrylate (GelMA) was prepared following the method described previously [22, 23]. Briefly, a 10% (w/v) gelatine solution was obtained by dissolving gelatine from porcine skin type A (Sigma-Aldrich) in phosphate buffer saline (PBS; pH 7.4) (Gibco) at 50 °C under stirring conditions for approximately 2 h. Methacrylic anhydride (MA) (Sigma-Aldrich) at 5% v/v was added at a rate of 0.5 ml min^{-1} and left to react for 1 h while stirring. Then, the solution was centrifuged at 1200 rpm for 3 min and the reaction was stopped by adding Milli-Q water to the supernatant. The resulting solution was dialyzed using 6–8 kDa of molecular weight cut-off (MWCO) membranes (Spectra/por, Spectrumlabs) against Milli-Q water at 40 °C, which was replaced every 4 h for 3 d. The pH of the dialyzed products was adjusted to 7.4. Samples were frozen overnight at −80 °C and lyophilized for 4 and 5 d (Freeze Dryer Alpha 1-4 LD Christ). The resulting products were stored at −20 °C until further use.

The successful methacrylation of the synthesized GelMA was analyzed by nuclear magnetic resonance (NMR) spectroscopy [24]. ^{1}H-NMR spectra were acquired using a Bruker DMX-500 high resolution NMR spectrometer (400 MHz) (Bruker). Spectra were collected from non-methacrylate gelatine as a control. To that end, GelMA solutions (1 ml) were prepared at 10 mg ml^{-1} in deuterium oxide. All spectra were collected with Mnova NMR software (Mestrelab Research). To quantitatively determine the amount of methacrylate amines in the GelMA polymer solutions, we employed the Habeeb Method [25]. This method is based on the fact that primary amines react with 2,4,6-Trinitrobenzene sulfonic acid (TNBS) (Sigma-Aldrich) to form a highly chromogenic derivative solution that can be measured by absorbance. Briefly, gelatine and GelMA polymers were dissolved at a concentration of 0.5 mg ml^{-1} in sodium bicarbonate buffer (NaHCO3, 0.1M; pH 8.4, in Milli-Q water) (Sigma-Aldrich) at 40 °C under stirring conditions. To generate a standard curve, 100 μl of increasing concentrations of gelatine solution and 100 μl of GelMA solution at 0.5 mg ml^{-1} were placed in a 96 well plate. 50 μl of TNBS 0.01% solution in sodium bicarbonate buffer was added to each well and the mixture was incubated for 2 h at 37 °C in complete darkness. The TNBS reaction was stopped by adding 50 μl of sodium dodecyl sulfate 10% (SDS) (Sigma-Aldrich) and 25 μl of hydrochloric acid (HCl, 1 M) (Panreac) to each well. The absorbance of the resulting solutions was measured at 335 nm using a spectrophotometer (Infinite M200 PRO Multimode Microplate Reader, Tecan). A linear calibration curve that relates the absorbances of the gelatine solution titrations to the free amine percentage (X) in the sample was established. Then, the degree of methacrylation of the GelMA samples was calculated as: methacrylated amines (%) $= 100 - X$.

2.2. Fabrication of GelMA and GelMA-PEGDA hydrogels

GelMA polymer solutions containing two different concentrations of total macromers (7.5% and 12.5% w/v) were dissolved in Dulbecco's modified eagle medium (DMEM) without Phenol red (Gibco, Thermo Fisher Scientific) and complemented with 1% Penicillin-Streptomycin (Sigma-Aldrich) at 65 °C under stirring conditions. In addition, GelMA and PEGDA polymer solutions containing the same concentrations of total macromers (7.5% and 12.5% w/v) but different percentages of both polymers, namely 3.75% w/v GelMA- 3.75% w/v PEGDA and 7.5% w/v GelMA-5% w/v PEGDA, were prepared as follows: PEGDA, with a molecular weight of 4000 Da (Polysciences), was dissolved at 65 °C in DMEM without Phenol red (Gibco, Thermo Fisher Scientific) and complemented with 1% Penicillin-Streptomycin (Sigma-Aldrich) under stirring conditions for 2 h. Then, PEGDA solutions were filtered and mixed with the corresponding percentages of GelMA. Next, 2-Hydroxy-4′-(2-hydroxyethoxy)-2-methylpropiophenone photoinitiator (Irgacure D-2959) (Sigma-Aldrich) was added to the polymer solutions at a concentration of 0.5% w/v (see schemes in figure 1(a)).

All polymer solutions were kept at 37 °C for about ~30 min before use. Hydrogel polymerization was performed following a previously described methodology [26]. Briefly, an array of circular pools (6.5 or 10 mm in diameter) were produced by punching polydimethylsiloxane (PDMS) Sylgard 184 (Dow Corning) membranes (prepared at a ratio 10:1 w/w between the pre-polymer and the curing agent and cured at room temperature for 24 h). The thickness of the hydrogel

IOP Publishing Biofabrication 12 (2020) 025008 A Vila et al

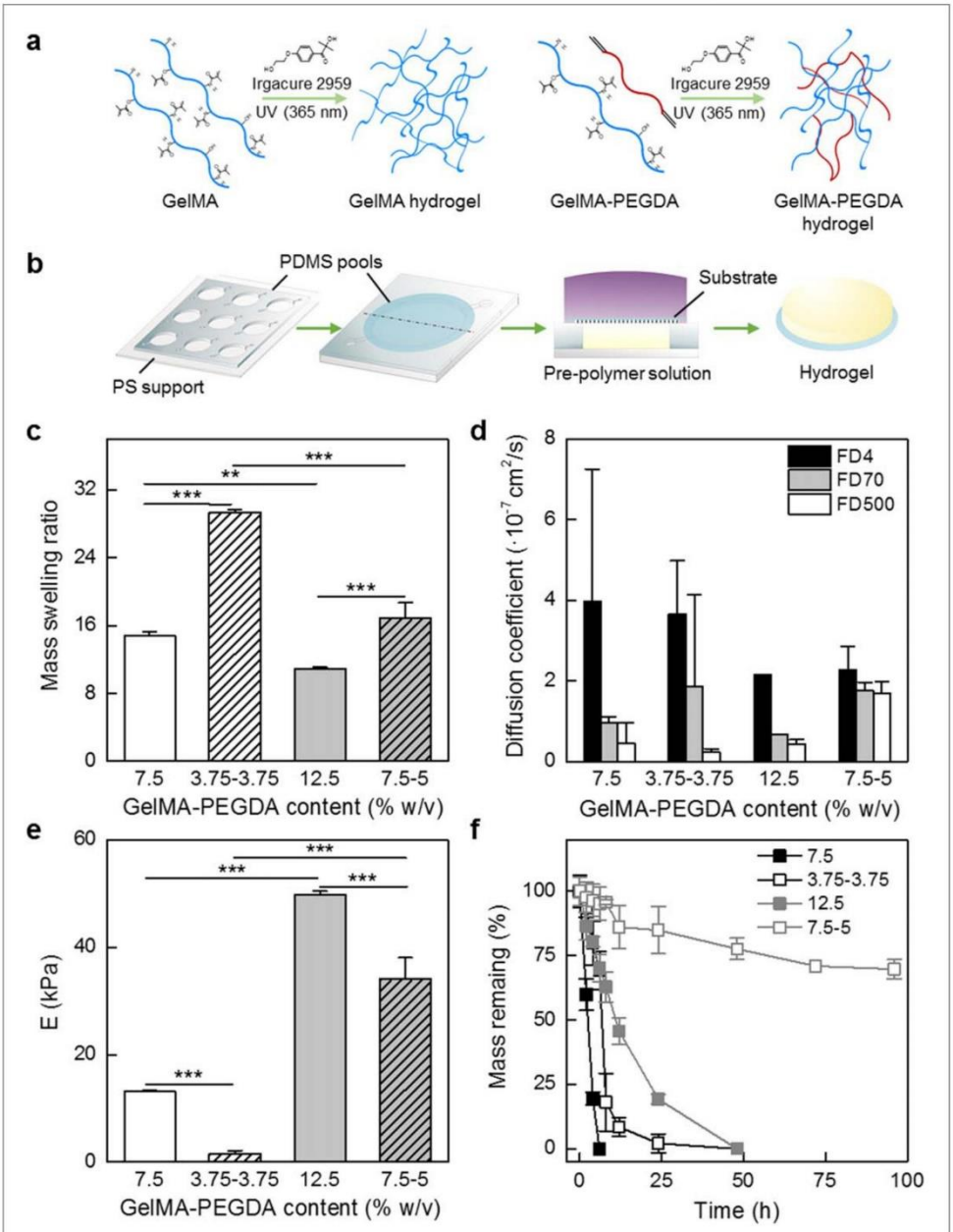

Figure 1. (a) Schematic of the GelMA and GelMA-PEGDA photopolymerization reaction and co-networks formed. (b) Schematic of the single-step photo-crosslinking process employed. Pre-polymer solution was poured into a PDMS pool and covered with a cover glass or a porous membrane which both act as substrates. UV exposure produces either a single or an array of photo-crosslinked hydrogel networks. (c) Mass swelling ratio, (d) diffusion coefficient for different molecule sizes (FD500 = 500 kDa, with a hydrodynamic diameter of 32 nm; FD70 = 70 kDa, hydrodynamic diameter of 11.6 nm; FD4 4 kDa, hydrodynamic diameter of 2.8 nm), (e) apparent elastic modulus, E, and (f) degradation upon collagenase incubation (shown as mass remaining with time), for different GelMA networks and GelMA-PEGDA co-networks: 7.5 (7.5% w/v GelMA), 3.75–3.75 (3.75% w/v GelMA-3.75% w/v PEGDA), 12.5 (12.5% w/v GelMA), 7.5-5 (7.5% w/v GelMA-5% w/v PEGDA). Values are shown as mean ±SD ($n = 3$). $^{**}p < 0.005$ and $^{***}p < 0.001$.

was defined by the height of the PDMS pools. Pools were mounted on top of polystyrene (PS) supports. Either silanized glass coverslips with a diameter of 12 mm or Tracketch® polyethylene terephthalate (PET) membranes with 5 μm pore size (Sabeu GmbH & Co) were then used as substrates covering the tops of the PDMS pools. Polymer solutions were poured into the pool array and flood exposed to UV light to form

disc-shaped hydrogels. UV light exposure took place in a MJBA mask aligner (SUSS MicroTech) equipped with an i-line filter ($\lambda = 365$ nm) emitting an energy dose (power density × time) of 1.88 J cm^{-2} (see scheme of the process in figure 1(b)). Before each exposure, the incidental power density (power per surface unit) on the surface of the samples was measured using a UV-power meter (Model 1000, SUSS MicroTech) to properly adjust the exposure time. After UV exposure, unreacted polymer and photoinitiator were washed out with warmed PBS at 37 °C. Then, samples were kept submerged in PBS at 4 °C to reach the equilibrium swelling before further characterization.

2.3. Characterization of GelMA and GelMA-PEGDA hydrogels

2.3.1. Analysis of co-network homogeneity

We determined the presence of GelMA and the microscopic homogeneity of the GelMA-PEGDA co-networks by the fluorescent labeling of the GelMA chains. For this purpose, discs of 10 mm in diameter and 1 mm in thickness, obtained by exposing to a UV dose of 3.00 J cm^{-2}, were fabricated onto glass coverslip substrates. Hydrogels were incubated overnight with a 0.02 mM solution of Rhodamine-NHS (Sigma-Aldrich) at 4 °C, which labels GelMA chains. After extensive washing in PBS, hydrogels were imaged using confocal microscopy (LSM 800, Zeiss). The average intensity was measured from the maximum Z projections of stacks of images collected from the first 50 μm of each hydrogel.

2.3.2. Mass swelling analysis

Hydrogel swelling was investigated on hydrogel discs (10 mm in diameter and 1 mm in height) photopolymerized with a UV dose of 1.88 J cm^{-2} onto glass coverslips covered with porous PET membranes (5 μm pore size). Since PET membranes tend to absorb UV light behaving as filters [26], they were used to fabricate hydrogels with mechanical properties comparable to those employed in the cell culture experiments. Right after polymerization, hydrogels were weighed (m_c) and kept submerged in PBS at 37 °C to induce swelling for one week, exchanging the PBS buffer every other day. Then, hydrogels were carefully wiped with a KimWipe tissue (Kimtech Science) to remove any excess liquid and weighed again (m_s). Finally, samples were detached from the glass coverslips, frozen overnight at −80 °C, lyophilized (Freeze Dryer Alpha 1-4 LD Christ) and weighed once more (m_d). The mass swelling ratio for the GelMA and GelMA-PEGDA hydrogel co-networks was then calculated as the ratio between the mass due to swelling (difference between swollen and dry polymer) and the mass of the dry polymer

$$Mass\ swelling\ ratio = \left(\frac{m_s - m_d}{m_d}\right).$$

2.3.3. Diffusion coefficient and mesh size analysis

Molecular diffusion is an important network property of the hydrogels affecting mass-transport. To estimate the molecular diffusion in the GelMA samples, we used the Flory–Rehner theory [27] in its modified form by Peppas and Merrill [28]. The measured masses of the hydrogels right after fabrication (m_c), in equilibrium swelling (m_s), and in their dry state (m_d) were used to calculate the polymer volume fraction of the hydrogels in their swollen ($\nu_{2,s}$) and relaxed ($\nu_{2,r}$) states as well as their estimated mesh sizes ξ. Details of the calculation can be found in the supplementary information which is available online at stacks.iop.org/BF/12/025008/mmedia. Since this model is not well suited to determine quantitatively the properties of hydrogel co-networks [29], we studied the influence of PEGDA within the GelMA networks by analyzing the diffusion profiles of dextran fluorescent molecules of different molecular weights as they passed through the hydrogels. GelMA and GelMA-PEGDA hydrogel discs (6.5 mm in diameter and 1 mm in height) were fabricated on top of porous PET membranes (5 μm pore size) using a UV dose of 1.88 J cm^{-2}. Hydrogels were mounted on 24-well polycarbonate Transwell® filter inserts (Corning Costar) using double-sided pressure-sensitive adhesive rings (Adhesives Research) as described elsewhere [26]. Then, 200 μl of solutions containing dextrans at 0.25 mg ml^{-1} in PBS were loaded in the apical chambers while adding 600 μl of PBS to the basolateral chambers. Dextran molecules of 4 kDa (FITC-Dextran), 70 kDa (Rhodamine-Dextran), and 500 kDa (FITC-Dextran) (all from Sigma-Aldrich) were used separately. The Transwell® plates were incubated at 37 °C. At regular intervals (from 0 to 240 min), 50 μl were sampled from the basolateral compartments and replaced with 50 μl of PBS. Collected samples were transferred to 96 black well plates and FITC or Rhodamine fluorescence was measured at excitation/emission wavelengths of 490/525 nm and 540/625 nm, respectively, using an Infinite M200 PRO Multimode microplate reader (Tecan). The changing concentration of dextrans over time was determined using standard calibration curves. Apparent diffusion coefficients (D_{app}) for each dextran were calculated as

$$D_{app} = \frac{P_{app} \cdot h}{K},$$

where h is the height of the hydrogels, K the hydrogel/water partition coefficient (assumed to be 1), and P_{app} the apparent permeability. P_{app} was obtained from the change in cumulative diffusion of the dextran over time (figure S3) [30]. The effects of PEGDA on the network structure's mesh size were evaluated by comparing the apparent diffusion coefficients of the GelMA-PEGDA

hydrogel co-networks to their GelMA counterparts (with equivalent macromer compositions).

2.4. Mechanical properties analysis

The mechanical properties of hydrogels are important physical cues that direct cell behavior. For their measurement, we fabricated discs on top of coverslips covered with a porous PET membrane. Pools, 10 mm in diameter and about 3 mm in height, were photopolymerized with an energy dose of 3.76 J cm^{-2} (double the standard dose to ensure photopolymerization across the entire thickness). After swelling in PBS, hydrogel diameters were no longer uniform and had to be re-punched to obtain consistent 10 mm diameter samples. Sample heights were accurately determined using a high precision Mitutoyo calliper (Mitutoyo Corporation). A Zwick-Roell Z0.5TN testing machine (Zwick Roell Group) was used to obtain stress–strain curves from compression assays at room temperature. Stress–strain curves were recorded limiting the strain rate to 5% min^{-1} and the maximum strain to 50%. An initial load of 5 mN was applied to facilitate proper contact between the hydrogels and the compression plates. The apparent elastic modulus of the samples was determined using TestXpert II, v.3.41 analysis software from the slope of the linear region of the stress–strain curves, corresponding to a strain of 10%–20%.

2.5. Degradation analysis

To investigate the degradation properties of GelMA and GelMA-PEGDA co-networks, we fabricated disc-shaped hydrogels (10 mm in diameter and 1 mm in thickness) on top of untreated cover glasses by applying a UV exposure dose of 3.00 J cm^{-2}. After fabrication, hydrogels were detached from the cover glasses and left to swell in an Eppendorf tube with 1 ml of PBS. After swelling, PBS was replaced by 1 ml of collagenase type II 2.5 U ml^{-1} solution (Sigma-Aldrich) and incubated at 37 °C for 96 h while regularly removing collagenase solution by centrifuging the samples for 5 min at 8000 rpm. The undigested hydrogels were washed twice by adding Milli-Q water and centrifuged before decanting the supernatant. Then, the hydrogels were freeze-dried (Freeze Dryer Alpha 1-4 LD Christ) and weighed. The mass remaining percentage was determined by comparing the mass before ($t = 0$) and after (t) enzyme incubation:

$$Mass\ remaning\ (\%) = \frac{M_{(t)}}{M_{(t=0)}} \cdot 100.$$

2.6. Fabrication and characterization of cell-laden GelMA-PEGDA hydrogels

NIH-3T3 fibroblasts (ATCC® CRL-1658™) were used as cell model to mimic the stromal compartment of the intestinal tissue. Fibroblasts were expanded and maintained in 75 cm^2 flasks in high glucose DMEM (Gibco, Thermo Fisher Scientific), supplemented with 10% v/v fetal bovine serum (FBS) (Gibco, Thermo Fisher Scientific) and 1% v/v Penicillin/Streptomycin (Sigma-Aldrich). NIH-3T3 were grown in an incubator at 37 °C and 5% CO_2 (exchanging the medium every other day) and passaged twice a week. To produce cell-laden hydrogels, NIH-3T3 (5×10^6 cells ml^{-1}) were trypsinised and re-suspended in pre-polymer solutions containing the polymers and 0.5% w/v Irgacure 2959 photoinitiator in DMEM supplemented with 1% v/v Penicillin/Streptomycin. DMEM without Phenol red was employed to avoid potential effects during photopolymerization. Cell-containing polymer solutions were kept at 37 °C before polymerization. Hydrogels (6.5 mm in diameter and 0.5 mm high) were fabricated on silanized PET membranes (5 μm pore size) (figure 2(a)), by exposing them to a UV dose of 1.88 J cm^{-2}. Unreacted polymer and photoinitiator were washed out with warm cell culture medium supplemented with 10% of Penicillin/Streptomycin and 1/250 of normocin (Invitrogen). Cell-laden hydrogels were then attached to Transwell® inserts using PSA rings and cultured for 7 d in an incubator at 37 °C and 5% CO_2, exchanging the medium every other day. L-Ascorbic acid at 50 μg ml^{-1} (Sigma-Aldrich) was added every other day to the cell culture medium to stimulate the production of ECM [31].

Cell viability on cell-laden hydrogels was investigated using a calcein-AM/ethidium homodimer Live/Dead kit (Invitrogen) 1 and 7 d after cell encapsulation and monitored via confocal laser-scanning microscope (LSM 800, Zeiss). Image processing and cell viability quantification was performed manually using ImageJ v.1.49b software (http://rsb.info.nih.gov/ij, NIH) to determine the percentage of viable cells at each time point.

2.7. Fabrication and functional characterization of a 3D model of the intestinal mucosa

2.7.1. Fabrication of the 3D model

Fibroblast-laden GelMA-PEGDA hydrogels were produced as described above to generate a model of the intestinal stromal compartment. Immediately after fabrication, Caco-2 cells (ATCC® HTB-37™) were seeded on top of the hydrogels to represent the epithelial component of the tissue. Caco-2 cells were maintained in 75 cm^2 flasks in high glucose DMEM (Gibco, Thermo Fisher Scientific), supplemented with 10% v/v FBS (Life Technologies), 1% v/v Penicillin/Streptomycin (Sigma-Aldrich), and 1% v/v of non-essential amino acids (Gibco, Thermo Fisher Scientific). Cells were kept in an incubator at 37 °C and 5% CO_2 (exchanging the medium every other day) and passaged weekly. Then, Caco-2 cells were seeded at a density of 7.5×10^5 cells cm^{-2} on the fibroblast-laden 7.5% w/v GelMA-5% w/v PEGDA hydrogel discs

IOP Publishing Biofabrication 12 (2020) 025008 A Vila et al

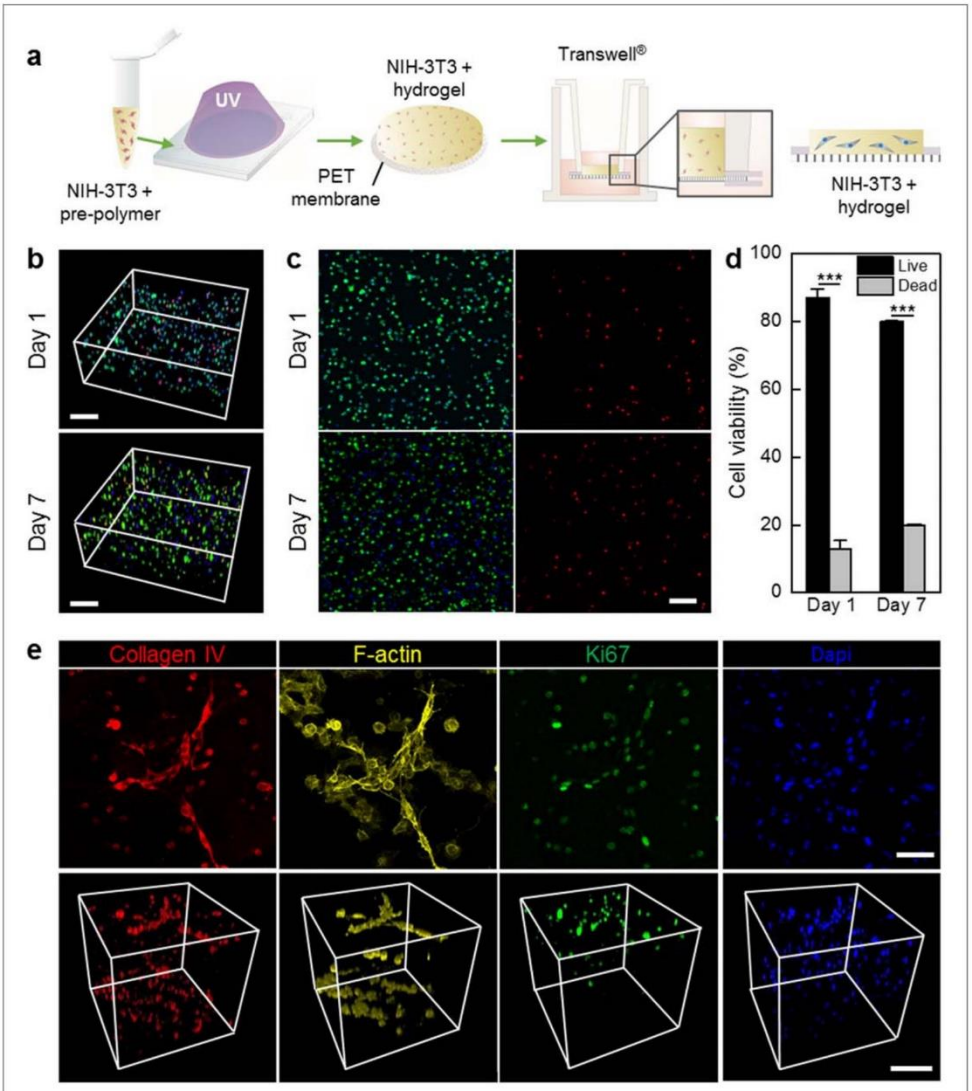

Figure 2. (a) Schematic to illustrate the NIH-3T3 fibroblast encapsulation process in the hydrogel co-network. (b) Confocal 3D reconstruction of the hydrogel co-network showing the spatial distribution of the NIH-3T3 embedded cells on days 1 and 7 after live/dead assays (live cells stain in green, dead cells in red). Dapi was used to stain the nuclei. Scale bars: 200 μm. (c) Maximum intensity projections of samples shown in panel (b). Scale bar: 100 μm. (d) Quantification of cell viability at days 1 and 7 after encapsulation based on live/dead staining. Values are the mean percentage of cell viability $\pm$SD ($n = 3$), $^{***}p < 0.001$. (e) Immunostaining for Collagen IV, F-actin, and Ki67 of hydrogel co-networks with embedded NIH-3T3 fibroblasts after 7 d in culture shown as maximum intensity projections (top panels) and confocal 3D reconstruction (bottom panels). Scale bars: 50 μm (top) and 100 μm (bottom panels).

(6.5 mm in diameter, 0.5 mm high) fabricated onto PET porous membranes and mounted on Transwell® inserts. Control experiments were performed by seeding Caco-2 cells on fibroblast-free hydrogels with the same composition. Additionally, Caco-2 cells were seeded on standard 24-well polycarbonate Transwell® filter inserts (0.4 μm pore size) at a density of 7.5×10^5 cells cm^{-2}. Cells were cultured for 21 d, exchanging the medium every other day. The medium composition used for the co-culture was identical to the one used for the Caco-2 cells with the addition of L-ascorbic acid every other day.

2.7.2. Immunofluorescence and histological analysis

The characteristic morphology and polarization of Caco-2 cells forming an epithelial barrier were studied by immunostaining after culturing for 21 d. Samples were fixed with 10% neutral buffered formalin solution (Sigma-Aldrich) at 4 C for 1 h, permeabilized with 0.5% Triton-X (Sigma-Aldrich) and blocked with 1%

bovine serum albumin (Sigma-Aldrich), 3% donkey serum (Millipore), and 0.3% Triton-X. Primary antibodies against ZO-1 (Abcam) (2 μg ml^{-1}) and β-catenin (Abcam) (1 μg ml^{-1}) were incubated overnight at 4 °C under shacking conditions. Samples were then incubated with secondary antibodies and/or Rhodamine-Phalloidin (Cytoskeleton) (0.07 μM) for 2 h at 4 °C under shacking conditions. Anti-goat Alexa 488 (Invitrogen, Thermo Fisher Scientific) and anti-rabbit Alexa 647 (Invitrogen, Thermo Fisher Scientific) (4 μg ml^{-1}) were used as secondary antibodies. Finally, samples were incubated with DAPI (Thermo Fisher Scientific) (5 μg ml^{-1}) for 30 min.

For the hydrogel-embedded fibroblasts, cell morphology and extracellular matrix (ECM) proteins production were analyzed by immunofluorescence, following the same protocol described above. After fixation, permeabilization, and blocking steps, primary antibodies against Collagen IV (Biorad) (1.6 μg ml^{-1}) were incubated overnight at 4 °C under shacking conditions. Then, secondary antibodies anti-goat Alexa 488 (Invitrogen, Thermo Fisher Scientific) (4 μg ml^{-1}) and/or Rhodamine Phalloidin (Cytoskeleton) (0.07 μM) were incubated for 2 h at 4 °C under shacking conditions. Finally, samples were incubated with DAPI (5 μg ml^{-1}) for 30 min. After immunostaining, hydrogels were mounted facing downward onto glass coverslips and imaged using a confocal laser-scanning microscope (LSM 800, Zeiss). 500 μm PDMS spacers were employed to prevent sample damage. A drop of Fluoromount G (Southern Biotech) was added to preserve the dyes and prevent the sample from drying. Acquired Z-stacks were processed using Image J software. For a better visualization of the embedded cells across the entire height of the hydrogel, stained hydrogels were embedded and cross-sectioned using the optimal cutting temperature (OCT) technique. First, samples were incubated overnight with 30% sucrose (Sigma-Aldrich) at 4 °C, then embedded in OCT (Tissue-Tek® O.C.T. Compound, Sakura® Finetek). OCT tissue sections (~7 μm in thickness) were cut, air dried, and stored at −80 °C for further analysis. Alternatively, some samples were embedded in paraffin for later hematoxylin-eosin staining. These samples were embedded in an automatic tissue processor machine (Tissue Tek VIP, Sakura) following routine procedures and resulting in paraffin-embedded sections of about 3 μm thick. After being cut and air dried, these samples were further dried overnight at 60 °C and then stored at room temperature before hematoxylin and eosin staining. For later imaging, both types of hydrogel slices were mounted on a glass coverslip using Fluoromount G (Southern Biotech) and visualized using a confocal laser-scanning microscope (LSM 800, Zeiss).

2.7.3. TEER and permeability studies

The integrity of the barrier developed by the epithelial cells on the fibroblast-laden hydrogels and control samples was monitored every two days throughout the culture period (21 d). For this purpose, the transepithelial resistance (TEER) between the two compartments of the Transwell® chambers was measured using an EVOM2 Epithelial voltohmmeter with an STX3 electrode (World precision Instruments). Measured resistance values were corrected by subtracting the resistances of the porous PET membranes and the hydrogels. TEER values were normalized to the total surface area of the epithelial monolayers. After 21 d, permeability was measured using fluorescent-labeled dextrans (4 kDa FITC dextran, FD4, and 70 kDa rhodamine dextran, FD70) as model compounds, and insulin as biological model drug. In brief, cells were washed with DMEM without Phenol red (Gibco, Life Technologies) and 200 μl of the test solutions containing 0.5 mg ml^{-1} dextrans or 0.25 mg ml^{-1} insulin were added to the apical side of the Transwell® inserts. Then, 600 μl of DMEM without Phenol red were added to the basolateral compartments. Samples were collected from the basolateral compartments at given time points followed by buffer replacement. During the experiment, cells were incubated at 37 °C on a horizontal shaker at 50 rpm. Samples were then analyzed by measuring the fluorescence using an Infinite M200 PRO Multimode microplate reader (Tecan) or by an insulin ELISA kit (Mercodia). The apparent permeability (P_{app}) was determined from the change in cumulative diffusion of the dextran over time [30].

2.7.4. Epithelial barrier disruption

The impact of the stromal cells on barrier recovery after tight-junction disruption was studied after 21 d of culturing by disrupting the barrier with ethylenediaminetetraacetic acid (EDTA) (Sigma-Aldrich). 5 mM solution of EDTA in high glucose DMEM supplemented with 10% v/v FBS, 1% v/v Penicillin/Streptomycin and 1% v/v of non-essential amino acids, were added to the apical (200 μl) and basolateral (600 μl) compartments. After 5 min of incubation, samples were washed with PBS and stored at 37 °C in DMEM, measuring TEER values at given time points.

2.8. Data analysis and statics

The data are presented as the mean ± standard deviation (SD). The graphs were plotted using OriginPro 8.5 software (OriginLab). In the case of normal distributions, differences between groups were compared through a one-way analysis of variance (ANOVA). Turkey's test was performed as indicated in the figure legends. Differences were considered as statistically significant if $p < 0.05$.

IOP Publishing Biofabrication 12 (2020) 025008 A Vila et al

3. Results

3.1. Photopolymerized GelMA and GelMA-PEGDA co-networks provide hydrogels with tuneable network properties

NMR spectroscopy of the methacrylation of the synthesized GelMA (figure S1) yield bands at 5.3 ppm and the 5.6 ppm in the spectra of the GelMA samples, characteristic of the double bonds of the methacrylate groups. Additionally, the decrease of a band at 3.0 ppm reveals the reaction of the methacrylic anhydride (MA) with the ε-amino groups from the Lysines in the gelatine [24]. These results confirm the success of the gelatine methacrylation process. By using the Habeeb Method [25], we found that adding 5% v/v of MA to the gelatine resulted in a polymer with a high degree of methacrylation (76.7% $\pm$ 2.1%). This parameter represents the percentage of ε-amino groups that are modified by the reaction, which determine the relative influence of the physical and chemical crosslinking mechanisms and, in turn, the mechanical properties of the final hydrogel [32]. As mechanical properties have been identified as critical cues affecting cellular behavior [33], polymers with high degrees of methacrylation promoting chemical crosslinking are claimed to provide a more mechanically stable and cell-friendly environment [18].

GelMA, PEGDA and GelMA-PEGDA polymeric solutions were mixed with a photoinitiator (Irgacure 2959) placed in circular PDMS pools and crosslinked by UV, using exposure doses from 1 to 3.76 J cm^{-2} (figures 1(a) and (b)) to form disc-shaped hydrogels. With this exposure conditions, only PEGDA polymers exhibited a complete lack of cross-linking at the macromer concentrations used. For all the solutions tested, UV dose of less than 1 J cm^{-2} lead to poorly crosslinked networks or no crosslinking at all.

GelMA has been shown to precipitate in GelMA-PEGDA co-networks when using high concentrations of PEG polymers of high molecular weight [34]. Through microscope imaging analysis of the distribution of fluorescence labeled GelMA chains we verified that GelMA precipitations did not occur in our composite hydrogel. We also did not observe any phase-segregation indicating the formation of homogeneous co-networks during the polymerization process (figure S2).

The swelling properties of polymeric networks depend on both the pore size and the polymer-solvent interaction and are important as they can affect the diffusive and mechanical properties of the material [20, 26, 35]. In here, hydrogel swelling as a function of the total macromer concentration of the polymer (7.5% w/v or 12.5% w/v), showed that a higher macromer content led to significant decreases in swelling ratios for both the GelMA and GelMA-PEGDA samples (figure 1(c)). This is a consequence of denser network structures that have higher crosslinking densities. In addition, the incorporation of PEGDA has a strong impact on the swelling properties of the co-network, increasing the hydrogels ability to attract and store water (figure 1(c)). This effect, attributed to the higher hydrophilicity of the PEGDA polymeric chains, was more evident in samples with a lower macromer content (swelling ratio increased by 100% when adding PEGDA on 7.5% w/v samples and only by 54% when adding PEGDA on 12.5% w/v samples). This result is in agreement with previous findings [17].

Diffusivity analyses of dextran compounds of different molecular size were performed to gain insight on the porous nature of the hydrogels. Our results showed that the permeability of large to medium sized molecules such as FD500 and FD70 with molecular weights of 500 and 70 kDa and hydrodynamic diameters of 32 and 11.6 nm, respectively [36], were hindered by the hydrogels, while the smaller FD4 with 4 kDa of molecular weight and 2.8 nm of hydrodynamic diameter [37] could diffuse more easily (figure S3). This effect was consistent for all the different hydrogels compositions (figure 1(d)). For FD4, the diffusion coefficient decreased with increasing macromolecular content. This behavior agrees with experimental diffusivity coefficients measured for GelMA networks [38]. We computed the values for the mesh size of PBS-swollen GelMA networks following Peppas and Merrill modifications proposed for the Flory–Rehner theory [27] (see supplementary Material and Methods), and found that those decreased from about 21 nm to about 16 nm when the macromer content was increased from 7.5% to 12.5% w/v. PEGDA-containing hydrogels did not show significant differences in diffusivity properties with respect to their GelMA counterparts (figure 1(d)), which suggests that mesh size is unaffected by the addition of PEGDA.

The mechanical properties of GelMA and GelMA-PEGDA hydrogels were evaluated in compression assays. The stress–strain curves recorded did not show any sample failure, even at the maximum strain level of 50%. This demonstrates that all hydrogels have a linear behavior as elastomers within the load range and the conditions of the assay. The apparent elastic modulus significantly increased for higher macromer content, both in the GelMA and GelMA-PEGDA samples (figure 1(e)), as would be expected for denser networks. For identical macromer contents, the addition of PEGDA led to a decrease in the apparent elastic modulus, particularly (>90% decrease) for low (7.5% w/v) macromer content.

The effects of adding PEGDA agree with those produced by a less dense network that allows higher water storage. Therefore, by co-polymerizing GelMA with PEGDA, the mechanical properties have become tuneable (here with apparent elastic moduli ranging from 2 to 50 kPa) and comparable to those reported for soft tissues *in vivo* (1–100 kPa) [39]. We next investigated the effect of having GelMA-PEGDA co-networks on hydrogel degradation by incubating the different samples with collagenase. Our results showed that

GelMA hydrogels containing 7.5% and 12.5% w/v of macromer were completely degraded after 4 and 24 h, respectively (figure 1(f)). We also found that for a given macromer content, the addition of PEGDA to form GelMA-PEGDA hydrogel co-networks retarded the degradation.

Samples containing 7.5% w/v of GelMA and 5% w/v of PEGDA were only 30% degraded after 96 h of collagenase incubation, preserving their mechanical integrity (figure 1(f)). Any attempt to provide cells with artificial ECM environments should synchronize the degradation rate needed for matrix remodeling with the rate of production of new ECM by the laden cells [17]. We found that GelMA-PEGDA hydrogels are able to modulate their degradation rates as the synthetic PEGDA component provides long-term mechanical integrity while the hydrogel-laden cells can attach, proliferate, and secrete their own ECM.

Overall, our GelMA-PEGDA co-networks are thus highly tuneable matrices in which water content, pore size, mechanical properties, and degradability can be tailored to suit the requirements of tissue-specific microenvironments

3.2. GelMA-PEGDA hydrogel co-networks support fibroblast 3D cultures

Based on the degradation results for the GelMA and GelMA-PEGDA samples and the long culture times required for the proper formation of intestinal epithelial cells (usually 3 weeks) [40], we selected the co-networks formed by 7.5% GelMA—5% PEGDA for the cellular experiments. NIH-3T3 fibroblasts were mixed with the GelMA-PEGDA polymer solution and the photoinitiator before encapsulating them through exposure to a UV dose of 1.88 J cm^{-2} (figure 2(a)). Disc-shaped hydrogels (6.5 mm in diameter and 0.5 mm thick) were initially loaded with 5×10^6 cells ml^{-1} cells. The hydrogel thickness was selected by considering that cell viability is limited by oxygen diffusion and computing the maximum hydrogel thickness for cell survival for NIH-3T3 cells (3 mm considering 2×10^7 cells ml^{-1}) [5]. The samples were fabricated on porous membranes and mounted on Transwell® inserts (figure 2(a)).

Cell viability of the encapsulated cells was evaluated through live/dead assays and confocal microscopy. One day after encapsulation, cells were evenly distributed throughout the hydrogel and, although there were some non-viable cells (stained in red), the majority were alive (stained in green) (figures 2(b), (c)). Overall, cell viability, computed as the ratio between alive and dead cells, was greater than 85% right after encapsulation (figure 2(d)). It has been previously shown that short-term cell viability after cell encapsulation decreases over time due to the stress induced by the photo-crosslinking process (UV irradiation, presence of radical species), and to the swelling caused by the incubation with cell culture medium.

To evaluate these effects on our hydrogels, we analyzed cell viability of the encapsulated cells at later culture time points. We found that at 7 d of culture, the cells were still evenly distributed along the thickness of the hydrogels (figure 2(b), lower panel) and only a not statistically significant decrease of less than 10% in cell viability was observed (figure 2(c), lower panel and figure 2(d)). After 14 and 21 d of culture, cell viability had decreased considerably with most viable cells being located at or near the surface of the hydrogels (figure S4). These results agree with previous findings where 3D environments have been reported to decrease cell metabolic activity and induce growth arrest, compared to two-dimensional equivalents, leading to a metabolic steady state when cultured for long periods [16, 41]. We next tested whether fibroblasts embedded in GelMA-PEGDA hydrogels were functional secreting ECM proteins. Specifically, we analyzed the expression of collagen IV as relevant ECM protein of the stromal compartment and epithelial basement membrane. Immunostaining showed that embedded fibroblasts cultured for 7 d had spread thorough the hydrogel and were actively producing collagen IV (figure 2(e)). In addition, embedded fibroblasts tested positive for the Ki67 proliferation marker after 7 d (figure 2(e)). Fibroblasts that were growing closer to the surface of the hydrogel proliferated more and exhibit a broader spread morphology compared to cells located in the interior of the hydrogel (figure 2(e), bottom panels). We hypothesize that these characteristics could be associated to hypoxic conditions and mass-transport issues inherent to the 3D cell culture microenvironment [39]. To test whether this limitation is particular to our GelMA-PEGDA hydrogel co-network formulation or whether it might be overcome in future experiments, we conducted a pilot experiment with cell-laden hydrogels cultured in custom-made bioreactors, previously developed in our laboratory, with medium perfusion for 21 d [42]. We observed that the viable fibroblasts were homogenously distributed throughout the entire hydrogel when cultured in this bioreactor (figure S4). However, for practical reasons, we chose to continue with the static Transwell® set-up in the work reported here.

Overall, our results show that GelMA-PEGDA co-networks guarantee a high level of viability and secretory functions of the encapsulated fibroblasts for at least 7 d in culture, making them convenient candidates for developing the stromal component of 3D *in vitro* models of intestinal mucosa.

3.3. GelMA-PEGDA hydrogel co-networks mimic the epithelial and stromal components of the intestinal mucosa

We next tested the capability of an epithelial intestinal cell line, Caco-2, to adhere and grow onto 7.5%

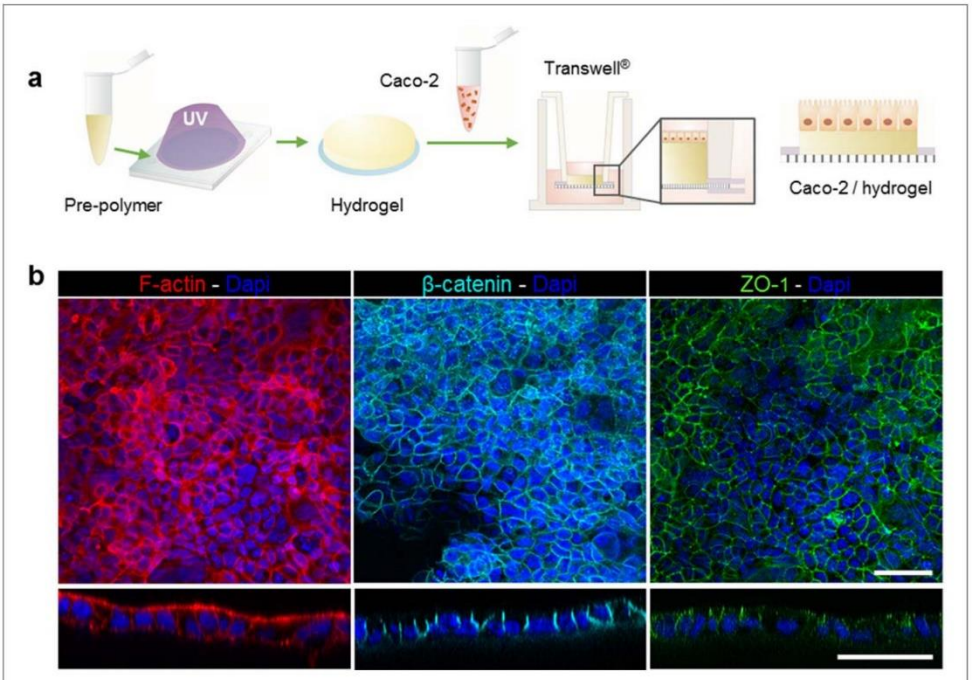

Figure 3. (a) Schematic to illustrate the Caco2 epithelial cells seeding method on the hydrogel co-network. (b) Maximum intensity projections of immunostainings for F-actin, β-catenin, and ZO-1 on the epithelial cell monolayer formed on top of the hydrogel co-networks (upper panels) and orthogonal sections (bottom panels). Dapi was used to stain the nuclei. Scale bars: 50 μm.

GelMA—5% PEGDA hydrogel co-networks. For this purpose, disc-shaped hydrogels 6.5 mm in diameter and 0.5 mm in height were photo-crosslinked by applying a UV exposure dose of 1.88 J cm^{-2}. The samples were fabricated onto porous polymeric membranes and mounted in Transwell® inserts. We next seeded 7.5 $\times$ 10^5 Caco-2 cells cm^{-2} onto the hydrogels and followed their behavior throughout the culture. Our results show that Caco-2 cells were able to adhere, spread, and proliferate on the surface of our hydrogels. After 21 d of culture, confocal microscopy images revealed the formation of a densely packed monolayer of Caco-2 cells covering the entire surface of the hydrogel (figure S5). Visualizing β-catenin and ZO-1 markers via immunofluorescence reveal the typical cobblestone-like shape of epithelial layers (figure 3(b), upper panels), while the cross-sections (figure 3(b), lower panels) show columnar, highly polarized cells exhibiting apical F-actin and ZO-1 expression, with β-catenin expression confined to the basolateral side of the monolayers. These results suggest that Caco-2 cells can form an epithelial monolayer on the GelMA-PEGDA hydrogel co-networks.

By combining the fibroblast-laden GelMA-PEGDA hydrogels with the culture of epithelial monolayers sitting on top of them we then obtained an *in vitro* model of the intestinal mucosa. NIH-3T3 cells were encapsulated at a density of 5 $\times$ 10^6 cells ml^{-1} following the method described in the previous section to generate fibroblasts-laden hydrogels that were mounted in Transwell® inserts and seeded with Caco-2 cells as described before (figure 4(a)). After 21 d of culture, the hydrogels showed good mechanical integrity and could be processed to perform histological studies. Hematoxylin-eosin staining of the construct's cross-sections about 3 μm thick showed the formation of a continuous epithelial cell monolayer on top of the constructs and even distribution of fibroblasts throughout the hydrogel co-network (figure 4(b)). Immunostaining showing apical F-actin and basolateral β-catenin confirmed the correct polarization of the epithelial monolayer formed on top of the mucosa-like hydrogel constructs. At this point in time, fibroblasts were mostly of a round shape while expressing collagen IV, which appears to have accumulated at the epithelial basement membrane (figure 4(c)), suggesting their capacity to remodel the surrounding matrix. Based on these results, our GelMA-PEGDA hydrogel co-networks appear as excellent candidates to produce long-lasting *in vitro* models of the intestinal mucosa that would allow to mimic *in vivo* interactions between stromal and epithelial cells under physiological and pathological conditions.

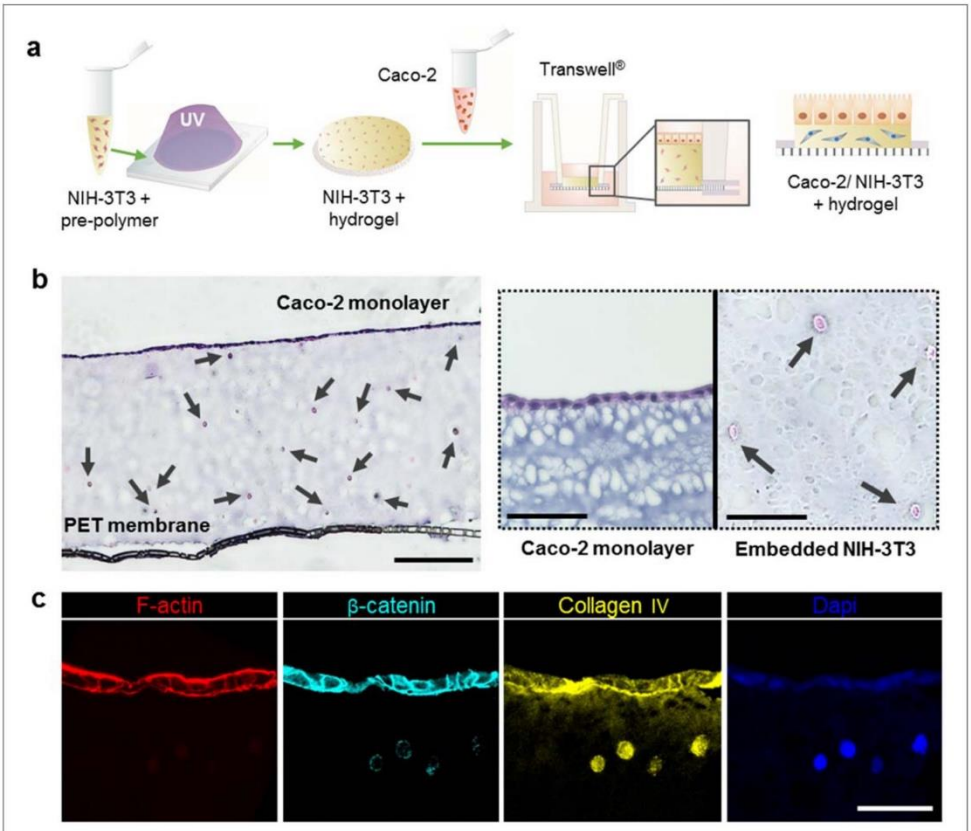

Figure 4. (a) Schematic to illustrate the NIH-3T3 fibroblast and Caco2 epithelial cell co-culture method in the hydrogel co-networks. (b) Cross-section of haematoxylin and eosin stained co-culture samples in hydrogel co-networks showing the formation of an intact epithelial monolayer at the top and a uniform distribution of the NIH-3T3 fibroblasts (arrows) throughout the hydrogel (left panel). The right panels shows detailed views of both cell types. Scale bars: 150 μm (left) and 50 μm (right). (c) Immunostainings for F-actin, β-catenin, and Collagen IV of a co-culture sample in hydrogel co-networks. Scale bar: 50 μm. DAPI was used to stain the nuclei. All samples were fixed and stained after 21 d of culture.

3.4. Evaluation of the stromal component effect on the barrier properties of the intestinal mucosa model

As a proof of concept, we employed our 3D model of intestinal mucosa to assess *in vitro* the effect of fibroblasts on the intestinal epithelial monolayer growth and barrier function. As functional hallmarks for epithelial barrier integrity and permeability, we measured the transepithelial electrical resistance (TEER) and the apparent permeability (P_{app}) to paracellular model compounds of the epithelial monolayers grown under different experimental conditions. Hydrogel discs laden with fibroblasts were fabricated onto porous membranes, mounted on Transwell® inserts and seeded with Caco-2 cells following the methods earlier described. In addition, we used hydrogels discs without fibroblasts and seeded with Caco-2 cells, and Caco-2 cell monolayers grown directly on porous membranes, which is the current gold-standard culture format for these assays [43] (figure 5(a)). Immunofluorescence images of the samples after 8 d of culture show that epithelial cells grown on fibroblast-laden hydrogels formed a continuous flat epithelial monolayer that fully covered the hydrogel surface. In contrast, on fibroblasts-free hydrogel samples the epithelial cells formed a discontinuous layer with dome-shaped structures (figure 5(b)). TEER, which is directly related to the tightness of the epithelial barrier, increased in all samples including epithelial cells with increasing culture time (figure 5(c)), indicating the formation of an epithelial monolayer with effective barrier properties. In contrast, fibroblast-laden hydrogels without epithelial cells on top (controls) did not show any significant change from the basal TEER background values (figure S6), which conclusively demonstrates that the increase in TEER was due to the formation of an epithelial barrier. TEER values of Caco-2 epithelial monolayers grown on GelMA-PEGDA hydrogels were significantly lower (up to four-fold) than for cells grown on hard Transwell® inserts (figure 5(c)). It should be noted that TEER values of Caco-2 cell monolayers grown on hard porous membranes increase already after 2–3 d in culture, while cells

IOP Publishing Biofabrication 12 (2020) 025008 A Vila et al

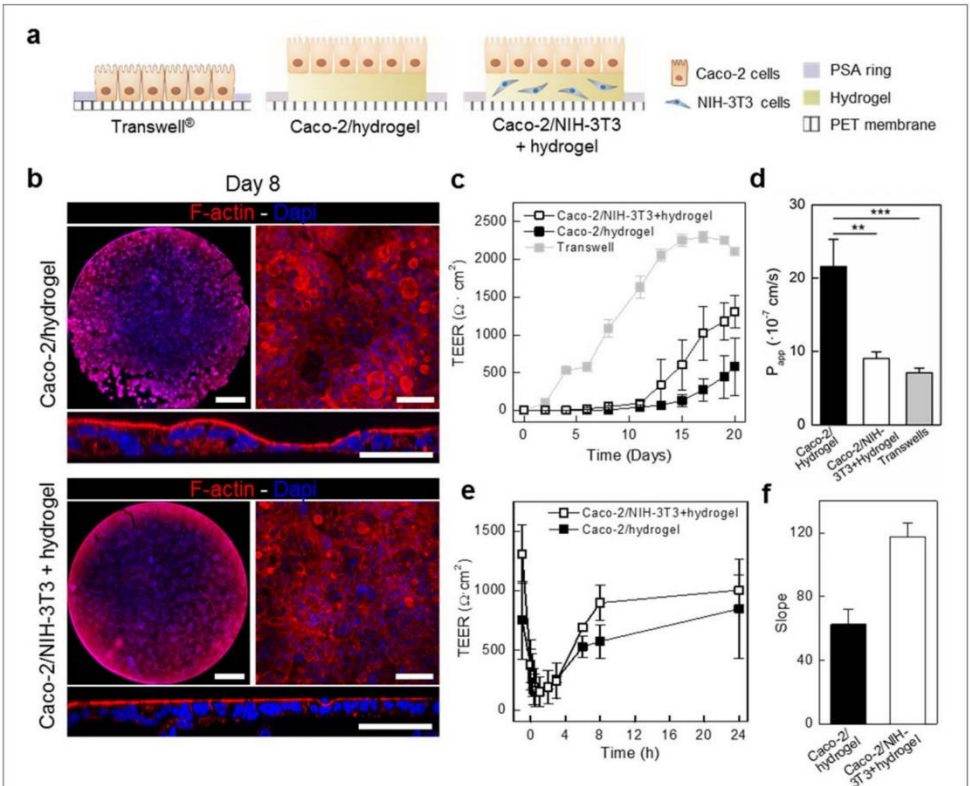

Figure 5. (a) Schematic illustration of the analyzed cell culture configurations. (b) Immunostainings for F-actin and nuclei of Caco-2 cells grown on top of hydrogel co-networks without (top images) and with (bottom images) embedded NIH-3T3 cells after 8 d in culture. Left panels show tile-scan images of the entire hydrogel surface (0.33 cm^2) (scale bar 1 mm), right panels are magnification images (scale bar 50 μm), and bottom panels are cross-sections views (scale bar 50 μm) of the corresponding samples. (c) Transepithelial electrical resistance (TEER) as function of cell culture time for epithelial monolayers grown on conventional Transwells® (gray) and on top of hydrogel co-networks with (white) and without (black) embedded NIH-3T3 fibroblasts. (d) Apparent permeability (Papp) of FITC-dextran 4 kDa (FDA) through epithelial monolayers grown on conventional Transwell® (gray) and on top of hydrogel co-networks with (white) and without (black) embedded NIH-3T3 fibroblasts. Values are mean ±SD ($n = 3$). (e) TEER evolution upon EDTA treatment of the epithelial monolayer grown on hydrogel co-networks in the presence or absence of embedded NIH-3T3. (f) Change of TEER over time from panel (e). Values are mean ±SD ($n = 3$). $^{**}p < 0.005$ and $^{***}p < 0.001$.

grown on GelMA-PEGDA hydrogels did not show an increase until 11–12 d of culture. This indicates a delay in epithelial layer formation when cells are grown on hydrogel substrates. It has been shown that the physical properties of cellular microenvironments play a crucial role in regulating cell division [44], collective cell migration [45], and, more importantly, in the maturing of tight junctions [46]. We therefore attribute the delay in epithelial monolayer formation and lower TEER values in the hydrogel-containing samples to the soft mechanical properties of the GelMA-PEGDA hydrogels (apparent elastic modulus of about 35 kPa) compared to the Transwell® inserts (about 2 GPa). This is also in agreement with previous findings for soft natural [16, 47] or synthetic hydrogels [26] which yield physiologically realistic values while hard porous membranes typically result in unrealistically high TEER values [48]. Hydrogel-based materials thus present near *in vivo*-like mechanical properties providing cells with an appropriate environment to grow and form epithelial monolayers that closely resemble the *in vivo* tissue barrier properties. Also, the change in TEER over time (slope) differed considerably between fibroblast-laden or fibroblasts-free GelMA-PEGDA hydrogels. The presence of fibroblasts clearly accelerated the monolayer formation and the development of tight junctions, which led to TEER values having increased 2.5-fold by day 21 (figure 5(c)). To further characterize the barriers, we investigated their permeability using dextrans of different molecular weights as tracers for paracellular transport through tight junctions. Consistent with the lower TEER values, the epithelial barriers formed onto the GelMA-PEGDA hydrogels were more permeable to small 4 kDa dextran than those formed on Transwells® inserts (figure 5(d)). Moreover, among the hydrogel samples, those containing embedded fibroblasts showed less epithelial permeability than those without fibroblasts (figure 5(d)). This permeability was size-selective, as the transport of the large 70 kDa

IOP Publishing Biofabrication 12 (2020) 025008 A Vila et al

dextran was significantly hindered (figure S7). These results indicate that the presence of embedded fibroblasts in the hydrogel had a positive effect on the formation of a continuous and uniform epithelial monolayer with mature tight junctions that lead to higher TEER and lower permeability than in epithelial monolayer formed on hydrogels devoid of fibroblasts. As a biological relevant model drug, we evaluated the permeability of insulin across the fibroblast-laden GelMA-PEGDA hydrogel (figure S8). The apparent permeability coefficent (P_{app}) obtained was $6 \pm 1 \times 10^{-8}$ cm s^{-1}, an order of magnitude higher than reported values for conventional Caco-2 monolayers on Transwell membranes [49, 50]. This result was again consistent with the lower TEER values observed for the hydrogel-containing samples. Overall, these results showed that Caco-2 cells grown on fibroblast-laden GelMA-PEGDA hydrogels form a more physiological barrier, correlating better with the *in vivo* intestinal permeability and TEER values [51].

3.5. Effects of stromal components on the recovery of the barrier function of the intestinal epithelium

We used our *in vitro* model of the intestinal mucosa to mimic the loss of epithelial barrier integrity, a common occurrence under specific pathological conditions. Epithelial monolayers grown on fibroblast-laden or fibroblast-free GelMA-PEGDA hydrogels were grown for 21 d as previously described, and then treated shortly with the calcium-chelating agent EDTA to disrupt the tight junctions and increase permeability. Epithelial integrity was monitored by measuring TEER values at different time points from the moment we added the EDTA to 24 h after removing it. As expected, treatment with EDTA reduced the TEER values in both samples to basal levels (figure 5(e)). After removing EDTA, TEER values recovered due to the recovery of the tight junctions and associated barrier integrity of the epithelial monolayers. Interestingly, TEER recovered more quickly in epithelial monolayers grown on fibroblast-laden hydrogels than in those formed on fibroblast-free hydrogels (figures 5(e), (f)). These results indicate that the presence of stromal fibroblasts not only affects the Caco-2 monolayer growth rate, morphology, and permeability, but also the rate of recovery of a barrier following a temporary disruption of the tight junctions.

4. Discussion

Intestinal epithelial-stromal interactions play an important role in regulating fundamental biological processes both under physiological and pathological conditions [9, 21, 52, 53]. It is therefore crucial to engineer more physiologically relevant *in vitro* models of intestinal mucosa that represent not only the epithelial but also the cellular and matrix components of the stroma. Despite recent advances, the set-ups are often highly complex which limits their use in routine assays [15, 54]. Furthermore, most studies employed biodegradable hydrogels of only natural origins [14, 16], which greatly compromises the mechanical stability of the constructs over time and, thus, their life span.

Here we have presented a simple procedure to fabricate a co-network formed by gelatine methacrylate (GelMA), a natural-derived polymer, and poly(ethylene glycol) diacrylate (PEGDA), a synthetic polymer, to produce a mechanically stable and long-lasting 3D model of the intestinal mucosa, which posses apparent elastic modulus values similar to those found *in vivo* (≈40 kPa) [55, 56]. The covalently crosslinked GelMA-PEGDA co-networks possess adjustable swelling, mesh size, degradability, and mechanical properties, resulting in a versatile system that can emulate the physicochemical properties of tissue extracellular matrices, which combine rigid and soft networks to provide mechanical stability, cell-adhesion properties, and ECM remodeling capabilities [17, 54]. We demonstrated that GelMA-PEGDA hydrogel co-networks can sustain viable and functional embedded fibroblasts that emulate the cellular component of the stromal compartment of the intestinal mucosa. In addition, we could show that epithelial cell monolayers can be successfully grown on top of the fibroblast-laden hydrogels. After 21 d in culture, epithelial monolayers formed on GelMA-PEGDA co-networks were nicely polarized and expressed typical epithelial markers. The effective tissue barrier function of the epithelial monolayers was evaluated by TEER and permeability measurements. We found that both were closer to physiological values reported for the intestine (100–400 Ω cm^2) [57] when epithelial cells were grown on hydrogel co-networks than on standard Transwells®. Using a model of pathological intestinal barrier disruption, we showed that the presence of fibroblasts in the artificial stroma accelerated the recovery of the tight junctions and the barrier function of the damaged epithelium returning them to physiological levels. Remarkably, the effects of the NIH-3T3 fibroblasts on the Caco-2 epithelial cells were noticeable despite using fibroblasts of a murine non-intestinal origin at low densities. NIH-3T3 fibroblasts have been extensively used in co-cultures with murine but also with human cells as feeder layers [58]. While it is well known that NIH-3T3 favors cell growth through paracrine signaling, the underlying mechanisms are still not fully understood. Co-cultures of fibroblasts and Caco-2 epithelial cells in conventional Transwell® inserts have been reported to enhance epithelial proliferation and differentiation via paracrine effects of the fibroblasts such as hepatocyte growth factor [52] or keratinocyte growth factor [59]. No tissue specificity for the fibroblast action was detected in these studies. In addition, mesenchymal-stromal cells have also been reported to accelerate tight junction assembly in

epithelial monolayers [46]. Paracrine signaling also seems to be the main signaling source of NIH-3T3 fibroblasts in our mucosa model, as their growth appeared inhibited and we did not see any physical interaction between them and the epithelial cells.

Overall, our results demonstrate that GelMA-PEGDA hydrogel co-networks might be good candidates to produce long-lasting *in vitro* models of the intestinal mucosa with the epithelial and mesenchymal compartment being represented in a cell-spatial configuration recapitulating the one found *in vivo*. Combining natural and synthetic polymers to generate the scaffold we could ensure both the integrity of the construct for long periods of time (at least 21 d of culture) and the compatibility with cell growth and functionality of the embedded cells. Furthermore, we showed that embedded fibroblasts do express collagen IV, which indicates their capacity to remodel the surrounding matrix by creating new matrix or by degrading the existing one [16]. Thus, our PEGDA-GelMA hydrogel co-networks would allow to mimic *in vivo* interactions between mesenchymal and epithelial cells that would help us understanding better biological processes that depend on cell migration, cell–cell interactions and cell-matrix interactions, both under physiological and pathological conditions.

5. Conclusion

Our intestinal mucosa model based on GelMA-PEGDA hydrogel co-networks was able to mimic some of the features attributed to mesenchymal-epithelial interactions such as enhanced epithelial cell proliferation and barrier permeability, diffusivity properties that allow paracrine effects and accelerated tight junction recovery. As added benefits, our 3D model possesses a tissue-like architecture that includes both stromal and epithelial compartments arranged in a spatially relevant manner as well as *in vivo*-like mechanical properties of the substrate. This enables to model cell-to-cell and cell-to-matrix interactions with *in vivo*-like accuracy, which translates into more physiological values of intestinal permeability hallmarks (TEER and permeability). Our model provides a simplistic but still meaningful approach to obtain more physiologically relevant *in vitro* epithelial models at the cellular and functional levels. It can therefore be used to improve predictions of intestinal permeability in drug studies or to implement better epithelial disease models where an accurate reproduction of the interaction between different cell compartments is of crucial importance. These GelMA-PEGDA co-networks should be able to accommodate additional relevant stromal cellular components such as the immune system (pivotal for regulating inflammatory responses, metabolic and cancerogenic processes) while being sufficiently versatile to mimic other simple or stratified epithelial tissues such as oesophagus, stomach, or skin.

Acknowledgments

Funding for this project was provided by a European Union Horizon 2020 ERC grant (agreement no. 647863—COMIET), the CERCA Programme/Generalitat de Catalunya (2017-SGR-1079), and the Spanish Ministry of Economy and Competitiveness (TEC2014-51940-C2-2-R, TEC2017-83716-C2-1-R, and the Severo Ochoa Programme for Centres of Excellence in R&D 2016–2019). MG-D would like to acknowledge financial support through the BEST Postdoctoral Programme, funded by the European Commission under the Horizon 2020 Marie Skłodowska-Curie Actions COFUND scheme (grant agreement no. 712754) and by the Severo Ochoa programme of the Spanish Ministry of Science and Competitiveness (Grant SEV-2014-0425, 2015–2019). The collaboration of the MicroFabSpace from IBEC is gratefully acknowledged. The results presented here only reflect the views of the authors; the European Commission is not responsible for any use that may be made of the information it contains.

ORCID iDs

Núria Torras https://orcid.org/0000-0001-5027-7428
María García-Díaz https://orcid.org/0000-0002-4794-5437
Óscar Castaño https://orcid.org/0000-0001-9212-784X
Elisabeth Engel https://orcid.org/0000-0003-4855-8874
Vanesa Fernández-Majada https://orcid.org/0000-0003-4287-5086
Elena Martínez https://orcid.org/0000-0002-6585-4213

References

[1] Hunyady B, Mezey E and Palkovits M 2000 *Acta Physiol. Hung.* **87** 305–28
[2] Turner J R 2009 *Nat. Rev. Immunol.* **9** 799–809
[3] Vancamelbeke M and Vermeire S 2017 *Expert Rev. Gastroenterol. Hepatol.* **11** 821–34
[4] Artursson P and Karlsson J 1991 *Biochem. Biophys. Res. Commun.* **175** 880–5
[5] Yanagawa F, Kaji H, Jang Y-H, Bae H, Yanan D, Fukuda J, Qi H and Khademhosseini A 2011 *J. Biomed. Mater. Res.* A **97** 93–102
[6] Bischoff S C, Barbara G, Buurman W, Ockhuizen T, Schulzke J-D, Serino M, Tilg H, Watson A and Wells J M 2014 *BMC Gastroenterol.* **14** 1–25
[7] Wang K, Wu L-Y, Dou C-Z, Guan X, Wu H-G and Liu H-R 2016 *Gastroenterol. Res. Pract.* **2016** 9686238
[8] Maresca M, Pinton P, Ajandouz E H, Menard S, Ferrier L and Oswald I P 2018 Overview and comparison of intestinal organotypic models, intestinal cells, and intestinal explants used for toxicity studies *Current Topics in Microbiology and Immunology* (Berlin: Springer) pp 1–18

[9] Bosman F T, de Bruïne A, Flohil C, van der Wurff A, ten Kate J and Dinjens W W 1993 *Int. J. Dev. Biol.* **37** 203–11
[10] Martínez E, St-Pierre J P and Variola F 2019 *Adv. Phys.* X **4** 1–28
[11] Torras N, García-Díaz M, Fernández-Majada V and Martínez E 2018 *Frontiers Bioeng. Biotechnol.* **6** 1–7
[12] Duval K, Grover H, Han L-H, Mou Y, Pegoraro A F, Fredberg J and Chen Z 2017 *Physiology* **32** 266–77
[13] Turnbull I C *et al* 2014 *FASEB J.* **28** 644–54
[14] Li N, Wang D, Sui Z, Qi X, Ji L, Wang X and Yang L 2013 *Tissue Eng.* C **19** 708–19
[15] Matsusaki M, Hikimoto D, Nishiguchi A, Kadowaki K, Ohura K, Imai T and Akashi M 2015 *Biochem. Biophys. Res. Commun.* **457** 363–9
[16] Pereira C, Araújo F, Barrias C C, Granja P L and Sarmento B 2015 *Biomaterials* **56** 36–45
[17] Daniele M A, Adams A A, Naciri J, North S H and Ligler F S 2014 *Biomaterials* **35** 1845–56
[18] Fu Y, Xu K, Zheng X, Giacomin A J, Mix A W and Kao W J 2012 *Biomaterials* **33** 48–58
[19] Aubin H, Nichol J W, Hutson C B, Bae H, Sieminski A L, Cropek D M, Akhyari P and Khademhosseini A 2010 *Biomaterials* **31** 6941–51
[20] Nichol J W, Koshy S T, Bae H, Hwang C M, Yamanlar S and Khademhosseini A 2010 *Biomaterials* **31** 5536–44
[21] Powell D W, Pinchuk I V, Saada J I, Chen X and Mifflin R C 2011 *Annu. Rev. Physiol.* **73** 213–37
[22] Van Den Bulcke A I, Bogdanov B, De Rooze N, Schacht E H, Cornelissen M and Berghmans H 2000 *Biomacromolecules* **1** 31–8
[23] Loessner D, Meinert C, Kaemmerer E, Martine L C, Yue K, Levett P A, Klein T J, Melchels F P W, Khademhosseini A and Hutmacher D W 2016 *Nat. Protocols* **11** 727–46
[24] Li X, Chen S, Li J, Wang X, Zhang J, Kawazoe N and Chen G 2016 *Polymers* **8** 1–15
[25] Habeeb A F S A 1966 *Anal. Biochem.* **14** 328–36
[26] Castaño A G, García-Díaz M, Torras N, Altay G, Comelles J and Martínez E 2019 *Biofabrication* **11** 025007
[27] Flory P J and Rehner J 1943 *J. Chem. Phys.* **11** 512–20
[28] Peppas N A and Merrill E W 1977 *J. Appl. Polym. Sci.* **21** 1763–70
[29] Okeowo O and Dorgan J R 2006 *Macromolecules* **39** 8193–202
[30] Kontturi L-S, Collin E C, Murtomäki L, Pandit A S, Yliperttula M and Urtti A 2015 *Eur. J. Pharm. Biopharm.* **95** 387–97
[31] Caballero D and Samitier J 2017 *ACS Appl. Mater. Interfaces* **9** 4159–70
[32] Benton J A, DeForest C A, Vivekanandan V and Anseth K S 2009 *Tissue Eng.* A **15** 3221–30
[33] Engler A J, Sen S, Sweeney H L and Discher D E 2006 *Cell* **126** 677–89
[34] Hönig W and Kula M R 1976 *Anal. Biochem.* **72** 502–12
[35] Peppas N A, Hilt J Z, Khademhosseini A and Langer R 2006 *Adv. Mater.* **18** 1345–60
[36] SIGMA 2010 Fluorescein Isothiocyanate-Dextran 1–5 https://sigmaaldrich.com/content/dam/sigma-aldrich/docs/Sigma/Product_Information_Sheet/1/fd4pis.pdf
[37] TdB Labs. 1997 FITC—dextran1–3 https://tdblabs.se/products/fluorescent-derivatives/fitc-derivatives/fitc-dextran/
[38] Kaemmerer E, Melchels F P, Holzapfel B M, Meckel T, Hutmacher D W and Loessner D 2014 *Acta Biomater.* **10** 2551–62
[39] Swift J *et al* 2013 *Science* **341** 1240104
[40] Cai Y, Xu C, Chen P, Hu J, Hu R, Huang M and Bi H 2014 *J. Pharmacol. Toxicol. Methods* **70** 175–81
[41] Wells R G 2008 *Hepatology* **47** 1394–400
[42] Valls-Margarit *et al* 2019 *Stem Cell Rep.* **13** 1–14
[43] Rodriguez-Boulan E, Kreitzer G and Müsch A 2005 *Nat. Rev. Mol. Cell Biol.* **6** 233–47
[44] Uroz M, Wistorf S, Serra-Picamal X, Conte V, Sales-Pardo M, Roca-Cusachs P, Guimerà R and Trepat X 2018 *Nat. Cell Biol.* **20** 646–54
[45] Sunyer R *et al* 2016 *Science* **353** 1157–61
[46] Rowart P, Erpicum P, Krzesinski J-M, Sebbagh M and Jouret F 2017 *Stem Cells Int.* **2017** 9717353
[47] Sung J H, Yu J, Luo D, Shuler M L and March J C 2011 *Lab Chip* **11** 389–92
[48] Le Ferrec E, Chesne C, Artusson P, Brayden D, Fabre G, Gires P, Guillou F, Rousset M, Rubas W and Scarino M L 2001 *Altern. Lab. Anim.* **29** 649–68
[49] Wood K M, Stone G M and Peppas N A 2010 *Acta Biomater.* **6** 48–56
[50] Liu J, Werner U, Funke M, Besenius M, Saaby L, Fanø M, Mu H and Müllertz A 2019 *Int. J. Pharm.* **560** 377–84
[51] Gupta V, Doshi N and Mitragotri S 2013 *PLoS One* **8** e57136–57136
[52] Göke M, Kanai M and Podolsky D K 1998 *Am. J. Physiol.* **274** G809–18
[53] Haffen K, Simon-Assmann P, Kedinger M, Grenier J F and Zweibaum Z 1981 *C. R. Seances Acad. Sci.* III **293** 807–12
[54] Wang H and Heilshorn S C 2015 *Adv. Mater.* **27** 3717–36
[55] Dou Y, Gregersen S, Zhao J, Zhuang F and Gregersen H 2001 *Med. Eng. Phys.* **23** 557–66
[56] Liao D, Yang J, Zhao J, Zeng Y, Vinter-Jensen L and Gregersen H 2003 *Med Eng Phys* **25** 413–8
[57] Srinivasan B, Kolli A R, Esch M B, Abaci H E, Shuler M L and Hickman J J 2015 *J. Lab. Autom.* **20** 107–26
[58] Hynds R E, Bonfanti P and Janes S M 2018 *EMBO Mol. Med.* **10** 139–50
[59] Visco V, Bava F A, D'Alessandro F, Cavallini M, Ziparo V and Torrisi M R 2009 *J. Cell. Physiol.* **220** 204–13